



**Ekaterina
Tsipis**

**Condutores mistos contendo níquel e cobalto
para aplicações como eléctrodos de PCES:
Relações entre propriedades de transporte,
físico-químicas e electroquímicas**

**Nickel- and cobalt-containing mixed conductors
for SOFC electrode applications:
Relationships between transport, physicochemical
and electrochemical properties**

UA-SD



255612



**Ekaterina
Tsipis**

**Condutores mistos contendo níquel e cobalto para
aplicações como eléctrodos de PCES:
Relações entre propriedades de transporte, físico-químicas e
electroquímicas**

dissertação apresentada à Universidade de Aveiro para cumprimento dos requisitos necessários à obtenção do grau de Doutor em Ciência e Engenharia de Materiais, realizada sob a orientação científica do Doutor Jorge Frade, Professor Catedrático do Departamento de Engenharia Cerâmica e do Vidro, e do Doutor Vladislav Kharton, Investigador Principal do Departamento de Engenharia Cerâmica e do Vidro

Apoio financeiro da FCT e do FSE no âmbito do III Quadro Comunitário de Apoio.

o júri

presidente

Prof. Dr. Armando da Costa Duarte
professor catedrática da Universidade de Aveiro

Prof. Dr. Jorge Ribeiro Frade
professor catedrático da Universidade de Aveiro

Prof. Dr. Adélio Miguel Magalhães Mendes
professor associado da Faculdade de Engenharia da Universidade do Porto

Dr. Vladislav Vadimovich Kharton
investigador principal convidado da Universidade de Aveiro

Dr. João Carlos Bentes Waerenborgh
investigador auxiliar do Instituto Tecnológico Nuclear, Sacavém

Dra. Elisabeth Djurado
senior researcher, Laboratory d'Electrochimie et de Physico-Chimie des Matériaux et des Interfaces (LEPMI), Institut National Polytechnique de Grenoble, France

acknowledgements

I am sincerely grateful to all people and organizations without whose help this work would be unrealizable:

- my supervisors, Prof. Jorge Frade and Dr. Vladislav Kharton, for encouraging and advising me;
- Prof. Fernando Marques, for helpful discussions and interest in this work;
- Fundação para a Ciência e Tecnologia, for funding this work under the grant BD/6827/2001;
- Drs. Eugene Naumovich, Aleksey Yaremchenko, Andrei Kovalevsky, Nikolai Vyshatko, Filipe Figueiredo, Duncan Fagg, and Aliaksandr Shaula, for the experimental assistance and helpful discussions;
- Dr. Mikhail Patrakeev, Prof. Pedro Núñez and Dr. João Waerenborgh, for their valuable collaboration;
- functionaries and technicians of the Department of Ceramics and Glass Engineering and Central Laboratory (University of Aveiro), for the everyday help;
- my parents, for their confidence, patience and support.

palavras-chave

Pilhas de Combustível de Electrólito Sólido, Eléctrodo, Condutividade Iónica, Condutividade Electrónica, Expansão Térmica, Permeabilidade ao Oxigénio, Estabilidade de Fase, Condutor Misto, Cátodos, Ânodos, Sobretenção

resumo

Este trabalho é dedicado ao desenvolvimento de novos materiais de eléctrodo para pilhas de combustível de electrólito sólido, operando a temperaturas intermédias. São analisados os efeitos das propriedades de transporte iónico e electrónico e o papel da permuta superficial no desempenho electroquímico de materiais de cátodo ou ânodo com estruturas dos tipos zircão, $(\text{Ce},\text{M})\text{O}_{4+\delta}$ com $\text{M}=\text{Ca}$ ou Sr , lamelar $\text{La}_2(\text{Ni},\text{M})\text{O}_{4+\delta}$ com $\text{M}=\text{Co}$ ou Cu ou $\text{YBa}(\text{Co},\text{Fe})_4\text{O}_{7+\delta}$, perovskite $\text{La}_{0.9}\text{Sr}_{0.1}(\text{Al},\text{Fe})_{0.85}\text{Mg}_{0.15}\text{O}_{3-\delta}$ e $(\text{La}_{0.3}\text{Sr}_{0.7})_{1-x}(\text{Co},\text{M})\text{O}_{3-\delta}$ com $\text{M}=\text{Al},\text{Ga}$, fluorite $\text{TbMO}_{4-\delta}$ com $\text{M}=\text{Zr},\text{Hf}$ e pirocloro $(\text{Gd},\text{Ca})_2\text{Ti}_2\text{O}_{7-\delta}$. É dada ênfase a propriedades influentes no desempenho dos eléctrodos, designadamente as componentes de condutividade iónica e electrónica, a permeabilidade ao oxigénio, variações estequiométricas, expansão térmica e estabilidade de fases. Entre os materiais de cátodo merecem destaque $\text{La}_2\text{Ni}_{0.8}\text{Cu}_{0.2}\text{O}_{4+\delta}$ e $\text{YBa}(\text{Co},\text{Fe})_4\text{O}_{7+\delta}$ que exibem expansão térmica relativamente baixa, apreciável condução mista e adequada actividade electroquímica quando usados com electrólitos sólidos à base de galato de lantânio $\text{La}_{1-x}\text{Sr}_x\text{Ga}_{1-y}\text{Mg}_y\text{O}_{3-\delta}$. Pelo contrário, as perovskites à base de LaCoO_3 possuem elevada condutividade iónica e electrónica mas a sua expansão térmica é excessiva, tornando-os incompatíveis com os electrólitos sólidos usuais. No caso dos ânodos, o melhor desempenho foi observado para materiais com uma fase condutora iónica estável em condições redutoras, (p.e. zircónia estabilizada ou $\text{Gd}_{1.86}\text{Ca}_{0.14}\text{Ti}_2\text{O}_{7-\delta}$), e uma fase contendo Ce, (p.e. $\text{Ce}_{0.8}\text{Gd}_{0.2}\text{O}_{2-\delta}$ ou $\text{Ce}_{0.8}\text{Ca}_{0.2}\text{VO}_{4+\delta}$). Algumas modificações da camada superficial originam redução significativa das perdas por polarização.

keywords

Solid Oxide Fuel Cell, Electrode, Ionic Conductivity, Electronic Transport, Thermal Expansion, Oxygen Permeation, Phase Stability, Mixed Conductor, IT SOFC cathode, Anode, Overpotential.

abstract

This work was dedicated to the development of novel electrode materials for intermediate temperature solid oxide fuel cells. One studied the effects of ionic and electronic transport properties and the role exerted by surface exchange on the electrochemical performance of cathode or anode materials with different structure types, namely zircon type $(\text{Ce},\text{M})\text{O}_{4+\delta}$ with $\text{M}=\text{Ca}$ or Sr , layered $\text{La}_2(\text{Ni},\text{M})\text{O}_{4+\delta}$ with $\text{M}=\text{Co}$ or Cu and $\text{YBa}(\text{Co},\text{Fe})_4\text{O}_{7+\delta}$, perovskite $\text{La}_{0.9}\text{Sr}_{0.1}(\text{Al},\text{Fe})_{0.85}\text{Mg}_{0.15}\text{O}_{3-\delta}$ and $(\text{La}_{0.3}\text{Sr}_{0.7})_{1-x}(\text{Co},\text{M})\text{O}_{3-\delta}$ with $\text{M}=\text{Al},\text{Ga}$, fluorite $\text{TbMO}_{4-\delta}$ with $\text{M}=\text{Zr},\text{Hf}$ and pyrochlore $(\text{Gd},\text{Ca})_2\text{Ti}_2\text{O}_{7-\delta}$. Special emphasis is given to properties playing major effects on the electrode performance such as the ionic and electronic conductivity contributions, oxygen permeability, oxygen stoichiometric changes, thermal expansion and phase stability. Promising cathode materials $\text{La}_2\text{Ni}_{0.8}\text{Cu}_{0.2}\text{O}_{4+\delta}$ and $\text{YBa}(\text{Co},\text{Fe})_4\text{O}_{7+\delta}$, possessing relatively low thermal expansion, significant mixed conductivity and suitable electrocatalytic activity in contact with solid electrolytes based on lanthanum gallate $\text{La}_{1-x}\text{Sr}_x\text{Ga}_{1-y}\text{Mg}_y\text{O}_{3-\delta}$. Though LaCoO_3 -based perovskites possess high ionic and electronic conductivities, their thermal expansion is excessive, and prevents their applicability with usual solid electrolytes. The best anodic performance was observed for composite anodes containing a stable mixed conductor under reducing conditions (e.g. stabilized zirconia or $\text{Gd}_{1.86}\text{Ca}_{0.14}\text{Ti}_2\text{O}_{7-\delta}$), and another phase containing Ce (e.g. $\text{Ce}_{0.8}\text{Gd}_{0.2}\text{O}_{2-\delta}$ or $\text{Ce}_{0.8}\text{Ca}_{0.2}\text{VO}_{4+\delta}$). Suitable surface modifications yield significant decrease in polarisation losses.

Table of Contents

Introduction	1
Part 1: Literature review: electrode materials for intermediate-temperature SOFCs	2
1.1. Operation principles of solid oxide fuel cells	2
1.2. Intermediate-temperature SOFCs: basic approaches and technologies	4
1.3. Solid electrolyte materials	6
1.3.1. Ionic conductivity	7
1.3.2. Stability and electronic conductivity	10
1.3.3. Thermal expansion	12
1.4. Electrode reaction mechanisms	13
1.4.1. Cathode processes	14
1.4.2. Anode reactions	25
1.4.3. Role of ionic transport in electrode materials	32
1.4.4. Effects of solid electrolyte surface	37
1.4.5. Effects of current collection	39
1.5. Electrode materials for IT SOFCs	41
1.5.1. Cathodes	41
1.5.1.1. Manganites	41
1.5.1.2. Ferrites	48
1.5.1.3. Cobaltites	52
1.5.1.4. Nickelates	56
1.5.1.5. Cuprates	59
1.5.1.6. Composite materials	60
1.5.2. Anodes	64
1.5.2.1. Me-YSZ cermets	64
1.5.2.2. CeO ₂ -based materials	68
1.5.2.3. Alternative anode compositions	69
1.5.3. Surface modification of solid electrolyte	72
1.5.4. Modification of electrode layers	74
1.6. Concluding remarks: promising directions in the developments of novel electrode materials	76
Part 2: Experimental	77
2.1. Synthesis and ceramic processing	77
2.2. X-ray diffraction, chemical analysis, IR absorption spectroscopy and Mössbauer spectroscopy	80
2.3. Microstructural studies	81
2.4. Dilatometry and thermal analysis	81
2.5. Measurements of the total electrical conductivity and Seebeck coefficient	82
2.6. Oxygen transport properties	83
2.6.1. Faradaic efficiency studies	84
2.6.2. Determination of oxygen permeation fluxes	86

2.6.3. E.m.f. measurements	87
2.7. Fabrication and electrochemical studies of electrode layers	88
2.7.1. Electrode fabrication	88
2.7.2. Cell configuration and measuring set-ups	89
2.7.3. Selection of glass-ceramic sealants	89
2.7.4. Electrochemical measurements	91
2.7.5. Reproducibility tests and assessment of materials interaction	92
Part 3: Cobalt- and nickel-containing phases promising for cathode applications	93
3.1. General characterization	93
3.1.1. $\text{La}_{0.3}\text{Sr}_{0.7}\text{CoO}_3$ -based perovskites	93
3.1.2. $\text{YBaCo}_4\text{O}_{7+\delta}$ and its derivatives	97
3.1.3. La_2NiO_4 -based nickelates	102
3.2. Oxygen ionic transport	106
3.2.1. Surface-limited oxygen transport in $\text{La}_{0.3}\text{Sr}_{0.7}\text{CoO}_3$ -based solid solutions	106
3.2.2. Oxygen ionic conductivity of $\text{YBaCo}_4\text{O}_{7+\delta}$	109
3.2.3. Oxygen permeability of $\text{La}_2\text{Ni}(\text{M})\text{O}_{4+\delta}$ (M = Co, Cu) ceramics	112
3.3. Role of synthesis method: case studies	116
3.4. Electrical properties vs. temperature and oxygen partial pressure	118
3.4.1. Cobalt-containing perovskites	118
3.4.2. Yttrium-barium cobaltite	126
3.4.3. K_2NiF_4 -type $\text{La}_2\text{Ni}(\text{M})\text{O}_{4+\delta}$ (M = Co, Cu)	128
3.5. Thermal expansion	133
3.6. Selection of cathode compositions	135
Part 4: Ion-conducting oxide materials as components of cermet anodes	136
4.1. Zircon-type $\text{Ce}_{1-x}\text{A}_x\text{VO}_{4+\delta}$ (A = Ca, Sr)	136
4.1.1. Structure, ceramic microstructure and thermal expansion	136
4.1.2. Oxygen ionic and p-type electronic conduction	142
4.1.3. Electrical conductivity and Seebeck coefficient vs. $p(\text{O}_2)$	148
4.1.4. Stability in reducing atmospheres	149
4.2. Perovskite-type $\text{La}_{0.9}\text{Sr}_{0.1}\text{Al}_{0.85-x}\text{Mg}_{0.15}\text{Fe}_x\text{O}_{3-\delta}$	153
4.2.1. General characterization	154
4.2.2. Transport properties at atmospheric oxygen pressure	156
4.2.3. Total conductivity vs. oxygen partial pressure	159
4.2.4. Partial ionic and electronic conductivities	163
4.2.5. Thermopower behavior and comments on the hole transport mechanism	166
4.3. Fluorite-related $\text{TbMO}_{4-\delta}$ (M = Zr, Hf)	168
4.3.1. Structure and microstructure	168
4.3.2. Thermal expansion	171
4.3.3. Ionic and electron-hole conductivities under oxidizing conditions	172
4.3.4. Transport properties in reducing atmospheres	175

4.4. Gd _{2-x} Ca _x Ti ₂ O _{7-δ} pyrochlores	178
4.4.1. Characterization of ceramic materials	178
4.4.2. Partial ionic and p-type electronic conductivities	183
4.4.3. Transport properties under high p(O ₂) gradients	188
4.4.4. Grain-boundary effects: a case study and selected conclusions	189
4.5. Partial ionic and electronic conductivities of anode components	193
Part 5: Processing and electrochemical activity of mixed-conducting electrodes	196
5.1. SOFC cathode layers in contact with LSGM electrolyte	196
5.1.1. Fabrication of porous cathode layers	196
5.1.2. Electrochemical behavior of La ₂ Ni _{0.8} Cu _{0.2} O _{4+δ} cathodes	198
5.1.3. YBaCo ₄ O ₇ -based electrodes	202
5.1.4. Critical role of ceramic microstructure and effects of surface modification	205
5.1.5. Concluding remarks: factors determining electrochemical activity	207
5.2. Cellulose-precursor synthesis of SOFC anode components	208
5.3. Electrochemical performance of cermet anodes	213
5.3.1. Fabrication and characterization of porous anode layers	213
5.3.2. Effects of metal/oxide ratio and phase components	214
5.3.3. Other factors influencing anode performance	218
5.3.4. Surface modification of cermet layers	222
5.3.5. Final remarks	224
Conclusions	225
Future research: selected aspects	230
References	232
Appendixes	257
Appendix 1: Properties of selected glass-ceramics	257
Appendix 2: Mössbauer spectroscopy results	260
Appendix 3: List of publications containing major results of the thesis	263
List of symbols	265
List of abbreviations	269
Index of Materials	271

Introduction

The development of alternative power sources providing high efficiency and minimum environmental pollutions presents a serious problem. One family of such devices is the solid oxide fuel cells (SOFCs). Their use is, however, still limited due to economic reasons. Commercialization of the SOFC-based generators requires a considerable decrease in the power-specific production costs, which can be achieved by (i) increasing the cell performance, (ii) further developments of the SOFC production technologies, and (iii) decreasing cost of the construction materials by reducing the operation temperature. These problems can be partly solved by decreasing the cell operation temperature. In the intermediate-temperature (IT) range, the performance of conventional electrode materials is insufficient and the anode and cathode polarization losses become critical, making it necessary to search for the new materials.

The major goal of this work is to elaborate novel electrode materials for the IT SOFC applications, with a special emphasis on the properties important for practical use, including partial electronic and ionic conductivities, oxygen permeability, nonstoichiometry variations, thermal expansion, phase stability and electrode performance. Particular objectives are:

- to prepare a series of layered oxide cobaltite and nickelate materials with perovskite-related or nonperovskite structure, perform their detailed characterization in a wide range of temperatures and oxygen partial pressures and investigate basic trends in the electrochemical behavior of materials most promising for IT SOFC cathode applications;
- to synthesize a series of mixed ionic-electronic conducting oxide phases with fluorite-, pyrochlore-, zircon- and perovskite-related structures, investigate their stability and transport properties under the SOFC operation conditions and test their performance as the anode components;
- to study the influence of synthesis route, microstructure and grain boundary effects on the ionic and electronic transport and electrode properties;
- to elaborate techniques for preparation of submicron oxide powders in order to fabricate porous oxide and cermet electrode layers with homogeneous well-developed microstructure and high electrochemical activity;
- to evaluate the functional roles of oxide and metal components in the IT SOFC anode behavior in order to develop physico- and electrochemical background for cermet optimization;
- to assess major factors determining the IT SOFC cathodes performance and to select the possible strategies for their further improvements.

Part 1: Literature review: electrode materials for intermediate-temperature SOFCs

1.1. Operation principles of solid oxide fuel cells

Solid oxide fuel cells (SOFCs) are electrochemical devices directly converting a chemical energy of fuel oxidation into the electrical energy and heat, using solid oxide as an electrolyte (oxygen anion conductor). The latter serves also as a barrier that prevents mixing of the fuel and oxidant steams. SOFCs operate at elevated temperatures (873 - 1273 K) where significant ionic conduction appears. With respect to the other types of fuel cells, such as alkaline fuel cell (AFC), polymer electrolyte membrane fuel cell (PEMFC), phosphoric acid fuel cell (PAFC) and molten carbonate fuel cell (MCFC), SOFCs attract a great interest due to their high energy-conversion efficiency, fuel flexibility including the prospects to directly operate on natural gas, environmental safety and a possibility to recover exhaust heat [1-9]. A single cell comprises a dense solid electrolyte in contact with porous anode and cathode, onto which a fuel and an oxidant, respectively, are continuously supplied (Fig.1.1).

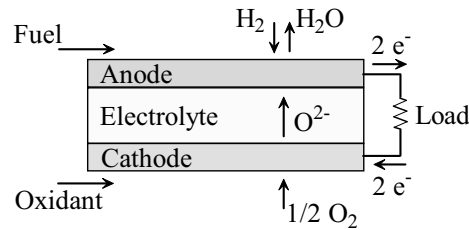


Fig.1.1. Schematic representation of H₂-fueled SOFC.

Except for hydrogen, a variety of other fuels, including hydrocarbons (e.g. methane) and carbon monoxide can also be used in SOFCs [1-9]. Electrical current is generated due to the electrochemical reactions at the electrodes, namely, reduction of the oxidant (oxygen from air) at the cathode:



and oxidation of fuel by the oxygen ions diffused through the electrolyte, at the anode:



Due to high operating temperatures, the steam reforming and water gas shift reaction may also occur:



producing hydrogen that is easier oxidized at the anode [1,2,5-7,9].

The electrons evolved from the anode are supplied through the external load to the cathode. The open-circuit cell voltage E^0 is determined by the Nernst equation:

$$E^0 = \frac{RT}{4F} \ln \left[\frac{p(\text{O}_2)^{\text{cathode}}}{p(\text{O}_2)^{\text{anode}}} \right] \quad (1.7)$$

where $p(\text{O}_2)$ is the oxygen partial pressure at the electrode; R , F , and T are the universal gas constant, the Faraday constant and the absolute temperature, respectively. The voltage losses in SOFCs are determined by ohmic losses in the cell components and their interfaces, and by the polarization of the electrodes (η):

$$E = E^0 - IR_{\text{total}} - \eta_{\text{anode}} - \eta_{\text{cathode}} \quad (1.8)$$

where E is the cell voltage, I is the current through the cell, and R_{total} is the total ohmic resistance.

Solid electrolytes should possess maximum ionic conductivity to reduce the ohmic losses and minimum electronic conductivity to reduce the leakage current, over a wide range of the oxygen partial pressures. The anode and the cathode should provide a fast electronic conduction, and also high catalytic activity to fuel oxidation and reduction of molecular O_2 , respectively. In addition, the materials choice for SOFC technologies is limited for a number of general requirements. All the SOFC components must be compatible in terms of thermal expansion and be thermodynamically stable under cell operation and fabrication conditions. Also, the chemical expansion of the component materials, as well as cation interdiffusion and chemical interactions between them should be minimized or, preferably, absent.

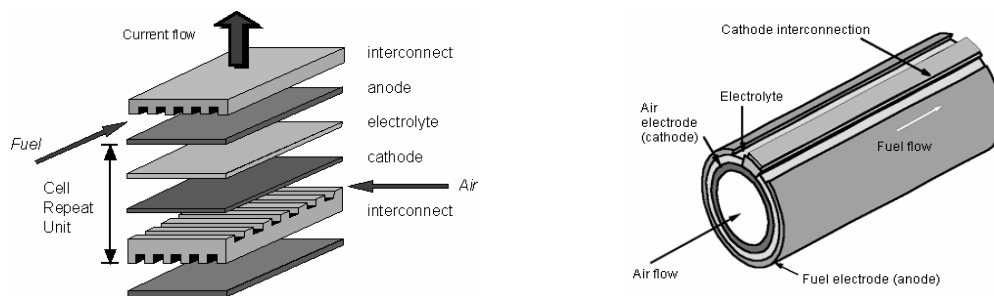


Fig.1.2. Schematic of planar (left) and tubular (right [13]) SOFC designs.

The SOFC operating at 1273 K on the MgO-ZrO_2 or $\text{Y}_2\text{O}_3\text{-ZrO}_2$ electrolyte with Fe_3O_4 cathode and iron or carbon anode was first proposed by Baur and Preis [2,3,10] in 1937. In 1962 Weissbart and Ruka [2,3,11], at Westinghouse Electric, used Pt-electrodes because of their high conductivity and catalytic activity. Due to a lower cost, later the Ni-based anodes became widely used. Tedmon et al. [2,3,12], at General Electric, applied in 1969 the $\text{PrCoO}_{3-\delta}$ perovskite cathode

showing the high performance but excessively large thermal expansion. A number of other ceramic materials, mostly perovskite-type, were then tested as the cathodes. The common materials used in SOFCs up to now are: yttria-stabilized zirconia as the electrolyte, Sr-doped $\text{LaMnO}_{3-\delta}$ as the cathode and Ni-zirconia cermets as the anode [1-9,13,14].

Two principal cell designs of SOFCs are being developed: planar and tubular, illustrated in Fig.1.2. By the geometrical arrangement, these can be electrolyte-, anode- or cathode- supported, depending on the thickness of the components. In order to achieve commercially feasible productivity, the individual cells are combined into stacks by the electrically-conductive gas-tight interconnectors joining the elements in series or in parallel. Fig.1.3 shows the examples of stack arrangement on the basis of planar and tubular SOFC concepts.



Fig.1.3. The 1.7kW SOFC module (48-cell stack) operating on methane at 1273 K, elaborated by Tokyo Gas [14] (left), and a stack connected by a nickel felt, elaborated by Siemens Westinghouse [13] (right).

In spite of the advantages with respect to the commercial electric power generation engines, practical application of SOFCs is still limited for the economical reasons, particularly as a result of the high costs of component materials and fabrication methods [1-7].

1.2. Intermediate-temperature SOFCs: basic approaches and technologies

Decreasing operation temperature of SOFCs down to 773 - 973 K, preserving the high performance, is desirable due to important economical and technological advantages. The SOFC-based power plants are commercially viable provided their production costs count less than approximately 0.6-0.8 Euro/W [3-5], while at present this sum is several times higher. Developments of intermediate temperature solid oxide fuel cells (IT SOFCs) are expected to reduce manufacturing costs, in particular by using the low-cost construction materials, such as stainless steels as the interconnects. Another advantage of IT SOFCs is the increase in the mechanical

durability of the stack due to reduced degradation of the cell materials, which may be caused by high operation temperatures and by the thermal cycling, and due to the possibility of using the alternative materials instead of fragile glass-ceramic sealants for the cell hermetic encapsulation. Furthermore, the low operation temperature is favorable for the small, kW-scale SOFC stacks not supposed to be integrated with gas turbines [3,5,15] because this enables to decrease heat losses.

Table 1.1

Comparison of the maximum power densities obtained for planar single cells operating on H₂-H₂O fuel

Cell type	Electrolyte	Cathode	Anode	T, K	Power density, W/cm ²	Ref.
Anode-supported	YSZ	YSZ-La _{0.85} Sr _{0.15} MnO ₃	Ni-YSZ	1073	0.7	[24]
Anode-supported	YSZ	YSZ-La _{0.8} Sr _{0.2} MnO ₃	Ni-YSZ	923-1073	0.8-1.8	[25]
Anode-supported	YSZ	YSZ-La _{0.8} Sr _{0.2} MnO ₃	Cu-CeO ₂	1073	0.31	[8]
Anode-supported	Ce _{0.8} Gd _{0.2} O ₂ (CGO)	La _{0.8} Sr _{0.2} Fe _{0.8} Co _{0.2} O ₃	Ni-CGO	773	0.14	[26]
Anode-supported	Double-layer yttria-doped ceria and zirconia (CYO-YSZ)	La _{0.8} Sr _{0.2} Co _{0.2} Fe _{0.8} O ₃ -CYO composite	Ni-YSZ	973-1073	0.47-0.89	[27]
Cathode-supported	YSZ with cathode and anode CYO interlayers	La _{0.85} Sr _{0.15} MnO ₃	Ni-YSZ	973-1073	0.30-0.87	[28]
Electrolyte-supported	La _{0.9} Sr _{0.1} Ga _{0.8} Mg _{0.2} O ₃	Sm _{0.6} Sr _{0.4} CoO ₃	Ni	1073	0.44	[29]
Electrolyte-supported	La _{0.9} Sr _{0.1} Ga _{0.8} Mg _{0.2} O ₃ +2 wt % Al ₂ O ₃ with cathode and anode Ce _{0.8} Sm _{0.2} O _{1.9} (CSO) interlayers	Pr _{0.6} Sr _{0.4} MnO ₃ -CSO composite	Ni-YSZ	1073	0.245	[30]

Reducing of SOFC operating temperature is associated, however, with increasing role of electrode polarization as a performance-limiting factor, since an apparent activation energy for the polarization resistance is typically higher than that for ionic transport in solid electrolytes [16,17]. Optimization of the cathode and anode compositions and microstructures are, therefore, necessary to achieve sufficiently low overpotentials in the intermediate-temperature range [1,3,16-20]. The ohmic resistance of the electrolytes is also exponentially increasing on cooling (Fig.1.4). In order to keep a sufficiently high level of oxygen ionic transport at reduced temperatures, two approaches can be used: the application of thinner layers of conventional electrolytes, e.g. yttria-stabilized zirconia (YSZ), or the elaboration of alternative electrolyte materials with a higher ionic conduction. The former concept gave rise to the developments of electrode-supported planar intermediate-temperature cells. To produce the electrolyte films, electrode supports and thin

electrode layers, a number of techniques were exploited, for instance, chemical and electrochemical vapor deposition (CVD and ECVD), electrostatic spray deposition (ESD), vacuum plasma spraying (VPS), physical vapor deposition (PVD), laser-deposition, sputtering, electrophoresis, sol-gel method, spray-pyrolysis, screen-printing, tape casting, slurry-coating methods, co-firing, etc. [1-3,21-23]. The majority of these technologies are time- and capital-consuming. Table 1.1 compares the performance of various types of single planar IT SOFCs.

1.3. Solid electrolyte materials

Yttria-stabilized zirconia (YSZ) with cubic fluorite-type structure is one of the most common commercially-produced solid electrolytes. In addition to ZrO_2 -based materials [31-40], one can list the other well-known solid electrolytes derived from ThO_2 , HfO_2 , CeO_2 and $\delta-Bi_2O_3$ [5,15,31,32,41-47]. Among the materials with fast oxygen ionic transport, discovered during last 15-17 years, are $LaGaO_3$ -based perovskites, doped $Bi_4V_2O_{11}$ (BIMEVOX) series, $La_2Mo_2O_9$ -based (LAMOXY) phases, $Ba_2In_2O_5$ -derived phases with perovskite- and brownmillerite-like structures, doped $Gd_2Ti_2O_{7-\delta}$ pyrochlores and apatite-type $Ln_{10-x}B_6O_{26\pm\delta}$ ($B = Si$ or Ge) derivatives [30,31,47-57].

Materials deserving no interest for the electrochemical applications due to their specific disadvantages, are not considered below and are only mentioned for the comparison. For example, bismuth oxide-based phases, exhibiting maximum level of oxygen ionic conductivity known to the moment, are however characterized by excessively high lattice expansion on heating, thermodynamic instability under reducing conditions, volatilization of bismuth oxide and extremely high reactivity with the electrode materials, preventing their use as SOFC electrolytes [44]. $La_2Mo_2O_9$ and LAMOXY phases can be regarded as solid electrolytes only under oxidizing conditions below 1000-1100 K, while increasing temperature or decreasing $p(O_2)$ results in a substantial n-type electronic conductivity [53]. In addition, these exhibit a high thermal expansion and may degrade under moderately reducing conditions [53]. $Ba_2In_2O_5$ derivatives may interact with water vapor and CO_2 , leading to a degradation in performance even under oxidizing conditions [31]. Doped HfO_2 and ThO_2 materials possess lower oxygen ionic and higher electronic transport in air than their ZrO_2 - and CeO_2 -based analogous, and also higher costs [41]. Significant radioactivity of thoria is another serious problem for the practical application.

Designing the electrolyte materials for SOFCs is directed, in general, towards enhancing the stability limits under reducing conditions, increasing the ionic conductivity and suppressing the electronic transport in a wide range of oxygen pressures and temperatures. The oxygen ionic conductivity, the key criterion for the solid electrolytes, is defined by the number of ionic charge carriers and by their mobility. These can be increased using an appropriate doping. For the

materials where the ionic transport occurs via the oxygen vacancy diffusion mechanism, i.e. for most phases mentioned above, probably except for the apatite- and brownmillerite-type materials, acceptor-type doping and/or cation deficiency may increase the oxygen vacancy concentration. Note that this effect is less important for the phases with internal structural disorder, providing a sufficient level of ionic defects; one example is δ -Bi₂O₃. Another factor influencing the ionic transport relates to defect association and ordering processes. When the dopant content becomes excessively high, the positively charged oxygen vacancies may associate with the acceptor cations; that would reduce the effective concentration of mobile ion species. The doping-induced ordering processes in the oxygen sublattice may result even in the phase transitions, e.g. the disordered perovskite may order into the brownmillerite-type structure. Except the concentration of solute cations, their radius plays also an important role in the transport properties and the phase stability. As a rule, the highest ionic conductivity corresponds to materials where the ionic radii of the dopant and cations constituting the host lattice are close. The larger difference in these radii causes the local strains of the lattice, destabilizing the structure and increasing tendencies to ordering and/or phase transformations, as typical for the fluorite-type ZrO₂-based solid solutions with rare- and alkaline-earths [33,38,39]. Another comment is that, in many cases, the properties of ion-conducting oxide materials are sensitive to the microstructural phenomena and to the presence of phase impurities. In particular, silica often segregates at the grain boundaries of solid-electrolyte ceramics, dramatically increasing the boundary resistance. Moderate alumina additions may be effective to “clean” the grain boundaries from SiO₂ without an essential blocking effect on the transport properties, as observed for YSZ-Al₂O₃ composites [58,59], whereas higher content of refractory Al₂O₃ decreases the ionic conductivity [59].

1.3.1. Ionic conductivity

Among the zirconium dioxide polymorphs, the high-temperature cubic fluorite phase shows the highest level of oxygen ionic transport ([33] and references therein). Incorporation of alkaline- and rare-earth elements partially or completely stabilizes this cubic modification to the lower temperatures and creates the oxygen vacancies. Increasing content of the dopant cations above certain level leads to their progressive association with oxygen vacancies and to a decrease in ionic conductivity [33,34,38,39], Fig.1.4A. The highest ionic transport in zirconias corresponds, therefore, to the minimum dopant concentration, sufficient for stabilization of cubic phase [33]. In the ZrO₂-Ln₂O₃ systems, the maximum ionic transport corresponds to the solid solutions with Ln = Yb, Lu, Sc or Y cations [33-37] with the smallest ionic radii, closer to that of Zr⁴⁺ [60]. Yb- and Lu-containing compounds are disadvantageous due to their high costs. Zr_{1-x}Y_xO_{2-x/2} and Zr_{1-x}Sc_xO_{2-x/2} ceramics show the highest ionic conductivity at x = 0.08-0.11 and 0.09-0.11, respectively. In the

ZrO₂-MO systems (M = alkaline-earth cation), the cubic fluorite-type solid solutions existing below 1473 K were found only for the Ca-substituted compositions. The maximum conductivity of Zr_{1-x}Ca_xO_{2-x} ceramics, corresponding to x = 0.13-0.15 [33], is substantially lower than that of Zr_{1-x}Ln_xO_{2-x/2} [33]. In fact, even for the most-conductive materials derived from zirconium dioxide, the level of ionic conductivity allows their application as IT SOFC electrolytes only in the form of films with 10-100 micron-scale thickness.

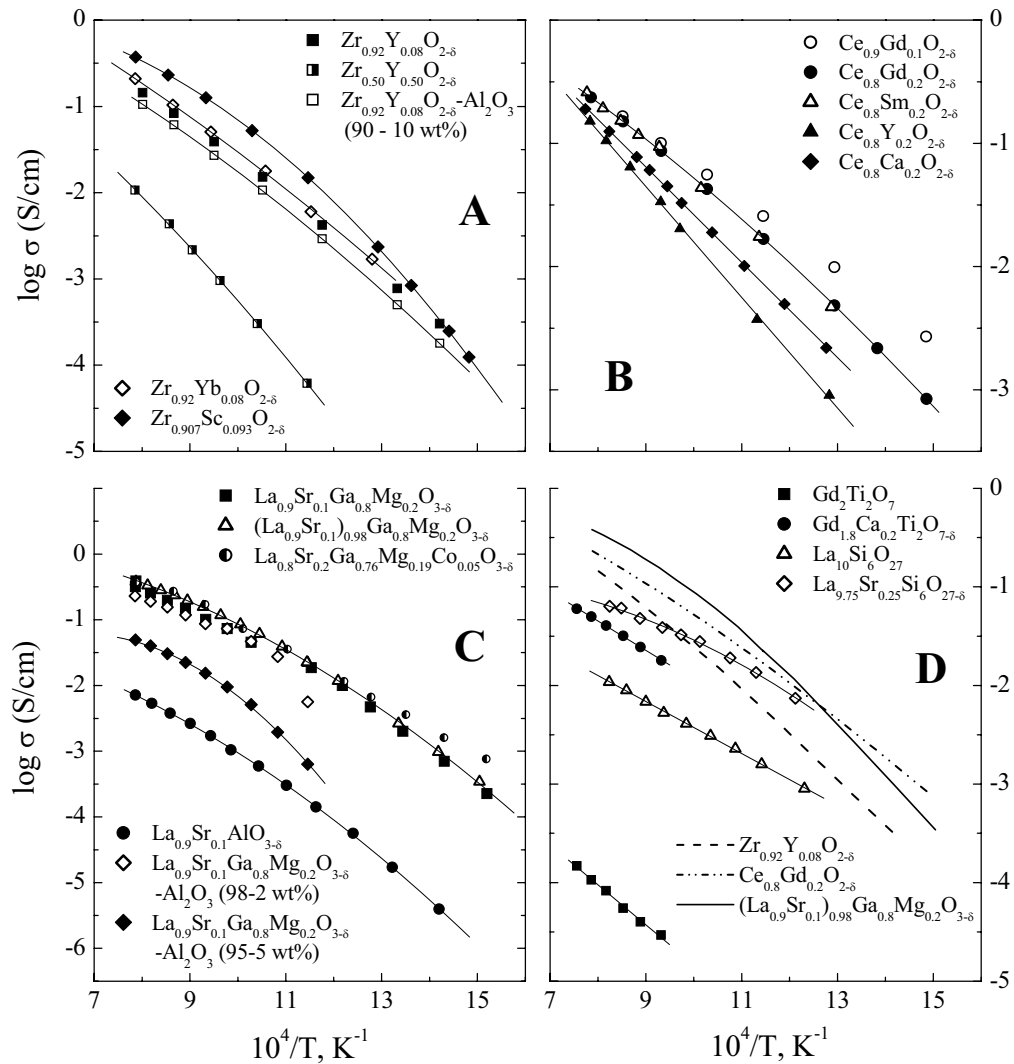


Fig.1.4. Temperature dependencies of the total conductivity of solid electrolytes based on ZrO₂ (A, [34-37]), CeO_{2-δ} (B, [5,42,43]), (La,Sr)(Ga,Mg)O_{3-δ} (C, [30,49,50]), (La,Sr)AlO_{3-δ} (C, [61]) and (La,Sr)₁₀Si₆O₂₇ (D, [56]) and the bulk oxygen ionic conductivity of (Gd,Ca)Ti₂O_{7-δ} (D, [54]). The data on La_{0.9}Sr_{0.1}Ga_{0.8}Mg_{0.2}O_{3-δ} with 5% Al₂O₃ additions correspond to p(O₂) = 1 atm, all other data were obtained in air.

With respect to the stabilized zirconias, cubic fluorite-type phases based on cerium dioxide possess significantly higher ionic transport dominating under oxidizing conditions (Fig.1.4A-D). In addition, these materials exhibit no phase transitions in air, which makes them attractive for the applications at reduced temperatures. Among the $\text{CeO}_{2-\delta}\text{-Ln}_2\text{O}_3$ and $\text{CeO}_{2-\delta}\text{-MO}$ solid solutions, the highest level of oxygen ionic transport is found for Gd- or Sm-doped compositions at x values in $\text{Ce}_{1-x}\text{Ln}_x\text{O}_{2-\delta}$ varying from 0.10 to 0.20 [41-43]. Fig.1.4B illustrates selected data on the total conductivity in air. As for the $\text{Ce}_{1-x}\text{Ln}_x\text{O}_{2-\delta}$ solid solutions, substitution of cerium with M^{2+} leads to a higher oxygen ion transport [41]. The solubility of the alkaline-earth cations in Ce-sublattice is, however, quite limited, decreasing on cooling and leading to separation of MCeO_3 perovskite-like phases [41].

Another group of materials, promising as solid electrolytes for the IT SOFCs and showing higher ionic conductivity in comparison with stabilized zirconia (Fig.1.4, C and D), are the doped lanthanum gallates with ABO_3 perovskite-type structure [48]. Incorporation of lower-valence cations of an appropriate radius into A- and B-sites of LaGaO_3 increases the oxygen ionic conductivity. The highest ionic conductivity is achieved when LaGaO_3 is doped with strontium rather than calcium or barium [48]. Mg^{2+} , the only bivalent cation with stable oxidation state and ionic radius close to that of Ga^{3+} [60], can be introduced into the B sublattice [48]. For $\text{La}_{1-x}\text{Sr}_x\text{Ga}_{1-y}\text{Mg}_y\text{O}_{3-\delta}$ (LSGM) materials, the optimized composition providing maximum ionic transport is found at $x = 0.10\text{-}0.20$ and $y = 0.15\text{-}0.20$. Further increase in M^{2+} content in the lattice, or introducing of more than 2% A-site substoichiometry, increases the oxygen vacancy concentration, but leads to extensive association processes and/or segregation of secondary phases, thus decreasing ionic transport [48,49]. Contrary to the ceria- and zirconia-based systems [41], minor (<10 mol%) Ga-doping with cations having variable oxidation state, such as cobalt or iron, leads to increasing ionic transport in LSGM ceramics in the low-temperature range [50,51], Fig.1.4C, while the electronic conductivity is still acceptable for the practical use [50].

Despite a relatively low level of ionic conductivity (Fig.1.4D), the materials derived from LnAlO_3 perovskites, $\text{A}_{10-x}(\text{SiO}_4)_6\text{O}_{2+\delta}$ ($A = \text{La, Pr, Nd, Sm, Gd, Dy}$) apatites and $\text{Gd}_2\text{Ti}_2\text{O}_7$ pyrochlores are still of interest due to their relatively low costs. One possible application of these ceramics are the protective surface layers at the anode-side of LaGaO_3 - or CeO_2 -based electrolytes, exposed to reducing atmospheres or the components of the composite solid electrolytes. In most perovskite and apatite materials, the oxygen ionic conductivity increases with increasing A-site dopant radius. The highest level of ionic transport was achieved for $\text{La}_{1-x}\text{Sr}_x\text{AlO}_{3-\delta}$ at $x = 0.10$ [61], for $\text{Gd}_{2-x}\text{Ca}_x\text{Ti}_2\text{O}_{7-\delta}$ at $x = 0.20$ [54] and for $\text{La}_{10-x}\text{Sr}_x\text{Si}_6\text{O}_{27}$ at $x = 0.25$ [56] and $\text{La}_{9.33+x/3}\text{Si}_{6-x}\text{Al}_x\text{O}_{26}$ series at $x = 1.5$ [57].

1.3.2. Stability and electronic conductivity

For the $Zr_{1-x}Sc_xO_{2-x/2}$ systems, partial ordering and/or decomposition of metastable cubic and rhombohedral solid solutions result in relatively fast ageing [33,39]. For instance, the conductivity of 10 mol% Sc-doped zirconia drops by 2 % after exposure in atmospheric air for 83 h at 1273 K and by 7 % at 1123 K [39]. Ytria-stabilized zirconia, characterized by lower costs and higher stability [33,38,39], is considered as more feasible. $Zr_{1-x}Ca_xO_{2-x/2}$ fluorite solid solutions even with high Ca-content are still metastable, decomposing below 1123 K into a stable $CaZrO_3$ perovskite and ZrO_2 [33]. In air, the p-type electronic conductivity of zirconia-based solid solutions is much lower than that in doped ceria and lanthanum gallate phases. For example, the electronic contribution to the total conductivity of $Zr_{0.9}Y_{0.1}O_{2-\delta}$ is less than 0.05 % at 1273 K. The oxygen ionic conductivity of yttria-stabilized zirconia is kept predominant down to at least 10^{-25} at 1173 K [32]. This low- $p(O_2)$ boundary of electrolytic domain is quite similar for all $ZrO_2-Ln_2O_3$ systems. Comparative data on the electronic transport is summarized in Table 1.2.

Table 1.2

Comparison of the parameters of electronic transport in solid electrolyte ceramics, under oxidizing conditions

Composition	T, K	$p(O_2)$, atm	t_e	σ_e , mS/cm	Ref.
$Zr_{0.9}Y_{0.1}O_{2-\delta}$	1273	0.21	5.0×10^{-5}		[41]
$Zr_{0.9}Sc_{0.1}O_{2-\delta}$	1273	0.21	3.8×10^{-4}		[41]
$Zr_{0.85}Ca_{0.15}O_{2-\delta}$	1273	0.21	8.6×10^{-4}		[41]
$Ce_{0.8}Gd_{0.2}O_{2-\delta}$	873	0.21	6.9×10^{-4}	0.003	[45]
	973	0.21	1.1×10^{-3}	0.015	
	1123	1.0	3.7×10^{-3}	0.42	[43]
$La_{0.9}Sr_{0.1}Ga_{0.8}Mg_{0.2}O_{3-\delta}$	1073	0.21		0.36	[52]
	1073	10^{-3}	1.0×10^{-2}		[49]
$(La_{0.9}Sr_{0.1})_{0.98}Ga_{0.8}Mg_{0.2}O_{3-\delta}$	1073	10^{-3}	4.7×10^{-3}		[49]
$Gd_{1.9}Ca_{0.1}Ti_2O_{7-\delta}$	1073	1.0	0.11	2.1	[54]
$La_{0.9}Sr_{0.1}AlO_{3-\delta}$	1073	0.21	0.64	1.9	[61]

Note: t_e and σ_e are the total electronic (p- and n-type) transference number and the total electronic conductivity, respectively.

Contrary to zirconia, the cubic fluorite-type polymorph of $CeO_{2-\delta}$ exists in air within all temperature range until the melting point [41]. In air, the level of p-type electronic conductivity in gadolinia-doped ceria is rather low [43,45], Table 1.2. Decreasing oxygen pressure leads, however, to reduction of cerium accompanied with increasing electronic conductivity [41] and significant volume changes, which implies mechanical instability under SOFC operation conditions, i.e. under

the large $p(\text{O}_2)$ gradients. Increasing the dopant content in $(\text{Ce,Ln})\text{O}_{2-\delta}$ decreases the stability in reducing atmospheres below 1000-1173 K [15,43]. In order to partially suppress these disadvantages, the fuel cell operation temperature should be reduced below 873 K [15]. In particular, 10 mol% Gd-doped ceria is considered as a prospective electrolyte material for the SOFCs operating at 773 K [5,15]. At this low temperature, however, the electrochemical activity of common electrode materials is usually insufficient to provide a high cell performance.

Contrary to zirconia-based solid electrolytes, the conductivity of the doped lanthanum gallate ceramics does not degrade in air [31]. In oxidizing atmospheres, the level of p-type electronic conductivity in LaGaO_3 -based electrolytes [52] is higher than in gadolinia-doped ceria [43,45], especially at reduced temperatures, e.g. at 973 K the difference becomes one order of magnitude. Nevertheless, the electronic conductivity of LSGM is still minor (Table 1.2) and has no essential effect on the electrolyte performance. The unfavorable factors limiting the applications of Ga-containing ceramics are Ga^{3+} reduction and gallium oxide volatilization at decreased $p(\text{O}_2)$, possible segregation of secondary phases during ceramics sintering, and interactions with electrode materials. Choosing appropriate ceramic processing techniques and cell fabrication and exploitation conditions enable to avoid these problems. Under reducing conditions, n-type electronic conductivity of LSGM ceramics is comparable, or even smaller, with respect to stabilized zirconia electrolytes [32,52]. If comparing with ceria-based electrolytes, the doped lanthanum gallates preserve the dominating ionic transport with negligible electronic contribution down to substantially lower oxygen pressures [52], which makes them advantageous for the IT SOFC applications. For example, the low- $p(\text{O}_2)$ boundary of the electrolytic domain where the contribution of electronic conductivity to the total transport in $\text{La}_{0.9}\text{Sr}_{0.1}\text{Ga}_{0.8}\text{Mg}_{0.2}\text{O}_{3-\delta}$ reaches 1 %, corresponds to the oxygen partial pressure of less than 10^{-30} atm at 1073 K [49], while for $\text{Ce}_{0.8}\text{Gd}_{0.2}\text{O}_{2-\delta}$ this value is as high as approximately 10^{-15} atm [44].

The $(\text{La,Sr})\text{AlO}_{3-\delta}$ perovskites and pyrochlore-type $(\text{Gd,Ca})_2\text{Ti}_2\text{O}_{7-\delta}$ possess a substantial p-type electronic conductivity under oxidizing conditions [54,61], Table 1.2, but are significantly more stable to reduction and component volatilization compared to the doped $\text{CeO}_{2-\delta}$ and $\text{LaGaO}_{3-\delta}$ ceramics. In air, the electron transference numbers of $\text{Gd}_{1.9}\text{Ca}_{0.1}\text{Ti}_2\text{O}_{7-\delta}$, 0.07-0.11 at 1073 - 1223 K [54], are close to the maximum level allowable for solid electrolytes. Taking into account the low costs of raw materials, the use of $(\text{Gd,Ca})_2\text{Ti}_2\text{O}_{7-\delta}$ phases for high-temperature applications seems possible. At 873-1173 K, the ionic contribution to total conductivity of $\text{La}_{0.9}\text{Sr}_{0.1}\text{AlO}_{3-\delta}$ is smaller than 40 % under air/ O_2 gradient and is ≥ 90 % under 4% H_2 /air gradient [61]. The performance of lanthanum-strontium aluminates under oxidizing conditions is, thus, relatively poor.

1.3.3. Thermal expansion

Alkaline-earth-doped lanthanum gallates at lower temperatures than 1073 K, $\text{Gd}_2\text{Ti}_2\text{O}_7$ and stabilized zirconia ceramics exhibit similar and moderate thermal expansion coefficients (TECs), Table 1.3. This is an important advantage of these materials with respect to the $(\text{Ce,Ln})\text{O}_{2-\delta}$ solid solutions, the thermal expansion of which is slightly higher, close to LSGM doped with transition metal cations (Table 1.3). One of the strategies to use ceria-based materials refers to the application of a protective layer of more redox stable electrolyte at the low- $p(\text{O}_2)$ surface of doped ceria [27]. However, the thermal expansion mismatch may lead to the microcrack formation and mechanical degradation of ceramics on thermal and redox cycling. The long-term operation of such cells seems, therefore, problematic. In addition, possible chemical interactions between the electrolyte materials may result in the formation of highly-resistive interface layers, deteriorating the cell performance [43,62].

Table 1.3

Comparison of the average linear thermal expansion coefficients of solid electrolyte ceramics in air

Composition	T, K	$\bar{\alpha} \times 10^6, \text{K}^{-1}$	Ref.
$\text{Zr}_{0.92}\text{Y}_{0.08}\text{O}_{2-\delta}$	300-1273	10.0	[35]
$\text{Zr}_{0.92}\text{Y}_{0.08}\text{O}_{2-\delta} - \text{Al}_2\text{O}_3$ (90-10 wt%)	300-1273	9.7	[35]
$\text{Zr}_{0.85}\text{Y}_{0.15}\text{O}_{2-\delta}$	303-1273	10.9	[63]
$\text{Zr}_{0.5}\text{Y}_{0.5}\text{O}_{2-\delta}$	293-1273	9.4	[33]
$\text{Ce}_{0.9}\text{Gd}_{0.1}\text{O}_{2-\delta}$	773	12.4	[46]
	853	12.5	
$\text{Ce}_{0.8}\text{Gd}_{0.2}\text{O}_{2-\delta}$	773	12.5	[46]
	853	12.6	
	303-1073	12.5	[63]
	303-1273	12.7	
$\text{La}_{0.9}\text{Sr}_{0.1}\text{Ga}_{0.8}\text{Mg}_{0.2}\text{O}_{3-\delta}$	303-1073	10.4	[30]
	300-1473	11.9	[49]
	303-1073	10.9	[63]
	$(\text{La}_{0.9}\text{Sr}_{0.1})_{0.98}\text{Ga}_{0.8}\text{Mg}_{0.2}\text{O}_{3-\delta}$	300-1473	11.8
$\text{La}_{0.9}\text{Sr}_{0.1}\text{Ga}_{0.8}\text{Mg}_{0.2}\text{O}_{3-\delta} - \text{Al}_2\text{O}_3$ (95-5 wt%)	303-1073	9.9	[30]
$\text{La}_{0.9}\text{Sr}_{0.1}\text{Ga}_{0.76}\text{Mg}_{0.19}\text{Co}_{0.05}\text{O}_{3-\delta}$	300-1473	12.7	[50]
$\text{Gd}_2\text{Ti}_2\text{O}_{7\pm\delta}$	323-1273	10.8	[55]

The incorporation of Ln_2O_3 into ceria facilitates Ce^{4+} reducibility below 1173 K [15] and induces an additional volume expansion on decreasing oxygen pressure. No essential chemical expansion was observed for the LSGM ceramics. For example, the TEC values obtained for

$\text{La}_{0.9}\text{Sr}_{0.1}\text{Ga}_{0.8}\text{Mg}_{0.2}\text{O}_{3-\delta}$ in air and in 4% H_2 were found equal within the limits of experimental uncertainty [30].

It should be mentioned that small amounts of highly-dispersed Al_2O_3 may improve sinterability and mechanical properties of YSZ and $(\text{La,Sr})(\text{Ga,Mg})\text{O}_{3-\delta}$ ceramics, particularly due to suppressed grain growth in the course of sintering [30,33,58,59]. These alumina additions to solid electrolyte ceramics enable also to decrease thermal expansion (Table 1.3).

In summary, gadolinia-doped $(\text{La,Sr})(\text{Ga,Mg})\text{O}_{3-\delta}$ and ceria are the most promising electrolyte materials for IT SOFCs, whereas yttria-stabilized zirconia having relatively low ionic conductivity in the intermediate-temperature range can only be used in the film form. The high n-type conductivity of $(\text{Ce,Gd})\text{O}_{2-\delta}$ in reducing atmospheres, resulting in the internal leakage currents, limits their applicability to a great extent. Low-cost $(\text{Gd,Ca})_2\text{Ti}_2\text{O}_{7-\delta}$ can be used, in particular, as a component of the multilayer or composite electrolytes.

1.4. Electrode reaction mechanisms

To design the electrodes with advanced electrochemical properties, a deep knowledge on the mechanisms of electrode reactions is necessary. The electrode reaction consists of a number of serial and/or parallel steps, which can be divided into transport and heterogeneous; in the course of latter, various intermediate electrochemically-active components may be formed. The characteristic steps of the gas electrode reactions include transport in the gas phase to (or from) the gas/electrode or gas/electrolyte interface, adsorption (or desorption) at these surfaces, diffusion to (or from) the reaction zone, and transfer reactions [32,64-70]. The reaction path and the rate-limiting step are dependent of numerous factors, such as the electrode and electrolyte properties and morphology, gas phase composition and pressure, thermal and electrochemical pre-history [32,64-66,69,71]. The electrochemical process is believed to occur in the vicinity (within few microns) of triple-phase boundary (TPB) [32,64,72], the junction of the gas, electronic or mixed conductor (electrode) and ionic conductor (electrolyte), whose length is mostly determined by the electrode microstructure, formed during electrode fabrication. Actual location of the electrochemically active sites depends generally on the volume and surface transport properties of the electrode and electrolyte materials.

On the absence of external current, dynamic equilibrium related to the equal rates of forward and backward reactions, is established at the electrode. The rate of oxygen exchange with the gas phase at the equilibrium electrode potential is reflected by the exchange current, I_0 [32]. The I_0 quantity characterizes only the steps related to activation polarization, such as adsorption/desorption, chemical reaction or charge-transfer reaction [32]. The limiting current, I_{lim} , corresponding to the maximum gradient of electrochemically active component concentration, can be realized for transport processes as well as for adsorption or chemical reaction steps [32]. When

the current I is passed or drawn through the cell, the electrode potential ϕ deviates from the equilibrium value ϕ^0 . This deviation is characterized by the quantity of overpotential $\eta = \phi - \phi^0$. At microstructural level, the reasons for electrode polarization include local changes in the concentration of electrochemically active components. The electrode polarization resistance defined as:

$$R_{\eta} = \frac{d\eta}{dI} \quad (1.9)$$

in the case of small polarization and a linear I - η dependence [32,64,65], is interrelated with the exchange or limiting current

$$R_{\eta} = \frac{RT}{nF \cdot I_0} \quad \text{or} \quad R_{\eta} = \frac{RT}{nF \cdot I_{lim}} \quad (1.10)$$

where n is a number depending on the rate-determining step(s). The most widely used tool for the investigations of electrode kinetics is based on the electrochemical impedance spectroscopy and current interruption methods. The problems which may hamper the proper understanding of the electrode kinetics are analyzed in [73].

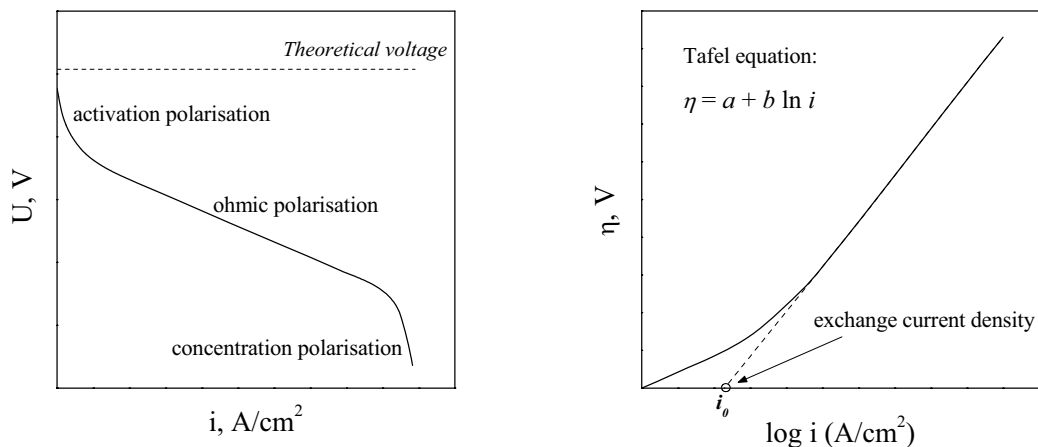


Fig.1.5. Examples of current density dependencies of fuel cell voltage (left) and electrode overpotential (right).

1.4.1. Cathode processes

The overall cathode reaction of oxygen reduction is expressed by Eq.(1.1). Historically the electrode reactions were first studied on the metal electrodes in contact with solid electrolyte (usually YSZ), which are still considered as appropriate model systems for analysis of processes at the gas electrodes [32,64-68,70-72,74-76]. However, even for these relatively simple systems, the electrode reaction mechanisms are complex and their models are still ambiguous. First of all, the

reaction zone expands from TPB over the electrolyte or electrode surfaces [32,64,69,74]. As all solid electrolytes possess some electronic conduction (see Chapter 1.3.2), the electrochemically active sites may be located at the gas/electrolyte interface with electronic charge carriers delivered along the electrolyte surface. In addition, high cathodic overpotentials or currents may result in a partial reduction of the electrolyte surface and increasing electronic transport, favoring the oxygen exchange with electrolyte [64]. In the case of electrodes where oxygen may dissolve in the bulk or form surface compounds, oxygen reduction may directly take place at the electrode/electrolyte interface, as was clearly shown for the $O_2, Ag | YSZ$ [32,74]. For mixed ionic-electronic conducting oxide phases used as the SOFC cathodes, the reaction zone may also spread into the gas/electrode interface with the subsequent transfer of reduced oxygen species to the electrolyte along the electrode surface and/or through the electrode bulk. Also, in some cases, another triple-phase boundary of gas/mixed conductor/current collector, should be taken into account [76]. Thus, despite the numerous experimental and theoretical investigations (see, for example, [32,64-89]) of various-type cathodes, identification of the exact reaction mechanism and rate-determining step(s), remains one of the most difficult but the most important tasks. A variety of simplified steps of the cathode reaction and the formulae for particular cases of polarization processes are summarized below, with emphasis on the porous oxide cathodes with mixed oxygen ionic and electronic conductivity.

General equations for diffusion processes

The diffusion processes are generally described by Fick's first and second laws [90]:

$$j_i = -D_i \cdot \nabla c_i = -\frac{c_i D_i}{RT} \cdot \nabla \mu_i \cdot \left(\frac{d \ln a_i}{d \ln c_i} \right) \quad (1.11)$$

$$\frac{\partial c_i}{\partial t} = \nabla (D_i \nabla c_i) \quad (1.12)$$

where j_i is the flux density, c_i is the concentration, a_i is the activity, D_i is the diffusion coefficient and μ_i is the chemical potential of diffusing i -species, and t is the time. The last part of Eq.(1.11) is written taking into account Wagner's law. The reaction rate-determining diffusion of molecular oxygen in the gas phase (including pores in the electrode layer) appears at reduced oxygen partial pressures and is characterized by the limiting current and reciprocal polarization resistance, both proportional to $p(O_2)$ [64,79]. The gas phase can be treated as an ideal binary mixture of O_2 and a diluent gas B [77]. Taking into account the diffusion and convection processes at moderate total gas pressure, and assuming an absence of homogeneous gas-phase reactions, one can write [79]:

$$j_{O_2} = -D_{O_2-B} \cdot \nabla c_{O_2} + c_{O_2} v \quad \text{and} \quad \frac{\partial c_{O_2}}{\partial t} = D_{O_2-B} \nabla^2 c_{O_2} - v \nabla c_{O_2} \quad (1.13)$$

where D_{O_2-B} is the gas-phase binary (O_2 -B) diffusion coefficient, v is the molar gas velocity. Gas-phase diffusion can be expressed by Eqs.(1.13) at large pore diameters compared to the mean free path of the gas molecules; the transport in the small pores is described by the Knudsen diffusion [91], taking into account the interaction with pore walls. The bulk diffusion should be considered along with the Knudsen effects; then, considering tortuous path through the porous media, the effective oxygen diffusion coefficient, $D_{O_2}^{eff}$, is given by [25,79,91]:

$$D_{O_2}^{eff} = \frac{P}{\tau_g} \cdot \frac{D_{O_2-B} \cdot D_{O_2}^K}{D_{O_2-B} + D_{O_2}^K} \quad (1.14)$$

where $D_{O_2}^K$ is the Knudsen diffusion coefficient of oxygen, τ_g is the gas-phase tortuosity, P is the porosity. As the diffusion coefficient of molecular oxygen in pores is at least 6 orders of magnitude greater than that of oxygen ions in solids [69], usually the O_2 diffusion is not rate-determining for the air electrode until approaching a limiting current. For example, in case of $La_{0.6}Sr_{0.4}Fe_{0.8}Co_{0.2}O_{3-\delta}$ in contact with $Ce_{0.9}Gd_{0.1}O_{2-\delta}$ electrolyte, possible gas-phase diffusion polarization was indicated by changing the shape of electrode impedance spectra at $p(O_2)$ below ~ 0.1 atm. [79]. The gas-diffusion limitations for the $O_2, Pt | YSZ$ cathode were discarded down to 10^{-3} atm [67,68].

Oxygen transport through the solid electrolyte bulk occurs under the gradients of both chemical and electrical (ϕ) potentials, typically via vacancy migration [77,79]. Using Eq.(1.11) and Ohm's law, the current density i is found as:

$$i = \frac{-\sigma_v}{2F} \nabla \phi_v \quad (1.15)$$

where σ_v is the conductivity and $\phi_v = \mu_v + zF\phi$ is the electrochemical potential of oxygen vacancies in the electrolyte bulk. It should be noted that vacancy redistribution at the electrode/electrolyte interface may lead to the non-linear potential distribution in the electrolyte bulk [64,78]. The role of nonuniform current and potential distribution in the electrolyte using a two-dimensional model was evaluated in the theoretical work [84]. Polarization caused by the ohmic potential drop in the solid electrolyte as function of the cathode microstructure was also discussed in Ref.[78]. As a rule, the ohmic losses, comprised by the IR term in Eq.(1.8), can be separated from the electrode polarization.

The oxygen ion and electron transport through the bulk of a mixed conductor obeys Wagner's law, stating the interrelated fluxes of ionic and electronic charge carriers. Under the absence of external electrical current, the oxygen flux through a dense mixed conductor, placed in the oxygen chemical potential gradient, is given by [83,90,92]:

$$j_{O_2} = \frac{1}{16F^2L} \int_{\mu_1}^{\mu_2} \frac{\sigma_{ion} \cdot \sigma_e}{\sigma_{ion} + \sigma_e} d\mu_{O_2} \quad (1.16)$$

where μ_1 and μ_2 are the oxygen electrochemical potentials at the gas/mixed conductor permeate and feed interfaces, σ_{ion} and σ_e are the partial ionic and electronic conductivities and L is the average length of the migration path. In the framework of the porous electrode theory, Eq.(1.16) is rewritten taking into account the porosity and the solid-phase tortuosity; examples of the alternative expressions for the transport through solid mixed-conductor in a porous layer can be found in [77,79].

General equations for interfacial processes

Molecular oxygen from the gas phase may be chemisorbed at the surface of noble-metal electrodes to form ad-atoms [64,65], which is expressed by



where s is an active site at the surface. Oxygen adsorption at the oxide electrode or electrolyte surfaces may occur via various mechanisms and may be conjugated with the charge-transfer reaction(s) [66]. Numerous forms of adsorbed oxygen species are assumed in literature, in particular O_2 , O , O_2^- , O_2^{2-} , O^- or O^{2-} . The adsorption isotherm, in the simplest case representing reaction Eq.(1.17) at relatively low surface coverage, obeys the Henry equation [64,93]:

$$[\text{O}_{\text{ad}}] = K \cdot p(\text{O}_2)^{1/2} \quad (1.18)$$

where K is the adsorption equilibrium constant related to the interatomic adsorbent-adsorbate interaction.

The oxygen pressure dependence of the polarization resistance of Pt electrodes is characterized by a minimum [32,64], attributed to the Pt oxidation and/or to the adsorption kinetics determined by the Langmuir isotherm [64]. The latter assumes a homogeneous adsorbent surface and a uniform adsorption enthalpy distribution along this surface, independent of the presence of adsorbates which are considered non-interacting. The Langmuir isotherm is given for dissociative adsorption Eq.(1.17) by [64,93,94]:

$$\theta_{\text{O}} \equiv \frac{[\text{O}_{\text{ad}}]}{[\text{O}_{\text{ad}}]_{\text{max}}} = \frac{K \cdot p(\text{O}_2)^{1/2}}{1 + K \cdot p(\text{O}_2)^{1/2}} \quad (1.19)$$

where θ is the relative surface coverage and $[\text{O}_{\text{ad}}]_{\text{max}}$ is the maximum concentration of ad-atoms, corresponding to the completely packed monolayer of adsorbed oxygen species, or the total number of sites available for adsorption. For real systems, the adsorption enthalpy decreases (in absolute value) with surface covering [64,93]; therefore, the applicability of Eq.(1.19) needs often a careful analysis and, in general, Eq.(1.19) should be written in an integral form [64].

For the case of substantially non-uniform adsorbent surface, the Temkin isotherm equation is simplified, at moderate coverage, to [64]:

$$[O_{ad}] = [O_{ad}]_{max} \cdot \frac{RT}{\alpha_0} \cdot \ln \left[\beta_0 p(O_2)^{1/2} \right] \quad (1.20)$$

where α_0 and β_0 are the parameter characterizing the extent of inhomogeneity and the adsorption coefficient at the sites with maximum adsorption enthalpy, respectively. Similar approximation was suggested in [93] for a binary gas adsorption. The oxygen adsorption/desorption process on $O_2, Pt | YSZ$ electrode was modeled in [68] as occurring via the formation of intermediate chemisorbed oxygen molecule with subsequent dissociation or desorption.

The information about the actual mechanisms of oxygen adsorption, dissociation and reduction at the solid oxide surface is, in fact, still scarce. Based on the ratio of the oxygen self-diffusion coefficients and the surface exchange coefficients, it was concluded [69,79] that, for optimized cathode microstructures with grain diameter of about 1 μm and TPB length per unit area greater than 10^4 cm^{-1} , the oxygen reduction should be governed by an interfacial oxygen exchange process unless the surface transport of oxygen ions to the TPB is rate-determining. The flux density of oxygen chemisorption-dissociation can be expressed by a kinetic equation [64]:

$$j_{O_2} = j_{O_2}^0 \cdot (1 - \theta_O^2) \quad (1.21)$$

where $j_{O_2}^0$ is the exchange flux density of oxygen dissociative adsorption. For the limiting oxygen adsorption, the current density is generally defined in [76, 94] by:

$$i = 4F \cdot \left[k_1 \cdot p(O_2) \cdot (1 - \theta_{O,st})^2 - k_1' \cdot \theta_{O,st}^2 \right] \quad (1.22)$$

where k_1 and k_1' are the constants of forward and backward processes Eq.(1.17) and $\theta_{O,st}$ is the steady-state coverage. The situation, when adsorption of molecular oxygen is retarding with the subsequent dissociation of adsorbed O_2 -s being in the virtual equilibrium, was considered in [95] postulating:

$$i = 4F \cdot k_a p(O_2) \cdot (1 - \theta_{O_2} - \theta_O) \quad (1.23a)$$

$$\theta_{O_2} \cdot (1 - \theta_{O_2} - \theta_O) = K_d \cdot \theta_O^2 \quad (1.23b)$$

where k_a and K_d are the oxygen adsorption and equilibrium dissociation constants, respectively. This process can also be considered as dissociation of the oxygen molecule in the gas phase in immediate proximity to the solid surface, followed by the adsorption of the oxygen atoms [96].

The case of limiting charge-transfer electrochemical reactions should be considered using the Butler-Volmer equation [32,64,67,85,90]:

$$i = i_0 \left[\exp \left(\frac{\alpha n F \eta}{RT} \right) - \exp \left(- \frac{\beta n F \eta}{RT} \right) \right] \quad (1.24)$$

where n is the number of electrons participating in the rate-determining step, α and β are the charge transfer coefficients, i and i_0 are the electrical current and exchange current densities, respectively. Eq.(1.24) is linearized to the ohmic electrode polarization at low overpotentials $|\eta|$ and shows a Tafel-like behavior at large $|\eta|$ [66]. The equation:

$$i = i_0 \left[\exp\left(\frac{\alpha F \eta}{RT}\right) - \exp\left(-\frac{\beta F \eta}{RT}\right) \right] + C \frac{d\eta}{dt} \quad (1.25)$$

where C is the capacitance of the interface, was used in [79] to describe interfacial charge-transfer reactions with a single activated rate-limiting step. η is stated to be proportional to the difference in the electrochemical potential of the transported species (vacancy, electron, etc.) across the interface.

Two typical combinations of adsorption/charge transfer/diffusion steps are shown in Fig.1.6. It is quite clear that even for the simple electrode systems, there are a great number of paths, spatially expanding the reaction zone. In addition, the possibility of parallel interfacial processes to occur cannot be *a priori* discarded. When the electrode polarization is determined by several limiting steps, it is very difficult or impossible to isolate them without precisely controlled morphology and composition of the interfaces; the latter situation is, however, far from experimental realization.

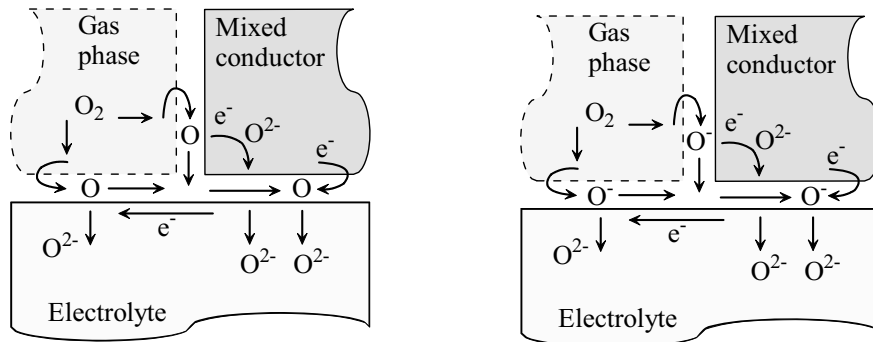


Fig.1.6. Examples of electrochemical reaction pathway for a porous mixed-conducting oxygen electrode, showing surface diffusion of O ad-atoms (left) and O⁻ sub-ions (right).

Selected models for one and several limiting steps

One version of the possible steps sequence for oxygen reduction at the surface of mixed-conducting oxide cathode (MC) was proposed as [79]:



where $(\text{O}_2\text{-s})^-$ and $(\text{O-s})^-$ are the adsorbed oxygen O_2^- and O^- sub-ions, respectively. In order to describe these processes, the authors [79] proposed an equation similar to that obtained for charge-transfer reactions, irrespective of the limiting step:

$$r = r_0 \left[\exp\left(\frac{\alpha_f}{RT} \Delta\phi_s\right) - \exp\left(\frac{-\alpha_b}{RT} \Delta\phi_s\right) \right] \quad (1.27)$$

where r is the rate of the limiting step, r_0 is the so-called exchange neutral flux density, α_f and α_b are constants depending on the specific reaction mechanism, and $\Delta\phi_s = \frac{1}{2} \phi_{\text{O}_2}^{\text{gas}} + \phi_{\text{V}_\text{O}}^{\text{MC}} - 2\phi_{\text{h}}^{\text{MC}}$ is the electrochemical potential difference between the reactants and the products.

For the case of two or more concurrent limiting steps, one possible approach can be based on the example of O_2 , Pt | YSZ electrode, where electrochemically active component is not soluble. Such an electrode was considered [32,66] as a tightly contacted with electrolyte discontinuously long metallic stripe of a fixed width. The relative roles of the interfacial diffusion rate of oxygen ad-atoms chemisorbed at the metallic electrode and the surface exchange rate were analyzed in Ref.[66]. In the case of the rate-limiting diffusion along the electrode/electrolyte interface which depends, in turn, on the rate of charge-transfer reaction, the current density was expressed by the Butler-Volmer-form equation [66]:

$$i = \frac{(i_0 \cdot 2eDc_0)^{1/2}}{l} \left[\exp\left(\frac{3F\eta}{2RT}\right) - \exp\left(-\frac{F\eta}{2RT}\right) \right] \quad (1.28a)$$

or

$$i = \left[\frac{l}{(i_0 \cdot 2eDc_0)^{1/2}} + \frac{l}{2e\gamma c_0} \exp\left(-\frac{F\eta}{2RT}\right) \right]^{-1} \cdot \left[\exp\left(\frac{3F\eta}{2RT}\right) - \exp\left(-\frac{F\eta}{2RT}\right) \right] \quad (1.28b)$$

where l is the stripe half-width, c_0 is the equilibrium concentration of oxygen adatoms, D is their interfacial diffusion coefficient and γ is a constant. Eqs.(1.28a) and (1.28b) are obtained for different boundary conditions.

For the competing charge-transfer, surface diffusion and dissociative adsorption, another equation was derived [68]:

$$i = i_0 \cdot A \cdot \left[\exp\left(\frac{3(1-\beta)F\eta}{7RT}\right) - \exp\left(-\frac{3\beta F\eta}{4RT}\right) \right] \quad (1.29)$$

where A is the electrochemically-active area near the TPB, was simulated; the latter two steps are assumed parallel. The effect of surface coverage on these processes were also discussed ([68] and cited references).

The models for a limiting step involving conjugated processes of interfacial diffusion/migration and heterogeneous exchange, was also discussed in Ref.[32]. For the

dissociative adsorption of oxygen coupled with diffusion along the gas/metal interface (GM), the electrical current per unit TPB length is found as [32]:

$$i = i_0^{\text{GM}} \left[\exp\left(\frac{6F\eta_1}{RT}\right) - 3 \exp\left(\frac{2F\eta_1}{RT}\right) + 2 \right]^{1/2} \quad (1.30)$$

Provided the constant oxygen ion concentration at the electrolyte surface, the current corresponding to the diffusion along the metal/electrolyte interface (ME) conjoined with the oxygen transfer to (or from) the electrolyte can be expressed as [32]:

$$i = i_0^{\text{ME}} \left[\exp\left(\frac{(1+\alpha)F\eta_2}{RT}\right) - \theta_0 \exp\left(-\frac{\beta F\eta_2}{RT}\right) \right] \quad (1.31)$$

where θ is the ratio of the oxygen atom concentration at the GM to the equilibrium concentration. These overpotential-current dependencies were obtained assuming that: (i) the widths of gas/metal and gas/electrolyte interfaces are much smaller than the corresponding penetration depths of the surface diffusion, (ii) the oxygen diffusion coefficient in the adsorption layer is concentration-independent, and (iii) the adsorption isotherm obeys the Henry equation. Dependence of the total overpotential on current was obtained from Eqs.(1.30) and (1.31), both expressing the interrelated exchange process and the interface diffusion; in this case, however, only numerical solution is possible [32]. Nevertheless, it was concluded [32] that decreasing $p(\text{O}_2)$ leads to the dominating limitations by Eq.(1.30), while the reaction rate becomes determined by Eq.(1.31) on increasing $p(\text{O}_2)$. The other processes illustrated in Fig.1.6, except for the oxygen transport through the electrode bulk, can be described by the analogous current-overpotential equations involving relative concentrations of O^- subions or electron-holes instead of θ_0 [32].

One important comment should be made for the case when two processes are rate-determining, whatever the reaction path. In such situation, one cannot principally determine characteristics of the separate steps from the results of polarization measurements only. Note also that the processes reflected by Eqs.(1.30) or (1.31) have a mixed character combining the activation and concentration polarization effects. The ratio of diffusion- and exchange-related contributions should change with the electrode depth [32]. As a result, the oxygen activity at the electrode surface may change by several orders of magnitude, decreasing for the cathode and increasing for the anode polarization. Such $p(\text{O}_2)$ variations may cause irreversible changes in the microstructure and properties of the electrodes.

Similar phenomena, including the adsorbate transport along the electrode/electrolyte interface may take place for the porous perovskite-type oxide cathodes [85]; for metallic electrodes such a reaction pathway was analyzed using two-dimensional model [84]. The effect of cathodic polarization or current on the microstructure and morphology of the $(\text{La}_{0.8}\text{Sr}_{0.2})_{1-x}\text{MnO}_{3-\delta}$ ($x = 0-$

0.05) porous layers in contact with 3 mol% Y_2O_3 - ZrO_2 electrolyte were attributed to the formation and migration of oxygen vacancies and manganese ions on the electrode surface [86].

For a mixed-conductor electrode, competitive bulk and surface oxygen transport was discussed in numerous works, e.g. [64,72,79,81-85,87,97,98]. Both these processes and their relative roles depend on the oxygen ion conductivity of the cathode material under given conditions, as discussed below. In turn, the conductivity of the cathode layer (σ) should be influenced by the equilibrium with gas environment and by the local overpotential caused by deviations of oxygen activity from the equilibrium values. The reaction mechanism including charge transfer, oxygen adsorption and O^{2-} diffusion through the electrode bulk, was discussed in Ref.[64], assuming that these two effects can be isolated and taking into account the boundary conditions at the mixed conductor/metallic current collector contact. In the case of the overpotential-independent total conductivity, for the adsorption regime the current through the unit triple-phase boundary is interrelated with overpotential as [64]:

$$i = \left[2RT\sigma S j_0 \left(\exp\left(\frac{2F\eta_0}{RT}\right) - \frac{2F\eta_0}{RT} - 1 \right) \right]^{1/2} \quad (1.32)$$

where S is the effective electrode surface area on which the electrochemical reaction takes place, and j_0 is the exchange flux density. The adsorption becomes rate-limiting when the oxygen activity in the gas phase is reduced due to high cathodic polarization. For the retarding oxygen ion diffusion through the electrode bulk

$$i = \left(\frac{2FD_i p(O_2)^{1/m}}{d} \right)^{1/2} \cdot \left[\exp\left(-\frac{2F\eta_0}{RT}\right) + \frac{2F\eta_0}{RT} - 1 \right]^{1/2} \quad (1.33)$$

where D_i is the effective $p(O_2)$ -independent diffusion coefficient, d is the effective thickness of the diffusion layer, and the m parameter is determined by the oxygen ion formation mechanism in the mixed conductor under equilibrium conditions. When the electrochemical reaction $O + 2e^- \rightleftharpoons O^{2-}$ is the rate-limiting step, the current taken from the unit triple-phase boundary is [64]:

$$i = \left(\frac{2RTi_0 S \sigma}{F} \right)^{1/2} \cdot \left[\exp\left(\frac{F\eta_0}{RT}\right) - \exp\left(-\frac{F\eta_0}{RT}\right) \right] \quad (1.34)$$

In the extreme cases of high polarization conditions, Eqs.(1.30)-(1.34) present Tafel-like dependencies. Under the low polarization when $|2F\eta/RT| \ll 1$:

$$i = \eta_0 \cdot \left(\sigma S \frac{2F}{RT} \right)^{1/2} \cdot \left(\frac{1}{i_0} + \frac{1}{2Fj_0} + \frac{d}{2FD_i p(O_2)^m} \right)^{-1/2} \quad (1.35)$$

where the resistances of all three steps: charge transfer, oxygen adsorption and O^{2-} diffusion through the electrode bulk in series, were taken into account [32,64]. Note that in Eqs.(1.30)-(1.35)

the effective width of the layer where the electrochemical reaction occurs, is assumed much smaller than the electrode thickness.

Table 1.4

The $p(\text{O}_2)$ exponent (m) for the polarization resistance experimentally obtained for various cathodes in contact with zirconia or ceria* based electrolytes

Cathode	Microstructure	T, K	$p(\text{O}_2)$, atm	- m	Ref.
Pt	porous film or mesh	833-983	$<10^{-2}$	1/2	[64]
	point	1115	$>10^{-3}$	1/2	[65]
	point	1115	$<10^{-4}$	2/3	[65]
Pt-YSZ	porous	1273	$10^{-2} - 1$	9/10	[74]
Pd	-	-	-	1/2	[32]
Ag	point	966-1139	$>10^{-6}$	1/2	[65]
Au	point	1211	$>10^{-3}$	1/2	[65]
		1211	$<10^{-3}$	1/4	
$\text{La}_{1-x}\text{Sr}_x\text{MnO}_3$ ($x=0.1-0.4$)	point	1233	$10^{-5} - 1$	1/2	[87]
	point, after high cathodic polarization	1233	$10^{-5} - 1$	3/8	[87]
$(\text{La}_{0.82}\text{Sr}_{0.18})_{0.82}\text{MnO}_3$	porous	1123-1273	$10^{-2} - 0.21$	0.45 - 0.86 (R2)	[107]
$\text{La}_{0.85}\text{Sr}_{0.15}\text{MnO}_3$	porous	1073-1170	$10^{-3} - 1$	1/4 (R2), 1 (R3)	[108]
$\text{La}_{0.8}\text{Sr}_{0.2}\text{MnO}_3$	porous	1073-1273	$<10^{-3}$	1	[109]
	porous	1073-1273	$10^{-3} - 1$	1/2	[109]
$\text{La}_{0.8}\text{Sr}_{0.2}\text{MnO}_3$	porous	823-1073	$10^{-3} - 1$	1/6	[110]
$\text{La}_{1-x}\text{Sr}_x\text{MnO}_3$ ($x=0.3-0.7$)	porous	1073	$10^{-2}-0.5$	3/4	[88]
$\text{La}_{0.63}\text{Sr}_{0.27}\text{MnO}_3$	dense	973-1173	$10^{-3} - 1$	negative	[83]
$\text{La}_{0.81}\text{Sr}_{0.09}\text{MnO}_3$	dense	1073	$10^{-3} - 1$	0	[94]
SrMnO_3	porous	1073	$10^{-2}-0.5$	1/2	[88]
$\text{La}_{0.6}\text{Ca}_{0.4}\text{MnO}_3$	porous	>1173	$<10^{-3}$	1	[106]
	porous	973-1173	$10^{-3} - 1$	1/2	[106]
$\text{La}_{0.6}\text{Ca}_{0.4}\text{MnO}_3$	porous	1073	$6 \times 10^{-4} - 1$	1/3	[111]
$\text{La}_{1-x}\text{Sr}_x\text{CoO}_3$ ($x=0-0.7$)	porous	873-1073	$10^{-2}-0.5$	1/4	[88]
$\text{La}_{0.6}\text{Sr}_{0.4}\text{CoO}_3$	dense	1073	$10^{-4} - 1$	1/2*	[94]
$\text{Sm}_{0.5}\text{Sr}_{0.5}\text{CoO}_3$	dense	1073	$10^{-4} - 1$	1/2*	[113]
$\text{La}_{1-x}\text{Sr}_x\text{CoO}_3$ ($x=0.2-0.4$)	porous	1023	$10^{-2} - 1$	0.2 - 0.4*	[112]
$\text{La}_{1-x}\text{Sr}_x\text{FeO}_3$ ($x=0.3-0.7$)	porous	1073	$10^{-2} - 0.5$	3/4	[88]
$\text{La}_{0.6}\text{Sr}_{0.4}\text{FeO}_3$	porous	1073	$2 \times 10^{-4} - 1$	0.17	[111]
$\text{La}_{1.9}\text{Sr}_{0.1}\text{CuO}_4$	porous	1073	$10^{-3} - 1$	0.08	[111]
$\text{La}_{0.7}\text{Sr}_{0.3}\text{CrO}_3$	porous	1073	$10^{-2} - 0.5$	1/2	[88]

In the case when the overpotential affects the electronic conductivity of electrode layer, the oxygen pressure dependence can be assumed to vary as $\sigma_e = \sigma_e^0 \cdot p(\text{O}_2)^{1/v}$, where σ_e^0 is the electronic conductivity at unit $p(\text{O}_2)$. If the oxygen delivery to the reaction zone is limiting, the overpotential and oxygen pressure are interrelated by the Nernst law [64]. Then the overpotential dependence of conductivity is $\sigma_e = A^0 \cdot \exp\left(\frac{nF\eta}{vRT}\right)$, where A^0 is the equilibrium electronic conductivity of the mixed conductor. The general current-voltage relation along the TPB is expressed as [64]:

$$i = A^0 \cdot A^{1/2} \cdot \left[\frac{a_1 - a_2}{(a_1 + 2b)(a_2 + 2b)} + \frac{\exp((a_1 + 2b)\eta_0)}{a_1 + 2b} - \frac{\exp((a_2 - 2b)\eta_0)}{a_2 + 2b} \right]^{1/2} \quad (1.36)$$

where $b = \frac{nF}{vRT}$; $A = \frac{4FSj_0}{A^0}$, $a_1 = \frac{2F}{RT} - b$ and $a_2 = -b$ for the adsorption regime;

$A = \frac{8FD_i p(\text{O}_2)^{1/m} S}{A^0 d}$, $a_1 = -b$ and $a_2 = -\frac{2F}{RT} - b$ for the regime of limiting ion transport;

$A = \frac{8FD(\text{O}_2)p(\text{O}_2)S}{A^0 d}$, $a_1 = \frac{4F}{RT} - b$ and $a_2 = -b$ for the regime of limiting transport of molecular

oxygen. The sign of the b coefficient in Eq.(1.36) coincides with that of $1/v$ parameter, where positive or negative value corresponds to the p- or n-type electron transport, respectively. Often, these equations may be simplified yielding the Tafel-type polarization curves or the limiting currents, associated with reduced electronic conductivity of the electrode material under polarization [64]. In Ref.[96], the electronic conductivity was described as a function of electric potential on the mixed conductor, oxygen partial pressures and overpotentials at the cathode and anode.

The reaction mechanism represented by:



and two additional pathways with O_{ad}^- formation through $\text{O}_{2,\text{ad}}^-$ at the electrode surface or at the TPB were considered in Ref.[89] for the $\text{La}_{0.85}\text{Sr}_{0.15}\text{MnO}_{3-\delta}$ cathode. In all cases, the oxygen adsorbates were assumed diffusing along the electrode surface. The models were suggested for a single rate-determining step and for two serial processes governing the electrode kinetics, with

other steps being in virtual equilibrium [89]. In particular, when the steps Eq.(1.37b) and (1.37c) are rate-determining, the following equation was obtained:

$$i = i_{0,2} \cdot i_{0,3} \cdot \left[\exp\left(\frac{2F\eta}{RT}\right) - 1 \right] \cdot \left[i_{0,2} \cdot \exp\left(\frac{F\eta}{RT}\right) + i_{0,3} \cdot \exp\left(\frac{F\eta}{2RT}\right) \right]^{-1} \quad (1.38)$$

where $i_{0,2}$ and $i_{0,3}$ are the exchange current densities of the steps Eq.(1.37b) and (1.37c), proportional for low surface coverage to $p(\text{O}_2)^{3/8}$ and $p(\text{O}_2)^{1/4}$, respectively [89].

One of the classical methods of investigating the electrode reaction kinetics is the electrochemical impedance spectroscopy (EIS). Analysis of the electrode response with appropriate equivalent circuits reflecting the model electrochemical process, was performed, for example, in Refs.[64,67,68,77,79,87,99,100]. In this respect, the works [101,102], suggesting a general theoretical framework to study the multi-step reaction mechanisms in aqueous systems, are also worth noting. Contrary to the simple model systems with precisely determined microstructures, ascribing exact physical meaning to the equivalent circuit elements, which represent the process at the porous mixed-conducting electrode, appears quite ambiguous. This leads to difficulties in determining the oxygen reduction kinetics. The literature data on oxygen partial pressure dependencies of the total electrode polarization resistance (Table 1.4) and exchange (or limiting) current is also, in many cases, inconsistent. For the anodes based on metallic nickel, the situation seems even more complex [103,104,105].

1.4.2. Anode reactions

The general relationships for transport and charge-transfer processes, given in Chapter 1.4.1, become more complex in the case of the anode reactions where at least two components in the gas phase should be accounted. Again, as for the investigations of the cathode process, the model anode systems are widely studied, in particular metallic Pt and Ni with a high electrocatalytic activity [114]. Nonetheless, the results are relevant for the practical applications as most common anode compositions are based on Ni-YSZ cermets. The majority of these studies are focused on the oxidation of H_2 , for the sake of simplicity. There are, however, two other important reasons for the attention to H_2 -containing fuels. For most anode materials, the electrochemical activity for H_2 oxidation is higher compared to CO and CH_4 . The performance of SOFCs fueled by hydrocarbon conversion products, is primarily dependent on the content of H_2 and H_2O in the fuel gases. Also, the use of H_2 -fueled SOFCs is associated with zero emission of green house gases.

The high operation temperatures and catalytic activity of the anode materials enable internal reforming of methane in addition to the electrochemical oxidation, as noted in Chapter 1.1. The reactions Eqs.(1.5) and (1.6) are characterized by the standard enthalpies ΔH_{298}^0 of 206 and -41 kJ/mol, respectively. Although the former may be partially compensated by the exothermic

oxidation of generated H₂ and CO, Eqs.(1.2) and (1.3) [115], the presence of endothermic process Eq.(1.5) leads to large temperature gradients in and along anode structures [115]. In addition to the steam reforming of methane, CO₂ reforming may take place: CH₄+CO₂ ⇌ 2H₂+2CO, ΔH₂₉₈⁰ = 247 kJ/mol [116]. It is also important that metallic nickel may catalyze methane pyrolysis (cracking) and Boudouard reaction (CO disproportionation), both resulting in carbon formation [117]:



Progressive carbon deposition at the anode leads to performance degradation. This coking might be partially suppressed by optimizing operation temperature and pressure, increasing current density, increasing amount of steam and/or CO₂ in the fuel, and using catalytic additives ([116-122] and references cited).

As for any electrode, the reaction mechanism and the electrode properties depend on the morphology of anode layer. For the SOFC anodes, these microstructural effects are, evidently, of special importance [104,123,73]. One particular problem is that during the cell operation, irreversible changes in the morphology and TPB may occur, particularly, sintering of the electrode particles is favored at high temperatures and/or under the high current densities [64,124,125]. The key polarization characteristics measured for porous anode structures are found different from those obtained for the model point- and pattern- type systems [104,126]. The developments of SOFC anodes are therefore directed to the controlled reaction kinetics, improvement of the electrocatalytic activity, reduction of the polarization resistance and optimization of the electrode microstructure and design.

H₂-H₂O electrode

One feature of the anode processes is that the gas-diffusion limitations become very important. In particular, contrary to the oxygen reduction, the counter-diffusion of reactant(s) and product(s) should be necessarily taken into account. Mass flows in the opposite directions may not be equal, resulting in the net mass transport in one direction [91,127]. In framework of the mean transport pore model [128], assuming an isotropic porous media with the cylindrical capillary pores of average radius *r*, the isothermal gas diffusion in a multicomponent gas mixture can be described using the modified Maxwell-Stefan equation and Knudsen diffusion [115,128]. The diffusion flux is defined by the dusty gas model in a similar way [128]. The steady-state net diffusion flux of a binary gas mixture, *j*, is simplified to the form [115]:

$$j = \frac{Pc_{\text{total}}D_{AB}}{\tau L} \cdot \ln \left(\frac{D_{AB} + K_A r}{D_{AB} + K_A r \cdot M_A^{1/2} M_B^{-1/2}} \right) \quad (1.41)$$

where c_{total} is the total molar concentration of the gas mixture, L is the thickness,

$K_A = \frac{2}{3} \cdot \left(\frac{8RT}{\pi M_A} \right)^{1/2}$ is the Knudsen number of the gas A, M_A and M_B are the molecular weights of

A and B molecules. The net permeation flux density was suggested [115] to include contributions from the Knudsen flow, the slip flow at the wall, and the viscous flow. For H₂-H₂O mixture in Ni-YSZ cermet medium at 30% porosity the effective diffusion coefficient, D^{eff} , was estimated to be 10^{-2} to 10^{-1} cm²/s at 1273 K, with mean-free path of a molecule of 0.1 μm [129].

The analysis of concentration and activation contributions to the polarization of electrolyte-supporting Ni-YSZ anodes, fueled with humidified hydrogen, indicated a performance-limiting transport of gaseous species through porous electrode media [25]. The effective binary gas diffusion coefficient estimated from the polarization curves, is 0.1-0.2 cm²/s at 923-1073 K, increasing on heating.

The hydrogen oxidation mechanisms for bare Ni and Ni-YSZ composite anodes are essentially similar [123]. The H₂ oxidation kinetics on Ni-YSZ cermet was analyzed [130] studying overpotential dependencies on the current density, gas composition and temperature, using the current-interruption method; the atmosphere at the anode was modeled as a continuously stirred tank reactor. For low polarization, the charge-transfer and the surface diffusion of adsorbates were assumed to be not rate-determining. Then, under equilibrium:



Assuming that the overpotential depends on the O_{ad} coverage, the polarization curve was finally described by [130]:

$$\eta = \frac{RT}{2F} \cdot \ln \left(1 + \frac{i \cdot f \cdot K}{i \cdot S + 2F \cdot x_{\text{H}_2\text{O}} \cdot f} \right) \quad (1.43)$$

where f is the gas flow rate, K is composed from the equilibrium constant of Eq.(1.42d) and the rate constants of the backward reactions Eqs.(1.42c) and (1.42d), $x_{\text{H}_2\text{O}}$ is the mole fraction of H₂O molecules in the inlet gas, and S is the anode surface area. The anode material with a larger O coverage under equilibrium conditions was found to have a smaller overpotential [130].

The relevance of concentration polarization for the performance of Ni-YSZ anodes was stressed in Refs.[126,129]. One important case, namely the coverage-dependent diffusion limitations at high current densities, was considered in [126]; the hypothesis on the slow surface diffusion of hydrogen, dissociatively adsorbed at the metal or electrolyte surface, is in agreement with characteristic diffusion times, longer than the residence of OH⁻ and H₂O adsorbates. The competitive adsorption of the reactants and product gases was described by the Langmuir isotherm [126]:

$$\theta_i = \frac{K_i \cdot p_i}{1 + \sum_i K_i \cdot p_i} \quad (1.44)$$

where p_i is the partial pressure of i species.

A very interesting attempt of state-space modeling of (H₂-H₂O), Ni | YSZ pattern anode [105] was based on the following assumptions: (i) the electrochemical reactions take place only at Ni surface and directly at TPB, (ii) both H₂ and H₂O adsorption is nonactivated, (iii) three atom reactions are excluded as most improbable, (iv) surface diffusion is fast, and (v) gas phase limitations are absent and H₂O is involved in two surface reactions, namely Eq.(1.42c) and $H_2O_{ad} + O_{ad} \rightleftharpoons 2OH_{ad}$. The simulation of impedance data was, however, rather unsuccessful; no unambiguous conclusion could be drawn on the reaction mechanism. The authors [131] assumed, oppositely, the rate-determining step for the process on Ni-YSZ cermet to be the reaction of two H atoms adsorbed at the Ni surface and one O ad-atom at the YSZ surface, to produce water molecule at the Ni surface. Again, however, the calculated current dependencies on the H₂ and H₂O partial pressures, using the Langmuir adsorption isotherm, provide only qualitative description of the experimental data [131].

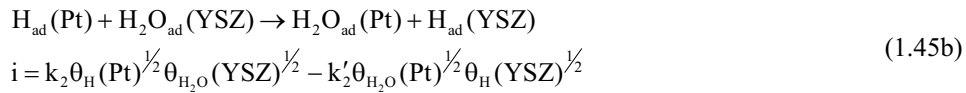
Fitting of the Ni-YSZ cermet anode polarization curves with the Nernst-type concentration equation and empirical Butler-Volmer type rate equation, suggested that the reaction is dominated by two steps, one of which is the charge-transfer reaction affected by $p(H_2O)$ and $p(H_2)$ [132]. The same conclusion was drawn analysing the impedance spectra, which consisted of two clearly separated arcs [133]. The presence of YSZ in the cermet was shown to be important for the anode microstructure and the reaction kinetics, with no effect on the anode reaction mechanism [133]. The active thickness of the Ni-YSZ cermet anode, found around 10 μm for a layer with fine microstructure, was ascribed to the ionic conductivity of YSZ network [104]. The maximum performance of Ni-YSZ (50-50 vol%) anode at 1123-1273 K was found at approximately 14% vapor content in the H₂-H₂O gas mixtures [132]. Accordingly, it was concluded [134] for H₂-H₂O fueled Ni-YSZ anode that below 1118 K, the oxidation of hydrogen atoms on the Ni surface is rate-determining. Increasing temperature accelerates the charge-transfer reaction; then an additional reaction step, possibly adsorption, becomes important for the overall kinetics.

Another one-dimensional microscopic model of an electronic conductor - ionic conductor anode, assuming steady-state conditions, uniform temperature and pressure distributions and homogeneous phases, was developed in Ref.[127]. The concentrations of reactants and products were included into the Butler-Volmer equation; the set of equations, describing the ionic and electronic transport, gas-phase diffusion in the anode layer and the electrochemical reaction at TPB, was solved numerically. Decreasing the particle size was concluded to reduce the overpotential due to larger active surface area until the certain limit when the concentration polarization starts to deteriorate electrode performance [127].

For the porous Pt electrodes, two processes were suggested as limiting, depending on the range of oxygen activity (a_{O^*}) at the YSZ surface near the TPB [70]. The first, at $a_{O^*} > 10^{-10}$, was expressed by Eq.(1.42c) with the rate equation

$$i = k_2 \theta_H (Pt)^{1/2} \theta_{OH} (YSZ)^{1/2} - k'_2 \theta_{H_2O} (Pt)^{1/2} \theta_s (YSZ)^{1/2} \quad (1.45a)$$

The second proposed process governing the kinetics when $a_{O^*} < 10^{-12}$ was:



Eqs.(1.45) were obtained, assuming a Langmuir-type adsorption and predominant H_{ad} adsorbates at Pt surface and OH_{ad} radicals at YSZ surface. The H_2 reduction mechanism on the stripe pattern Ni electrode occurred different from that on porous Pt [124]. Namely, either the dissociative adsorption, or the surface diffusion of adsorbed reactants were found rate-determining.

Table 1.5

Exponents of the polarization resistance versus $p(H_2)^m$ and $p(H_2O)^n$ dependencies for various anodes in contact with YSZ electrolyte

Anode	Microstructure	T, K	m	n	Ref.
Pt	porous	973-1073	-1/4 – 1/4	-1/2 – -1/4	[71,104]
Ni	point pattern	1248	-1/2 – 1/2	-1/2	[138]
		973-1073	0	negative	[124]
	fine cermet	1123	0 – 1/2	negative	[124]
		973	-0.24 – -0.11	-0.67 – -0.32	[137]
Ni - YSZ	coarse cermet	1273	-3/20 – 0	-1/5 – -3/10	[156]
	porous	1023-1273	~ 0		[131]
	porous	1123-1273		-1	[139]
Ni - yttria-doped TZP	porous	1123-1273	-1/10	-1/2	[132]

The anode process was modeled in [64,135] for the pattern metallic stripe electrode in H₂-H₂O or CO-CO₂ atmospheres, via various mechanisms comprising surface diffusion of H₂, H₂O or CO, CO₂ molecules, O atoms and/or electrons. The mechanisms of anodic reactions involving water vapor molecules were analyzed in Refs.[136,137].

CO-CO₂ electrode

In the CO-CO₂ atmospheres, the electrochemical reaction rate on Pt- and Ni-based electrodes is substantially lower compared to H₂-H₂O [9,77,124]. For CO oxidation on porous Pt electrode, the rate of the process Eq.(1.3) was suggested determined by the chemical reactions of adsorbed species at Pt and YSZ surfaces, identified as [140]:



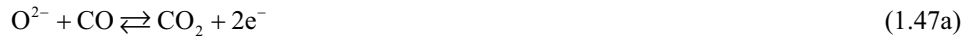
with the rate equations:

$$i = k_1 p(\text{CO})^{1/2} a_{\text{O}}^{1/2} - k'_1 p(\text{CO}_2)^{1/2} \quad (1.46c)$$

$$i = k_2 p(\text{CO}) - k'_2 p(\text{CO}_2)^{1/2} a_{\text{O}}^{-1/2} \quad (1.46d)$$

where, a_{O} is the oxygen activity at the YSZ surface near TPB, and the role of the Boudouard process becomes critical in CO-rich atmospheres.

The case when the reaction zone expands along electrolyte surface and the electrons are supplied to metal through this surface, was considered in [32,135,141], assuming fast sorption of CO and CO₂, and the reaction at the electrolyte/gas interface expressed as:



The final equations for the current per unit TPB length:

$$i = i_0^{\text{ME}} \left[\theta_{\text{e}} \exp\left(\frac{\alpha F \eta}{2RT}\right) - \exp\left(-\frac{(1+\beta)F\eta}{2RT}\right) \right] \quad (1.47b)$$

$$i = i_0^{\text{GE}} (\theta_{\text{e}}^3 - 3\theta_{\text{e}} + 2)^{1/2} \quad (1.47c)$$

are analogous to those generated in [32,135] for the process on oxygen electrode limited by diffusion of O atoms, Eqs.(1.30) and (1.31), or O⁻ ions along the electrolyte surface. In the latter case, reactions at the electrolyte/metal and electrolyte/gas interfaces were assumed to be:



In Eqs.(1.47b) and (1.47c), Θ_{e} is the electron concentration at TPB, normalized to the equilibrium value. At high anodic polarization the current may however approach the limiting value while the

cathodic polarization obeys the Tafel-like equation, probably due to inducing n-type conductivity at the electrolyte surface [32,135].

For a mixed-conducting anode layer, the polarization curves theoretically derived [64] assuming overpotential-independent total conductivity, were similar to those of the oxygen electrode, Eqs.(1.32)-(1.34), with the limiting currents depending on the CO and CO₂ (or H₂ and H₂O) pressures. In the case of overpotential-dependent conductivity, the solution for CO-CO₂ atmosphere was [64]:

$$i = A^0 \cdot A^{1/2} \cdot \left[\frac{a_1 - a_2}{(a_1 + 2b)(a_2 + 2b)} + \frac{\exp((a_1 + 2b)\eta_0)}{a_1 + 2b} - \frac{\exp((a_2 - 2b)\eta_0)}{a_2 + 2b} \right] \quad (1.49)$$

where $b = \frac{2F}{vRT}$ and v is determined from the dependence of electrode material conductivity on local partial pressures of gaseous species. When the adsorption or diffusion of CO molecules is impeded $A = \frac{2S \cdot i_{01}}{A^0}$, $a_1 = -b$ and $a_2 = -\frac{2F}{RT} - b$, while for the limiting CO₂ adsorption or diffusion $A = \frac{2S \cdot i_{02}}{A^0}$, $a_1 = \frac{2F}{RT} - b$ and $a_2 = -b$ [64].

CH₄-H₂O electrode

The electrochemical oxidation of CH₄ is characterized by slower kinetics in comparison with CO and H₂ [119,142]. The power densities produced by the lanthanum-strontium manganite (LSM) | CYO | YSZ | CYO | Ni-YSZ cathode-supported cells with Ni-YSZ anodes, fueled by wet methane, were found about 20% lower compared to humidified hydrogen fuel due to higher anode resistance [28,116]. The likely reaction path may include hydrogen generation owing to reforming of methane, circulating over the anode, with the steam produced by hydrogen oxidation at TPB [119]. Under low fuel utilization conditions, the reaction mechanism on porous Ni-YSZ anodes was suggested as methane cracking followed by the electrochemical oxidation of carbon [118]. Taking into account the competitive C and OH adsorption on the Ni surface, the optimum H₂O concentration to maximize the reforming rate corresponds to $p(\text{H}_2\text{O})/p(\text{CH}_4) = 0.25 - 0.5$; to avoid the carbon deposition, this value should be higher than 0.15 [117]. The anodic overpotential may modify electrode catalytic activity, especially at reduced temperatures (so-called NEMCA effect), increasing the rate of steam reforming and suppressing coking [117].

A significant role at intermediate temperatures can also be played by the oxidative coupling of methane [143]. This effect is mainly determined by kinetic factors [9]. Numerical simulations of the catalytic oxidation and conversion of methane over Pt anode were performed for transient one-dimensional flow configurations [143]. This formalism can be used, however, to

describe only the catalytic systems with known surface-reaction mechanism and rate constants. A comprehensive analysis of the processes related to the oxidation and oxidative coupling of methane by moderate oxygen additions, particularly over dispersed Ni catalysts, was presented in Ref.[121]. The CO₂ formation was found preferable with respect to CO when the reaction temperature decreases from 1160 down to 760 K. Completely reduced nickel catalysts showed a higher selectivity towards CO formation if compared partially reduced or oxidized [121]. The bare and Mo-doped Ni-YSZ cermets were tested in an YSZ tubular cell and showed a high activity towards methane reforming [122]. The presence of molybdenum was found to suppress the carbon deposition [122]. The mechanism of methane oxidation by oxygen over the YSZ surface was proposed in Ref.[144]. Two parallel oxidation pathways, namely the partial and total oxidation were identified [144].

Ref.[145] presents a comprehensive review of the catalytic routes for syngas and hydrogen production, including partial oxidation, autothermal reforming, combined and CO₂ reforming; the energy efficiencies of direct and indirect methane conversion are compared.

1.4.3. Role of ionic transport in electrode materials

Incorporation of the oxygen-ion conducting materials into the electrode layer results in the spatial expanding of the electrochemical reaction zone along the electrode/gas and electrode/electrolyte interfaces, thus reducing electrode overpotentials. As noted above, the electrode reaction path and rate may directly depend on the ionic conductivity (σ_o) of the electrode materials, which influences the kinetics and relative role of adsorption/desorption, charge and mass transfer at the electrode surface and in the bulk, and also the processes at electrolyte surface. However, no linear correlations between the ionic conductivity in the electrode material and specific electrocatalytic properties of porous electrode layers often observed [146,147].

Cathodes

For mixed-conducting cathode layers, at least three competitive reaction paths for oxygen reduction, including diffusion in pores with subsequent discharge at TPB, oxygen transport through the electrode bulk and along the electrode surface, may take place (Fig.1.6). Due to complexity of these processes, numerous models [17,32,64,76,77,79,81-85,87,89,94-100,106,108,109,112,113] were developed but had quite a limited applicability. Nonetheless, these models make it possible to understand particular aspects of the cathode reaction and, often, to predict the materials behavior. Among relevant examples, one should mention the continuum mass-transport model [97] to describe the competition between the surface and bulk pathways, predicting a critical role of the vacancy concentration. The results seem in a good agreement with experimental data on La₁₋

$x\text{Sr}_x\text{MnO}_{3-\delta}$ (LSM) cathodes [148]. The numerical finite element calculations showed that the reaction path including the oxygen ion transport through the bulk of a conventional mixed conductors, in favor of the surface diffusion, is rather unlikely [81,82]. In particular, the current density was found to be distributed essentially along the TPB, with the polarization resistance being almost proportional to the reciprocal TPB length. The level of ionic conductivity, which can be achieved for the common cathodes, seems insufficient for essential spatial expansion of the electrochemically-active zone into the electrode/electrolyte interface [81,82]. An opposite situation may however be observed. In the case of significant role of the oxygen exchange limitations at the electrode surface, the reaction zone may expand into the entire electrode/electrolyte interface [81,82]. For instance, for porous $\text{La}_{0.6}\text{Ca}_{0.4}\text{Fe}_{0.8}\text{Co}_{0.2}\text{O}_{3-\delta} | \text{Ce}_{0.9}\text{Sm}_{0.1}\text{O}_{2-\delta}$ cathode possessing a high level of ionic conductivity, the electrode kinetics is influenced by both surface exchange rate and the solid-state oxygen diffusion [79]. For the materials characterized by fast oxygen ion transport in the lattice, such as $(\text{La,Sr})(\text{Co,Ni})\text{O}_{3-\delta}$ or $(\text{La,Sr or Ca})(\text{Co,Fe})\text{O}_{3-\delta}$ [79,92], the oxygen penetration depth into the electrode grain may reach several microns [79]. The thickness of the electrochemically-active layer of a porous mixed-conducting cathode typically decreases with increasing rate of the surface reaction and with decreasing bulk transport of ionic or electronic defects [77]. The surface-exchange and tracer diffusion coefficients for a number of promising cathode materials are summarized in Refs.[149,150].

A comparative study of the oxygen reduction reactions on porous $\text{La}_{0.82}\text{Sr}_{0.18}\text{MnO}_3$ and $\text{La}_{0.6}\text{Sr}_{0.4}\text{Co}_{0.2}\text{Fe}_{0.8}\text{O}_3$ electrodes at 973-1173 K in air showed that for the manganite cathode, with a lower ionic conductivity, the reaction is controlled by the oxygen dissociative adsorption and surface diffusion at reduced temperatures, and by the oxygen ion migration into zirconia electrolyte at higher temperatures [17]. Both the surface and bulk diffusion processes provide significant contributions to the overall reaction kinetics on $(\text{La,Sr})(\text{Co,Fe})\text{O}_3$ electrodes [17]. At 873 K, $\text{La}_{0.8}\text{Sr}_{0.2}\text{Co}_{0.8}\text{Fe}_{0.2}\text{O}_3$ and $\text{LaFe}_{0.5}\text{Ni}_{0.5}\text{O}_3$ materials having the higher oxygen ion mobility than the manganite-based cathodes, showed sufficiently high performance in contact with $\text{Ce}_{0.8}\text{Gd}_{0.2}\text{O}_{2-\delta}$ electrolyte [43]. The electrochemical activity as a function of transport properties of the cathode material is discussed using the examples of Pt, Au, Ag, $\text{La}_{0.8}\text{Sr}_{0.2}\text{MnO}_3$ and $\text{La}_{0.84}\text{Sr}_{0.16}\text{CoO}_3$ in contact with 20 mol% Sm- or Gd-doped ceria electrolyte [96], and Pt, $(\text{La}_{0.6}\text{Sr}_{0.4})_{0.9}\text{MnO}_3$, $(\text{La,Sr})\text{CoO}_3$, $\text{Sm}_{0.6}\text{Sr}_{0.4}\text{CoO}_3$, $\text{La}_{0.6}\text{Sr}_{0.4}\text{FeO}_3$ and $\text{La}_{0.75}\text{Sr}_{0.25}\text{CrO}_3$ electrodes applied onto $\text{La}_{0.9}\text{Sr}_{0.1}\text{Ga}_{0.8}\text{Mg}_{0.2}\text{O}_{3-\delta}$ [29]. In agreement with other works (Chapter 1.5.1), better performance is observed for the electrodes exhibiting a faster ion transport. For example, the overpotentials of the cobaltite cathode were found about 6 times lower than those of manganite, at 973 K [96].

The electrochemical characteristics of $\text{La}_{0.81}\text{Sr}_{0.09}\text{MnO}_3$ and $\text{La}_{0.6}\text{Sr}_{0.4}\text{CoO}_3$ electrodes of various microstructures were studied in contact with YSZ or samaria-doped ceria electrolytes

[94,150]; a large surface area and a high ionic conductivity of the cathodes promote oxygen reduction. The gas/electrode interfacial processes are especially important for the cobaltite-based electrodes [27,151].

At temperatures below 1073 K, the rate-determining steps for oxygen reduction on $\text{La}_{1-x}\text{Sr}_x\text{BO}_3$ (B = Cr, Mn, Fe, Co) layers, sputtered onto YSZ ceramics, were identified as the charge-transfer process for the cobaltites, the dissociation of oxygen molecules on the surface of ferrites and manganites, and oxygen diffusion along the surface of $(\text{La,Sr})\text{CrO}_3$ electrode [88]. The performance of the sputtered electrodes at fixed x increases in the sequence $\text{Cr} < \text{Fe} < \text{Mn} < \text{Co}$. The high cathodic activity of $(\text{La,Sr})\text{CoO}_3$ films was attributed to a large effective reaction zone due to the high oxygen ionic conductivity and catalytic activity of the electrode material, while the poor electrode properties of chromite were suggested to result from the low oxygen ion diffusivity [88]. Note that the activity of LaBO_3 towards the oxygen evolution reaction in liquid electrolytes may be related to the electronic configuration of B-site cations [152].

A dense $\text{La}_{0.63}\text{Sr}_{0.27}\text{MnO}_3$ layer applied onto the YSZ electrolyte was used to clarify the effects of oxygen ionic and electronic conductivities of the cathode material on the oxygen reduction kinetics [83]. The results were found quite different from those obtained for similar cathodes with other microstructures (Table 1.4). The polarization of porous $(\text{La,Sr})\text{MnO}_3$ cathodes was drastically reduced by Sr doping, which has no essential effect in the case of dense electrode layers [153]. This confirms that oxygen reduction on the cathodes with rather low ionic conductivity is limited by the surface rather than bulk transport. The adsorption/desorption kinetics was found dominating the oxygen reduction on both $\text{La}_{0.6}\text{Sr}_{0.4}\text{CoO}_3$ [94] and $\text{Sm}_{0.5}\text{Sr}_{0.5}\text{CoO}_3$ [113] dense cathodes. At the same time, the latter material has a higher ionic conductivity, and exhibits smaller overpotentials. The electrode resistance of porous $(\text{La,Sr})\text{CoO}_3$ layers decreases with increasing vacancy diffusion coefficient [112].

One should note that the ionic conductivity in the cathode layer is affected by both $p(\text{O}_2)$ and overpotential, as it was mentioned in Chapter 1.4.1. This complicates theoretical studies of the ionic transport effects on the cathode performance and their experimental validation. Moreover, the processes of surface exchange and charge transfer reactions, occurring at the gas/cathode and cathode/electrolyte interfaces respectively, are often inter-correlated. This is due to the well-known correlation between bulk ionic conductivity and surface exchange parameters [150], and to the effects of ionic charge carrier concentration on the interfacial exchange rate. The nature of contact between the mixed conductor and electrolyte is also of key importance [77], particularly, when blocking layers may form. In other words, the reaction kinetics is determined by both bulk and interface properties of the cell components, both electrode and electrolyte, and their interaction. For instance, the results on $\text{La}_{1-x}\text{Sr}_x\text{MnO}_{3\pm\delta}$ | YSZ cathodes with $x = 0.1-0.4$ at 973-1273 K and oxygen

pressures of 10^{-5} -1 atm [154] suggest no unambiguous relation of their electrochemical activity and equilibrium nonstoichiometry probably as a result of different fabrication methods and firing temperatures varying from 1473 to 1673 K.

Anodes

The conventional anode materials for SOFCs are the cermets of electronically conducting Ni and ionically conducting YSZ; the latter is added into electrode layer to prevent sintering of Ni particles, to elongate the electrochemical reaction zone, to match the thermal expansion, and to increase stability with respect to redox cycling. For example, no significant sintering of yttria-stabilized zirconia was observed in Ni-YSZ anodes after 4000 h at 1273 K [155]. Note however, that it is often difficult to separate the effects caused by enhanced ionic conductivity, improved electrical contacts between the metallic grains and the changes in catalytic behavior caused by such additions.

Stabilized zirconia was suggested to play an important role in the formation of well-developed microstructure of Ni-based anodes and to improve the fuel oxidation kinetics, without essential influence on the reaction mechanism [123,133]. The extension of electrochemically active zone, up to 10-20 μm from the electrolyte surface at 1273 K, relates presumably to the conductivity of YSZ network [104,156]. The enhanced oxygen supply at the anode side should promote water decomposition by trapping H atoms at the surface to produce hydroxyle radicals [105]. The high-frequency response in the impedance spectra of these anodes was attributed to the charge-transfer process from Ni to YSZ in combination with the ionic resistivity of YSZ grains [156]. The use of $\text{Zr}_{0.94}\text{Y}_{0.06}\text{O}_2$ instead of $\text{Zr}_{0.85}\text{Y}_{0.15}\text{O}_2$ (Fig.1.7) slightly decreases polarization of Ni-YSZ cermets with comparable microstructures [157], despite the lower ionic conductivity of partially-stabilized zirconia.

Incorporation of catalytically-active pure or partially substituted ceria was proved to enhance the performance of conventional anode cermets [8,19,20,43,157-161]. The use of doped cerium dioxide, having a significant mixed ionic-electronic conductivity under reducing conditions [43], might be even advantageous with respect to undoped $\text{CeO}_{2-\delta}$ [157]. As for Ni-stabilized zirconia anodes, the cermets comprising doped ceria show improved performance compared to the pure nickel, at least due to a reduced diffusion overpotential, which results from the enhanced effective electrode area [19].

Despite the higher ionic and electronic conductivity (Fig.1.4), the polarization resistance of Ni-CGO anodes was found, however, higher than that of Ni-YSZ cermets with the same volume fraction of nickel, 40 vol% [162], probably due to the insufficient thermomechanical stability of the former materials. The likely reason relates to extensive volume changes caused by the oxygen

partial pressure or current variations; excessively large concentrations of ceria-based components in the cermets may, therefore, have an unfavorable effect. On the contrary, stabilized zirconia possesses essentially constant oxygen stoichiometry and, hence, volume under the anode operation conditions, but insufficient ionic conductivity in the intermediate-temperature range.

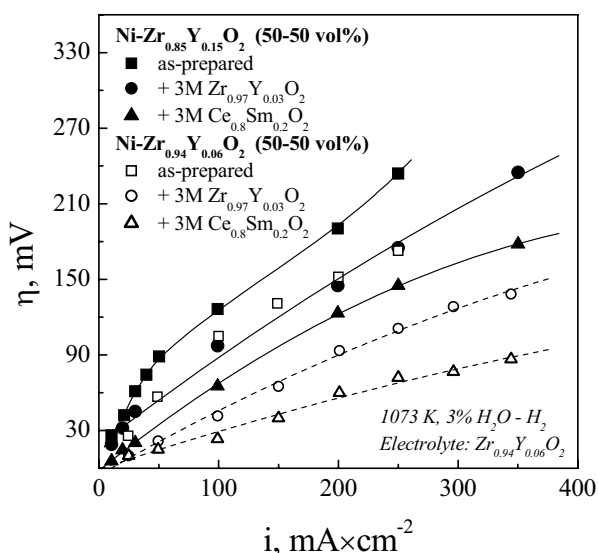


Fig.1.7. Current dependencies of overpotential for Ni-YSZ anodes before and after impregnation with 3M nitrate solutions containing zirconium and yttrium or cerium and samarium cations [157]. “M” denotes the molar concentration.

Although the ceria-based oxides might be, in principle, used as anode materials without any metallic component [159], the presence of metallic phase seems still necessary to maintain a sufficient level of the electronic transport. Note that, even under strongly reducing conditions, the total electrical conductivity of doped cerium dioxide is several orders of magnitude lower than that of Ni. As a result, the performance of ceria-based anode layers is usually worse if compared to the cermets containing the same oxides [162]. The incorporation of even small amounts (1-3 wt%) of dispersed Ni on the surface of mixed-conducting anodes enhances the electrode performance [162].

A comparative study of Ni - Zr_{0.85}Y_{0.15}O_{1.93}, Ni - Ce_{0.9}Gd_{0.1}O_{1.95}, Ce_{0.6}Gd_{0.4}O_{1.8}, La_{0.75}Sr_{0.25}Cr_{0.97}V_{0.03}O_{3-δ} and Zr_{0.71}Y_{0.12}Ti_{0.17}O_{1.94}, all having different levels of oxygen ion conduction, was reported [162]. For the mixed-conducting oxide anodes, the higher ionic conductivity decreases the total electrode polarization resistance. A similar correlation between the ionic conductivity in the cermet layers made of 5 wt% Ni - Ce_{0.8}Sm_{0.2}O_{2-δ}, Ni - Ce_{0.8}Gd_{0.2}O_{2-δ}, Ni - Nd_{0.9}Ca_{0.1}Ga_{0.9}Co_{0.1}O_{3-δ}, Ni - La_{0.9}Sr_{0.1}Ga_{0.8}Mg_{0.115}Co_{0.085}O_{3-δ}, Ni - Gd₂Ti₂O₇ and pure Ni, and their anodic overpotential was found in Ref.[19]. In principle, further improvement of the electrode activity could be expected from replacement of YSZ, playing a stabilizing role with respect to redox cycling and Ni sintering under the anode operation conditions, with alternative materials having a higher electrocatalytic activity and/or ionic conductivity.

1.4.4. Effects of solid electrolyte surface

The ionic and electronic conductivities of the solid electrolyte material are relevant not only to the ohmic losses and leakage current of the cell, respectively. The electrolyte properties have also a strong influence on the electrochemical processes (see, e.g. [163-165]). As a general rule, the electrode polarization resistance increases with the electrolyte total resistance [20,76,163,165-167]; several typical examples are given in Fig.1.8. This relationship was theoretically explained by the non-uniform electrode theory [76] with locally variable R_{η} due to discrete contacts of electrode assembled with the electrolyte surface. The effect of the ionic current distribution at the electrolyte surface on the population of active sites for oxygen incorporation was mentioned in Ref.[168].

Whatever the current distribution, the overall exchange rate is a function of the oxygen-vacancy and electron concentrations and mobilities at the electrolyte surface, depending on the electrolyte composition, oxygen pressure and temperature. As mentioned above, all solid electrolytes possess some electronic conductivity, the type and level of which at the surface should be sensitive to the overpotential. Therefore, the concentration of electrons or electron holes at the surface layers of solid electrolyte may substantially differ from that in the material bulk [169]. The same statement is true for the vacancies since oxygen molecules adsorb from the gas phase at the solid electrolyte surface directly filling vacant sites or through the intermediate complex (O , V_o^{\bullet}) (see [167] and references cited). Nevertheless, the surface and bulk charge-carrier concentrations are expected to correlate.

The oxygen ionic conductivity of the electrolyte was shown to affect the electrode kinetics of various metallic cathodes, although for zirconia-based materials with relatively similar properties these differences are found insignificant [65]. The latter observation contradicts, however, to the data of other authors (e.g. [20,76,163]). Minor (0.03 mol%) doping of (La,Sr)(Ga,Mg)O₃ material with iron, increasing ionic and electronic transport, leads to lower ohmic losses and anode overpotentials [164]. 10 mol% doping of YSZ solid electrolyte with variable-valence cations, such as Pr, Mn, Fe and Co, decreases the cathodic polarization of platinum layers 2-10 times with respect to pure YSZ at 1073 K; cobalt incorporation is most effective [170]. This behavior can be attributed, at least partly, to the spreading of the electrode reaction zone due to the enhanced electronic conductivity of the electrolyte surface [170].

A direct correlation between the ionic conductivity of the electrolyte material and the cathode polarization resistance was revealed for metallic electrodes in contact with stabilized zirconia, doped thoria and ceria electrolytes ([169] and references cited) and for the mixed-conducting $Ln_{0.7}Sr_{0.3}Co_{0.7}Fe_{0.3}O_{3-\delta}$ applied onto the $Bi_{1.5}Y_{0.5}O_3$, $BaCe_{0.8}Gd_{0.2}O_3$, $Ce_{0.9}Sr_{0.1}O_2$ and YSZ electrolytes [165]. Such behavior was explained in terms of rate-determining charge transfer

process at the electrode/electrolyte interface [165], and in terms of electrocatalytic properties of the electrolyte surface [169]. The influence of ionic conductivity in zirconia solid electrolytes doped with ytterbia or yttria, on the polarization characteristics of Pt or $\text{La}_{0.85}\text{Sr}_{0.15}\text{MnO}_3$ cathodes was studied in [163]. The exchange current density was found to increase proportionally to the ionic conductivity of the solid electrolyte material, at least below 1173 K; the transport of O^{2-} ions at the electrode/electrolyte interface was suggested to dominate the cathode performance when the exchange at the surface is sufficiently fast [163]. A similar behavior was observed by the same authors [20] for $\text{Ce}_{0.8}\text{Sm}_{0.2}\text{O}_2$ -based anodes applied onto Sc-, Yb- and Y-stabilized zirconia electrolytes with different levels of ionic conductivity, in H_2O - H_2 atmospheres.

The surface oxygen exchange coefficients of the doped ceria are higher than those of zirconia ceramics [150]. At 1073 K, the polarization resistances of $\text{La}_{0.6}\text{Sr}_{0.4}\text{MnO}_{3\pm\delta}$ cathode and Ni-YSZ (20-80 wt%) anode were reduced by a factor of 3-21 and 6-150, respectively, by using doped ceria electrolyte or ceria-containing composite [166]. Qualitatively similar results were obtained for the layered cells of ceria-based electrolyte with YSZ protective layer at the fuel side [167].

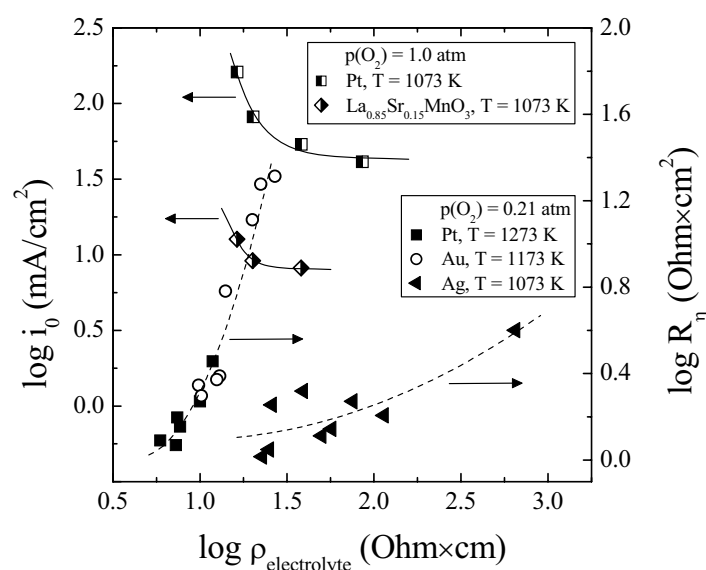


Fig.1.8. Polarization resistance [163] and exchange current density [76] of metallic and oxide electrodes vs. electrolyte resistivity controlled by the Ln^{3+} doping in $(\text{Zr,Ln})\text{O}_2$.

The effects of electrolyte composition on the electrode performance may also originate from the materials chemical interaction, resulting in the formation of ionically-insulating phases limiting oxygen transfer [112,146]. One classical example is related to the $(\text{La,Sr})\text{BO}_{3-\delta}$ ($\text{B} = \text{Mn}, \text{Fe}, \text{Co}$) perovskites reacting with YSZ to form lanthanum and strontium zirconates [89,111,112].

No blocking layers are expected in the case of doped ceria [146] where, however, the cation interdiffusion decreases ionic conductivity of the electrolyte surface [43]. The diffusion of transition metal cations increases electronic and, for LSGM, ionic conductivities, promoting oxygen exchange; a similar influence is often observed when Ba^{2+} is incorporated into the lanthanum gallate lattice [112,164,168,170,172]. The latter trend explains high performance of $(\text{La,Ba})\text{CoO}_{3-\delta}$ cathodes in contact with Co-substituted $(\text{La,Sr})(\text{Ga,Mg})\text{O}_3$ [173]. Note that a relatively high performance of $\text{Pr}_{0.8}\text{Sr}_{0.2}\text{CoO}_{3-\delta}$ cathodes on $\text{Ce}_{0.9}\text{Gd}_{0.1}\text{O}_{2-\delta}$ at 973-1173 K, which was up to 2-4 times lower than in contact with YSZ, can also be partly ascribed to a negligible interaction in the former case [174]. Finally, the electrode performance is often influenced by impurities on the electrolyte surface. The results of $^{16}\text{O}/^{18}\text{O}$ exchange [175] suggest that the surface oxygen exchange of YSZ decreases linearly with the increasing content of impurity oxides, particularly SiO_2 , CaO and Na_2O , accumulated at the outermost surface layer.

1.4.5. Effect of current collection

The influence of current path constrictions on the ohmic and overpotential losses was clearly demonstrated using Pt mesh current collectors of different geometric spacing [78]. Both types of polarizations increase on decreasing contact area [78]. This dependence is influenced by the electrode microstructure and the current collector properties [78]. Assuming that the mean conduction path from current collector through the cathode layer to the solid electrolyte is 1/6 of the distance between neighboring Pt wires, the in-plane resistance of the cathode layer, R^c , can be estimated as [76]:

$$R^c = \frac{\rho^c}{12N^c \cdot \delta^c} \quad (1.50)$$

where ρ^c is the specific resistivity of a porous cathode layer, N^c is the number of square grids per unit area of cathode, and δ^c is the cathode thickness. A small effective electrode area and inhomogeneous current distribution is expected for the electrodes with an insufficiently large number of three-phase contacts either with electrolyte or with current collector, resulting in a smaller in-plane electrode resistance and a higher ohmic loss in the electrolyte [78]. These situations are schematically illustrated in Fig.1.9. Higher conductivity of the electrode layer makes it possible to use rarefied current collector.

In the case of relatively thick porous electrodes, the electrode layer itself can effectively collect the current [80]. Increasing the thickness above a critical limit leads however to higher electrode polarization, while the ohmic losses (primarily due to the electrolyte resistivity) tend to a plateau [78]. Therefore, an optimized microstructure comprising one ultra-thin mixed conductor layer covered by a porous current-collecting layer of coarse grains was suggested for the IT SOFC

cathodes [80]. The electronic conductivity of the mixed-conducting layer should be higher than 1 S/cm [80].

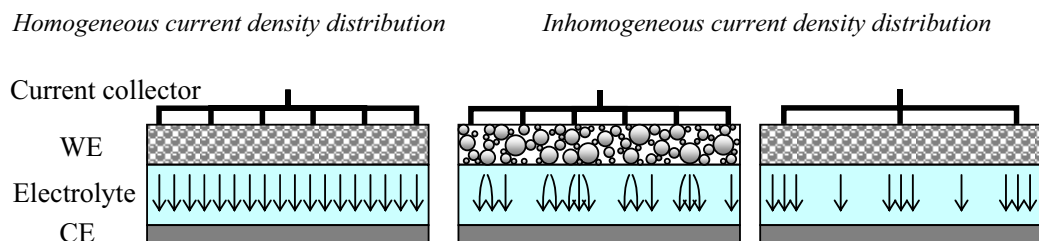


Fig.1.9. Schematic drawing of current distributions in the electrolyte, depending on the cathode microstructure and current collector geometry [78]. The flow of oxygen ions is shown by arrows.

Effects of the contact area between $\text{Pr}_{0.80}\text{Sr}_{0.2}\text{MnO}_{3\pm\delta}$ cathode, Pt or Ag meshes or Ag foils were assessed in Ref.[176]. Although the influence of a current collecting material was not considered, increasing the contact area from 4.6 to 27.2 % decreased the cell resistance by 7.5 times, and increased the power density by 4 times. In agreement with earlier work [78], the constriction effect was suggested due to discrete contacts between the electrode and current collector; the contact area affected both ohmic resistance and overpotential [176]. The polarization resistance of dense In_2O_3 electrodes decreased after deposition of Pt on the surface instead of using one Pt wire [177], probably owing to similar reasons.

Another necessary comment is that volatilization of current collector components may lead to the electrode degradation, particularly due to partial blocking of surface and TPB. This has a critical importance for the cells with oxidation-resistant alloys containing chromium, which tends to volatilize in the form of oxide- and oxy-hydroxide compounds [178,179].

1.5. Electrode materials for IT SOFCs

Despite the effects of electrode microstructure, cell fabrication conditions and solid electrolyte surface, the electrode performance is still dominated, first of all, by the properties of electrode materials determined by their chemical composition and structure. In the next Chapters, the materials relevant for the practical applications due to adequate electrochemical activity, conductivity and stability under the operation conditions are mainly considered. Fig.1.10 compares the total conductivity levels in several perovskite-related phases, representative for the corresponding groups of electrode materials.

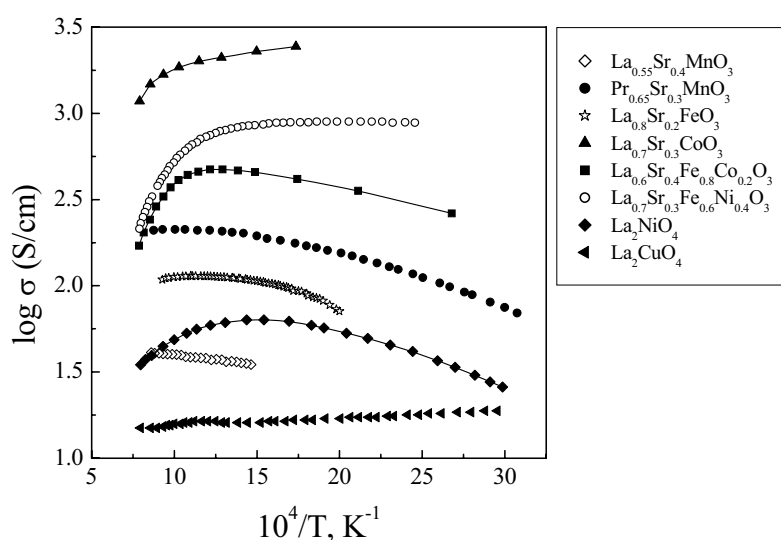


Fig.1.10. Temperatures dependencies of the total conductivity for various perovskite-related ceramics in air [188,224,227,228,257,258,288].

1.5.1. Cathodes

1.5.1.1. Manganites

Perovskite-type manganites $(Ln,A)MnO_{3\pm\delta}$ (Ln = lanthanoid or Y; A = Ca, Sr, Ba, Pb, Cd) possess a substantial level of the electronic conductivity and thermal expansion compatible with stabilized zirconia electrolytes [146,180], making them attractive as cathodes for high-temperature cells. In fact, lanthanum-strontium manganites are state-of-the-art cathode materials of SOFCs operating at 1173-1273 K.

Formation of perovskite-like $LnMnO_{3\pm\delta}$ phases was established for all the Ln-Mn-O systems, except for $Ln = Ce$ ([146] and cited references). Ilmenite-type $LnMn_2O_5$ are stable in air up to 1370 K for $Ln = Nd, Sm, Eu, Gd, Tb, Dy, Ho$, and up to 1270 K for $Ln = Er, Yb, Lu, Y$. Only the perovskite-type solid solutions with a relatively large range of oxygen stoichiometry and A:B

cation ratio variations are known to exist under oxidizing conditions in the $\text{La}_2\text{O}_3\text{-MnO}_x$ system. Doping of $\text{LnMnO}_{3+\delta}$ with divalent metal cations (Ca, Sr, Ba, Pb) leads to increasing Mn^{4+} concentration, which determines the electrical and magnetic properties of the manganites [146,181-183]. The solubility limit of Ca, Sr, Ba and Pb in the perovskite lattice of $\text{Ln}_{1-x}\text{A}_x\text{MnO}_{3-\delta}$ (Ln = La, Pr, Nd, Sm, Gd) corresponds to x varying from 0.4 to 0.7 [146,182,184,185]. $\text{Ln}_{0.6}\text{Sr}_{0.4}\text{MnO}_{3-\delta}$ (Ln = Y, Yb) were also reported as single perovskite-type phases [186]. $\text{Ce}_{1-x}\text{Sr}_x\text{MnO}_3$ perovskites were obtained at x = 0.1-0.3 [187]. When the alkaline-earth dopant concentration in $\text{Ln}_{1-x}\text{A}_x\text{MnO}_{3-\delta}$ is low, 0-20 mol%, A-site substoichiometry increases the stability of perovskite crystal lattice, while the rare-earth oxide may isolate from the nominally cation-stoichiometric compositions ([188,189] and references cited). $(\text{Ln,A})_2\text{MnO}_4$ with K_2NiF_4 -type structure may form after reduction of the respective perovskites [146,190]. One possible exception relates to $(1.2 < x < 1.5)$, which can be synthesized via annealing in air at 1623 K [190].

The perovskite manganites possess predominantly electronic and rather negligible oxygen-ionic conductivity; their transport properties and electrode activity of manganite perovskites is strongly dependent on the nonstoichiometry. The electrocatalytic effect under high cathodic polarization is usually attributed to the additional oxygen vacancy generation at the electrode surface [87,148,191]. The $\text{La}_{1-x}\text{Sr}_x\text{MnO}_{3\pm\delta}$ phases are characterized by oxygen-hyperstoichiometry of 0.02-0.11 at x = 0-0.2 in air below 1273 K [146,154]. Electronic conduction in $\text{LnMnO}_{3+\delta}$, typically occurring via hole hopping, increases with Ln^{3+} cation radius [146].

The electrical conductivity and Seebeck coefficients of the $\text{Ln}_{1-x}\text{A}_x\text{MnO}_{3\pm\delta}$ solid solutions at moderate A^{2+} concentrations increase with x, in a good correlation with the fraction of Mn^{4+} ions [146,147,182,183]; typical trends are illustrated by Figs. 1.11 and 1.12. The maximum conductivity, corresponding to the x values of 0.2-0.5, shifts towards lower dopant concentrations on heating. Further increase in x leads to decreasing conductivity, which is associated with decreasing mobility of the electronic charge carriers and in some cases an apparent transition from p- to n-type and/or secondary phase segregation [146]. In the series $\text{Ln}_{0.7}\text{Sr}_{0.3}\text{MnO}_{3\pm\delta}$ (Ln = La, Pr, Nd, Sm and Gd), the highest conductivity corresponds to $\text{Nd}_{0.7}\text{Sr}_{0.3}\text{MnO}_{3\pm\delta}$ above 760 K and to $\text{Pr}_{0.7}\text{Sr}_{0.3}\text{MnO}_{3\pm\delta}$ at lower temperatures [181].

A summary of the average thermal expansion coefficients of manganite ceramics is given in Table 1.6. Notice that both the TEC and electrical conductivity values are often influenced by the sample pre-history [146,180]. Decreasing rare-earth cation radii in $\text{Ln}_{1-x}\text{A}_x\text{MnO}_{3\pm\delta}$ (at fixed A^{2+} concentration) suppresses the lattice expansion on heating. For the solid solutions with the maximum conductivity, the TECs are sufficiently close to those of stabilized zirconia electrolytes (Tables 1.3 and 1.6). An optimum TEC compatibility of $\text{Ln}_{1-x}\text{Sr}_x\text{MnO}_{3\pm\delta}$ with stabilized zirconia

electrolytes increases from $x = 0.1-0.15$ for $\text{Ln} = \text{La}$, and to $x = 0.3-0.5$ for Gd-containing manganites [181].

Table 1.6

Average linear thermal expansion coefficients $\bar{\alpha}$ of manganite ceramics in air
[43,63,146,147,181-183,186,192,199,204]

Composition	T, K	$\bar{\alpha} \times 10^6, \text{K}^{-1}$	Composition	T, K	$\bar{\alpha} \times 10^6, \text{K}^{-1}$
$\text{La}_{0.99}\text{MnO}_3$	300-1370	11.2	$\text{Pr}_{0.80}\text{Sr}_{0.20}\text{MnO}_3$	300-1270	9.6
$\text{La}_{0.94}\text{Sr}_{0.05}\text{MnO}_3$	300-1370	11.7		300-1270	10.1
$\text{La}_{0.89}\text{Sr}_{0.10}\text{MnO}_3$	300-1370	12.0	$\text{Pr}_{0.75}\text{Sr}_{0.25}\text{MnO}_3$	300-1170	10.2
$\text{La}_{0.79}\text{Sr}_{0.20}\text{MnO}_3$	300-1370	12.4	$\text{Pr}_{0.70}\text{Sr}_{0.30}\text{MnO}_3$	300-1270	10.6
	300-1270	11.1		300-1070	11.1
$\text{La}_{0.69}\text{Sr}_{0.30}\text{MnO}_3$	300-1370	12.8	$\text{Pr}_{0.65}\text{Sr}_{0.30}\text{MnO}_3$	300-1270	11.6
$\text{La}_{0.65}\text{Sr}_{0.30}\text{MnO}_3$	300-1270	12.3	$\text{Pr}_{0.60}\text{Sr}_{0.40}\text{MnO}_3$	570-1270	12.0
$\text{La}_{0.69}\text{Sr}_{0.30}\text{MnO}_3$	300-1270	12.0		300-1270	11.6
$\text{La}_{0.50}\text{Sr}_{0.40}\text{MnO}_3$	300-1100	11.3	$\text{Pr}_{0.50}\text{Sr}_{0.50}\text{MnO}_3$	300-1270	12.2
$\text{La}_{0.50}\text{Sr}_{0.30}\text{MnO}_3$	300-1100	12.3	$\text{Pr}_{0.70}\text{Ca}_{0.30}\text{MnO}_3$	570-1270	11.9
$\text{La}_{0.30}\text{Sr}_{0.50}\text{MnO}_3^*$	300-1100	11.9	$\text{Nd}_{0.80}\text{Sr}_{0.20}\text{MnO}_3$	300-1270	9.6
LaMnO_3	320-580	7.7	$\text{Nd}_{0.75}\text{Sr}_{0.25}\text{MnO}_3$	300-1170	10.7
	580-1100	11.8	$\text{Nd}_{0.70}\text{Sr}_{0.30}\text{MnO}_3$	300-1270	10.3
$\text{La}_{0.90}\text{Sr}_{0.10}\text{MnO}_3$	300-1270	9.9		300-1070	11.1
$\text{La}_{0.80}\text{Sr}_{0.20}\text{MnO}_3$	300-1270	11.2	$\text{Nd}_{0.65}\text{Sr}_{0.30}\text{MnO}_3$	300-1270	9.7
	340-540	7.7	$\text{Nd}_{0.60}\text{Sr}_{0.40}\text{MnO}_3$	300-1270	11.2
$\text{La}_{0.70}\text{Sr}_{0.30}\text{MnO}_3$	300-1270	11.7	$\text{Nd}_{0.50}\text{Sr}_{0.50}\text{MnO}_3$	300-1270	12.1
$\text{La}_{0.60}\text{Sr}_{0.40}\text{MnO}_3$	570-1270	13.0	$\text{Nd}_{0.50}\text{Ca}_{0.50}\text{MnO}_3$	500-1200	11.3
	320-1100	11.7	$\text{Sm}_{0.70}\text{Sr}_{0.30}\text{MnO}_3$	300-1270	9.9
	300-1100	11.3	$\text{Sm}_{0.60}\text{Sr}_{0.40}\text{MnO}_3$	300-1270	10.4
	300-1270	12.0	$\text{Sm}_{0.50}\text{Sr}_{0.50}\text{MnO}_3$	300-1270	11.4
$\text{La}_{0.50}\text{Sr}_{0.50}\text{MnO}_3$	300-1100	12.1	$\text{Gd}_{0.80}\text{Sr}_{0.20}\text{MnO}_3$	300-1270	3.8
	300-1270	12.2	$\text{Gd}_{0.70}\text{Sr}_{0.30}\text{MnO}_3$	300-1270	9.5
	320-1100	12.3	$\text{Gd}_{0.65}\text{Sr}_{0.30}\text{MnO}_3$	300-1270	9.9
$\text{La}_{0.80}\text{Ca}_{0.20}\text{MnO}_3$	320-520	6.3	$\text{Gd}_{0.60}\text{Sr}_{0.40}\text{MnO}_3$	300-1270	10.2
	550-1050	10.6	$\text{Gd}_{0.50}\text{Sr}_{0.50}\text{MnO}_3$	300-1270	10.9
$\text{La}_{0.60}\text{Ca}_{0.40}\text{MnO}_3$	350-1050	9.3	$\text{Gd}_{0.50}\text{Ca}_{0.50}\text{MnO}_3$	300-1070	10.0
$\text{La}_{0.50}\text{Ca}_{0.50}\text{MnO}_3$	350-1050	10.7	$\text{Yb}_{0.50}\text{Ca}_{0.50}\text{MnO}_3$	300-1100	10.2
$\text{La}_{0.60}\text{Pb}_{0.40}\text{MnO}_3$	550-1100	9.2	$\text{Y}_{0.50}\text{Ca}_{0.50}\text{MnO}_3$	450-670	3.0
$\text{La}_{0.50}\text{Pb}_{0.50}\text{MnO}_3$	300-1100	10.4		670-1100	9.1

*manganese oxide phase impurities

The acceptor-type doping into the A-site of $\text{LaMnO}_{3+\delta}$ substantially reduces the cathodic polarization, Figs.1.11 and 1.12. Dependencies of the electrode polarization resistances and overpotentials of $\text{Ln}_{1-x}\text{A}_x\text{MnO}_{3\pm\delta}$ on the alkaline-earth cation concentration exhibit a minimum at $x = 0.3-0.7$ at 1073-1273 K, which shifts, in general, to lower dopant concentrations when temperature or A-site cation radius increases. The most widely used cathodes of SOFC are, however, $(\text{La}_{1-x}\text{Sr}_x)_{1-y}\text{MnO}_{3\pm\delta}$ with $x = 0.10-0.30$ and $y = 0-0.20$ due to a better thermal expansion matching with YSZ (Tables 1.3 and 1.6). Introducing deficiency in A-sublattice of manganites increases their cathode performance [146,147,188,189,193], a result of suppressed chemical reactivity with zirconia electrolyte higher vacancy content, and, often, faster ionic conduction in the electrode material. The latter seems less important, since the electrochemical properties of manganite-based electrode layers are weakly dependent on oxygen ion transport [147]. The minimum overpotentials correlate usually with the values of total electrical conductivity, Figs.1.11 and 1.12.

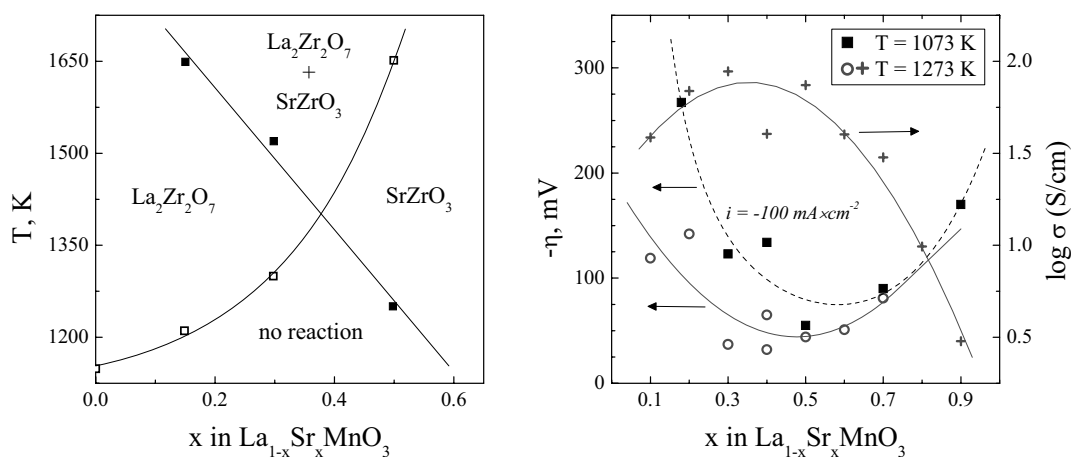


Fig.1.11. Approximate temperatures corresponding to the start of extensive interaction between $\text{La}_{1-x}\text{Sr}_x\text{MnO}_3$ and ZrO_2 , forming $\text{La}_2\text{Zr}_2\text{O}_7$ or SrZrO_3 (left) [194]. Cathodic overpotentials [17,88,185,186] and conductivities in air [185] of $\text{La}_{1-x}\text{Sr}_x\text{MnO}_3$ (right).

One of the most important factors determining the performance of $\text{Ln}_{1-x}\text{A}_x\text{MnO}_{3\pm\delta}$ manganite cathode layers is their interaction with zirconia ceramics during the cell fabrication and operation, resulting in the formation of AZrO_3 -based perovskite and $\text{Ln}_2\text{Zr}_2\text{O}_7$ pyrochlore layers. This increases both the ohmic losses due to the low conductivity of the products, and the polarization losses due to blocking of oxygen transfer [194]. In the LaMnO_3 -YSZ system, $\text{La}_2\text{Zr}_2\text{O}_7$ starts to form already at 1170 K, Fig.1.11 (left). As an example, annealing the cells with $\text{La}_{1-x}\text{A}_x\text{MnO}_{3\pm\delta}$ ($\text{A} = \text{Ca}$ and Sr , $x = 0.0-1.0$) electrode layers and YSZ electrolyte at 1473 K resulted in

higher overpotentials [185]. The porous $\text{La}_{0.85}\text{Sr}_{0.15}\text{MnO}_{3-\delta}$ electrode fired at 1573 K onto the YSZ surface, showed a worse electrochemical activity compared to cathodes sintered at 1373 and 1473 K [89]. The polarization resistance of $\text{La}_{0.8}\text{Sr}_{0.2}\text{MnO}_3$ | YSZ cathode measured at 1073-1273 K, was increased by a factor of 14-25 with increasing fabrication temperature from 1623 to 1773 K [109]. The $\text{La}_{0.6}\text{Pb}_{0.4}\text{MnO}_{3-\delta}$ cathode showed a better performance compared to $\text{La}_{0.6}\text{Sr}_{0.4}\text{MnO}_{3-\delta}$, partly due to decreased interaction with the electrolyte [146,147,182,196].

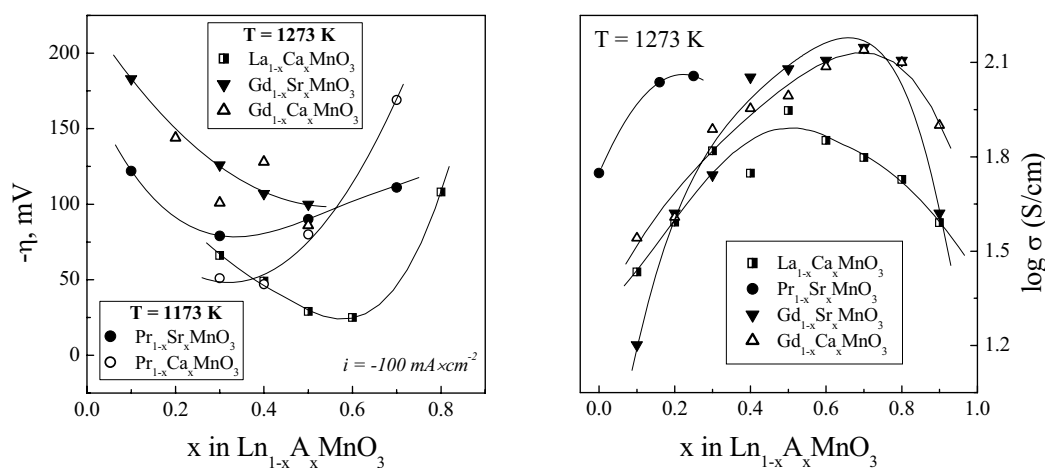


Fig.1.12. Cathodic overpotentials (left) and total conductivities in air (right) of selected $\text{Ln}_{1-x}\text{A}_x\text{MnO}_3$ [184-186,192,199].

For the $\text{Ln}_{1-x}\text{Sr}_x\text{MnO}_{3\pm\delta}$ ($\text{Ln} = \text{La}, \text{Pr}, \text{Nd}, \text{Sm}$ and Gd) perovskites, the reactivity with YSZ to form $\text{Ln}_2\text{Zr}_2\text{O}_7$ pyrochlore phase is lower for the compositions having a smaller lanthanoid radius [181]. This results from decreasing stability of rare-earth zirconate pyrochlores with respect to the corresponding fluorite structures. The reactivity of $\text{Pr}_{0.6}\text{Sr}_{0.4}\text{MnO}_{3-\delta}$ with YSZ was found much smaller compared to the $\text{La}_{0.6}\text{Sr}_{0.4}\text{MnO}_3$ material, being negligible up to 1373 K [186]. At temperatures up to 1573 K, $\text{Nd}_{1-x}\text{Sr}_x\text{MnO}_{3\pm\delta}$ ($x = 0.1-0.4$) seems the least reactive with zirconia in terms of both $\text{Ln}_2\text{Zr}_2\text{O}_7$ and SrZrO_3 formation [181]. Except for $(\text{Gd},\text{Sr})\text{MnO}_3$ systems, 30 mol% Sr-doped $\text{Ln}_{1-x}\text{Sr}_x\text{MnO}_{3\pm\delta}$ were found the most stable in contact with YSZ [181,194]. For the $\text{Gd}_{1-x}\text{A}_x\text{MnO}_{3\pm\delta}$ ($\text{A} = \text{Ca}$ and Sr) compositions with $x = 0-0.8$, no reaction occurred after annealing at 1273 K for 96 h. The separation of $\text{Gd}_2\text{Zr}_2\text{O}_7$ and Mn_3O_4 phases was indicated by XRD at 1373 and 1473 K, respectively; the formation of AZrO_3 was identified within all temperature range, 1373-1673 K [184]. The Ca-doped compositions were reported [184] to be more chemically stable in contact with zirconia, which contradicts to the data on $\text{La}_{1-x}\text{A}_x\text{MnO}_{3\pm\delta}$ [185].

The formation of blocking layers is closely related to the catio stoichiometry, being favorable for the A-site stoichiometric and Mn-deficient electrodes [189,191,197]. A significant A-site deficiency may inhibit this topotactic reaction [111,189,198]. Under the cell operating conditions, the zirconate formation can also be suppressed due to reducing oxygen activity at the cathode side, which may lead to dissociation and re-dissolution of the blocking layers [189,195].

The electrochemical performance of Sr- and Ca-doped rare-earth manganites is quite similar [184,185]. In the $\text{La}_{1-x}\text{A}_x\text{MnO}_{3\pm\delta}$ ($\text{A} = \text{Ca}, \text{Sr}, x = 0.0-1.0$) series, $\text{La}_{0.5}\text{Sr}_{0.5}\text{MnO}_{3-\delta}$ and $\text{La}_{0.7}\text{Ca}_{0.3}\text{MnO}_3$ show the highest conductivities at 1273 K, whereas the best cathodic properties were found at $x = 0.3-0.7$ for Sr- and $x = 0.5-0.7$ for Ca-substituted compositions [185]. Analogously, maximum conductivity and electrochemical activity in $\text{Ln}_{0.6}\text{Sr}_{0.4}\text{MnO}_{3-\delta}$ and $\text{Pr}_{1-x}\text{Sr}_x\text{MnO}_{3\pm\delta}$ systems was found for $\text{Pr}_{0.6}\text{Sr}_{0.4}\text{MnO}_{3-\delta}$ [186]. A correlation between electrochemical properties and total electrical conductivity, which can be observed until the chemical interaction with zirconia deteriorated the performance, suggests that the surface concentration of electronic charge carriers and/or Mn^{4+} states affect electrocatalytic activity towards oxygen reduction [185]. Whatever the role of electronic defects, the cathodic performance can be clearly improved incorporating variable-valence $\text{Pr}^{4+/3+}$; typical examples relate to $\text{Pr}_{0.6}\text{Sr}_{0.4}\text{MnO}_{3-\delta}$ [186] and $\text{Pr}_{0.7}\text{Ca}_{0.3}\text{MnO}_{3-\delta}$ [199] exhibiting superior properties.

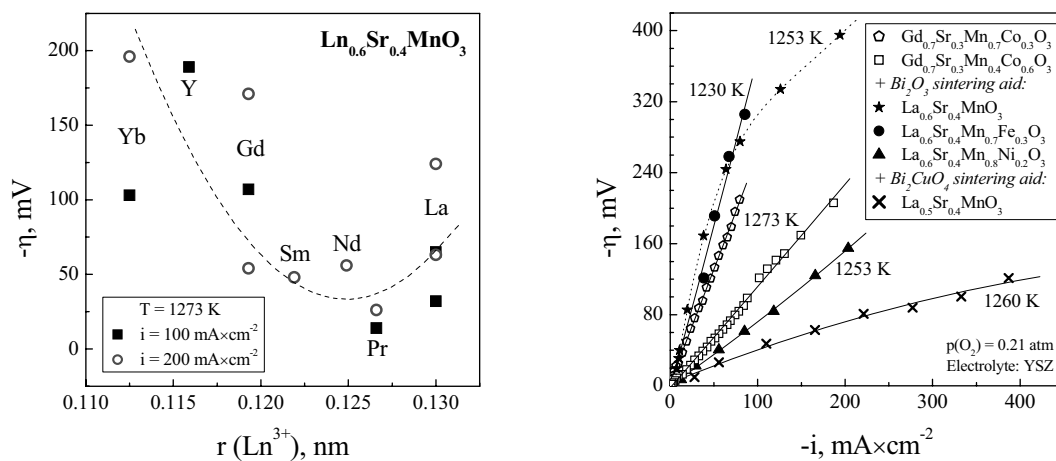


Fig.1.13. Cathodic overpotentials of porous $\text{Ln}_{0.6}\text{Sr}_{0.4}\text{MnO}_3$ | YSZ electrodes [184-186] as function of the ionic radius of Ln^{3+} cations in 8-fold coordination (left), and overpotential-current dependencies of $\text{O}_2, (\text{Ln}, \text{Sr})(\text{Mn}, \text{M})$ | YSZ half-cells fabricated with and without sintering aids [146,196,200,201,203] (right).

For long-term annealing at 1473 K, Ca-doped compositions appear more reactive with zirconia than Sr-substituted manganites [185], probably due to increasing thermodynamic stability of the perovskite phases when tolerance factor increases. On the other hand, detection of the trace

amounts of zirconates is often difficult, which leads to numerous contradictions in the experimental data. As an example, the cathodic polarization curves of $\text{Ln}_{0.7}\text{Sr}_{0.3}\text{MnO}_{3-\delta}$ ($\text{Ln} = \text{La}, \text{Pr}, \text{Nd}, \text{Sm}$ and Gd) at 1273 K were reported essentially identical for all compositions within the limits of experimental uncertainty [181], which is contrary to the results [186], Fig.1.13. To avoid the interaction between the perovskite and zirconia phases the electrode sintering temperature and time should be minimized. This can be achieved using various sintering aids. Additions of small amounts of CuO , Bi_2O_3 or Bi_2CuO_4 to the manganite ceramics improve both the sinterability and electrical conductivity and often enhance electrochemical activity [146,147,182,196,200,201].

Partial substitution of manganese with other elements enables significant variations in the conductivity, thermal expansion and oxygen permeability of $(\text{La},\text{Sr})(\text{Mn},\text{M})\text{O}_{3-\delta}$ ($\text{M} = \text{Ti}, \text{Fe}, \text{Co}, \text{Ni}, \text{Cu}, \text{Al}$) ceramics, and in the electrochemical activity of manganite-based electrodes [146,147,180,200-202]. The performance of $\text{La}_{0.6}\text{Sr}_{0.4}\text{Mn}_{1-x}\text{M}_x\text{O}_{3-\delta}$ layers applied onto YSZ increases with the incorporation of moderate amounts of the transition metal cations into the B sublattice, although, again, no direct correlation between the oxygen ion transport through the ceramic material and the electrochemical activity of the corresponding porous electrode could be identified. The electrical conductivity of the $\text{La}_{0.6}\text{Sr}_{0.4}\text{Mn}_{1-x}\text{Fe}_x\text{O}_{3-\delta}$ ($x = 0-0.5$) solid solutions decreases with iron additions, while the electrochemical properties remain essentially unchanged. The electronic conductivity of $\text{LaMn}_{1-x}\text{Ni}_x\text{O}_{3\pm\delta}$ ($x = 0-0.5$) and $\text{La}_{0.6}\text{Sr}_{0.4}\text{Mn}_{1-x}\text{Ni}_x\text{O}_{3-\delta}$ ($x = 0-0.4$) monotonically increases with x ([146,200] and cited references). Doping $\text{La}_{0.6}\text{Sr}_{0.4}\text{MnO}_{3-\delta}$ with iron or nickel drastically decreases the ionic conductivity [146], which might be ascribed to the formation of defect associates. Thermal expansion of the $(\text{La},\text{Sr})\text{Mn}_{1-x}\text{M}_x\text{O}_{3-\delta}$ ($\text{M} = \text{Fe}, \text{Ni}$) ceramics is essentially independent of the dopant concentration [146,200,201]. The substitution of nickel for manganese in the $\text{La}_{0.6}\text{Sr}_{0.4}(\text{Mn},\text{Ni})\text{O}_{3-\delta}$ perovskite-type solid solutions leads to a pronounced increase in the electrochemical activity of porous electrode layers, Fig.1.13. Aluminium doping of $(\text{La},\text{Sr})\text{MnO}_{3\pm\delta}$ decreases the reactivity with YSZ and total conductivity [202]. Doping with cobalt leads to increasing conductivity and TECs of $(\text{Ln},\text{M})\text{Mn}_{1-x}\text{Co}_x\text{O}_{3-\delta}$ [146,203]. The substitution of Mn with up to 50 mol% Co in $\text{Gd}_{0.8}\text{Sr}_{0.2}\text{Mn}_{1-y}\text{Co}_y\text{O}_{3-\delta}$ and $\text{Gd}_{0.7}\text{Ca}_{0.3}\text{Mn}_{1-y}\text{Co}_y\text{O}_{3-\delta}$ was reported effective to improve the conductivity and cathodic properties in contact with YSZ, also preserving thermal expansion compatible with that of electrolyte ceramics [203]. However, although $\text{Gd}_{1-x}\text{M}_x\text{Mn}_{1-y}\text{Co}_y\text{O}_{3-\delta}$ are less reactive compared to the La-containing analogues [203], their relatively low performance (Fig.1.13) might result from the interaction with the electrolyte.

1.5.1.2. Ferrites

The number of iron-containing phases stable in air and presenting an interest for the high-temperature electrochemical applications, significantly exceeds that in manganite systems. The perovskite-type $\text{LnFeO}_{3-\delta}$ phases exist in air for $\text{Ln} = \text{La-Yb}$ and Y [206]. $\text{LaFeO}_{3-\delta}$ is stable in air up to 2158 K [207]; A-site doping decreases the perovskite phase stability. The cubic perovskite lattice of $\text{SrFeO}_{3-\delta}$ transforms into oxygen vacancy-ordered $\text{SrFeO}_{2.5+\delta}$ brownmillerite at $p(\text{O}_2) < 10^{-4}$ atm and $T < 1123$ K [208], with intermediate $\text{Sr}_n\text{Fe}_n\text{O}_{3n-1}$ ($n = 2, 4, 8$) phases [209]. In Sr-Fe-O system, various intergrowth structures, including $\text{Sr}_3\text{Fe}_2\text{O}_{6+\delta}$ with a Ruddlesden-Popper structure, $\text{Sr}_4\text{Fe}_6\text{O}_{13+\delta}$, $\text{SrFe}_{12}\text{O}_{19}$ are also formed [206,209]. Among the ferrite materials, the phases with disordered perovskite-like structure possess the highest level of the electronic and ionic conductivity [210]. Decreasing A-site cation radius may promote ordering processes in the perovskite lattice, having an unfavorable effect on the oxygen ion transport. $\text{La}_{2-x}\text{Sr}_x\text{FeO}_{4\pm\delta}$ ($x = 1-1.4$) materials adopt the K_2NiF_4 -type structure over a wide range of oxygen stoichiometries up to 1473 K in air and under reducing conditions [190,211]. The results of Mössbauer spectroscopy, iodometric titrations and structural analysis suggest that at ambient temperature, $\text{La}_{2-x}\text{Sr}_x\text{FeO}_4$ are oxygen-stoichiometric in air, while the Fe^{4+} fraction increases with x [211]. As for the manganites, the electrical conductivity of perovskite ferrites under oxidizing conditions is predominantly p-type electronic, occurring via a small-polaron hopping mechanism. The incorporation of divalent cations increases both the iron oxidation state and the oxygen vacancy concentration, typically enhancing mixed conductivity of $(\text{Ln,A})\text{FeO}_{3-\delta}$ (Table 1.7). The $\text{La}_{1-x}\text{Sr}_x\text{FeO}_{3-\delta}$ series exhibits a maximum in partial electronic and oxygen ionic conductivities for $x = 0.5$ in low- $p(\text{O}_2)$ regimes [212], while higher strontium content results in oxygen vacancy ordering and deterioration of transport properties. The $\text{La}_{2-x}\text{Sr}_x\text{FeO}_4$ ceramics shows maximum conductivity, 10-25 S/cm, at $x = 1.2-1.3$ and 673-1273 K [190].

The materials of $(\text{La,Sr})\text{FeO}_{3-\delta}$ system possess excessively high thermal and chemically-induced expansion, incompatible with common solid electrolytes such as doped lanthanum gallate, ceria or stabilized zirconia. The lattice expansion can be considerably suppressed by partial substitution of iron with cations having a more stable oxidation state, which reduces oxygen nonstoichiometry variations with temperature and oxygen partial pressure. This can be achieved via isovalent doping, e.g. by Ga^{3+} or Al^{3+} [213-216], or the substitution with other transition metals such as chromium or titanium [210,217-220]. Contrary to perovskite ferrites, an essentially linear expansion behavior on heating was observed for both a and c unit cell parameters of the $\text{La}_{2-x}\text{Sr}_x\text{FeO}_{4\pm\delta}$ ($x = 1-1.4$) ceramics, masking Fe–O bond lengthening due to the changes in the Fe^{3+} fraction [211].

At 1673 K, the rate of $\text{La}_2\text{Zr}_2\text{O}_7$ formation between YSZ and $\text{LaFeO}_{3-\delta}$ is much lower than for lanthanum manganite [202]. The incorporation of moderate amounts (up to 30 mol%) of Al^{3+} into the B-sites of $\text{La}_{0.8}\text{Sr}_{0.2}\text{FeO}_{3-\delta}$ further suppresses the interaction with zirconia and has no essential effect on the total electrical conductivity [202]. The Mn-substituted ferrites were found most stable to the zirconate formation at 1273 K compared to $(\text{La}_{0.6}\text{A}_{0.4})_{1-x}\text{Fe}_{0.8}\text{M}_{0.2}\text{O}_{3-\delta}$ ($x = 0, 0.1$; $\text{A} = \text{Sr}, \text{Ca}$; $\text{M} = \text{Cr}, \text{Co}, \text{Ni}$) perovskites, but tend to promote the cubic to monoclinic phase transition of zirconia on long annealing; doping with Co or Ni increases the reactivity [221,222]. The A-site substoichiometry enhances the stability of these perovskites in contact with YSZ. In the case of $\text{La}_{1-x}\text{A}_x\text{Co}_{0.2}\text{Fe}_{0.8}\text{O}_{3-\delta}$ ($\text{A} = \text{Sr}, \text{Ca}$; $x = 0-0.5$) interaction at 1373 K [223], formation of CoFe_2O_4 was detected in addition to $(\text{Sr,Ca})\text{ZrO}_3$ and $\text{La}_2\text{Zr}_2\text{O}_7$ phases; for some compositions, monoclinic zirconia was also observed. XRD analysis of $\text{La}_{0.8}\text{Sr}_{0.2}\text{FeO}_3$ -YSZ reaction mixtures indicated no strontium or lanthanum zirconate formation even at 1673 K [224]. However, at temperatures higher than 1273 K, a significant shift in the perovskite diffraction peaks corresponding to a unit cell volume expansion, suggests the incorporation of Zr^{4+} cations; the latter results in lower electrical conductivity in the cathode layer [224]. The anode-supported SOFCs utilizing a $\text{La}_{0.8}\text{Sr}_{0.2}\text{FeO}_{3-\delta}$ cathode and YSZ electrolyte demonstrated an improved performance on the incorporation of a Sm-doped CeO_2 layer between the cathode and YSZ electrolyte [224]. Increasing Sr content in $\text{La}_{1-x}\text{Sr}_x\text{FeO}_{3-\delta}$ up to 50 mol% reduces cathode overpotentials in contact with YSZ solid electrolyte, Fig.1.14.

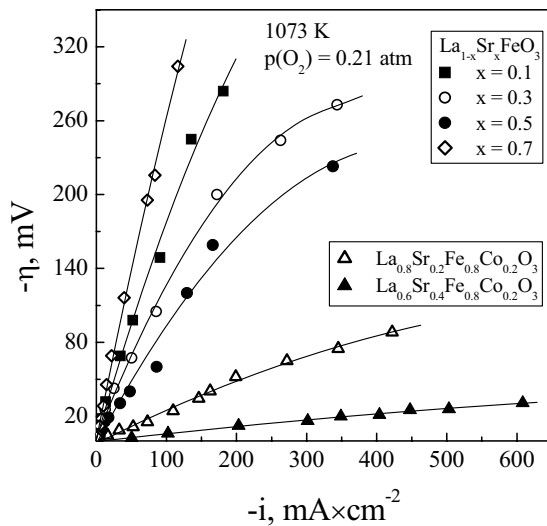


Fig.1.14. Current dependence of cathodic overpotential of $\text{La}_{1-x}\text{Sr}_x\text{FeO}_3$ [88] and $\text{La}_{1-x}\text{Sr}_x\text{Fe}_{0.8}\text{Co}_{0.2}\text{O}_3$ [17,43] electrodes in contact with YSZ and ceria-based electrolytes, respectively.

Decreasing the SOFC operating temperature reduces oxygen vacancy concentration in oxide electrodes and the role of ionic conductivity increases significantly. One well-known example is the substitution of iron with cobalt, which increases ionic transport and reduces cathodic

overpotentials of $(\text{La,Sr})(\text{Fe,Co})\text{O}_{3-\delta}$ (LSFC), Fig.1.14. On the other hand, the apparent thermal expansion also increases (Table 1.7).

The $\text{La}_{1-x}\text{Sr}_x\text{Co}_{1-y}\text{Fe}_y\text{O}_{3-\delta}$ perovskites and their A-site deficient derivatives [225-228] are of special interest for cathode applications. As a rule, the p-type electronic transport in these phases increases on cobalt doping and with moderate Sr additions. On the creation of A-site vacancies in $\text{La}_x\text{Sr}_y\text{Fe}_{0.8}\text{Co}_{0.2}\text{O}_{3-\delta}$ ($x = 0.4-0.6$, $y = 0.2-0.4$), the conductivity and thermal expansion both decrease due to the charge compensation mechanism via increasing oxygen deficiency [228]; the hole transport increases with La/Sr ratio. For $\text{Ln}_{0.8}\text{Sr}_{0.2}\text{Fe}_{0.8}\text{Co}_{0.2}\text{O}_{3-\delta}$ ($\text{Ln} = \text{La-Gd}$) systems, decreasing the radius of rare-earth cation lead to a lower stability, limiting the solid solution formation ranges, and to reduced thermal expansion and total conductivity [229].

An optimum combination of transport and physicochemical properties in $(\text{La,Sr})(\text{Fe,Co})\text{O}_{3-\delta}$ system is accepted for compositions close to $\text{La}_{0.6}\text{Sr}_{0.4}\text{Fe}_{0.8}\text{Co}_{0.2}\text{O}_{3-\delta}$ considered as promising for cathode applications in contact with ceria-based electrolytes. The ionic conductivity and electrochemical activity of LSFC increase with cobalt and strontium concentrations, but further doping increases the thermal expansion excessively [17,43,225-227,230]. At 973-1173 K, a porous $\text{La}_{0.6}\text{Sr}_{0.4}\text{Fe}_{0.8}\text{Co}_{0.2}\text{O}_{3-\delta}$ electrode layer in contact with $\text{Ce}_{0.8}\text{Sm}_{0.2}\text{O}_2$ solid electrolyte showed 9-42 times lower cathodic overpotentials compared to $\text{La}_{0.82}\text{Sr}_{0.18}\text{MnO}_{3-\delta} | \text{YSZ}$ half-cells [17]; this difference increases on reducing temperature. $\text{La}_{0.6}\text{Sr}_{0.4}\text{Fe}_{0.8}\text{Co}_{0.2}\text{O}_{3-\delta}$ double-layer cathode comprising one thin dense and one thick porous layer, applied onto the 10 mol% or 20 mol% Gd-doped ceria electrolytes, exhibits the resistance as low as $0.5 \text{ Ohm}\times\text{cm}^2$ at 793 K [231].

Table 1.7

Total conductivity and thermal expansion of $\text{La}_{1-x}\text{Sr}_x\text{Fe}_{1-y}\text{Co}_y\text{O}_{3-\delta}$ ceramics in air

x	y	Total conductivity, S/cm		Average TECs		Ref.
		873 K	1073 K	T, K	$\bar{\alpha} \times 10^6, \text{K}^{-1}$	
0	0.2	0.8	4.5	373-773	13.1	[226]
				873-1173	17.5	[226]
0.1	0.2	44	59	573-1173	16.0	[226]
0.1	1.0	1267	1210			[227]
0.2	0	93	93	573-1173	12.6	[225]
			109			[224]
0.2	0.1	116	123	473-1173	14.5	[225]
0.2	0.2	175	191	373-1073	15.4	[226]
		127	149	373-1073	15.4	[225]
		77	87	303-1273	14.8	[227]
		176	164	973	12.5	[229]

Table 1.7 (continued)

0.2	0.3	187	224	373-1173	16.5	[225]
0.2	0.4	339	287	373-1173	17.6	[225]
0.2	0.5	287	325	373-1173	18.7	[225]
0.2	0.6	414	455	373-1173	20.0	[225]
0.2	0.7	743	776	373-1173	20.3	[225]
0.2	0.8	1049	996	373-1173	20.7	[225]
				470-1070	15.4	[43]
0.2	0.9	1142	1071	373-1173	20.1	[225]
0.2	1.0	1373	1235	373-1173	19.7	[225]
0.2	1.0	1689	1521	303-1273	18.5	[227]
0.3	0.2	240	205	373-973	14.6	[226]
		159	159	303-1273	16.0	[227]
0.3	1.0	1972	1676	303-1273	19.2	[227]
				303-1073	17.5	[63]
				303-1273	19.2	
0.4	0.2	335	279	373-873	15.3	[226]
		275	333	303-1273	17.5	[227]
		460	330	973	15.3	[228]
				1273	19.9	
0.4	1.0	2035	1595	303-1273	20.5	[227]
0.5	1.0	1899	1356	303-1273	22.3	[227]
0.6	0.2			373-673	16.8	[226]
0.6	0.8			373-1273	21.2	[253]
0.6	1.0	1810	1156	303-1273	25.1	[227]
0.7	0	61	44	303-1273	25.6	[227]
0.7	0.1	90	61	303-1273	24.8	[227]
0.7	0.2	51	46	303-1273	27.1	[227]
0.7	0.3	63	54	303-1273	27.1	[227]
0.7	0.4	95	83	303-1273	23.9	[227]
0.7	0.5	132	93	303-1273	23.5	[227]
0.7	0.6	173	129	303-1273	24.1	[227]
0.7	0.7	286	217	303-1273	24.7	[227]
0.7	0.8	480	388	303-1273	21.0	[227]
0.7	0.9	1369	837	303-1273	19.2	[227]
0.7	1.0	1474	912	303-1273		[227]
				303-1273	25.0	[290]
0.8	1.0	810	578	303-1273	25.6	[227]
0.9	1.0	335	191	303-1273	26.0	[227]

1.5.1.3. Cobaltites

Compared to ferrite-based materials, perovskite-related cobaltites are characterized by higher electrochemical activity, faster oxygen-ionic and p-type electronic conductivities and greater oxygen permeability [232-254]. However, thermal expansion of cobaltites is also substantially higher, Table 1.7, making these materials compatible with a very limited number of solid electrolytes such as derivatives of δ -Bi₂O₃ and Bi₂VO_{5.5- δ} . Phase relationships in Co-containing multicomponent oxide systems are quite similar to those with iron oxide; the major differences relevant for this review, refer to a higher oxygen deficiency and lower thermodynamic stability of cobaltite phases, particularly at low chemical potentials. Detailed information on the phase relations, thermodynamics and structure in Co-containing systems can be found in Refs.[146,190, 232-238] and references cited. As for the manganite and ferrite-based electrodes, the primary attention for electrochemical applications is focused on La(Sr)CoO_{3- δ} perovskites and their B-site substituted derivatives, and on the Sr(Co,M)O_{3- δ} (M = Ti, Cr, Mn, Fe) systems.

Other attractive examples are the tetragonal Ln₄Co₃O₁₀ (Ln = La, Pr, Nd) and K₂NiF₄-type (Ln,A)₂CoO_{4± δ} (Ln = La, Pr, Nd; A - alkaline-earth cation) existing at moderately reducing oxygen partial pressures [146,190,234]. One should also mention tetragonal and orthorhombic LnBaCo₂O₅ (Ln = Y, Tb, Dy, Ho) [235,236] and hexagonal LnBaCo₄O₇ (Ln = Y, Ho) [237,238]. The HoBaCo₄O₇ was reported to contain only di- and trivalent cobalt [237], which might be beneficial for suppressing the thermal expansion. The information on high-temperature transport and electrochemical properties of the latter phases is, however, very scarce.

The electrical conductivity of LnCoO_{3- δ} , predominantly p-type electronic, is significantly higher compared to manganite analogues (Table 1.7 and Fig.1.15). Incorporation of divalent cations into the A-sublattice of La_{1-x}A_xCoO_{3- δ} increases the concentrations of Co⁴⁺ and oxygen vacancies, resulting in a drastic increase of the electronic and ionic transport and surface exchange rates. A transition to metallic conductivity is observed for La_{1-x}A_xCoO_{3- δ} (Ln = La, Pr, Nd, Sm) solid solutions in air at $x \geq 0.25-0.30$ [146]. At 873-1273 K, the maximum total electrical conductivity of the La_{1-x}Sr_xCoO_{3- δ} series corresponds to $x = 0.2-0.4$, shifting towards lower x on heating [227]. The electrical properties of the La_{1-x}Ba_xCoO_{3- δ} system are quite close to those of the strontium-doped cobaltites. Introducing cation vacancies or bismuth cations into the A sublattice leads often to decreasing ionic and electronic conductivities, although the effects of A-site deficiency are determined by particular charge compensation mechanisms dependent on La:Sr concentration ratio [146,240]. For La_{2-x}Sr_xCoO_{4± δ} ($x = 0.7-1.0$), the conductivity above 873 K in air becomes comparable to that of A₂BO₄ nickelates, 80-100 S/cm [190].

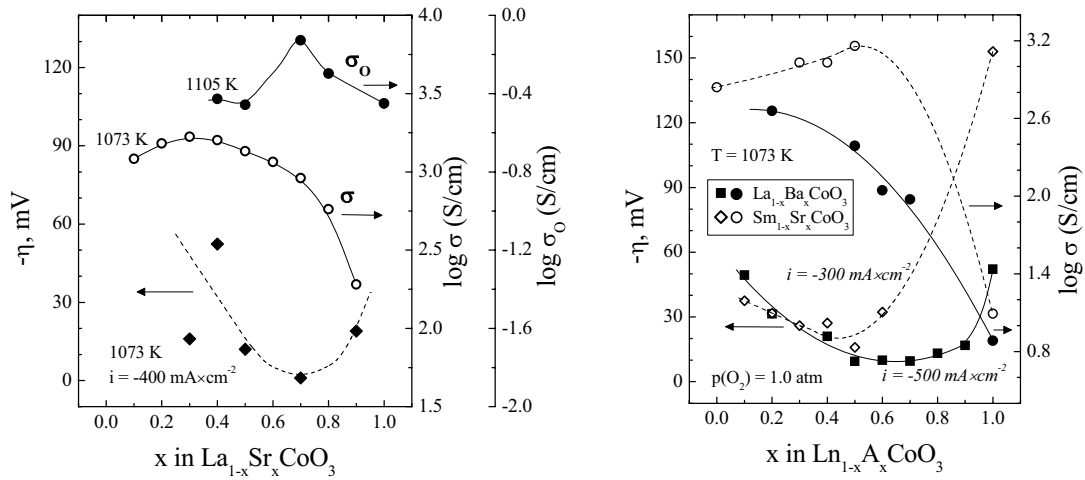


Fig.1.15. Cathodic overpotentials of $\text{La}_{1-x}\text{Sr}_x\text{CoO}_3$ | YSZ porous electrodes [88,250], and total [227] and oxygen ionic [239] conductivities of $\text{La}_{1-x}\text{Sr}_x\text{CoO}_3$ ceramics in air (left); cathodic overpotentials in contact with LSGM-based electrolytes and total electrical conductivity of $\text{Sm}_{1-x}\text{Sr}_x\text{CoO}_3$ [247] and $\text{La}_{1-x}\text{Ba}_x\text{CoO}_3$ [173] (right).

The ionic conductivity and oxygen permeation fluxes through $\text{LnCoO}_{3-\delta}$ were shown to increase with the Ln^{3+} cation radii [146,239,240]. The dopant concentration dependences of the ionic conductivity in $\text{Ln}_{1-x}\text{A}_x\text{CoO}_{3-\delta}$ have quite a complex nature, being determined by oxygen nonstoichiometry, cobalt ion oxidation states, defect association and, often, grain-boundary processes. For $\text{La}_{1-x}\text{Sr}_x\text{CoO}_{3-\delta}$ series, the maximum ionic transport is observed at x about 0.7 [146,239,240]. In fact, higher ionic conduction for cobaltite-based systems is only known for Bi-containing materials and perovskite phases derived from $\text{A}(\text{Co,Fe})\text{O}_{3-\delta}$ ($\text{A} = \text{Sr, Ba}$) which exhibit, however, poor mechanical properties and sinterability. Further increase of strontium content in $\text{La}_{1-x}\text{Sr}_x\text{CoO}_{3-\delta}$ leads to decreasing oxygen transport due to progressive defect association and phase separation [239]. Even for $\text{La}_{0.3}\text{Sr}_{0.7}\text{CoO}_{3-\delta}$, electron microscopy and spectroscopic studies revealed vacancy-ordered microdomains with low oxidation state of Co cations [241]; this ordering is expected to increase with Sr concentration, resulting in lower oxygen ion transport.

The excessively high TECs of cobaltite materials (Table 1.7), associated with extensive oxygen nonstoichiometry variations and numerous transitions in the electronic sublattice when temperature increases [92,146,242,243], limit their applications as the SOFC cathodes. In $\text{La}_{1-x}\text{Sr}_x\text{CoO}_{3-\delta}$ series, the minimum TEC value averaged at 300-1270 K was obtained at $x = 0.2$ to be $18.5 \times 10^{-6} \text{ K}^{-1}$ [227]. The thermal expansion of Mn- and Fe-substituted $\text{La}(\text{Sr})\text{CoO}_{3-\delta}$ monotonically decreases on doping but cannot be reduced to the level of $\text{La}(\text{Sr})\text{MnO}_{3-\delta}$ or $\text{La}(\text{Sr})\text{FeO}_{3-\delta}$ without lowering the Co concentration to very small values (for example [244,245]). This, in turn, is

associated with a decrease in electronic conductivity and electrochemical activity. For various intergrowth structures stabilising Co^{2+} and Co^{3+} cations, thermal expansion is considerably lower compared to the perovskites [190]; an importance of the spin state ordering of cobalt ions and semiconductor-to-metal transition for the expansivity of cobaltites was noted in [244]. The thermomechanical incompatibility of cobaltite electrodes and common solid electrolyte materials may lead to apparently high overpotentials, caused by poor electrical contact and interface cracks. One example relates to the data on $\text{La}_{0.6}\text{Ca}_{0.4}\text{CoO}_{3-\delta}$ layers applied onto YSZ [111], where the polarization resistance seems overestimated.

Cobaltite cathodes exhibit a superior electrochemical performance with respect to common electrode materials based on $\text{La}(\text{Sr})\text{MnO}_{3-\delta}$, Fig.1.15. This may be of great interest for IT SOFCs, performance of which is substantially limited by the electrode polarization. For example, the maximum power density obtained with LSGM-based cells and identical Ni anodes at 1273 K, increased in the sequence $\text{La}_{0.75}\text{Sr}_{0.25}\text{CrO}_{3-\delta} < (\text{La}_{0.6}\text{Sr}_{0.4})_{0.9}\text{MnO}_{3-\delta} < \text{La}_{0.6}\text{Sr}_{0.4}\text{FeO}_{3-\delta} < (\text{La},\text{Sr})\text{CoO}_{3-\delta}$ [29,247]. $\text{La}_{1-x}\text{Sr}_x\text{CoO}_{3-\delta}$ perovskites applied onto the YSZ electrolyte, showed very low overpotentials at 1073 K, with minimum at $x = 0.7$ [88]. $(\text{Gd},\text{Sr})\text{CoO}_{3-\delta}$ cathodes had a worse performance in contact with YSZ compared to $(\text{La},\text{Sr})\text{CoO}_{3-\delta}$ [248], contrary to the results obtained for LSGM electrolyte [29]. Among the $\text{Ln}_{0.6}\text{Sr}_{0.4}\text{CoO}_{3-\delta} | \text{La}_{0.9}\text{Sr}_{0.1}\text{Ga}_{0.8}\text{Mg}_{0.2}\text{O}_{3-\delta}$ cathodes ($\text{Ln} = \text{La}, \text{Sm}, \text{Nd}, \text{Gd}, \text{Pr}$), the composition with $\text{Ln} = \text{Sm}$ showed a highest performance in pure oxygen at 1073-1273 K [29]. A fuel cell involving one ordered macropore-structured $\text{Sm}_{0.5}\text{Sr}_{0.5}\text{CoO}_{3-\delta}$ cathode with 140 nm sized pores prepared using a template of monodispersed polystyrene spheres, CGO electrolyte and Ni-CGO cermet anode showed the maximum power density of 0.27 W/cm^2 at 873 K [249]. The overpotential of $\text{La}_{0.6}\text{Sr}_{0.4}\text{CoO}_{3-\delta}$ cathodes with optimized microstructure, applied onto the YSZ electrolyte coated by the thin and dense samaria-doped ceria interlayer, was less than 100 mV at current density of 800 mA/cm^2 and 1073 K in air, and as low as 50 mV at 400 mA/cm^2 [250].

As the p-type conductivity in perovskite-type cobaltites is exceptionally high, hole transport has no effect on the electrode performance. For instance, the overpotential dependence on the La:Ba ratio in $\text{La}_{1-x}\text{Ba}_x\text{CoO}_{3-\delta}$ cathodes applied onto $\text{La}_{0.8}\text{Sr}_{0.2}\text{Ga}_{0.8}\text{Mg}_{0.115}\text{Co}_{0.05}\text{O}_{3-\delta}$ electrolyte has a minimum at $x = 0.5-0.7$ at 1073 K; this minimum does not correlate with the total conductivity variations (Fig.1.15). Note that the surface exchange rate of $(\text{La},\text{Ba})\text{CoO}_{3-\delta}$ increases with Ba concentration [173]. Selected data on maximum power density of cells comprising perovskite cobaltite cathodes are listed in Table 1.8. When applied onto LSGM electrolyte, the electrochemical activity of $(\text{La},\text{Ba})\text{CoO}_{3-\delta}$ seems slightly higher compared to $(\text{Sm},\text{Sr})\text{CoO}_{3-\delta}$ cathodes, both performing better than $(\text{La},\text{Sr})\text{CoO}_{3-\delta}$ [173,247].

Table 1.8

Performance of H₂-fueled SOFCs with cobaltite cathodes

Cathode	Electrolyte/ thickness, mm	Anode	T, K	Maximum power density, W/cm ²	Ref.
La _{0.9} Sr _{0.1} CoO ₃	YSZ / 0.5	Ni	1273	0.39	[29]
			1073	0.05	
La _{0.9} Sr _{0.1} CoO ₃	LSGM / 0.5	Ni	1273	0.93	[29]
			1073	0.38	[247]
La _{0.6} Sr _{0.4} CoO ₃	LSGM / 0.5	Ni	1273	0.71	[29]
			1073	0.21	
La _{0.6} Sr _{0.4} CoO ₃	LSGM / 0.5	Co	1273	0.53	[29]
La _{0.2} Sr _{0.8} CoO ₃	LSGM / 0.5	Ni	1073	0.44	[173]
La _{0.2} Ca _{0.8} CoO ₃	LSGM / 0.5	Ni	1073	0.46	[173]
La _{0.4} Ba _{0.6} CoO ₃	LSGMC / 0.4	Ni	873	0.12	[173]
La _{0.2} Ba _{0.8} CoO ₃	LSGM / 0.5	Ni	1073	0.52	[173]
Sm _{0.6} Sr _{0.4} CoO ₃	LSGM / 0.5	Ni	1073	0.44	[29]
Sm _{0.5} Sr _{0.5} CoO ₃	LSGM / 0.5	Ni	1073	0.53	[173]
			873	0.08	[247]
Sm _{0.5} Sr _{0.5} CoO ₃	CGO / 0.03	Ni-CGO	873	0.27	[249]

LSGMC denotes the La_{0.8}Sr_{0.2}Ga_{0.8}Mg_{0.115}Co_{0.05}O_{3-δ} electrolyte

For the B-site substituted (La,A)(Co,M)O_{3-δ} (M = Ti, Cr, Mn, Fe, Ni, Cu, Ga, Mg) solid solutions, the basic composition-property relations are quite similar to those in the manganite- and ferrite-based systems [146]. The information on the electrochemical properties of moderately doped cobaltites is often contradicting, especially for materials with relatively similar composition, where the difference in electrochemical behavior are primarily related to dissimilar sinterability, microstructure and interaction with solid electrolytes. In the case of Ln_{0.4}Sr_{0.6}Co_{0.8}Fe_{0.2}O_{3-δ} (Ln = La, Pr, Nd, Sm, Gd) series on YSZ electrolyte, the highest electrochemical activity was found for the Nd-containing composition [251]. Contrary, for Mn-doped Ln_{0.6}Sr_{0.4}Co_{0.8}Mn_{0.2}O_{3-δ} (Ln = La, Nd, Sm, Gd,), lowest overpotentials in contact with Ce_{0.8}Gd_{0.2}O₂ electrolyte were obtained when Ln = La [245]. The Y_{0.8}Ca_{0.2}Co_{1-x}Fe_xO_{3-δ} perovskites with x = 0.1-0.7 are stable in air at least up to 1473 K, whereas the Fe-free cobaltite (x = 0) decomposes into the binary oxides [252]. In the latte series, the Y_{0.8}Ca_{0.2}Co_{0.7}Fe_{0.3}O_{3-δ} | YSZ cathode showed the highest activity which is, however, comparable to that of manganite electrodes, and a thermal expansion coefficient of 10.5×10⁻⁶ K⁻¹, quite close to that of common electrolyte ceramics. During the cathode fabrication process, the interaction of Y_{0.8}Ca_{0.2}Co_{0.7}Fe_{0.3}O_{3-δ} and YSZ resulted in Co₂FeO₄ spinel formation while no significant degradation in the cell performance with time was observed at 1173-1273 K;

the formation of highly-resistive zirconate phases seems avoided [252]. The electrochemical activity of $Y_{0.9}Co_{0.5}Mn_{0.5}O_{3-\delta}$, having a perovskite structure and TEC close to $10 \times 10^{-6} \text{ K}^{-1}$, was found low [244].

Finally, one should note that the cobaltite materials may interact with zirconia easier than manganites, but yield no reaction products with ceria (e.g. [245,250]), although non-negligible cation interdiffusion is still possible. In the case of LSGM electrolytes, a substantial Co diffusion into the substrate without formation of blocking layers takes place [253].

1.5.1.4. Nickelates

The thermodynamic stability of $LaMO_{3-\delta}$ based perovskites and the average oxidation state of M cations in air increase in a sequence $Cu < Ni < Co < Fe < Mn$ [146,190,254]. Perovskite-like $LaNiO_{3-\delta}$ is stable at $p(O_2) = 0.21-1.0 \text{ atm}$ only at temperatures below 1123-1173 K; further heating leads to the decomposition into $La_2NiO_{4+\delta}$ with K_2NiF_4 -type structure and nickel oxide, through the formation of Roddlesden-Popper type $La_4Ni_3O_{10}$ and $La_3Ni_2O_7$ phases [146,255,256]. Decreasing the Ln^{3+} cation radius and acceptor-type doping lead to a decrease in the thermodynamic stability. The phase decomposition limiting the practical application of $LaNiO_{3-\delta}$ based perovskites in SOFCs, may be partly suppressed by appropriate doping into the B sublattice. The solid solutions $La(Ni,M)O_{3-\delta}$ ($M = Ga, Cr, Mn, Fe, Co$) containing 50-60 mol% of nickel retain perovskite-type structure at elevated temperatures [146,256,257]. In particular, $La_{1-y}Sr_yNi_{1-x}Fe_xO_{3-\delta}$ are stable in air at least up to 1673 K when $x > 0.5$; doping with Sr destabilizes the $La(Ni,Fe)O_{3-\delta}$ lattice [257].

In ternary Ln-M-O systems with $Ln = La, Pr$ or Nd , and $M = Ni$ or Cu , the K_2NiF_4 -type compounds are the most stable under oxidizing and moderately reducing conditions [146,206]. This layered structure consists of perovskite layers alternating with rock-salt LaO sheets. On heating above 423 K in air, $La_2NiO_{4+\delta}$ exhibits a first-order phase transition from the orthorhombic (S.G. Fmmm) to the tetragonal (S.G. I4/mmm) polymorph [258]. In air, the equilibrium oxygen hyperstoichiometry of $La_2NiO_{4+\delta}$, resulting from the incorporation of interstitial oxygen into the rock-salt layers, is $\delta = 0.14-0.15$ at 300 K and decreases on heating above 700 K and on alkaline-earth doping [190,258-261]; $La_{2-x}Sr_xNiO_{4\pm\delta}$ are oxygen-deficient at $x \geq 1.0$ [146,260]. The concentration ranges of existing solid solutions for the $La_{2-x}A_xNiO_{4\pm\delta}$ series correspond to $x = 0-1.4$ for $A = Sr$, $x = 0-1.0$ for $A = Ba$, and $x = 0-0.5$ for $A = Ca$ [146,190,260]. $La_2Ni_{1-x}Co_xO_{4+\delta}$ are stable in air only at $x \leq 0.2$ [262]; a continuous solid solution exists in the pseudobinary $La_2NiO_4-La_2CuO_4$ system [258]. The substitution of Cu for Ni decreases the oxygen excess in the lattice [258].

Table 1.9

Thermal expansion of selected Ni- and Cu-containing ceramics in air

Composition	T, K	$\bar{\alpha} \times 10^6, \text{K}^{-1}$	Ref.
La ₂ NiO ₄	290-1170	13.7	[259]
La ₂ NiO ₄	300-1270	13.0	[258]
La ₂ NiO ₄	300-1270	11.9	[190]
La _{1.7} Sr _{0.3} NiO ₄	300-1270	11.3	[190]
La _{1.6} Sr _{0.4} NiO ₄	300-1270	13.2	[190]
La _{1.4} Sr _{0.6} NiO ₄	300-1270	11.0	[190]
La ₂ Ni _{0.98} Fe _{0.02} O ₄	300-1100	13.2	[263]
La ₂ Ni _{0.90} Fe _{0.10} O ₄	300-1100	12.8	[263]
LaPrNi _{0.90} Fe _{0.10} O ₄	300-1100	13.4	[263]
La ₂ Ni _{0.88} Fe _{0.02} Cu _{0.10} O ₄	300-1100	10.5	[263]
La _{1.9} Sr _{0.1} Ni _{0.98} Fe _{0.02} O ₄	300-1100	12.5	[263]
La _{1.9} Sr _{0.1} Ni _{0.90} Fe _{0.10} O ₄	300-1100	12.7	[263]
La ₂ Ni _{0.50} Cu _{0.50} O ₄	290-1270	12.8	[258]
La ₂ CuO ₄	290-520	8.6	[258]
	520-1170	13.8	
Pr ₂ CuO ₄	300-1070	10.2	[263]
Nd ₂ CuO ₄	300-1050	10.1	[263]
La ₂ Cu _{0.98} Co _{0.02} O ₄	300-460	7.1	[263,265]
	470-1050	12.2	
La ₂ Cu _{0.90} Co _{0.10} O ₄	300-1080	13.2	[263,265]
LaNi _{0.7} Fe _{0.3} O ₃	300-1270	12.1	[256]
LaNi _{0.6} Fe _{0.4} O ₃	300-1270	11.4	[256]
LaNi _{0.5} Fe _{0.5} O ₃	300-1270	10.9	[256]
LaNi _{0.5} Fe _{0.5} O ₃	300-1100	11.9	[43]
LaNi _{0.6} Co _{0.4} O ₃	300-1270	15.0	[256]
LaNi _{0.6} Mn _{0.4} O ₃	300-1270	10.8	[256]
La _{0.6} Sr _{0.4} Ni _{0.5} Mn _{0.5} O ₃	300-1100	12.1	[200]
La _{0.6} Sr _{0.4} Ni _{0.4} Mn _{0.6} O ₃	300-1100	12.5	[200]
La _{0.6} Sr _{0.4} Ni _{0.3} Mn _{0.7} O ₃	350-1100	12.5	[200]
La _{0.6} Sr _{0.4} Ni _{0.2} Mn _{0.8} O ₃	300-1100	12.7	[43,200]

The total conductivity of La₂NiO₄-based phases is predominantly p-type electronic in the entire p(O₂) range where the K₂NiF₄-type phases exist [146,190,258,260,263]. The hole conduction occurs, most likely, via a small-polaron transport [146,258], although further studies are necessary to identify microscopic mechanisms. The level of electronic conductivity in the Ln₂MO_{4+δ} (M = Fe, Co, Ni, Cu) compounds and their derivatives is lower when compared to their perovskite oxide

analogues, but is sufficiently high for electrode applications [146,190]. On doping La_2NiO_4 with strontium, the conductivity of the ceramics increases and becomes pseudometallic at $x = 1.0$ [146,190]; the incorporation of ≤ 25 mol% of copper has a moderate effect on the level of electronic transport. At the same time, while the melting point of La_2NiO_4 is rather high, lanthanum cuprate forms liquid phase at approximately 1323 ± 10 K [206]. Doping of La_2NiO_4 with copper considerably improves the sinterability [258], which enables to reduce the electrode layers fabrication temperature. $\text{LaNiO}_{3-\delta}$ exhibits a metallic-like conductivity as high as 1.1×10^3 S/cm at room temperature [146]. The maximum electronic conductivity of $\text{La}_{1-y}\text{Sr}_y\text{Ni}_{1-x}\text{Fe}_x\text{O}_3$ at 873-1073 K corresponds to $(1-x+y) = 0.6$ [258].

La_2NiO_4 -based phases show a relatively high oxygen ion conductivity [146,258,259,260,263,264], which is 5-10 times lower than that of oxygen-deficient perovskites $\text{SrCo}_{1-x}\text{Fe}_x\text{O}_{3-\delta}$ ($x = 0.2-0.5$) and $\text{La}_{1-x}\text{Sr}_x\text{CoO}_{3-\delta}$ ($x = 0.6-0.8$), but remarkably higher compared to lanthanum-strontium ferrite and manganite electrode materials. Doping with Sr decreases oxygen permeability [259]. The bulk ionic transport in La_2NiO_4 -based phases occurs via diffusion of interstitial ions in the rock-salt-type layers and vacancies in the perovskite layers of K_2NiF_4 -type structure; the oxygen permeation through dense nickelate membranes is limited as a rule by both ionic conductivity of ceramic bulk and the surface exchange rate [263]. Partial substitution of nickel with higher valence cations, such as Fe or Co, results in higher oxygen hyperstoichiometry and has often a positive effect on the ionic transport [261,263].

On the contrary to perovskite-type cobaltites, La_2NiO_4 -based phases exhibit a relatively low thermal and chemically-induced expansion [43,146,258-260,263]. The apparent TEC values of most K_2NiF_4 -type nickelates, close to 13×10^{-6} K^{-1} (Table 1.9), are compatible with thermal expansion of solid oxide electrolytes for IT SOFCs. The $\text{LaNi}_{1-x}\text{Fe}_x\text{O}_3$ ($x \geq 0.4$) perovskites also possess a reasonably low thermal expansion, Table 1.9 and [256].

The Information on nickelate-based cathodes is still rather limited. $\text{LaNiO}_{3-\delta}$ [255] and $\text{La}_{1-y}\text{Sr}_y\text{Ni}_{1-x}\text{Fe}_x\text{O}_{3-\delta}$ [257] were suggested as the cathode materials for IT SOFCs, but not evaluated as yet. $\text{LaNi}_{0.5}\text{Fe}_{0.5}\text{O}_{3-\delta}$ cathodes exhibited a high electrocatalytic activity in contact with $\text{Ce}_{0.8}\text{Gd}_{0.2}\text{O}_{2-\delta}$ solid electrolyte at 873 K [43], better than lanthanum-strontium manganites. Surface modification of the nickelate electrode layers with praseodymium oxide enabled further decreasing their polarization [43]. Porous $\text{Ln}_2\text{NiO}_{4+\delta}$ ($\text{Ln} = \text{La}, \text{Nd}, \text{Pr}$) layers deposited onto YSZ, showed a very good performance at 773-1073 K in air [264]; the cathodic overpotentials were lower than those observed for LSM under the same current and temperature conditions. Ageing tests during one month under *dc* conditions revealed a decrease in the polarization resistance, without significant interaction between $\text{Ln}_2\text{NiO}_{4+\delta}$ and zirconia [264]. The area-specific resistivity of porous $\text{La}_2\text{Ni}_{0.9}\text{Co}_{0.1}\text{O}_{4+\delta}$ electrode layers is lower in contact with $\text{La}_{0.9}\text{Sr}_{0.1}\text{Ga}_{0.8}\text{Mg}_{0.2}\text{O}_{3-\delta}$ solid electrolyte

compared to $\text{Ce}_{0.9}\text{Gd}_{0.1}\text{O}_{2-\delta}$, at 773-1073 K [262]; long-term annealing of both cells at 1273 K leads to the formation of secondary phases, $\text{La}_3\text{Ni}_2\text{O}_7$ and La_2O_3 , suggesting diffusion of Co and Ni into the electrolyte ceramics. Typical examples illustrating the electrochemical behavior of nickelate- and cuprate-based electrodes are presented in Fig.1.16.

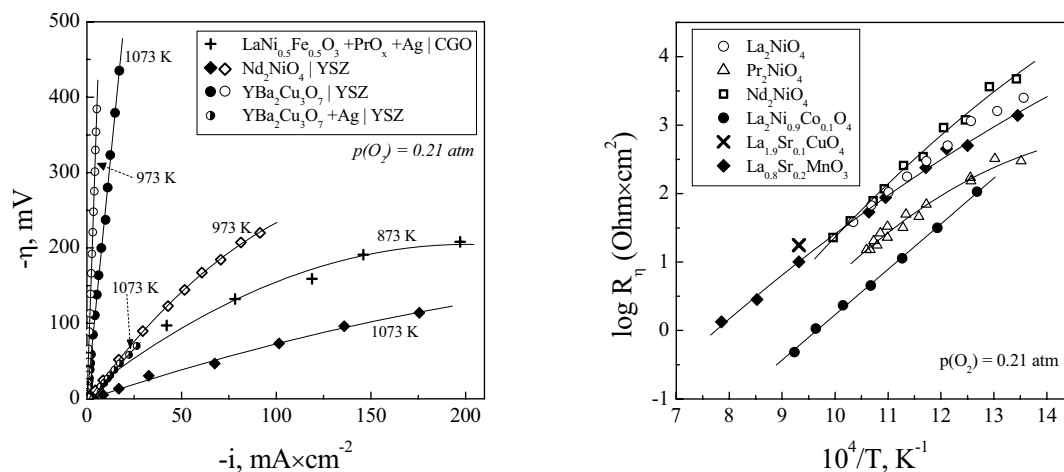


Fig.1.16. Current density dependencies of cathodic overpotentials for nickelate and cuprate electrodes ([43,95,264], left); temperature dependencies of the polarization resistance of porous cathode layers, all in contact with YSZ electrolyte, except for $\text{La}_2\text{Ni}_{0.9}\text{Co}_{0.1}\text{O}_4$ measured on LSGM ceramics ([111,152,262,264], right).

1.5.1.5. Cuprates

No perovskite compounds exist in the ternary Ln-Cu-O systems at oxygen pressures close to atmospheric; the Ln_2CuO_4 and $\text{Ln}_2\text{Cu}_2\text{O}_5$ phases are most stable in air [146,206]. As for perovskites, the thermodynamic and thermal stabilities of Ln_2CuO_4 (Ln = La, Pr, Nd, Sm, Eu, Gd) decrease with decreasing rare-earth cation radius; $\text{Ln}_2\text{Cu}_2\text{O}_5$ exhibit an opposite behavior [146]. The equilibrium oxygen hyperstoichiometry of $\text{La}_2\text{CuO}_{4\pm\delta}$ is low, about 0.01 at 300-1273 K in air [258]. In these conditions, the orthorhombic (S.G. Bmab) lattice of La_2CuO_4 transforms on heating into tetragonal (S.G. I4/mmm) [258]. In terms of dopant solubility in both sublattices, the behavior of La_2CuO_4 is quite similar to that of $\text{La}_2\text{NiO}_{4+\delta}$ ([146,265] and references cited).

The total conductivity of La_2CuO_4 ceramics has a pseudometallic character (Fig.1.10) and varies in the range 15-20 S/cm at 300-1273 K, being lower than that of $\text{La}_2\text{NiO}_{4+\delta}$ [146,258]. The electrical transport in other rare-earth cuprates (Ln = Pr-Gd) is temperature-activated and increases with the Ln^{3+} radius and on acceptor-type doping [146]. Incorporating up to 30 mol% cobalt into

the copper sublattice of La_2CuO_4 leads to increasing oxygen hyperstoichiometry and decreasing electrical conductivity, with a minor effect on thermal expansion [265].

The oxygen diffusion and surface exchange coefficients of the $\text{La}_{2-x}\text{Sr}_x\text{CuO}_{4+\delta}$ ($x = 0-0.20$) are rather low [258,266,267]. The oxygen transport mechanism in layered cuprates is still unclear, though some assumptions [266,267] were made in favor of the vacancy diffusion. The diffusivity along the perovskite layers (a - b planes) is considerably faster as compared to the c direction through sequential perovskite and rock-salt-type layers [266]. The rate of oxygen transport in $\text{La}_{2-x}\text{Sr}_x\text{CuO}_{4+\delta}$ solid solutions increases slightly with x in the range 0-0.07, and then decreases dramatically for $x = 0.07-0.20$ [266,267]. Doping with Ni increases the oxygen diffusion coefficients of $\text{La}_2(\text{Cu},\text{M})\text{O}_{4+\delta}$ [258]. Analogously, small (≤ 10 mol%) cobalt additions increase the oxygen permeability, determined by both surface oxygen exchange and bulk ionic conduction [263]. Note also that increasing oxygen content in another well-known cuprate, $\text{YBa}_2\text{Cu}_3\text{O}_{7-\delta}$, results in higher permeation fluxes and ionic conductivity [268].

The rare-earth cuprates, either pure or moderately doped with transitional metals, are quite compatible with the solid electrolyte ceramics (Table 1.9). On the other hand, literature data on electrochemical behavior of cuprate-based electrodes at high temperatures are scarce, as for nickelates. In general, the performance of cuprate cathodes is worse with respect to the nickelate analogues. This results, first of all, from lower ionic transport and lower stability. The latter factor is responsible for a greater reactivity with solid electrolytes and additional sintering under operation conditions, leading to microstructural degradation.

Typical examples include $\text{La}_{1.9}\text{Sr}_{0.1}\text{CuO}_4$ cathodes measured in contact with YSZ solid electrolyte; both SrZrO_3 and $\text{La}_2\text{Zr}_2\text{O}_7$ based solid solutions were identified at the electrode/electrolyte interface after firing at 1373 K, forming the thick (20-30 μm) diffusion layer [111] deteriorating electrochemical properties. $\text{YBa}_2\text{Cu}_3\text{O}_{7-\delta}$ possessing significant mixed conductivity was proposed as the cathode material for SOFCs, but showed cathode performance insufficient for practical applications [95].

1.5.1.6. Composite materials

Composite electrodes comprising a mixture of one electronically-conducting cathode material and one solid-electrolyte component, as a rule, improved performance due to a greater number of triple-phase contacts and good adherence to the electrolyte. Another advantage of the composite electrode concept is a possibility to adjust thermal expansion. The activity of such electrodes is determined by properties of all components and their volume ratio, with critical influence of the connectivity and size of the component particles [269-272]. In general, the TPB is

electrochemically active provided the electrons, oxygen ions and gas all percolate through the electronic conductor, ionic conductor and pores, respectively.

Although there is no unambiguous correlation between the ionic conductivity of cathode material and the electrochemical performance (Chapter 1.4.3), additions of the oxygen ionic conductors, e.g. stabilized zirconia enables definitely to reduce polarization of manganite electrodes, Fig.1.17. This influence is, however, strongly dependent on the phase interaction between LSM and zirconia. The polarization resistance of LSM-YSZ composite at 1223 K was found to decrease with YSZ content up to 40-45 wt%, when the solid electrolyte grains were well connected; further YSZ additions lead to a sharp increase in the ohmic resistance of the electrode layers [270]. Additions of 50 wt% YSZ into $\text{La}_{0.85}\text{MnO}_{3-\delta}$ electrode decrease the polarization resistance from 0.77 to 0.16 $\text{Ohm}\times\text{cm}^2$ at 1173 K [273]. In the case of $\text{La}_{0.8}\text{Sr}_{0.2}\text{MnO}_{3-\delta}$ cathode, adding YSZ leads to a lower polarization resistance and oxygen dissociative adsorption as the rate limiting step, due to spatial enlargement of the reaction zone, as suggested in Ref.[274]. Similar results were also reported for 50 vol% YSZ in $\text{La}_{0.8}\text{Sr}_{0.2}\text{MnO}_{3-\delta}$ layers, where an additional arc appeared in the impedance spectra was attributed to YSZ grain boundaries in the cathode layer [110]. A decrease in the polarization resistance of $(\text{La}_{0.75}\text{Sr}_{0.25})_{0.95}\text{MnO}_3$ -YSZ (50-50 wt%) composites applied onto the YSZ substrate was achieved after reducing the electrode sintering temperature from 1573 down to 1423 K [269], as a result of smaller grain size, longer TPB and/or less pronounced interaction of the components.

Such a behavior is in agreement with theoretical calculations using a random resistor networks model [275], predicting minimum polarization resistance at 30-60 vol% fraction of the electronically-conducting phase. A number of other theoretical approaches, including the effective medium approximation, percolation theory and various microscopic models ([276,277] and references cited) may also be useful to predict selected aspects of the composites behavior. However,, modeling of the transport and electrochemical processes in composites is much more complicated with respect to single-phase mixed-conductors, even porous.

Using ceria-based materials as components of the composite cathodes is beneficial compared to zirconia (Fig.1.17), due to an absence of blocking layers and the higher ionic conductivity of doped ceria. The minimum interfacial resistance of $\text{La}_{0.8}\text{Sr}_{0.2}\text{MnO}_3$ - $\text{Ce}_{0.8}\text{Gd}_{0.2}\text{O}_{2-\delta}$ composite cathodes were studied in contact with YSZ at 873-1023 K was achieved at 45-55 wt% $\text{Ce}_{0.8}\text{Gd}_{0.2}\text{O}_{2-\delta}$ content in the composite; the corresponding value, approximately 0.49 $\text{Ohm}\times\text{cm}^2$ at 1023 K, is 2-3 times lower than that of LSM-YSZ composites [278]. The optimum composition of $\text{La}_{0.8}\text{Sr}_{0.2}\text{MnO}_3$ - $\text{Ce}_{0.7}\text{Bi}_{0.3}\text{O}_{2-\delta}$ layers on YSZ can be estimated as 30-50 wt% of $\text{Ce}_{0.7}\text{Bi}_{0.3}\text{O}_{2-\delta}$ [279]; the minimum polarization resistance at 973 K was 1.78 $\text{Ohm}\times\text{cm}^2$.

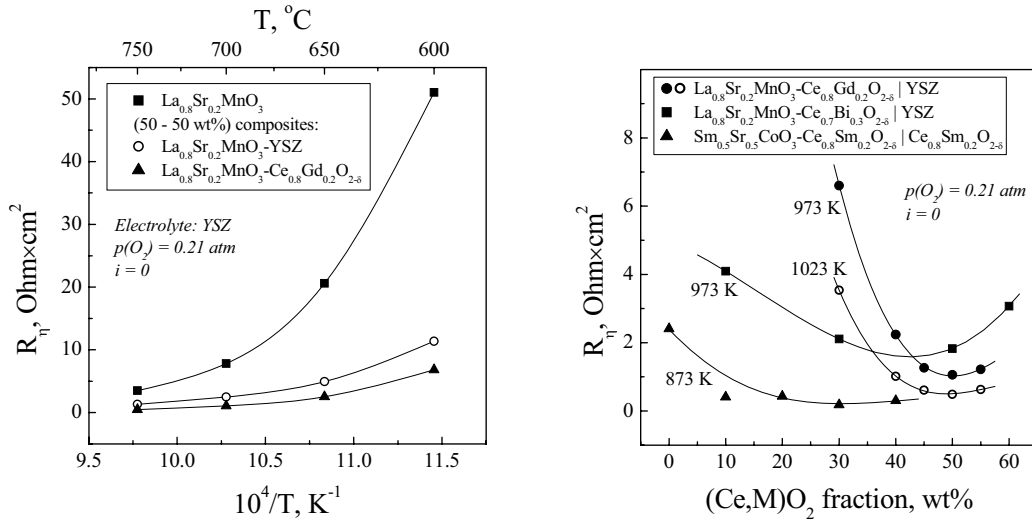


Fig.1.17. Temperature (left) and composition (right) dependencies of the polarization resistance for various composite cathodes [278-280].

In spite of the high oxygen ionic conduction of the cobaltite-based materials (Table 1.10), their electrode performance may also be improved by doped ceria additions. This is primarily associated with possible matching of the thermal expansion coefficients, enabling to improve electrode/electrolyte contact, and with changes in the exchange mechanisms. For example, a significant decrease in the polarization resistance of $\text{La}_{0.6}\text{Sr}_{0.4}\text{Co}_{0.2}\text{Fe}_{0.8}\text{O}_{3-\delta}$ cathodes, up to 10 times, was achieved adding 50 vol% $\text{Ce}_{0.8}\text{Gd}_{0.2}\text{O}_{2-\delta}$ content; the R_η values were as low as 0.33 and 0.01 $\text{Ohm}\times\text{cm}^2$ at 873 and 1023 K, respectively [281]. The $\text{La}_{0.6}\text{Sr}_{0.4}\text{Co}_{0.8}\text{Fe}_{0.2}\text{O}_3\text{-Ce}_{0.8}\text{Gd}_{0.2}\text{O}_{2-\delta}$ (70-30 wt%) composite applied onto $\text{Ce}_{0.8}\text{Sm}_{0.2}\text{O}_{2-\delta}$ ceramics, with subsequent deposition of Ag layer, showed an interfacial resistance lower than 1 $\text{Ohm}\times\text{cm}^2$ at 873 K [282]. The $\text{La}_{1-x}\text{Sr}_x\text{CoO}_{3-\delta}\text{-Ce}_{0.8}\text{Sm}_{0.2}\text{O}_{2-\delta}$ cathodes in contact with the YSZ- $\text{Ce}_{0.8}\text{Sm}_{0.2}\text{O}_{2-\delta}$ bilayer electrolyte exhibit best performance at 40 to 60 wt% ratio of the components; the power density of the anode-supported cell achieved 1.8 W/cm^2 at 1073 K [283]. The polarization resistance of $\text{Sm}_{0.5}\text{Sr}_{0.5}\text{CoO}_{3-\delta}\text{-Ce}_{0.9}\text{Sm}_{0.1}\text{O}_{2-\delta} | \text{Ce}_{0.9}\text{Gd}_{0.1}\text{O}_{2-\delta}$ composite electrode was reported to be about 0.4 $\text{Ohm}\times\text{cm}^2$ at 973 K [284]. Even moderate (10 wt%) $\text{Ce}_{0.8}\text{Sm}_{0.2}\text{O}_{2-\delta}$ additions into $\text{Sm}_{0.5}\text{Sr}_{0.5}\text{CoO}_{3-\delta}$ cathode, in contact with $\text{Ce}_{0.8}\text{Sm}_{0.2}\text{O}_{2-\delta}$, had a dramatic effect on the polarization; the minimum R_η value, < 0.18 $\text{Ohm}\times\text{cm}^2$ at 873 K, was found for 30 wt% $\text{Ce}_{0.8}\text{Sm}_{0.2}\text{O}_{2-\delta}$ addition [280].

Table 1.10

Oxygen ionic conductivity of oxide materials in air

Composition	T, K	σ_o , S/cm	Ref.
La _{0.95} Sr _{0.05} MnO ₃	1173	1.1×10^{-7}	[205]
La _{0.90} Sr _{0.10} MnO ₃	1273	2.1×10^{-6}	[205]
La _{0.80} Sr _{0.20} MnO ₃	1173	5.9×10^{-7}	[205]
	1273	5.8×10^{-6}	
La _{0.79} Sr _{0.20} MnO ₃	1273	8×10^{-6}	[98]
La _{0.65} Sr _{0.30} MnO ₃	1073	1.7×10^{-4}	[288]
Pr _{0.65} Sr _{0.30} MnO ₃	1073	3.4×10^{-4}	[288]
La _{0.70} Ba _{0.30} CoO ₃	1273	3.0×10^{-2}	[173]
La _{0.60} Sr _{0.40} FeO ₃	1073	5.6×10^{-3}	[288]
La _{0.60} Sr _{0.40} CoO ₃	1073	0.22	[288]
	1105	0.37	[239]
La _{0.50} Sr _{0.50} CoO ₃	1073	9.3×10^{-2}	[288]
La _{0.30} Sr _{0.70} CoO ₃	1073	0.76	[288]
	1105	0.75	[239]
La _{0.20} Sr _{0.80} CoO ₃	1105	0.51	[239]
SrCoO ₃	1105	0.35	[239]
La _{0.75} Sr _{0.20} Mn _{0.8} Co _{0.2} O ₃	1073	3.1×10^{-5}	[288]
Pr _{0.75} Sr _{0.20} Mn _{0.8} Co _{0.2} O ₃	1073	1.1×10^{-4}	[288]
La _{0.8} Sr _{0.2} Fe _{0.9} Co _{0.1} O ₃	1073	2.2×10^{-3}	[288]
La _{0.8} Sr _{0.2} Fe _{0.8} Co _{0.2} O ₃	1073	2.3×10^{-3}	[288]
Pr _{0.8} Sr _{0.2} Fe _{0.8} Co _{0.2} O ₃	1073	1.5×10^{-3}	[288]
La _{0.8} Sr _{0.2} Fe _{0.2} Co _{0.8} O ₃	1073	4×10^{-2}	[288]
La _{0.65} Sr _{0.30} Fe _{0.8} Co _{0.2} O ₃	1073	4×10^{-3}	[288]
La _{0.6} Sr _{0.4} Fe _{0.8} Co _{0.2} O ₃	1073	8×10^{-3}	[288]
La _{0.6} Sr _{0.4} Fe _{0.2} Co _{0.8} O ₃	1073	5.8×10^{-2}	[288]
La _{0.6} Sr _{0.4} Fe _{0.2} Co _{0.8} O ₃	1173	0.2	[289]
Y _{0.8} Ca _{0.2} Co _{0.7} Fe _{0.3} O ₃	923	2.4×10^{-6}	[252]
	973	8.3×10^{-6}	
	1023	2.0×10^{-5}	
La ₂ Zr ₂ O ₇	1273	10^{-4}	[290]

Further developments of standard perovskite-containing cathodes include grading the material to overcome thermal expansion mismatch and reactivity problems. The polarization resistance of functionally graded La_{0.85}Sr_{0.15}MnO₃-YSZ cathodes, where the composition gradually changes from YSZ to LSM was shown to decrease as the level of grading increases; it was concluded that regions containing less than 20 wt% LSM, below the percolation limit, should be

avoided [285,286]. Comparison of functionally graded cathodes comprising the first layers made of $(\text{La}_{0.85}\text{Sr}_{0.15})_{0.9}\text{MnO}_{3-\delta}$ and different solid electrolytes (50-50 wt%), namely YSZ or $\text{Ce}_{0.9}\text{Gd}_{0.1}\text{O}_{2-\delta}$ [286], revealed a strong positive impact of ceria incorporation; the polarization resistance of CGO-containing cathodes was lower up to one order of magnitude at 973-1273 K.

Composite cathodes comprising noble metals are of interest as model systems, but their practical use is very unlikely due to economical reasons. These systems are not considered in the present review; the corresponding information can be found in [287] and references cited.

1.5.2. Anodes

1.5.2.1. Me-YSZ cermets

The ceramic-metal composites (cermets) of YSZ and Ni, where the metallic phase combines the functions of electronic conductor and catalyst, are the commonly used anode materials of SOFCs. Additions of YSZ prevent sintering of Ni particles, enlarge the active reaction zone and enable to adjust thermal expansion, Table 1.11, [155,291,292]. As the composite layers should provide percolation paths for electrons, oxygen ions and gas, the cermet performance is strongly dependent on the microstructure-related factors, such as processing conditions and starting materials.

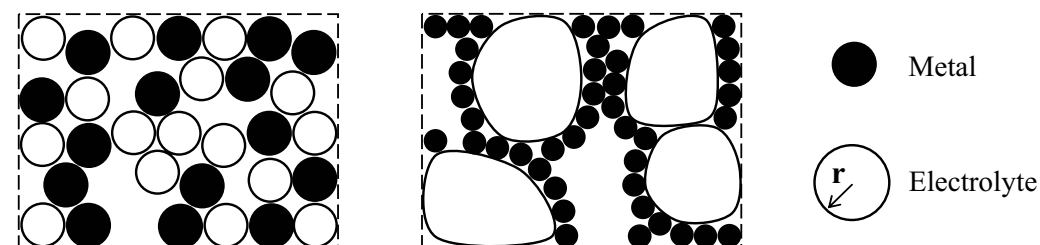


Fig.1.18. Schematic illustrations of the anode microstructures at $r(\text{electrolyte}) \approx r(\text{metal})$, left, and $r(\text{electrolyte}) > r(\text{metal})$, right.

The lowest voltage losses and electrode resistance of the Ni-YSZ anodes is usually observed when TPB is as long as possible [293]. This can be achieved, in particular, using small Ni particles and high YSZ to Ni particle ratio, Figs.1.18 and 1.19. For example, a mixture of fine and coarse YSZ particles was suggested [294] to tune the microstructure and properties of the cermets. On the other hand, a significant improvement was attained when fabricating the anodes from mechanically-processed powder, with a resultant microstructure comprising submicron Ni and YSZ particles and uniformly distributed micron-sized pores [295].

Considerable emphasis is focused on theoretical modeling of porous cermets in order to guide the design of high-performance SOFC anode. Among these studies, one should mention the pore, random resistor network and random packing sphere models [296]. These approaches can also be classified [297] according to the type of microstructural analysis; particular cases include modeling of corrugated layers of the electrode material covered by a thin film of electrolyte or *vice versa* (thin film model), a random packing of particles (Monte Carlo calculations), or using a macroscopic averaged description of the disordered electrode structure (macroscopic porous-electrode model). Modeling of composite anodes behavior by three-dimensional impedance networks [298] showed that their response may be more complex than those corresponding to a single interface between an electrode and an electrolyte particle; a distortion of the spectrum at high frequencies and/or clearly distinguishable extra arcs may appear when the system is close to or below the percolation threshold for the electronic conduction. An important conclusion is that simply ascribing the arcs in the Nyquist plots to definite steps of the electrode reaction is often problematic.

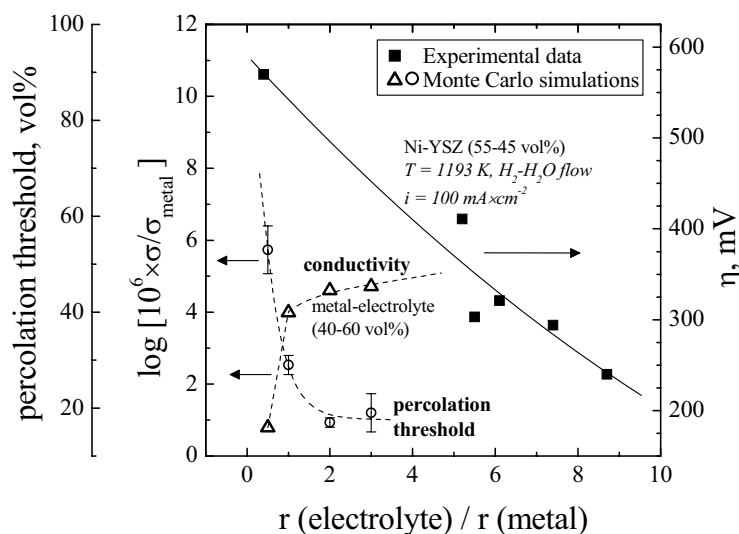


Fig.1.19. Relative electrical conductivity of metal-electrolyte (40-60 vol%) composite and metal percolation threshold estimated by the Monte Carlo method for random packing [300], and measured overpotentials of Ni - $\text{Zr}_{0.85}\text{Y}_{0.15}\text{O}_2$ anode [293], as functions of the particle size ratio.

For the composites consisting of one electronic and one oxygen ionic conductor with similar grain sizes, the percolation threshold is expected to correspond to approximately 30 vol% metallic phase [299]. This estimation is in agreement with experimental data (Fig.1.20), where a significant scatter is, however observed due to microstructural factors. The electrical conductivity

of porous Ni - YSZ composites in hydrogen atmosphere was reported to exhibit a semiconductor-like behavior up to 30 vol% Ni, becoming metallic at 50 vol% Ni [292]; other authors [291,300] found a metallic conduction for the compositions containing 20-30 vol% Ni. For instance, the use of combustion synthesis [300] and Ni-coated graphite particulates in tape-casted composites [301] enabled to change the behavior of Ni-YSZ cermets in the vicinity of nickel percolation limit, increasing the conductivity of zirconia-rich materials. The YSZ fraction, optimum for electrochemical performance, is dependent on the anode synthesis and fabrication conditions. This fraction corresponds usually to 30-60 vol% YSZ (Fig.1.21). One typical example is found in Ref.[302], where a minimum polarization resistance at 1273 K in hydrogen was observed for 60 vol% zirconia fraction, whereas the ohmic resistance decreased with Ni content as expected.

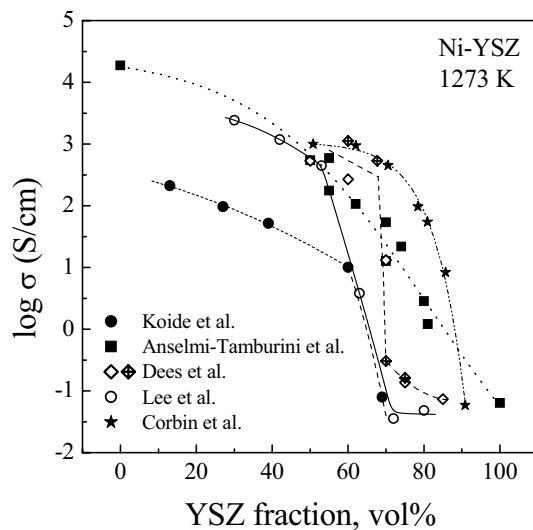


Fig.1.20. Total conductivity of Ni - YSZ cermets with various microstructures as function of the YSZ content, in H₂-H₂O or N₂ atmosphere [299,301-304].

At high Ni concentrations and at elevated temperatures, the microstructure and properties of Ni - YSZ cermets undergo fast degradation due to coarsening of the metal particles. For instance, a 33% decrease in the conductivity measured at 298 K was revealed for reduced 56 wt% NiO - YSZ mixture after an exposure at 1273 K in 4%Ar-3%H₂-H₂O for 4000 h [155]. The rate of increasing polarization of Ni - Zr_{0.85}Y_{0.15}O_{2-δ} (51-49 vol% or 67 wt% NiO) electrode in 50% H₂-N₂ atmosphere 1200-1281 K and current density of 300 mA/cm² was as high as 14 μV/h [125]. Another factor requiring to decrease metal concentration in the cermets is the anode layer stability to redox cycling. As an example, the polarization loss of Ni - YSZ (65-35 mol%) anode at 1223 K increased by 18% after the triple redox cycling of the cell [305].

In order to increase n-type electronic conductivity of zirconia-based phase, Ti^{4+/3+} cations can be dissolved in the fluorite lattice [306]. However, Ti incorporation decreases ionic conductivity of zirconia. The mechanical stability of Ni - (Ti-doped YSZ) cermets can also be

improved by titania doping [291,306]. In fact, the performance of cermets with pure and Ti-doped YSZ is quite similar [306].

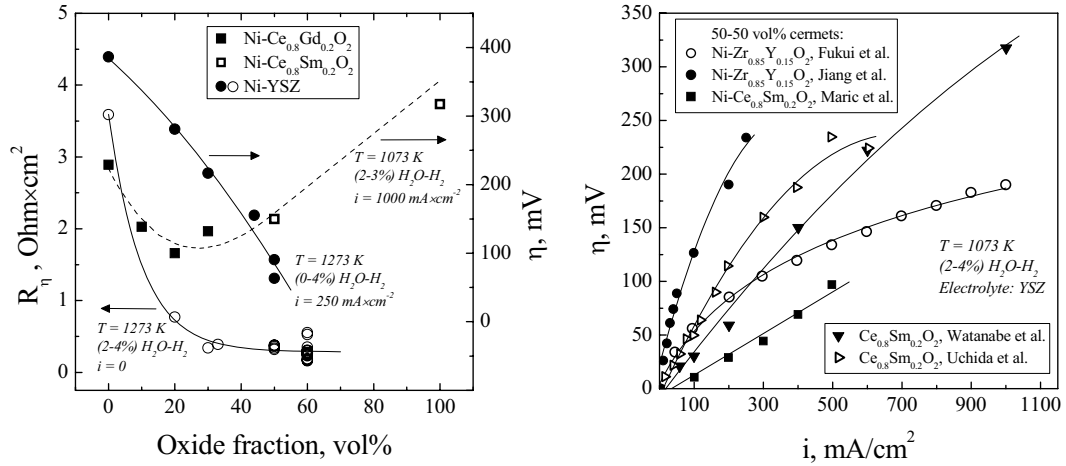


Fig.1.21. Polarization resistance and overpotentials of Ni - YSZ [132,134,135,156,162,306], Ni - CGO | LSGM [19], Ni - (Ce,Sm)O $_2$ | LSGM cermets [312] and (Ce,Sm)O $_2$ | YSZ anodes [307], left, and the current density dependencies of anodic polarization of various electrode layers [157,294,310,311,314], right.

Table 1.11

Average thermal expansion coefficients of Ni-based composite and oxide ceramics

Composition	T, K	$\bar{\alpha} \times 10^6, K^{-1}$	Ref.
Ni	-	16.5	[291]
Zr $_{0.85}$ Y $_{0.15}$ O $_2$	303-1273	10.9	[63]
Zr $_{0.85}$ Y $_{0.15}$ O $_2$	323-1273	10.3	[304]
Ni - Zr $_{0.85}$ Y $_{0.15}$ O $_2$ (40-60 vol%)	303-1273	12.6	[63]
Zr $_{0.94}$ Y $_{0.06}$ O $_2$	298-1273	10.5	[291]
Ni - Zr $_{0.94}$ Y $_{0.06}$ O $_2$ (30-70 vol%)	298-1273	12.7	[291]
Ni - Zr $_{0.94}$ Y $_{0.06}$ O $_2$ (40-60 vol%)60	298-1273	13.1	[291]
Ni - Zr $_{0.94}$ Y $_{0.06}$ O $_2$ (45-55 vol%)	298-1273	13.3	[291]
La $_{0.9}$ Sr $_{0.1}$ CrO $_3$	303-1273	10.7	[63]
La $_{0.79}$ Sr $_{0.20}$ CrO $_3$	623-1273	11.1	[63]
La $_{0.7}$ Ca $_{0.3}$ Cr $_{0.5}$ Ti $_{0.5}$ O $_3$	303-1273	10.1	[63]
La $_{0.7}$ Sr $_{0.3}$ Cr $_{0.8}$ Ti $_{0.2}$ O $_3$	303-1273	10.7	[63]
La $_{0.4}$ Sr $_{0.5}$ Ti $_{0.6}$ Fe $_{0.4}$ O $_3$	303-1053	10.2	[219]

Due to carbon deposition on the Ni-containing cermets in hydrocarbon-fueled SOFCs, attention was drawn to the electrodes based on metallic copper, which has a considerably lower catalytic activity for C-C bond formation [160,307]. The use of Cu-YSZ or (Cu,Ni) alloy-YSZ

cermets may, indeed, decrease coking in CH₄-containing atmospheres. However, the electrochemical performance of these anodes is lower than that of conventional Ni-YSZ. Therefore, further optimization of SOFC anode materials is still desirable to decrease polarization losses and to suppress carbon deposition for the cells using fossil fuels. One possible approach to enhance the electrochemical activity of conventional anode cermets, consisting of metallic Ni and yttria-stabilized zirconia (YSZ), refers to the incorporation of catalytically-active phases containing ceria [19,20,157-159].

1.5.2.2. CeO₂-based materials

First attempts to use ceria as anode material in H₂- and CO-containing atmospheres were performed in 1960s (e.g. [308]). Ceria-based phases have a very high activity for carbon oxidation [309], beneficial for the operation using hydrocarbon fuels and biogas. Another important advantage relates to mixed ionic and n-type electronic conductivity of reduced ceria, enlarging the electrochemical reaction zone.

Methane oxidation over Ce_{0.9}Gd_{0.1}O_{2-δ} resulted in total combustion at 573 K; only a minor amount of carbon formed at higher temperatures [309]. Ce_{0.9}Gd_{0.1}O_{2-δ} oxidized methane to CO₂ and H₂O at around 573 K and only small amounts of carbon are formed on this oxide at higher temperatures [309]. The electrochemical behavior of Ce_{1-x}Sm_xO_{2-δ} (x = 0-0.4) anodes in contact with YSZ electrolyte was evaluated in [310,311]; the composition with x = 0.2 showed a maximum power density in humidified hydrogen at 1073-1273 K [310]. At the same time, although no carbon deposition was detected on Ce_{0.6}Gd_{0.4}O_{2-δ} anode after the operation for 1000 h at 1273 K and steam to carbon ratio of 0.3, the electrocatalytic activity of pure gadolinia-doped ceria was found insufficient to provide a direct methane oxidation [159]. Note that the electronic conduction of ceria-based materials may also be insufficient to avoid critical ohmic losses, thus requiring to introduce a metal component.

Porous Ni-Ce_{0.8}Sm_{0.2}O_{2-δ} layers deposited onto the La_{0.9}Sr_{0.1}Ga_{0.8}Mg_{0.2}O_{3-δ} and fired at 1523-1573 K are characterized by a well-developed microstructure and good electrochemical performance, but exhibit a sharp increase in both the polarization and ohmic resistances when sintered at higher temperatures [312]. Apart from the extensive grain growth observed at 1623 K, a significant Ni diffusion into the electrolyte ceramics was detected [312]. A similar behavior, making it necessary to decrease the sintering temperature from 1773 down to 1523-1573 K, was found for Ni - Ce_{0.9}Gd_{0.1}O_{2-δ} | Ce_{0.9}Gd_{0.1}O_{2-δ} [313] and Ni - Ce_{0.8}Sm_{0.2}O_{2-δ} | YSZ [314]. At 1073 K, the maximum power density and minimum anode overpotentials of Ni - Ce_{0.8}Gd_{0.2}O_{2-δ} cermet in contact with La_{0.9}Sr_{0.1}Ga_{0.8}Mg_{0.2}O_{3-δ} correspond to 10-20 vol% of Ce_{0.8}Gd_{0.2}O_{2-δ}, increasing with the electrode sintering temperature [19]. The best performance of ceria-based cermets annealed at

1473 K can be achieved at 20-40 vol% of the oxide phase (Fig.1.21), which is smaller than the amount of zirconia required to minimize the Ni-YSZ anode polarization. The overpotentials of 95 wt% Ni - 5 wt% $\text{Ce}_{0.8}\text{M}_{0.2}\text{O}_{2-\delta}$ (M = Sm, Gd) anodes was slightly lower for M = Sm than for CGO-containing composition, both measured in contact with $\text{La}_{0.9}\text{Sr}_{0.1}\text{Ga}_{0.8}\text{Mg}_{0.2}\text{O}_{3-\delta}$ [19]. The polarization resistance of Ni - $\text{Ce}_{0.8}\text{Sm}_{0.2}\text{O}_{2-\delta}$ | $\text{Ce}_{0.8}\text{Sm}_{0.2}\text{O}_{2-\delta}$ anode was increasing with *dc* current [161]; the experimental errors could be caused by the electronic current in the electrolyte. Similar behavior might result from the volume changes and nickel oxidation due to the oxygen permeation through the electrolyte. As mentioned in Chapter 1.4.3, the Ni-ceria cermet suffer from the dimensional instabilities caused by the local $p(\text{O}_2)$ variations and excessive thermal expansion; the presence of one redox-stable phase in the anode layers is, therefore, desirable to avoid these problems. The content and distribution of such stabilizing additions should be, however, optimized. The Ni - ($\text{Ce}_{0.9}\text{Ca}_{0.1}\text{O}_{2-\delta}$ - YSZ) cermet shows lower overpotentials and anode interfacial resistances than Ni - YSZ [315], though in all cases the performance was worse than for the optimized Ni - YSZ cermet known in literature. The electrochemical activity of $\text{Zr}_{0.57}\text{Y}_{0.15}\text{Ce}_{0.15}\text{Ti}_{0.13}\text{O}_{2-\delta}$ as anode and as a component of Ni- and Cu-containing cermet is inferior compared to the conventional Ni - YSZ [316]. Among these groups of cermet, the anode obtained after reduction of $\text{CuO} - \text{Zr}_{0.57}\text{Y}_{0.15}\text{Ce}_{0.15}\text{Ti}_{0.13}\text{O}_{2-\delta}$ (60-40 wt%) showed the best performance at 773 K; the microstructural degradation of this layer was observed above 873 K [316]. Note also that the performance of Ni-based cermet containing ion-conducting $\text{Nd}_{0.9}\text{Ca}_{0.1}\text{Ga}_{0.9}\text{Co}_{0.1}\text{O}_{3-\delta}$ and $\text{Nd}_{0.9}\text{Ca}_{0.1}\text{Ga}_{0.8}\text{Mg}_{0.115}\text{Co}_{0.085}\text{O}_{3-\delta}$ perovskites or pyrochlore $\text{Gd}_2\text{Ti}_2\text{O}_7$ was substantially worse than that of ceria-containing electrodes [19].

A direct oxidation of various hydrocarbon fuels was successfully performed using Cu-(Ce,Sm) $\text{O}_{2-\delta}$ anodes dispersed in YSZ matrix [8,23]. The additions of ceria considerably improved the performance of Cu-YSZ anodes which is, however, still lower than that of Ni-containing cermet. At 973-1073 K, the maximum power densities achieved 0.22-0.31 W/cm² in hydrogen and 0.12-0.18 in n-butane atmospheres when using 60 μm -thick YSZ electrolyte, Cu - CeO_2 - YSZ (40-20-40 wt%) anode and LSM - YSZ cathode.

1.5.2.3. Alternative anode compositions

The search for alternative anode materials is primarily focused on perovskite-related structures, which are tolerant to extensive substitution and possess better transport properties with respect to other structural families such as spinel and C-type. Fig.1.22 compares the low- $p(\text{O}_2)$ stability limits of various oxide phases with high electronic conductivity. The cobaltite-, manganite- and ferrite-based compounds are clearly unstable under the SOFC anode conditions, while chromites and titanates may, in principle, be considered as fuel electrode components.

At the intermediate temperatures, LaCrO_3 is quite inert for steam reforming and for carbon deposition [119,142,322]. Alkaline-earth doping in the lanthanum sublattice enhances the conductivity [146] and electrochemical activity [142] of lanthanum chromite, most likely due to increasing oxidation state of Cr cations. Perovskite-type $\text{La}_{0.8}\text{Ca}_{0.2}\text{CrO}_{3-\delta}$ perovskite was evaluated [309,323] as a SOFC anode for complete oxidation of dry methane. Both oxidation and surface dissociation of CH_4 took place above 773 K; during complete oxidation, the carbon deposition was negligible. The electrode properties of doped chromites are poor, a result of relatively low conductivity under anodic conditions. Extremely high polarization resistances were measured for anodes made of $\text{La}_{0.8}\text{Sr}_{0.2}\text{CrO}_{3-\delta}$ and its derivatives in H_2 - H_2O and CH_4 - H_2O atmospheres even at elevated temperatures, up to 1223 K [324,325]. Analogously to the data [323], no carbon formation was detected for $\text{La}_{0.8}\text{Sr}_{0.2}\text{Cr}_{0.95}\text{Ru}_{0.05}\text{O}_{3-\delta}$ [324] and $\text{La}_{0.8}\text{Sr}_{0.2}\text{Cr}_{0.97}\text{V}_{0.03}\text{O}_{3-\delta}$ [326]. The latter composition exhibits a low activity towards steam reforming, being completely passive for the direct methane oxidation [325,326]; the polarization resistance of $\text{La}_{0.75}\text{Sr}_{0.25}\text{Cr}_{0.97}\text{V}_{0.03}\text{O}_{3-\delta}$ electrode is very high even in 3% H_2O - H_2 atmosphere [162]. The properties of $\text{La}_{1-x}\text{A}_x\text{Cr}_{1-y}\text{M}_y\text{O}_{3-\delta}$ (A = Ca, Sr; M = Ti, Fe, V, Nb) perovskite materials, relevant to the anode applications, were systematically studied in [327]; however, no composition appropriate for the use as fuel cell anode can be selected in this family. For instance, the chromium-rich solid solutions show low electrical transport; the iron-containing ceramics are characterized by a high chemically-induced expansion leading to mechanical instability. As volume expansion of the chromite-based materials on reduction may be suppressed by Ti doping [63], attention was drawn to the multicomponent oxide systems based on $\text{La}(\text{Cr},\text{Ti})\text{O}_3$. The $\text{La}_{0.4}\text{Sr}_{0.6}\text{Cr}_{0.8}\text{Ti}_{0.2}\text{O}_{3-\delta}$ electrode was found active for hydrogen oxidation, but its performance was insufficient for practical use [327]. The thermodynamic stability and catalytic activity of $\text{La}_{1-x}\text{A}_x\text{Cr}_{1-y}\text{M}_y\text{O}_{3-\delta}$ (A = Ca, Sr; M = Mg, Mn, Fe, Co, Ni) systems were analyzed in Refs.[323,324]. The Sr- and Mn-doped phases maintain perovskite lattice under the SOFC anode conditions; other substitutions had a destabilizing effect, although their decomposition is often prevented by kinetic limitations [321]. The incorporation of Ca, Sr, Mn, Fe and Ni improved the activity for CH_4 oxidation and reforming; doping by Mg and Co has inhibiting effect [322]. Note that Co- and Mn-substituted chromites showed the lowest cracking activity, in contrast to the Fe-containing materials [322]. $\text{La}_{0.75}\text{Sr}_{0.25}\text{Cr}_{0.5}\text{Fe}_{0.5}\text{O}_{3-\delta}$ was reported stable in reducing environment [328], probably due to kinetically stagnated decomposition [321]; this composition showed, again, poor electrochemical properties in wet CH_4 . The high catalytic activity and acceptable anode performance of 10 mol% Ni doped chromites [322] seem to originate from the Ni metal segregation on reduction. The $(\text{La}_{0.75}\text{Sr}_{0.25})_{1-x}\text{Cr}_{0.5}\text{Mn}_{0.5}\text{O}_{3-\delta}$ series, which is more promising for high-temperature SOFC anodes, demonstrated better properties: at $x = 0$, the polarization resistances in wet H_2 and CH_4 at 1173 K were 0.26 and 0.87 $\text{Ohm}\times\text{cm}^2$, respectively [229]. In

general, the chromite-based materials which are thermodynamically stable both in oxidizing and reducing atmospheres, show poor electrode properties. Doping with transition metals into the B sublattice increases their electrical conductivity and electrochemical activity, but deteriorates phase stability.

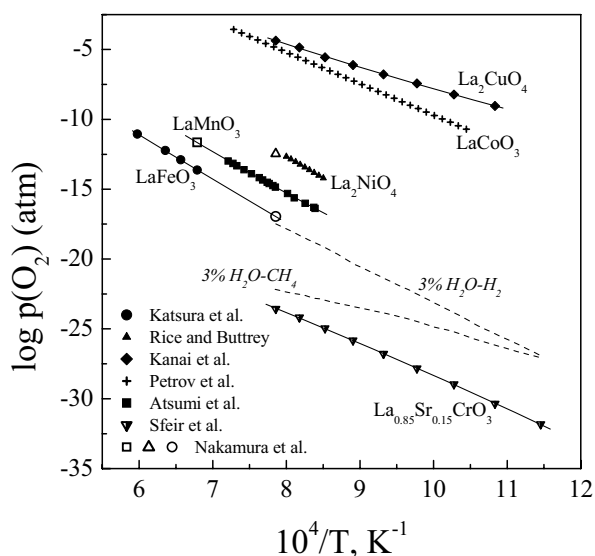


Fig.1.22. Low- $p(\text{O}_2)$ stability boundaries of various oxide phases [234,254,317-321] and oxygen chemical potentials typical for SOFC anodes.

High n-type electronic conductivity under reducing conditions is known for Ti-containing perovskites and perovskite-related lattices. Typical example is $\text{La}_{0.4}\text{Sr}_{0.6}\text{TiO}_{3-\delta}$, showing the conductivity of approximately 60 S/cm at 1173 K [327]. However, the structure and transport properties of titanates tend to degrade irreversibly on oxidation [296]. To some extent, this can be avoided by compositional optimization. The $(\text{Sr},\text{Y})(\text{Ti},\text{M})\text{O}_{3-\delta}$ ($\text{M} = \text{Co}, \text{Al}, \text{V}, \text{Cu}, \text{Ga}, \text{Mn}, \text{Ni}, \text{Fe}$) series were investigated [330] as possible anodes for YSZ or LSGM-based SOFCs; a promising combination of properties, including the total conductivity of 82 S/cm at 1073 K and $p(\text{O}_2) \approx 10^{-19}$ atm, structural stability over a wide range of temperatures and oxygen pressures and thermal expansion compatible with solid oxide electrolytes, was reported for $\text{Sr}_{0.86}\text{Y}_{0.08}\text{TiO}_{3-\delta}$. The maximum power density, 58 mW/cm² at 1173 K, was obtained using $\text{Sr}_{0.85}\text{Y}_{0.10}\text{Ti}_{0.95}\text{Co}_{0.05}\text{O}_{3-\delta}$ anode [330]. Although such performance is insufficient, these materials can be used as the support compositions or anode components. The $\text{Mg}_{2-x}\text{Ti}_x\text{O}_4$ ($x = 0-0.5$) spinels are only stable in air up to 773 K [331]. The A-site deficient $\text{Sr}_{1-3x/2-y/2}\text{La}_x\text{Ti}_{1-y}\text{Nb}_y\text{O}_3$ were synthesized single-phases at $x = 0-0.6$ and $y = 0$, or at $y = 0-0.4$ and $x = 0$ [332]; these remain stable down to $p(\text{O}_2) = 10^{-20}$ atm and have the maximum conductivity of 7 S/cm at 1203 K [332]. The polarization resistance of $\text{La}_2\text{Sr}_4\text{Ti}_6\text{O}_{19}$ anodes was 2.97 and 8.93 Ohm \times cm² at 1173 K in wet H_2 and CH_4 , respectively; in hydrogen, the power density generated by 0.3 mm YSZ-based cell with LSM cathode achieved 76

mW/cm² [335]. In summary, the titanate-based phases having relatively high electrical conductivity at low oxygen pressures are usually unstable in air. The substitution stabilizing these compounds under oxidizing conditions has unfavorable effects on the transport properties, electrode performance and stability in reducing atmospheres.

Other families considered for SOFC applications comprise $A_{0.6}Nb_{1-x}M_xO_3$ ($A = Ba, Sr, Ca, La$; $M = Mg, Ni, Mn, Cr, Fe, In, Ti, Sn$) with the tungsten bronze structure and heavily doped zirconia [334-337]. A typical composition is $Sr_{0.2}Ba_{0.4}Nb_{0.8}Ti_{0.2}O_3$, which showed the electronic conductivity lower than 10 S/cm at 1203 K and $p(O_2) = 10^{-20}$ atm, the TEC value of $7 \times 10^{-6} K^{-1}$ at 298-1273 K in air, and rather low anode performance [334]. The polarization resistance of about 2 Ohm \times cm² was reported for $Ti_{0.22}Y_{0.16}Zr_{0.92}O_2$ electrode at 1123 K in flowing 3% H_2O - H_2 [162]. In the Sc-Y-Zr-Ti-O system, a potentially interesting composition is $Sc_{0.15}Y_{0.05}Zr_{0.62}Ti_{0.18}O_2$ [336]. Such materials cannot be, however, used for single-phase electrodes.

1.5.3. Surface modification of solid electrolyte

Whatever the effect of electrolyte ionic conductivity on the electrode reaction mechanisms, the exchange current of solid electrolyte ceramics can often be enhanced modifying the surface layers. The well-established methods of electrolyte surface modification relate to a local increase of the electronic transport [338] and to the incorporation of catalytically-active particles, in particular transition metal cations [169,339-343]. The dopant selection for the surface layers should, however, take into account the possible diffusion into electrolyte bulk in the course of cell operation in order to avoid excessive leakage currents. Long-term experiments are usually necessary to verify the absence of such effects. In addition to doping of the electrolyte surface, morphological modifications can also be employed [231,272]. In particular, etching of $Ce_{0.8}Gd_{0.2}O_{2-\delta}$ ceramics with hydrofluoric acid prior to the electrode layer deposition is reported effective to remove the surface siliceous phases and to promote surface roughening, resulting in high performance of LSFC cathode [231]. The polarization resistance of LSM-YSZ composite cathodes was reduced applying a layer of coarse YSZ particles onto the electrolyte surface prior to electrode fabrication, due to the lengthening of active TPB [274]. A careful mechanical treatment can also be used for the same purpose.

Ceria doping of the YSZ surface was found to promote water vapor electrolysis on the point metallic electrodes due to electrocatalytic effects and an enlargement of the electrochemical reaction zone, resulting from higher concentration of the mobile electrons [169,340]; the electronic charge carriers can be injected into the surface of zirconia electrolytes already at relatively low cathodic polarization.

The implantation of ^{56}Fe into the YSZ surface up to 8×10^{16} at/cm^2 with the penetration depth of about 30 nm, was performed in [171,341,342]. In agreement with data of other authors [65], the presence of Fe^{3+} in the zirconia surface layer has no essential effect on the rate-determining steps for oxygen reduction on porous Au electrodes [171]. At the same time, the exchange current density increased by 10-50 times at 773-1073 K [171,342]. The implanted layers were stable up to 973-1073 K; further heating leads to the iron dissolution in the YSZ bulk [341,342]. The surface implantation of Ce or Mn into YSZ was carried out [337] with the insertion depth of 150-300 nm. At 1023 K, the polarization resistance of Pt electrodes deposited onto the surface-modified electrolyte was drastically decreased in comparison with pure YSZ, especially for cerium implantation. On the other hand, the ion implantation method is not commercially feasible [339].

Another technique for the electrolyte surface modification, via deposition of active components and subsequent firing (e.g. [344]), is simpler and more effective for practical applications, except for the obvious limitations in case of thin electrolyte films. The comparison of various dopants incorporated into YSZ surface, showed the best results for Ni and Mn at the anode and cathode sides, respectively [344]; the maximum power density for such SOFC was about 425 mW/cm^2 at 1173 K. Manganese incorporation into zirconia was also suggested to inhibit blocking layer formation at the LSM | YSZ interface and to facilitate the charge transfer process [195].

An improvement in the surface exchange kinetics of YSZ was observed on surface doping by iron [343]. This effect was attributed, however, to the removal of unfavorable phase impurities (SiO_2 , CaO and Na_2O). The deposition of iron oxide may partially the surface suppress the segregation of impurities in YSZ in the course of processing [343]. The authors [343] suggested also that no improvement in the surface exchange rate of zirconia by using catalytically active species can be achieved if YSZ is clean enough. Such an assumption, based on the comparison of tracer diffusion profiles in surface-unmodified and iron-modified samples, seems questionable considering other literature data, including the results on single YSZ crystals [339,345].

Surface-modification of YSZ with PrO_x and $\text{La}_{0.7}\text{Sr}_{0.3}\text{CoO}_{3-\delta}$ resulted in a dramatic increase in oxygen exchange rate [345]. A significant improvement in the power density of a single-chamber SOFC, where CH_4 -air mixture is supplied onto both electrodes made of Pt and Au, was achieved modifying the YSZ electrolyte surface by praseodymium oxide [346]. The modification was performed painting the YSZ ceramics with a saturated aqueous solution of $\text{Pr}(\text{NO}_3)_3$ at the cathode side and subsequent thermal treatment; the thickness of activating layer was 2-3- μm [346].

The use of yttria-doped ceria layers between the electrolyte and electrodes was reported to suppress carbon deposition, to preserve high cell voltages, and to reduce interfacial resistances of LSM cathode and Ni-YSZ anode [28,116]. The use of such layers may be, however, associated

with instabilities due to cation interdiffusion, thermal expansion mismatch and secondary phase segregation at the interface, all increasing the cell resistance [43,62].

1.5.4. Modification of electrode layers

In addition to the use of sintering aids, which can be added into electrode compositions to decrease the sintering temperature and to preserve high surface area, the electrodes can be further activated during or after fabrication, applying a highly-dispersed electrocatalytically active component onto the electrode and electrolyte surfaces. A number of methods, including impregnation with cation-containing solutions or suspensions and subsequent calcination, coating with oxide gels or slurries to form thin layers, and deposition of catalysts onto the electrode particles prior to the layer formation, are known in literature.

The application of highly dispersed noble metals onto the surface of manganite, cobaltite- and cuprate-based cathodes and ceria-based anodes provides a considerable improvement of their performance [95,250,296,310,311]. These additives are, however, quite expensive. The use of less expensive silver is possible generally below 1023-1073 K, due to fast volatilization at higher temperatures. Nonetheless, additions of silver to the electrode composition before thermal treatment and/or impregnation of sintered electrode layers with Ag-containing solutions, is often effective to reduce cathode overpotentials [95,196,146,347,348]. Selected results are shown in Figs.1.16 and 1.23. Note, however, that the electrocatalytic effect of minor Ag additions is strongly dependent on the starting powder morphology and sintering conditions, which determine the distribution of remaining Ag in the electrode system. For example, no positive impact was observed for $\text{La}_{0.65}\text{Sr}_{0.3}\text{MnO}_3$ cathodes synthesized by the Pechini method, with homogeneously distributed 0.1-2.0 wt% Ag [349]. Minor (0.3-3 wt%) additions of nickel onto the anode surface were found to significantly decrease the polarization resistance of mixed-conducting $\text{Ce}_{0.6}\text{Gd}_{0.4}\text{O}_2$, $\text{La}_{0.75}\text{Sr}_{0.25}\text{Cr}_{0.97}\text{V}_{0.03}\text{O}_3$ and $\text{Ti}_{0.22}\text{Y}_{0.16}\text{Zr}_{0.92}\text{O}_2$ oxide anodes and Ni- $\text{Ce}_{0.9}\text{Gd}_{0.1}\text{O}_2$ (40-60 vol%) cermet; no essential effect was found in the case of Ni- $\text{Zr}_{0.92}\text{Y}_{0.16}\text{O}_2$ (40-60 vol%) layers [162].

For oxygen-containing atmospheres, praseodymia can be used as an activating agent to reduce polarization of the oxide and metal electrodes [32,146]. The influence of praseodymia modification on the performance of manganite-based cathodes is illustrated by Fig.1.23. The overpotentials of dense In_2O_3 | YSZ electrodes decrease after the deposition of PrO_x thin layer, obtained by the nitrate decomposition [177].

The manganite electrodes can also be activated applying other perovskite materials with higher electrochemical activity, such as cobaltites, onto the surface; in this case, the thermal expansion mismatch is less important due to high porosity. For example, screen-printing of $(\text{La,Sr})\text{CoO}_{3-\delta}$ over manganite layers resulted in considerably lower overpotentials [350]. The

impregnation by the aqueous solution of nitrates prepared via the dissolution of $\text{La}_{0.5}\text{Sr}_{0.5}\text{CoO}_{3-\delta}$ or $\text{Pr}_{0.5}\text{Sr}_{0.5}\text{CoO}_3$ in nitric acid, enabled to reduce polarization of $\text{La}_{0.6}\text{Sr}_{0.4}(\text{Mn,Fe})\text{O}_{3-\delta}$ cathodes [201]. Analogously, a drastic decrease in the polarization resistance of $\text{La}_{0.7}\text{Sr}_{0.3}\text{CoO}_{3-\delta}$, 10-100 times, was achieved after surface modification via the impregnation with a solution of metal acetates of the same cation composition [351]. As for PrO_x deposition, such an improvement cannot be attributed to a single factor determining electrode activity. This type of modification increases specific surface area, improves the contact between electrode grains and between electrode and electrolyte, and enlarges the TPB.

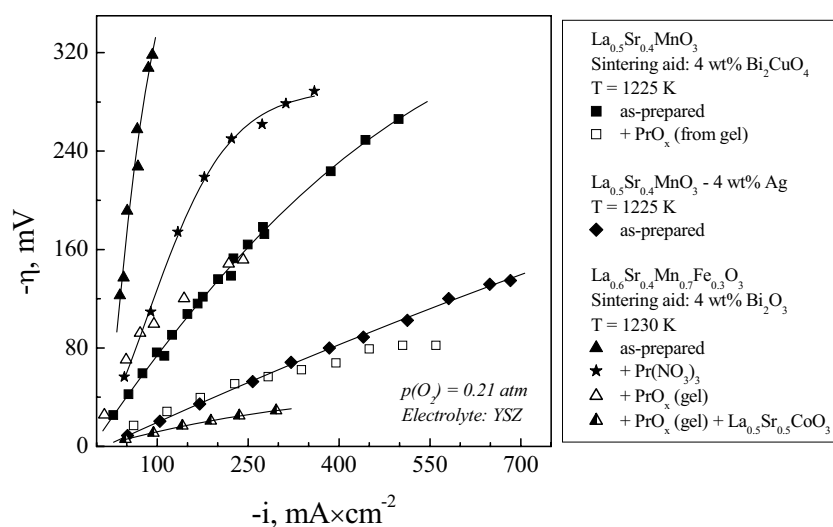


Fig.1.23. Current dependencies of cathodic overpotentials of (La,Sr)(Mn,Fe) O_3 electrodes before and after the surface modification [146,196,201].

The effects of impregnation of Ni - YSZ cermets and $\text{La}_{0.72}\text{Sr}_{0.18}\text{MnO}_3$ cathodes with fine $\text{Zr}_{0.97}\text{Y}_{0.03}\text{O}_2$, CeO_2 and $\text{Ce}_{0.8}\text{Sm}_{0.2}\text{O}_2$ oxide particles, via immersing electrode layers in the acidic solutions of metal nitrates, were assessed in Ref.[157]. In all cases, the performance was considerably improved (Fig.1.8). Furthermore, sintering, grain growth and agglomeration of the metal particles in cermet anodes were effectively inhibited; ceria incorporation into the anodes was found most favorable, as expected [157].

An additional impact can be provided decreasing the particle size of the oxide activating agents down to nanoscale level. In combination with a greater surface area, this should affect both transport and electrocatalytic properties due to a reduced defect formation energy and high concentration of grain boundaries on the surface [352,353]. For instance, nanocrystalline ceria

exhibits a substantially higher electronic conduction and faster oxygen exchange if compared to the materials with micron-sized grains [352,353].

1.6. Concluding remarks: promising directions in the developments of novel electrode materials

The major prospects in SOFC developments are directed towards decreasing the cell operation temperatures, which increases the role of cathode and anode polarization. As concluded from Chapter 1.5.1, an optimum cathode material for the IT SOFCs can hardly be proposed to the moment; each group of known materials possesses a number of specific disadvantages limiting the practical use. Since the properties of perovskite-type solid solutions are usually intermediate with respect to end members, improving one parameter relevant to the electrode application results often in deteriorating the others. The same statement is valid for ceramic anodes (see Chapter 1.5.2.3). At the same time, the performance of state-of-the-art cathodes and anodes currently used in the SOFC technology is obviously insufficient for the operation at reduced temperatures. This makes it necessary to search for new materials, highly active for the oxygen reduction and fuel oxidation processes and satisfying all general requirements for the SOFC electrodes.

For the cathodes, one promising strategy relates to the assessment of cobaltite and nickelate phases with intergrowth structures. In the anode developments, alternative redox-stable and catalytically-active phases should be tested and the role of components should be clarified in detail, especially in the intermediate temperature range. In parallel, simple and economically feasible methods of electrode processing are to be explored. These should enable the fabrication of uniform optimized microstructures of the porous electrode layers and their subsequent activation, the importance of which was discussed in Chapters 1.4, 1.5.3 and 1.5.4. An additional enhancement of the electrochemical activity could be expected using the nanocrystalline ceramic additives, further sintering of which should be rather limited at intermediate temperatures. To elaborate appropriate methodology of the electrode developments more in-depth study into the electrode reaction mechanisms may be desirable. Of great importance, is also the analysis of empirical knowledge based on the reliable and systematic experimental data on the electrode properties of promising materials, making it possible to optimize their compositions and microstructure. In the current literature, the electrode reactions were primarily investigated in contact with zirconia solid electrolytes. Taking into account the contributions of electrolyte surface (Chapter 1.4.4), the electrode activity may alter depending on the solid electrolyte material. The information on electrochemical behavior of electrode materials, either common or new, in contact with lanthanum gallate-based ionic conductors is scarce, although these electrolyte family is among most promising for IT SOFCs.

Part 2: Experimental

2.1. Synthesis and ceramic processing

The conditions of the powders and ceramics processing are summarized in Table 2.1. Most of the chemicals used for the synthesis as starting materials, were produced by Merck, Aldrich, Fluka or Riedel-de Haën companies (>99.9 % purity). In the case of $\text{Ce}_{0.8}\text{Gd}_{0.2}\text{O}_{2-\delta}$, $\text{Zr}_{0.85}\text{Y}_{0.15}\text{O}_{2-\delta}$ (Y8SZ), $\text{Zr}_{0.9}\text{Y}_{0.1}\text{O}_{2-\delta}$ and $(\text{La}_{0.9}\text{Sr}_{0.1})_{0.98}\text{Ga}_{0.8}\text{Mg}_{0.2}\text{O}_{3-\delta}$, commercially available powders and ceramics (Rhodia, Tosoh and Praxair) were used.

Single-phase powders of zircon-type $\text{Ce}_{1-x}\text{Ca}_x\text{VO}_{4+\delta}$ ($x = 0, 0.1, 0.2$) and $\text{Ce}_{0.9}\text{Sr}_{0.1}\text{VO}_{4+\delta}$, pyrochlore-type $\text{Gd}_{2-x}\text{Ca}_x\text{Ti}_2\text{O}_{7\pm\delta}$ ($x = 0.10, 0.14$) and $\text{Gd}_{2-x}\text{Ca}_x\text{Ti}_2\text{O}_{7\pm\delta}$ ($x = 0.05, 0.10, 0.14$) with additions of ~3 mol% SiO_2 ; K_2NiF_4 -type $\text{La}_2\text{Ni}_{0.9}\text{Co}_{0.1}\text{O}_{4+\delta}$, hexagonal $\text{YBaCo}_4\text{O}_{7+\delta}$, and perovskite-type $\text{La}_{0.3}\text{Sr}_{0.7}\text{CoO}_{3-\delta}$ powders were synthesised via a standard ceramic technique from high-purity $\text{Ce}(\text{NO}_3)_3 \cdot 6\text{H}_2\text{O}$, V_2O_5 , SrCO_3 , CaCO_3 , Gd_2O_3 , TiO_2 , $\text{Ni}(\text{NO}_3)_2 \cdot 6\text{H}_2\text{O}$, Y_2O_3 , BaCO_3 , $\text{Co}(\text{NO}_3)_2 \cdot 6\text{H}_2\text{O}$ and La_2O_3 . Before weighting, gadolinium, titanium, yttrium and lanthanum oxides were annealed in air at 1173-1473 K for 2-3 h to remove adsorbates. The stoichiometric amounts of starting materials were mixed and then calcined in air in alundum crucibles, typically at 823-1273 K for 5-10 h. The final solid-state reactions were conducted in air at 1123-1623 K for 5-25 h, with multiple intermediate regrindings under ethanol using an agate mortar and pestle. $\text{CeV}_{0.9}\text{M}_{0.1}\text{O}_4$ ($\text{M} = \text{Fe}, \text{Ni}, \text{Cu}$) were synthesized in a similar way as $\text{Ce}_{1-x}\text{A}_x\text{VO}_{4+\delta}$, but contained ceria impurities.

Submicron powders of $\text{La}_2\text{Ni}_{0.8}\text{Cu}_{0.2}\text{O}_{4+\delta}$ and $\text{La}_2\text{Ni}_{0.9}\text{Co}_{0.1}\text{O}_{4+\delta}$ with K_2NiF_4 -type structure, hexagonal $\text{YBaCo}_{4-x}\text{Fe}_x\text{O}_{7+\delta}$ ($x = 0, 0.4, 0.8$), and perovskite-like $(\text{La}_{0.3}\text{Sr}_{0.7})_{0.97}\text{CoO}_{3-\delta}$, $\text{La}_{0.3}\text{Sr}_{0.7}\text{Co}_{0.8}\text{M}_{0.2}\text{O}_{3-\delta}$ ($\text{M} = \text{Al}, \text{Ga}$) and $\text{La}_{0.90}\text{Sr}_{0.10}\text{Al}_{0.85-x}\text{Fe}_x\text{Mg}_{0.15}\text{O}_{3-\delta}$ ($x = 0.20-0.60$) were prepared by the glycine-nitrated process (GNP), a self-sustaining combustion technique using nitrates of metal components as an oxidant and glycine ($\text{NH}_2\text{CH}_2\text{COOH}$) as a fuel and chelating agent [354]. This synthesis method is suitable to obtain homogeneous multicomponent oxide powders with a large specific surface area [354], especially when the solid-state reaction is stagnated due to kinetic reasons. The starting materials were $\text{La}(\text{NO}_3)_3 \cdot 6\text{H}_2\text{O}$, $\text{Ni}(\text{NO}_3)_2 \cdot 6\text{H}_2\text{O}$, $\text{Cu}(\text{NO}_3)_2 \cdot 2.5\text{H}_2\text{O}$, $\text{Co}(\text{NO}_3)_2 \cdot 6\text{H}_2\text{O}$, $\text{Y}(\text{NO}_3)_3 \cdot 6\text{H}_2\text{O}$, $\text{Fe}(\text{NO}_3)_3 \cdot 9\text{H}_2\text{O}$, SrCO_3 or $\text{Sr}(\text{NO}_3)_2$, Ga_2O_3 , $\text{Al}(\text{NO}_3)_3 \cdot 9\text{H}_2\text{O}$, $\text{Mg}(\text{NO}_3)_2 \cdot 6\text{H}_2\text{O}$. For the synthesis, the stoichiometric amounts of metal nitrates were dissolved in distilled water; barium carbonate and gallia were preliminarily dissolved in an aqueous solution of nitric acid. Then glycine was added to the solution in an equivalent ($\text{La}_2\text{Ni}_{0.8}\text{Cu}_{0.2}\text{O}_{4+\delta}$) or double (all other cases) amount to the stoichiometric one, calculated assuming the only gaseous reaction products to be N_2 , CO_2 and H_2O . Portions of a solution were

placed into 2 l beaker, covered with a steel grid and evaporated on a hot plate until autoignition. The resultant foam-like powders were calcined in air at 1073-1273 K for 2 h to remove organic residues and then ball-milled. $\text{La}_{0.90}\text{Sr}_{0.10}\text{Al}_{0.65}\text{M}_{0.20}\text{Mg}_{0.15}\text{O}_{3-\delta}$ (M = Co, Ni), which occurred to be unobtainable as single phases, were prepared analogously to the iron-containing materials, but with additional treatments at 1373-1673 K.

Table 2.1

Details of the powder and ceramic synthesis and processing, in air

Composition	Calcination/Synthesis		Sintering		Relative density, %
	T, K	Time*, h	T, K	Time*, h	
<i>Standard ceramic route</i>					
$\text{Ce}_{1-x}\text{A}_x\text{VO}_{4+\delta}$ (A = Ca, Sr; x = 0-0.2)	873-1123	10-30	1423-1653	2-8	93-99
$\text{Gd}_{2-x}\text{Ca}_x\text{Ti}_2\text{O}_{7\pm\delta}$ (x = 0.10-0.14),	1273-1623	35	1823	4	99
$\text{Gd}_{2-x}\text{Ca}_x\text{Ti}_2\text{O}_{7\pm\delta}$ (x = 0.05-0.14)- SiO_2			1723-1773		91-95
YBaCo ₄ O _{7+δ} (Method 1)	1073-1273	10	1523	2	98
$\text{La}_{0.3}\text{Sr}_{0.7}\text{CoO}_{3-\delta}$					93
$\text{La}_2\text{Ni}_{0.9}\text{Co}_{0.1}\text{O}_{4+\delta}$ (Method 1)	1423-1593	30	1723	2	96
<i>Glycine-nitrate process</i>					
$\text{La}_2\text{Ni}_{0.9}\text{Co}_{0.1}\text{O}_{4+\delta}$ (Method 2)	1073	2	1543	2	97
$\text{La}_2\text{Ni}_{0.8}\text{Cu}_{0.2}\text{O}_{4+\delta}$	1073	2	1503	2	98
$(\text{La}_{0.3}\text{Sr}_{0.7})_{1-x}\text{Co}_{1-y}\text{M}_y\text{O}_{3-\delta}$ (M = Al, Ga; x = 0-0.03; y = 0-0.2)	1073-1273	2	1423-1553	2	97-98
YBaCo ₄ O _{7+δ} (Method 2),	1073/1273	2/5	1473	2	78-93
YBaCo _{4-x} Fe _x O _{7+δ} (x = 0.4, 0.8)					
$\text{La}_{0.9}\text{Sr}_{0.1}\text{Al}_{0.85-x}\text{Fe}_x\text{Mg}_{0.15}\text{O}_{3-\delta}$ (x = 0.2-0.6)	1273	2	1673	2-4	90-91
<i>Cellulose-precursor technique</i>					
$\text{Ce}_{0.8}\text{Gd}_{0.2}\text{O}_{2-\delta}$ (CGO)	1173	2	-	-	
NiO - $\text{Ce}_{0.8}\text{Gd}_{0.2}\text{O}_{2-\delta}$	1173	2	-	-	
CuO - $\text{Ce}_{0.8}\text{Gd}_{0.2}\text{O}_{2-\delta}$	1173	2	-	-	
<i>Mechanically-activated synthesis</i>					
TbZrO _{4-δ}	-	-	1473	6	>90
TbHfO _{4-δ}	-	-	1473	6	>90
<i>Commercially available powders</i>					
8 mol% Y ₂ O ₃ -stabilized zirconia (Zr _{0.85} Y _{0.15} O _{2-δ} or Y8SZ)	-	-	1873	8	>95
Zr _{0.90} Y _{0.10} O _{2-δ}	-	-			>95
$(\text{La}_{0.9}\text{Sr}_{0.1})_{0.98}\text{Ga}_{0.8}\text{Mg}_{0.2}\text{O}_{3-\delta}$ (LSGM)	-	-	1673	4	95

* the total time of all synthesis steps is given

Nanocrystalline powders of single-phase fluorite-type $\text{Ce}_{0.8}\text{Gd}_{0.2}\text{O}_{2-\delta}$ (CGO) and two-phase NiO - $\text{Ce}_{0.8}\text{Gd}_{0.2}\text{O}_{2-\delta}$ (50-50 mol%) and CuO - $\text{Ce}_{0.8}\text{Gd}_{0.2}\text{O}_{2-\delta}$ (50-50 mol%) mixtures, were obtained by the cellulose-precursor method, earlier tested for synthesis of other mixed conductors (e.g. [158]). This technique is based on the combustion of structure-modified cellulose containing the metal salts. In the course of synthesis, the starting cellulose fiber was reacted with 65-70% solution of nitric acid, resulting in formation of so-called Knecht compound, $(\text{C}_6\text{H}_{10}\text{O}_5 \cdot \text{HNO}_3)_n$; the latter was then hydrolyzed in order to increase sorption ability of the template. The prepared structure-modified cellulose matrix was impregnated with 1.2 - 1.5 ml/g of 0.25-1.00 M aqueous solutions of the corresponding metal nitrates, $\text{Ce}(\text{NO}_3)_3 \cdot 6\text{H}_2\text{O}$, $\text{Gd}(\text{NO}_3)_3 \cdot 6\text{H}_2\text{O}$, $\text{Ni}(\text{NO}_3)_2 \cdot 6\text{H}_2\text{O}$ and $\text{Cu}(\text{NO}_3)_2 \cdot 2.5\text{H}_2\text{O}$. Then the cellulose fibers were dried and ignited on a hot plate, forming oxide fiber retaining the precursor texture. In order to ensure complete firing of carbon-containing residuum, the materials were annealed in air at 1173 K for 2 h. The oxide fibers were readily destroyable into fine powders by light mechanical action.

Single-phase fluorite-related $\text{TbZrO}_{4-\delta}$ and $\text{TbHfO}_{4-\delta}$ were synthesized from mechanically activated stoichiometric mixtures of high-purity terbium, zirconium and hafnium oxides. The 20g batch of initial oxide mixture was loaded into cylindrical vial (volume of 125 ml) with steel balls (5 mm in diameter); the powder to balls weight ratio was 0.5-0.7. The mechanical activation was performed in air following the method employed in Ref.[355], in a high-energy eccentric-type vibration mill at 1200 rpm for 10 h.

In order to identify possible microstructural effects on the transport properties, $\text{YBaCo}_4\text{O}_{7+\delta}$ and $\text{La}_2\text{Ni}_{0.9}\text{Co}_{0.1}\text{O}_{4+\delta}$ samples were prepared using two different synthesis methods, namely the standard ceramic technique and the glycine-nitrate process, hereafter referred to as Method 1 and Method 2, respectively.

Formation of single phases or multiphase mixtures was verified by X-ray diffraction analysis, as described in Chapter 2.2. The powders synthesized via a standard ceramic or glycine-nitrate routes were ball-milled for 4 hours in a nylon container with 9-20 mm zirconia balls in ethanol media, dried and uniaxially pressed at 200-400 MPa into disks (12-18 mm in diameter) of various thicknesses. Gas-tight ceramics, were sintered in air at 1423 – 1773 K for 2-8 h and slowly (2-4 K/min) furnace-cooled down to room temperature, in order to achieve equilibrium oxygen stoichiometry. Mechanically-treated $\text{TbMO}_{4-\delta}$ powders were pressed into discs of 10 mm diameter at 30 MPa, placed into a furnace preheated to 523 K, and then fired in air at 1473 K for 6 h with subsequent slow cooling. This procedure was selected on the basis of experimental data on phase development in the activated mixtures. After sintering, the Ba-containing samples were kept in dry CO_2 -free air for 10-20 days. Except for $\text{YBa}(\text{Co},\text{Fe})_4\text{O}_{7+\delta}$ and $\text{TbMO}_{4-\delta}$, density of the ceramic materials, determined by the standard picnometric technique, was higher than 90% of the

theoretical value calculated from XRD data. Disc and bar-shaped samples of necessary sizes were then cut off using a diamond saw and polished with diamond discs, SiC papers and diamond pastes.

2.2. X-ray diffraction, chemical analysis, IR absorption spectroscopy and Mössbauer spectroscopy

Phase purity was confirmed by X-ray diffraction (XRD) analysis for the oxide powders, as prepared or obtained by grinding of the ceramic samples. XRD patterns were recorded in atmospheric air on a series Rigaku D/Max-B X-ray powder diffractometer; a Philips X'Pert MPD apparatus with a Pt heating strip was used for the high-temperature XRD studies. In both cases the scans were obtained in Cu-K α radiation ($\lambda = 0.154178$ nm), within 2Θ range from 10 to 120° with step 0.02° and 3-7 s/step. Room temperature XRD was performed for either equilibrated samples or for the materials quenched in liquid nitrogen. In order to assess phase changes on heating and under reduction, porous ceramics were annealed at fixed temperatures in flowing oxygen, air (purified from water vapour and CO $_2$, when necessary), Ar, O $_2$ -Ar or H $_2$ O-H $_2$ -N $_2$ gas mixtures for 2-50 hours, with subsequent slow (1-2 K/min) or fast (10 K/min) cooling in the same flow, or quenching. The oxygen partial pressure was independently measured by an oxygen sensor. High-temperature XRD studies were carried out at 298-1223 K in air and under vacuum of approximately 2×10^{-9} atm. The Fullprof software [356] was employed to calculate unit cell parameters, to verify lattice symmetry, and to estimate the amount of secondary phases in multiphase materials. In the case of partial decomposition, structural parameters of the major phase were refined on the first step; then the secondary phase was included in the refinement.

The cation composition of selected samples was confirmed by inductively coupled plasma – optical emission spectroscopy (ICP-OES) analysis (Jobin Yvon JY 70 plus), which showed, in all cases, no essential deviations from their nominal compositions within the limits of experimental error. Infrared (IR) absorption spectra were collected at room temperature in the frequency range 250-4000 cm $^{-1}$, using the KBr pellet technique and a SPECORD M-80 instrument.

In order to evaluate the valent states of iron cations in the oxide phases, Mössbauer spectroscopy was used. Mössbauer spectra were collected by Dr. João C. Waerenborgh at the Chemistry Department of the Instituto Tecnológico e Nuclear (Sacavém) in the framework of collaborative research with the University of Aveiro. For these studies, selected samples were annealed at 973 and 1223 K in air during 4-5 h, with subsequent quenching in liquid nitrogen. The Mössbauer spectra were obtained at 295 and 20 K in transmission mode using a conventional constant-acceleration spectrometer and a 25 mCi ^{57}Co source in a Rh matrix; the low-temperature data were obtained using a liquid-helium flow cryostat with a temperature stability of ± 0.5 K. The velocity scale was calibrated using α -Fe foil. The absorbers were obtained by pressing the

powdered samples (5 mg of natural Fe/cm²) into perspex holders. The spectra were fitted to Lorentzian lines using a non-linear least-squares method; the isomer shifts (IS) are given relative to metallic α -Fe at room temperature. The relative areas and widths of both peaks in a quadrupole doublet were kept equal during refinement. The summary of the results is presented in Appendix 2.

2.3. Microstructural studies

The microstructure inspections of oxide powders and fibers, and fractured or polished ceramics were performed by a scanning electron microscopy combined with energy dispersive spectroscopy SEM/EDS using a Hitachi S-4100 microscope. The powders were mixed with ethanol and deposited onto a glass plate before applying onto the holder. The ceramic materials with a smooth surface were prepared by mechanical polishing on the silicon carbide papers #600-2400 and diamond pastes 1/4-3 μm , sequentially decreasing the abrasive roughness. Then the samples were ultrasonically cleaned and thermally etched for 0.3-1 h in order to remove residual carbon and to visualize grain boundary phenomena; the temperature of etching was 150-200 K below the sintering temperature.

The submicron-sized powders were characterized by transmission electron microscopy (TEM) coupled with EDS on a Hitachi H-9000 microscope. The powders were applied onto the Cu- or Ni-grid holders from ultrasonically-dispersed suspension in ethanol. The electron diffraction studies with 300 kV beam were employed to evaluate the crystallization processes. Inhomogeneities in the cation distribution were assessed using the EDS analysis.

2.4. Dilatometry and thermal analysis

Dilatometric data were obtained in air using a Bahr DIL801L, Linseis L70 or Linseis L75V series dilatometers, all with alumina measuring cell, at 298-1373 K with a heating/cooling rates of 3-5 K/min. These studies were used to assess the shrinkage behavior and to calculate the thermal expansion coefficients (TECs). For the dilatometric analysis, the rectangular samples were cut from green compacts or sintered ceramics.

Thermogravimetric and differential thermal analyses (TG/DTA) were carried out on a Setaram LabSys TG-DTA16 or Setaram SetSys 16/18 instruments in a flow of air or 10%H₂-90%N₂ mixture. The powdered samples prepared by grinding ceramics were preliminarily annealed in air at 1273 K with subsequent 1 K/min cooling down to room temperature. TG/DTA measurements were performed in air, with 3-5 K/min ramp rate. Alternatively, the measurement regime included heating to a desired temperature (1-3 K/min) in air flow, equilibration at this temperature for few hours, flushing the apparatus with argon, exposure in flowing 10%H₂-90%N₂ mixture and then heating to 1373 K in the same flow in order to ensure complete reduction to

oxides with constant stoichiometry and metals. The total oxygen content in air was then calculated from the latter results.

2.5. Measurements of the total electrical conductivity and Seebeck coefficient

The total electrical conductivity (σ) was measured by 4-probe *dc* technique, van der Pauw method or *ac* impedance spectroscopy (Hewlett Packard HP 4284A precision LCR meter, frequency range 20 Hz-1 MHz), using ceramic bars and/or discs. The impedance data were collected in flowing air, argon and 10% H_2 -90% N_2 mixture and analyzed using the “Equivalent Circuit” program [357]. The values of the activation energy (E_a) for conductivity were calculated by the standard Arrhenius equation:

$$\sigma = \frac{A_0}{T} \exp\left(-\frac{E_a}{RT}\right) \quad (2.1)$$

where A_0 is the pre-exponential factor.

The isothermal measurements of the $p(\text{O}_2)$ dependencies of total conductivity (4-probe *dc*) and Seebeck coefficient (α) were performed at 973-1223 K on two separate bar-shaped samples placed inside a hermetical cell of YSZ (Fig.2.1). This cell was equipped with an electrochemical oxygen pump and a sensor, isolated from each other by a glass-ceramic sealant. For the thermoelectric power measurements, the sample was squeezed between two B-type thermocouples, one end of which served also as a potential probe for measuring thermal e.m.f. of the sample. The system was initially evacuated with a vacuum pump and filled with O_2 - CO_2 gas mixture. In the course of measurements, the oxygen partial pressure was varied by the solid-electrolyte oxygen pump, continuously pumping oxygen in or out the cell, and controlled by the sensor. The criteria for equilibration of a sample after a change in either $p(\text{O}_2)$ or temperature included the relaxation rates of the conductivity and thermopower less than 0.05 %/min and $0.001 \mu\text{V}\times\text{K}^{-1}\times\text{min}^{-1}$, respectively. Due to stagnated gas diffusion and compositional instabilities at oxygen partial pressures from 10^{-6} down to 10^{-11} - 10^{-9} atm, resulting in hysteresis phenomena and, possibly, non-equilibrium values of the conductivity and Seebeck coefficient, this $p(\text{O}_2)$ range was usually excluded from consideration. At higher and lower oxygen pressures, the transport properties of single phase materials were completely reproducible, within the limits of standard experimental error. The thermopower was determined under a temperature differential of 10-15 K; the higher potential was formally assigned to a hotter end of the sample. The Seebeck coefficients were then corrected to that of corresponding Pt-Rh alloy.

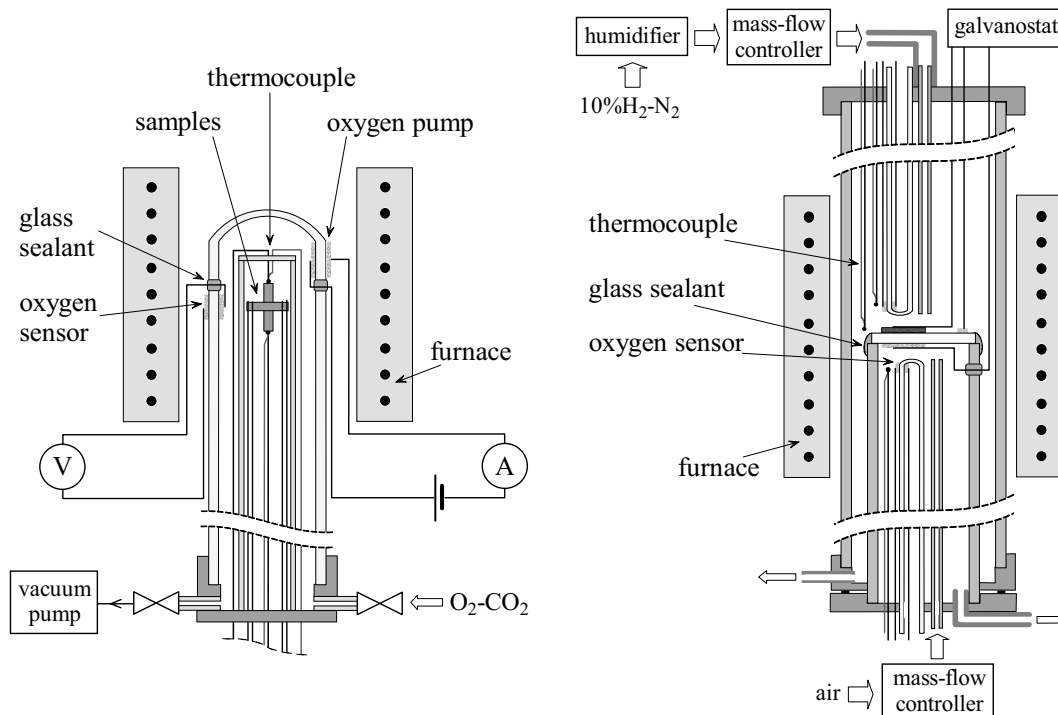


Fig.2.1. Schematic drawings of the experimental set-ups for the measurements of total conductivity and Seebeck coefficient vs. $p(O_2)$ (left) and electrode polarization (right).

The evaluation of the low- $p(O_2)$ phase stability boundary was based on the data on total conductivity and thermopower vs. oxygen partial pressure. The Seebeck coefficient defined as a voltage generated in a material under unit temperature gradient, is a function of charge carrier concentration and mobility, both being very sensitive with respect to the phase composition. The same is for the electronic and ionic conductivities. The oxygen pressure, at which the slope of $\log(\sigma) - \log p(O_2)$ and $\alpha - \log p(O_2)$ dependencies starts to change stepwise, was considered as the stability limit at a given temperature. Further reducing of oxygen partial pressure leads to a drastic, usually irreversible degradation of the electrical properties due to phase decomposition.

2.6. Oxygen transport properties

The oxygen transport parameters (permeability, transference numbers and ionic conductivity), were measured only for dense gas-tight ceramics. Both sides of the disc-shaped sample (diameter 9-11 mm) were polished until the necessary thickness and a mirror surface were achieved. The gas-tightness was then tested under the total gas pressure of 2 atm. When necessary, Pt electrodes (Engelhard paste) were painted onto both sides of the sample and annealed at 1223-1273 K.

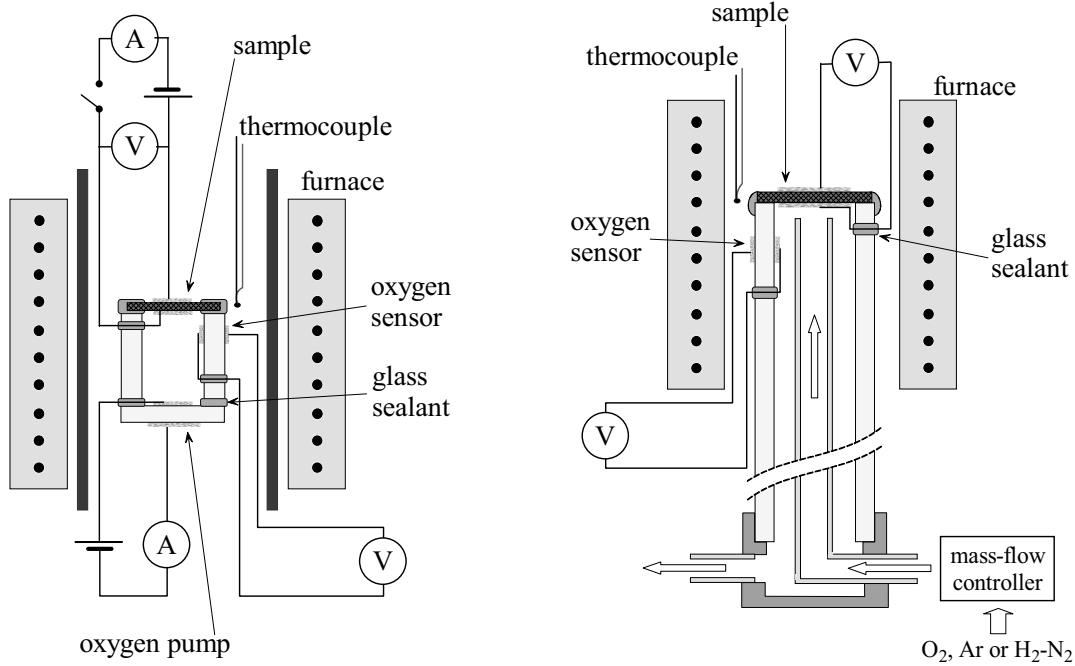


Fig.2.2. Schematic assemblies of experimental set-ups for the faradaic efficiency (left) and e.m.f. (right) measurements.

2.6.1. Faradaic efficiency studies

The oxygen ion transference numbers ($t_o = \sigma_o / (\sigma_o + \sigma_e)$ where σ_o and σ_e are the partial ionic and electronic conductivities), were determined by the faradaic efficiency (FE) technique, based on the comparison of the total electrical current driven through the sample by an applied *dc* voltage, and the corresponding oxygen flux. Most of the measurements were carried out under zero oxygen chemical potential (μ) gradient in atmospheric air at 973-1223 K. The measuring cells comprising an oxygen pump and a sensor made of YSZ solid electrolyte, sealed together with the glass-ceramics (see Chapter 2.7.3), are illustrated in Fig.2.2 (left). After sealing of a gas-tight ceramic sample with porous Pt electrodes onto preliminarily prepared zirconia cell, a direct current I_{total} was passed through the sample pumping oxygen into the cell, and a current I_o was simultaneously passed through the pump, removing oxygen from the cell. The time-independent current values were adjusted to provide sensor e.m.f. values (E_{sens}) to be constant and close to zero:

$$E_{\text{sens}} = \frac{RT}{4F} \ln \left(\frac{p_2}{p_1} \right) \approx 0 \quad (2.2)$$

where p_1 and p_2 were the oxygen partial pressures inside and outside the cell. In steady-state conditions, oxygen chemical potential gradients across the membrane were therefore negligible. The steady oxygen fluxes through the sample (J_{total}) and a pump (J_o) are defined as:

$$J_{\text{total}} = t_{\text{O}} \cdot I_{\text{total}} \cdot (4F)^{-1} \quad \text{and} \quad J_{\text{O}} = I_{\text{O}} \cdot (4F)^{-1} \quad (2.3)$$

Since these fluxes should be equal, the oxygen ion transference number can be determined:

$$t_{\text{O}} = \frac{I_{\text{O}}}{I_{\text{total}}} \quad (2.4)$$

Decreasing temperature and/or oxygen partial pressure in the measuring cells is known to increase errors in the transference number determination by the classical faradaic efficiency and e.m.f. techniques due to a greater role of electrode polarization, which may be significant in the case of materials with dominant ionic transport. When the effect of electrode processes, tested combining the faradaic efficiency data with impedance spectroscopy was found negligible, t_{O} values were calculated from Eq.(2.4). Otherwise, the modifications of FE method were employed to take the electrode polarization resistance (R_{η}) into account and to increase accuracy of the transference number determination. For small ionic currents, the electrode overpotential (η) linearly depends on current as $\eta = R_{\eta} \cdot I_{\text{O}}$. Fig.2.3A illustrates the equivalent circuit for a mixed conductor with polarizable electrodes. The total current through the sample and ionic current through the pump are related to applied voltage (U) via Ohm's law:

$$I_{\text{total}} = \left(\frac{1}{R_{\text{O}} + R_{\eta}} + \frac{1}{R_{\text{e}}} \right) \cdot U \quad \text{and} \quad I_{\text{O}} = \frac{U}{R_{\text{O}} + R_{\eta}} \quad (2.5)$$

where R_{O} and R_{e} are the bulk ionic and electronic resistances, respectively. Here R_{η} corresponds to the sum of the polarisation resistances of both electrodes. The apparent transference number ($t_{\text{O}}^{\text{obs}}$) is related to the true t_{O} as [358,359]:

$$t_{\text{O}}^{\text{obs}} = \frac{R_{\text{e}}}{R_{\text{O}} + R_{\text{e}} + R_{\eta}} = t_{\text{O}} \cdot \left(1 + \frac{R_{\eta}}{R_{\text{O}} + R_{\text{e}}} \right)^{-1} \quad (2.6)$$

As follows from equivalent circuit (Fig.2.3), at small currents and overpotentials, the t_{O} values can be calculated from a combination of faradaic efficiency data and bulk resistance of the sample (R_{bulk}) obtainable by *ac* techniques such as impedance spectroscopy:

$$t_{\text{O}} = 1 - \frac{R_{\text{bulk}} \cdot (I_{\text{total}} - I_{\text{O}})}{U}; \quad R_{\text{bulk}} = \frac{R_{\text{O}} \cdot R_{\text{e}}}{R_{\text{O}} + R_{\text{e}}} \quad (2.7)$$

Each t_{O} value was averaged from 2-4 experimental data points. The oxygen ionic conductivity was calculated from data on total conductivity and transference numbers as $\sigma_{\text{O}} = \sigma \times t_{\text{O}}$. In the case of measurements under $p(\text{O}_2)$ gradient, the results were corrected for the steady oxygen permeation fluxes, independently measured prior to the faradaic efficiency.

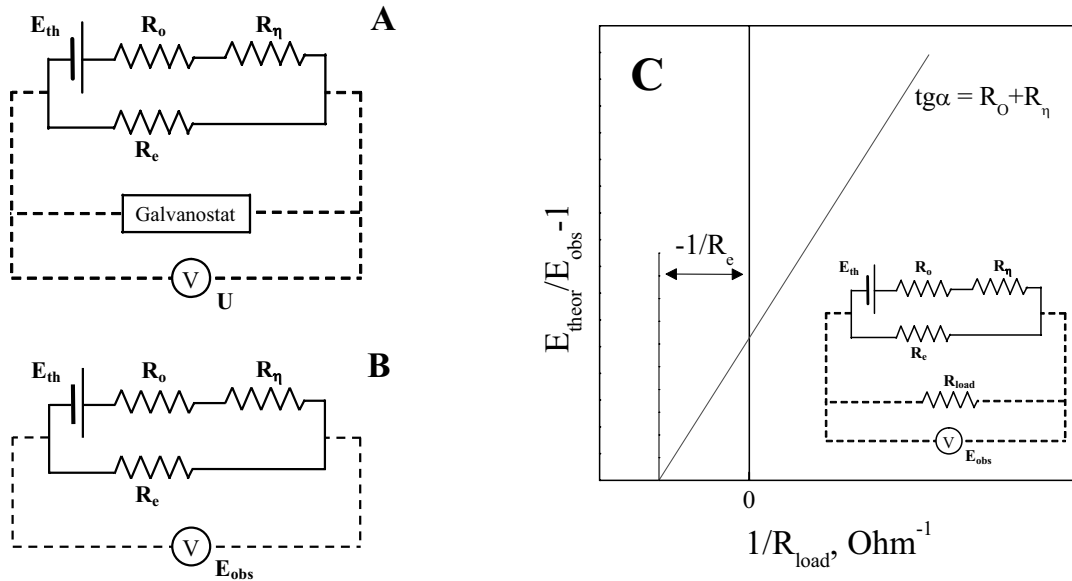


Fig.2.3. Equivalent circuits for the faradaic efficiency measurements (A) and classical e.m.f. technique (B), and illustration of Gorelov's modification of the e.m.f. method (C).

2.6.2. Determination of oxygen permeation fluxes

When a ceramic membrane having mixed oxygen ionic and electronic conductivity is placed under an oxygen chemical potential differential, the interrelated fluxes of oxygen ions and electrons are induced, as discussed in Chapter 1.4.1, Eq.(1.16). The oxygen permeation (OP) processes through dense ceramics were analyzed in terms of permeation flux density of molecular oxygen j [$\text{mol}\times\text{s}^{-1}\times\text{cm}^{-2}$] and specific oxygen permeability $J(\text{O}_2)$ [$\text{mol}\times\text{s}^{-1}\times\text{cm}^{-1}$], interrelated as ([146] and cited references):

$$J(\text{O}_2) = \frac{RT \cdot d \cdot j}{\mu_2 - \mu_1} = j \cdot d \cdot \left(\ln \frac{p_2}{p_1} \right)^{-1} \quad (2.8)$$

where d is the membrane thickness, μ_1 (p_1) and μ_2 (p_2) are the μ_{O_2} ($p(\text{O}_2)$) values at the membrane permeate and feed sides, respectively ($\mu_2 > \mu_1$, $p_2 > p_1$). The quantity $J(\text{O}_2)$, proportional to $j \times d$ by definition, is suitable to identify limiting effects of surface oxygen exchange kinetics on the oxygen permeation analysing the membrane thickness dependencies of the permeation fluxes. In the case of negligible effect of the processes at the membrane/gas boundaries when the integral form of the Wagner law is observed, the values of oxygen permeability should be thickness-independent, whilst the permeation fluxes should increase with decreasing d . In this case, the overall steady-state oxygen permeation flux through the membrane can be represented as [90,92]:

$$j \equiv \frac{I_o}{4F \cdot S} = \frac{1}{16F^2 d} \int_{\mu_1}^{\mu_2} \frac{\sigma_o \cdot \sigma_e}{\sigma_o + \sigma_e} d\mu = \frac{1}{16F^2 d} \int_{\mu_1}^{\mu_2} t_o \cdot (1 - t_o) \cdot \sigma d\mu \quad (2.9)$$

where S is the surface area. The t_o and σ_o values can be estimated from Eq.(2.9) and the total conductivity data:

$$t_o = \frac{1}{2} \pm \frac{1}{2} \cdot \left(1 - \frac{4d \cdot I_o}{S \cdot E_{sens} \cdot \sigma} \right)^{1/2} \quad (2.10)$$

If the overall oxygen transport is limited by the surface exchange rate only, the oxygen fluxes should not depend on the thickness at given oxygen chemical potential gradient and the permeability should increase with increasing d due to a decreasing role of the exchange rates. The ceramic membranes with different thicknesses from 0.5 to 1.4 mm were measured in the electrochemical cells similar to those used for the FE measurements (Fig.2.2). The membrane feed side was exposed to atmospheric air (0.21 atm), while p_1 was varied from 5×10^{-3} to 0.1 atm.

2.6.3. E.m.f. measurements

The electro-motive force (emf) technique is based on the measurement of the open-circuit voltage of a cell placed under an oxygen chemical potential gradient. For an oxygen concentration cell with negligible electrode polarisation resistance, the oxygen ion transference number averaged in the given oxygen pressure range is obtained from the ratio of the measured emf (E_{obs}) and theoretical Nernst voltage (E_{theor}) as (Eq.(1.7)):

$$t_o = \frac{E_{obs}}{E_{theor}} \quad (2.11)$$

As for the FE measurements, significant polarisation resistance may lead to underestimated ion transference numbers. For the small currents through the cell, when the polarization curve obeys a linear law, the process is represented by equivalent circuit Fig.2.3B and Eq.(2.6) is applied. For the measurements, a modification of the emf method proposed by Gorelov [358] was used, simulating an increase of the electronic conductivity with an external variable resistance (R_{load}) and measuring the cell voltage as a function of R_{load} . From the corresponding equivalent circuit (Inset of Fig.2.3C) one can easily obtain the relation:

$$\frac{E_{theor}}{E_{obs}} - 1 = (R_o + R_\eta) \cdot \left(\frac{1}{R_e} + \frac{1}{R_{load}} \right) \quad (2.12)$$

As long as $R_{load} \gg R_{bulk}$, the function $(E_{theor}/E_{obs}-1)$ against reciprocal R_{load} can be approximated by a simple linear regression with (R_o+R_η) slope (Fig.2.3C). R_e can be found from an absolute term. The oxygen ion transference number can thus be obtained as $t_o = 1 - R_{bulk}/R_e$, where the bulk resistance (Eq.2.7) is independently measured by *ac* impedance spectroscopy.

The t_o values were determined at 873-1223 K by the modified emf technique under O₂/air, air/Ar or air/10%H₂-N₂ gradients; the gas flow rates of 50-250 ml/min were fixed by Bronkhorst mass-flow controllers. The ion transference numbers obtained by the emf method are averaged in the oxygen chemical potential gradient, which can be expressed using Wagner's law as:

$$\bar{t}_o = \frac{1}{\mu_2 - \mu_1} \cdot \int_{\mu_1}^{\mu_2} t_o \, d\mu = \left(\ln \frac{p_2}{p_1} \right)^{-1} \cdot \int_{p_1}^{p_2} \frac{\sigma_o}{\sigma_o + \sigma_e} \cdot \frac{1}{p(O_2)} \, dp(O_2) \quad (2.13)$$

Substituting the models for the partial conductivities as functions of oxygen pressure can make it possible to determine the equilibrium t_o values at fixed $p(O_2)$.

Eq.(2.12) may fail for highly polarizable electrodes, or when η vs. I deviates from the assumed linear relation. In this case, R_η should be replaced with η/I . Then the overpotential and ionic current can be expressed as:

$$\eta = E_{\text{theor}} - E_{\text{obs}} \cdot \left(1 + \frac{R_o}{R_e} + \frac{R_o}{R_{\text{load}}} \right) \quad (2.14a)$$

$$I = E_{\text{obs}} \cdot \left(\frac{1}{R_e} + \frac{1}{R_{\text{load}}} \right) \quad (2.14b)$$

The partial electronic resistance derived as illustrated in Fig.2.3C, may thus be combined with the experimental data on E_{obs} vs. R_{load} . One should examine the $\eta - I$ dependence to avoid the conditions of limiting current density and to verify if the overpotential increases faster than current on varying the external load resistance. Linearity of $E_{\text{theor}}/E_{\text{obs}} - 1$ vs. $1/R_{\text{load}}$ can be considered as a first criterion to confirm the applicability of emf measurements under short-circuit conditions. One alternative criterion is based on the values of dimensionless overpotential $F\eta/RT$. If the electrode kinetics can be approximated by the Butler-Volmer type equations, Eq.(1.24), nearly constant polarization resistance can be expected when the values of $F|\eta|/RT$ are lower than approximately 0.2. Otherwise, only sufficiently higher values of external resistance should be used to ensure that relative changes in current remain small.

2.7. Fabrication and electrochemical studies of electrode layers

2.7.1. Electrode fabrication

The electrode layers were studied in contact with LSGM or Zr_{0.9}Y_{0.1}O_{2-δ} electrolytes. Sintered dense disc-shaped ceramics with the diameter of about 17 mm were polished to thickness of 0.9-1.9 mm, cleaned and tested for gas-tightness under the total gas pressure of 2 atm. Porous electrodes were screen-printed (screen 32 HD - SSThal) or brush-painted onto the LSGM ceramics and annealed in air for 2 h at various temperatures. The electrode diameter was 4.8-7.2 mm, thickness was about 30-40 μm and sheet density varied from 10 to 20 mg/cm². The details

concerning formation of the porous cathode and anode layers are described in Chapters 5.1.1 and 5.3.1, respectively.

2.7.2. Cell configuration and measuring set-ups

The electrode polarization measurements were carried out by the electrochemical impedance spectroscopy using the 3-electrode technique. The cell geometry, chosen according to works [74,360], is illustrated in Fig.2.4. The counter electrode (CE) was symmetrical to the working electrode, the reference electrode (RE, diameter of about 1 mm) was placed 5-7 mm away from the WE; both CE and RE were painted with Pt paste (Engelhard) and fired at 1273 K. The slight changes in geometry were verified not to influence the results.

Pt gauze (Engelhard) or wire (diameter of 0.5 mm), were used as a current collector (CC), Fig.2.4 (B and C). In the case of the cathode layers, the CC configuration had no essential influence on the polarization characteristics.

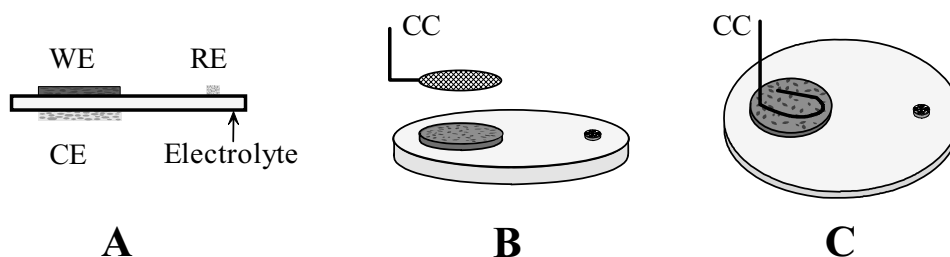


Fig.2.4. Geometrical arrangement of the electrochemical cells for the measurements of the electrode properties.

The experiments were performed in the cell (Fig.2.1, right) with separated WE and CE zones in flowing air and O₂-Ar mixtures (flow rate of 25 ml/min) for the cathode measurements and in flowing humidified 10%H₂-90%N₂ gas mixture for the anode; air was supplied to the CE in all cases. The composition of gas mixtures was settled by Bronkhorst mass-flow controllers; the oxygen partial pressure at both sides was controlled by electrochemical oxygen sensors to vary in the range from 4×10^{-4} to 1 atm at the cathode and 1×10^{-25} - 2×10^{-19} atm at the anode. The cathode layers were also tested in a similar set-up as in Fig.2.1 in open air without sealing the sample and p(O₂) control.

2.7.3. Selection of glass-ceramic sealants

The glass-ceramic materials were used for the cell hermetization in high-temperature zone. The sealants should satisfy numerous requirements, including chemical stability, good adhesion to the cell components, minimum electrical conductivity and electrochemical permeability, and

adequate mechanical and thermal properties. The stability of seals with commercial Pyrex is usually insufficient due to thermal expansion mismatch and/or interaction with SOFC components. Therefore, a series of alternative glass-ceramics based on the multicomponent system SiO_2 (30-65 mol%) – Al_2O_3 (0-6%) – MgO (0-40%) – CaO (0-25%) – BaO (10-18%) were obtained and studied. The nominal compositions and physicochemical, mechanical and transport properties of selected sealants are shown in Table 2.2 and Appendix 1 (Figs.A1.1-A1.5).

Moderate amounts of YSZ and TiO_2 with submicron particle size were introduced into the compositions before melting in order to achieve external nucleation, to modify crystal growth rate, and to optimize physicochemical properties. In most cases, as-prepared materials were completely amorphous, while the crystal phases were grown after annealing at elevated temperatures (Fig.A1.1).

Table 2.2

Composition and properties of glass-ceramics

Designation	S2	S3	S5	S7
Main components (weight ratio)	$\text{SiO}_2\text{-Al}_2\text{O}_3\text{-CaO-BaO}$ (100-9-38-53)	$\text{SiO-Al}_2\text{O-Ca-BaO}$ (100-16-30-88)	SiO-Mg-BaO (100-50-68)	SiO-Mg-BaO (100-17-64)
Additives	Y8SZ, 16.4 wt%	TiO_2	CaO, Y3SZ	CaO, Y3SZ
T_{sealing} , K	1220 - 1240	1430 - 1460	1470 - 1490	1375 - 1385
$\bar{\alpha} \times 10^6$, K^{-1} (T, K)	8.02 ± 0.02 (350 - 1040)	8.65 ± 0.02 (350 - 1000)	11.47 ± 0.04 (400 - 1000)	8.45 ± 0.03 (490 - 970)
Rupture modulus, MPa	103 ± 19	85 ± 21	121 ± 24	-
Vicker's hardness, GPa	0.69 ± 0.06	0.52 ± 0.07	>1	-
$J(\text{O}_2)^{1123}$, $\text{mol}\times\text{s}^{-1}\times\text{cm}^{-1}$		$< 8 \times 10^{-12}$	$< 8 \times 10^{-12}$	-

Notes:

- The modulus of rupture and the Vicker's hardness were measured at room temperature using a LR 30K machine (Lloyd Instruments, UK) and M-type microhardness-tester (Shimadzu, Japan), respectively.
- The specific oxygen permeability $J(\text{O}_2)$ was measured under air/ $\text{H}_2\text{-H}_2\text{O-N}_2$ gradients, corresponding to the e.m.f. of a YSZ sensor of 1.10-1.15 V, using a set-up similar to Fig.2.2 (right). The thickness of glass-ceramic sample was 1.0 ± 0.1 mm; the data are averaged for 80-100 h of testing.

Typical microstructures demonstrating the quality of interfaces between glass-ceramics and solid electrolytes, fractured after sealing, are shown in Fig.A1.3. For most cells, a relatively good adhesion and negligible interaction with YSZ and CGO are observed, whilst LSGM may form reaction layers when the sealing temperature is higher than 1450 K. Nonetheless, the used sealants provide a better stability in contact with LSGM, compared to Pyrex. One should also note that moderate additions of zirconia seem to increase mechanical strength (Table 2.2), although this effect is within the limits of experimental uncertainty. Fig.A1.2 presents the temperature dependencies of relative elongation of the glass-ceramic materials; the TEC values are close to

those of solid electrolytes and alumina. The total conductivity (Fig.A1.4) was found essentially independent of composition; no attempts to clarify the mechanism of electrical transport were undertaken. The long-term stability tests under SOFC operation conditions were performed using YSZ electrochemical cells comprising one oxygen pump and a sensor, similar to that shown in Fig.2.2 (left) but in hermetical chamber with a gas inlet and outlet and an additional oxygen sensor. Gas-tight membranes, made of glass-ceramics or YSZ, were sealed onto the cell in air. Then these cells were placed into flowing H₂-H₂O-N₂ mixtures; the current through the pump was adjusted to provide time-independent sensor emf, thus compensating leakages. Except for noise, the variations of sensor emf of the cells are related to the changes of oxygen partial pressure inside these cells. In all cases, no degradation at temperatures below 1150 K during 300-1000 h was found, as illustrated by Fig.A1.5. At higher temperatures, however, the long-term stability of glass-ceramic sealants under O₂-N₂/H₂-H₂O-N₂ is often insufficient; the leakage drastically increases after 300-700 h. The XRD studies showed that the degradation phenomena are associated with different crystallization mechanisms in reducing and oxidizing conditions, leading to re-crystallization of the sealants under SOFC operation conditions.

For sealing of the electrochemical cells, the prepared glass-ceramics were ball-milled and the fraction with particle size smaller than 90 μm was sifted out. The paste of this powder with ethanol was deposited on the junction of cell components, annealed at necessary temperature for 10-30 min and 1-2 K/min cooled down. Since the S3 or S5 glass-ceramics should be heated above 1440 and 1470 K, respectively, and are essentially non-reactive with YSZ, these were chosen to seal an oxygen pump to a sensor of the cell shown in Fig.2.1 (left) and the cells for oxygen permeability and faradaic efficiency measurements (Fig.2.2, left). The concentration cell Fig.2.2 (right) was sealed with S3 or S7 glass-ceramics. For the OP, FE and emf measurements, the sample was sealed to the YSZ sensor with S7 sealant, except for the cases when the TEC value of the studied material was more compatible with Pyrex. As S3 and S5 suffer from the interaction with LSGM solid electrolyte and degradation in reducing atmospheres, the S2 sealant was used in the cells for electrode tests (Fig.2.1, right).

2.7.4. Electrochemical measurements

The measurements were performed in the galvanostatic mode using an AUTOLAB PGSTAT20 instrument at 873 - 1073 K. The overpotential (η) was calculated as:

$$\eta = U - I \cdot R \quad (2.15)$$

where U is the steady-state potential difference between the WE and RE, I is the current between WE and CE, and I×R is the ohmic contribution to the total potential drop. The values of the ohmic resistance, R, were determined from the corresponding impedance spectra collected in the

frequency range from 10 mHz to 50 kHz. The impedance spectroscopy data were also used to calculate the electrode polarization resistance, R_{η} , which can be derived as the difference between the low- and high-frequency intercepts of the electrode part of impedance spectra. The highest current density values were 360 mA/cm² and 300 mA/cm² for the cathode and anode, respectively. The time-dependencies of the potential under *dc* polarization were measured *a priori*; the time necessary to attain steady-state conditions was 0.5-2 h.

2.7.5. Reproducibility tests and assessment of materials interaction

The reproducibility of electrochemical data was verified studying 2-3 similar electrodes prepared under identical conditions. Additional tests were performed on one and the same sample after each measurement cycle to check whether the results are reproducible after the temperature variations and polarization treatments.

As-prepared electrode layers and the cells after electrochemical measurements were examined by XRD, SEM/EDS, TEM/EDS and ICP analyses in order to reveal possible changes in phase composition and microstructure.

Part 3: Cobalt- and nickel-containing phases promising for cathode applications

This Chapter is centered on the characterization of cobaltite and nickelate phases studied as potential cathode materials for IT SOFCs. Perovskite-type cobaltites, possessing a high electrochemical activity, suffer from excessive thermal expansion. To some extent, the lattice expansion might be reduced by doping, particularly by incorporating Al^{3+} or Ga^{3+} cations having a stable oxidation state, which should decrease chemical contribution to the thermal expansion. The cobaltite and nickelate phases with layered structures are expected to have a lower thermal expansion in combination with high mixed conductivity and cathode activity. However, to date of this work, the information on transport and electrochemical properties of these materials is scarce.

3.1. General characterization

3.1.1. $\text{La}_{0.3}\text{Sr}_{0.7}\text{CoO}_3$ -based perovskites

SEM inspections showed that GNP-synthesised $\text{La}_{0.3}\text{Sr}_{0.7}\text{CoO}_{3-\delta}$ based powders consisted of submicron-sized particles (Inset in Fig.3.1). As expected, these powders demonstrate an enhanced sintering ability; one example of which is illustrated by Fig.3.1. The densification of green compacts starts already at 1000-1100 K, with a maximum shrinkage at 1170-1180 K. However, the materials with sufficiently high density (Table 2.1) can be sintered only at 1423-1553 K.

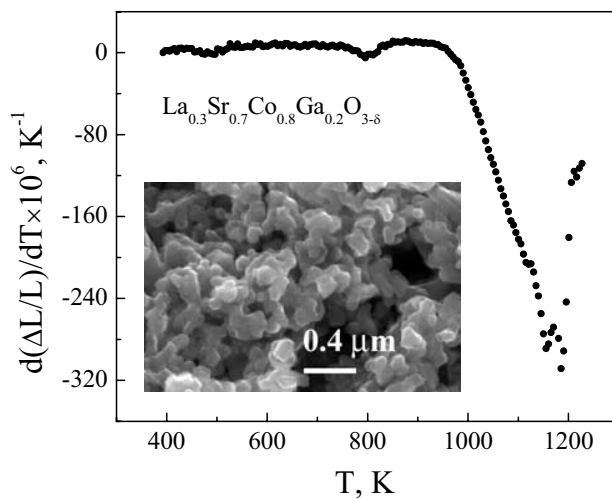


Fig.3.1. Relative shrinkage of $\text{La}_{0.3}\text{Sr}_{0.7}\text{Co}_{0.8}\text{Ga}_{0.2}\text{O}_{3-\delta}$ green compacts. Inset shows SEM micrograph of as-synthesized powder annealed at 1073 K.

Typical microstructures of fractured $\text{La}_{0.3}\text{Sr}_{0.7}\text{CoO}_3$ -based ceramics are shown in Fig.3.2. The grain size of $\text{La}_{0.3}\text{Sr}_{0.7}\text{Co}_{0.8}\text{Ga}_{0.2}\text{O}_{3-\delta}$ material, 20 to 70 μm , is substantially higher than that of the other two ceramics, due to the higher sintering temperature. Minor traces of a glassy phase are observed at the grain boundaries, indicating a liquid phase-assisted sintering process. Notice,

however, that no essential inhomogeneities in the cation distribution between grain bulk and boundaries were detected by EDS, in all cases.

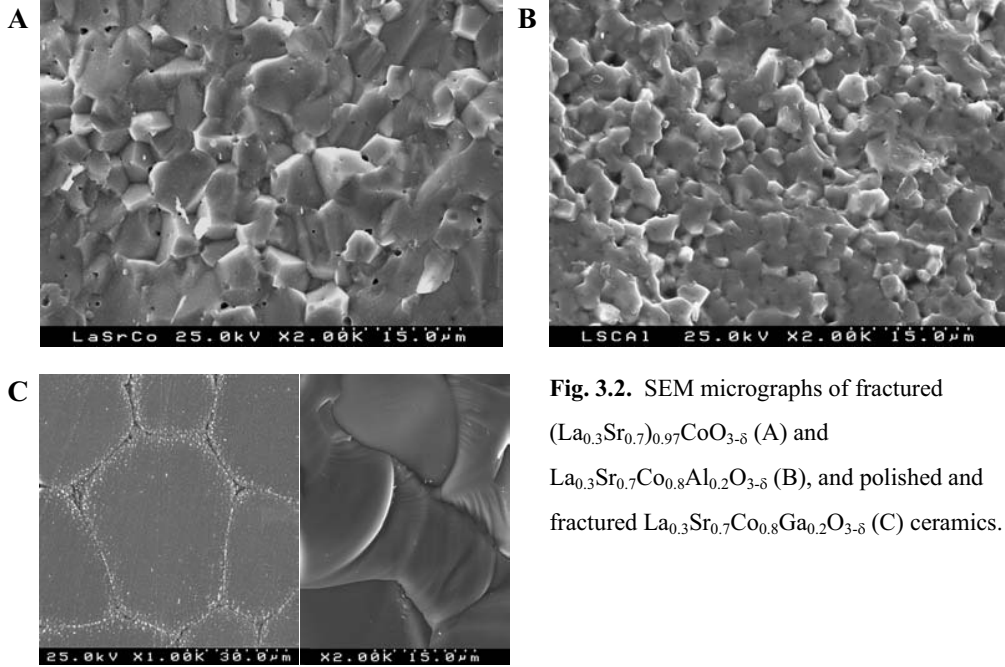


Fig. 3.2. SEM micrographs of fractured $(\text{La}_{0.3}\text{Sr}_{0.7})_{0.97}\text{CoO}_{3-\delta}$ (A) and $\text{La}_{0.3}\text{Sr}_{0.7}\text{Co}_{0.8}\text{Al}_{0.2}\text{O}_{3-\delta}$ (B), and polished and fractured $\text{La}_{0.3}\text{Sr}_{0.7}\text{Co}_{0.8}\text{Ga}_{0.2}\text{O}_{3-\delta}$ (C) ceramics.

Table 3.1

Properties of $\text{La}_{0.3}\text{Sr}_{0.7}\text{CoO}_3$ -based ceramics

Composition	Relative density, %	Unit cell parameter a, nm	Average linear thermal expansion coefficient in air		Activation energy for the oxygen permeation fluxes*	
			T, K	$\bar{\alpha} \times 10^6, \text{K}^{-1}$	T, K	$E_a, \text{kJ/mol}$
$\text{La}_{0.3}\text{Sr}_{0.7}\text{CoO}_{3-\delta}$	92.6	0.3836	300 - 750	19.6 ± 0.5	1023 - 1153	77 ± 5
$(\text{La}_{0.3}\text{Sr}_{0.7})_{0.97}\text{CoO}_{3-\delta}$	97.5	0.3837	750 - 1100	28.8 ± 0.5	1073 - 1173	106 ± 12
			390 - 640	17.5 ± 0.3		
$\text{La}_{0.3}\text{Sr}_{0.7}\text{Co}_{0.8}\text{Al}_{0.2}\text{O}_{3-\delta}$	97.2	0.3846	790 - 1160	29.7 ± 0.5	1103 - 1173	124 ± 2
			390 - 790	17.4 ± 0.2		
$\text{La}_{0.3}\text{Sr}_{0.7}\text{Co}_{0.8}\text{Ga}_{0.2}\text{O}_{3-\delta}$	96.5	0.3871	790 - 1240	28.3 ± 0.4	1073 - 1223	78 ± 11
			360 - 710	15.9 ± 0.5		
			710 - 1030	27.9 ± 0.4		

* the permeation fluxes correspond to the oxygen pressure gradient of 0.209/0.066 atm and the membrane thickness of 1.00 mm.

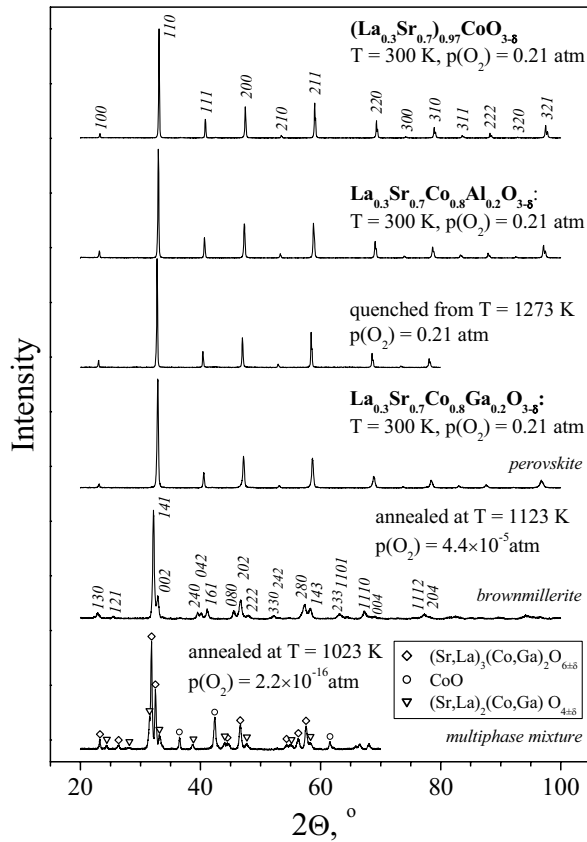


Fig.3.3. XRD patterns of $\text{La}_{0.3}\text{Sr}_{0.7}\text{CoO}_3$ -based ceramics thermally treated in various atmospheres.

XRD analysis confirmed that all studied materials, $(\text{La}_{0.3}\text{Sr}_{0.7})_{0.97}\text{CoO}_{3-\delta}$, $\text{La}_{0.3}\text{Sr}_{0.7}\text{Co}_{0.8}\text{Al}_{0.2}\text{O}_{3-\delta}$ and $\text{La}_{0.3}\text{Sr}_{0.7}\text{Co}_{0.8}\text{Ga}_{0.2}\text{O}_{3-\delta}$, are single-phase and have the cubic perovskite structure (space group $\text{Pm}\bar{3}\text{m}$) characteristic of the parent compound, $\text{La}_{0.3}\text{Sr}_{0.7}\text{CoO}_{3-\delta}$ [239]. Selected examples of XRD patterns are shown in Fig.3.3. Doping with Al^{3+} and Ga^{3+} leads to increasing unit cell parameters (Table 3.1). Taking into account the ionic radii of B-site cations [60], one may conclude that the substitution of aluminum or gallium for cobalt decreases the Co^{4+} fraction, as for tetravalent iron in the $\text{La}_{0.3}\text{Sr}_{0.7}\text{Fe}(\text{Ga})\text{O}_{3-\delta}$ system [215]. The minor lattice expansion due to creation of A-site cation vacancies results, most likely, from increasing anion repulsion. No structural changes were observed on heating in air up to 1273 K, while reducing oxygen partial pressure down to approximately 10^{-5} atm results in a transition into the brownmillerite-like phases (Fig.3.3).

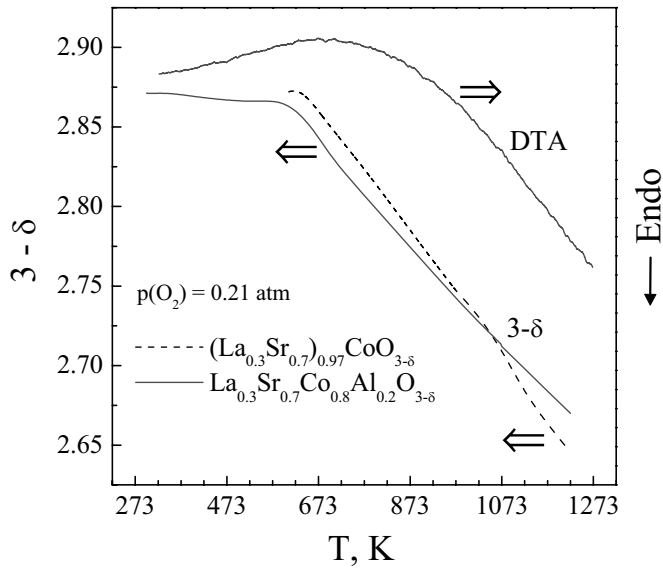


Fig.3.4. Temperature dependencies of the oxygen content in $\text{La}_{0.3}\text{Sr}_{0.7}\text{CoO}_3$ -based phases and one example of DTA curve, in air.

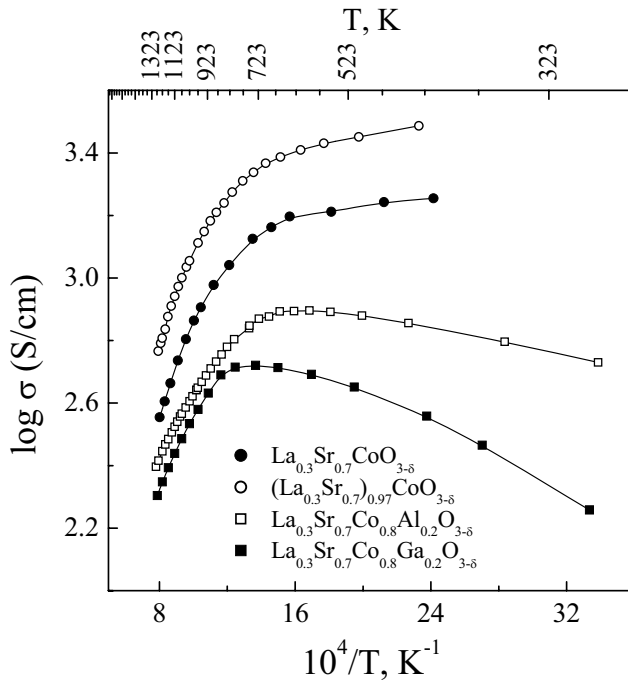


Fig.3.5. Temperature dependencies of the total conductivity of $\text{La}_{0.3}\text{Sr}_{0.7}\text{CoO}_3$ -based ceramics in air.

The total conductivity of perovskite-type cobaltites is predominantly p-type electronic [239,240]; the progressive increase of the oxygen deficiency leads, in particular, to a lower concentration of electron holes and thus decreases the conductivity when temperature increases. Examples of oxygen stoichiometry variations in air calculated from the thermogravimetric results under reduction in a flowing 10% H_2 -90% N_2 mixture, illustrating this trend, are shown in Fig.3.4.

The conductivity of $(\text{La}_{0.3}\text{Sr}_{0.7})_{0.97}\text{CoO}_{3-\delta}$ is substantially higher compared to the A-site-stoichiometric material (Fig.3.5), indicating the higher concentration of Co^{4+} ions. Incorporation of Al^{3+} and Ga^{3+} , having constant oxidation state, decreases the concentration of B sites contributing to the electron-hole conduction, and leads to a lower electronic transport. As for $\text{La}_{0.3}\text{Sr}_{0.7}(\text{Fe,Ga})\text{O}_{3-\delta}$ [215,216], Ga- and Al- substitution results not only in lower charge carrier concentration, but also in decreasing hole mobility provided by the Co–O–Co bonds [361], a part of which becomes blocked by dopant cations. This is reflected by the higher activation energy for the total conductivity of $\text{La}_{0.3}\text{Sr}_{0.7}\text{Co}_{0.8}\text{M}_{0.2}\text{O}_{3-\delta}$ ($\text{M} = \text{Al}, \text{Ga}$) than that of $\text{La}_{0.3}\text{Sr}_{0.7}\text{CoO}_{3-\delta}$ in the low-temperature range (Fig.3.5).

3.1.2. $\text{YBaCo}_4\text{O}_{7+\delta}$ and its derivatives

The crystal structure of $\text{YBa}(\text{Co,Fe})_4\text{O}_7$ (Fig.3.6), firstly reported for $\text{HoBaCo}_4\text{O}_7$ [237], comprises two distinct cobalt sites, *Co1* and *Co2*, both tetrahedrally-coordinated. The *Co1:Co2* concentration ratio is 3:1; the space group was reported as $\text{P6}_3\text{mc}$ [237,238] (Fig.3.7). The large Ba^{2+} cations occupy cavities between alternating layers of (*Co1*) O_4 tetrahedra and layers composed by (*Co2*) O_4 and octahedrally-coordinated Y^{3+} . The synthesized submicron powders (Fig.3.8A) contained apparently a significant amount of amorphous or partially crystallized phases, as indicated by electron diffraction (Fig.3.8B). XRD analysis showed that as-prepared $\text{YBaCo}_{4-x}\text{Fe}_x\text{O}_7$ ceramics were single-phase (Figs.3.7 and 3.9). In agreement with literature data [238], their crystal lattice was identified as hexagonal, space group $\text{P6}_3\text{mc}$ (Fig.3.7). Iron doping increases *a* parameter and leads to the unit cell contraction along *c* axis (Table 3.2). Under oxidizing conditions at elevated temperatures, the YBaCo_4O_7 structure is stable (Fig.3.9B).

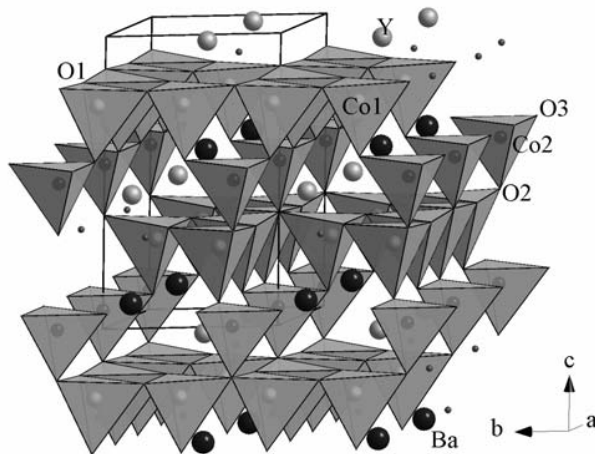


Fig.3.6. Crystal structure of YBaCo_4O_7 according to the model from Ref.[237]; solid lines show one hexagonal unit cell.

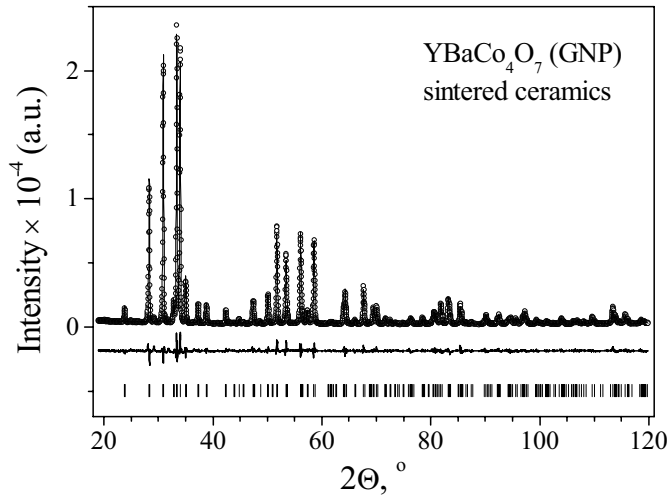


Fig.3.7. An example illustrating the quality of Fullprof analysis.

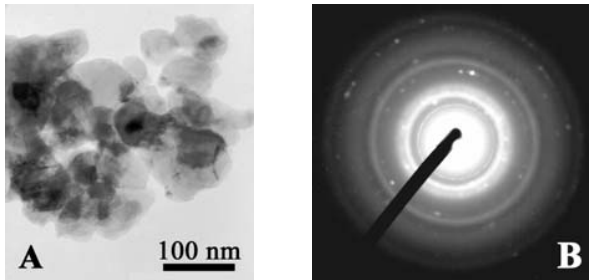


Fig.3.8. Bright-field TEM image (A) and electron diffraction pattern (B) of as-prepared YBaCo₄O₇ powder.

Table 3.2

Properties of YBaCo_{4-x}Fe_xO_{7+δ} ceramics in air

x	Unit cell parameters		Average linear thermal expansion coefficient		Activation energy for total conductivity	
	a, nm	c, nm	T, K	$\bar{\alpha} \times 10^6, K^{-1}$	T, K	E _a , kJ/mol
0 (Method 1)	0.6302(2)	1.0243(9)	420 - 660	9.00±0.09*	620 - 1070	21.7±0.2
			750 - 1270	7.61±0.02*	1090 - 1250	22.5±0.4
0 (Method 2)	0.6303(5)	1.0248(3)	470 - 760	7.29±0.04*	270 - 770	20±2
			800 - 1220	7.27±0.05*	1080 - 1250	21±4
0.4			290 - 975	9.74±0.02**	615 - 935 1160 - 1275	21±6 21±3
0.8	0.6313(2)	1.0273(8)				

* heating rate of 5 K/min;

** heating rate of 2 K/min, with dwells at every 50 K.

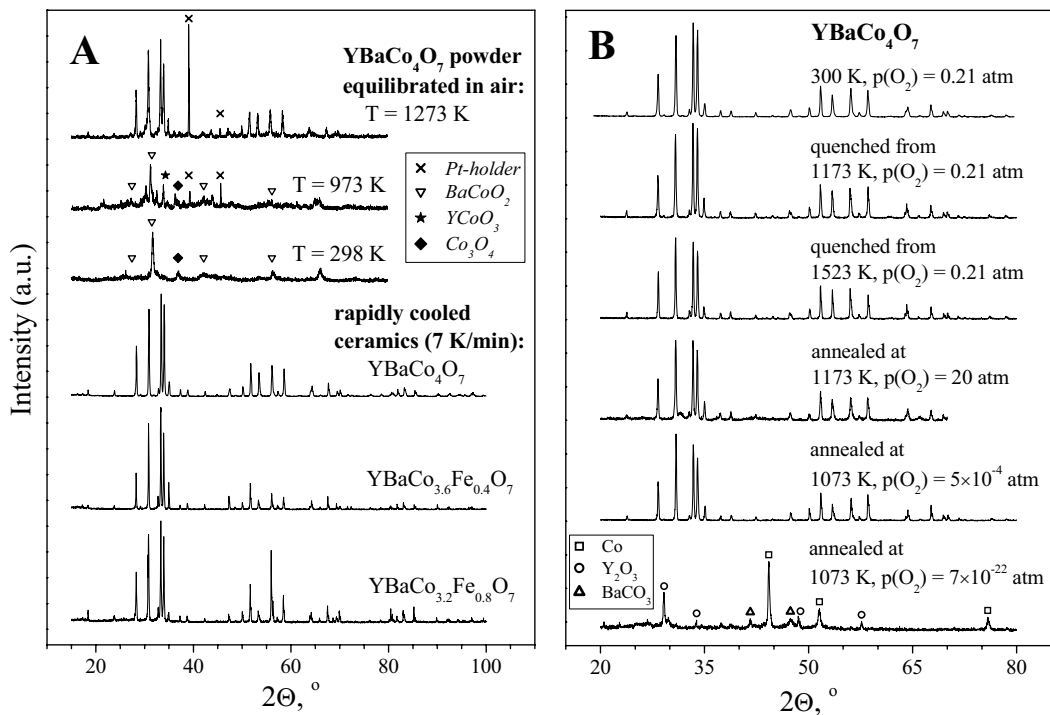


Fig.3.9. High-temperature XRD patterns of YBaCo_4O_7 in air (top) and room-temperature XRD patterns of $\text{YBa}(\text{Co,Fe})_4\text{O}_7$ ceramics sintered at 1473 K (bottom) (A); XRD patterns of $\text{YBaCo}_4\text{O}_{7+\delta}$ after treatments in various atmospheres (B).

SEM/EDS analysis confirmed an absence of substantial grain-boundary anomalies. Fig.3.10 compares typical microstructures of materials prepared by ceramic technique (Method 1) and GNP (Method 2). The grain size varies in the range 2 to 10 μm , being slightly larger for the material synthesized via the former method due to higher sintering temperature.

The data on ion transference numbers and thermopower, given below, indicate that the transport in YBaCo_4O_7 -based materials is predominantly electronic with p-type charge carriers, as for other cobalt-containing phases (e.g. [225] and references cited). Moderate doping of YBaCo_4O_7 with iron decreases electron-hole transport (Fig.3.11, A and B). At temperatures up to 930-1040 K, the total conductivity in air exhibits an ordinary semiconductor-like behavior (Fig.3.11). The activation energy is 20-21 kJ/mol. Further heating results, however, in a drastic increase of the σ values; then the conductivity decreases back to the initial level at 1190-1220 K. The anomalous conductivity increment is reproducible on cooling, with a hysteresis shift. The activation energies before and after this transition are equal within the limits of experimental error (Table 3.2). Such a behavior may indicate that $\text{YBa}(\text{Co,Fe})_4\text{O}_7$ solid solutions are metastable below 900-1050 K.

Indeed, high-temperature XRD data collected after 5 h exposure at each temperature confirm the existence of hexagonal phase at 1273 K, whereas on cooling the YBaCo_4O_7 powder decomposes with partial amorphization (Fig.3.9A). These structural changes were further verified by the XRD analysis of a series of $\text{YBaCo}_4\text{O}_{7+\delta}$ powder samples annealed in air purified from water vapor and CO_2 at various temperatures from 773 to 1523 K with subsequent quenching in liquid nitrogen (Fig.3.9B). In the case of dense ceramic materials, the phase changes are kinetically-stagnated. For instance, the conductivity relaxation time was up to 250 h under conditions close to the transformation (Inset in Fig.3.12B); at higher and lower temperatures, typical transient times varied from 0.3 to 4 h. The slow decomposition enables to obtain single-phase solid solutions based on YBaCo_4O_7 without quenching [238].

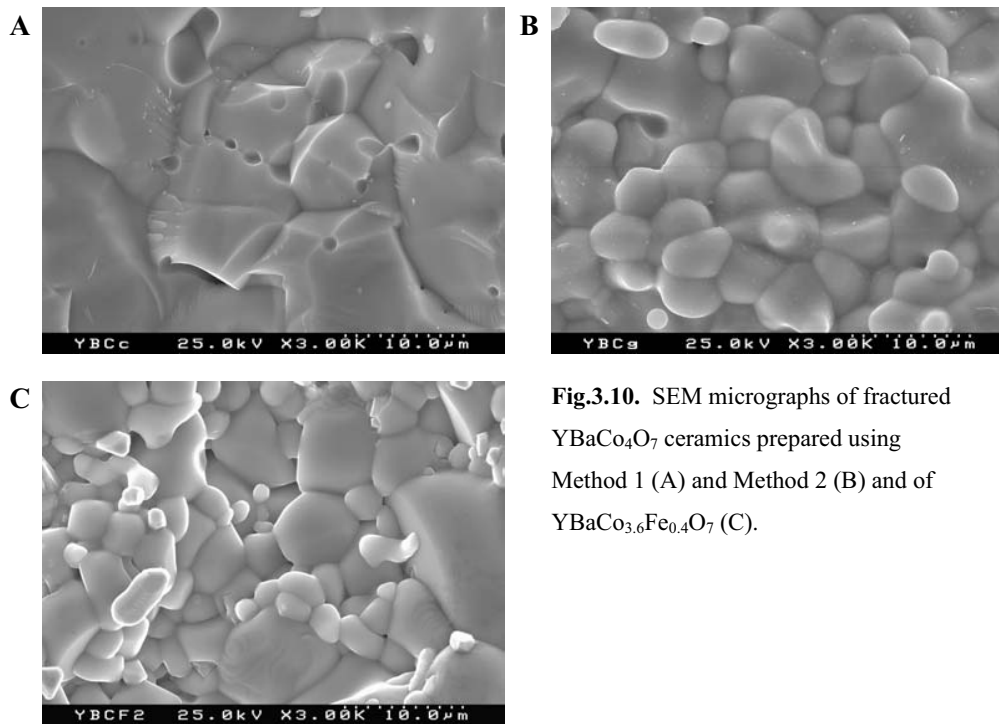


Fig.3.10. SEM micrographs of fractured YBaCo_4O_7 ceramics prepared using Method 1 (A) and Method 2 (B) and of $\text{YBaCo}_{3.6}\text{Fe}_{0.4}\text{O}_7$ (C).

The total oxygen content in the high-temperature phase, YBaCo_4O_7 , where the average oxidation state of cobalt is +2.25, was found almost equal to the nominal value; the nonstoichiometry is less than 0.01 (Fig.3.12A). On the contrary, the decomposition products formed at low temperatures contain approximately 8.4 oxygen atoms per 4 cobalt cations. Hence, the phase changes are associated with instability of Co^{2+} state under oxidizing conditions on cooling, when all cobalt ions tend to become trivalent. Note that such extensive weight losses on heating in air observed at 1110-1200 K, cannot be attributed to BaCO_3 decomposition on the surface, characteristic of Ba-containing oxide materials. In the course of thermogravimetric

measurements, the powder was heated (3 K/min) to 1273 K in dried CO₂-free air, followed by the cooling/heating cycles at 973-1273 K with 1 K/min rate and dwells for 3-20 h with the temperature step of 50 K. The oxygen losses on heating are accompanied with two endothermic effects at approximately 1135 and 1170 K.

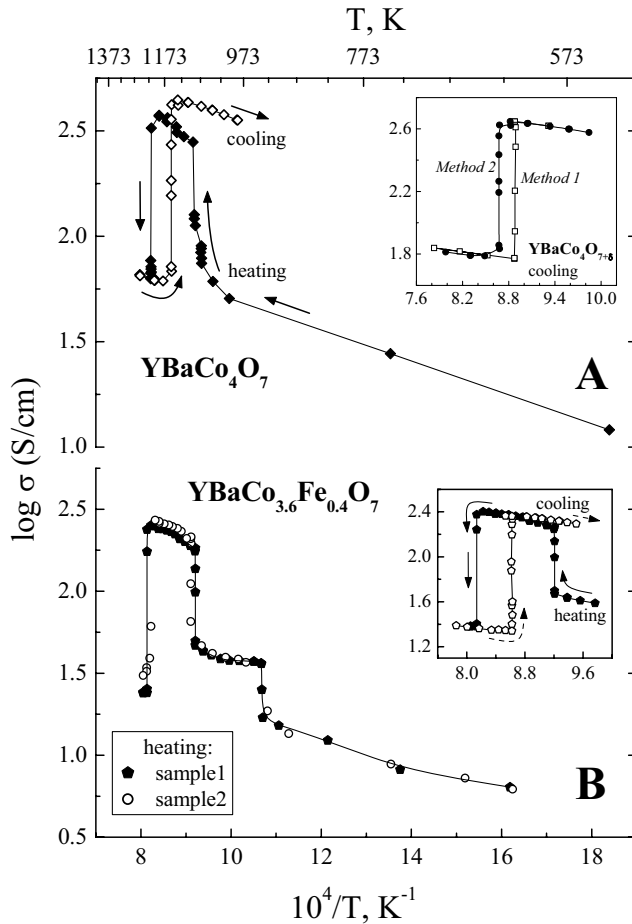


Fig.3.11. Temperature dependencies of the total conductivity of YBaCo₄O₇ (A) and YBaCo_{3.6}Fe_{0.4}O₇ (B) on heating and cooling.

The behavior of thermal expansion of the YBaCo_{4-x}Fe_xO₇ ceramics is similar to that of the total conductivity. Up to the temperatures where phase changes are observed, the TECs are essentially constant; one example is given in Fig.3.12B. In this temperature range, no volume changes were found during prolonged isothermal annealing steps. Increasing temperature above 920-970 K results in a sharp contraction, reflected as a decrease in apparent TECs down to negative values. As for the conductivity, on further heating the volume and the thermal expansion coefficients increase back to the initial level. Phase decomposition on cooling leads to irreversible volume contraction. Note also that shrinkage of the ceramics due to additional sintering is very unlikely since 93-97% density was already achieved in the course of sintering at 1473-1523 K.

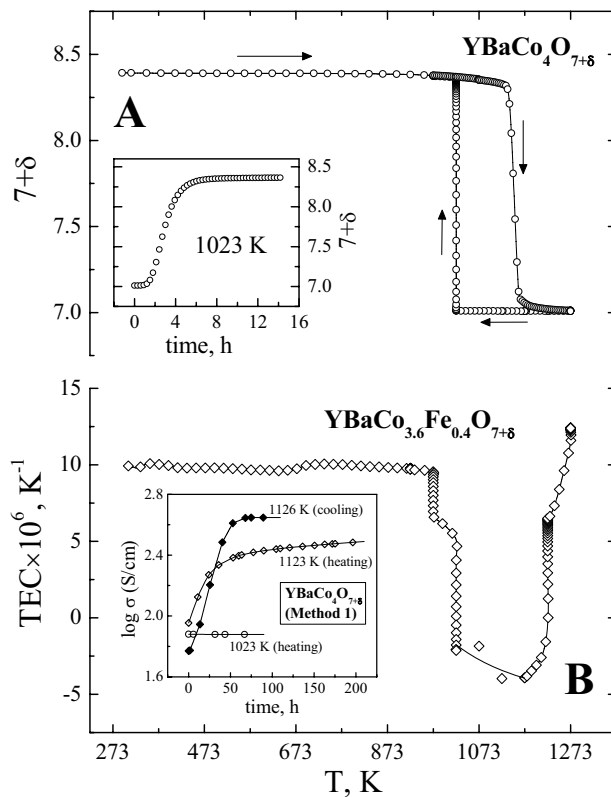


Fig.3.12. Temperature dependencies of the oxygen content in $\text{YBaCo}_4\text{O}_{7+\delta}$ (A) and linear thermal expansion coefficient of $\text{YBaCo}_{3.6}\text{Fe}_{0.4}\text{O}_{7+\delta}$ (B), in air. Insets show an example of transient TG curve of $\text{YBaCo}_4\text{O}_{7+\delta}$ powder at fixed temperature and time dependencies of total conductivity in air after temperature variations, performed with a rate of 5 K/min.

In the temperature range where $\text{YBaCo}_{4-x}\text{Fe}_x\text{O}_{7+\delta}$ solid solutions are thermodynamically stable, no time degradation of the thermal expansion and electrical properties was observed. The XRD analysis of ceramic materials demonstrated no phase changes after prolonged thermal treatments, up to 1000 h.

3.1.3. La_2NiO_4 -based nickelates

The X-ray and electron diffraction studies demonstrated that complete formation of crystalline $\text{La}_2\text{Ni}_{1-x}\text{M}_x\text{O}_{4+\delta}$ ($\text{M} = \text{Co}, \text{Cu}; x = 0.1-0.2$) with K_2NiF_4 -type lattice can be achieved at temperatures around 1200 K. For example, XRD pattern of the GNP-synthesized powder annealed at 1073 K shows traces of phase impurity, which cannot be identified due to very low intensity of the corresponding peaks (Fig.3.13). After sintering of ceramics and electrodes at 1473-1543 K, no secondary phases are observed. One example of selected-area electron diffraction (SAED) pattern typical for the crystallites in electrode layers is given as Inset of Fig.3.13. Both the powder and ceramics of $\text{La}_2\text{Ni}_{0.9}\text{Co}_{0.1}\text{O}_{4+\delta}$ synthesized via the standard ceramic route were found single-phase. The parameters of tetragonal unit cells (space group $I4/mmm$) refined from the XRD data (Table 3.3) agree well with literature [263,362] and are weakly dependent on the dopant nature and

concentration. The differences between materials obtained using the standard ceramic route and the GNP (Methods 1 and 2, respectively) are discussed in Chapter 3.3.

Table 3.3

 Properties of $\text{La}_2\text{NiO}_{4+\delta}$ -based ceramics in air

Composition	Unit cell parameters, nm	Average linear thermal expansion coefficient		Activation energy		
		T, K	$\bar{\alpha} \times 10^6, \text{K}^{-1}$	Process	T, K	$E_a, \text{kJ/mol}$
$\text{La}_2\text{Ni}_{0.8}\text{Co}_{0.1}\text{O}_4$ (Method 1)	a = 0.38711(4) c = 1.2656(5)	400-1250	12.8 ± 0.1	Total conduction	300-625	15.4 ± 0.1
				Oxygen permeation	973-1223	171 ± 6
$\text{La}_2\text{Ni}_{0.8}\text{Co}_{0.1}\text{O}_4$ (Method 2)	a = 0.3864(1) c = 1.266(3)	400-1250	14.2 ± 0.1	Total conduction	300-625	15.1 ± 0.3
				Oxygen permeation		
$\text{La}_2\text{Ni}_{0.8}\text{Cu}_{0.2}\text{O}_4$	a = 0.3858(0) c = 1.2787(3)	400-1240	13.3 ± 0.1	Total conduction	300-750	8.6 ± 0.1
				Oxygen permeation		

Note: E_a for oxygen permeability was calculated for oxygen partial pressure gradient of 0.209 / 0.021 atm.

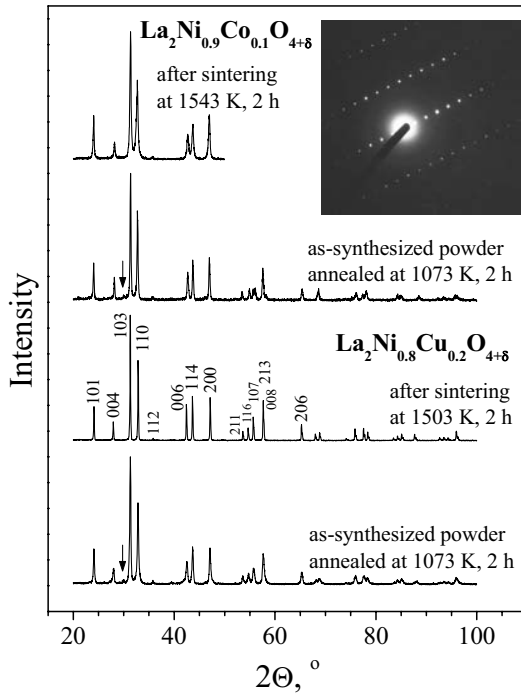


Fig. 3.13. XRD patterns of $\text{La}_2\text{NiO}_{4+\delta}$ based GNP-prepared powders and sintered ceramics. Arrow in the patterns of as-synthesized powder indicates minor impurity peak, unidentified due to low intensity. Inset shows SAED pattern of the $\text{La}_2\text{Ni}_{0.8}\text{Cu}_{0.2}\text{O}_{4+\delta}$ cathode layer sintered at 1473 K for 2 h.

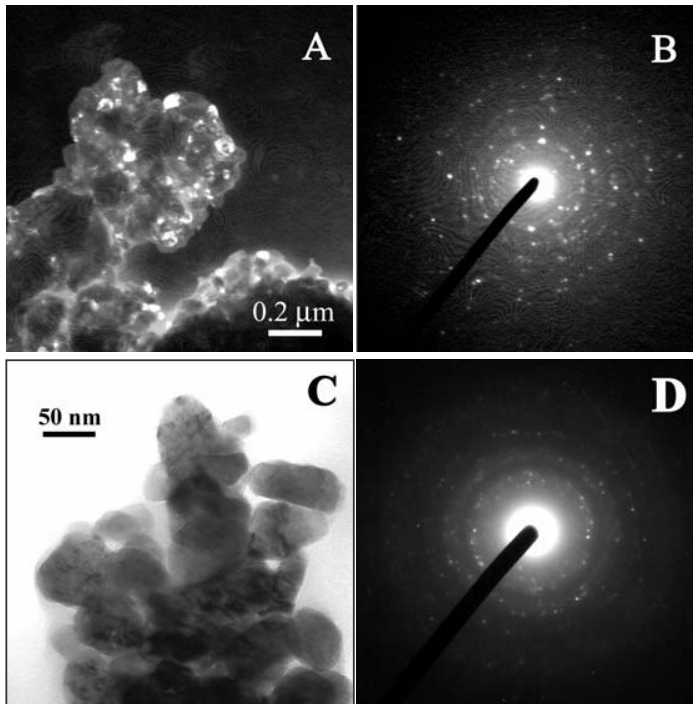


Fig. 3.14 Dark-field TEM image (A) and electron diffraction pattern (B) of $\text{La}_2\text{Ni}_{0.9}\text{Co}_{0.1}\text{O}_{4+\delta}$, and bright-field TEM image (C) and electron diffraction pattern (D) of $\text{La}_2\text{Ni}_{0.8}\text{Cu}_{0.2}\text{O}_{4+\delta}$ powders after the GNP and annealing in air at 1073 K.

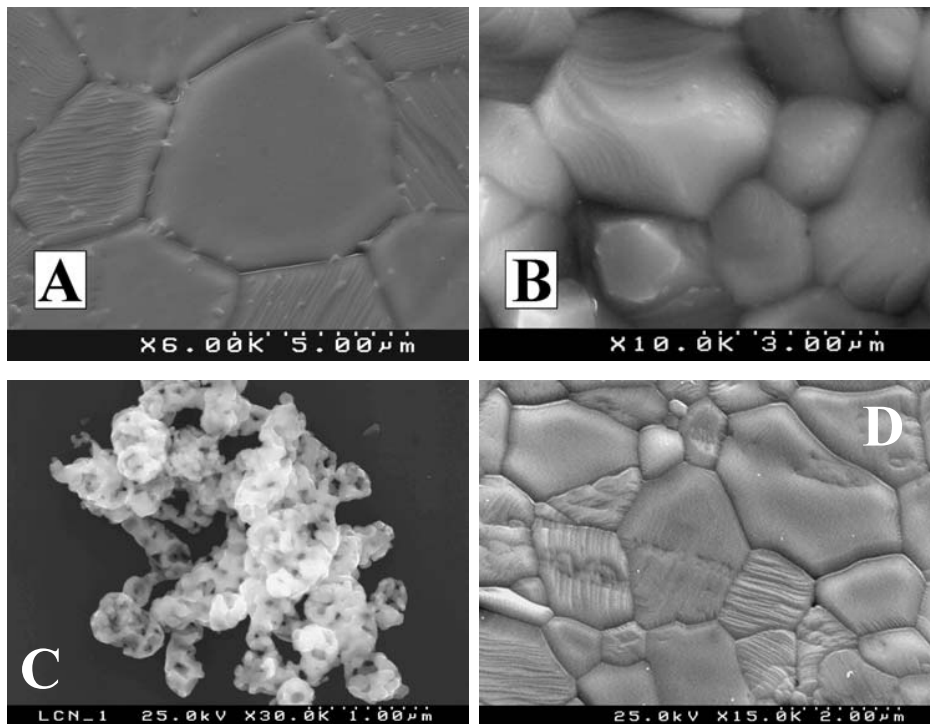


Fig.3.15. SEM micrographs of $\text{La}_2\text{Ni}_{0.9}\text{Co}_{0.1}\text{O}_{4+\delta}$ ceramics prepared by Method 1 (A) and Method 2 (B) and of $\text{La}_2\text{Ni}_{0.8}\text{Cu}_{0.2}\text{O}_{4+\delta}$ powder synthesized via GNP and annealed at 1073 for 2 h (C) and sintered ceramics(D).

TEM inspection showed that the particle size in the powder, prepared by the GNP with subsequent annealing at 1073 K is submicron, 30-90 nm (Fig.3.14). Due to agglomeration, this powder has a foam-like microstructure (Fig.3.15C) with a large surface area. The active sintering accompanied with complete crystallization of GNP-synthesized $\text{La}_2\text{NiO}_{4+\delta}$ based phases starts at approximately 1100-1200 K (Fig.3.16). The high density ceramics and mechanically stable electrode layers can be obtained after sintering at higher temperatures (Table 2.1 and Chapter 5.1.1). The sintering results in grain growth, up to 0.2 - 8 μm (Fig.3.15). As expected, doping with copper assisted the sintering process and allowed decreasing the final heat-treatment temperature of ceramics (Table 2.1), while preserving the smaller grains (Fig.3.15D). The EDS analysis of ceramics and electrode layers confirmed homogeneous cation distribution, within the limits of experimental uncertainty; no segregation at the grain boundaries was detected.

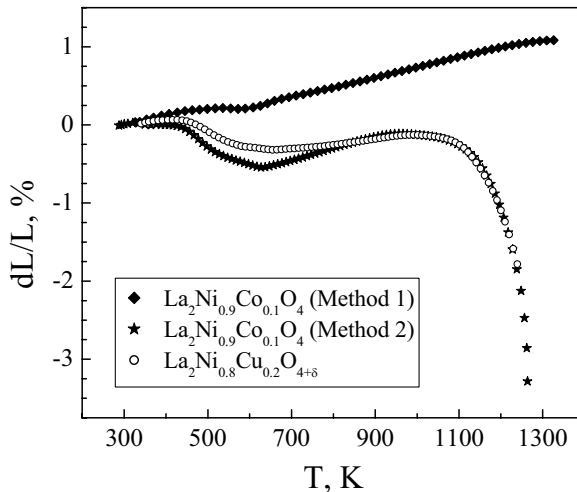


Fig.3.16. Shrinkage of green compacts of GNP- and ceramic route-synthesized nickelates in air (ramp rate of 5 K/min).

Below approximately 750 K, the total conductivity of $\text{La}_2\text{Ni}_{1-x}\text{M}_x\text{O}_{4+\delta}$ ($\text{M} = \text{Co}, \text{Cu}$; $x = 0.1-0.2$) exhibits a semiconductor-like behavior (Fig.3.17); the activation energies are listed in Table 3.3. At higher temperatures, an apparent transition to a metallic-like behavior is observed. Similar trends are typical for most La_2NiO_4 -based materials [258,260,263]. It should be separately mentioned that, as for other nickelates, the conductivity of studied materials is predominantly p-type electronic [258,260,263]; the oxygen ion transference numbers estimated using the oxygen permeation data are lower than 10^{-3} . The pseudometallic dependencies of the conductivity on temperature result from oxygen losses on heating, leading to a decrease in p-type charge carrier concentration; the electron-hole transport mechanism remains, most probably, small-polaronic, though the direct experimental proofs are necessary. The total conductivity values of $\text{La}_2\text{Ni}_{0.8}\text{Cu}_{0.2}\text{O}_{4+\delta}$, varying in the range 50-85 S/cm at 800-1300 K in air, are sufficiently high for SOFC cathode applications.

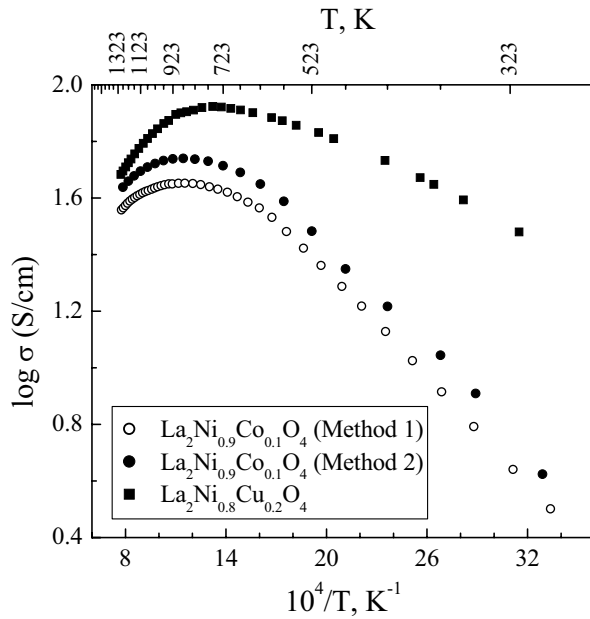


Fig.3.17. Temperature dependencies of total conductivity of La_2NiO_4 -based materials, in air.

3.2. Oxygen ionic transport

3.2.1. Surface-limited oxygen transport in $\text{La}_{0.3}\text{Sr}_{0.7}\text{CoO}_{3-\delta}$ -based solid solutions

Figs. 3.18 and 3.19 present the data on oxygen permeation fluxes through $\text{La}_{0.3}\text{Sr}_{0.7}\text{CoO}_{3-\delta}$ -based ceramic membranes of various thickness, and the corresponding values of the specific oxygen permeability calculated by Eq.(2.8). The behavior of $\text{La}_{0.3}\text{Sr}_{0.7}\text{CoO}_{3-\delta}$ and $(\text{La}_{0.3}\text{Sr}_{0.7})_{0.97}\text{CoO}_{3-\delta}$ membranes (Fig.3.18) indicates that the effects of both surface oxygen exchange and bulk ambipolar conduction are significant (see Chapter 2.6.2). Namely, decreasing membrane thickness leads to lower permeation fluxes, whereas $J(\text{O}_2)$ increases due to a decreasing role of the surface exchange. The influence of interfacial processes becomes greater on reducing oxygen partial pressure and temperature. These observations are in agreement with the isotopic exchange data [363], which demonstrated, in particular, that the activation energy for bulk oxygen diffusion in $\text{La}_{0.3}\text{Sr}_{0.7}\text{CoO}_{3-\delta}$ is considerably higher than that for exchange rate.

In contrast to undoped $\text{La}_{0.3}\text{Sr}_{0.7}\text{CoO}_{3-\delta}$, the effect of surface exchange kinetics on the permeability of $\text{La}_{0.3}\text{Sr}_{0.7}\text{Co}_{0.8}\text{Al}_{0.2}\text{O}_{3-\delta}$ and $\text{La}_{0.3}\text{Sr}_{0.7}\text{Co}_{0.8}\text{Ga}_{0.2}\text{O}_{3-\delta}$ ceramics seems to decrease with decreasing temperature (Fig.3.19). Similar phenomenon was earlier observed for Ga-substituted $\text{La}_{0.3}\text{Sr}_{0.7}\text{FeO}_{3-\delta}$ [216]. If comparing the levels of oxygen permeation fluxes through $\text{La}_{0.3}\text{Sr}_{0.7}\text{CoO}_{3-\delta}$ -based materials (Fig.3.20), one may conclude that the B-site doping decreases bulk ionic conduction without essential influence on their exchange rates. Most likely, the strong difference in

the covalence of Co–O and M–O bonds leads to local distortions near the dopant cations, blocking neighboring oxygen sites.

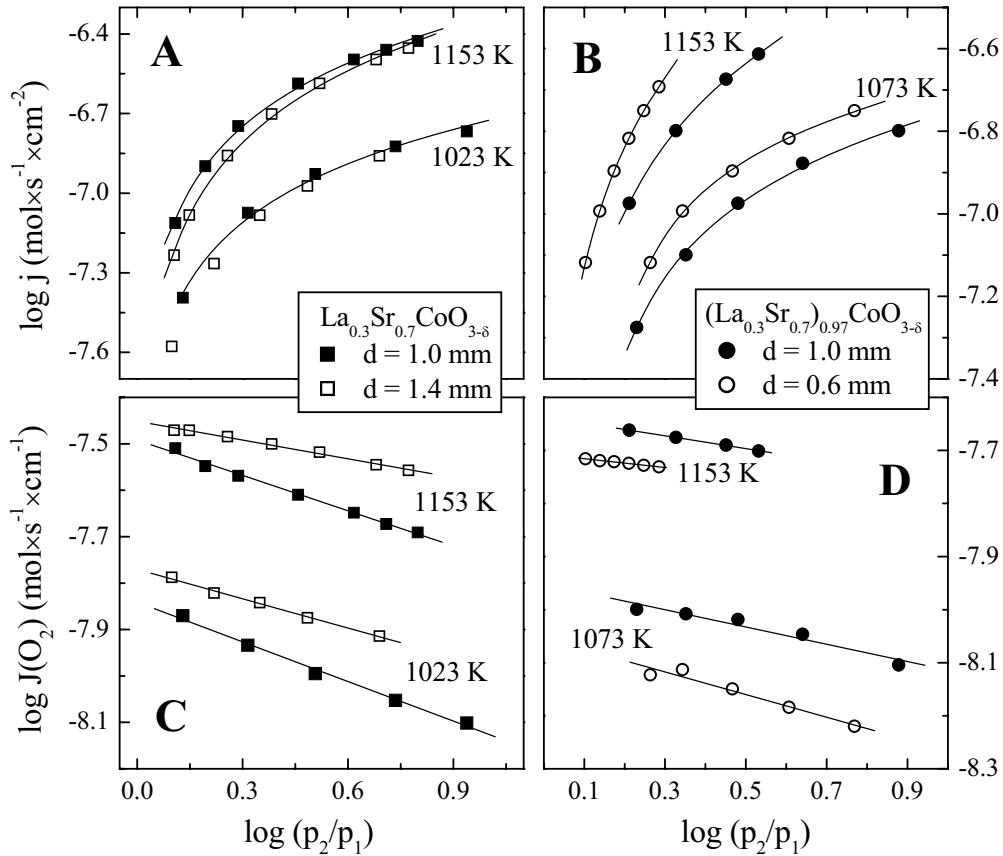


Fig.3.18. Dependence of the oxygen permeation fluxes (A,B) and specific oxygen permeability (C,D) of $\text{La}_{0.3}\text{Sr}_{0.7}\text{CoO}_{3-\delta}$ (A,C) and $(\text{La}_{0.3}\text{Sr}_{0.7})_{0.97}\text{CoO}_{3-\delta}$ (B,D) membranes on the oxygen partial pressure gradient.

In the case of $(\text{La}_{0.3}\text{Sr}_{0.7})_{0.97}\text{CoO}_{3-\delta}$, the oxygen permeability is also lower with respect to the A-site-stoichiometric analogue (Fig.3.20). Such a behavior confirms that the creation of A-site cation vacancies is mainly compensated by the formation of Co^{4+} , in agreement with the total conductivity data (Fig.3.5). This results in increasing Co–O bond strength, reflected by a substantial increase in the activation energy for oxygen transport (Table 3.1). Analogous effect is observed when aluminum is substituted for cobalt.

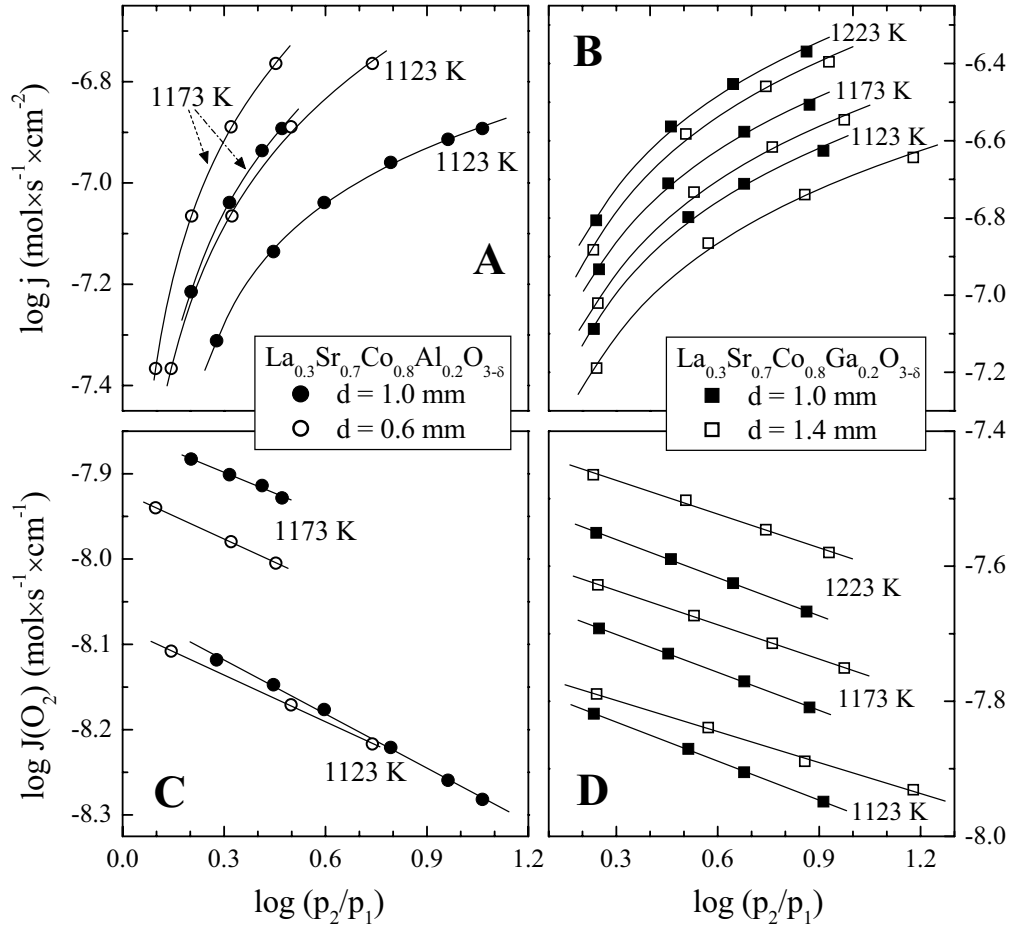


Fig.3.19. Dependence of the oxygen permeation fluxes (A,B) and specific oxygen permeability (C,D) of $\text{La}_{0.3}\text{Sr}_{0.7}\text{Co}_{0.8}\text{Al}_{0.2}\text{O}_{3-\delta}$ (A,C) and $\text{La}_{0.3}\text{Sr}_{0.7}\text{Co}_{0.8}\text{Ga}_{0.2}\text{O}_{3-\delta}$ (B,D) membranes on the oxygen partial pressure gradient.

Finally, although the oxygen-vacancy ordering processes in the cobaltite lattice at temperatures below 1100 K [241] are clearly visible in the Arrhenius plots of oxygen permeation fluxes (Fig.3.20), the role of partial ordering processes seems significantly lower in comparison with $\text{La}_{0.3}\text{Sr}_{0.7}\text{Fe}(\text{M})\text{O}_{3-\delta}$ ($\text{M} = \text{Al}, \text{Ga}$) perovskites [210,216]. As a result, although the oxygen ionic conduction in $\text{La}_{0.3}\text{Sr}_{0.7}\text{CoO}_3$ -based phases is substantially faster than that in ferrites, the defects in the cation sublattices and/or structural distortions have a deteriorating influence on the oxygen transport.

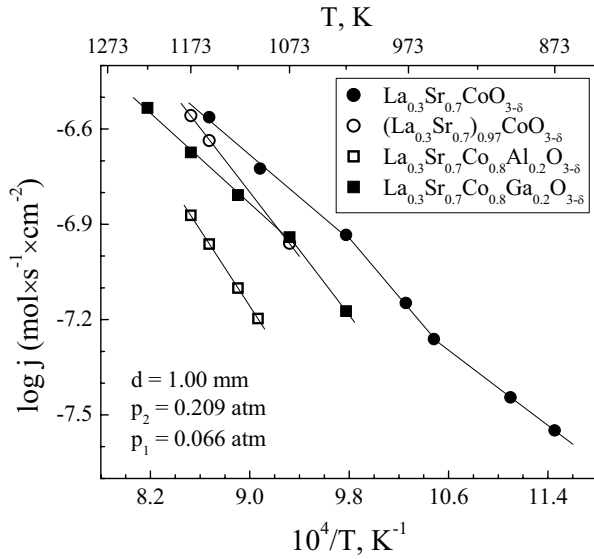


Fig.3.20. Temperature dependence of the oxygen permeation fluxes through $\text{La}_{0.3}\text{Sr}_{0.7}\text{CoO}_{3-\delta}$ -based ceramics under a fixed oxygen partial pressure gradient.

3.2.2. Oxygen ionic conductivity of $\text{YBaCo}_{4-x}\text{Fe}_x\text{O}_{7+\delta}$

The oxygen ionic transport properties were determined by the measurements of oxygen permeation and faradaic efficiency within the temperature range where no time-degradation of ceramics was observed. The ion transference numbers of $\text{YBaCo}_{4-x}\text{Fe}_x\text{O}_{7+\delta}$ ($x = 0-0.8$) at 1073-1223 K in air vary in the range $(0.4-4.5) \times 10^{-4}$, increasing with temperature and iron content (Table 3.4). The partial oxygen-ionic conductivity calculated from the transference numbers and total conductivity, is essentially independent of iron concentration (Table 3.5).

Table 3.4

Oxygen ion transference numbers of $\text{YBaCo}_{4-x}\text{Fe}_x\text{O}_{7+\delta}$ ceramics

T, K	x = 0 (Method 1)	x = 0 (Method 2)		FE d = 1.0 mm	x = 0.4	x = 0.8
	OP d = 0.6 mm	OP			FE d = 1.0 mm	FE d = 1.0 mm
		d = 0.6 mm	d = 1.0 mm			
1223	1.8×10^{-4}	1.5×10^{-4}	1.8×10^{-4}	9.1×10^{-5}	3.4×10^{-4}	4.2×10^{-4}
1173	1.7×10^{-4}	1.4×10^{-4}	1.5×10^{-4}	7.2×10^{-5}	3.0×10^{-4}	3.9×10^{-4}
1123	1.2×10^{-4}	1.1×10^{-4}	1.2×10^{-4}			
1073	2.9×10^{-5}		3.9×10^{-5}		1.1×10^{-4}	

Notes:

- the FE measurements were performed under zero oxygen chemical potential gradient in air;
- the transference numbers calculated from the OP data are averaged in the p_1 range from 0.05 to 0.10 atm, at fixed $p_2 = 0.21$ atm;
- d is the membrane thickness.

The results of faradaic efficiency studies, performed under zero oxygen chemical potential in air, show that the oxygen ionic contribution to the total conductivity of $\text{YBaCo}_4\text{O}_{7+\delta}$ at 1173-1223 K is lower than 0.01% (Table 3.4). Therefore, for the $\text{YBaCo}_4\text{O}_{7+\delta}$ membrane placed under an oxygen chemical potential gradient, the ambipolar conductivity determining oxygen transport through membrane bulk is governed by the ionic conduction; the effect of p-type electronic conductivity is expected negligible. In order to identify if the overall oxygen transport is influenced by surface exchange kinetics in addition to bulk diffusion, the oxygen permeation fluxes were measured as function of the membrane thickness (Fig.3.21). The obtained data suggest a presence of minor surface limitations to the permeation flux, the role of which increases with decreasing temperature. However, the difference in the $J(\text{O}_2)$ values of membranes with different thickness is comparable to experimental error.

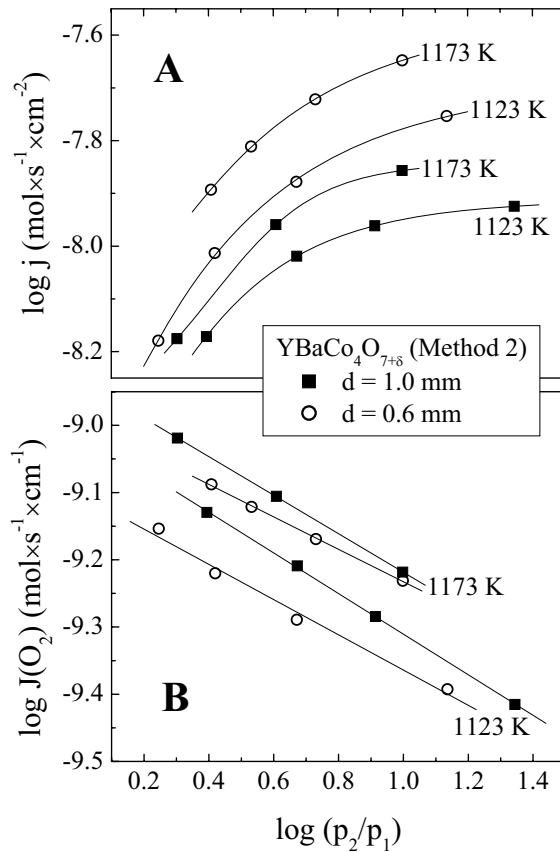


Fig.3.21. Dependencies of the oxygen permeation fluxes (A) and specific oxygen permeability (B) of $\text{YBaCo}_4\text{O}_{7+\delta}$ membranes, prepared using Method 2, on the oxygen partial pressure gradient.

The values of oxygen ionic conductivity and transference numbers, calculated from the permeation data using Eq.(2.10), are similar within the limits of experimental uncertainty (Tables 3.4 and 3.5). Moreover, these values are in a reasonable agreement with those measured by the faradaic efficiency method if taking into account that, due to a higher permeate-side oxygen

pressure in the latter case, the ion transference numbers determined by the FE technique should be lower than those calculated from the OP data, as the conductivity decreases on reducing $p(\text{O}_2)$, as shown in Chapter 3.4.2. One may therefore conclude that the surface exchange effects on the oxygen permeation through $\text{YBaCo}_4\text{O}_{7+\delta}$ based ceramics at 1073-1223 K can be neglected.

Table 3.5

Oxygen ionic conductivity of $\text{YBaCo}_4\text{O}_{7+\delta}$ (mS/cm)
evaluated from the data on oxygen permeation and total conductivity

T, K	Method 1 d = 0.60 mm	Method 2	
		d = 0.60 mm	d = 1.00 mm
1223	11.6	9.7	11.3
1173	10.4	8.5	9.4
1123	6.7	6.4	7.0
1073	1.6	-	2.1

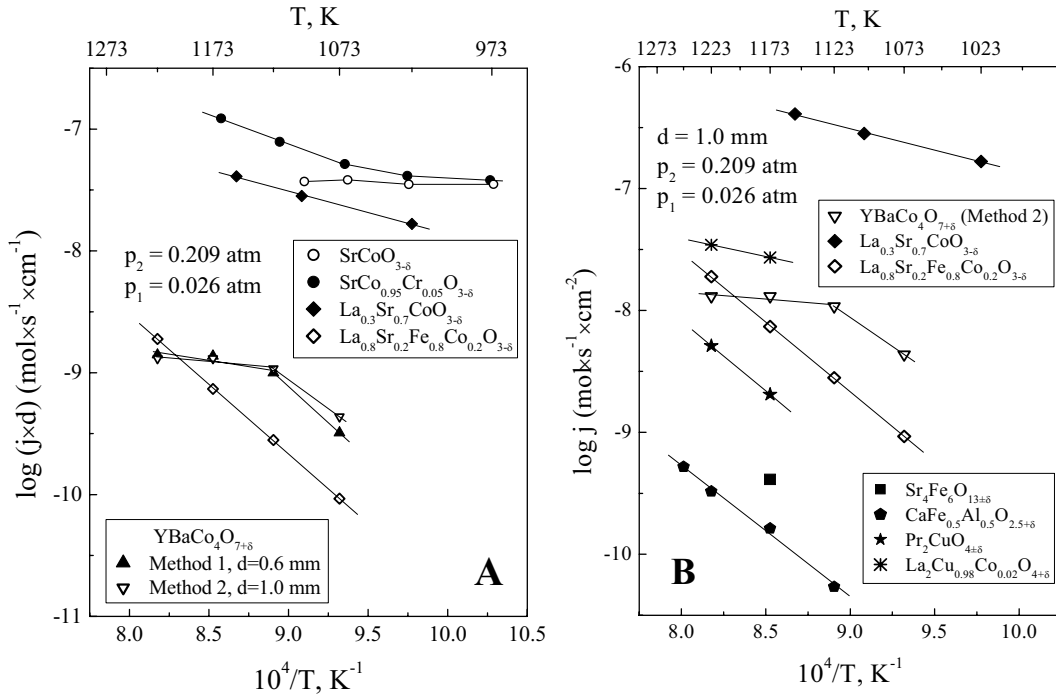


Fig.3.22. Temperature dependence of the oxygen permeation fluxes through $\text{YBaCo}_4\text{O}_{7+\delta}$ ceramics, normalised to the membrane thickness, under a fixed oxygen partial pressure gradient; data [364-367] on $\text{SrCoO}_{3-\delta}$ ($d = 1.20$ mm), $\text{SrCo}_{0.95}\text{Cr}_{0.05}\text{O}_{3-\delta}$ ($d = 2.10$ mm), $\text{La}_{0.3}\text{Sr}_{0.7}\text{CoO}_{3-\delta}$ ($d = 1.00$ mm) and

$\text{La}_{0.8}\text{Sr}_{0.2}\text{Fe}_{0.8}\text{Co}_{0.2}\text{O}_{3-\delta}$ ($d = 1.00$ mm) are shown for comparison (A). Comparison of the oxygen permeation fluxes through various mixed-conducting materials [263,364,365,368,369] (B).

Fig.3.22A compares the level of oxygen permeation fluxes through $\text{YBaCo}_4\text{O}_{7+\delta}$ ceramics and several Co-containing perovskites [364-367]. In order to provide a comparison of membranes with different thickness, the permeation fluxes are expressed as $j \times d$. The permeability of oxygen-deficient materials based on $\text{SrCoO}_{3-\delta}$ is 30-150 times higher than that of $\text{YBaCo}_4\text{O}_{7+\delta}$. At the same time, the ionic transport in undoped $\text{SrCoO}_{3-\delta}$ at 973-1100 K shows a negligible dependence on temperature, as for $\text{YBaCo}_4\text{O}_{7+\delta}$ at 1123-1223 K. In both cases this behaviour is ascribed to temperature-induced phase transitions. Strontium cobaltite with cubic perovskite structure is stable under oxidising conditions at temperatures above 1120-1220 K and undergoes a series of phase transformations on cooling; depending on moderate $p(\text{O}_2)$ variations a number of phases, such as brownmillerite-type $\text{Sr}_2\text{Co}_2\text{O}_{5+\delta}$ and rhombohedral $\text{Sr}_6\text{Co}_5\text{O}_{15}$, may be formed [233,367]. Cubic perovskite $\text{SrCo}_{0.95}\text{Cr}_{0.05}\text{O}_{3-\delta}$ decomposes into a phase mixture on cooling down to temperatures below 1000 K, resulting in a drastic drop of the apparent activation energy for oxygen permeation. Similar behavior is characteristic for most SrCoO_3 -based ceramics where the concentration of dopants is insufficient to stabilise cubic perovskite lattice [366,367].

With respect to perovskite $\text{La}_{0.8}\text{Sr}_{0.2}\text{Fe}_{0.8}\text{Co}_{0.2}\text{O}_{3-\delta}$ that belongs to another series of materials promising for SOFCs and oxygen membranes [365], $\text{YBaCo}_4\text{O}_{7+\delta}$ exhibits considerably higher oxygen permeation at 1073-1173 K (Fig.3.22). This level of oxygen transport is also greater than that in layered Fe-containing phases such as $\text{Sr}_4\text{Fe}_6\text{O}_{13\pm\delta}$ [368] or $\text{CaFe}_{0.5}\text{Al}_{0.5}\text{O}_{2.5+\delta}$ [369], but is rather moderate if compared to K_2NiF_4 -type cuprates [263]. Fig.3.22B presents an overview on the oxygen permeability of various intergrowth materials.

3.2.3. Oxygen permeability of $\text{La}_2\text{Ni}(M)\text{O}_{4+\delta}$ ($M = \text{Co}, \text{Cu}$) ceramics

The results of faradaic efficiency measurements confirmed that the conductivity of $\text{La}_2\text{NiO}_{4+\delta}$ based materials is predominantly electronic. The oxygen ionic contribution to total conductivity, which can be estimated from the ratio between oxygen flux and total current passed through a membrane by an applied dc voltage, is lower than 0.5%. As an example, Table 3.6 shows the data on faradaic efficiency of $\text{La}_2\text{Ni}_{0.9}\text{Co}_{0.1}\text{O}_{4+\delta}$ prepared by Method 2, under zero oxygen partial pressure gradient in air. The ionic contribution is as low as 0.11% at 1223 K and decrease on cooling. This suggests that, under an oxygen chemical potential gradient, electronic transport should have no essential effect on the oxygen transport through the membrane bulk.

Table 3.6

Faradaic efficiency of $\text{La}_2\text{Ni}_{0.9}\text{Co}_{0.1}\text{O}_{4+\delta}$ ceramics, prepared by Method 2,
under zero oxygen chemical potential gradient in air

T, K	Total current through membrane, $\text{mA}\times\text{cm}^{-2}$	Oxygen flux through membrane, $\text{mA}\times\text{cm}^{-2}$	Voltage applied to the electrodes of sample, mV	Faradaic efficiency, %
1223	348.5	0.398	19.8	0.114
	174.2	0.197	9.90	0.113
1173	296.2	0.215	16.8	0.073
	148.1	0.109	8.42	0.074
1073	374.6	0.084	21.3	0.023
	188.0	0.048	10.7	0.025

Note: The voltage between electrodes consists of several contributions, including the electrical potential drops on the current collectors, electrodes and membrane bulk, and is thus higher than expected from the total conductivity of membrane material.

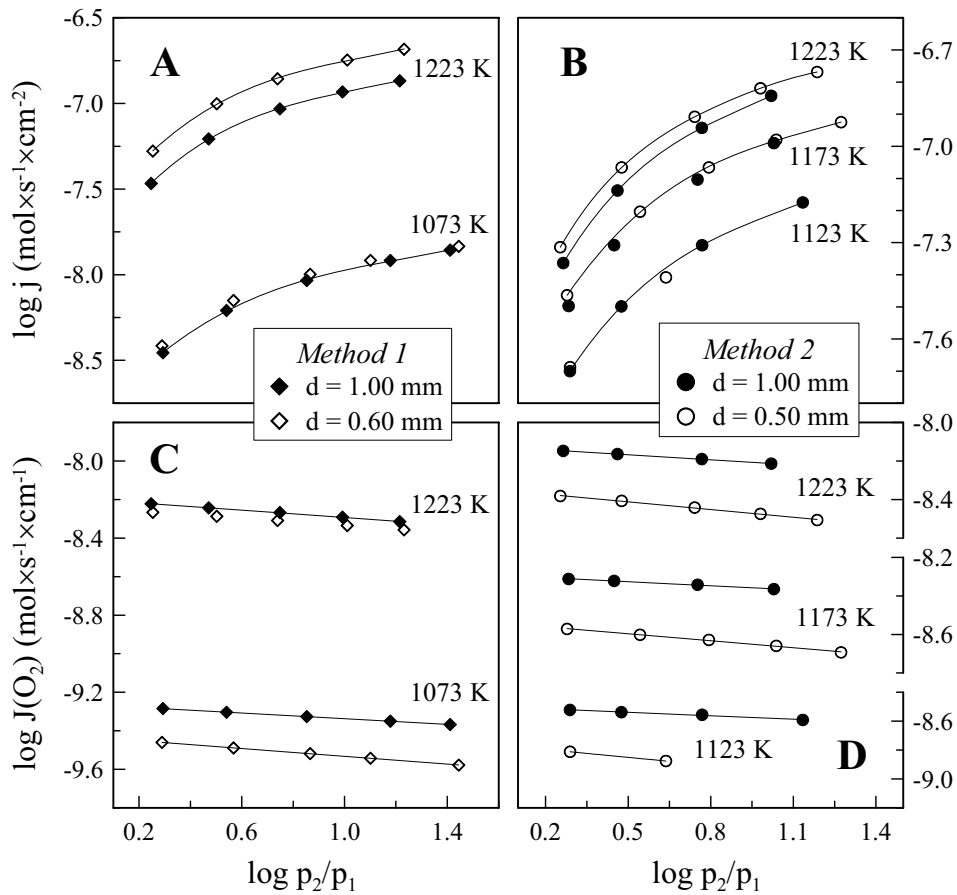


Fig.3.23. Dependencies of oxygen permeation fluxes (A, B) and specific oxygen permeability (C, D) of $\text{La}_2\text{Ni}_{0.9}\text{Co}_{0.1}\text{O}_{4+\delta}$ membranes, prepared by the different methods, on oxygen partial pressure gradient under oxidizing conditions.

Figs.3.23 and 3.24 present the dependencies of oxygen permeation fluxes and specific oxygen permeability of $\text{La}_2\text{Ni}_{0.9}\text{Co}_{0.1}\text{O}_{4+\delta}$ and $\text{La}_2\text{Ni}_{0.8}\text{Cu}_{0.2}\text{O}_{4+\delta}$ membranes of different thickness on the oxygen partial pressure gradient in oxidizing conditions. These results unambiguously indicate that the overall oxygen transport is limited by both bulk ionic conduction and surface exchange rates, similar to other La_2NiO_4 -based materials [263]. Irrespective of ceramic processing route, the permeation fluxes decrease with increasing membrane thickness at 1223 K and become almost independent of thickness below 1173 K (Figs.3.23, A and B, and 3.24A), whilst the specific oxygen permeability increases with d (Fig.3.23, C and D, and 3.24B). Hence, the limiting role of interfacial exchange increases with decreasing temperature; below 1173 K the permeation is controlled by the exchange kinetics. Despite that the incorporation of cobalt and copper cations into $\text{La}_2\text{NiO}_{4+\delta}$ lattice may increase surface exchange rate [261], such an enhancement is obviously insufficient to achieve bulk-controlled oxygen transport, especially at reduced temperatures. This behavior suggests that the cathodic performance of $\text{La}_2\text{Ni}_{1-x}\text{M}_x\text{O}_{4+\delta}$ ($M = \text{Co}, \text{Cu}$) may be limited by the surface exchange processes.

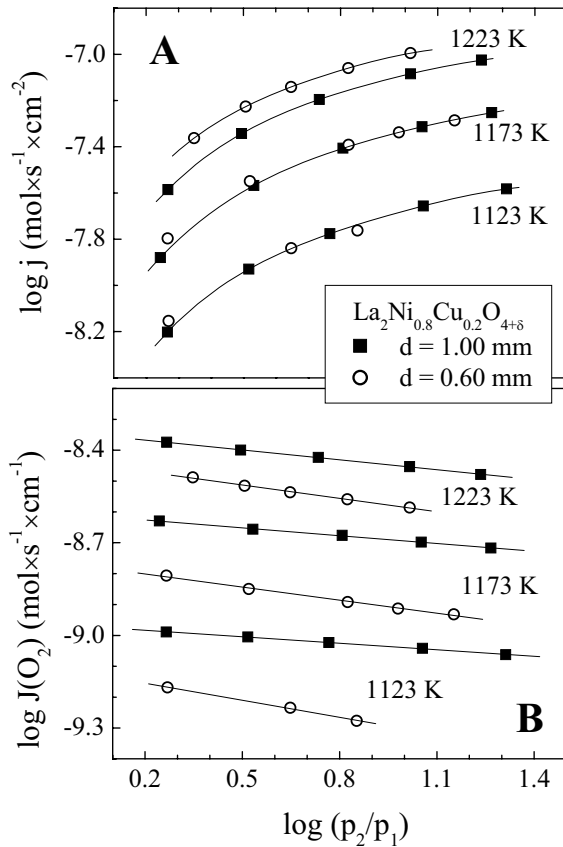


Fig.3.24. Oxygen permeation fluxes through $\text{La}_2\text{Ni}_{0.8}\text{Cu}_{0.2}\text{O}_{4+\delta}$ membranes vs. oxygen partial pressure gradient.

Fig.3.25 compares oxygen permeation through $\text{La}_2\text{Ni}_{0.9}\text{Co}_{0.1}\text{O}_{4+\delta}$ and $\text{La}_2\text{Ni}_{0.8}\text{Cu}_{0.2}\text{O}_{4+\delta}$ and other prospective cathode materials having TECs compatible with LSGM, under a fixed oxygen chemical potential gradient. The membrane thickness was 1.0 mm in all cases, except for $\text{La}_{0.7}\text{Sr}_{0.3}\text{MnO}_{3-\delta}$ where the permeation flux was measured for the ceramics with $d = 0.6$ mm and then normalized. Detailed information on the alternative electrode materials, including thermal expansion, oxygen permeability and total conductivity, is found elsewhere [43,370-372]. In general, LaMnO_3 - and SrMnO_3 -based phases exhibit a low ionic transport inappropriate for IT SOFC cathodes. Oxygen permeability of $\text{LaFe}(\text{Ni})\text{O}_{3-\delta}$ perovskites is determined by the vacancy concentration and achieves sufficient level only for $\text{LaFe}_{0.5}\text{Ni}_{0.5}\text{O}_{3-\delta}$, the composition close to solid solution formation limit [372]. The permeability of $\text{La}_2\text{Ni}_{0.8}\text{Cu}_{0.2}\text{O}_{4+\delta}$ ceramics is similar to that of $\text{LaGa}_{0.65}\text{Mg}_{0.15}\text{Ni}_{0.20}\text{O}_{3-\delta}$; the TECs of the latter composition, $(17.0\text{-}18.4)\times 10^{-6} \text{ K}^{-1}$ at 773-1273 K [370], are excessively high to provide stable operation in contact with LSGM. Also, the total electrical conductivity of $\text{LaGa}_{0.65}\text{Mg}_{0.15}\text{Ni}_{0.20}\text{O}_{3-\delta}$, varying in the range of 1.2-1.4 S/cm at 1073 K [370], is significantly lower compared to that of K_2NiF_4 -type nickelates (Fig.3.17). $\text{La}_2\text{Ni}_{0.9}\text{Co}_{0.1}\text{O}_{4+\delta}$ shows the highest ionic transport among this group of materials. Thus, due to relatively high oxygen permeability and moderate thermal expansion, phases derived from $\text{La}_2\text{NiO}_{4+\delta}$ can be considered as promising candidates for IT SOFC cathode materials.

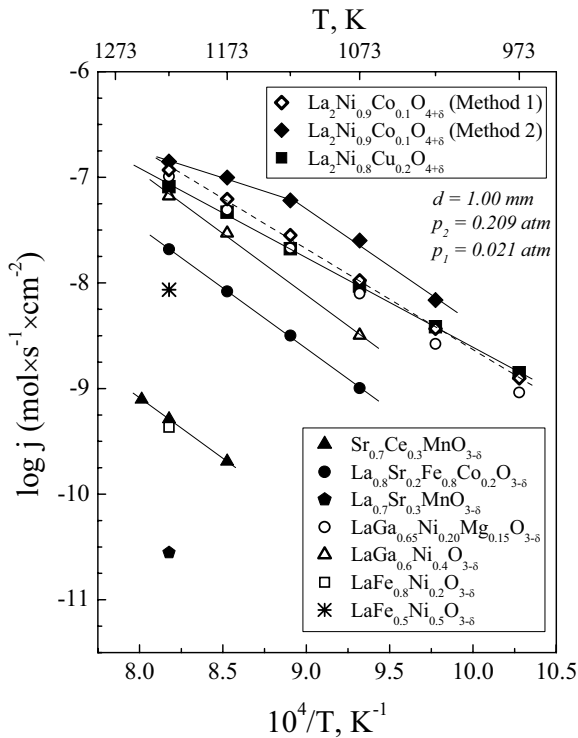


Fig.3.25. Comparison of oxygen permeation fluxes through various ceramic materials, having TECs compatible with LSGM [43,370-372], under fixed oxygen pressure gradient. The data for $\text{La}_{0.7}\text{Sr}_{0.3}\text{MnO}_3$, measured for membrane thickness of 0.60 mm, is normalized to 1.00 mm [43].

3.3. Role of synthesis method: case studies

The preparation procedure may significantly affect both ionic conductivity and oxygen surface exchange of ceramic materials [353,364,370], though interpretation of observed phenomena is often ambiguous due to complex nature of transport processes at the grain boundaries and on the surface. The oxygen ionic conductivity of single-phase materials, prepared by a similar method with monotonous variation of the processing conditions, typically increases with increasing grain size due to lower grain-boundary resistance [353,364,370]. At the same time, LaCoO_{3-δ} ceramics prepared using different powder synthesis techniques, but having similar grain sizes, showed drastically different level of the ionic transport; the surface exchange limitations for LaGa_{0.65}Ni_{0.20}Mg_{0.15}O_{3-δ} membranes were found considerably higher in the case of material with larger grains ([370] and references cited). In order to identify possible effects of the synthesis method on the microstructure and transport properties, YBaCo₄O_{7+δ} and La₂Ni_{0.9}Co_{0.1}O_{4+δ} samples were prepared using the solid-state reaction (Method 1) and the glycine-nitrate process (Method 2).

The grain size of YBaCo₄O_{7+δ} ceramics prepared using Methods 1 and 2 is 8-10 μm and 2-7 μm, respectively (Fig.3.10). Note that the latter powder was annealed at 1273 K in order to obtain single-phase ceramics after sintering. As it was mentioned in Chapter 3.1.2, in general the microstructures of these materials are similar. No phase impurities were found by XRD and SEM/EDS in both cases. As a result, the unit cell parameters are quite close (Table 3.2). The phase decomposition on cooling indicated by XRD, TG/DTA and dilatometry techniques and electrical conductivity measurements, is observed at similar temperatures; one example of conductivity data comparing behavior of ceramic route- and GNP-synthesized samples, is shown by Inset of Fig.3.11A. At temperatures above 750 K, the average TECs of materials prepared by two different methods are quite close, (7.3-7.6)×10⁻⁶ K⁻¹ (Table 3.2). In the low-temperature range, the difference in TECs is slightly higher, probably due to an experimental error that might originate, in particular, from hysteresis phenomena related to the phase metastability. The transport properties of YBaCo₄O_{7+δ}, including the electronic and ionic conductivities and oxygen permeability are found essentially independent of the synthesis method (Table 3.2, Inset in Fig.3.11A, Fig.3.22B). Thus, moderate differences in the microstructure of YBaCo₄O_{7+δ} ceramics prepared by Methods 1 and 2 have a minor effect on the materials properties.

The dilatometric studies of La₂Ni_{0.9}Co_{0.1}O_{4+δ} green compacts revealed a considerably higher sinterability of GNP-synthesized powder (Fig.3.16). In this case, pronounced sinterization starts around 1100 K, while a green compact of powder synthesized by Method 1 does not shrink at least up to 1340 K. Using Method 2 made it possible to decrease the processing temperature by 180 K and to sinter ceramics with 96-97% density at 1543 K (Table 2.1). SEM/EDS revealed no significant difference in the microstructures of La₂Ni_{0.9}Co_{0.1}O_{4+δ} ceramics prepared by different

methods, except for the grain size. As for $\text{YBaCo}_4\text{O}_{7+\delta}$, the use of Method 2 resulted in smaller grains (1-3 μm), whereas in case of Method 1 the grain size was in range 4-8 μm (Fig.3.15 A and B). The larger grains of the material prepared by the standard ceramic route result, obviously, from extensive heat treatments, including longer annealing time of the powder and higher sintering temperature of the ceramics.

At the same time, the variations in lattice parameters, thermal expansion and total conductivity of $\text{La}_2\text{Ni}_{0.8}\text{Co}_{0.1}\text{O}_{4+\delta}$ (Table 3.3 and Fig.3.17) are higher than the corresponding experimental errors, suggesting a significant difference between the ceramics prepared by different techniques. Comparison of the unit cell parameters with literature [373] may indicate a lower Co concentration in the grain bulk of material synthesized by Method 2, which may result, in particular, from cobalt segregation at the grain boundaries. This seems consistent with the differences in total conductivity (Fig.3.17), since p-type electronic transport in $\text{La}_2\text{Ni}_{1-x}\text{Co}_x\text{O}_{4+\delta}$ decreases with Co additions [373]. However, for both preparation methods, no traces of liquid phase formation at the grain boundaries were observed (Fig.3.15); the cation distribution was apparently homogeneous within the limits of experimental uncertainty of the EDS method. One alternative explanation may refer to a greater concentration of extended defects in the ceramics made from the nanosized non-single-phase powder, obtained via glycine-nitrate process. On the contrary to GNP synthesis, the particle size of the single-phase powder prepared by Method 1 is of micron-scale, available for evaluation by SEM. For the material synthesized by Method 2, the ceramic grains are formed from a substantially large number of nanosized particles. The resultant high concentration of extended defects may lead to local inhomogeneities in the point defect distribution in this material, affecting both lattice parameters and transport properties. An analogous behavior was observed for $\text{LaGa}_{0.65}\text{Ni}_{0.20}\text{Mg}_{0.15}\text{O}_{3-\delta}$ ceramics prepared using two similar techniques [370]. Slightly higher TEC of samples prepared by Method 2 may, again, be attributed to higher concentration of extended defects; as a rule, increasing defects concentration leads to increase in thermal expansion of ceramics.

Fig.3.25 compares the oxygen permeation fluxes through $\text{La}_2\text{Ni}_{0.9}\text{Co}_{0.1}\text{O}_{4+\delta}$ membranes prepared by two different techniques, under a fixed oxygen partial pressure gradient. The material synthesized by Method 2 exhibits higher oxygen permeability within the entire temperature range. Similar differences in behavior were earlier observed for $\text{LaGa}_{0.65}\text{Ni}_{0.20}\text{Mg}_{0.15}\text{O}_{3-\delta}$ [370] prepared by the standard ceramic route and via the GNP (inset in Fig.3.25). The data on oxygen permeation and faradaic efficiency of $\text{LaGa}_{0.65}\text{Ni}_{0.20}\text{Mg}_{0.15}\text{O}_{3-\delta}$ indicated faster exchange kinetics for the GNP-synthesized membranes, with no essential effect of processing route on the bulk transport properties [370]. Although the data on $\text{La}_2\text{Ni}_{0.9}\text{Co}_{0.1}\text{O}_{4+\delta}$ do not allow unambiguous conclusion, one may assume that the higher oxygen permeation through nickelate membranes prepared via the GNP

is also associated with faster oxygen exchange. The possible cobalt segregation at grain boundaries, if any, should not significantly affect bulk oxygen transport as the oxygen diffusion coefficients in $\text{La}_2\text{Ni}_{1-x}\text{Co}_x\text{O}_{4+\delta}$ ($x = 0-0.2$) are essentially independent of cobalt content [261]. Moreover, the bulk ionic conductivity, which typically increases with grain size [374], may even be higher for the material prepared by Method 1 due to larger grains (Fig.3.16, A and B). One possible explanation may therefore refer to a greater concentration of extended defects in the material prepared by Method 2; this may lead to a higher concentration of active centers on the surface, accelerating interfacial exchange processes. Nonetheless, the overall permeation fluxes through GNP-synthesized $\text{La}_2\text{Ni}_{1-x}\text{Co}_x\text{O}_{4+\delta}$ membranes at temperatures below 1200 K are still determined by the exchange kinetics (Fig.3.23). The stability limits of the materials obtained using two various methods were very similar; their difference was within the limits of experimental error.

3.4. Electrical properties vs. temperature and oxygen partial pressure

3.4.1. Cobalt-containing perovskites

The oxygen partial pressure dependencies of the total conductivity and Seebeck coefficient of $(\text{La}_{0.3}\text{Sr}_{0.7})_{0.97}\text{CoO}_{3-\delta}$, $\text{La}_{0.3}\text{Sr}_{0.7}\text{Co}_{0.8}\text{Al}_{0.2}\text{O}_{3-\delta}$ and $\text{La}_{0.3}\text{Sr}_{0.7}\text{Co}_{0.8}\text{Ga}_{0.2}\text{O}_{3-\delta}$, Figs.3.26 and 3.27, confirm predominant p-type electronic transport under oxidizing conditions, as for the parent compound [239]. The conclusion, that the p-type conduction is dominant, is in agreement with oxygen permeation data discussed in Chapter 3.2.1. Although the calculation of exact values of the oxygen ionic conductivity is impossible due to a significant interfacial effect on the oxygen permeation, the estimates of the ionic contribution to the total conductivity are less than 0.5%, in all cases. Reducing $p(\text{O}_2)$ down to approximately 10^{-4} atm is accompanied with an increase in the thermopower and a decrease in the p-type conductivity owing to decreasing hole concentration.

Table 3.7

Reciprocal slope* of the $p(\text{O}_2)$ dependencies of the total conductivity for $\text{La}_{0.3}\text{Sr}_{0.7}\text{Co}_{0.8}\text{Ga}_{0.2}\text{O}_{3-\delta}$ ceramics

T, K	$(\text{La}_{0.3}\text{Sr}_{0.7})_{0.97}\text{CoO}_{3-\delta}$	$\text{La}_{0.3}\text{Sr}_{0.7}\text{Co}_{0.8}\text{Al}_{0.2}\text{O}_{3-\delta}$	$\text{La}_{0.3}\text{Sr}_{0.7}\text{Co}_{0.8}\text{Ga}_{0.2}\text{O}_{3-\delta}$	
	$9.4 \times 10^{-5} - 3.7 \times 10^{-1}$ atm	$1.8 \times 10^{-4} - 3.7 \times 10^{-1}$ atm	$1.3 \times 10^{-3} - 2.1 \times 10^{-2}$ atm	$2.1 \times 10^{-2} - 3.4 \times 10^{-1}$ atm
973	12.1 ± 0.2	11.9 ± 0.5	6.6 ± 0.5	8 ± 1
1023	9.9 ± 0.3	11.4 ± 0.4	5.4 ± 0.2	7.5 ± 1
1073	9.1 ± 0.3	11.2 ± 0.4	4.9 ± 0.2	7 ± 2
1123	8.8 ± 0.4	11.0 ± 0.4	4.8 ± 0.8	7 ± 3
1173	8.9 ± 0.3	11.1 ± 0.4	5 ± 1	8 ± 3
1223	9.9 ± 0.3	11.8 ± 0.6	5 ± 2	9.9 ± 0.1

* The model for conductivity: $\sigma = \sigma_p^0 p(\text{O}_2)^{1/m}$, where m and σ_p^0 are constants.

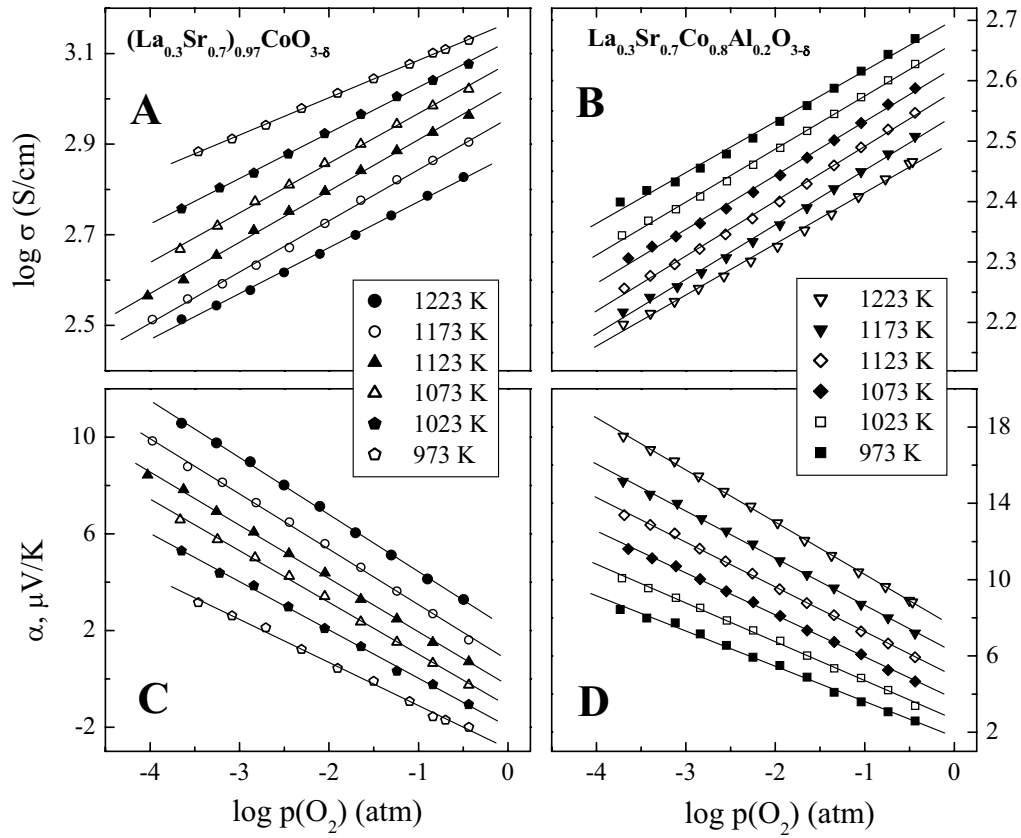


Fig.3.26. Oxygen partial pressure dependencies of the total conductivity (A,B) and Seebeck coefficient (C,D) of $(\text{La}_{0.3}\text{Sr}_{0.7})_{0.97}\text{CoO}_{3-\delta}$ (A,C) and $\text{La}_{0.3}\text{Sr}_{0.7}\text{Co}_{0.8}\text{Al}_{0.2}\text{O}_{3-\delta}$ (B,D) under oxidizing conditions. Solid lines are for visual guidance only.

At the same time, the slope of logarithmic σ vs. $p(\text{O}_2)$ dependencies of $(\text{La}_{0.3}\text{Sr}_{0.7})_{0.97}\text{CoO}_{3-\delta}$ and $\text{La}_{0.3}\text{Sr}_{0.7}\text{Co}_{0.8}\text{Al}_{0.2}\text{O}_{3-\delta}$, 1/12 to 1/9 (Table 3.7), is 5-10 times higher than that of $(\alpha x e/k)$ vs. $\ln p(\text{O}_2)$ curves. The $p(\text{O}_2)$ dependencies of total conductivity and Seebeck coefficient of $\text{La}_{0.3}\text{Sr}_{0.7}\text{Co}_{0.8}\text{Ga}_{0.2}\text{O}_{3-\delta}$ perovskite (Fig.3.28) are clearly non-linear, with a maximum slope at moderate oxygen partial pressures varying from 10^{-3} to 2×10^{-2} atm. In this $p(\text{O}_2)$ range, the exponent of σ vs. $p(\text{O}_2)^{1/m}$ dependencies (Table 3.7) is close to 1/6, a classical value for a mixed conductor with moderate oxygen nonstoichiometry [90]. For the Seebeck coefficient, the slope of α vs. $\ln p(\text{O}_2)$ is, again, considerably lower than $(-k/6e)$, which could be expected in case of a simple band mechanism of the hole conduction. In combination with relatively high values of the hole mobility discussed below, such trends suggest itinerant behavior of the p-type charge carriers, with the density of states and mobility both increasing when the oxygen nonstoichiometry decreases. This conforms to the literature data on $\text{La}_{1-x}\text{Sr}_x\text{CoO}_{3-\delta}$ ($x \geq 0.4$) perovskites [375-377].

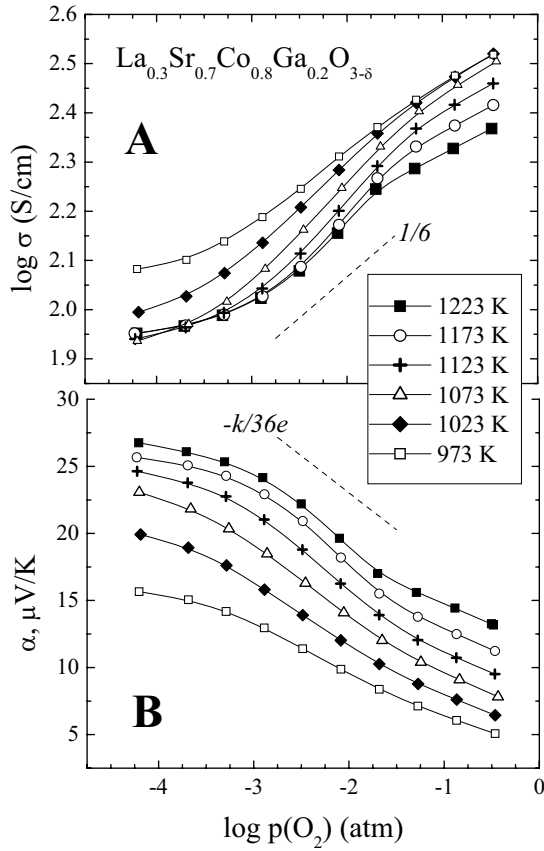


Fig.3.27. Oxygen partial pressure dependencies of the total conductivity (A) and Seebeck coefficient (B) of $\text{La}_{0.3}\text{Sr}_{0.7}\text{Co}_{0.8}\text{Ga}_{0.2}\text{O}_{3-\delta}$ under oxidizing conditions. Solid lines are for visual guidance only.

Note, however, that a hopping mechanism with $p(\text{O}_2)$ -dependent mobility cannot yet be entirely excluded. It should also be mentioned that the behavior of $(\text{La}_{0.3}\text{Sr}_{0.7})_{0.97}\text{CoO}_{3-\delta}$ and $\text{La}_{0.3}\text{Sr}_{0.7}\text{Co}_{0.8}\text{Al}_{0.2}\text{O}_{3-\delta}$ may differ from that of $\text{La}_{0.3}\text{Sr}_{0.7}\text{Co}_{0.8}\text{Ga}_{0.2}\text{O}_{3-\delta}$ due to larger interatomic distances in the Ga-doped phase (Table 3.1), leading to a higher degree of electron localization in the latter [375,376]. As a particular result, the conductivity of $\text{La}_{0.3}\text{Sr}_{0.7}\text{Co}_{0.8}\text{Ga}_{0.2}\text{O}_{3-\delta}$ is substantially lower than that of the Al-containing analogue (Fig.3.5).

The variations of the electrical properties as function of oxygen partial pressure can be analyzed on the examples of $(\text{La}_{0.3}\text{Sr}_{0.7})_{0.97}\text{CoO}_{3-\delta}$ and $\text{La}_{0.3}\text{Sr}_{0.7}\text{Co}_{0.8}\text{Al}_{0.2}\text{O}_{3-\delta}$, assuming no essential association of the point defects. The role of n-type electronic charge carriers formed due to cobalt disproportionation can also be neglected under oxidizing conditions [375,377]. In this situation, the concentrations of electron holes (p) and oxygen vacancies (δ) of $(\text{La}_{0.3}\text{Sr}_{0.7})_{1-x}\text{Co}_{1-y}\text{Al}_y\text{O}_{3-\delta}$ are related via the equilibrium with gas phase and the electroneutrality condition:

$$K_{\text{ex}} = \frac{p(\text{O}_2)^{1/2} \cdot \delta \cdot (1 - y - p)^2}{(3 - \delta) \cdot p^2} \quad (3.1)$$

$$2\delta + p = 0.7 + 2.3x \quad (3.2)$$

where K_{ex} is the equilibrium constant and all defect concentrations correspond to one perovskite formula unit. Using the experimental values of oxygen nonstoichiometry in air determined by thermogravimetry (Fig.3.4), one can directly calculate K_{ex} at $p(\text{O}_2) = 0.21$ atm. Then Eq.(3.1) can be solved for p as function of the oxygen pressure. In turn, hole concentration is used to assess the mobility of p-type electronic charge carriers (μ_p) and the apparent density of states (N^*):

$$\sigma \approx \sigma_p = e \cdot \mu_p \cdot p / V_{\text{uc}} \quad (3.3)$$

$$\alpha = \frac{k}{e} \cdot \ln \left(\frac{N^*}{p} \right) \quad (3.4)$$

where V_{uc} is the unit cell volume calculated from the XRD data. Note that Eq.(3.4) neglects the transported heat of holes, and also possible site-exclusion and spin degeneracy effects. The results of these estimations are presented in Figs. 3.28 and 3.29.

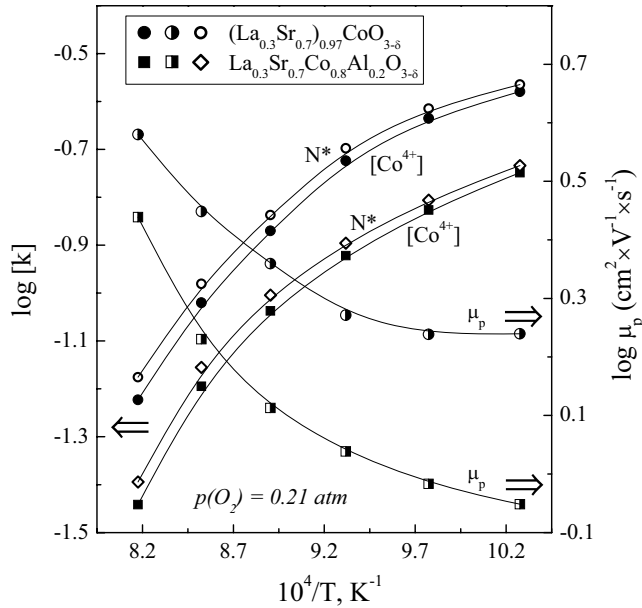


Fig.3.28. Temperature dependencies of the calculated values of electron-hole concentration and density of states per formula unit, and hole mobility for cobaltite perovskites in air (see text).

As expected from literature [375,376], the density of states decreases on heating at fixed $p(\text{O}_2)$, when the oxygen deficiency increases (Fig.3.28). The N^* estimates are significantly lower than the total concentration of cobalt cations, a result of itinerant behavior of the electrons of Co(IV)O_6 complex [375]. Most likely, the occupation of cobalt cations, whose nearest neighborhood comprises oxygen vacancies, is energetically unfavorable due to coulombic forces; the concentration of Co^{3+} contributing to the hole transport is, therefore, relatively low. At the same time, the difference between p and N^* increases with temperature, in agreement with the band

model proposed by Mineshige et al. [376]; this is accompanied with increasing hole mobility. The values of μ_p , $0.9\text{--}3.8\text{ cm}^2\times\text{V}^{-1}\times\text{s}^{-1}$ at $973\text{--}1223\text{ K}$ in air, are considerably higher than the characteristic threshold of approximately $0.1\text{ cm}^2\times\text{V}^{-1}\times\text{s}^{-1}$, considered as a rough criterion separating polaron and broad-band conductors. One should also note that the increase in hole mobility with increasing oxygen pressure (Fig.3.29) is often observed in perovskite-related phases (e.g. [215]). This may be associated with progressive association of oxygen vacancies and Co^{2+} ions on reducing $p(\text{O}_2)$, decreasing concentration of the cobalt sites available for hole hopping. Another possible explanation refers to the perovskite unit cell contraction when the oxygen nonstoichiometry decreases and the average oxidation state of cobalt cations increases [215]. This leads to a greater overlap of cobalt and oxygen electron orbitals and, thus, to a stronger covalency of Co–O–Co bonds, providing higher mobility [361].

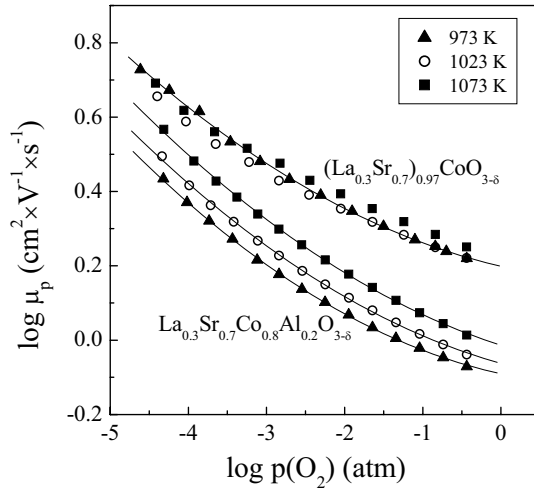


Fig.3.29. Estimated electron-hole mobility of $(\text{La}_{0.3}\text{Sr}_{0.7})_{0.97}\text{CoO}_{3-\delta}$ and $\text{La}_{0.3}\text{Sr}_{0.7}\text{Co}_{0.8}\text{Al}_{0.2}\text{O}_{3-\delta}$ (see text).

Fig.3.30 compares the estimated oxygen nonstoichiometry of $\text{La}_{0.3}\text{Sr}_{0.7}\text{Co}_{0.8}\text{Al}_{0.2}\text{O}_{3-\delta}$ and literature data on $\text{La}_{0.3}\text{Sr}_{0.7}\text{CoO}_{3-\delta}$ [378]. As for $\text{La}_{0.3}\text{Sr}_{0.7}\text{Fe}(\text{Ga})\text{O}_{3-\delta}$ [215], the oxygen deficiency of Al-substituted cobaltite is higher with respect to the parent compound, in agreement with structural and dilatometric data (Table 3.1). The δ vs. $p(\text{O}_2)$ curves of $\text{La}_{0.3}\text{Sr}_{0.7}\text{Co}_{0.8}\text{Al}_{0.2}\text{O}_{3-\delta}$ exhibit a tendency to saturation at $\delta \rightarrow 0.35$, when most cobalt cations become trivalent. Further reduction leads to a transition of perovskite into brownmillerite-type phase isostructural to $\text{Sr}_2\text{Co}_2\text{O}_5$ (space group *Ibmm*, No.34-1475), revealed by XRD (Fig.3.3). In these conditions, the electrical properties are essentially $p(\text{O}_2)$ -independent (Figs.3.31 and 3.32). Note, however, that the pseudometallic character of p-type electronic transport is kept until decomposition of the brownmillerite-like polymorphs.

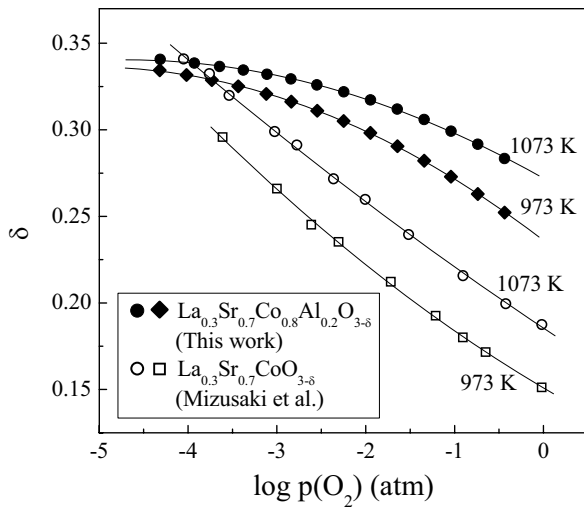


Fig.3.30. Oxygen nonstoichiometry of $\text{La}_{0.3}\text{Sr}_{0.7}\text{Co}_{0.8}\text{Al}_{0.2}\text{O}_{3-\delta}$ determined in air by thermogravimetric analysis and estimated for lower oxygen pressures (see text). Data on oxygen deficiency of $\text{La}_{0.3}\text{Sr}_{0.7}\text{CoO}_{3-\delta}$ [378] are shown for comparison.

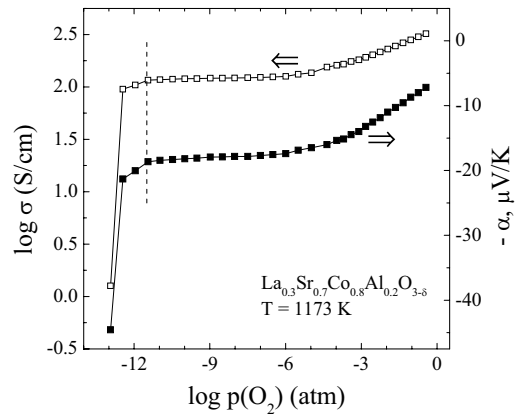
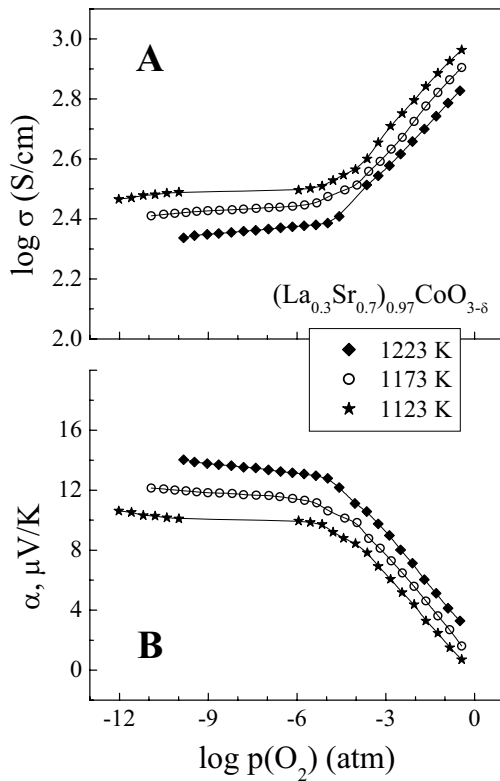


Fig.3.31. Oxygen pressure dependencies of the total conductivity (A) and Seebeck coefficient (B) of $(\text{La}_{0.3}\text{Sr}_{0.7})_{0.97}\text{CoO}_{3-\delta}$ in the $p(\text{O}_2)$ range where the single perovskite-related phases exist and those of $\text{La}_{0.3}\text{Sr}_{0.7}\text{Co}_{0.8}\text{Al}_{0.2}\text{O}_{3-\delta}$ (C) at 1173 K, illustrating the relationships between phase composition and electrical properties (see text). Dashed line indicates approximate stability limit of the brownmillerite-like phase.

Another important data which can be derived from the measurements of electrical properties vs. oxygen pressure, is the low- $p(\text{O}_2)$ phase stability boundaries. Typical examples of oxygen partial pressure dependencies of total conductivity and Seebeck coefficient of

$\text{La}_{0.3}\text{Sr}_{0.7}\text{CoO}_{3-\delta}$ based materials in a wide $p(\text{O}_2)$ range are presented in Figs.3.31 and 3.32. The behavior of electrical properties of $\text{La}_{0.3}\text{Sr}_{0.7}\text{Co}_{0.8}\text{Ga}_{0.2}\text{O}_{3-\delta}$ suggests the presence of, at least, four distinct phase domains ascertained by XRD. For oxygen pressures greater than approximately $(7-10)\times 10^{-5}$ atm (Domain I), decreasing $p(\text{O}_2)$ leads to a significant increase in thermopower and a decrease in conductivity, both indicating dominant pseudometallic electron-hole transport. Domain II corresponds to a plateau-like behavior at the oxygen pressures below $(5-7)\times 10^{-5}$ atm. The low- $p(\text{O}_2)$ boundary of this domain varies from 8×10^{-15} up to 3×10^{-9} atm when temperature increases in the range 973-1223 K. For Domain II, the electrical properties are almost independent of $p(\text{O}_2)$, keeping the tendencies characteristic of a pseudometallic p-type conduction. According to the XRD data (Fig.3.3), Domains I and II correspond to the perovskite- and brownmillerite-type polymorphs of $\text{La}_{0.3}\text{Sr}_{0.7}\text{Co}_{0.8}\text{Ga}_{0.2}\text{O}_{3-\delta}$. Further reduction leads to the formation of multiphase mixtures consisting of $(\text{Sr},\text{La})_3(\text{Co},\text{Ga})_2\text{O}_6$ - and $(\text{La},\text{Sr})_2(\text{Co},\text{Ga})\text{O}_4$ -based solid solutions and CoO; this is accompanied by a moderate decrease in conductivity (Domain III).

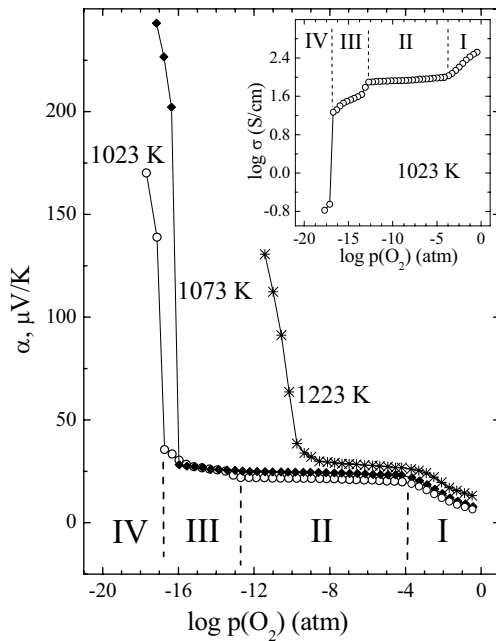


Fig.3.32. Examples of the oxygen partial pressure dependencies of Seebeck coefficient of $\text{La}_{0.3}\text{Sr}_{0.7}\text{Co}_{0.8}\text{Ga}_{0.2}\text{O}_{3-\delta}$. Inset shows $p(\text{O}_2)$ dependence of the total conductivity at 1023 K. Dashed lines indicate approximate phase boundaries at 1023 K (see text).

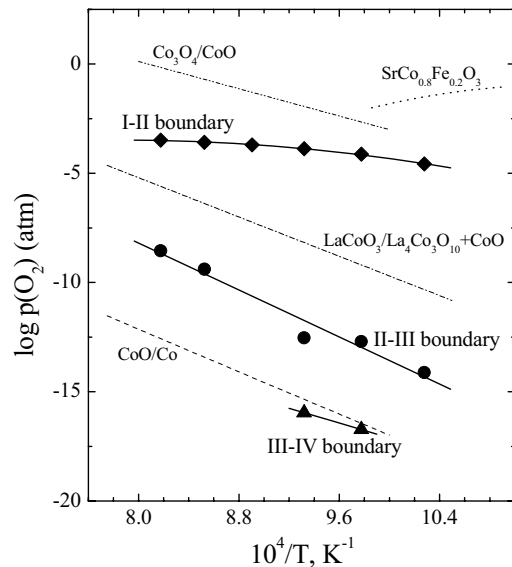


Fig.3.33. Approximate phase stability boundaries of $\text{La}_{0.3}\text{Sr}_{0.7}\text{Co}_{0.8}\text{Ga}_{0.2}\text{O}_{3-\delta}$, evaluated from the data on total conductivity and Seebeck coefficient as functions of $p(\text{O}_2)$. Literature data on Co_3O_4 [381], CoO [381], $\text{LaCoO}_{3-\delta}$ [234], and $\text{SrCo}_{0.8}\text{Fe}_{0.2}\text{O}_{3-\delta}$ [382] are shown for comparison.

Finally, at oxygen pressures close to Co/CoO boundary [379], the oxide phase mixture is reduced to metallic cobalt and binary metal oxides, which results in a dramatic conductivity drop (Domain IV in Fig.3.33). Based on the XRD analysis of $\text{La}_{0.3}\text{Sr}_{0.7}\text{Co}_{0.8}\text{Ga}_{0.2}\text{O}_{3-\delta}$ samples quenched after annealing at various $p(\text{O}_2)$, such a decomposition mechanism is quite similar to that reported for $\text{La}_{0.3}\text{Sr}_{0.7}\text{CoO}_{3-\delta}$ at 1373 K [380]. $(\text{La}_{0.3}\text{Sr}_{0.7})_{0.97}\text{CoO}_{3-\delta}$ and $\text{La}_{0.3}\text{Sr}_{0.7}\text{Co}_{0.8}\text{Al}_{0.2}\text{O}_{3-\delta}$ materials show analogous reduction mechanism. Decreasing $p(\text{O}_2)$ below 10^{-12} - 10^{-9} atm results in formation of multiphase mixtures comprising $(\text{Sr},\text{La})_3\text{Co}_2\text{O}_6$ - and $(\text{La},\text{Sr})_2\text{CoO}_4$ -based solid solutions and CoO; this is accompanied with a moderate decrease in the total conductivity and an increase in thermopower (Fig.3.31). Then, at oxygen partial pressures close to the CoO/Co boundary [379], a drastic irreversible degradation of the electrical properties is observed due to the separation of metallic Co and binary metal oxides. The corresponding phase changes were verified by XRD analysis of the samples, annealed at various $p(\text{O}_2)$ and quenched. The approximate phase boundaries, thus evaluated from the conductivity and Seebeck coefficient data, are almost equal (Fig.3.31C).

Fig.3.33 compares phase boundaries of $\text{La}_{0.3}\text{Sr}_{0.7}\text{Co}_{0.8}\text{Ga}_{0.2}\text{O}_{3-\delta}$ with the stability limits of binary cobalt oxides [379,381], and perovskite-type $\text{LaCoO}_{3-\delta}$ [234] and $\text{SrCo}_{0.8}\text{Fe}_{0.2}\text{O}_{3-\delta}$ [382]. The transition “perovskite \leftrightarrow brownmillerite” occurs at oxygen partial pressures 10^2 - 10^4 times lower than the decomposition limits of Co_3O_4 and $\text{SrCo}_{0.8}\text{Fe}_{0.2}\text{O}_{3-\delta}$, but about 10^3 times higher than that of lanthanum cobaltite. The unusual behavior of $\text{SrCo}_{0.8}\text{Fe}_{0.2}\text{O}_{3-\delta}$ is associated with complex reduction mechanism; in moderately reducing atmospheres $\text{Sr}(\text{Co},\text{Fe})\text{O}_{3-\delta}$ perovskites transform into brownmillerite-type $\text{Sr}_2(\text{Co},\text{Fe})_2\text{O}_5$ at temperatures above 900-1100 K and to a mixture of hexagonal $\text{Sr}_6(\text{Co},\text{Fe})_5\text{O}_{15}$ and Co_3O_4 at low temperatures (Refs.[382,383] and references cited). If compared to the reduction of $\text{LaCoO}_{3-\delta}$ yielding $\text{La}_4\text{Co}_3\text{O}_{10}$ and CoO [234], the decomposition of brownmillerite modification of $\text{La}_{0.3}\text{Sr}_{0.7}\text{Co}_{0.8}\text{Ga}_{0.2}\text{O}_{2.5\pm\delta}$ occurs at lower $p(\text{O}_2)$, but is characterized by a similar enthalpy. It is noteworthy that, in the case of $\text{La}_{0.3}\text{Sr}_{0.7}(\text{Fe},\text{Ga})\text{O}_{3-\delta}$, the transition from disordered perovskite to the brownmillerite-like modifications have no essential effect on the oxygen ionic conductivity [216].

The low- $p(\text{O}_2)$ stability limits of brownmillerite modifications of the studied cobaltite materials are presented in Fig.3.34. For comparison, the phase boundaries of CoO [379] and perovskite-type $\text{LaCoO}_{3-\delta}$ [234] are shown. Whilst the decomposition of lanthanum cobaltite occurs via formation of $\text{La}_4\text{Co}_3\text{O}_{10}$ and CoO at moderate oxygen chemical potentials [234], doping with strontium has a positive effect on the stability of mixed-conducting membrane materials in terms of phase separation, changing the decomposition mechanism towards the formation of single brownmillerite-like phases at moderate $p(\text{O}_2)$. The stability of brownmillerite-like

$\text{La}_{0.3}\text{Sr}_{0.7}\text{Co}_{0.8}\text{Ga}_{0.2}\text{O}_{2.5\pm\delta}$ is slightly worse with respect to $(\text{La}_{0.3}\text{Sr}_{0.7})_{0.97}\text{CoO}_{2.5\pm\delta}$ and $\text{La}_{0.3}\text{Sr}_{0.7}\text{Co}_{0.8}\text{Al}_{0.2}\text{O}_{2.5\pm\delta}$, probably due to the tendency to gallium oxide volatilization in reducing atmospheres or lower covalency of the Co–O bonds.

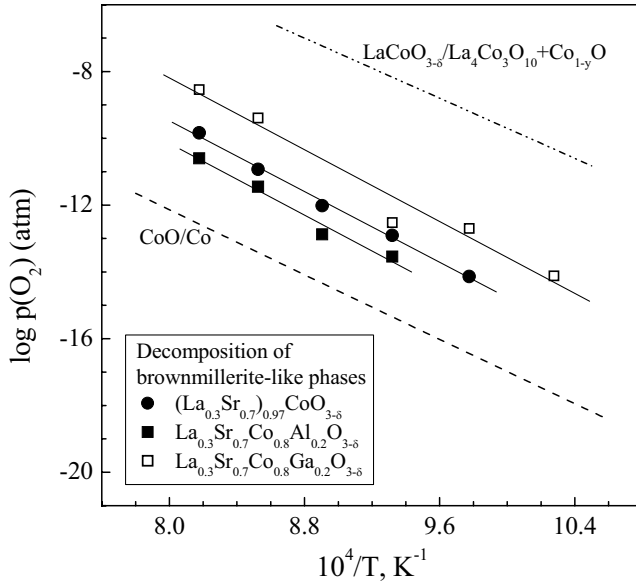


Fig.3.34. Approximate phase stability limits of $\text{La}_{0.3}\text{Sr}_{0.7}\text{CoO}_3$ -based materials, evaluated from the data on electrical properties vs. $p(\text{O}_2)$. Literature data on $\text{LaCoO}_{3-\delta}$ [234] and CoO [379] are shown for comparison.

3.4.2. Yttrium-barium cobaltite

Representative examples of the $p(\text{O}_2)$ -dependencies of total conductivity and Seebeck coefficient are shown in Figs.3.35 and 3.36. The electrical properties of $\text{YBaCo}_4\text{O}_{7+\delta}$ ceramics at 973–1023 K are essentially independent of the oxygen partial pressure until decomposition of a metastable phase; the stability boundaries confirmed by XRD (Fig.3.9B) are marked in Fig.3.36 by dashed lines. This behaviour is typical for oxide phases where the oxygen stoichiometry variations with oxygen pressure are very low. Within all studied $p(\text{O}_2)$ range, the Seebeck coefficient was found positive. As the oxygen ion transference numbers of $\text{YBaCo}_4\text{O}_{7+\delta}$ are lower than 10^{-3} (Table 3.2), the sign of thermopower indicates that the conductivity is predominantly p-type electronic.

At 1073–1223 K, an oxygen pressure-dependent phase transition is observed (Fig.3.35). Reducing $p(\text{O}_2)$ from 0.5 down to 10^{-4} atm leads to a lower total conductivity and higher thermopower, both showing large hysteresis phenomena. Upon further reduction, the electrical properties become essentially $p(\text{O}_2)$ -independent (Fig.3.36). The transition observed on reduction occurs in the same temperature range as phase changes in air (Fig.3.11) and has evidently the same nature. Note that, except for the peak intensity distribution, no essential differences are observed in

the XRD patterns of yttrium-barium cobaltite samples annealed at $p(\text{O}_2) = 5 \times 10^{-4}$ atm and 20 atm, i.e. at oxygen chemical potentials far from atmospheric, at temperatures where the $\text{YBaCo}_4\text{O}_{7+\delta}$ phase should be stable (Fig.3.9B).

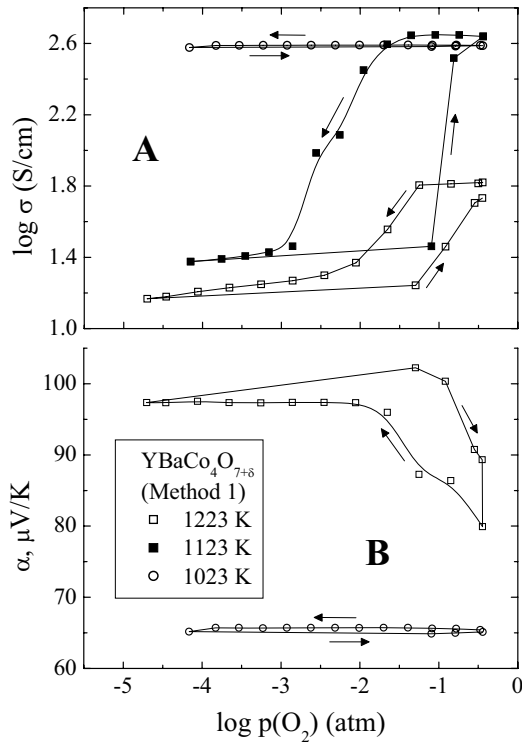


Fig.3.35. Oxygen partial pressure dependencies of the total conductivity (A) and Seebeck coefficient (B) of $\text{YBaCo}_4\text{O}_{7+\delta}$ under oxidising conditions. Arrows show the direction of $p(\text{O}_2)$ changes.

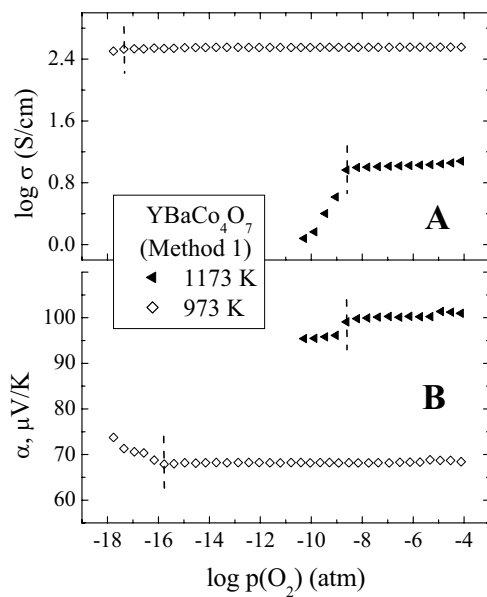


Fig.3.36. Oxygen partial pressure dependencies of the total conductivity (A) and Seebeck coefficient (B) of $\text{YBaCo}_4\text{O}_{7+\delta}$, under moderately oxidising and reducing conditions. Dashed lines indicate the phase stability limit.

Decreasing oxygen partial pressures below approximately 2×10^{-16} atm at 973 K and 3×10^{-9} atm at 1173 K results in a decomposition of $\text{YBaCo}_4\text{O}_{7+\delta}$ phase, accompanied with irreversible degradation of the electrical properties and poor reproducibility of results. Fig.3.37 compares the stability boundary of $\text{YBaCo}_4\text{O}_{7+\delta}$, estimated from the $p(\text{O}_2)$ -dependencies of the Seebeck coefficient as shown in Fig.3.36, with literature data on cobalt oxide [381] and perovskite-type lanthanum cobaltite [234]. The decomposition of yttrium-barium cobaltite occurs at oxygen partial pressures 10^2 - 10^4 times higher than that for CoO , but considerably lower with respect to $\text{LaCoO}_{3-\delta}$ where the basic oxidation state of cobalt cations is $3+$. This suggests that $\text{YBaCo}_4\text{O}_{7+\delta}$ decomposes into a mixture of binary metal oxides when most Co^{3+} cations are converted into Co^{2+} ; further reduction leads to the formation of metallic cobalt (Fig.3.9).

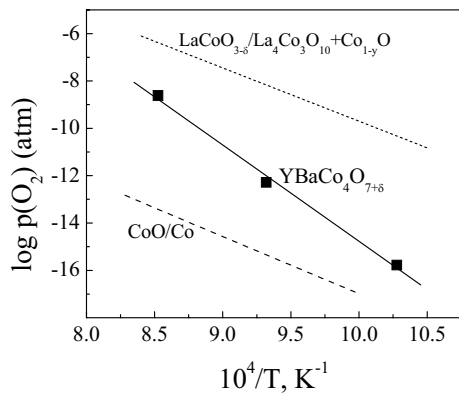


Fig.3.37. Low- $p(\text{O}_2)$ stability boundary of $\text{YBaCo}_4\text{O}_{7+\delta}$ phase, evaluated from the data on Seebeck coefficient vs. oxygen pressure. Literature data on CoO [381] and $\text{LaCoO}_{3-\delta}$ [234] are shown for comparison.

3.4.3. $K_2\text{NiF}_4$ -type $\text{La}_2\text{Ni}(M)\text{O}_{4+\delta}$ ($M = \text{Co}, \text{Cu}$)

Figs.3.38 and 3.39 present $p(\text{O}_2)$ -dependencies of the electrical properties of $\text{La}_2\text{Ni}(M)\text{O}_{4+\delta}$ in oxidizing and reducing conditions. Reducing oxygen partial pressure leads to a lower total conductivity, whilst the Seebeck coefficient has positive sign and increases, thus confirming dominant electron-hole transport, within the phase stability domain. It should be noted that the oxygen-ion transference numbers of La_2NiO_4 -based phases in air, estimated from the oxygen permeation data (Figs.3.23 and 3.24), are lower than 0.002. Although such estimates are crude due to surface-exchange limitations to the oxygen transport, they still suggest that the partial ionic transport can be neglected for the analysis of electrical properties as function of the oxygen pressure. Moreover, due to significant interstitial-migration contribution to the ionic transport [263], the oxygen ionic conductivity of $K_2\text{NiO}_4$ -type nickelates is expected to decrease with reducing $p(\text{O}_2)$. A pseudometallic behavior of total conductivity of $\text{La}_2\text{Ni}_{0.9}\text{Co}_{0.1}\text{O}_{4+\delta}$ and $\text{La}_2\text{Ni}_{0.8}\text{Cu}_{0.2}\text{O}_{4+\delta}$ remains under reduction at 973-1223 K until the phase decomposition (Figs.3.38 and 3.39).

In oxidizing conditions, $\log \sigma - \log p(O_2)$ and $\alpha - (k/e) \ln p(O_2)$ curves of $\text{La}_2\text{Ni}_{0.9}\text{Co}_{0.1}\text{O}_{4+\delta}$ and $\text{La}_2\text{Ni}_{0.8}\text{Cu}_{0.2}\text{O}_{4+\delta}$ are non-linear; their slope decreases with increasing oxygen pressure and with decreasing temperature, being lower than 1/10 (Figs.3.38, 3.39A and 3.39C). Such behavior agrees well with the literature data on $\text{La}_2\text{NiO}_{4+\delta}$, $\text{La}_{2-x}\text{Sr}_x\text{NiO}_{4+\delta}$ and $\text{La}_2\text{Ni}_{0.5}\text{Cu}_{0.5}\text{O}_{4+\delta}$ [260,387]. On the contrary, in the range of lower oxygen partial pressures, the same dependencies are linearized (Figs.3.38, 3.39B and 3.39D); the regression parameters of linear approximation are listed in Table 3.8. The exponent, $1/m$, is quite close to the value of 1/6, which can be obtained considering a simple point-defect equilibrium in lanthanum nikelate.

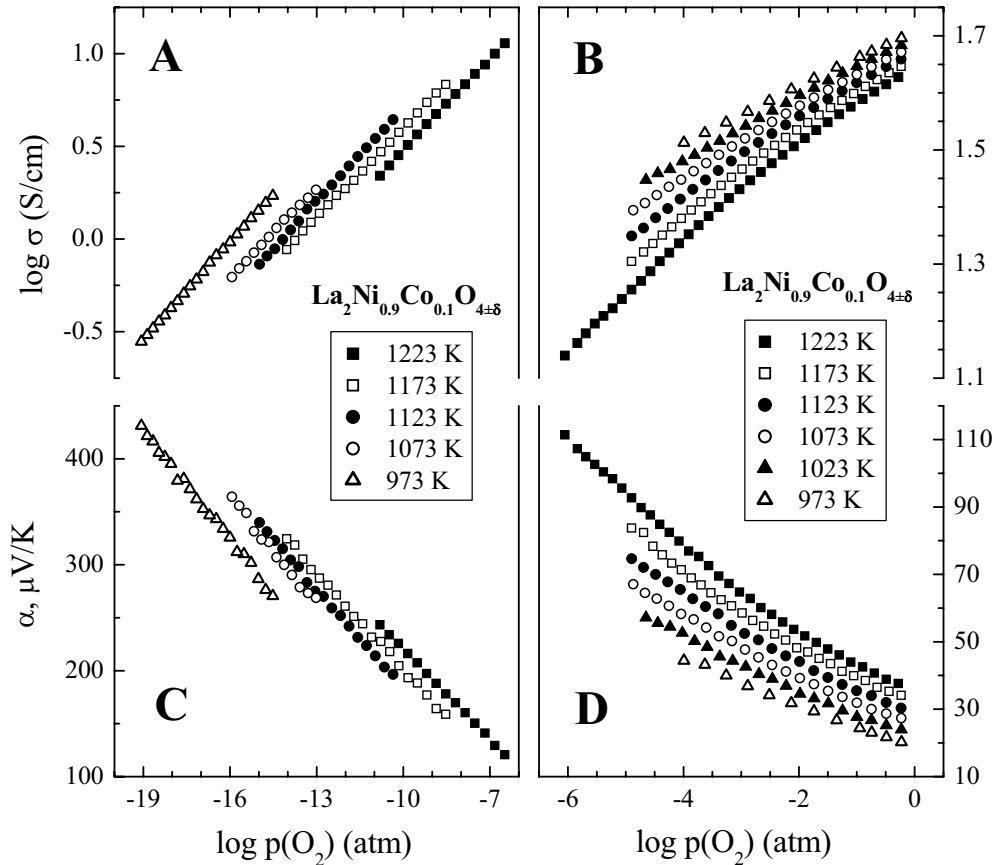


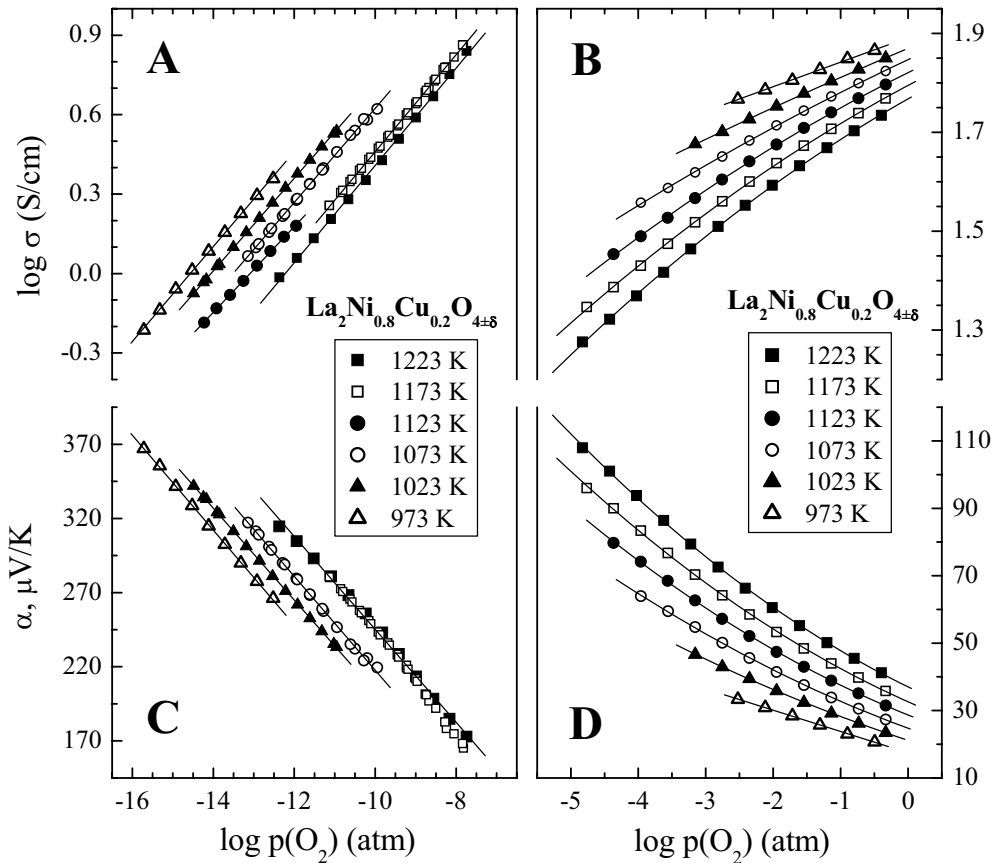
Fig.3.38. Oxygen partial pressure dependencies of the total conductivity (A,B) and Seebeck coefficient (C,D) of $\text{La}_2\text{Ni}_{0.9}\text{Co}_{0.1}\text{O}_{4\pm\delta}$ (Method 1) under oxidising (B,D) and reducing (A,C) conditions.

Table 3.8

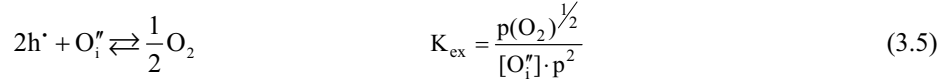
 Slope parameter m of $p(\text{O}_2)$ dependencies of the total conductivity* and thermopower** of $\text{La}_2(\text{Ni,M})\text{O}_{4+\delta}$

T, K	$\text{La}_2\text{Ni}_{0.9}\text{Co}_{0.1}\text{O}_{4+\delta}$ (Method 1)		$\text{La}_2\text{Ni}_{0.8}\text{Cu}_{0.2}\text{O}_{4+\delta}$	
	Total conductivity	Seebeck coefficient	Total conductivity	Seebeck coefficient
973	5.75 ± 0.05	5.7 ± 0.2	5.6 ± 0.1	6.2 ± 0.1
1023			5.72 ± 0.04	6.41 ± 0.05
1073	6.2 ± 0.2	5.8 ± 0.4	5.73 ± 0.08	6.3 ± 0.1
1123	5.92 ± 0.08	6.4 ± 0.1	6.1 ± 0.1	7.7 ± 0.4
1173	6.21 ± 0.06	6.6 ± 0.1	5.61 ± 0.05	5.8 ± 0.1
1223	6.08 ± 0.08	6.99 ± 0.06	5.4 ± 0.1	6.2 ± 0.2

 * model for conductivity vs. oxygen pressure: $\sigma = \sigma_p^0 \cdot p(\text{O}_2)^{1/m}$;

 ** model for Seebeck coefficient vs. oxygen pressure: $\alpha = -\frac{k}{e} \cdot \frac{1}{m} \cdot \ln p(\text{O}_2) + b$.

Fig.3.39. Oxygen partial pressure dependencies of the total conductivity (A,B) and Seebeck coefficient (C,D) of $\text{La}_2\text{Ni}_{0.8}\text{Cu}_{0.2}\text{O}_{4+\delta}$ under oxidising (B,D) and reducing (A,C) conditions.

Assuming interstitial oxygen ions (O_i'') and electron holes (h^\bullet) to be the main point defects, presenting at relatively low concentrations ($[O_i'']$ and p), the oxygen release process and corresponding equilibrium constant can be written as:



Particular electroneutrality condition is

$$2[O_i''] = p \quad (3.6)$$

If the hole mobility (μ_p) is independent of p-type charge carrier concentration, which is valid for a small-polaron conduction mechanism when the charge carrier concentration is low, Eq.(3.3) is applicable and, taking into account Eqs.(3.5 and 3.6),

$$\sigma \approx \sigma_p = e \cdot \mu_p \cdot p / V_{\text{uc}} = \sigma_p^0 \cdot p(O_2)^{1/6} \quad (3.7)$$

where σ_p^0 is a constant depending on temperature. On the other hand, the results of coulometric titration show that the oxygen nonstoichiometry in $\text{La}_2\text{NiO}_{4+\delta}$ based phases linearly depends on $\log p(O_2)$ [384]. Therefore, such simplified defect equilibria can only be applied under reducing conditions, when the concentration of point defects is low.

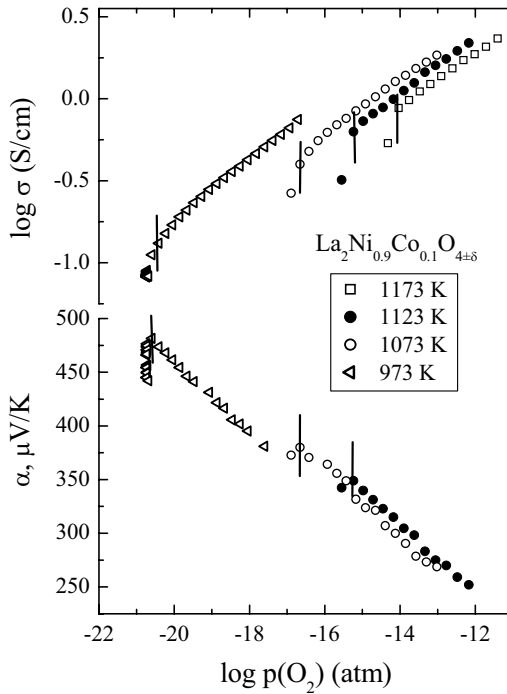


Fig.3.40. Illustration of phase stability limits estimation for $\text{La}_2\text{Ni}_{0.9}\text{Co}_{0.1}\text{O}_{4+\delta}$.

The phase stability boundaries of $\text{La}_2\text{Ni}_{0.9}\text{Co}_{0.1}\text{O}_{4+\delta}$ and $\text{La}_2\text{Ni}_{0.8}\text{Cu}_{0.2}\text{O}_{4+\delta}$ at reduced oxygen partial pressures, estimated from the data on total conductivity and Seebeck coefficient (Fig.3.40), are compared with literature data on binary metal oxides [135], $\text{La}_2\text{NiO}_{4+\delta}$ [318] and $\text{La}_2\text{CuO}_{4+\delta}$ [319] in Fig.3.41. Phase decomposition of substituted nickelates at 973-1173 K occurs at $p(\text{O}_2)$ values substantially lower with respect to NiO. A similar enlargement of the stability domain was earlier reported for K_2NiF_4 -type $\text{La}_2\text{CuO}_{4+\delta}$ [319], though in the latter case the decomposition mechanism is more complex than a single-step reduction into transition metal and lanthanum oxide. The phase boundary of $\text{La}_2\text{Ni}_{0.9}\text{Co}_{0.1}\text{O}_{4+\delta}$ is quite close to that of undoped $\text{La}_2\text{NiO}_{4+\delta}$ [318]. Therefore, the use of different synthesis methods and local compositional inhomogeneities, if any, should have no effect on the stability of Co-substituted nickelate. Incorporation of copper slightly decreases the phase stability limit, as expected regarding the considerably higher equilibrium oxygen pressures over $\text{Cu}_2\text{O}/\text{CuO}$ and $\text{Cu}/\text{Cu}_2\text{O}$ mixtures with respect to Ni/NiO and Co/CoO . Nevertheless, moderate substitution of nickel with other transition metal cations, having either higher or lower oxidation state, has a minor effect on the stability of $\text{La}_2\text{NiO}_{4+\delta}$ to reduction. It can be also noticed, that a deviation from the linear van't Hoff dependence, $\log p(\text{O}_2)$ vs. $1/T$, in the low-temperature range may indicate either the kinetically stagnated decomposition of the K_2NiF_4 -type phase, or a change in the phase decomposition mechanism at reduced temperatures.

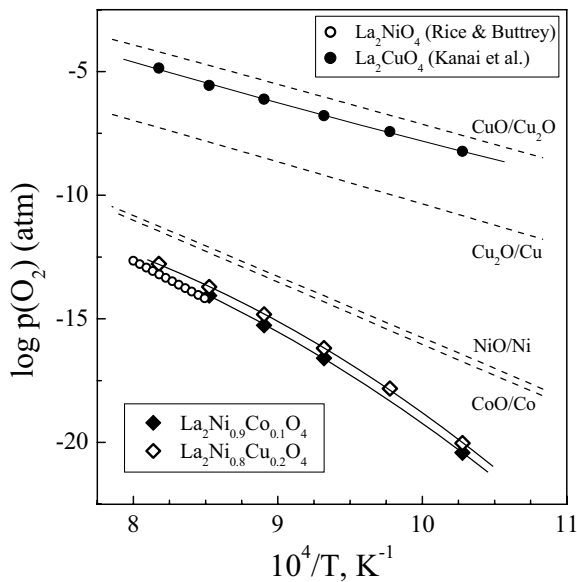


Fig.3.41. Phase stability limits of Ni-containing ceramics, determined from the data on total conductivity and Seebeck coefficient. Literature data on binary metal oxides [135], $\text{La}_2\text{NiO}_{4+\delta}$ [318] and $\text{La}_2\text{CuO}_{4+\delta}$ [319] are shown for comparison.

3.5. Thermal expansion

The dilatometric curves of $\text{La}_{0.3}\text{Sr}_{0.7}\text{CoO}_{3-\delta}$ -based ceramics in air are presented in Fig.3.42; Table 3.1 lists the average thermal expansion coefficients. A drastic increase in TEC values at temperatures above 700-800 K is typical for transition metal-containing perovskites [210,216] and originates from chemically-induced expansion of the lattice due to oxygen losses on heating. This lattice expansion correlates well with the data on total conductivity (Fig.3.5). As for $\text{La}_{0.3}\text{Sr}_{0.7}\text{Fe}(\text{M})\text{O}_{3-\delta}$ ($\text{M} = \text{Al}, \text{Ga}$) systems [210,216], thermal expansion of $\text{La}_{0.3}\text{Sr}_{0.7}\text{Co}_{0.8}\text{M}_{0.2}\text{O}_{3-\delta}$ is lower than that of lanthanum-strontium cobaltite, a result of reduced oxygen losses due to the substitution of variable-valence cobalt with the cations having stable oxidation state. On the contrary, the creation of A-site cation vacancies increases TEC in the high-temperature range; such a tendency indicates that the charge compensation occurs mainly via Co^{4+} formation, thus increasing variations of the oxygen nonstoichiometry on heating.

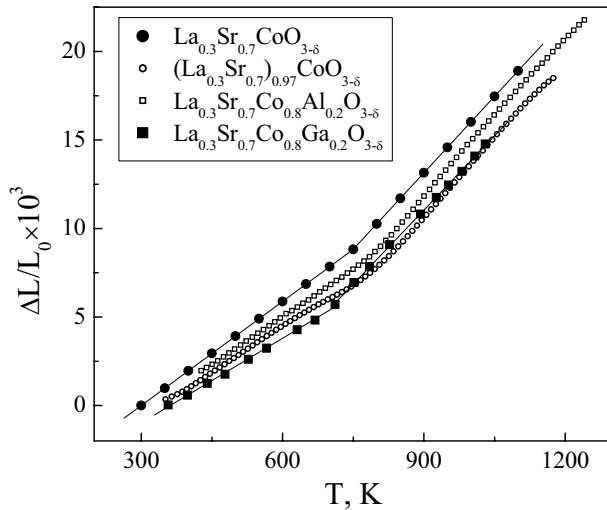


Fig.3.43. Dilatometric curves of $\text{La}_{0.3}\text{Sr}_{0.7}\text{CoO}_{3-\delta}$ -based ceramics in air.

Despite the first-order phase transitions at 1050-1100 K, accompanied with kinetically-stagnated oxygen stoichiometry variations, the dilatometric curves of YBaCo_4O_7 ceramics, measured with a heating rate of 5 K/min, were found almost linear (Fig.3.43). The average TEC values of the $\text{YBaCo}_{4-x}\text{Fe}_x\text{O}_7$ ceramics are $(7.3-9.0) \times 10^{-6} \text{ K}^{-1}$ for $x = 0$, and $9.7 \times 10^{-6} \text{ K}^{-1}$ for $x = 0.4$. This apparent linearity indicates that the phase transitions in ceramics are kinetically hampered, as discussed in Chapter 3.1.2. The isothermal dilatometric measurements showed a significant volume contraction at temperatures around 1173-1223 K as illustrated by the Inset of Fig.3.43; the average TEC on further cooling was close to that on heating.

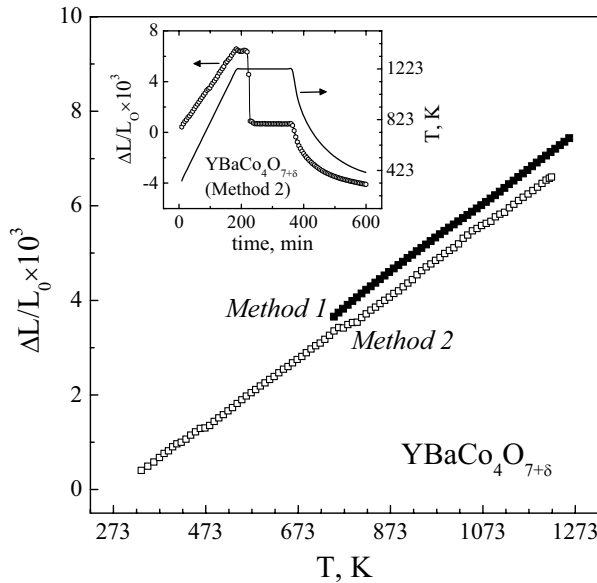


Fig.3.44. Dilatometric curves of $\text{YBaCo}_4\text{O}_{7+\delta}$ ceramics, prepared using Methods 1 and 2, on 5 K/min heating in air. Inset shows relative elongation in the course of heating, isothermal annealing at 1223 K, and subsequent cooling.

Thermal expansion of $\text{La}_2\text{Ni}_{0.9}\text{Co}_{0.1}\text{O}_{4+\delta}$ and $\text{La}_2\text{Ni}_{0.8}\text{Cu}_{0.2}\text{O}_{4+\delta}$ ceramics, studied by dilatometry at 300-1270 K in air, was found approximately linear (Fig.3.44). As for the total conductivity, the average TEC values of La_2NiO_4 -based ceramics, calculated from dilatometric data in air, are very similar, $(12.8\text{-}14.2)\times 10^{-6} \text{ K}^{-1}$ at 300-1200 K (Table 3.3), in agreement with literature data on other La_2NiO_4 -based materials [259,260,263]. The relatively low thermal expansion makes La_2NiO_4 -based materials compatible with IT SOFC solid electrolytes, such as LSGM or $\text{Ce}(\text{Gd})\text{O}_{2-\delta}$, having slightly lower but still very similar TEC values, $(10.4\text{-}12.6)\times 10^{-6} \text{ K}^{-1}$ (Table 1.3).

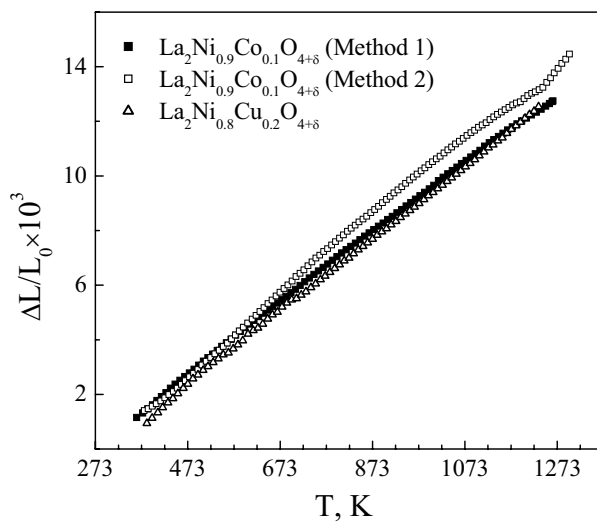


Fig.3.45. Dilatometric curves of $\text{La}_2\text{Ni}_{0.9}\text{Co}_{0.1}\text{O}_{4+\delta}$, prepared using Methods 1 and 2, and $\text{La}_2\text{Ni}_{0.8}\text{Cu}_{0.2}\text{O}_{4+\delta}$ ceramics on heating in air.

3.6. Selection of cathode compositions

Perovskite-type cobaltites, having the high electrochemical activity, possess the thermal expansion excessively high for their use as SOFC cathodes. Substitution of metal cations with stable 3+ oxidation state for Co decreases their TECs, but the thermal expansion is still incompatible with common solid electrolytes. The higher level of doping is expected to result in degradation of the transport properties and electrode performance.

Layered YBaCo_4O_7 and its derivatives possess an attractive combination of properties, which might be of interest for the high-temperature electrochemical applications. These include a significant mixed ionic-electronic conductivity and moderate thermal expansion. However, their practical application is hampered due to metastability at intermediate and low temperatures; extensive compositional modifications are necessary. Nonetheless, developments of novel $\text{YBaCo}_4\text{O}_{7+\delta}$ based compositions require to assess the electrochemical behavior of the parent composition.

Although the TECs of K_2NiF_4 -type nickelates are slightly higher with respect to LSGM solid electrolytes, $(10-12)\times 10^{-6} \text{ K}^{-1}$, these materials are still compatible in terms of thermal expansion. The maximum shrinkage at temperatures below 1400 K was found for $\text{La}_2\text{Ni}(\text{Cu})\text{O}_{4+\delta}$ system. In fact, Cu-containing materials seem to be the only La_2NiO_4 -based compositions, enabling to fabricate mechanically stable porous layers at temperatures below 1550 K without sintering aids. The use of higher temperatures may lead to passivation of nickelate cathodes and their interaction with solid electrolyte. Therefore, $\text{La}_2\text{Ni}_{0.8}\text{Cu}_{0.2}\text{O}_{4+\delta}$ phase, having a high total conductivity and substantial oxygen permeability, was chosen for testing of the electrochemical activity of cathode layers.

Part 4: Ion-conducting oxide materials as components of cermet anodes

The studies of IT SOFC anodes were focused both on a deeper understanding of relative roles of the cermet components and on the search for alternative oxide materials with high catalytic activity for fuel oxidation, stability under reducing conditions and moderate dimensional changes on redox cycling. Investigations of the phases belonging to different structural types and having different chemical composition are expected to enable selection of anode components. For these goals, fluorite-, pyrochlore- and perovskite-related materials are of special interest due to their substantial level of oxygen ionic transport and electrocatalytic properties.

4.1. Zircon-type $Ce_{1-x}A_xVO_{4+\delta}$ ($A = Ca, Sr$)

As shown in Chapter 1.5.2.2, the incorporation of ceria into the anodes, where most cerium cations are reduced to Ce^{3+} , leads to a considerable improvement of the SOFC performance. In order to evaluate whether the other cerium-containing phases may be of interest as anode components, $Ce_{1-x}A_xVO_4$ ($A = Ca, Sr$) were studied. Note that binary oxides of both cerium and vanadium exhibit high catalytic activity in reactions involving oxygen. $CeVO_4$ possesses a significant total conductivity [385], which can be considerably enhanced by substitution of cerium with divalent metal cations. The highest conductivity values in air were reported for $Ce_{0.8}Ca_{0.2}VO_4$ and $Ce_{0.9}Sr_{0.1}VO_4$ [385]; therefore, the studied composition range was limited to $x = 0.2$.

4.1.1. Structure, ceramic microstructure and thermal expansion

XRD studies showed that both synthesized powders and sintered ceramics of $Ce_{1-x}A_xVO_{4+\delta}$ were single-phase; one example of XRD pattern is given in Fig.4.1. The parameters of the tetragonal zircon-type structure are shown in Table 4.1 and Fig.4.2.

Table 4.1

Structure refinement results of $Ce_{1-x}A_xVO_{4+\delta}$ at room temperature

Composition	Unit cell parameters		Specific free volume	Average bond lengths, Å		Ce^{4+} fraction y, %	δ
	a, Å	c, Å		Ce – O	V – O		
$CeVO_4$	7.396(8)	6.496(9)	0.542	2.52	1.66	13	0.07
$Ce_{0.9}Sr_{0.1}VO_4$	7.381(0)	6.491(5)	0.519	2.52	1.68	24	0.06
$Ce_{0.9}Ca_{0.1}VO_4$	7.354(0)	6.472(0)	0.517	2.49	1.68	30	0.08
$Ce_{0.8}Ca_{0.2}VO_4$	7.314(5)	6.450(9)	0.512	2.49	1.64	33	0.03

Notes:

- the Ce – O bond lengths were averaged between Ce – O1 and Ce – O2 interatomic distances;
- y is the fraction of Ce^{4+} , estimated from the bond length values and multiplied by 100%;
- δ is the oxygen hyperstoichiometry calculated from y using the crystal electroneutrality law.

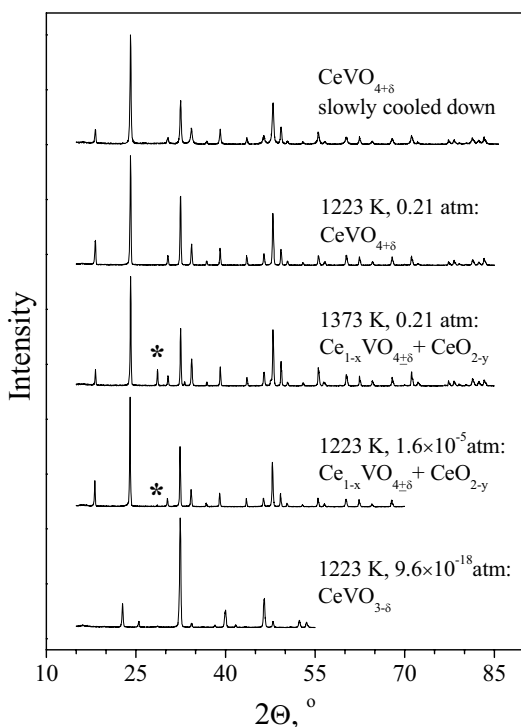


Fig.4.1. Examples of XRD patterns of $\text{CeVO}_{4+\delta}$ as-prepared and slowly cooled in air and quenched after annealing in various atmospheres, illustrating phase relationships discussed in the text. The strongest reflection of CeO_{2-y} is marked by asterisk.

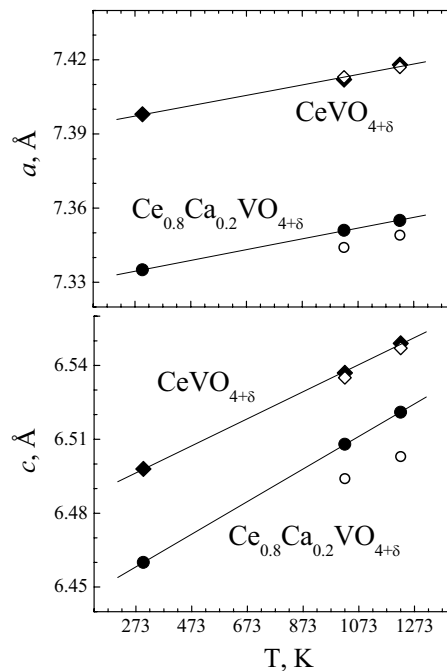


Fig.4.2. Temperature dependencies of the tetragonal unit cell parameters of zircon-type $\text{CeVO}_{4+\delta}$ and $\text{Ce}_{0.8}\text{Ca}_{0.2}\text{VO}_{4+\delta}$ in air (closed symbols) and in vacuum (open symbols).

Tetragonal distortion of the lattice, expressed by the a/c ratio, decreases when cerium is substituted with either calcium or strontium. Doping with alkaline-earth cations also leads to decreasing unit cell volume, in agreement with literature data [385,386]. This behavior suggests a charge compensation mechanism via formation of tetravalent cerium cations. The radii of Ca^{2+} and Ce^{3+} ions are similar, both smaller than that of Sr^{2+} ; 8-coordinated Ce^{4+} has a substantially smaller size than Ce^{3+} [60]. The lattice contraction is therefore attributed to forming Ce^{4+} cations, which was confirmed by the Seebeck coefficient and total conductivity results.

In order to estimate the oxidation states of cerium and vanadium, the cation-anion distances were calculated from the structure refinement results (Table 4.1). In the case of Ce ions, the existence of two non-equivalent oxygen positions in the lattice (O1 and O2, Fig.4.3) results in two different Ce–O distances; the average bond length values were taken for the estimations. The interatomic distances V–O, determined from the refinement data, were found to be similar to those estimated as the sum of O^{2-} and 4-coordinated V^{5+} radii [60], suggesting that the predominant

oxidation state of vanadium is 5+. For Ce–O bonds, however, the average length is smaller than that expected for $\text{Ce}^{3+}-\text{O}^{2-}$, but greater than estimated for $\text{Ce}^{4+}-\text{O}^{2-}$. Again, this might indicate the presence of a significant fraction of tetravalent cerium cations in the lattice. The fraction of Ce^{4+} , calculated assuming the Ce–O bond length to be the sum of average Ce-site cation and oxygen anion radii [60], increases from 13 to 33% with increasing dopant content (Table 4.1). The oxygen nonstoichiometry of $(\text{Ce}^{3+}_{1-y}\text{Ce}^{4+}_y)_{1-x}\text{A}_x\text{VO}_{4\pm\delta}$ is related to cerium oxidation state via the electroneutrality condition:

$$\delta = \frac{y - x - xy}{2} \quad (4.1)$$

where y is the fraction of Ce^{4+} . Calculations of the oxygen content showed that all title materials are possibly oxygen-hyperstoichiometric; the estimated δ values vary in the range from +0.03 to +0.08 at room temperature (Table 4.1). Although these estimations are very crude, the assumptions regarding oxygen hyperstoichiometry and increasing cerium oxidation state on doping are in agreement with the results on the total electrical conductivity, Seebeck coefficient, and partial ionic conductivity of $\text{Ce}_{1-x}\text{A}_x\text{VO}_{4\pm\delta}$, as discussed below.

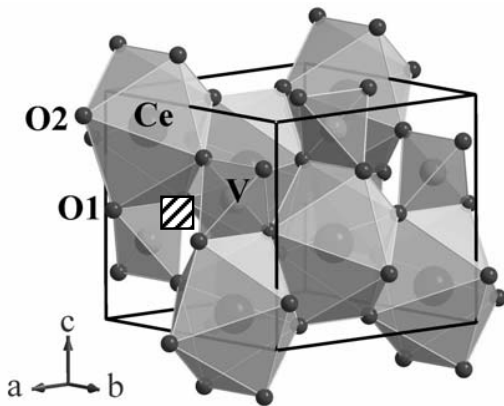


Fig.4.3. Fragment of zircon-type structure of $\text{Ce}_{1-x}\text{A}_x\text{VO}_{4\pm\delta}$. The square shows most probable position of hyperstoichiometric oxygen.

Finally, the structure of CeVO_4 was analysed to locate positions available for hyperstoichiometric oxygen. The incorporation of the extra oxygen ions into either V–O tetrahedra or Ce–O dodecahedra constituting the zircon-type lattice (Fig.4.3) seems unlikely. Such an incorporation would lead to an increase in the bond lengths due to increasing cation coordination numbers, which contradicts the refinement results (Table 4.1). The most likely location of a hyperstoichiometric anion is to be found in a void between two V–O tetrahedra, marked by square in Fig.4.3. These voids form 1/2 additional oxygen site per formula unit of $\text{CeVO}_{4\pm\delta}$; the hypothetical maximum oxygen nonstoichiometry of cerium orthovanadate, satisfying the lattice conservation condition, corresponds thus to the value of $\delta = +0.5$.

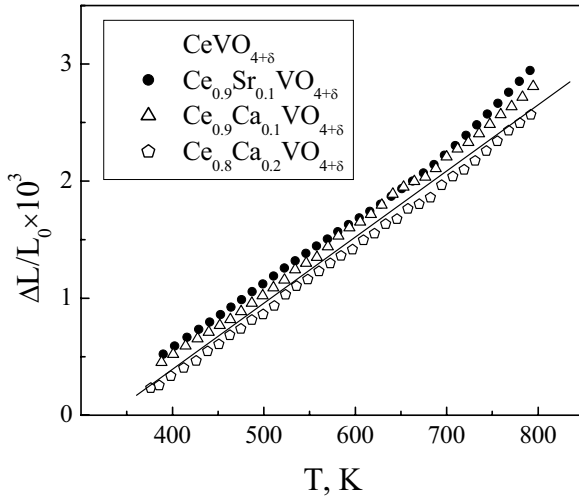


Fig.4.4. Dilatometric curves of $\text{Ce(A)VO}_{4+\delta}$ ceramics in air.

Table 4.2

Linear TECs of CeVO_4 and $\text{Ce}_{0.8}\text{Ca}_{0.2}\text{VO}_4$, calculated from high-temperature XRD data

Composition	$p(\text{O}_2)$, atm	T, K	$\alpha_a \times 10^6, \text{K}^{-1}$	$\alpha_c \times 10^6, \text{K}^{-1}$	$\alpha_v \times 10^6, \text{K}^{-1}$
CeVO_4	0.21	300-1123	2.8	8.5	4.7
	2×10^{-9}	1023-1223	2.3	9.2	4.6
$\text{Ce}_{0.8}\text{Ca}_{0.2}\text{VO}_4$	0.21	300-1123	2.9	10.2	5.4
	2×10^{-9}	1023-1223	3.1	6.8	4.3

Notes:

- α_a and α_c are the TEC values for the a and c axes of zircon lattice, respectively;
- α_v is the average linear TEC, related to the volume thermal expansion coefficient (β) as $\alpha_v = \beta/3$.

The temperature dependencies of the unit cell parameters calculated from high-temperature XRD data are linear within the temperature range of 300-1223 K (Fig.4.2). The thermal expansion has a significantly anisotropic character, being greater for c axis than for a . The linear thermal expansion coefficients are $(2.8-3.1) \times 10^{-6}$ and $(6.8-10.2) \times 10^{-6} \text{ K}^{-1}$ for the a and c parameters, respectively (Table 4.2). This corresponds to the average linear TECs (α_v), which can be estimated from the volume thermal expansion coefficients (β) as $\alpha_v = \beta/3$, to vary in the range $(4.3-5.4) \times 10^{-6} \text{ K}^{-1}$. The dilatometric curves of $\text{Ce}_{1-x}\text{A}_x\text{VO}_{4+\delta}$ ceramics are also linear (Fig.4.4). The average thermal expansion coefficients of $\text{Ce}_{1-x}\text{A}_x\text{VO}_{4+\delta}$, calculated from dilatometric data in air, vary in the very narrow range $(5.6-5.9) \times 10^{-6} \text{ K}^{-1}$ at 400-800 K (Table 4.3), being quite similar to the high-temperature XRD results. Note that the dilatometric TECs of $\text{Ce}_{0.9}\text{A}_{0.1}\text{VO}_{4+\delta}$ compounds, $5.85 \times 10^{-6} \text{ K}^{-1}$ for $\text{A} = \text{Ca}$ and $6.09 \times 10^{-6} \text{ K}^{-1}$ for $\text{A} = \text{Sr}$, were slightly higher than for two other compositions (Table 4.3).

Table 4.3

Properties of $Ce_{1-x}A_xVO_4$ ceramics

Composition	Relative density, %	$\bar{\alpha} \times 10^6, K^{-1}$ (400-800 K)	Activation energy in air, kJ/mol			
			Total conduction (400-1200 K)	Ionic transport (973-1223 K)	p-type transport (973-1223 K)	Hole mobility (1023-1223 K)
$CeVO_4$	99	5.64 ± 0.01	37.9 ± 0.8	112 ± 14	45 ± 7	-
$Ce_{0.9}Sr_{0.1}VO_4$	95	5.73 ± 0.01	34.8 ± 0.5	87 ± 7	39 ± 1	35 ± 1
$Ce_{0.9}Ca_{0.1}VO_4$	93	5.89 ± 0.01	35.2 ± 0.6	93 ± 8	42 ± 3	36 ± 6
$Ce_{0.8}Ca_{0.2}VO_4$	97	5.64 ± 0.01	34.6 ± 0.7	91 ± 9	40 ± 7	34 ± 9

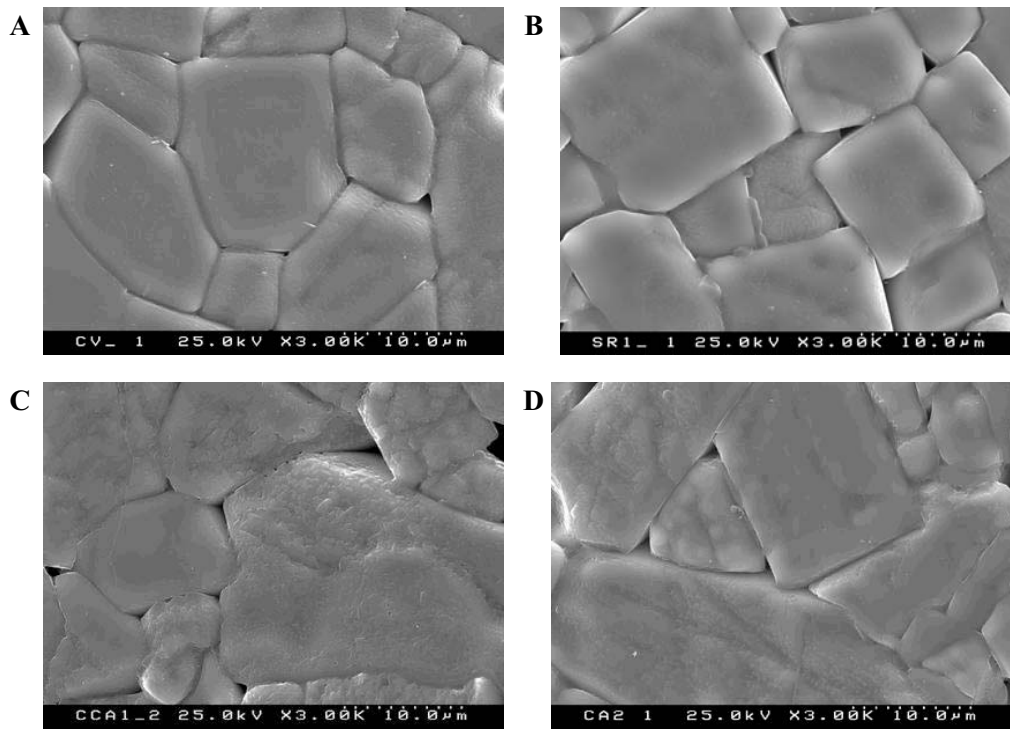


Fig.4.5. SEM micrographs of $CeVO_4$ (A), $Ce_{0.9}Sr_{0.1}VO_4$ (B), $Ce_{0.9}Ca_{0.1}VO_4$ (C), and $Ce_{0.8}Ca_{0.2}VO_4$ (D) ceramics.

The density of sintered samples was no less than 93% of their theoretical density calculated from XRD results (Table 4.3). SEM images reflecting microstructures typical for $Ce(A)VO_{4+\delta}$ ceramics, are presented in Fig.4.5. The average grain size was similar for all materials, varying in the range from 5 to 25 μm . Some traces of a liquid phase possibly assisted the sintering process were observed at the grain boundaries. Cation composition of the ceramic materials was, however, found to be uniform within the limits of experimental error of EDS analysis. Impedance spectroscopy confirmed a negligible effect of the grain boundaries on the conductivity.

The impedance spectra exhibit only a single arc, even at temperatures as low as 300-400 K (Fig.4.6). The capacity associated with this arc was less than $(6-7)\times 10^{-11}$ F/cm, which can be definitely attributed to the bulk process. Moreover, the total conductivity values obtained by different techniques, including 4-probe *dc* and van der Pauw methods and the *ac* impedance spectroscopy, were found equal within the limits of experimental uncertainty and very similar to the literature data [385]. This trend is essentially due to the main conductivity contribution, which is, as discussed below, p-type electronic; nevertheless, one cannot exclude the possibility of significant grain boundary blocking effects on a minor ionic conductivity contribution. No interfacial contribution to the total resistivity was also detected at intermediate oxygen partial pressures, as illustrated by the inset in Fig.4.6. In addition, it should be separately mentioned that the impedance spectroscopy showed no electrode effects, in agreement with very low values of the oxygen ion transference numbers of $Ce_{1-x}A_xVO_{4+\delta}$, discussed in the next Chapter.

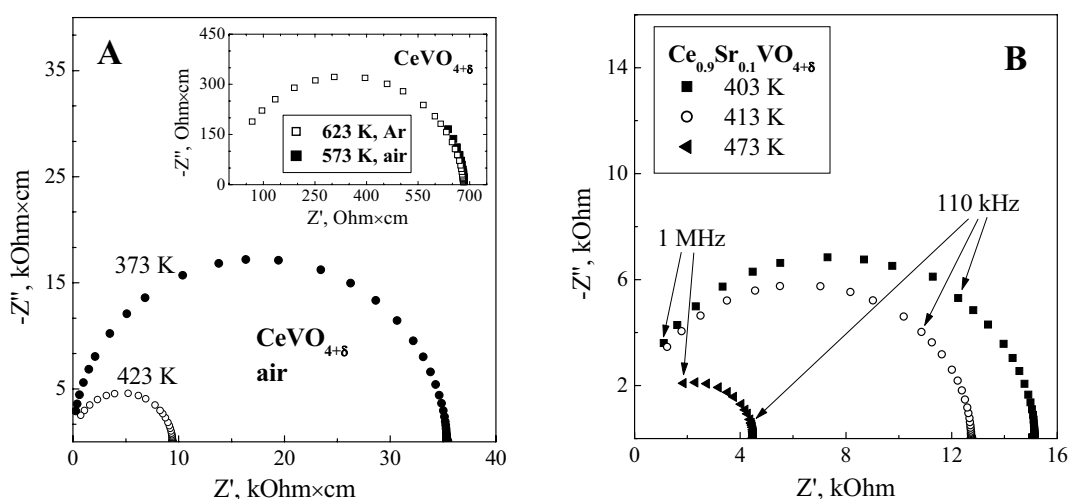


Fig.4.6. Examples of the impedance spectra of $CeVO_{4+\delta}$ (A) and $Ce_{0.9}Sr_{0.1}VO_{4+\delta}$ (B) ceramics, collected at 403-573 K in air and argon.

Fig.4.7A presents the temperature dependencies of the total conductivity of $Ce_{1-x}A_xVO_{4+\delta}$ ceramics in air, measured using impedance spectroscopy. The incorporation of alkali-earth cations increases electrical conductivity. The values of activation energy vary in the range 34-38 kJ/mol, slightly decreasing when dopant concentration increases (Table4.3). Taking into account that phase decomposition of zircon-type $Ce_{1-x}A_xVO_4$ may lead to a time degradation of the ionic and/or electronic transport, stability tests of the total conductivity and faradaic efficiency were carried out. Selected examples on the conductivity in air are shown in Fig.4.7B. At 973-1223 K the

transport properties of cerium vanadate-based ceramics were found to be essentially time-independent, which suggests an absence of phase changes, in agreement with XRD results. Therefore, one can assume that the data on ionic conductivity presented below are related to single zircon-type phases.

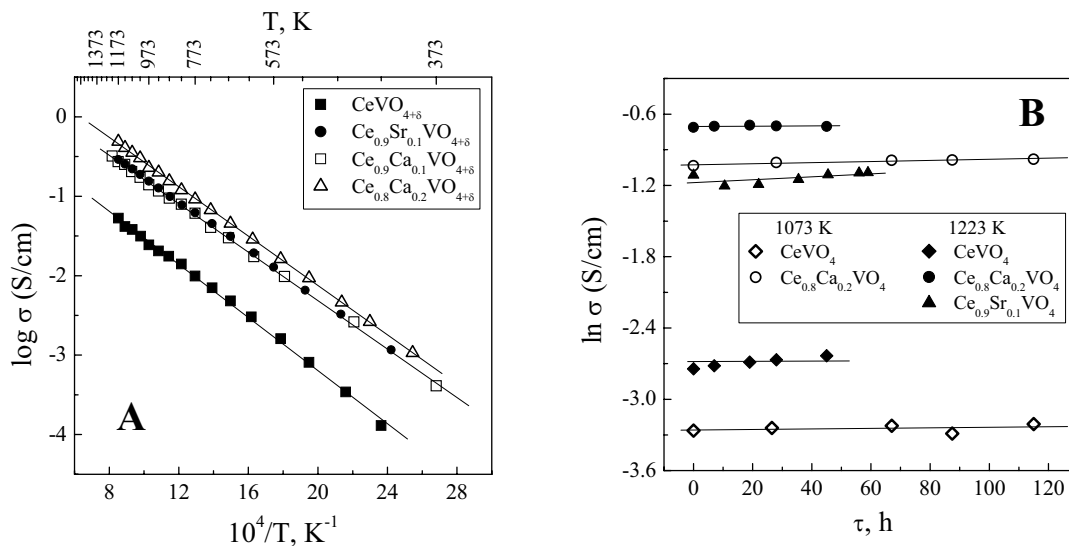


Fig.4.7. Temperature (A) and time (B) dependencies of total electrical conductivity of $\text{Ce}_{1-x}\text{A}_x\text{VO}_4$ ceramics in air.

4.1.2. Oxygen ionic and p-type electronic conduction

Fig.4.8 presents the oxygen ion transference numbers of $\text{Ce}_{1-x}\text{A}_x\text{VO}_{4+\delta}$ (A = Ca, Sr; x = 0-0.2) ceramics, determined by the faradaic efficiency measurements in air. The ion transference numbers vary in the range from 2×10^{-4} to 6×10^{-3} at 973-1223 K and increase with temperature. Increasing concentration of alkaline-earth cations leads to decreasing ionic contribution to the total conductivity. The conductivity enhancement on acceptor-type doping (Fig.4.7A) suggests that the p-type electronic conduction prevails. Arrhenius plots of partial oxygen-ionic and p-type electronic conductivities are shown in Figs.4.9 and 4.10A; the corresponding activation energies are listed in Table 4.3. In both cases, E_a values are found to decrease on doping.

The level of oxygen ionic conduction is quite similar for all studied materials, being dependent on the nature of divalent dopant cations rather than on their concentration (Fig.4.9). For instance, σ_o values of $\text{Ce}_{1-x}\text{Ca}_x\text{VO}_{4+\delta}$ with x = 0.1 and 0.2 are almost equal, within the limits of experimental error, being lower than those of $\text{Ce}_{0.9}\text{Sr}_{0.1}\text{VO}_{4+\delta}$. The structure refinement (Table 4.1) and electron-hole concentration calculations (see below) suggest significant oxygen excess. Some

authors [385,386,388] assumed cerium vanadate phase to be nearly oxygen-stoichiometric, with a prevailing charge compensation mechanism via the oxygen vacancy formation. In this case, however, a systematic increase in the ionic conduction with Ca content should be expected due to increasing concentration of ionic charge carriers, which is not observed experimentally. On the other hand, a coexistence of oxygen vacancies and interstitials with an intrinsic Frenkel-type equilibrium in the $\text{Ce}_{1-x}\text{Ca}_x\text{VO}_{4+\delta}$ lattice, like in $\text{La}_2\text{NiO}_{4+\delta}$ -based phases [263], cannot be entirely excluded.

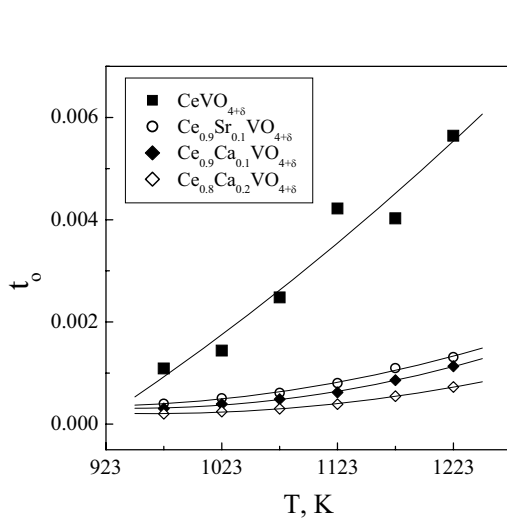


Fig.4.8. Temperature dependencies of the oxygen ion transference numbers of $\text{Ce}_{1-x}\text{A}_x\text{VO}_{4+\delta}$, determined by the faradaic efficiency measurements in air.

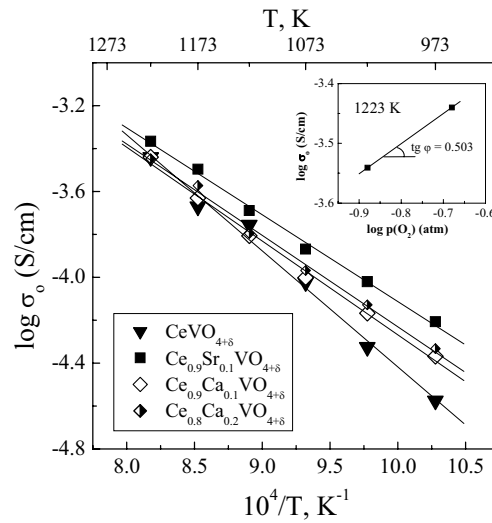


Fig.4.9. Temperature dependence of the oxygen ionic conductivity of $\text{Ce}_{1-x}\text{A}_x\text{VO}_{4+\delta}$ ceramics in air. Inset shows the ionic conductivity of $\text{CeVO}_{4+\delta}$ as a function of the membrane permeate-side oxygen pressure, with feed-side $p(\text{O}_2)$ fixed at 0.21 atm.

At 973-1073 K the ionic conductivity of undoped cerium vanadate is slightly lower, but becomes similar to that in $\text{Ce}(\text{Ca})\text{VO}_{4+\delta}$ at temperatures above 1100 K. Such a behavior could be attributed to a moderate oxygen uptake on heating $\text{CeVO}_{4+\delta}$ in air, revealed by TG measurements. The oxygen ionic conductivity of Sr-doped vanadate was found to be slightly higher with respect to Ca-containing compositions (Fig.4.9). Therewith, $\text{Ce}_{0.9}\text{Sr}_{0.1}\text{VO}_{4+\delta}$ and $\text{Ce}_{0.9}\text{Ca}_{0.1}\text{VO}_{4+\delta}$ possess essentially the same values of p-type conductivity and Seebeck coefficient and, thus, electron-hole concentration (Fig.4.10). As the latter is directly related to the oxygen hyperstoichiometry according to the crystal electroneutrality law, the concentrations of the ionic charge carriers in $\text{Ce}_{0.9}\text{Sr}_{0.1}\text{VO}_{4+\delta}$ and $\text{Ce}_{0.9}\text{Ca}_{0.1}\text{VO}_{4+\delta}$ are expected to be very similar; the higher ionic conduction in Sr-containing compound is hence related to a greater oxygen-ion mobility.

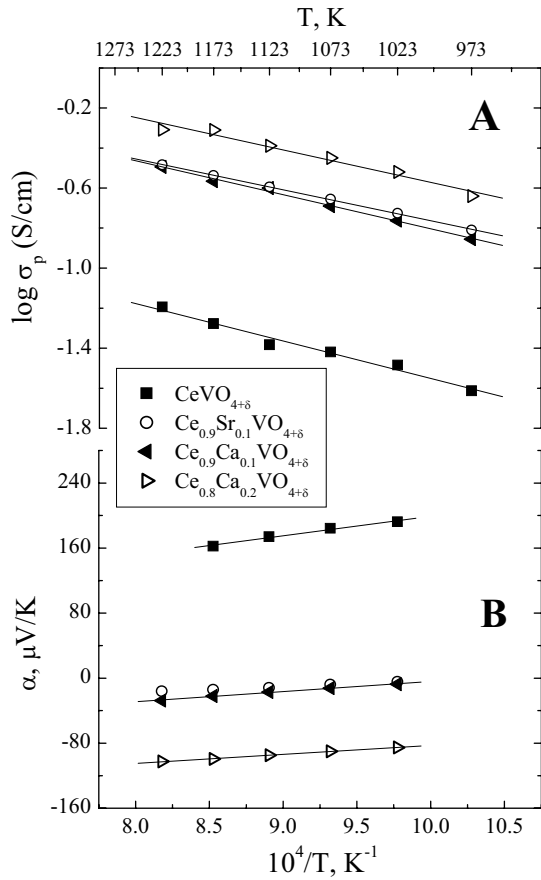


Fig.4.10. Temperature dependence of the partial p-type electronic conductivity (A) and Seebeck coefficient (B) of $Ce_{1-x}A_xVO_{4+\delta}$ ceramics in air.

Analogous tendencies in ABO_3 perovskite oxides, where increasing A-site cation radius leads to increasing ionic transport [239,263], can be explained in terms of various geometrical parameters, including the size of ion migration channels and free volume of the lattice [389,390]. In the case of zircon structure, however, these concepts seem rather invalid. As an example, Fig.4.11(left) shows a projection of $CeVO_4$ unit cell, drawn on the basis of structure refinement results and ionic radii from Ref.[60], in the direction perpendicular to c axis; the probable migration channels of oxygen interstitials in zircon-type lattice [391] are marked by circles. For $Ce_{1-x}A_xVO_{4+\delta}$ the size of these channels (so-called “bottlenecks”) is 30-40% smaller than the diameter of oxygen ion. Respectively, no correlation between the bottleneck size and ionic conductivity was found, as expected from this comparison. The specific free volume of the lattice of $Ce_{1-x}A_xVO_{4+\delta}$ (Table 4.1) is defined as $(V-V_{ion})/V$, where V is the unit cell volume and V_{ion} is the volume of ions constituting the cell [390]. Again, no correlation of the free volume with ionic conduction is observed.

The higher ionic conductivity of $Ce_{0.9}Sr_{0.1}VO_{4+\delta}$ with respect to other vanadates may hence be explained in terms of hypothesis [239], regarding possible influence of A-site cation

polarizability on the anion mobility, or assuming a strong cooperative effect in the processes of ion migration. The assumption [239] refers to increasing polarizability of A-site cations with similar charge when the average cation radius increases; this is expected to decrease cation-anion interaction and, thus, potential barrier for ion jumps. Such effect may explain variations of the oxygen ionic transport in a number of perovskite- and K_2NiF_4 -type mixed conductors [239,263]. One alternative hypothesis relates to a significant contribution of the oxygen jumps along $[1,1,-1]$ direction as illustrated by Fig.4.11(right); oxygen vacancies in these oxygen chains can be formed due to a Frenkel-type disorder. In this case, again, the size and polarizability of A-site cations is expected to play an important role.

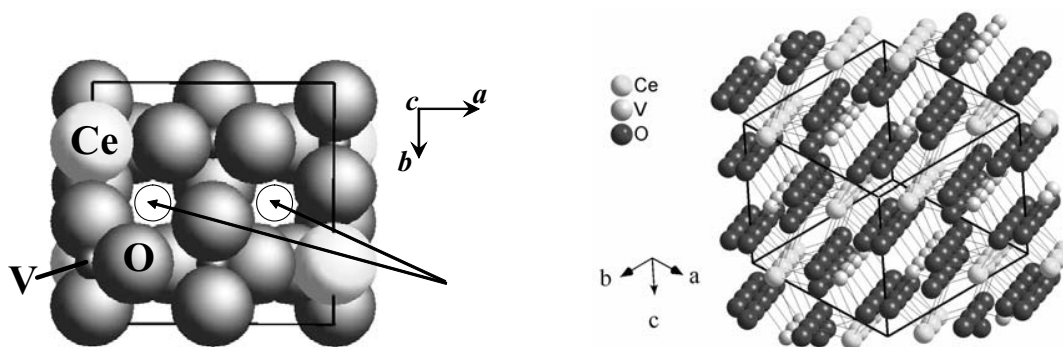


Fig.4.11. Projection of zircon-type lattice of $CeVO_{4+\delta}$, drawn using structure refinement results and ionic radii from Ref. (24). Square and circles show the unit cell and the most probable channel for the interstitial oxygen transport along c axis, respectively (left). Fragment of zircon-type structure of $Ce_{1-x}A_xVO_4$, showing the oxygen chains along $[1,1,-1]$ direction (right).

Contrary to the oxygen ionic conduction, the values of electronic conductivity (Fig.10A) and Seebeck coefficient (Fig.4.10B) are determined by the acceptor dopant concentration and are almost independent of the type of A-site substituent. In particular, $Ce_{0.9}Ca_{0.1}VO_{4+\delta}$ and $Ce_{0.9}Sr_{0.1}VO_{4+\delta}$ exhibit similar level of electron-hole transport. This behavior suggests the charge compensation mechanism via the formation of holes localized, most likely, on cerium cations, which has no essential effect on the anion charge carrier concentration. In combination with the negative slope of $\alpha - T$ dependencies (Fig.4.10B), the systematic increase in the conductivity on acceptor doping confirms that the p-type electronic conduction is dominant compared to n-type.

The Seebeck coefficient of pure $CeVO_{4+\delta}$ is positive (Fig.4.10B), in agreement with literature [385,387]. Doping with calcium and strontium leads to a change in the sign of thermoe.m.f.; the character of temperature dependencies of the electrical properties remains, however, similar to that of undoped cerium orthovanadate. Such a behavior results from increasing hole concentration and cannot be attributed to a transition from p- to n-type conduction. Taking into

account literature data [90] showing that electronic conduction in both cerium and vanadium oxides occurs via hopping mechanism, small-polaron conduction in $\text{Ce}_{1-x}\text{A}_x\text{VO}_{4+\delta}$ was assumed. In this case, neglecting transported heat of the holes, the Seebeck coefficient can be expressed as [90,392]:

$$\alpha = \frac{k}{e} \cdot \ln\left(\frac{N-p}{p}\right) \quad (4.2)$$

where p is the hole concentration, N is the total concentration of sites participating in the conduction process. Formally, the Seebeck coefficient will become negative when p exceeds $0.5 \times N$, i.e. if more than a half of sites, available for hopping in the lattice of $\text{Ce}_{1-x}\text{A}_x\text{VO}_{4+\delta}$, are occupied. The evaluated p/N ratio is increasing from 0.09-0.19 ($x = 0$) up to 0.72-0.77 ($x = 0.2$) in air at 1023-1223 K. Increasing calcium content leads to a greater p/N ratio and, hence, lower Seebeck coefficient, which becomes negative at $x \geq 0.1$. At the same time, the dominant oxidation state of vanadium in these conditions is $5+$ [385], and V^{5+} cations in vanadates contribute, as a rule, to n-type electronic transport [387]. Thus, cerium sublattice is supposed to provide the electron-hole conduction. This assumption is supported by the decrease in the tetragonal unit cell parameters on doping (Fig.4.2), suggesting the presence of cerium in $4+$ oxidation state since the ionic radius of 8-coordinated cations increases as $\text{Ce}^{4+} < \text{Ce}^{3+} \approx \text{Ca}^{2+} < \text{Sr}^{2+}$. Note that modest fractions of Ce^{4+} (9.7 % at 973 K) in undoped vanadate are actually non-contradicting to the X-ray absorption spectroscopy and TGA data [385,388], implying the basic oxidation state of cerium to be $3+$.

As a first approximation, one can assume the N value equal to the total concentration of cerium in the lattice. This hypothesis neglects possible blocking effects, making a part of cerium sites unavailable for electron-hole hopping (e.g. due to local distortions of the lattice near Ce^{4+} cations having relatively small size). Under this assumption, the concentration of p-type charge carriers may be estimated from thermopower using Eq.(4.2). Since p was calculated per one formula unit, the oxygen access was determined by Eq.(4.1), substituting $p = y(1-x)$. 10 mol% A^{2+} substitution for cerium leads to an unproportional (by 30-40%) increase in the hole concentration. This might suggest a promoted tendency for changing oxidation state of Ce cations to $4+$, which is more stable in air. The oxygen access is essentially the same (0.18-0.21 per unit formula) for all the doped compositions and is probably the maximum that the zircon-type structure can actually adopt. Hence, further calcium doping results in a proportional increase in Ce^{4+} fraction. The estimated oxygen access in pure $\text{CeVO}_{4+\delta}$, $\delta = 0.05-0.07$ at 1023-1223 K, is substantially lower than that of alkaline-earth containing phases and is quite close to the structure refinement results (Table 4.1). The high content of interstitial oxygen ions might prevent the lattice contraction caused by the presence of Ce^{4+} , leading to erroneous estimates from XRD data. Both p and δ only slightly increase on heating (Fig.4.12), in agreement with TG results showing an absence of significant weight variations, within the limits of experimental uncertainty.

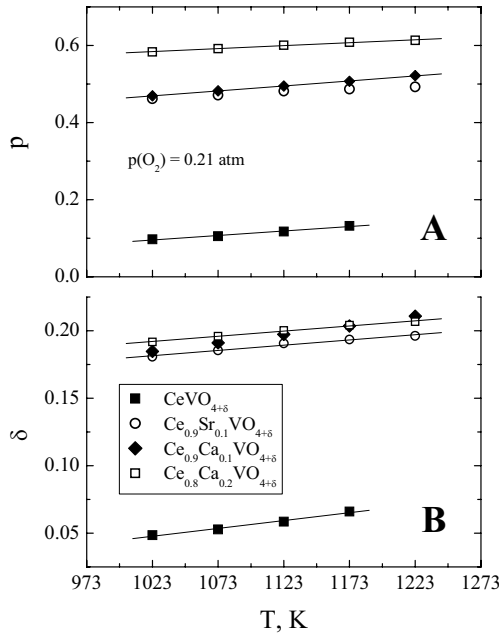


Fig.4.12. Electron-hole concentration (A) and oxygen hyperstoichiometry (B) per one formula unit of $\text{Ce}^{3+}_{1-x-p}\text{Ce}^{4+}_p\text{A}_x\text{VO}_{4+\delta}$, calculated from Eqs.(4.1) and (4.2).

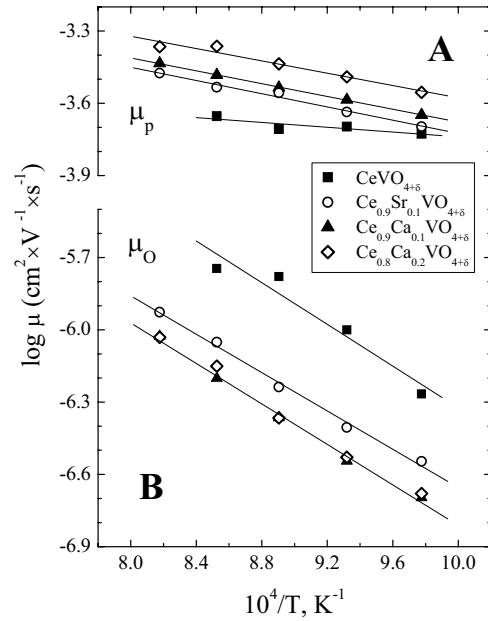


Fig.4.13. Electron-hole (A) and interstitial oxygen ion (B) mobilities in $\text{Ce}_{1-x}\text{A}_x\text{VO}_{4+\delta}$, calculated from Eq.(4.3).

The mobilities of electron holes and oxygen ions (μ_p and μ_o , respectively) plotted in Fig.4.13 were evaluated from [92,207]

$$\sigma_k = z_k e \cdot \mu_k \cdot [k] \cdot (N_{\text{fu}}/V_{\text{uc}}) \quad (4.3)$$

where ($z_k e$), σ_k and μ_k are the absolute charge, partial conductivity and mobility of k-species, $[k]$ is their concentration related to one formula unit, V_{uc} is the unit cell volume calculated from the XRD data, and N_{fu} is the number of formula units per unit cell (here $N_{\text{fu}} = 4$). The mobility of p-type charge carriers has a temperature-activated character, with E_a values similar to the conductivity (Table 4.3), and is of similar level for all materials, being below $10^{-3} \text{ cm}^2 \times \text{V}^{-1} \times \text{s}^{-1}$. This validates the small-polaron conduction mechanism. According to the estimates, about 40% theoretical interstitial-oxygen sites should be occupied in cerium vanadate containing alkaline-earth cations, which might explain noticeably lower oxygen ion mobility compared to the undoped composition. The μ_o values of $\text{Ce}_{0.9}\text{Sr}_{0.1}\text{VO}_{4+\delta}$ are slightly higher, probably due to the greater free volume in the lattice (Table 4.1) associated with the larger Sr^{2+} cations. The activation energies for the oxygen ion mobility, 85-92 kJ/mol, are quite close to those for the σ_o (Table 4.3).

4.1.3. Electrical conductivity and Seebeck coefficient vs. $p(O_2)$

Reducing oxygen partial pressure leads to decreasing total conductivity of $Ce_{1-x}A_xVO_{4+\delta}$, whilst the values of Seebeck coefficient were found to increase (Figs.4.14-4.16). Within the phase stability limits, these changes are relatively small: for example, the slope of σ vs. $p(O_2)$ logarithmic dependencies is as low as $5 \times 10^{-4} - 3 \times 10^{-2}$. Such a behavior is due to minor oxygen content variations in the studied range of temperatures and oxygen pressures, confirmed by TGA studies in atmospheres with various $p(O_2)$. In agreement with Ref.[387], the changes in δ values with temperature, determined by TGA, are comparable with the experimental error. The oxygen nonstoichiometry variations on changing oxygen pressure were also small, close to the level of experimental uncertainty.

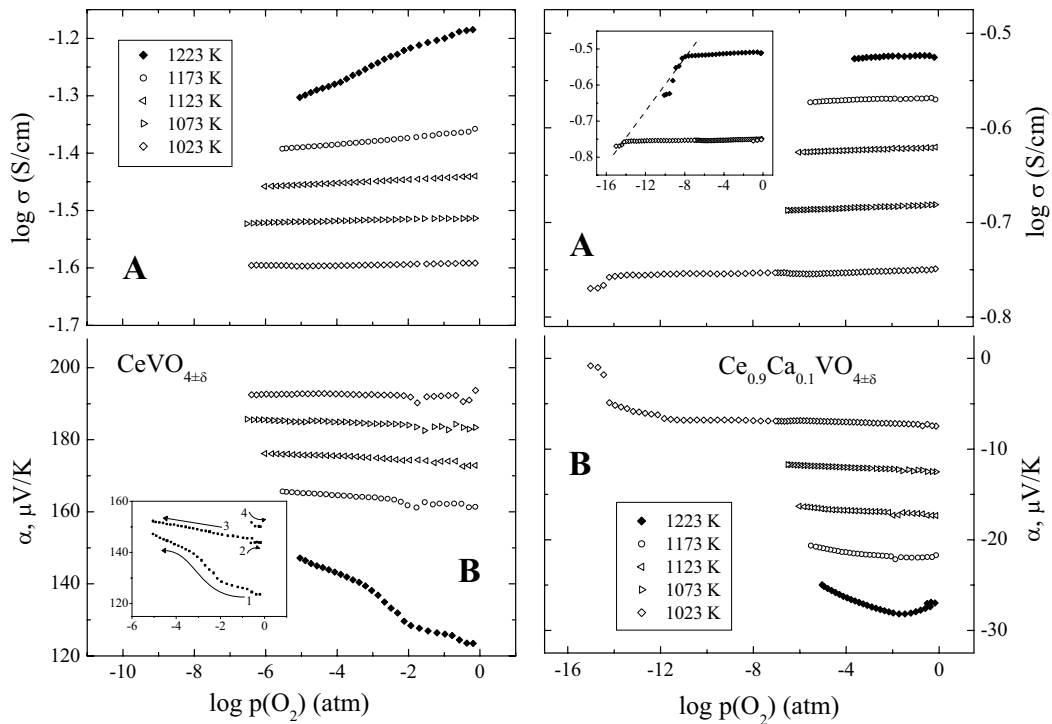


Fig.4.14. Oxygen partial pressure dependence of the total conductivity (A) and Seebeck coefficient (B) of $CeVO_{4+\delta}$. Inset illustrates irreversible behavior of thermopower after phase decomposition, with the numbers and arrows showing a sequence of $p(O_2)$ changes.

Fig.4.15. Oxygen partial pressure dependence of the total conductivity (A) and Seebeck coefficient (B) of $Ce_{0.9}Ca_{0.1}VO_{4+\delta}$. Inset illustrates estimations of the phase stability boundary from the thermopower data.

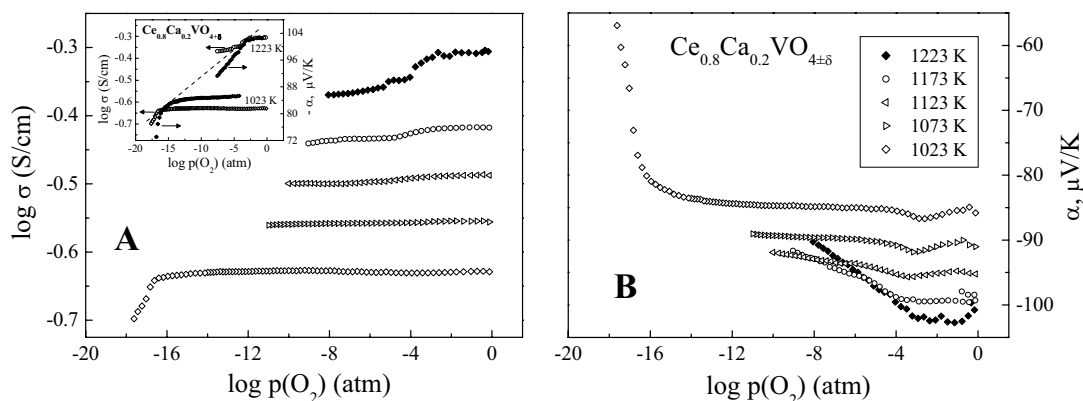


Fig.4.16. Oxygen partial pressure dependence of the total conductivity (A) and Seebeck coefficient (B) of $\text{Ce}_{0.8}\text{Ca}_{0.2}\text{VO}_{4\pm\delta}$. Inset illustrates estimations of the phase stability boundary.

Possible mechanisms of the electronic conduction in $\text{Ce}_{1-x}\text{A}_x\text{VO}_{4\pm\delta}$ are briefly discussed above. The oxygen pressure dependencies of thermopower and conductivity of $\text{CeVO}_{4\pm\delta}$ (Fig.4.14) unambiguously indicate the dominating role of electron holes in the charge transfer processes, which corresponds well to the literature data [385,387]. As for the variations with temperature, the character of $p(\text{O}_2)$ dependencies of the electrical properties of calcium-doped materials remains similar to that of undoped cerium orthovanadate, supporting such a conclusion.

Further decrease in $p(\text{O}_2)$ results in the decomposition of the zircon-type phases, which is associated with an irreversible drop in the conductivity and a poor reproducibility of the results; the decomposition phenomena are illustrated by Insets of Figs.4.14-4.16. Although the stability limit of undoped CeVO_4 at 1223 K is quite close to the atmospheric oxygen pressure, no phase changes were detected at this temperature in air.

4.1.4. Stability in reducing atmospheres

In atmospheric air, zircon-type phases $\text{Ce(A)VO}_{4\pm\delta}$ were found stable up to, at least, 1300 K. The high-temperature XRD data and the analysis of samples quenched in liquid nitrogen proved no phase changes. Increasing temperature to 1373 K results in the formation of two phases, CeO_2 and the corresponding A-site deficient zircon $\text{Ce}_{1-x}\text{VO}_{4\pm\delta}$. The content of CeO_{2-y} at 1373 K in air was observed to be as high as 30%; an example of the XRD pattern is given in Fig.4.1. This is contrary to the assumption [387] concerning a transformation of the zircon- to scheelite-type phase of CeVO_4 around 1173 K, suggested to explain the unusual conductivity behavior and the results of differential thermal analysis (DTA). The phenomena observed by the authors [387] might be, however, caused by CeO_2 separation.

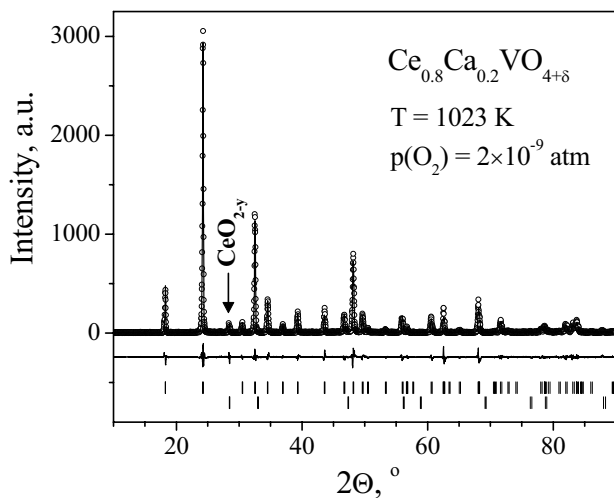


Fig. 4.17. Observed, calculated and difference XRD pattern of CeO_{2-y} -containing $\text{Ce}_{0.8}\text{Ca}_{0.2}\text{VO}_{4+\delta}$ ceramics at 1023 K in vacuum.

Although the thermal expansion coefficients in vacuum are quite similar to those in air (Table 4.2), reducing oxygen partial pressure down to 2×10^{-9} atm also leads to segregation of oxygen-deficient CeO_{2-y} and, thus, to the unit cell contraction (Fig.4.2). The amount of segregated cerium oxide at 1023-1223 K, estimated from the structure refinement results, was 3-5 mol% in the case of CeVO_4 and up to 12 mol% for $\text{Ce}_{0.8}\text{Ca}_{0.2}\text{VO}_4$; one example is shown in Fig.4.17. Similar behavior is observed for the samples annealed in a flow of argon, where $p(\text{O}_2) = 10^{-5}$ atm, at 1223 K (Fig.4.1). Further reduction of the oxygen partial pressure results in a transition of the zirconite-type phases into CeVO_3 -based perovskites (Fig.4.1). This transformation occurred for all samples annealed in a flow of 10% H_2 - 90% N_2 mixture at 973-1223 K. At 923 K, the conversion of $\text{Ce}_{0.8}\text{Ca}_{0.2}\text{VO}_4$ into $\text{Ce}(\text{Ca})\text{VO}_{3-\delta}$ perovskite was incomplete; only about 7 mol% of perovskite phase was formed after the reduction. However, such a behavior can be ascribed, most likely, to kinetic limitations.

Selected results on the phase relations in $\text{Ce}(\text{Ca})\text{VO}_{4\pm\delta}$ systems, evaluated from the XRD data at different temperatures and oxygen partial pressures, are summarized in Fig.4.18. The solid lines correspond to the stability boundaries estimated from $p(\text{O}_2)$ -dependencies of the total conductivity and Seebeck coefficient, as shown by Insets of Figs.4.15 and 4.16. The XRD results are in a good agreement with the phase boundary estimates. This means that a sharp decrease in the conductivity curves and the corresponding increase of Seebeck coefficient result from starting of cerium oxide segregation due to the decomposition process. The conductivity of CeO_{2-y} [41] is considerably lower than that of CeVO_4 -based phases (Fig.4.7A, [385]). The volume fraction of segregated cerium oxide is small but it may still affect the conductivity by preferential segregation at grain boundaries. Notice also that, in most cases, the changes in conductivity and Seebeck coefficient of $\text{Ce}_{1-x}\text{A}_x\text{VO}_{4+\delta}$ at reduced oxygen partial pressures were irreversible.

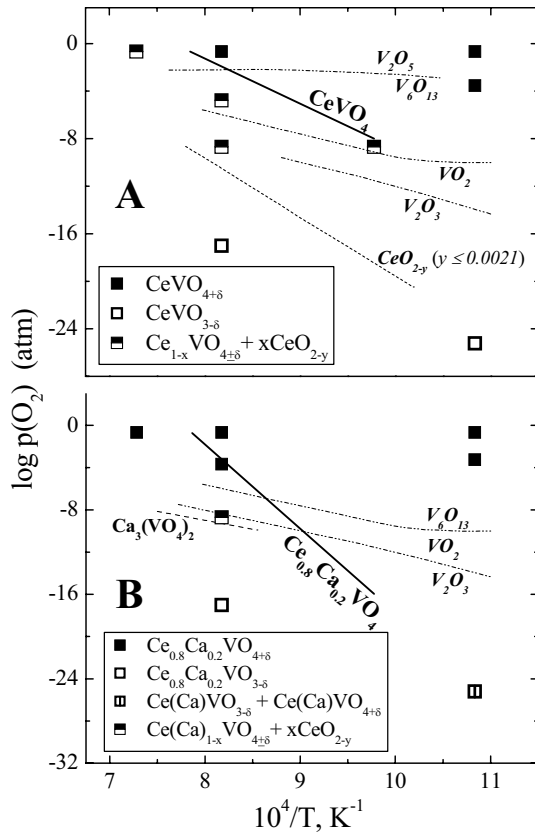


Fig.4.18. Selected results of XRD analysis and phase stability limits of $\text{CeVO}_{4+\delta}$ (A) and $\text{Ce}_{0.8}\text{Ca}_{0.2}\text{VO}_{4+\delta}$ (B). Solid lines correspond to the phase boundaries estimated from the data on conductivity and Seebeck coefficient. Dashed lines correspond to the stability limits of $\text{Ca}_3(\text{VO}_4)_2$ [393] and binary vanadium oxides [394]. Oxygen isoconcentration line in $\text{CeO}_{1.9979}$ [206] is shown for comparison.

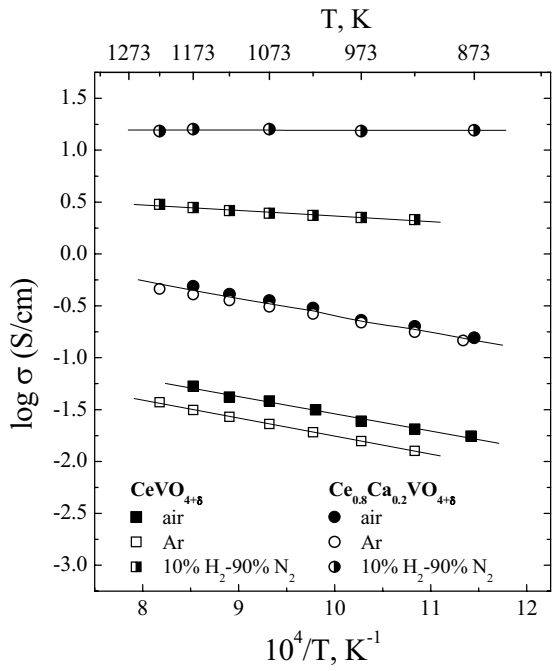
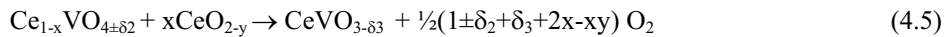
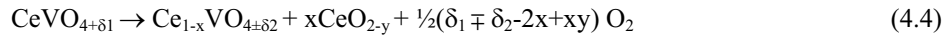


Fig.4.19. Temperature dependence of the total conductivity of $\text{CeVO}_{4+\delta}$ and $\text{Ce}_{0.8}\text{Ca}_{0.2}\text{VO}_{4+\delta}$ ceramics in various atmospheres.

In order to verify phase relationships assessed by XRD analysis, the temperature dependencies of total conductivity were studied in different atmospheres (Fig.4.19). For $\text{Ce}_{0.8}\text{Ca}_{0.2}\text{VO}_{4+\delta}$ ceramics which are single-phase both in air and in argon, the change in the oxygen partial pressure from 0.21 to 1×10^{-5} atm results in a slight decrease of the σ values. Contrary, the conductivity of undoped $\text{CeVO}_{4+\delta}$ in air is considerably higher than that in argon where the segregation of ceria is observed. When both compositions are converted into the perovskite phases in hydrogen atmosphere, the values of σ increase 10-80 times, in agreement with literature on perovskite-type vanadates [395]. The total conductivity of $\text{Ce}_{0.8}\text{Ca}_{0.2}\text{VO}_{3-\delta}$ shows a metallic behavior, being essentially independent of temperature.

The XRD and conductivity data show that at low oxygen pressures CeO_{2-y} segregates from the zircon-type phases; further reduction results in a conversion of the two-phase mixtures into perovskite phase. Therefore, the reduction mechanism of $\text{Ce}(\text{Ca})\text{VO}_{4\pm\delta}$ is more complex than one-step transformation “zircon \rightarrow perovskite”, suggested in Ref.[396]. This mechanism should include at least two stages, which may be expressed as



where δ_1 and δ_2 are the oxygen nonstoichiometry values of the cation-stoichiometric and A-site-deficient zircon phases, and δ_3 is the nonstoichiometry of perovskite. The latter phase is presumably oxygen-deficient, especially when significant amounts of the acceptor-type dopants are incorporated in the lattice.

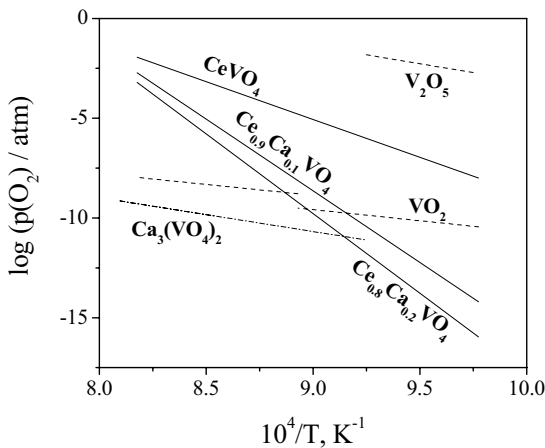


Fig.4.20. Phase stability limits of $\text{Ce}_{1-x}\text{Ca}_x\text{VO}_{4+\delta}$. Literature data on binary vanadium oxides [206,381] and $\text{Ca}_3(\text{VO}_4)_2$ [393] are shown for comparison.

Figs.4.18 and 4.20 compare the stability boundaries of $\text{Ce}(\text{Ca})\text{VO}_{4+\delta}$ with thermodynamic data on calcium vanadate [393] and binary oxides of vanadium and cerium [206,381,394]. In the case of vanadium oxides, dashed lines correspond to the phase boundaries between different V-O

phases [394]; for oxygen-deficient CeO_{2-y} [206] the dashed line relates to the fixed nonstoichiometry value, $y = 0.0021$. The first step of $\text{Ce}(\text{Ca})\text{VO}_{4+\delta}$ reduction is close to the oxygen partial pressures of $\text{V}_6\text{O}_{13} \rightarrow \text{VO}_2 \rightarrow \text{V}_2\text{O}_3$ transitions and can thus be associated with reducing of vanadium cations. The zircon-type lattice is expected to stabilize V^{5+} oxidation state, as for $\text{Ca}_3(\text{VO}_4)_2$ where decomposition takes place at $p(\text{O}_2)$ values close to VO_2 phase boundary. Further conversion into $\text{Ce}(\text{Ca})\text{VO}_{3-\delta}$ perovskite is related to the formation of Ce^{3+} and V^{3+} cations; the onset of the perovskite phase is observed mainly for conditions when both single oxides are reduced to the trivalent state.

Perovskite-type $\text{Ce}(\text{Ca})\text{VO}_{3-\delta}$ exhibits better transport properties than the zircon-type compounds, but its stability with respect to re-oxidizing is poor. Nevertheless, divalent additives may stabilize the perovskite phase by allowing partial re-oxidation of cerium and/or vanadium to higher valence states. From the point of view of the tolerance factor, one should expect an enhanced stability by allowing partial oxidation from V^{3+} to V^{4+} . On the contrary, oxidation of Ce^{3+} to Ce^{4+} should spoil the stability.

Doping with calcium leads to a considerable enlargement of the zircon phase stability domain (Fig.4.20), which is associated most probably with an increase in the concentrations of ionic species with higher valence states at a given value of $p(\text{O}_2)$. One thus expects that Ca doping increases the concentration of Ce^{4+} and suppresses the formation of V^{4+} . In fact, the decomposition of $\text{Ce}_{1-x}\text{Ca}_x\text{VO}_{4+\delta}$ takes place at values of $p(\text{O}_2)$ of 10^{-16} - 10^{-8} atm at 1020-1100 K, which are comparable to the stability boundaries of VO_2 and $\text{Ca}_3(\text{VO}_4)_2$. The ability to retain the highest oxidation state (V^{5+}) is thus enhanced by the tetrahedral coordination of vanadium cations in cerium orthovanadate and by additions of calcium, as observed in alkaline-earth vanadates [393]. Notice also that extrapolation of the stability limit of $\text{Ce}_{0.8}\text{Ca}_{0.2}\text{VO}_{4+\delta}$ to the low-temperature range suggests that this phase should be stable in the SOFC anode environments at temperatures below 950 K, when the decomposition is expected at $p(\text{O}_2) < 10^{-20}$ atm.

4.2. Perovskite-type $\text{La}_{0.9}\text{Sr}_{0.1}\text{Al}_{0.85-x}\text{Mg}_{0.15}\text{Fe}_x\text{O}_{3-\delta}$

As discussed in Chapter 1.5.1.2, the incorporation of aluminium cations having stable oxidation state into the perovskite-like structure of lanthanum-strontium ferrites partially suppresses the lattice expansion on heating and under changing $p(\text{O}_2)$, due to reduced oxygen nonstoichiometry variations. For deep analysis of the behavior of transition metal cations dissolved in a lattice of ions with stable oxidation state, $\text{La}_{0.90}\text{Sr}_{0.10}\text{Al}_{0.85-x}\text{Fe}_x\text{Mg}_{0.15}\text{O}_{3-\delta}$ system was selected as model. Doping with acceptor-type cations, Sr^{2+} and Mg^{2+} , was necessary to provide sufficient ionic conduction required for the electrochemical applications; in order to minimize local

inhomogeneities due to possible dopant segregation at the grain boundaries, the content of these cations was selected close to their maximum solubility in LaAlO_3 lattice.

4.2.1. General characterization

XRD analysis confirmed the formation of single-perovskite type phase after sintering ceramics of Fe-substituted materials, $\text{La}_{0.90}\text{Sr}_{0.10}\text{Al}_{0.85-x}\text{Fe}_x\text{Mg}_{0.15}\text{O}_{3-\delta}$ ($x = 0.20, 0.40$ and 0.50) at 1673 K (Fig.4.21). The crystal structure was identified as rhombohedrally distorted (space group $R\bar{3}c$); Fig.4.22 presents one example of the final structure refinement. At $x = 0.60$, minor impurity peaks were observed in the XRD patterns, suggesting that maximum solubility of iron in doped LaAlO_3 corresponds to $0.5 < x < 0.6$. Table 4.4 lists the unit cell parameters in hexagonal settings. The lattice expansion with increasing Fe content is due to the larger cation radius of iron with respect to aluminum [60]. As illustrated by the inset in Fig.4.22, no phase changes such as metallic Fe formation were detected using XRD analysis after annealing in flowing $\text{H}_2\text{-H}_2\text{O-N}_2$ gas mixtures at 1073-1223 K. Therefore, all data on the transport properties of Fe-containing compositions, presented below, correspond to single perovskite phases.

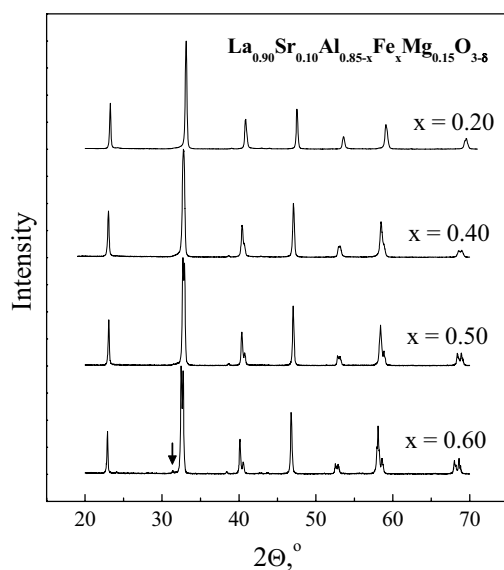


Fig.4.21. XRD patterns of $\text{La}_{0.90}\text{Sr}_{0.10}\text{Al}_{0.85-x}\text{Fe}_x\text{Mg}_{0.15}\text{O}_{3-\delta}$ ceramics, after sintering in air at 1673 K.

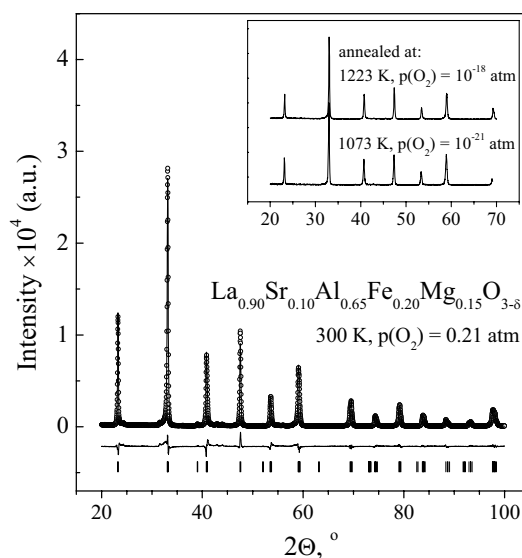


Fig.4.22. Observed, calculated and difference XRD pattern of $\text{La}_{0.90}\text{Sr}_{0.10}\text{Al}_{0.65}\text{Fe}_{0.20}\text{Mg}_{0.15}\text{O}_{3-\delta}$ ceramics, sintered at 1673 K in air and equilibrated with atmospheric oxygen at low temperatures. Inset shows XRD patterns after annealing at reduced oxygen pressures and quenching. All patterns were collected at room temperature.

Table 4.4

Properties of $\text{La}_{0.90}\text{Sr}_{0.10}\text{Al}_{0.85-x}\text{Fe}_x\text{Mg}_{0.15}\text{O}_{3-\delta}$ perovskite ceramics

x	Unit cell parameters (space group $R\bar{3}c$, PDF n° 167)		Linear thermal expansion coefficient in air		Activation energy for the total conductivity in air	
	a, nm	c, nm	T, K	$\bar{\alpha} \times 10^6, \text{K}^{-1}$	T, K	$E_a, \text{kJ/mol}$
0.20	0.5418(1)	1.3214(2)	410-1000	12.62±0.03	445-760	40±6
			1000-1300	17.9±0.1	955-1260	10.3±0.3
0.40	0.5473(3)	1.3303(6)	410-820	11.66±0.01	455-910	24.3±0.9
			1040-1520	18.01±0.01		
0.50	0.5483(0)	1.3301(6)	490-1000	13.22±0.01	560-910	21.3±0.6
			1000-1520	19.71±0.01		
0.60	0.5510(2)	1.3347(6)				

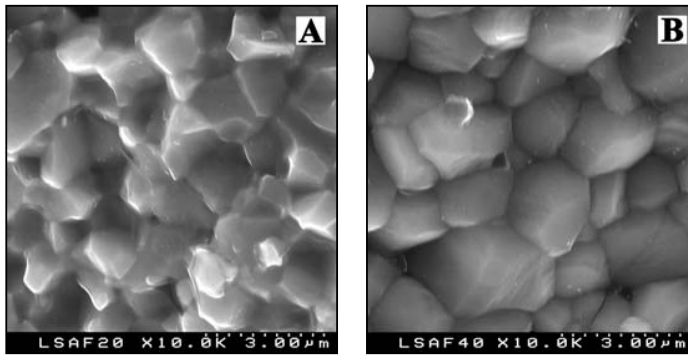


Fig.4.23. SEM micrographs of fractured $\text{La}_{0.90}\text{Sr}_{0.10}\text{Al}_{0.65}\text{Fe}_{0.20}\text{Mg}_{0.15}\text{O}_{3-\delta}$ (A) and $\text{La}_{0.90}\text{Sr}_{0.10}\text{Al}_{0.45}\text{Fe}_{0.40}\text{Mg}_{0.15}\text{O}_{3-\delta}$ (B) ceramics.

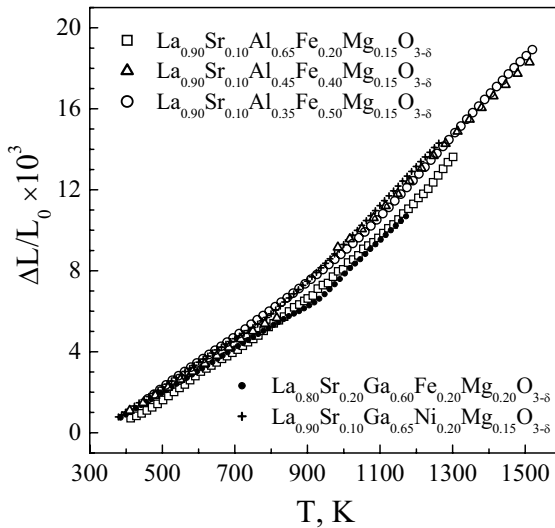


Fig.4.24. Dilatometric curves of $\text{La}_{0.90}\text{Sr}_{0.10}\text{Al}_{0.85-x}\text{Fe}_x\text{Mg}_{0.15}\text{O}_{3-\delta}$ ceramics, compared to those of $\text{La}_{0.8}\text{Sr}_{0.2}\text{Ga}_{0.6}\text{Fe}_{0.2}\text{Mg}_{0.2}\text{O}_{3-\delta}$ and $\text{La}_{0.90}\text{Sr}_{0.10}\text{Ga}_{0.65}\text{Ni}_{0.20}\text{Mg}_{0.15}\text{O}_{3-\delta}$ [397], in air.

Typical SEM micrographs of fractured $\text{La}_{0.90}\text{Sr}_{0.10}\text{Al}_{0.85-x}\text{Fe}_x\text{Mg}_{0.15}\text{O}_{3-\delta}$ samples are shown in Fig.4.23. The materials have homogeneous microstructures with minor porosity and small grains, characteristic of the ceramics prepared from GNP-synthesized powders. The grain size varies in the range 1-3 μm and is quite similar for all compositions. Neither secondary phase segregation nor essential grain-boundary anomalies could be identified by the SEM/EDS inspections.

The average TEC values of $\text{La}_{0.90}\text{Sr}_{0.10}\text{Al}_{0.85-x}\text{Fe}_x\text{Mg}_{0.15}\text{O}_{3-\delta}$ ceramics in air are $(11.7-19.7)\times 10^{-6} \text{ K}^{-1}$ (Table 4.4), generally increasing with x , especially in the high-temperature range. Fig.4.24 compares the dilatometric data on the Fe-doped aluminates and two LaGaO_3 -based mixed conductors [397]. In the low-temperature range, thermal expansion coefficients (TECs) of all these materials are similar. At temperatures above 900-1000 K, the thermal expansion of $\text{La}_{0.90}\text{Sr}_{0.10}\text{Al}_{0.65}\text{Fe}_{0.20}\text{Mg}_{0.15}\text{O}_{3-\delta}$ is close to that of $\text{La}_{0.8}\text{Sr}_{0.2}\text{Ga}_{0.6}\text{Fe}_{0.2}\text{Mg}_{0.2}\text{O}_{3-\delta}$, but lower if compared to $\text{La}_{0.90}\text{Sr}_{0.10}\text{Ga}_{0.65}\text{Ni}_{0.20}\text{Mg}_{0.15}\text{O}_{3-\delta}$. The apparent increase in TECs on heating is associated, most likely, with chemically induced expansion of the lattice due to increasing oxygen nonstoichiometry [213].

4.2.2. Transport properties at atmospheric oxygen pressure

The temperature dependencies of the total conductivity of $\text{La}_{0.90}\text{Sr}_{0.10}\text{Al}_{0.85-x}\text{Fe}_x\text{Mg}_{0.15}\text{O}_{3-\delta}$, in comparison with other LaAlO_3 - and LaGaO_3 -based phases [398-401], are presented in Fig.4.25. Doping with iron cations, which are the only variable-valence ions in the aluminate lattice, should obviously increase the number of sites participating in electronic transport and, thus, the electronic conductivity. For most Fe-containing perovskites including iron-doped LaAlO_3 and LaGaO_3 , the electronic conduction under oxidizing conditions is p-type [202,212,215,216,400,401]; a similar behavior can also be expected for $\text{La}_{0.90}\text{Sr}_{0.10}\text{Al}_{0.85-x}\text{Fe}_x\text{Mg}_{0.15}\text{O}_{3-\delta}$. Notice that the values of total conductivity (Fig.4.25) and the corresponding activation energy (Table 4.4) for the studied materials are close to those of LaGaO_3 -based analogues. In correlation with increasing thermal expansion (Fig.4.24), the conductivity starts to decrease at temperatures above 900-1000 K due to progressive oxygen losses and decreasing hole concentration on heating; analogous trends are typical for most Fe-containing perovskites [215,216]. This effect is more pronounced for the compositions where $\geq 40\%$ B sites are occupied with iron, since the oxygen nonstoichiometry variations should be proportional to the concentration of transition metal cations. At temperatures below 760-910 K the conductivity shows a semiconductor-like behavior.

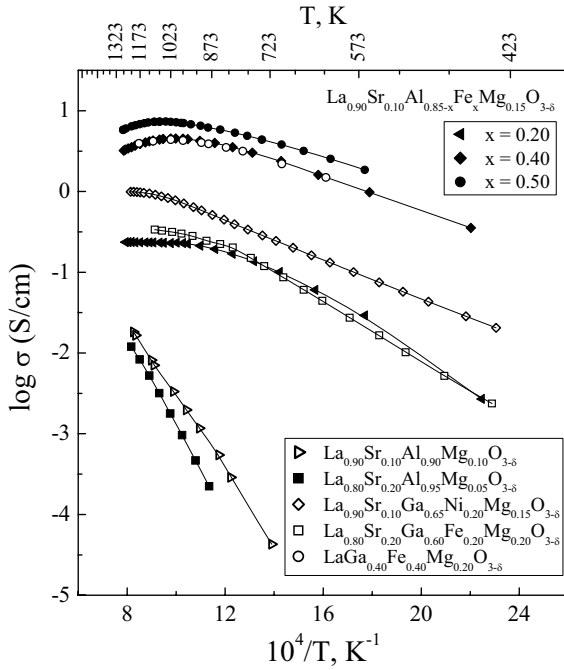


Fig.4.25. Temperature dependence of the total conductivity of $\text{La}_{0.90}\text{Sr}_{0.10}\text{Al}_{0.85-x}\text{Fe}_x\text{Mg}_{0.15}\text{O}_{3-\delta}$ ceramics in air. Data on $\text{La}_{0.9}\text{Sr}_{0.1}\text{Al}_{0.9}\text{Mg}_{0.1}\text{O}_{3-\delta}$ [398], $\text{La}_{0.80}\text{Sr}_{0.20}\text{Al}_{0.95}\text{Mg}_{0.05}\text{O}_{3-\delta}$ [399], $\text{La}_{0.90}\text{Sr}_{0.10}\text{Ga}_{0.65}\text{Ni}_{0.20}\text{Mg}_{0.15}\text{O}_{3-\delta}$ [401], $\text{La}_{0.8}\text{Sr}_{0.2}\text{Ga}_{0.6}\text{Fe}_{0.2}\text{Mg}_{0.2}\text{O}_{3-\delta}$ [401] and $\text{LaGa}_{0.4}\text{Mg}_{0.2}\text{Fe}_{0.4}\text{O}_{3-\delta}$ [400] are shown for comparison.

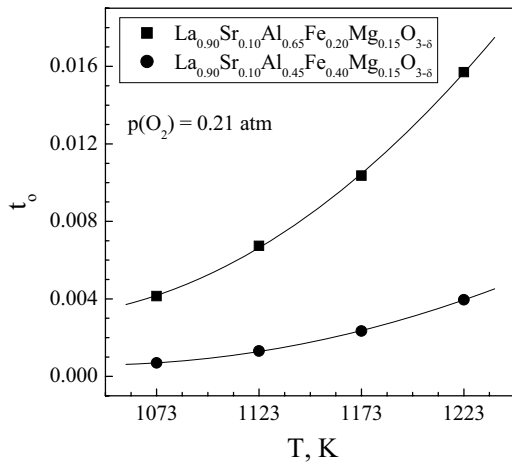


Fig.4.26. Temperature dependencies of the oxygen ion transference numbers of $\text{La}_{0.90}\text{Sr}_{0.10}\text{Al}_{0.85-x}\text{Fe}_x\text{Mg}_{0.15}\text{O}_{3-\delta}$ ceramics in air.

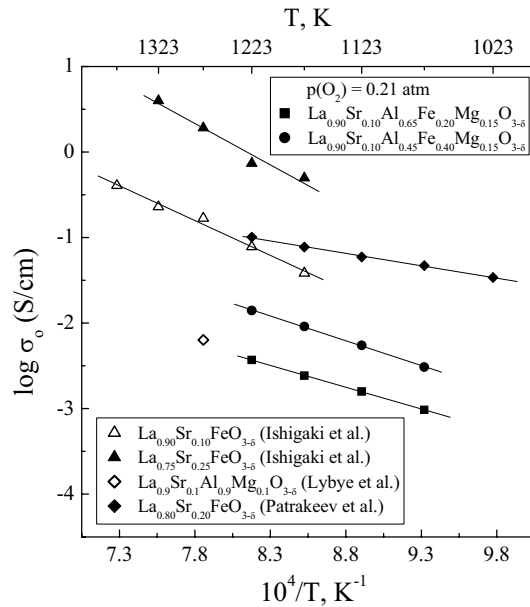


Fig.4.27. Temperature dependencies of the oxygen ionic conductivity of $\text{La}_{0.90}\text{Sr}_{0.10}\text{Al}_{0.85-x}\text{Fe}_x\text{Mg}_{0.15}\text{O}_{3-\delta}$ ceramics in air. Data on $\text{La}_{0.90}\text{Sr}_{0.10}\text{FeO}_{3-\delta}$ [402], $\text{La}_{0.75}\text{Sr}_{0.25}\text{FeO}_{3-\delta}$ [402], $\text{La}_{0.80}\text{Sr}_{0.20}\text{FeO}_{3-\delta}$ [212] and $\text{La}_{0.90}\text{Sr}_{0.10}\text{Al}_{0.90}\text{Mg}_{0.10}\text{O}_{3-\delta}$ [398] are shown for comparison.

The faradaic efficiency data (Fig.4.26) confirm that the electronic conduction is predominant in air. The oxygen ion transference numbers of $\text{La}_{0.90}\text{Sr}_{0.10}\text{Al}_{0.85-x}\text{Fe}_x\text{Mg}_{0.15}\text{O}_{3-\delta}$ vary from 6.9×10^{-4} to 1.6×10^{-2} at 1073-1223 K, increasing with temperature and decreasing when the iron content increases. For $\text{La}_{0.90}\text{Sr}_{0.10}\text{Al}_{0.65}\text{Fe}_{0.20}\text{Mg}_{0.15}\text{O}_{3-\delta}$, the σ_{O} values in air (Fig.4.27), calculated from the faradaic efficiency and total conductivity results, are similar to the ionic conductivity of analogous iron-free compositions [398]. This level of ionic transport is substantially lower than that in $\text{La}(\text{Sr})\text{FeO}_{3-\delta}$ [212,402], although literature data on the lanthanum-strontium ferrites show definite disagreements. As expected from ideal solid solution model, increasing iron content in $\text{La}_{0.90}\text{Sr}_{0.10}\text{Al}_{0.85-x}\text{Fe}_x\text{Mg}_{0.15}\text{O}_{3-\delta}$ leads to a higher ionic conduction. Comparison of the activation energies for various parameters describing ionic transport in ferrite- and aluminate-based phases is given in Table 4.5.

Table 4.5

Comparison of the activation energies for oxygen ionic transport parameters* of Fe- and Al-containing perovskites

Composition	Transport parameter	T, K	p(O ₂), atm	E _a , kJ/mol	Reference
$\text{La}_{0.9}\text{Sr}_{0.1}\text{Al}_{0.65}\text{Fe}_{0.20}\text{Mg}_{0.15}\text{O}_{3-\delta}$	σ_{O}	1073 - 1223	0.21	107±4	This work
		1073 - 1223	1×10^{-15}	102.1±0.7	
	$\sigma_{\text{O}}/[\text{V}_{\text{O}}^{\bullet\bullet}]$	1073-1223	0.21	98±4	
$\text{La}_{0.9}\text{Sr}_{0.1}\text{Al}_{0.45}\text{Fe}_{0.40}\text{Mg}_{0.15}\text{O}_{3-\delta}$	σ_{O}	1073 - 1223	0.21	120±9	This work
		1023 - 1223	1×10^{-15}	99±7	
	$\sigma_{\text{O}}/[\text{V}_{\text{O}}^{\bullet\bullet}]$	1023-1223	0.21	84±6	
$\text{La}_{0.9}\text{Sr}_{0.1}\text{Al}_{0.35}\text{Fe}_{0.50}\text{Mg}_{0.15}\text{O}_{3-\delta}$	σ_{O}	1023 - 1223	1×10^{-15}	80.7±0.8	This work
$\text{La}_{0.90}\text{Sr}_{0.10}\text{FeO}_{3-\delta}$	D_{V}	1173 - 1373	6.4×10^{-2}	79±25	[402]
$\text{La}_{0.75}\text{Sr}_{0.25}\text{FeO}_{3-\delta}$		1173 - 1323	6.4×10^{-2}	114±23	[402]
$\text{La}_{0.80}\text{Sr}_{0.20}\text{FeO}_{3-\delta}$	σ_{O}	1023 - 1223	1×10^{-19} - 1×10^{-7}	65±5	[212]
$\text{La}_{0.90}\text{Sr}_{0.10}\text{FeO}_{3-\delta}$	$j(\text{O}_2)$	1123 - 1323	$1 \times 10^{-3}/0.21$	178±7	[403]
$\text{La}_{0.80}\text{Sr}_{0.20}\text{FeO}_{3-\delta}$		1123 - 1323	$1 \times 10^{-3}/0.21$	199±18	[403]
$\text{La}_{0.90}\text{Sr}_{0.10}\text{Al}_{0.90}\text{Mg}_{0.10}\text{O}_{3-\delta}$	σ_{O}	1073-1273	1×10^{-18} -1.0	101	[404]
$\text{La}_{0.90}\text{Sr}_{0.10}\text{Al}_{0.90}\text{Mg}_{0.10}\text{O}_{3-\delta}$		1073	1×10^{-17} -1.0	87	[398]

* σ_{O} , D_{V} and $j(\text{O}_2)$ are the ionic conductivity, oxygen vacancy diffusion coefficient and oxygen permeation flux, respectively. The activation energy for $\sigma_{\text{O}}/[\text{V}_{\text{O}}^{\bullet\bullet}]$ quantity corresponds to that for the oxygen vacancy mobility.

4.2.3. Total conductivity vs. oxygen partial pressure

Selected results on the total conductivity and Seebeck coefficient of $\text{La}_{0.90}\text{Sr}_{0.10}\text{Al}_{0.85-x}\text{Fe}_x\text{Mg}_{0.15}\text{O}_{3-\delta}$ as a function of the oxygen partial pressure are presented in Figs.4.28 and 4.29. Due to stagnated gas-phase diffusion processes in the intermediate $p(\text{O}_2)$ range, the measurements at oxygen pressures from approximately 10^{-13} - 10^{-10} to 10^{-5} - 10^{-4} atm were skipped. Under oxidizing conditions, the total conductivity decreases with reducing $p(\text{O}_2)$, whereas the thermopower increases and has positive sign. This behavior unambiguously indicates that the electronic transport is dominantly p-type, in agreement with data on other Fe-containing perovskites [202,212,215,216,400,401,403]. When $p(\text{O}_2)$ is lower than 10^{-10} atm, the conductivity exhibits a plateau, suggesting that the electron-hole concentration becomes low and the oxygen ionic transport prevails. Similar behavior is often observed for transition metal-free phases derived from LaAlO_3 [398, 399]. The corresponding $p(\text{O}_2)$ range, becomes narrower with Fe-doping and increasing temperature.

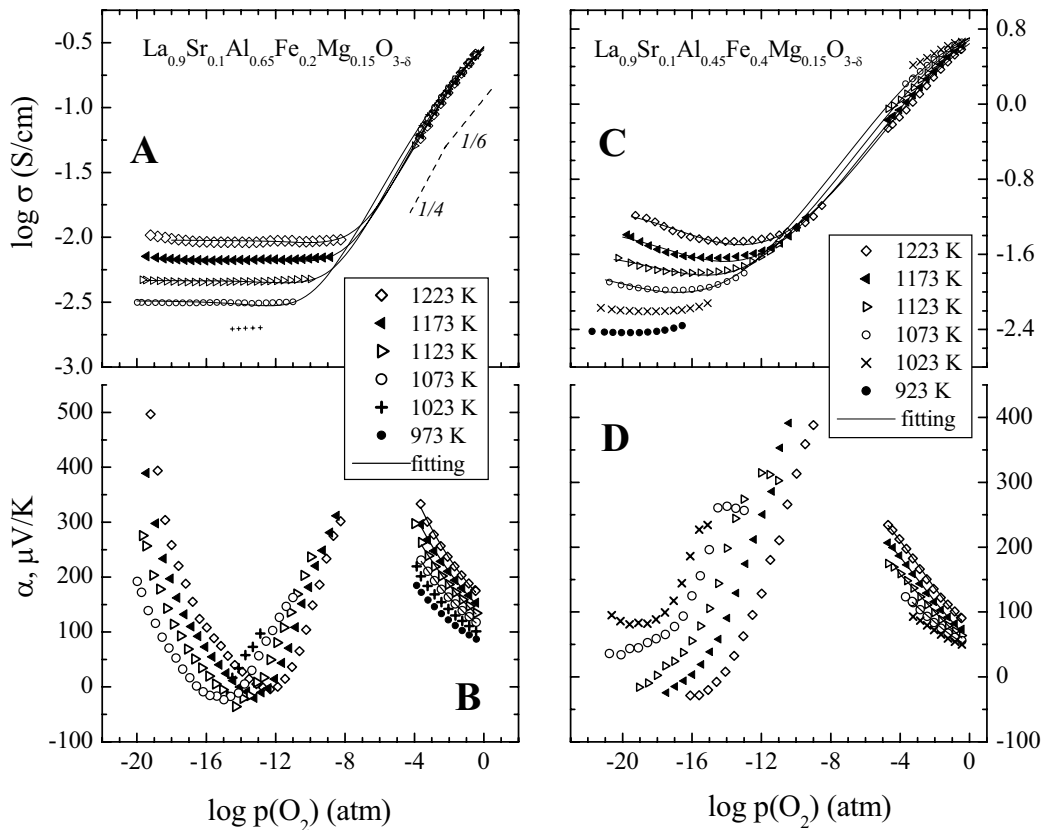


Fig.4.28. Oxygen partial pressure dependencies of the total conductivity (A,C) and Seebeck coefficient (B,D) of $\text{La}_{0.90}\text{Sr}_{0.10}\text{Al}_{0.65}\text{Fe}_{0.20}\text{Mg}_{0.15}\text{O}_{3-\delta}$ (A,B) and $\text{La}_{0.90}\text{Sr}_{0.10}\text{Al}_{0.45}\text{Fe}_{0.40}\text{Mg}_{0.15}\text{O}_{3-\delta}$ (C,D). Solid lines correspond to the best fit to experimental data (see text).

It should be separately mentioned that the total conductivity values corresponding to plateau in the σ - $p(\text{O}_2)$ dependencies (Fig.4.28, A and C) are 2-4 times higher than the oxygen ionic conductivity in air (Fig.4.27). As oxygen ion diffusion in perovskite oxides occurs via a vacancy mechanism [402], this tendency indicates a significant effect of oxygen chemical potential on the concentration of mobile ionic charge carriers when oxygen incorporation into the lattice under oxidizing conditions is reflected by the increase in p-type electronic conduction. On the contrary, under reducing conditions the plateau-like behavior of the total conductivity, particularly clearly observable for the 20 mol% Fe-doped aluminate (Fig.4.28A), supposes that the vacancy concentration becomes essentially $p(\text{O}_2)$ -independent. Further reduction, down to oxygen partial pressures below 10^{-17} - 10^{-14} atm, leads to an increasing role of n-type electronic conduction and probably also to the changes in oxygen transport behavior. Note that XRD analysis of $\text{La}_{0.90}\text{Sr}_{0.10}\text{Al}_{0.85-x}\text{Fe}_x\text{Mg}_{0.15}\text{O}_{3-\delta}$ ceramics, annealed at $p(\text{O}_2) = 10^{-20}$ - 10^{-18} atm and 1073-1223 K, showed no traces of phase decomposition; one example is illustrated by Inset of Fig.4.21.

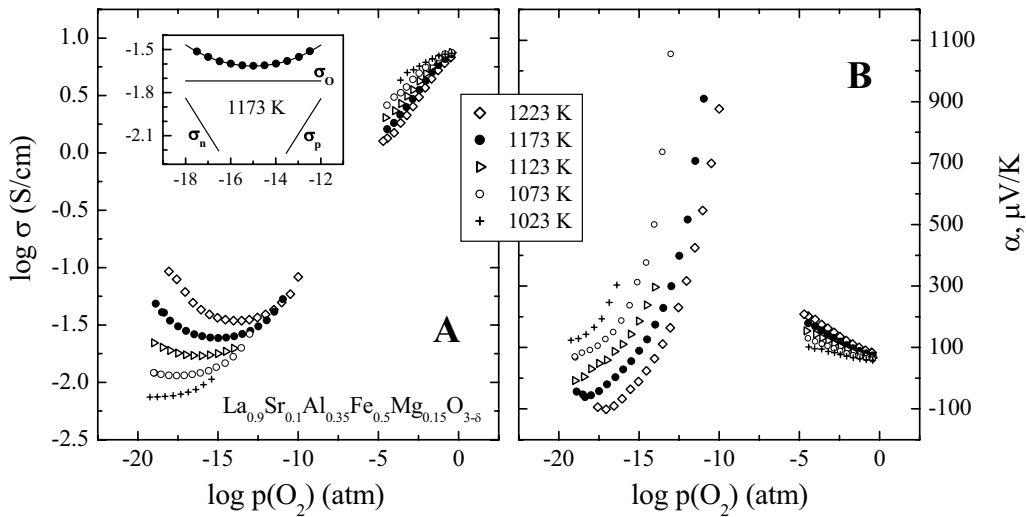


Fig.4.29. Oxygen partial pressure dependencies of the total conductivity (A) and Seebeck coefficient (B) of $\text{La}_{0.90}\text{Sr}_{0.10}\text{Al}_{0.35}\text{Fe}_{0.50}\text{Mg}_{0.15}\text{O}_{3-\delta}$. Inset shows an example of fitting at oxygen pressures close to the conductivity minimum (see text).

In order to assess the applicability of conventional point-defect models which were employed to describe transport in $\text{La}(\text{Sr})\text{FeO}_{3-\delta}$ ferrites [92,403], the defect formation processes is discussed on the examples of $\text{La}_{0.90}\text{Sr}_{0.10}\text{Al}_{0.65}\text{Fe}_{0.20}\text{Mg}_{0.15}\text{O}_{3-\delta}$ and $\text{La}_{0.90}\text{Sr}_{0.10}\text{Al}_{0.45}\text{Fe}_{0.40}\text{Mg}_{0.15}\text{O}_{3-\delta}$. In the former case, iron cations are in a relatively isolated state, being surrounded mainly by $\text{Al}^{3+}/\text{Mg}^{2+}$ in the perovskite lattice, while the concentrations of iron and aluminum in the B

sublattice are similar in the latter phase. The dependencies of total and partial conductivities on the oxygen pressure and temperature can be adequately analyzed assuming the electronic charge carrier localization on iron cations, with no essential association of the point defects. In this situation, the concentrations of Fe^{4+} and Fe^{2+} are equal to those of holes and electrons, respectively; these can be expressed via the equilibrium constants of iron disproportionation and oxygen exchange reactions (K_d and K_{ex}):

$$2\text{Fe}_{\text{Fe}}^{\times} \rightleftharpoons \text{Fe}'_{\text{Fe}} + \text{Fe}'_{\text{Fe}} \quad K_d = \frac{n \cdot p}{([\text{Fe}^{\text{total}}] - n - p)^2} = \exp\left(-\frac{\Delta H_d}{RT}\right) \quad (4.6)$$

$$2\text{Fe}'_{\text{Fe}} + \text{O}_o^{\times} \rightleftharpoons \frac{1}{2}\text{O}_2 + \text{V}_o'' + 2\text{Fe}_{\text{Fe}}^{\times} \quad (4.7a)$$

$$K_{ex} = \frac{p(\text{O}_2)^{1/2} \cdot \delta \cdot ([\text{Fe}^{\text{total}}] - n - p)^2}{(3 - \delta) \cdot p^2} = \exp\left(-\frac{\Delta H_{ex} - T \cdot \Delta S_{ex}}{RT}\right) \quad (4.7b)$$

where the Kröger-Vink notation [92,135,405,406] is used, all defect concentrations are related to one formula unit, and δ is the oxygen nonstoichiometry. The entropy of iron disproportionation process in Eq.(4.6) was found statistically insignificant and is hence skipped, in agreement with the results of Ref.[407]. The electroneutrality condition can be written as

$$2\delta + p = 0.25 + n \quad (4.8)$$

where 0.25 corresponds to the sum of Mg^{2+} and Sr^{2+} concentrations normalized to one formula unit.

The total conductivity is the sum of the partial ionic and p- and n-type electronic contributions:

$$\sigma = \sigma_o + \sigma_p + \sigma_n \quad (4.9)$$

The ionic conductivity can be expressed in terms of the random walk theory [406]:

$$\sigma_o = A_o^0 \cdot \delta \cdot (3 - \delta) \quad (4.10)$$

where A_o^0 is the T-dependent constant. Since the theoretical description of electronic transport may require complex relationships between the charge carrier concentration and the density of states, a series of alternative models were tested. In the simplest case, the partial electronic conductivity is assumed proportional to the charge carrier concentration, with $p(\text{O}_2)$ -independent mobility:

$$\sigma_p = B_p^0 \cdot p \quad (4.11a)$$

$$\sigma_n = B_n^0 \cdot n \quad (4.11b)$$

The A_o^0 and B_p^0 values can be expressed through the only parameter of K_{ex} from the results of the total conductivity and faradaic efficiency measurements in air (Figs.4.25-4.27), using Eqs.(4.7b), (4.8), (4.10) and (4.11), neglecting the concentration of electrons and substituting $p(\text{O}_2) = 0.21$ atm. From this system of equations, δ and p in air were obtained numerically for each temperature.

The model for non-linear regression analysis comprised Eqs.(4.6)-(4.11). Fitting of the data on total conductivity and transference numbers was performed using a procedure developed for the analysis of $p(\text{O}_2)$ - T - δ diagrams [407]. As the electronic transport in perovskite-type phases occurs via the B–O–B bonds [375], the conductivity may also be affected by the concentration of these bonds and, hence, of the oxygen ions. The most adequate results (Table 4.6) were obtained, however, using Eq.(4.11), while the other models yielded similar regression parameters with slightly higher errors. The quality of the separate fitting of data points for each temperature is illustrated by solid lines in Fig.4.28, A and C; fitting of all data vs. temperature and oxygen pressure simultaneously, gave essentially identical results. Due to a certain nonlinearity of the model, the weight of data points was settled using a function of reciprocal conductivity value. For the $\text{La}_{0.90}\text{Sr}_{0.10}\text{Al}_{0.65}\text{Fe}_{0.20}\text{Mg}_{0.15}\text{O}_{3-\delta}$ composition where the total iron content is relatively small, the number of data points under reducing conditions when the electron transport appears noticeable, is quite limited. This makes it impossible to analyze the behavior of n-type electronic conduction. The calculated values of electron-hole and oxygen vacancy concentrations in air are in a good agreement with the Mössbauer spectroscopy data (Fig.4.30 and Table A2.1 in Appendix 2).

Table 4.6

Regression parameters of the $\sigma(T, p\text{O}_2)$ dependence of $\text{La}_{0.90}\text{Sr}_{0.10}\text{Al}_{0.85-x}\text{Fe}_x\text{Mg}_{0.15}\text{O}_{3-\delta}$, for models with different relationships between the partial electronic conductivities and charge carrier concentration

x	T, K	Adjusted correlation coefficient		$\ln K_{\text{ex}}$	$\ln K_{\text{d}}$	N
		Conductivity	Thermopower			
0.2	1223	0.99981	0.998	-2.29±0.04	-4.2±0.5	0.415±0.009
	1173	0.99992	0.998	-2.65±0.03	-4.3±0.4	0.376±0.007
	1123	0.99995	0.998	-3.00±0.02	-4.6±0.6	0.340±0.007
	1073	0.99950	0.999	-3.68±0.08		0.339±0.005
0.4	1223	0.99949	0.998	-1.82±0.03	-10.4±0.7	0.267±0.004
	1173	0.99978	0.998	-2.21±0.02	-10.7±0.5	0.247±0.004
	1123	0.99984	0.998	-2.98±0.02		0.277±0.004
	1073	0.99986	0.998	-3.90±0.02		0.313±0.004

The mobilities of electron holes and oxygen vacancies (μ_p and μ_v) given in Fig.4.31 were evaluated from Eq.(4.3) with $N_{\text{fu}} = 6$. Both μ_p and μ_v follow an Arrhenius dependence on temperature. While for the ion migration this trend is usual, the temperature-activated character of hole mobility ($E_a = 30\text{-}32$ kJ/mol) unambiguously shows a small-polaron conduction mechanism. The values of μ_p , $(1.1\text{-}14.5) \times 10^{-3} \text{ cm}^2 \times \text{V}^{-1} \times \text{s}^{-1}$ at 1073-1223 K, are considerably lower than for $\text{La}_{0.9}\text{Sr}_{0.1}\text{FeO}_{3-\delta}$ [409], due to the lower concentration of B sites and Fe-O-Fe bonds participating in

the electronic transport in $\text{La}_{0.90}\text{Sr}_{0.10}\text{Al}_{0.85-x}\text{Fe}_x\text{Mg}_{0.15}\text{O}_{3-\delta}$ lattice. Moreover, these values are below the characteristic threshold of about $0.1 \text{ cm}^2 \times \text{V}^{-1} \times \text{s}^{-1}$, which is believed to be a rough criterion to separate polaron and broadband conductors. In addition, the 3+ and 4+ states of iron cations can be clearly distinguished in the Mössbauer spectra of $\text{La}_{0.90}\text{Sr}_{0.10}\text{Al}_{0.85-x}\text{Fe}_x\text{Mg}_{0.15}\text{O}_{3-\delta}$ ($x \leq 0.40$) (see Appendix 2) suggesting a hampered charge delocalization. This seems to result from relatively high concentrations of Al^{3+} and Mg^{2+} in the B sites. The mobility of n-type charge carriers is substantially lower than that of electron-holes (Fig.4.32), which is usual for the ferrite materials [212,409].

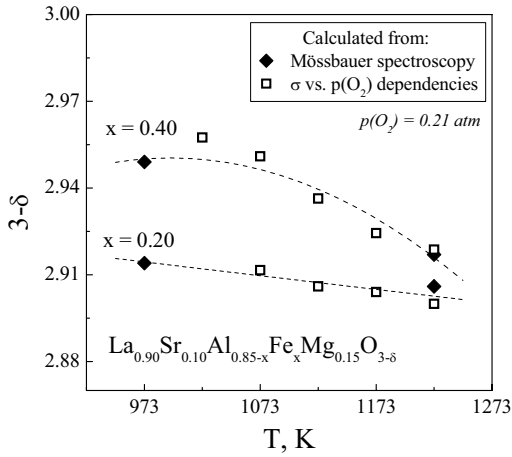


Fig.4.30. Temperature dependence of the oxygen content in $\text{La}_{0.90}\text{Sr}_{0.10}\text{Al}_{0.85-x}\text{Fe}_x\text{Mg}_{0.15}\text{O}_{3-\delta}$ in air.

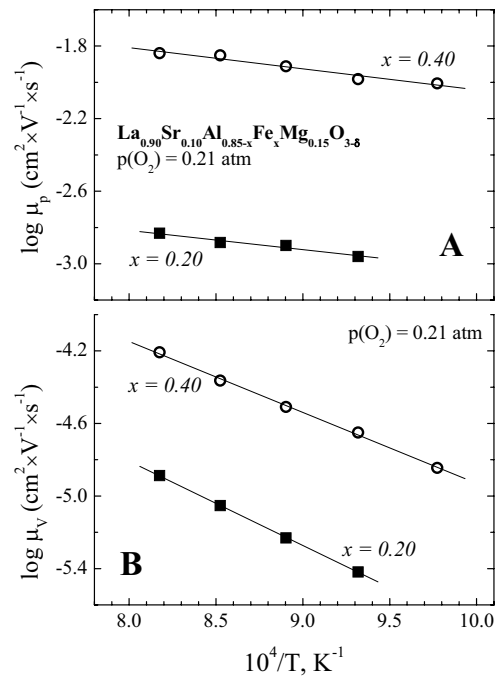


Fig.4.31. Temperature dependencies of electron-hole (A) and oxygen vacancy (B) mobility of $\text{La}_{0.90}\text{Sr}_{0.10}\text{Al}_{0.85-x}\text{Fe}_x\text{Mg}_{0.15}\text{O}_{3-\delta}$ in air.

4.2.4. Partial ionic and electronic conductivities

Fig.4.32 shows the calculated defect concentrations and partial conductivities of $\text{La}_{0.90}\text{Sr}_{0.10}\text{Al}_{0.85-x}\text{Fe}_x\text{Mg}_{0.15}\text{O}_{3-\delta}$ as functions of oxygen pressure. Under moderately reducing conditions, the observed tendencies are close to classical [92,406]; namely, the ionic conduction is almost constant and the partial electronic conductivities are proportional to $p(\text{O}_2)^{\pm 1/4}$. This situation is changed in oxidizing atmospheres and at $p(\text{O}_2) < 10^{-15}$ atm, when the average oxidation state of iron cations is far from 3+ and the chemical potential of oxygen vacancies becomes substantially

$p(\text{O}_2)$ -dependent. Nevertheless, as confirmed by the Mössbauer spectroscopy and by the hole mobility calculations, no delocalization of p-type electronic charge carriers is observed in $\text{La}_{0.90}\text{Sr}_{0.10}\text{Al}_{0.45}\text{Fe}_{0.40}\text{Mg}_{0.15}\text{O}_{3-\delta}$ within all studied $p(\text{O}_2)$ range.

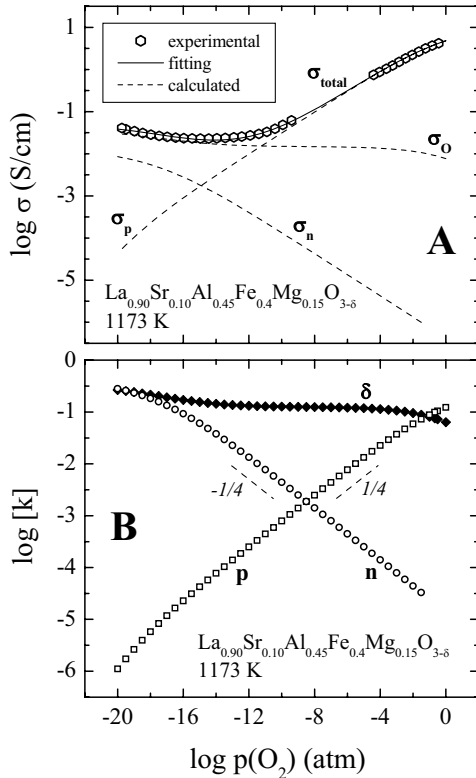


Fig.4.32 Oxygen partial pressure dependence of the total, oxygen ionic, and p- and n-type electronic conductivities of $\text{La}_{0.90}\text{Sr}_{0.10}\text{Al}_{0.45}\text{Fe}_{0.40}\text{Mg}_{0.15}\text{O}_{3-\delta}$ (A) and the corresponding defect concentrations related to one formula unit (B) at 1173 K. Solid line in (A) shows the fitting results (see text).

The proposed model suggests a change in the slope of logarithmic σ_p vs. $p(\text{O}_2)$ dependencies from $1/4$ under reducing conditions, where the chemical potential of oxygen vacancies is essentially independent of the oxygen chemical potential, down to $1/6$ at oxygen pressures close to atmospheric, where the vacancy chemical potential decreases with increasing $p(\text{O}_2)$. The latter situation is associated with decreasing ionic conductivity when $p(\text{O}_2)$ increases, due to a sharp decrease in the vacancy concentration (Fig.4.32). Similar trends in ionic conduction are known for other Fe-containing perovskites where most B sites are occupied with iron [216,408]. No degradation of ionic conduction on reduction, which may appear due to the formation of vacancy-ordered microdomains in ferrites, was observed in this work, probably owing to moderate concentrations of oxygen vacancies and iron cations.

The ionic conductivity exhibits almost linear dependence on oxygen deficiency, suggesting that the oxygen transport is limited by the vacancy concentration (Fig.4.33). The latter tendency well corresponds to the recent data on $\text{La}_{0.3}\text{Sr}_{0.7}(\text{Fe},\text{Al})\text{O}_{3-\delta}$ system [408], whereas the ionic

transport in Ga-substituted ferrites, $\text{La}_{0.3}\text{Sr}_{0.7}(\text{Fe,Ga})\text{O}_{3-\delta}$, is essentially independent of $p(\text{O}_2)$ and δ [216]. The activation energy for vacancy migration, 84-98 kJ/mol, is similar to that of $\text{La}_{0.9}\text{Sr}_{0.1}\text{Al}_{0.9}\text{Mg}_{0.1}\text{O}_{3-\delta}$ solid electrolyte without iron additions (Table 4.5).

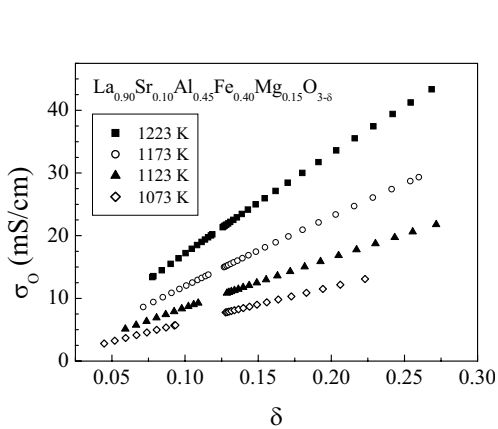


Fig.4.33. Oxygen ionic conductivity of $\text{La}_{0.90}\text{Sr}_{0.10}\text{Al}_{0.45}\text{Fe}_{0.40}\text{Mg}_{0.15}\text{O}_{3-\delta}$ as a function of the oxygen nonstoichiometry.

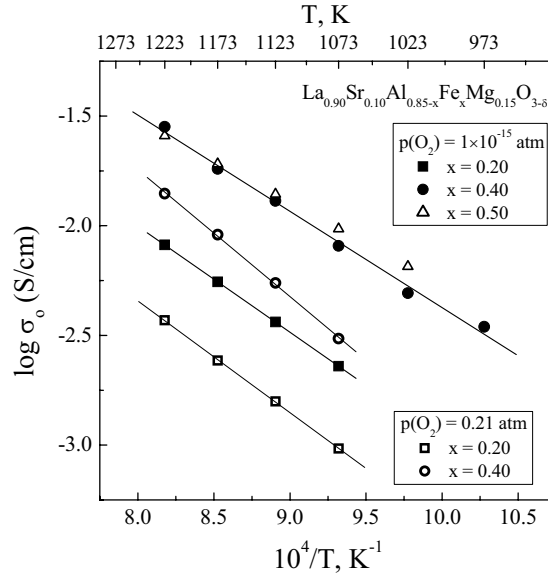


Fig.4.34. Temperature dependencies of the oxygen ionic conductivity of $\text{La}_{0.90}\text{Sr}_{0.10}\text{Al}_{0.85-x}\text{Fe}_x\text{Mg}_{0.15}\text{O}_{3-\delta}$ under oxidizing and reducing conditions.

Fig.4.34 compares the values of the partial ionic conductivity in air and under reducing conditions; the corresponding activation energies (E_a) are listed in Table 4.5. Since in the vicinity of minimum in the isothermal $\log \sigma - \log p(\text{O}_2)$ dependence, the oxygen ionic conductivity can be assumed constant and the slopes of partial electronic contributions tend to $\pm 1/4$, the data for $\text{La}_{0.90}\text{Sr}_{0.10}\text{Al}_{0.35}\text{Fe}_{0.50}\text{Mg}_{0.15}\text{O}_{3-\delta}$ presented in Fig.4.29A was fitted to a simplified model

$$\sigma = \sigma_{\text{O}} + \sigma_{\text{p}}^0 \cdot p(\text{O}_2)^{1/4} + \sigma_{\text{n}}^0 \cdot p(\text{O}_2)^{-1/4} \quad (4.12)$$

where σ_{p}^0 and σ_{n}^0 are the p- and n-type conductivities at unit oxygen partial pressure. One example of such fit is illustrated by Inset of Fig.4.29A; the adjusted correlation coefficients were higher than 0.999. The level of ionic conductivity at reduced $p(\text{O}_2)$ increases and its activation energy decreases with iron concentration due to the higher both concentration and mobility of oxygen vacancies. The σ_{O} values of 40 and 50 mol% doped $\text{La}_{0.90}\text{Sr}_{0.10}\text{Al}_{0.85-x}\text{Fe}_x\text{Mg}_{0.15}\text{O}_{3-\delta}$ become however similar in the high-temperature range. Due to decreasing contribution of the vacancy formation enthalpy, reducing $p(\text{O}_2)$ leads to a decrease in E_a values from 107-120 down to 99-102

kJ/mol. The activation energy becomes thus closer to the migration energy estimated from the $\sigma_o/[V_o^{\bullet\bullet}]$ ratio (Table 4.5). The vacancy formation enthalpy contribution under oxidizing conditions is expected to increase when the total iron content in the perovskite lattice and, thus, the absolute concentration of Fe^{4+} cations increases. As a result, the activation energy for ionic conductivity of $La_{0.90}Sr_{0.10}Al_{0.45}Fe_{0.40}Mg_{0.15}O_{3-\delta}$ in air is higher than that of $La_{0.90}Sr_{0.10}Al_{0.65}Fe_{0.20}Mg_{0.15}O_{3-\delta}$ (Table 4.5); a similar behavior is observed in $La_{1-x}Sr_xFeO_{3-\delta}$ ($x=0.10-0.25$) where the vacancy concentration is relatively low and Sr additions are partly compensated by Fe^{4+} formation [212].

4.2.5. Thermopower behavior and comments on the hole transport mechanism

The low level of hole mobility and its temperature-activated character both suggest a small-polaron mechanism for the p-type electronic conduction. At the same time, one should mention that these mechanisms may be more complex than simple hopping of the holes between Fe^{4+} and Fe^{3+} cations, as suggested in Ref.[409]. The adequacy of defect model used in this work implies that mobility of the p-type electronic charge carriers is essentially concentration-independent. At oxygen partial pressures close to atmospheric, the concentration of holes is comparable to the total iron content (Fig.4.32); in this situation one could expect a non-negligible effect of iron oxidation state on the oxygen incorporation reaction and hole migration processes if the conduction would occur due to hopping of strongly localized holes. In this case, the Seebeck coefficient of holes can be expressed by Eq.(4.2). Alternatively, if the electronic transport occurs via the band mechanism with concentration-independent density of states, the Eq.(3.4) is applied.

The ionic thermopower is determined by equilibrium at the electrodes maintained owing to the redox reaction [135]:



The oxygen ion Seebeck coefficient is then expressed as:

$$\alpha_{O^{2-}} = -\frac{t_o}{2e} \left(\frac{1}{2} \frac{d\mu_{O_2}}{dT} - \frac{\partial\mu_{O^{2-}}}{\partial T} + \frac{Q^0}{T} \right) \quad (4.14)$$

where Q^0 is the transported heat of oxygen ions. Taking into account the experiments for chemical potentials of molecular oxygen in the gas phase and of the oxygen ions in a mixed conductor, one may obtain [135]:

$$\alpha_{O^{2-}} = -t_o \cdot \frac{k}{e} \cdot \left(\frac{1}{2} \cdot \ln \frac{\delta}{3-\delta} + \frac{5}{8} \cdot \ln T + \frac{1}{4} \ln p(O_2) + \frac{Q^0}{2kT} + C \right) \quad (4.15)$$

where all constants are combined into one constant C.

Under reducing conditions, the change of equilibrium at the electrodes causes a shift of the heterogeneous part of the ionic thermopower, equivalent to a stepwise decrease of C [392]. For the experimental setup used in this work, this effect cannot be precisely accounted for due to possible presence of H_2/H_2O impurities in the CO/CO_2 atmosphere where only the resultant oxygen chemical potential is controlled. For oxidizing and moderately reducing atmospheres when the n-type electronic conduction is negligible, the experimental data on Seebeck coefficient of $La_{0.90}Sr_{0.10}Al_{0.85-x}Fe_xMg_{0.15}O_{3-\delta}$ ($x = 0.2$ and 0.4) as a function of $p(O_2)$ were fitted using a model:

$$\alpha = t_p \cdot \frac{k}{e} \cdot \ln \frac{N}{p} - t_o \cdot \frac{k}{2e} \cdot \left(\ln \frac{\delta}{3-\delta} + \frac{1}{2} \cdot \ln p(O_2) + C' \right) \quad (4.16)$$

where t_p is the p-type electronic transport number and C' is the constant which comprises C and the all terms in Eq.(4.15) depending only on temperature. The t_o and t_p values for each data point were calculated from results of the total conductivity fitting, while the nonlinear regression parameters included N and C' . Note that N may comprise a coefficient responsible for blocking a part of iron cations for the hole transfer [215].

Note that Eq.(4.2) was found inappropriate for the analysis of hole contribution to thermopower; Eq.(4.16), implying the p-independent density of states, was therefore applied. Indeed, such a model occurred to be sufficiently adequate (Table 4.6, Fig.4.28 B and D). The observed behavior can be explained in terms of the hypotheses formulated by Goodenough [375], who supposed a significant role of $O:2p^6$ valence band containing a large $O-2p_\sigma$ component in $LaFeO_3$ -based phases. Consequently, the holes in perovskite ferrites may prefer to occupy molecular orbitals (MOs) rather than a localized e orbital; trapping of two holes in MOs of a $Fe(V)O_6$ complex may also be assumed [375]. The calculated N values varying in the rather narrow range, 0.27-0.42 per one perovskite unit formula (Table 4.6), are practically independent of the composition and temperature. Therefore, sites available for holes hopping may probably be related to the total concentration of B sites rather than $[Fe^{3+}]$.

In summary, the redox behavior and transport properties of $La_{0.90}Sr_{0.10}Al_{0.85-x}Fe_xMg_{0.15}O_{3-\delta}$ ($x = 0.2 - 0.5$) can be adequately described by equilibrium processes of oxygen intercalation and iron disproportionation, with the thermodynamic functions independent of defect concentrations. Substantial level of oxygen ionic conductivity and relatively high stability allows the use of $La(Fe,Al)O_3$ -based mixed conductors for the anode applications.

4.3. Fluorite-related $TbMO_{4-\delta}$ ($M = Zr, Hf$)

As mentioned in Chapter 1.3.1, numerous fluorite- and pyrochlore-type oxide materials possess a significant oxygen ionic conductivity and thus can be used as the anode components. Among the pyrochlore systems, a high ionic conductivity was observed for $Gd_2Zr_2O_7$, $Tb_2Zr_2O_7$ and $Gd_2Ti_2O_7$ based phases [54,410]; the incorporation of variable-valence $Tb^{3+/4+}$ may play a positive role in the electrochemical kinetics. In the present work, $TbZrO_{4-\delta}$ and $TbHfO_{4-\delta}$ prepared via mechanically-activated synthesis were studied. This synthesis method, resulting in nano- and submicron-scale crystallites, often leads to enhanced defect concentrations, formation of metastable disordered phases and, subsequently, to considerable variations in the ionic and electronic transport properties (e.g. [33,352]). At the same time, theoretical prediction of such changes is difficult due to the complex nature of transport processes occurring at grain boundaries and in nanosized grains. Since $TbZrO_{4-\delta}$ and $TbHfO_{4-\delta}$ both possess A/B cation radius ratio close to the “pyrochlore-fluorite” boundary in the systems $Ln_2M_2O_{7+\delta}$ ($M = Zr, Hf$; Ln is rare-earth cation), mechanically-activated synthesis may have a strong effect on the structure and phase composition.

4.3.1. Structure and microstructure

The final structure refinement plots of $TbHfO_{4-\delta}$ and $TbZrO_{4-\delta}$ are given in Fig.4.35. For both compositions, Rietveld analysis was performed presuming two possible crystal structures, namely pyrochlore $Tb_2M_2O_{7+\delta}$ (space group $Fd\bar{3}m$, No.227) and fluorite $TbMO_{4-\delta}$ (space group $Fm\bar{3}m$, No.225). The pyrochlore lattice is distinguished from fluorite by ordering of the cations in $16d$ (1/2,1/2,1/2) and $16c$ (0,0,0) sites, and by the displacement of $48f$ oxygen. In XRD patterns this should be reflected by additional Bragg peaks, particularly (311) (for CuK_α radiation $2\theta \approx 28.5^\circ$) and (331) ($2\theta \approx 37.5^\circ$). These lines are not observed in the XRD patterns (Fig.4.35). Therefore, if considering XRD data only, the structure of both studied compounds should be described as cubic fluorite; Table 4.7 lists the unit cell parameters and agreement factors for the $Fm\bar{3}m$ space group. The lattice parameters of $TbHfO_{4-\delta}$ and $TbZrO_{4-\delta}$ are very similar, as a result of the similar radii of Zr^{4+} and Hf^{4+} cations [60]. One should separately note that the XRD results cannot exclude local ordering [410-412]. Moreover, in the case of $TbHfO_{4-\delta}$, the intensity of (311) and (331) Bragg peaks is expected to be very low due to only a small difference in the atomic scattering factors of hafnium and terbium; these reflections could hence be missed. As an attempt to reveal possible local ordering, selected area electron diffraction (SAED) and IR absorption studies were performed.

Table 4.7

Properties of TbHfO_{4-δ} and TbZrO_{4-δ} ceramics

Composition	Unit cell parameter *		Grain size, nm	Average linear thermal expansion coefficient		Activation energy for the total conductivity	
	S.G.	a, Å		T, K	$\bar{\alpha} \times 10^6, K^{-1}$	T, K	E _a , kJ/mol
TbHfO _{4-δ}	Fm $\bar{3}$ m	5.222(9)	50-150	600-1200	11.53±0.01	873-1123	44±1
				1200-1420	18.37±0.08	423-723	57±2
TbZrO _{4-δ}	Fm $\bar{3}$ m	5.221(1)	70-200	600-1200	12.36±0.02	773-1123	36±1
				1200-1420	20.28±0.07	373-723	49±1

* R_p, P_{wp} and χ^2 factors are equal to 7.15, 8.59 and 5.32 for Tb₂Hf₂O_{7+δ}, and 7.56, 6.82 and 2.68 for TbZrO_{4-δ}, respectively.

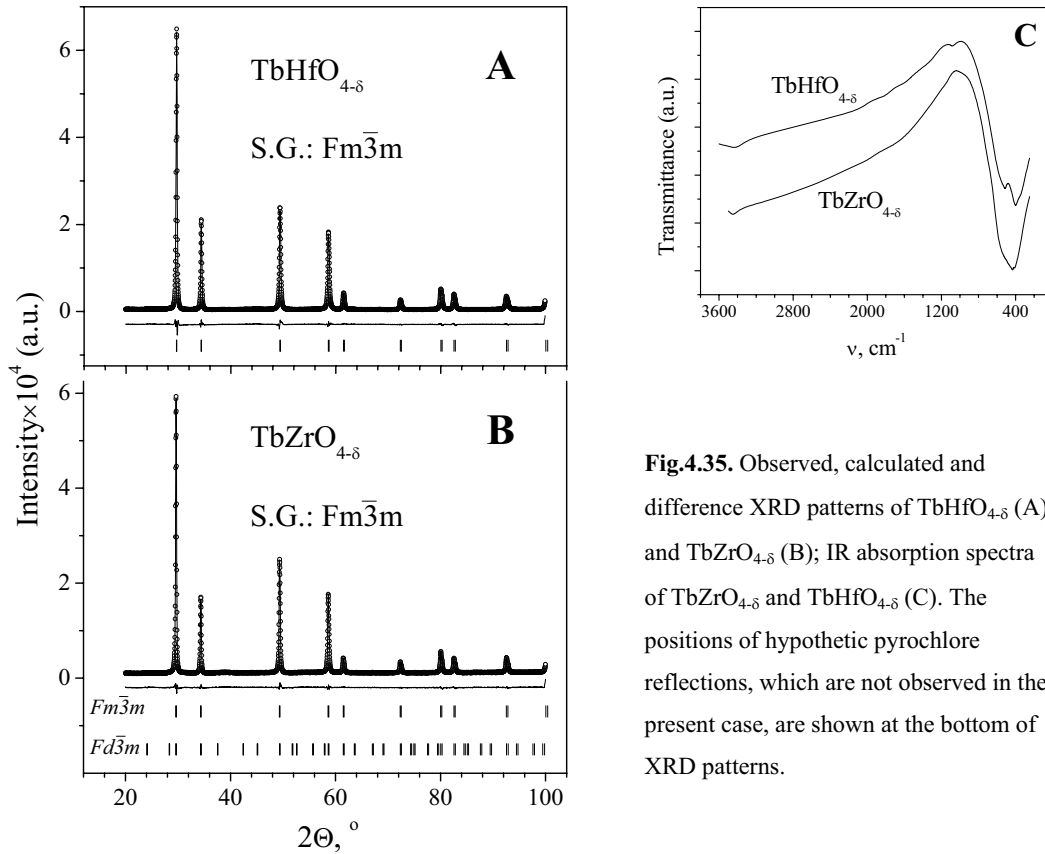


Fig.4.35. Observed, calculated and difference XRD patterns of TbHfO_{4-δ} (A) and TbZrO_{4-δ} (B); IR absorption spectra of TbZrO_{4-δ} and TbHfO_{4-δ} (C). The positions of hypothetic pyrochlore reflections, which are not observed in the present case, are shown at the bottom of XRD patterns.

Representative examples of the SAED patterns of TbHfO_{4-δ} and TbZrO_{4-δ} are shown in Fig.4.36, A and B. All observed reflections are consistent with fluorite structure; no superlattice spots or diffuse scattering characteristic of locally-ordered (Tb,Gd)₂Zr₂O₇ [412] can be seen in the electron diffraction patterns in both cases. At the same time, the IR spectrum of TbHfO_{4-δ} exhibits absorption bands at 400 and 510 cm⁻¹ (Fig.4.35C), typical for Ln₂Hf₂O₇ pyrochlore structure [413].

Such behavior indicates a partial pyrochlore-type ordering in terbium hafnate ceramics. The fact, that ordered microdomains cannot be distinguished in the course of standard TEM analysis, may be explained if their volume fraction is small and/or if their primary location is around grain boundaries. Also, one should take into account the very similar values of the atomic scattering factors of Hf and Tb, which should lead to weakening of possible superlattice reflections. In these conditions, detailed HRTEM studies are necessary to resolve microdomain formation.

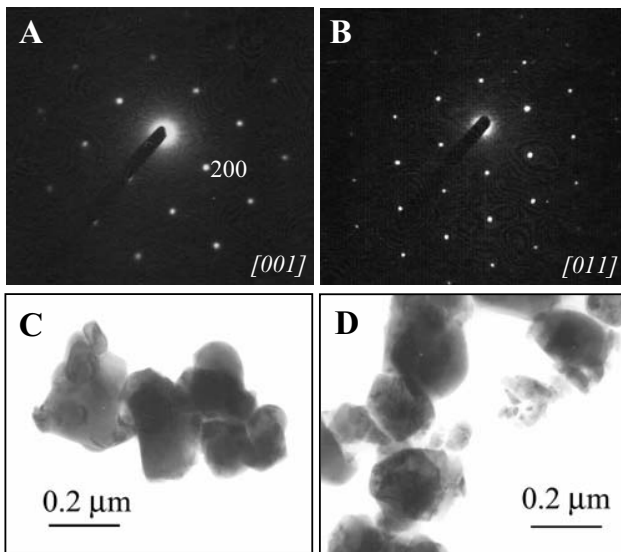


Fig.4.36. Selected area electron diffraction patterns of $\text{TbHfO}_{4.8}$ along [001] zone axis (A), and $\text{TbZrO}_{4.8}$ along [011] zone axis (B), and the bright-field TEM images of $\text{TbHfO}_{4.8}$ (C) and $\text{TbZrO}_{4.8}$ (D). SAED patterns can be indexed for the cubic fluorite cell.

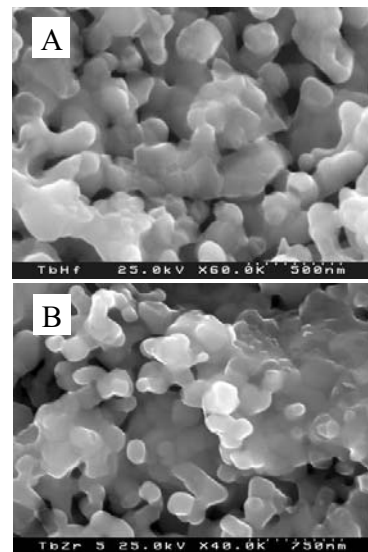


Fig.4.37. SEM micrographs of fractured ceramic samples: $\text{TbHfO}_{4.8}$ (A) and $\text{TbZrO}_{4.8}$ (B).

For $\text{TbZrO}_{4.8}$, no absorption band near 510 cm^{-1} is observed in the IR spectra (Fig.4.35C), in agreement with X-ray and electron diffraction data. Therefore, the structure of terbium zirconate can be identified as disordered fluorite-type. This may be considered as contradicting to the data of van Dijk et al. [410,412] who reported a short-range ordering in $\text{TbZrO}_{4.8}$ ceramics with micron-scale grain size, prepared using citrate method and sintered at 1823 K. Such a difference results, most probably, from the microstructural features of terbium zirconate obtained via mechanically-activated synthesis, where the grains are considerably smaller and a greater concentration of extended defects, such as dislocations, may be expected. In addition, the sintering conditions used in the present work were quite different from those reported by van Dijk et al. [410,412]. For instance, due to the strong effect of submicron grain size on the properties of ceramic materials, the use of sol-gel or organometallic-precursor techniques often leads to apparent stabilization of cubic

fluorite $Zr(Ln)O_{2-\delta}$ phases, the composition of which corresponds to multiphase domains in equilibrium phase diagrams, at temperatures below 1300-1350 K [33]. Another necessary comment is that the different behavior of $TbHfO_{4-\delta}$ and $TbZrO_{4-\delta}$ is in agreement with literature data [33,41] showing a higher thermodynamic stability of HfO_2 -containing pyrochlores with respect to ZrO_2 -based compounds, while the stabilized fluorite phases in HfO_2 - and ZrO_2 -based systems show the opposite tendency.

Typical SEM micrographs of fractured $TbMO_{4-\delta}$ samples are shown in Fig.4.37; Fig.4.36 presents examples of bright-field TEM images. The grain size distribution in both materials is quite uniform; no inhomogeneities in the cation distribution between grains and grain boundaries were detected by EDS analysis. The grain size, which is slightly smaller for terbium hafnate ceramics, varies from 50 to 200 nm. The low limit of this range, 50 nm, is close to crystallite size estimates from the XRD data, 46.4-50.2 nm. In addition, TEM studies indicated no traces of liquid phase or other grain-boundary phenomena, in agreement with the impedance spectroscopy data discussed below.

4.3.2. Thermal expansion

Dilatometric studies of $TbMO_{4-\delta}$ ceramics showed that heating up to temperatures, comparable to the temperature of final firing, leads to continuing shrinkage processes. One example illustrating such behavior is presented as Inset in Fig.4.38. The shrinkage starts at 1440-1460 K for $TbHfO_{4-\delta}$ and 1470-1490 K for $TbZrO_{4-\delta}$. This suggests that, although the conductivity degradation is observed at 1223 K, grain growth becomes extensive at significantly higher temperatures.

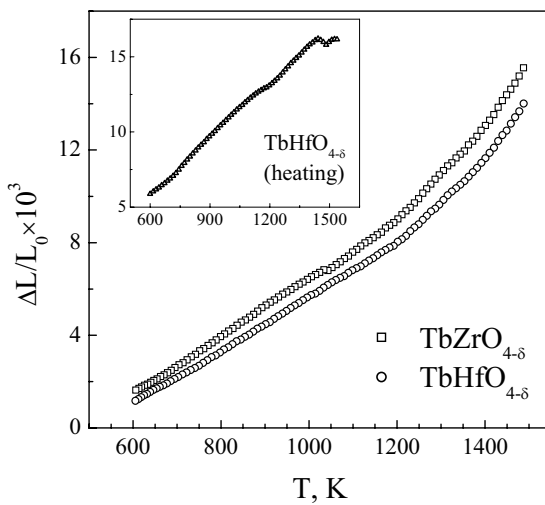


Fig.4.38. Dilatometric curves of $TbZrO_{4-\delta}$ and $TbHfO_{4-\delta}$ ceramics on cooling in air. Inset shows the curve of $TbHfO_{4-\delta}$ on heating up to 1600 K, illustrating the shrinkage behavior.

In the intermediate temperature range, 1200-1400 K, the dilatometric curves of TbMO_{4-8} show a considerable nonlinearity, probably associated with starting microstructural changes and oxygen losses from the lattice on heating (Fig.4.38). At lower temperatures, the dilatometric curves are approximately linear, with the average thermal expansion coefficients of $(11.5-12.5)\times 10^{-6} \text{ K}^{-1}$ (Table 4.7). These values are close to literature data on $\text{Y}_2(\text{Ti,Zr})_2\text{O}_7$ [414] and $\text{Ln}_2\text{Hf}_2\text{O}_7$ [41] pyrochlores, being slightly higher than TECs of stabilized zirconia and $\text{Gd}_2\text{Ti}_2\text{O}_7$ (Table 1.3).

4.3.3. Ionic and electron-hole conductivities under oxidizing conditions

Typical impedance spectra of TbHfO_{4-8} and TbZrO_{4-8} ceramics are presented in Figs.4.39 and 4.40, correspondingly. In all cases, no grain-boundary contribution was detected even at low temperatures (for example, inset in Fig.4.39A). The spectra collected in air consist of a bulk arc and a small electrode tail, the latter decreasing with reducing temperature. Such a behavior indicates that the p-type electronic contribution to the total conductivity is dominant in oxidizing atmospheres and possesses an activation energy lower than that for ionic conduction. Indeed, the oxygen ion transference numbers measured by the modified emf method under oxygen/air gradient, vary in the range 0.08-0.26 at 873-1123 K and increase with temperature (Table 4.8). A qualitatively similar trend, namely a higher activation energy for the ionic transport compared to p-type electronic, is characteristic of a number of fluorite- and pyrochlore-type phases containing variable-valence cations [33,41,54]. Fig.4.41 illustrates experimental data of the dependencies expressed by Eq.(2.12); no essential deviations from the linearity is observed, thus validating applicability of the modified emf technique.

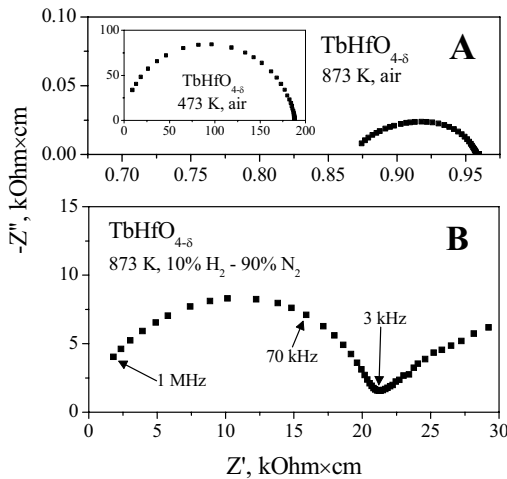


Fig.4.39. Impedance spectra of TbHfO_{4-8} ceramics in air (A) and in a flow of 10% H_2 -90% N_2 mixture (B).

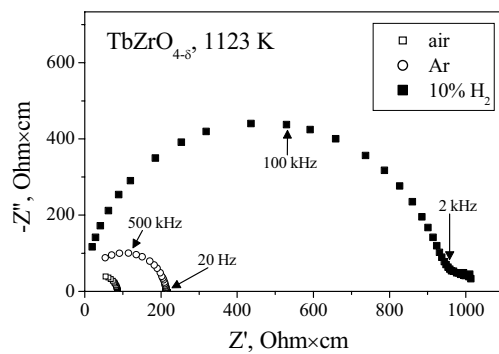


Fig.4.40. Impedance spectra of TbZrO_{4-8} ceramics in various atmospheres at 1123 K.

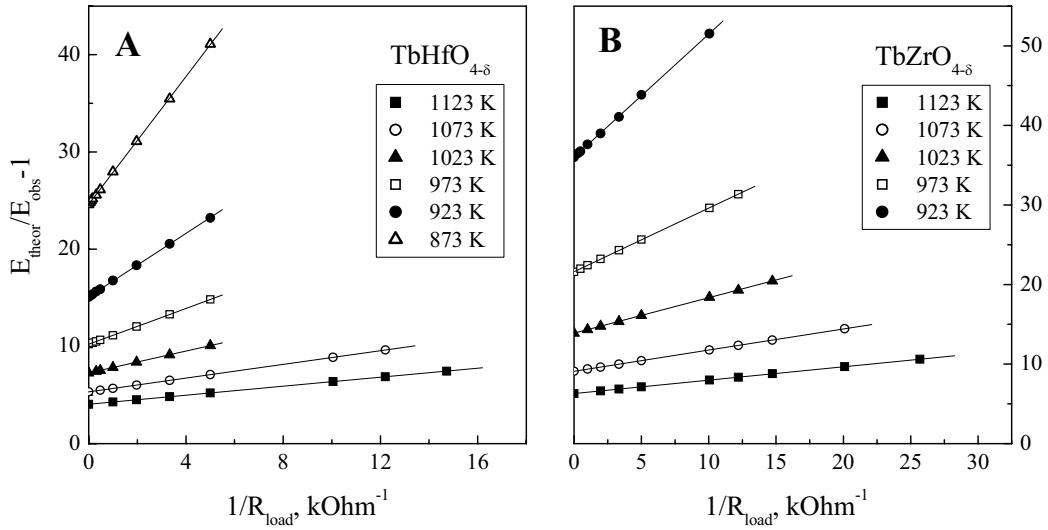


Fig.4.41. Measured e.m.f. of the cell Fig.2.2 (right) as a function of reciprocal external load resistance, for $\text{TbHfO}_{4-\delta}$ (A) and $\text{TbZrO}_{4-\delta}$ (B) ceramics under O_2/air gradient. Solid lines correspond to the fitting results using Eq.(2.12) as a regression model.

Table 4.8

Parameters of oxygen ion transport

Composition	Ion transference number under oxygen/air gradient		Activation energy for ionic and electronic conductivities, kJ/mol	
	T, K	t_o	$E_a(\sigma_o)$	$E_a(\sigma_p)$
$\text{TbHfO}_{4-\delta}$ (873 – 1123) K	1123	0.26	82±7	40±2
	1073	0.21		
	1023	0.17		
	973	0.14		
	923	0.11		
	873	0.09		
$\text{TbZrO}_{4-\delta}$ (923 – 1123) K	1123	0.25	83±9	29±2
	1073	0.20		
	1023	0.14		
	973	0.12		
	923	0.08		

Due to the cation ordering processes in $\text{TbHfO}_{4-\delta}$, the partial ionic and p-type electronic conductivities of terbium hafnate are both lower than those of $\text{TbZrO}_{4-\delta}$ (Fig.4.42). Again, this is an excellent agreement with literature data [33,41], showing that the pyrochlore-fluorite transition is accompanied with increasing ionic conduction, and that the transport properties of HfO_2 -based

materials are usually worse compared to ZrO₂-based ceramics. The latter trend results from a greater tendency to local ordering in hafnates [41]. Respectively, at 673-1123 K the total conductivity of TbZrO_{4-δ} is 3-5 times higher than that of TbHfO_{4-δ}, whereas the activation energy values are similar for both materials (Inset in Fig.4.42). Notice that changes in the slope of the Arrhenius curves at 600-700 K are related to oxygen losses on heating, which leads to decreasing p-type charge carrier concentration [415].

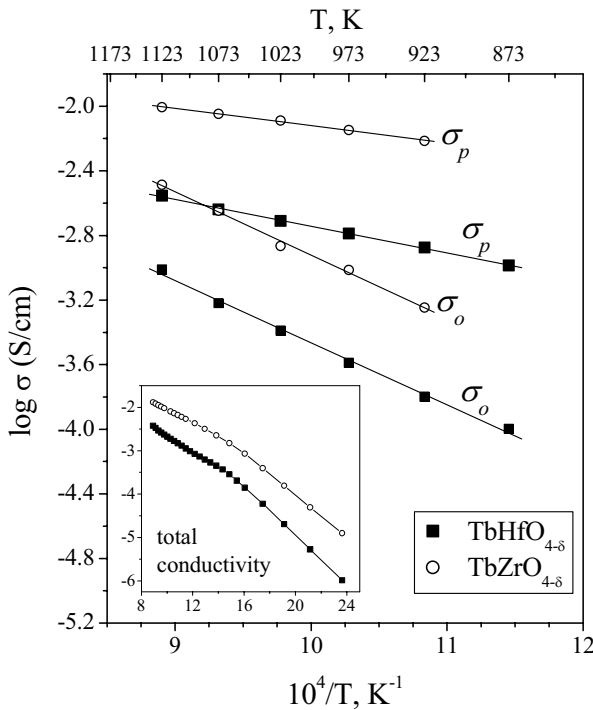


Fig.4.42. Temperature dependence of oxygen ionic and p-type electronic conductivity of TbMO_{4-δ} ceramics in air. Inset shows temperature dependence of the total conductivity.

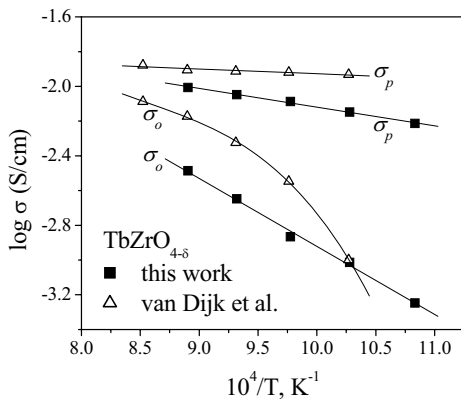


Fig.4.43. Comparison of the ionic and p-type electronic conductivities of submicron-crystalline TbZrO_{4-δ} ceramics with literature data [415] on material with micron-scale grains. In both cases the partial conductivities are calculated from the results on transference numbers and total conductivity.

Finally, Fig.4.43 compares the transport properties of TbZrO_{4-δ} ceramics with submicron grain size, prepared in this work, with data on the same material where the grains were 10-20 times larger [415]. In the latter case, both ionic and electron-hole conductivities are slightly higher. Such a difference seems quite surprising as the IR and SAED studies of TbZrO_{4-δ}, prepared via mechanical activation, showed no local ordering and the impedance spectroscopy indicated that the grain-boundary resistance is insignificant (Fig.4.40). On the contrary, SAED patterns of terbium zirconate studied by van Dijk et al. [410,412] clearly demonstrate short-range ordering phenomena; a considerable grain-boundary contribution is also observed in the impedance spectra [415]. The observed behavior could be explained by a greater concentration of extended linear defects (e.g. dislocations) trapping charge carriers in the ceramics prepared using mechanically-activated synthesis. HRTEM studies are necessary in order to verify such an assumption. Note that the impedance spectroscopy only distinguishes processes with differences in the relaxation frequency higher than one order of magnitude, and corresponding differences in capacitance. This might be insufficient to trace the electrical effects resulting from very high concentrations of linear defects. Another possible reason refers to point-defect association promoted by the enlarged grain boundary, which also might lead to increasing total bulk resistivity without a separate signal in the impedance spectra.

4.3.4. Transport properties in reducing atmospheres

When the oxygen partial pressure decreases, the impedance spectra of TbMO_{4-δ} ceramics undergo significant changes associated with an increase in the bulk resistance and a greater electrode response (Figs.4.39 and 4.40). This implies that the role of p-type electronic conductivity, dominant in air, decreases as expected. In the case of TbHfO_{4-δ}, the values of the oxygen ionic conductivity in oxidizing conditions are similar to the total conductivity in 10%H₂-90%N₂ mixture at 1023-1123 K (Fig.4.44A). Hence, at low oxygen pressures the transport becomes almost purely ionic. At the same time, the behavior in reducing conditions, particularly the high activation energy, suggests a decrease in the ionic conductivity with decreasing p(O₂), which may result from oxygen-vacancy association. The drop of ionic transport at low oxygen pressures is quite typical for fluorite-type materials, including acceptor-doped CeO₂. A more pronounced difference between the ionic conductivity in air and total conductivity under very reducing conditions is observed for TbZrO_{4-δ} (Fig.4.44B). As a particular result, the assumption [415] that the ionic conductivity of terbium zirconate in oxidizing conditions is equal to its total conductivity in reducing atmospheres appears quite questionable. One should also mention that the structural studies of TbMO_{4-δ} annealed in hydrogen atmosphere, indicated no significant changes in their crystal lattice.

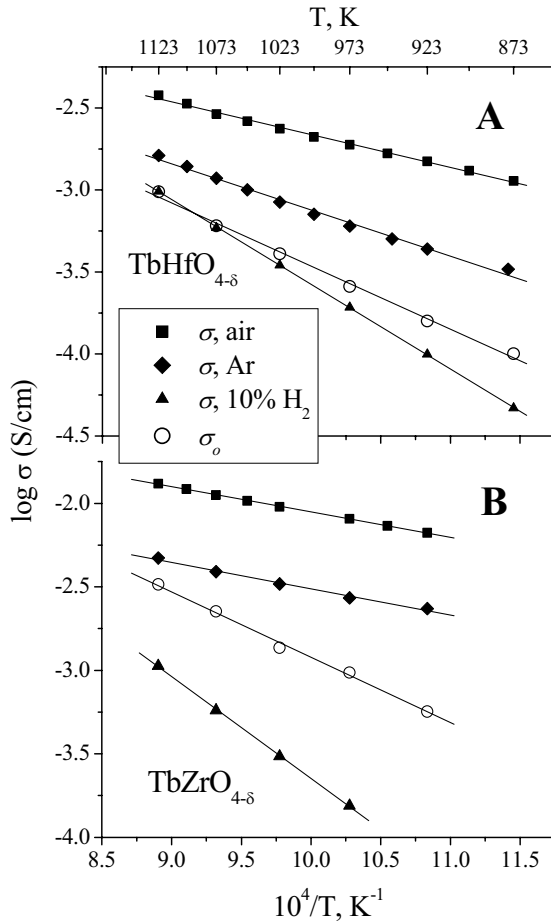


Fig.4.44. Temperature dependence of the total conductivity of $\text{TbHfO}_{4-\delta}$ (A) and $\text{TbZrO}_{4-\delta}$ (B) ceramics in air, argon and 10% H_2 -90% N_2 mixture, compared to the partial ionic conductivity under oxidizing conditions.

The oxygen pressure dependencies of Seebeck coefficient of $\text{TbHfO}_{4-\delta}$ and $\text{TbZrO}_{4-\delta}$ are presented in Figs.4.45 and 4.46, respectively. Taking the transference numbers (Table 4.8) into account, the thermopower in oxidizing conditions comprises ionic ($\alpha_{\text{O}_2^-}$) and electron-hole (α_p) contributions: $\alpha = \alpha_{\text{O}_2^-} + \alpha_p$. If the chemical potential of oxygen ions is essentially independent of oxygen partial pressure, Eq.(4.15) can be simplified to [392]:

$$\alpha_{\text{O}_2^-} = -t_o \cdot \left(\frac{k}{4e} \cdot \ln p(\text{O}_2) + \alpha_{\text{O}_2^-}^0 \right) \quad (4.17)$$

where $-\alpha_{\text{O}_2^-}^0$ is the ionic Seebeck coefficient at unit oxygen pressure and t_o . Such situation should take place for $\text{TbHfO}_{4-\delta}$ at temperatures above 1023 K when the ionic conductivity, essentially independent of $p(\text{O}_2)$, indicates that the oxygen-vacancy concentration is sufficiently high and, therefore, that minor variations in the oxygen nonstoichiometry should have no effect on the ion chemical potential. The electron-hole conductivity is defined analogous to Eq.(3.7) [392,410,415]:

$$\sigma_p = F \cdot \mu_p \cdot p = \sigma_p^0 \cdot p(\text{O}_2)^{1/m} \quad (4.18)$$

where m is constant and p has a dimensionality of mol/cm^3 . For solid electrolytes, the values of m are typically equal to 4. As shown for $\text{TbZrO}_{4-\delta}$ [415], p-type electronic transport occurs, most likely, via a hopping between terbium ions. In this case, p-type electronic contribution to the thermopower is [90,392,416]:

$$\alpha_p = t_p \cdot \frac{k}{e} \left(\ln \frac{N-p}{p} + \frac{q}{kT} \right) = t_p \cdot \frac{k}{e} \cdot \ln \left(\frac{N \cdot \mu_p \cdot F}{\sigma_p^0 \cdot p(\text{O}_2)^{1/m}} - 1 \right) + t_p \cdot \frac{q}{eT} \quad (4.19)$$

where N is the total concentration of sites participating in the conduction process, and q is the transported heat of electron holes, which can be neglected for most semiconductors [416]. For $\text{TbHfO}_{4-\delta}$, the ionic conductivity can be assumed $p(\text{O}_2)$ -independent at least at 1073-1123 K; the ion transference numbers can be expressed as [417]:

$$t_o = \frac{\sigma_o}{\sigma_o + \sigma_p^0 \cdot p(\text{O}_2)^{1/m}} \quad (4.20)$$

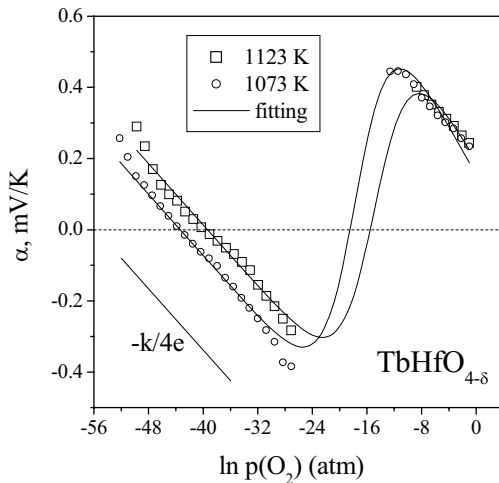


Fig.4.45. Oxygen partial pressure dependence of Seebeck coefficient of $\text{TbHfO}_{4-\delta}$. Solid lines indicate the fitting results (see text).

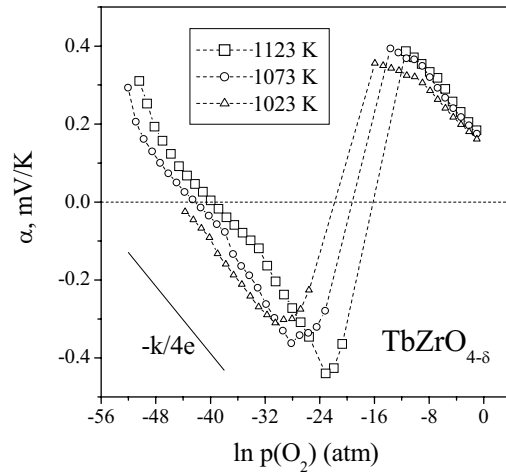


Fig.4.46. Oxygen partial pressure dependence of Seebeck coefficient of $\text{TbZrO}_{4-\delta}$. Dashed lines are for visual guidance.

Substitution of Eqs.(4.17-4.20) into α makes it possible to model $\alpha - \ln p(\text{O}_2)$ dependencies. The fitting results, shown in Fig.4.45 by solid lines, are considered as sufficiently adequate. A sharp increase in the Seebeck coefficient, found when $p(\text{O}_2)$ is lower than 10^{-22} - 10^{-21} atm, may result from the influence of oxygen-vacancy association starting to affect ion chemical potential at very reduced oxygen pressures. For $\text{TbZrO}_{4-\delta}$, the $p(\text{O}_2)$ -dependence of thermopower is qualitatively similar to that of $\text{TbHfO}_{4-\delta}$ (Fig.4.46). The ionic conductivity of $\text{TbZrO}_{4-\delta}$ at reduced

$p(\text{O}_2)$ is found substantially lower with respect to oxidizing conditions (Fig.4.44), most probably due to the vacancy-ordering processes. The simple model for Seebeck coefficient, valid for $\text{TbHfO}_{4-\delta}$, cannot therefore be applied in this case.

4.4. $\text{Gd}_{2-x}\text{Ca}_x\text{Ti}_2\text{O}_{7-\delta}$ pyrochlores

Pyrochlore phases based on $\text{Gd}_2\text{Ti}_2\text{O}_7$ were reported as promising solid electrolyte materials [54,55,414,418,419]. Acceptor-type doping of $\text{Gd}_2\text{Ti}_2\text{O}_7$ leads to a significant enhancement of the oxygen ionic transport; the maximum ionic conductivity was found for $\text{Gd}_{2-x}\text{Ca}_x\text{Ti}_2\text{O}_{7-\delta}$ with $x = 0.10-0.30$ [54,418]. The narrow composition range of $\text{Gd}_{2-x}\text{Ca}_x\text{Ti}_2\text{O}_{7-\delta}$ ($x = 0.10-0.14$) was selected to match the phases with most promising properties and to reassess contradictory literature data on pyrochlore phases with a significant level of the ionic conductivity [54,418,419].

4.4.1. Characterization of ceramic materials

XRD studies of $\text{Gd}_{2-x}\text{Ca}_x\text{Ti}_2\text{O}_{7-\delta}$ powders and ceramics showed a formation of single phases with pyrochlore structure. An example of final Rietveld plot, showing the quality of structure refinement, is given in Fig.4.47. The unit cell parameters of the materials with $x = 0.10$ and 0.14 are quite similar as the difference in their composition is rather small (Table 4.9).

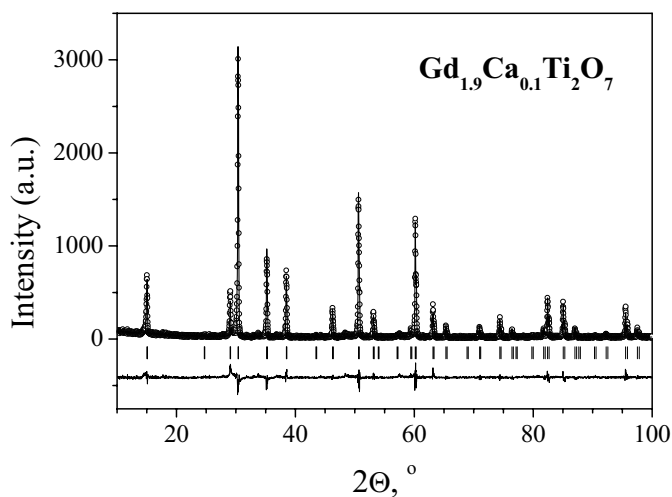


Fig.4.47. Observed, calculated and difference XRD pattern of $\text{Gd}_{1.90}\text{Ca}_{0.10}\text{Ti}_2\text{O}_{7-\delta}$.

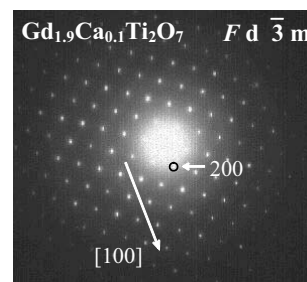


Fig.4.48. SAED pattern of $\text{Gd}_{1.90}\text{Ca}_{0.10}\text{Ti}_2\text{O}_{7-\delta}$.

At the same time, the analysis of cation-anion bond lengths in the pyrochlore lattice indicates that Ti-O octahedra contract and their distortion decreases when calcium concentration increases. These octahedra are formed by so-called O1 oxygen sites (position 48f mm u 1/8 1/8) and have an ideal form if $u = 0.3125$. Increasing x results in a clear decrease in the Ti-O1 distance, considerably larger than the experimental error; the parameter u for $Gd_{2-x}Ca_xTi_2O_{7-\delta}$ is higher than 0.3125, but decreases with x (Table 4.9). As pyrochlore structure is a cation-ordered derivative of the fluorite structure, a number of pyrochlore phases exhibit partial or complete disordering on heating; the latter process corresponds to a transformation of $A_2B_2O_7$ pyrochlore into a nonstoichiometric $(A,B)O_{3.5\pm\delta}$ fluorite lattice, one example of which refers to 50 mol% yttria-doped zirconia [33,41,414]. The lattice disorder leads, as a rule, to a greater oxygen ionic conduction [33,41,414].

Table 4.9

Structure refinement results of $Gd_{2-x}Ca_xTi_2O_{7-\delta}$

	$Gd_{1.90}Ca_{0.10}Ti_2O_{7-\delta}$	$Gd_{1.86}Ca_{0.14}Ti_2O_{7-\delta}$
Crystal system	cubic	
Space group	$Fd\bar{3}m$ (No 227)	
Unit cell parameter, Å	10.192(5)	10.193(1)
u	0.32431	0.32258
Interatomic distances, Å		
Ti – O1	1.955	1.948
Ti – O2	2.226	2.226
Gd – O1	2.540	2.553
Gd – O2	2.207	2.207
O1 – O1	2.651	2.658
O1 – O2	3.065	3.083
O2 – O2	4.413	4.414

Since partial cation disordering may also be induced by A-site doping [414], TEM examination of $Gd_{1.9}Ca_{0.1}Ti_2O_{7-\delta}$ fine-ground ceramic sample was carried out. An example of the electron diffraction pattern is presented in Fig.4.48. The inspection of TEM results showed no evidence of cation disorder; the lattice parameters calculated from the XRD and TEM data were very similar, within the limits of experimental error. Taking into account that thermally-induced cation disordering of pyrochlore-type compounds usually becomes significant only when temperature is higher than 1350-1500 K [33,41,414], the level of structural disorder in $Gd_{2-x}Ca_xTi_2O_{7-\delta}$ is expected to be rather negligible and essentially unaffected by temperature variations within the studied range (400-1223 K).

Fig.4.49 presents SEM micrographs, reflecting microstructures characteristic of $Gd_{2-x}Ca_xTi_2O_{7-\delta}$ ceramics. The average grain size is similar for both studied compositions and varies in the range 5 - 10 μm . In agreement with the pycnometric data (Table 4.10), the closed porosity of ceramic materials was very small. No traces of a liquid phase formation at the grain boundaries or phase impurities were detected by SEM/EDS analysis.

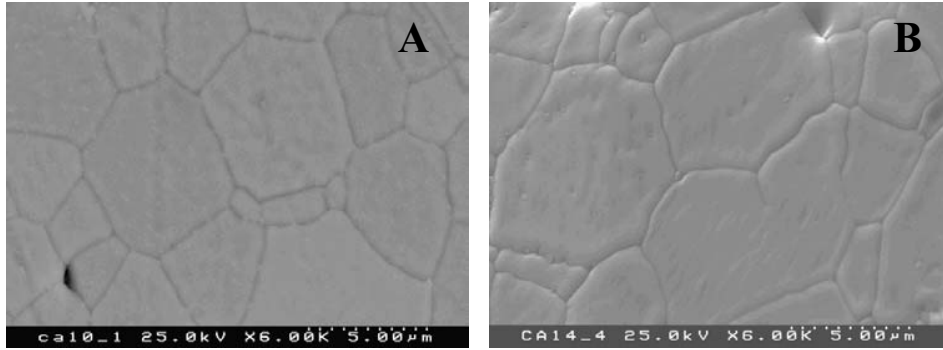


Fig.4.49. SEM micrographs of $Gd_{2-x}Ca_xTi_2O_{7-\delta}$ ceramics with $x = 0.10$ (A) and 0.14 (B).

Table 4.10

Properties of $Gd_{2-x}Ca_xTi_2O_{7-\delta}$ ceramics

Composition	d_{exp} g/cm ³	d_{exp}/d_{theor} %	$\bar{\alpha} \times 10^6, K^{-1}$ (400 - 1300 K)	Activation energy for the total conductivity	
				T, K	E_a , kJ/mol
x = 0.10	6.19	98.9	10.54 ± 0.02	670 - 820	96 ± 5
				820 - 1250	75 ± 2
x = 0.14	6.07	98.8	10.44 ± 0.03	500 - 820	97 ± 6
				820 - 1270	74 ± 1

Note: d_{exp} and d_{theor} are the experimental and theoretical density values, respectively.

Dilatometric curves of $Gd_{2-x}Ca_xTi_2O_{7-\delta}$ ceramics are close to linear within all studied temperature range, 400-1300 K (Fig.4.50). The average thermal expansion coefficients calculated from dilatometric data vary in the very narrow range $(10.4 - 10.6) \times 10^{-6} K^{-1}$ (Table 4.10). These TEC values are very similar to literature data on $Y_2(Ti,Zr)_2O_7$ pyrochlores [414] and to the TECs of stabilized zirconia ceramics [33].

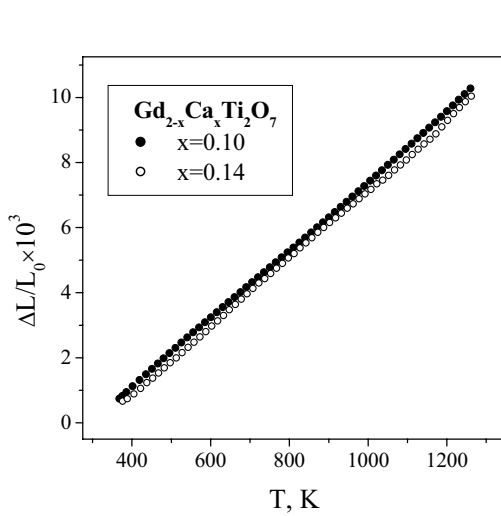


Fig.4.50. Dilatometric curves of $\text{Gd}_{2-x}\text{Ca}_x\text{Ti}_2\text{O}_{7-\delta}$ ceramics in air.

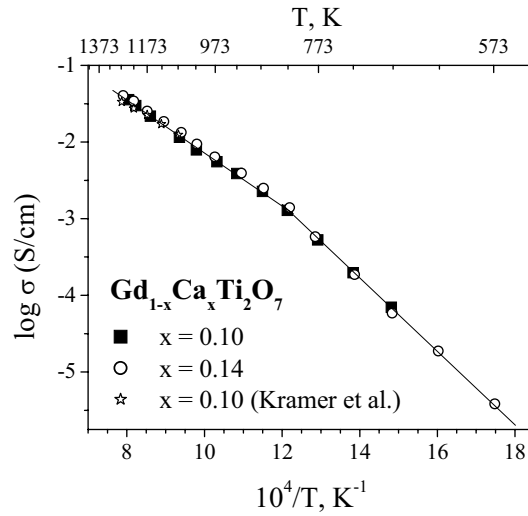


Fig.4.51. Temperature dependence of the total conductivity of $\text{Gd}_{2-x}\text{Ca}_x\text{Ti}_2\text{O}_{7-\delta}$ ceramics in air. Data from Ref. [54] on $\text{Gd}_{1.90}\text{Ca}_{0.10}\text{Ti}_2\text{O}_{7-\delta}$ are shown for comparison.

Temperature dependence of the total conductivity of $\text{Gd}_{2-x}\text{Ca}_x\text{Ti}_2\text{O}_{7-\delta}$ is shown in Fig.4.51. The conductivity is predominantly oxygen ionic (Table 4.11) and excellently coincides with results of Kramer and Tuller [54]. The significantly lower conduction level of the same compositions, reported in Ref.[419], may therefore result from specific features of $\text{Gd}_{2-x}\text{Ca}_x\text{Ti}_2\text{O}_{7-\delta}$ ceramics sintered at 1373 K, such as blocking grain boundaries in ceramics with fine grain sizes. Indeed, in the case of zirconia-based materials, low sintering temperatures are typically associated with a greater grain-boundary resistance [33]. The conductivity of $\text{Gd}_{1.86}\text{Ca}_{0.14}\text{Ti}_2\text{O}_{7-\delta}$ at temperatures above 823 K is slightly higher than that of $\text{Gd}_{1.90}\text{Ca}_{0.10}\text{Ti}_2\text{O}_{7-\delta}$, whereas in the low-temperature range σ values of both compositions are similar. The activation energy for the total conductivity increases from 74-75 kJ/mol at 823-1273 K up to 96-97 kJ/mol at 500-823 K (Table 4.10). According to TEM results and literature data [33,41,414], cation disordering of the pyrochlore titanates at temperatures around 800-850 K seems unlikely. The impedance spectroscopic data, examples of which are presented in Fig.4.52, A and B, indicate a negligible contribution of the grain boundaries to the total resistance within all studied temperature range (400-1300 K); the change in the activation energy at 823 K cannot thus be attributed to grain-boundary effects. Most probably, the observed change in E_a values is due to disordering in the oxygen sublattice on heating, which is quite typical for stabilized zirconia and hafnia [33,41]. The composition-independent conductivity in the low-temperature range may result from an association of oxygen

vacancies and calcium cations and/or from formation of ordered microdomains. At temperatures above 823 K, disordering in the oxygen sublattice leads to a lower activation energy due to decreasing contribution of the vacancy formation energy to E_a values down to zero; ionic conduction in the high-temperature range becomes dependent on the total oxygen-vacancy concentration, which increases with calcium content (Fig.4.51).

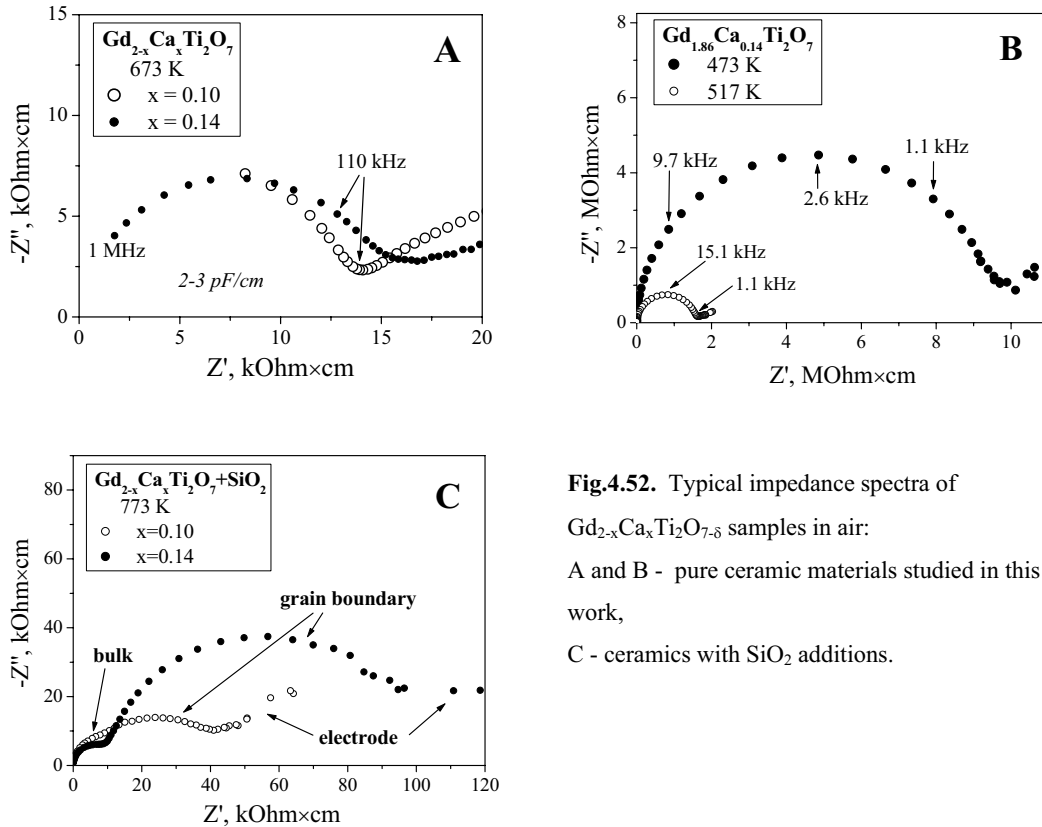


Fig.4.52. Typical impedance spectra of $Gd_{2-x}Ca_xTi_2O_{7-\delta}$ samples in air: A and B - pure ceramic materials studied in this work, C - ceramics with SiO_2 additions.

The impedance spectroscopic studies of $Gd_{2-x}Ca_xTi_2O_{7-\delta}$ ceramics demonstrated that in the studied temperature range grain-boundary resistance can be neglected. At all temperatures, only two arcs were observed in the impedance spectra; the high-frequency arc with a specific capacitance of about 10^{-12} F/cm is obviously associated with grain bulk conduction, whilst the low-frequency part of the spectra (10^{-7} - 10^{-6} F/cm) correspond to electrode processes. Representative examples of the impedance spectra at different temperatures are given in Fig.4.52, A and B. For comparison, Fig.4.52C presents the data of $Gd_{2-x}Ca_xTi_2O_{7-\delta}$ ceramics containing approximately 1.5 mol% of SiO_2 . Silica impurities are well known to segregate at grain boundaries of most solid-electrolyte ceramics and to dramatically increase boundary resistivity [15,33]. As for other solid electrolytes, additions of SiO_2 lead to appearance of a new intermediate-frequency arc in the impedance spectra of pyrochlore titanates (Fig.4.52C). This arc, having a specific capacity of (4-

$9) \times 10^{-9}$ F/cm at 773 K, can be undoubtedly attributed to the grain-boundary processes. The example shown in Fig.52C stresses that the measurement conditions, used in this work, provided a sufficient sensitivity to the grain boundary effects; the absence of intermediate-frequency phenomena in the impedance spectra of pure $\text{Gd}_{2-x}\text{Ca}_x\text{Ti}_2\text{O}_{7-\delta}$ ceramics is a conclusive proof of the negligible boundary contribution to the total resistance.

4.4.2. Partial ionic and p-type electronic conductivities

The oxygen ion transference numbers of $\text{Gd}_{2-x}\text{Ca}_x\text{Ti}_2\text{O}_{7-\delta}$ at 973-1223 K, determined by the modified faradaic efficiency technique under zero oxygen chemical potential gradient in air, vary from 0.95 to 0.97, slightly increasing when temperature decreases or calcium concentration increases (Table 4.11). Fig.4.53 presents examples of the experimental data obtained by the modified emf technique, plotted according to Eq.(2.12), and the polarization curves calculated from Eqs.(2.14). All dependencies are linear, validating the selected measurement conditions.

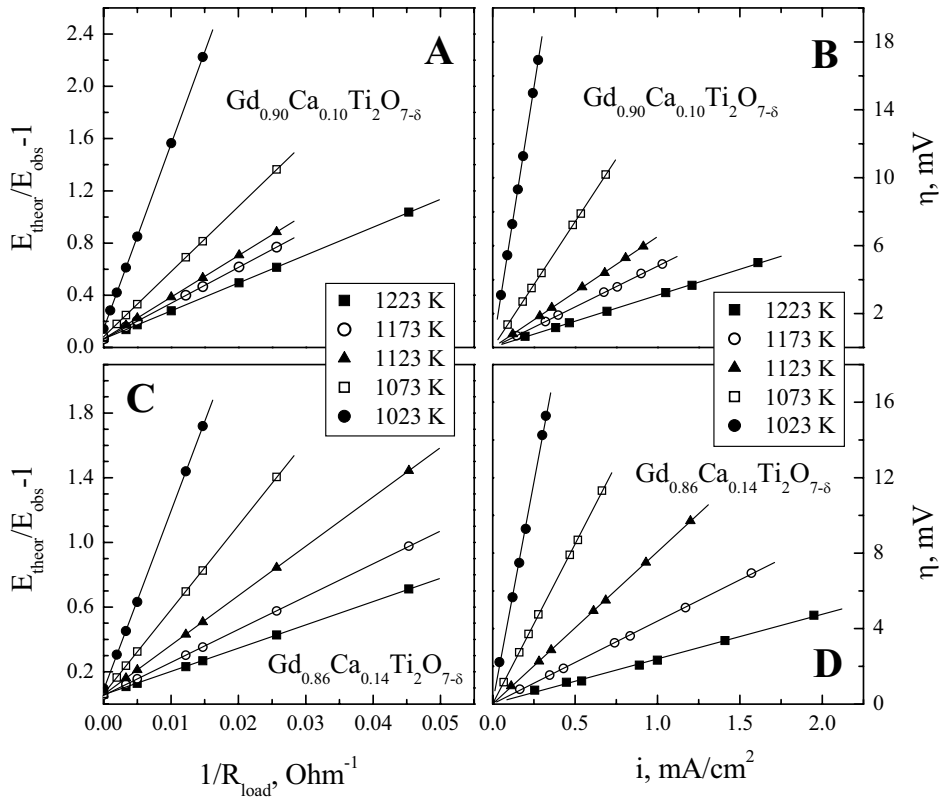


Fig.4.53. Measured e.m.f. of the cell Fig.2.2 (right) as a function of R_{load} (A,C) and overpotential vs. current dependencies (B,D) calculated from Eqs.(2.14), for $\text{Gd}_{2-x}\text{Ca}_x\text{Ti}_2\text{O}_{7-\delta}$ ceramics under O_2/air gradient. Solid lines correspond to the linear regression fit.

The faradaic efficiency technique and the emf method under oxygen/air gradient give very similar values of the transference numbers (Table 4.11) and electronic conductivity (Fig.4.54). These data confirm correctness of the measurement techniques and reliability of the results. The oxygen ionic conductivity in air is plotted in Fig.4.55.

Table 4.11

Parameters of the oxygen ionic transport in $Gd_{2-x}Ca_xTi_2O_{7-\delta}$ ceramics in air

x	Average ion transference numbers *			Activation energy for ionic and electron-hole conductivities (973 – 1223 K)**	
	T, K	\bar{t}_o (emf)	\bar{t}_o (FE)	E_a (σ_o), kJ/mol	E_a (σ_p), kJ/mol
x = 0.10	1223	0.952	0.952	77±4	91±2
	1173	0.956	0.955		
	1123	0.958	0.958		
	1073	0.960	0.959		
	1023	0.961	0.962		
	973	-	0.967		
x = 0.14	1223	0.960	0.956	74±2	87±3
	1173	0.966	0.958		
	1123	0.968	0.960		
	1073	0.972	0.962		
	1023	-	0.965		
	973	-	0.968		

* Each t_o value was averaged from 2-4 experimental data points.

** The oxygen ionic conductivity was calculated from the results on the total conductivity and transference numbers, determined by the faradaic efficiency method, as $\sigma_o = \sigma \times t_o$.

Tuller et al. [54,418] showed that electronic conductivity of $Gd_{2-x}Ca_xTi_2O_{7-\delta}$ in oxidizing conditions is predominantly p-type; the n-type contribution is negligibly small. Therefore, the equilibrium ion transference numbers can be written by Eq.(4.20). According to Ref.[54], ionic conduction in $(Gd,Ca)_2Ti_2O_{7-\delta}$ phases is independent of the oxygen partial pressure, which also agrees with the data on electrolytes [33,41,417]. For the measurements under a non-zero oxygen pressure gradient, either by emf or faradaic efficiency technique, the transference numbers are averaged in a given range of oxygen chemical potential as expressed by Eq.(2.13). Substitution of Eq.(4.20) into Eq.(2.13) and integration result in the following expression:

$$\bar{t}_o(p_2, p_1) = -m \cdot \ln \frac{k_1 \cdot p_2^{-1/m} + 1}{k_1 \cdot p_1^{-1/m} + 1} \cdot \left(\ln \frac{p_2}{p_1} \right)^{-1} \quad (4.21)$$

where $k_1 = \sigma_o/\sigma_p^0$. Fig.4.56A shows fitting results of the experimental dependence of the average

transference numbers on p_1 , determined by faradaic efficiency measurements at fixed $p_2 = 0.21$ atm, using Eq.(4.21) as regression model. Taking into account experimental error, this equation is considered to be adequate. The calculated value of m parameter, 4.7 ± 0.2 , is quite close to 4, the classical value for electron-hole transport in solid electrolytes.

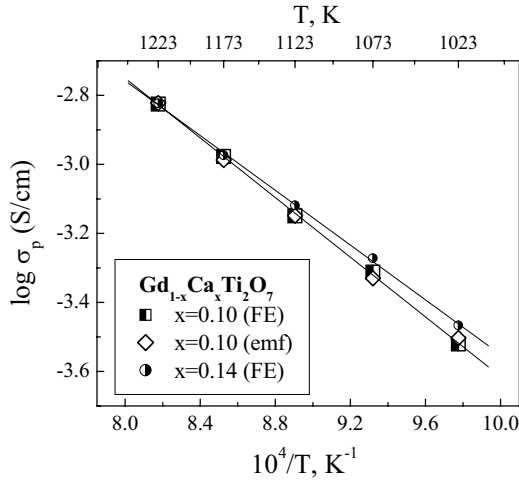


Fig.4.54. Temperature dependence of the p-type electronic conductivity of $Gd_{2-x}Ca_xTi_2O_{7-\delta}$ ceramics in air, calculated from the impedance spectroscopic, faradaic efficiency and emf results.

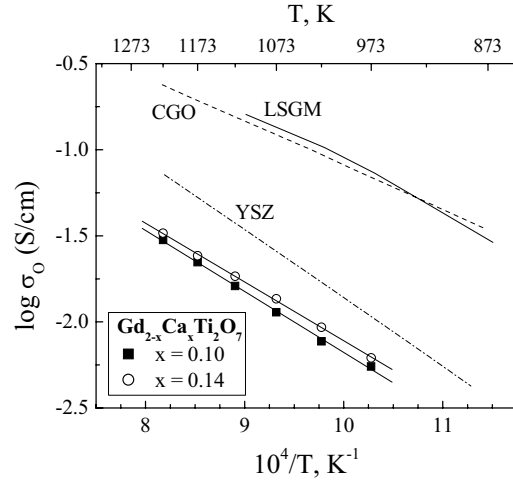


Fig.4.55. Temperature dependence of the oxygen ionic conductivity of $Gd_{2-x}Ca_xTi_2O_{7-\delta}$ in air. Data on $La_{0.80}Sr_{0.20}Ga_{0.85}Mg_{0.15}O_{3-\delta}$ (LSGM), $Ce_{0.80}Gd_{0.20}O_{2-\delta}$ (CGO) and $Zr_{0.90}Y_{0.10}O_{1.95}$ (YSZ), shown for comparison, are taken from Ref.[420].

In these conditions, if the surface exchange limitations to the overall oxygen transport through a pyrochlore membrane can be neglected, the permeation flux density (j) is described by Eq.(2.9). After substitution of Eq.(4.20), analytical solution of Eq.(2.9) is

$$j = \frac{RT \cdot m \cdot \sigma_o}{16F^2d} \cdot \ln \frac{\sigma_p^0 \cdot p_2^{1/m} + \sigma_o}{\sigma_p^0 \cdot p_1^{1/m} + \sigma_o} \quad (4.22)$$

Fig.4.56B compares experimental results on oxygen permeation through a $Gd_{1.90}Ca_{0.10}Ti_2O_{7-\delta}$ membrane and the corresponding predictions, calculated by Eq.(4.22) with the values of m , σ_o and σ_p^0 obtained by other methods. The parameters m and k_1 were determined by fitting of \bar{t}_o vs. p_1 dependence obtained by FE measurements (Fig.4.56A); the values of σ_o and σ_p^0 were extracted from the total conductivity in air (Fig.4.51) using the definitions $k_1 = \sigma_o/\sigma_p^0$ and $\sigma = \sigma_o + \sigma_p^0 \times p(O_2)^{1/m}$. The experimentally-measured and calculated permeation fluxes are very similar (Fig.4.56B), thus confirming that different methods are consistent with each other and that Eq.(4.22) is valid.

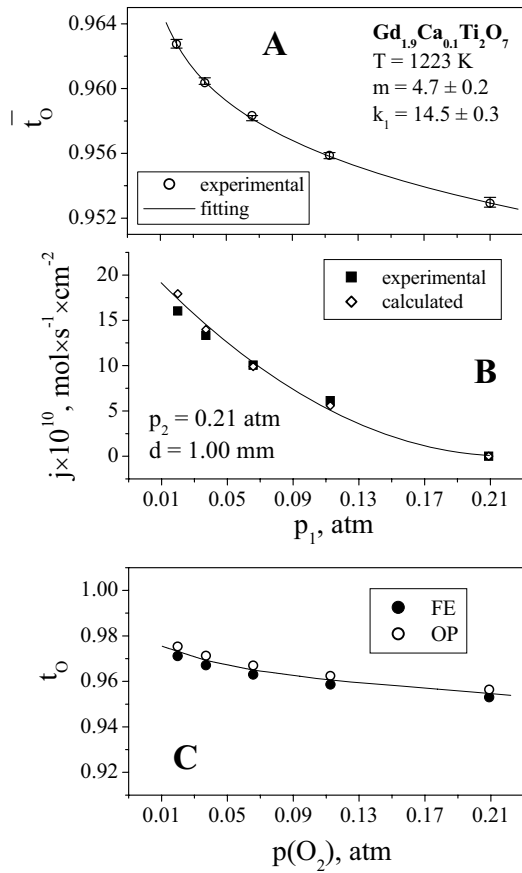


Fig.4.56. Dependencies of the average ion transference numbers (A) and oxygen permeation flux density (B) on the permeate-side oxygen pressure, and $p(\text{O}_2)$ dependence of equilibrium transference numbers of $\text{Gd}_{1.90}\text{Ca}_{0.10}\text{Ti}_2\text{O}_{7.8}$ at 1223 K calculated from these results (C). Solid line in A corresponds to best fit to the faradaic efficiency data using Eq.(4) as regression model. Solid lines in B and C are for visual guidance only.

Table 4.12

Average ion transference numbers of $\text{Gd}_{1.90}\text{Ca}_{0.10}\text{Ti}_2\text{O}_{7.8}$ under 10% H_2 -90% N_2 / air gradient, determined by the modified emf method

T, K	\bar{t}_o
1273	0.976±0.001
1223	0.982±0.001
1123	0.989±0.002

Fig.4.56C presents the equilibrium transference numbers, t_o , which were evaluated from the regression parameters of $\bar{t}_o - p_1$ and $j - p_1$ dependencies (Fig.4.56, A and B) expressed by Eqs.(4.21) and (4.22), respectively. Again, the results obtained using different measurement techniques are similar within the limits of experimental uncertainty. Thus, p-type electronic conductivity and oxygen permeability of $\text{Gd}_{2-x}\text{Ca}_x\text{Ti}_2\text{O}_{7.8}$ pyrochlores both can be adequately described by models, derived from relationships common for solid electrolytes [33,417].

Finally, Fig.4.57 shows the relative error in the ion transference numbers (\bar{t}_o^{obs}) determined by classical emf and faradaic efficiency methods, which appears due to electrode polarization in the measuring cells. The error was evaluated as

$$\frac{\Delta \bar{t}_o}{\bar{t}_o} = \frac{\bar{t}_o - \bar{t}_o^{\text{obs}}}{\bar{t}_o} \quad (4.23)$$

where \bar{t}_o values were measured by the modified techniques, taking polarization resistance into account. For the classical emf method [417], the transference numbers are estimated as the ratio

between the observed emf of an oxygen concentration cell and its theoretical Nernst voltage; in the case of classical arrangement of the faradaic efficiency measurements, ionic contribution to the total conductivity is estimated from the ratio of ionic and total currents through a mixed conductor. However, when electrode polarization is significant, these apparent transference numbers are considerably lower than the true t_o values. The relative error increases with decreasing oxygen partial pressure and temperature (Fig.4.57). The behavior of $(\text{Gd,Ca})_2\text{Ti}_2\text{O}_{7-\delta}$, illustrated by Fig.4.57, is similar to other solid electrolytes; most probably, this error might constitute a reason for the very low apparent transference numbers reported in Ref.[419].

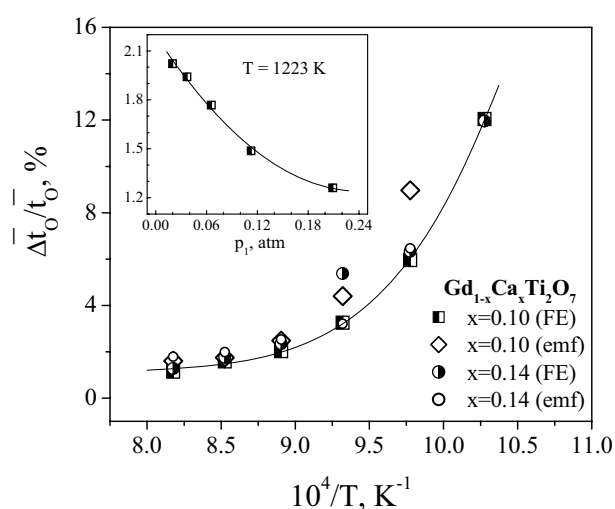


Fig.4.57. Relative error of the transference number determination by classical emf and faradaic efficiency methods, appearing due to electrode polarization.

Increasing calcium content in the lattice of $\text{Gd}_{2-x}\text{Ca}_x\text{Ti}_2\text{O}_{7-\delta}$ leads to a slight decrease in the activation energy for electron-hole transport in air (Table 4.12). As a result, the p-type conductivity of $\text{Gd}_{1.90}\text{Ca}_{0.10}\text{Ti}_2\text{O}_{7-\delta}$ at temperatures below 1100 K is lower than that of $\text{Gd}_{1.86}\text{Ca}_{0.14}\text{Ti}_2\text{O}_{7-\delta}$; at higher temperatures σ_p values are essentially independent of x (Fig.4.54). This phenomenon indicates that charge compensation of the acceptor-type doping occurs via the oxygen vacancy formation rather than via generation of any positive electronic charge carriers, which seems quite reasonable as the oxidation state of cations in the structure of $\text{Gd}_{2-x}\text{Ca}_x\text{Ti}_2\text{O}_{7-\delta}$ cannot further increase. The electron-hole conduction is therefore related to an intrinsic electronic disorder at least in the high-temperature range.

Due to the charge compensation mechanism via the oxygen vacancy formation, doping with calcium leads to increasing oxygen ionic conductivity (Fig.4.55). The observed activation energy for ionic transport, 74-77 kJ/mol at 973-1223 K (Table 4.12), is slightly higher compared to the data by Kramer and Tuller [54], who reported E_a values of $\text{Gd}_{2-x}\text{Ca}_x\text{Ti}_2\text{O}_{7-\delta}$ ($x = 0.10-0.20$) in the range 63-65 kJ/mol at 1073-1373 K. Such a difference may result from the different

temperature ranges, studied in the present work and in Ref.[54]. For instance, the activation energy for ionic conduction in stabilized zirconia typically increases with decreasing temperature due to a progressive association of mobile oxygen vacancies [33]. The values of E_a , calculated for $Gd_{2-x}Ca_xTi_2O_{7-\delta}$ ceramics, are comparable with those of well-known solid electrolytes, such as gadolinia-doped ceria (CGO) or La(Sr)Ga(Mg)O_{3-δ} (LSGM) [15,43,420]. However, the level of ionic conductivity in $(Gd,Ca)_2Ti_2O_{7-\delta}$ is lower 8-10 times (Fig.4.55).

4.4.3. Transport properties under high $p(O_2)$ gradients

The measurements of oxygen ion transference numbers by the modified emf method, performed under the gradient of 10% H_2 -90% N_2 / air, showed that in fuel cell operation conditions the electronic contribution to total conductivity of $Gd_{2-x}Ca_xTi_2O_{7-\delta}$ is relatively small, less than 3% (Table 4.11). This behavior is similar to LSGM electrolytes; the n-type electronic conduction induced in CGO ceramics in H_2 -containing atmospheres is considerably higher (see [43] and references cited). Hence, a decrease in the performance of SOFCs with pyrochlore solid electrolytes due to their electronic conductivity is expected to be rather negligible.

However, due to the low ionic conductivity of $(Gd,Ca)_2Ti_2O_{7-\delta}$ ceramics (Fig.4.55), the ohmic losses in model fuel cells with pyrochlore electrolytes are excessively high, resulting in a poor cell performance even at temperatures as high as 1223-1273 K (Figs.4.58 and 4.59). Fig.4.58 presents one example of the current dependencies of voltage and power density in a cell with $Gd_{1.90}Ca_{0.10}Ti_2O_{7-\delta}$ electrolyte membrane; the ohmic losses calculated from the impedance spectroscopy data are marked as IR. The ohmic contribution to the total voltage drop is up to 70%. This leads to almost linear current-voltage curves (Fig.4.59).

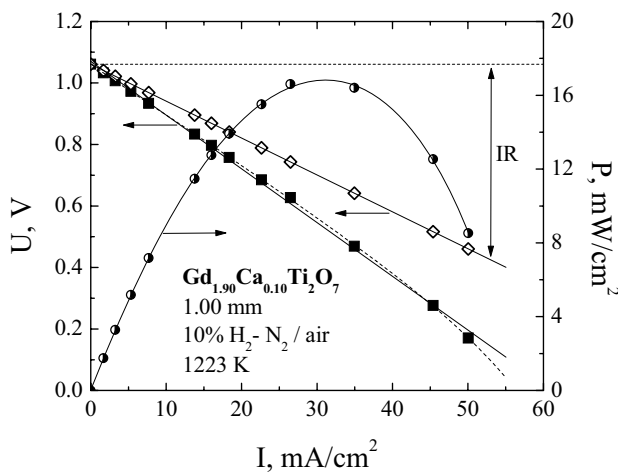


Fig.4.58. Current dependencies of the voltage and specific power density of one cell with $Gd_{1.90}Ca_{0.10}Ti_2O_{7-\delta}$ solid electrolyte and Pt electrodes at 1223 K. Ohmic losses calculated from impedance spectroscopic data are marked as IR.

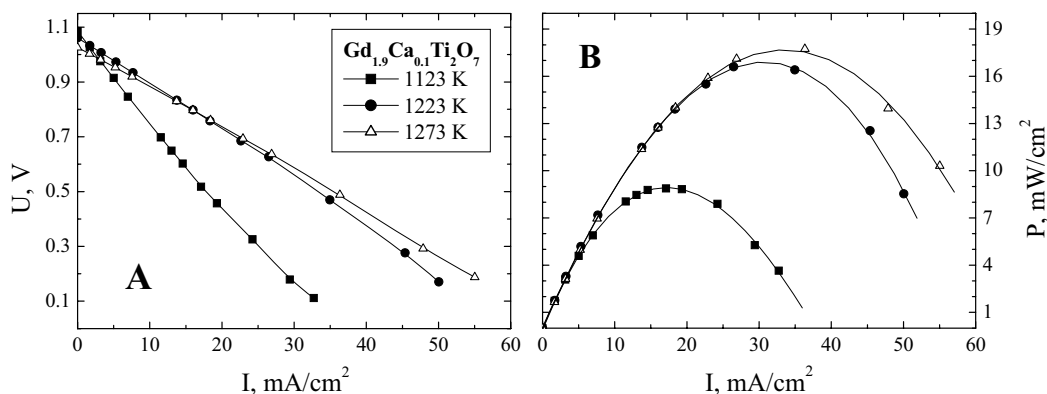


Fig.4.59. Current dependencies of the voltage and specific power density of a model fuel cell: 10% H_2 - N_2 , Pt | $Gd_{1.9}Ca_{0.1}Ti_2O_7$ | Pt, O_2 (air).

The maximum power density, shown by the cells with $(Gd,Ca)_2Ti_2O_{7-\delta}$ electrolyte and porous Pt electrodes at 1123-1273 K, varied from 8 to 18 mW/cm^2 , increasing with temperature (Fig.4.59). Such a performance is 10-20 times lower than the minimum necessary for commercial use. Although a definite improvement can be achieved by enhancing electrochemical activity of electrodes and by decreasing electrolyte thickness, it seems unlikely that pyrochlore titanates could be used in electrolyte-supported SOFCs. Therefore, due to low ionic conductivity of $(Gd,Ca)_2Ti_2O_{7-\delta}$, possible applications of these materials may refer to electrode-supported fuel cells where the thickness of solid-electrolyte film is less than 50-100 μm . The sufficiently high stability of pyrochlore phases in reducing environments and the moderate thermal expansion might be advantageous for these applications.

4.4.4. Grain-boundary effects: a case study and selected conclusions

Literature data [54,419] on the properties of titanate pyrochlores is rather contradictory. As an example, the oxygen ion transference numbers of $Gd_{1.9}Ca_{0.1}Ti_2O_{7-\delta}$ in pure oxygen, estimated from the $p(O_2)$ -dependence of the total conductivity [54], vary in the range 0.90 - 0.95 at 1073-1223 K, while t_o values determined by the classical emf method under an oxygen pressure gradient of $10^{-4}/0.21$ atm at 873-1023 K were reported to be as low as 0.18-0.20 [419]. One possible explanation for this conflicting evidence is the presence of distinct grain-boundary roles in such materials. In order to clarify the role of the boundaries, the transport properties of “pure” $Gd_{2-x}Ca_xTi_2O_{7-\delta}$ ($x = 0.10-0.14$) are compared to those of materials containing SiO_2 as an addition to increase the grain-boundary resistivity.. Silica is well known to segregate at the grain boundaries of most solid-electrolyte ceramics and to dramatically increase the boundary resistance [15].

Table 4.13

Properties of $Gd_{2-x}Ca_xTi_2O_{7-\delta}$ ceramics

Composition, x		Unit cell parameter a, Å	E _a for ionic and electronic conductivity* (973 – 1223 K)		t _o determined by faradaic efficiency measurements in air			
			E _a (σ _o), kJ/mol	E _a (σ _e), kJ/mol	1123 K	1173 K	1123 K	1073 K
pure	0.10	10.192(5)	83	97	0.952	0.955	0.958	0.959
	0.14	10.193(1)	78	90	0.956	0.958	0.960	0.962
with SiO ₂	0.10	10.185(1)	137	115	0.823	0.816	0.781	0.783
	0.14	10.179(2)	183	124	0.884	0.846	0.815	0.767

* Data corresponds to total (bulk + grain boundary) partial conductivities.

In the case of SiO₂-containing samples, trace amounts of a secondary phase, Ca₂Gd₈(SiO₄)₆O₂, were detected in the XRD spectra. The smaller unit cell parameters of these materials (Table 4.13) are probably due to A-site depletion of the surface layers of Gd_{2-x}Ca_xTi₂O_{7-δ} grains, due to partial reaction with silica and formation of Ca₂Gd₈(SiO₄)₆O₂. Typical microstructure of Gd_{2-x}Ca_xTi₂O_{7-δ} ceramics with silica additions is illustrated by Fig.4.60. Whilst no traces of liquid phase or other grain-boundary phenomena were detected by SEM analysis of the “pure” materials (Fig.4.49), needle-like crystallites growing up from the boundaries are observed in the case of fractured and thermally etched surfaces of silica-containing ceramics (Fig.4.60). The EDS studies indicated that these crystallites are significantly enriched with SiO₂.

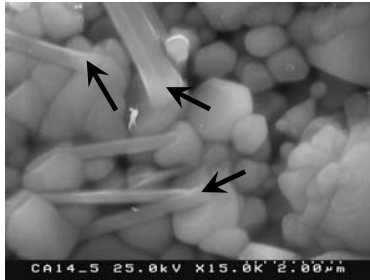


Fig.4.60. SEM micrograph of thermally etched SiO₂-containing Gd_{1.86}Ca_{0.14}Ti₂O_{7-δ} ceramics. The arrows indicate needle-like silica-rich phases.

Representative examples of the impedance spectra of Gd_{1.86}Ca_{0.14}Ti₂O_{7-δ} samples, without and with SiO₂ additions, are presented in Figs.4.61A and 4.61B, respectively. Incorporation of SiO₂ into the ceramics leads to the appearance of large intermediate-frequency arcs, having a specific capacity of about 10⁻⁸ F/cm at 873 K, attributed to the grain-boundary processes (Fig.4.61B). This is obviously due to the presence of the insulating siliceous phase at the boundaries. For “pure” ceramics the boundary resistivity was drastically lower. For example, the inset in Fig.4.61A illustrates the impedance spectra at low temperature, indicating that the grain bulk resistance dominates at 473 K. The total (bulk + boundary) conductivity of “pure” materials, measured by *ac*

impedance spectroscopy, is much higher than that of SiO₂-containing samples, while the bulk conductivity values of the ceramics with equal x were found quite similar. This confirms that, as expected, the minor amount of added silica results in a dramatic increase of the grain-boundary resistance.

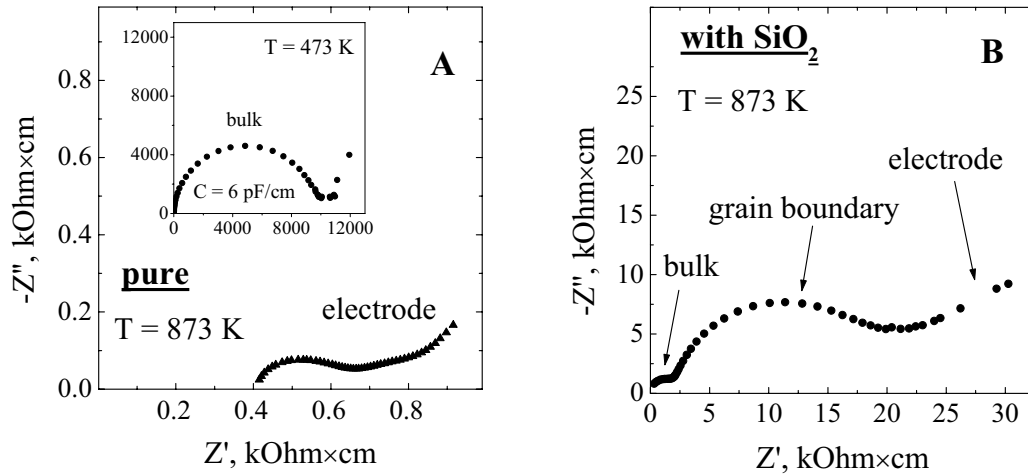


Fig.4.61. Typical impedance spectra of pure (A) and SiO₂-containing (B) Gd_{1.90}Ca_{0.10}Ti₂O_{7-δ} ceramics at 873 K in air. Inset shows spectrum of pure material at 473 K.

The oxygen ion transference numbers of “pure” pyrochlore ceramics in air, determined by the modified faradaic efficiency technique, vary from 0.952 to 0.962, increasing when temperature decreases or Ca-concentration increases (Table 4.11). For SiO₂-doped materials, these values are in the range 0.767-0.884 and increase with temperature. The transference numbers measured by the modified emf technique were similar to those obtained from faradaic efficiency data, confirming the reliability of these results. The observed behavior suggests that the highly resistive grain boundaries have a strong limiting effect on the ionic conduction, while their influence on the electronic transport is considerably smaller. This is in agreement with data on SrTiO₃ crystals [421], and can be interpreted using the classical equivalent circuit presented in Fig.4.62.

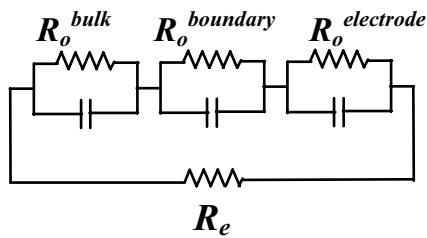


Fig.4.62. Simplified equivalent circuit providing the basis for the evaluation of the roles of grain-boundary resistance and electronic conduction on the measurable transport properties of a ceramic mixed conductor (see text).

A significant grain-boundary resistance contribution (R_o^{boundary}), comparable to the bulk resistance (R_o^{bulk}), leads to a large ionic resistance of the ceramics when compared to the intrinsic materials properties. As the ion transference number determined by *dc* techniques is $t_o = R_e / (R_e + R_o^{\text{bulk}} + R_o^{\text{boundary}})$, if the electronic resistance (R_e) is kept essentially unchanged, the apparent ion transference numbers decrease when the grain-boundary resistance increases.

Further analysis of the equivalent circuit (Fig.4.62) also shows that the apparent grain boundary resistance, directly estimated from impedance spectroscopy data (usually ascribed to the magnitude of the so-called intermediate frequency arc in the impedance spectra), might be significantly affected by the electronic conductivity. In fact, when the partial electronic conductivity exceeds a few percent of the total conductivity, the magnitudes of the bulk and grain boundary arcs are no longer a simple and direct result of these contributions. Therefore, for a correct determination of the grain-boundary resistance, impedance spectroscopy data should be combined with measurements of transference numbers.

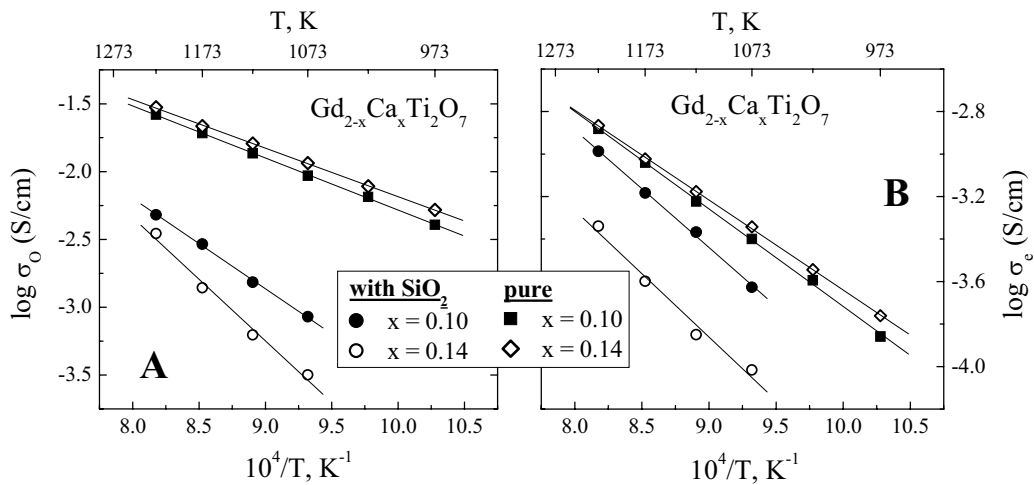


Fig.4.63. Temperature dependencies of the oxygen ionic (A) and p-type electronic (B) conductivities of $Gd_{2-x}Ca_xTi_2O_{7-\delta}$ ceramics in air. Data corresponds to the total (bulk + grain boundary) partial conductivities.

Fig.4.63 illustrates the influence of grain boundaries on the ionic and electronic conduction in $Gd_{2-x}Ca_xTi_2O_{7-\delta}$ ceramics. The effect of silica additions on the magnitude and activation energy of the oxygen ionic conductivity is much larger than that for electronic transport. In particular, the values of the electronic conductivity of pure and SiO_2 -containing $Gd_{1.90}Ca_{0.10}Ti_2O_{7-\delta}$ are quite similar, whereas the ionic conductivity values differ by a factor of 8-12. In the case of $Gd_{1.86}Ca_{0.14}Ti_2O_{7-\delta}$ the limiting effect of grain boundaries on both ionic and electronic transport is greater than that for $Gd_{1.90}Ca_{0.10}Ti_2O_{7-\delta}$ for unclear reasons at present. However, the decrease in the

ionic conduction is always considerably large if compared to the electronic conductivity. One should also note that whilst pure $\text{Gd}_{2-x}\text{Ca}_x\text{Ti}_2\text{O}_{7-\delta}$ pyrochlore ceramics exhibit dominant ionic transport in air and can thus be considered as solid electrolytes, the influence of the grain boundaries transforms these materials into mixed conductors with comparable levels of ionic and electronic transport, especially at low temperatures. Ion-blocking grain boundaries may be of interest for applications such as SOFC interconnectors, which should be impervious to oxygen; for solid electrolytes this effect is extremely undesirable.

4.5. Partial ionic and electronic conductivities of anode components

Figs.4.64 and 4.65 summarize the data on transport properties of the ion-conducting oxide materials selected as the components of fuel electrode. The values of total conductivity in Fig.4.64B correspond to $p(\text{O}_2) = 10^{-20}$ atm, which is close to the SOFC anode operation conditions. The oxygen ionic conductivity relates to atmospheric oxygen pressure; although these values cannot be used for quantitative analysis as the ionic transport is often $p(\text{O}_2)$ -dependent, their comparison may be useful to identify basic trends.

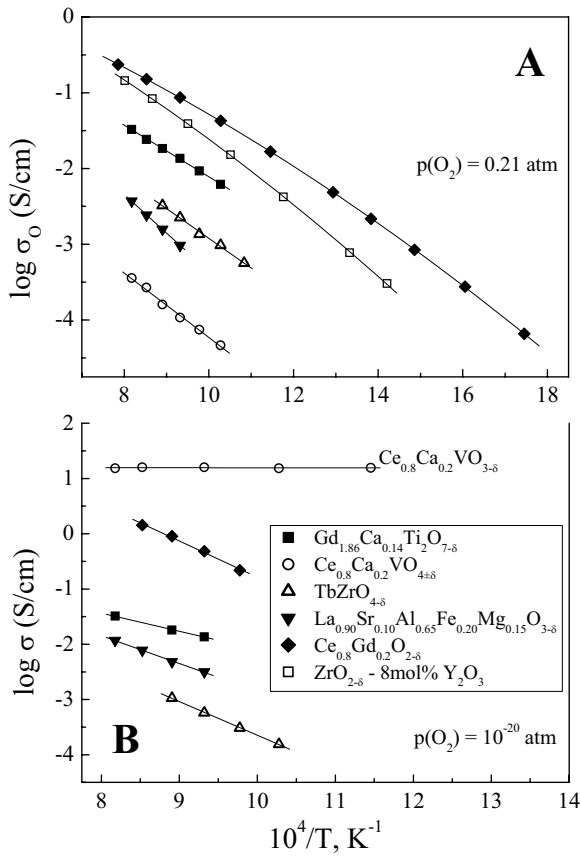


Fig.4.64. Comparison of oxygen ionic conductivity in air (A) and total conductivity at $p(\text{O}_2)=10^{-20}$ atm (B) for Y8SZ, $\text{Ce}_{0.8}\text{Gd}_{0.2}\text{O}_{2-\delta}$, $\text{TbZrO}_{4-\delta}$, $\text{Ce}_{0.8}\text{Ca}_{0.2}\text{VO}_{4+\delta}$, $\text{Gd}_{1.86}\text{Ca}_{0.14}\text{Ti}_2\text{O}_{7-\delta}$ and $\text{La}_{0.90}\text{Sr}_{0.10}\text{Al}_{0.65}\text{Fe}_{0.20}\text{Mg}_{0.15}\text{O}_{3-\delta}$.

As follows from Chapter 1.4, oxygen transport in the porous layer plays an important role in the anode performance. The transport properties of the electrode materials affect the adsorption/desorption of the reactant gases and the surface oxygen diffusion to the reaction zone; the oxygen transport through the electrode bulk may well be competitive to the latter process. This implies a relevance of ambipolar rather than simply oxygen-ionic conductivity of the oxide components. Despite the high ionic and substantial electronic conductivity of CGO under reducing conditions (Fig.4.64A, Fig.4.65A), the use of other materials with more stable oxygen content in the anode compositions may be of interest. Ca-doped cerium vanadates possessing the poorest ionic transport in air show the highest electronic conduction, even at low temperatures, when reduced to the perovskite phase. In addition, cerium vanadate based phases were reported [396] to have a high catalytic activity. Substitution of fluorite-type ceria with the phase having such a combination of properties, should enable to estimate relative roles of the ionic and electronic conductivities of Ce-containing additive in the anode layer. On the other hand, the influence of compositional variations of CeO₂-based phases on the electrochemical activity of cermets should still be assessed.

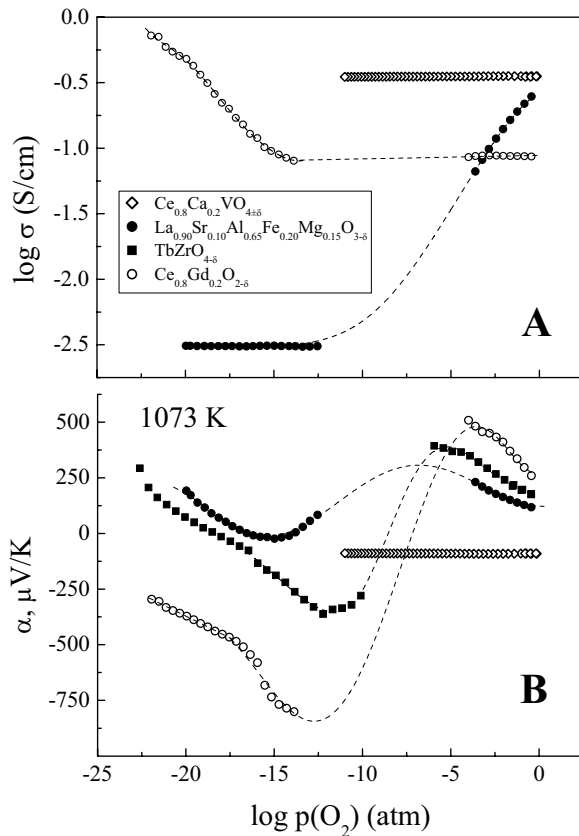


Fig.4.65. The oxygen partial pressure dependencies of the total conductivity (A) and Seebeck coefficient (B) of Ce_{0.8}Gd_{0.2}O_{2-δ}, TbZrO_{4-δ}, Ce_{0.8}Ca_{0.2}VO_{4+δ} and La_{0.90}Sr_{0.10}Al_{0.65}Fe_{0.20}Mg_{0.15}O_{3-δ}, at 1073 K.

The effect of oxygen ionic conductivity of zirconia in Me - YSZ and Me - YSZ-CeO_{2-δ} (or CGO) cermets on the anode performance remains still debatable (see Chapter 1.5.2.1); replacing YSZ with less conductive (Gd,Ca)₂Ti₂O_{7-δ}, TbZrO_{4-δ} or La_{0.9}Sr_{0.1}(Al,Fe)Mg_{0.15}O_{3-δ} phases, belonging to different structural types, might clarify if the properties of this component are critical. The use of titanate pyrochlores and aluminate-ferrite perovskites may be advantageous from the economic point of view, whereas the incorporation of variable-valence terbium cations into the fluorite-related structure could favorably modify the electrocatalytic activity of zirconia.

In order to reveal the roles of the ionically-conducting oxide components in the cermets, materials with quite a wide range of transport properties were studied. Within each group of oxide materials except for La_{0.90}Sr_{0.10}Al_{0.85-x}Fe_xMg_{0.15}O_{3-δ}, compositions showing maximum ionic conductivity were selected for fabrication and testing the anode layers. The phase stability to reduction was, in principle, sufficient in all cases. For the (La,Sr)(Al,Fe)O_{3-δ} perovskites, the thermal and low-p(O₂) stability is supposed to decrease on Fe doping. Although no degradation of transport properties was observed for all these materials, the anode operating conditions correspond to oxygen pressures far below Fe_xO/Fe boundary and the decomposition of phases with high iron content might be stagnated kinetically. Therefore, La_{0.90}Sr_{0.10}Al_{0.65}Fe_{0.20}Mg_{0.15}O_{3-δ} was used as the cermet component. Another advantage of this material is the lower variations of oxygen nonstoichiometry under reducing conditions, confirmed by essentially constant conductivity values (Fig.4.65A).

Part 5: Processing and electrochemical activity of mixed-conducting electrodes

The literature data summarized in Chapters 1.4 and 1.5 shows that a high electrochemical activity can only be expected when the specific surface area of the electrode layer is large and the size of component particles is small. This makes it necessary to use submicron oxide powders and to choose the thermal treatment conditions at which their sintering would be limited. In the present study, the glycine-nitrate process and cellulose-precursor technique were selected to obtain the electrode components. These synthesis methods are simple and enable to obtain homogeneous submicron oxide powders.

5.1. SOFC cathode layers in contact with LSGM electrolyte

5.1.1. Fabrication of porous cathode layers

Porous electrode layers of $\text{La}_2\text{Ni}_{0.8}\text{Cu}_{0.2}\text{O}_{4+\delta}$, $\text{YBaCo}_4\text{O}_{7+\delta}$ and $\text{YBaCo}_{3.2}\text{Fe}_{0.8}\text{O}_{7+\delta}$ powders prepared via the GNP and YBaCo_4O_7 -Ag (90-10 wt%) mixture were deposited onto the $(\text{La}_{0.9}\text{Sr}_{0.1})_{0.98}\text{Ga}_{0.8}\text{Mg}_{0.2}\text{O}_{3-\delta}$ ceramics and annealed for 2 h in air. The use of GNP-synthesized oxide powders, characterized in Chapters 3.1.2 and 3.1.3, makes it possible to fabricate porous cathode layers with well-developed homogeneous porous microstructure (Figs.5.1 and 5.2).

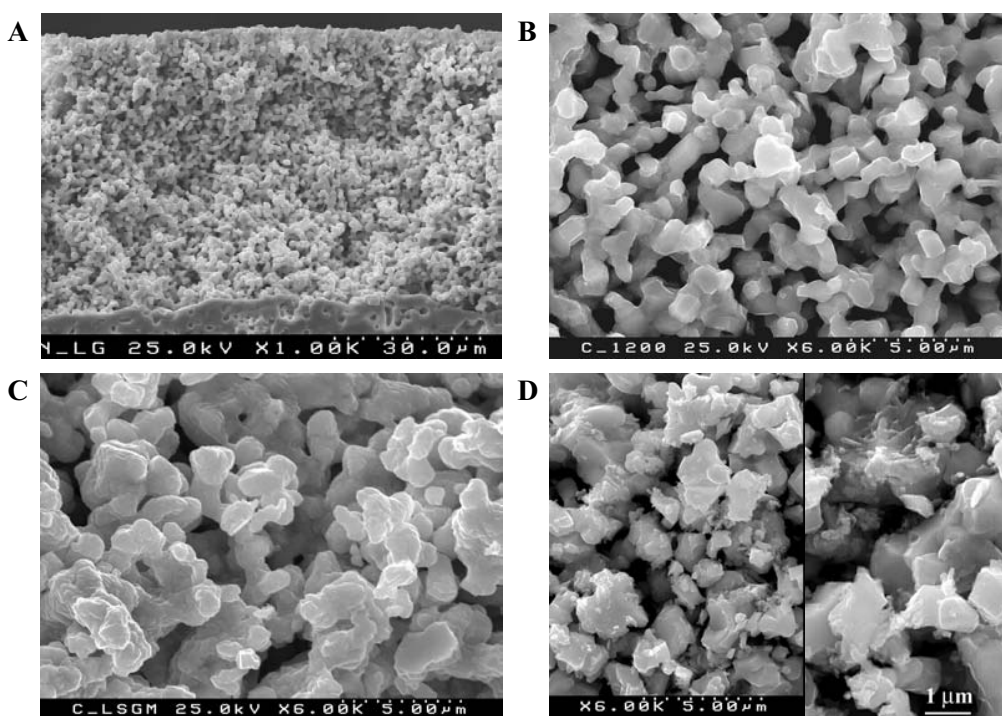


Fig.5.1. SEM micrographs of $\text{La}_2\text{Ni}_{0.8}\text{Cu}_{0.2}\text{O}_{4+\delta}$ cathode layers applied onto the surface of LSGM solid electrolyte, before (A) and after (B, C) polarization measurements, and following measurements after modification with PrO_x (D). Fabrication temperatures were 1473 K (A, B, D) and 1523 K (C).

In order to elucidate the microstructural effects on the electrode performance, the porous $\text{La}_2\text{Ni}_{0.8}\text{Cu}_{0.2}\text{O}_{4+\delta}$ cathode layers were prepared in two series, with different annealing temperatures (1473 and 1523 K). Formation of single K_2NiF_4 -type phase of $\text{La}_2\text{Ni}_{0.8}\text{Cu}_{0.2}\text{O}_{4+\delta}$ during sintering of electrode layers was confirmed by XRD and SAED analyses (Fig.3.13).

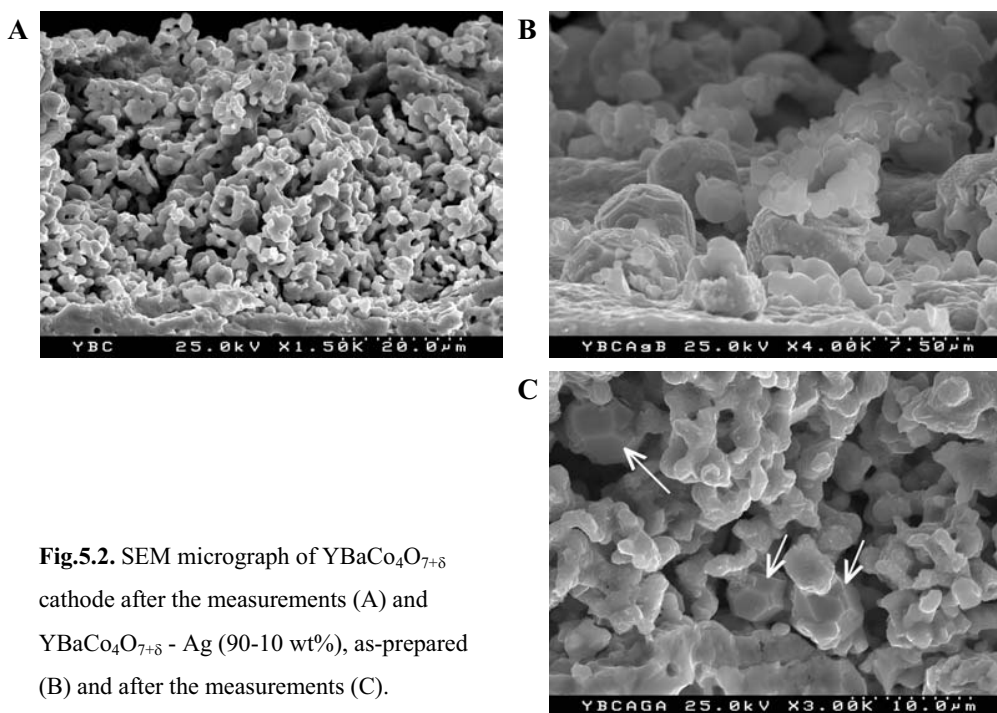


Fig.5.2. SEM micrograph of $\text{YBaCo}_4\text{O}_{7+\delta}$ cathode after the measurements (A) and $\text{YBaCo}_4\text{O}_{7+\delta}$ - Ag (90-10 wt%), as-prepared (B) and after the measurements (C).

Pure single-phase $\text{YBaCo}_{4-x}\text{Fe}_x\text{O}_{7+\delta}$ ($x = 0, 0.8$) and Ag-containing layers were sintered in air for 2 h at 1333-1343 and 1273 K, respectively. Highly-dispersed metallic silver (10 wt%) was added into a paste used for electrode fabrication on the basis of the results reported in Ref.[196]. Since the melting point of Ag (1234 K) is lower than the cell fabrication temperature, a significant part of silver is volatilised in the course of cathode sintering at 1273 K. According to TGA, these losses correspond to 8-10 wt% of total amount of metallic Ag. The SEM/EDS inspections showed that remaining silver spreads mainly along the electrolyte surface, but small amounts are present in the electrode bulk as well (Fig.5.2B and 5.2C). Similar behavior was earlier observed for Ag-containing $\text{La}_{0.5}\text{Sr}_{0.4}\text{MnO}_{3.8}$ cathodes [196]. The electrode morphology was practically unchanged after the electrochemical measurements; no essential Ag losses took place.

After the measurements, selected electrode layers were surface-modified with praseodymium oxide, according to results of [196]. The activation included impregnation with a $\text{Pr}(\text{NO}_3)_3 \cdot 5\text{H}_2\text{O}$ solution in ethanol, drying and annealing in air at 1073 K for 2 h; then the

overpotential-current dependencies were re-measured. In all cases, the absence of fast degradation processes was verified by the measurements of time dependencies of the overpotential at fixed currents during 50-200 h.

5.1.2. Electrochemical behavior of $\text{La}_2\text{Ni}_{0.8}\text{Cu}_{0.2}\text{O}_{4+\delta}$ cathodes

The impedance spectroscopy data were used to calculate polarization resistance; the current density and overpotential values varied in the ranges 0-220 mA/cm^2 and 0-350 mV, respectively; the time necessary to attain steady-state conditions was 0.5-10 h. Fig.5.3 shows representative impedance spectra. The high-frequency intercept of the arcs corresponds to the electrolyte and electrode series resistance. The electrode polarization resistance was determined as a difference between the high- and low-frequency intercepts. The reproducibility of results was separately checked after each measurement cycle; one example is shown in Fig.5.4.

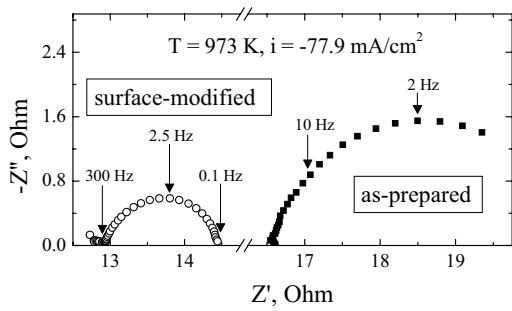


Fig.5.3. Typical impedance spectra of $\text{La}_2\text{Ni}_{0.8}\text{Cu}_{0.2}\text{O}_{4+\delta}$ cathode, as-prepared and surface-activated with PrO_x . Spectra obtained in the course of polarization measurements at 973 K in air.

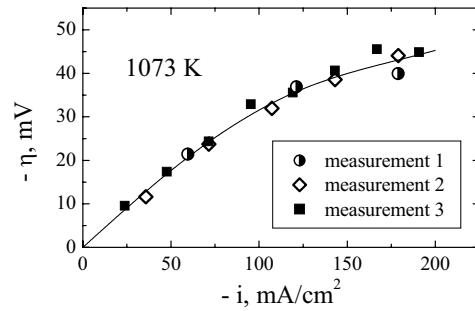


Fig.5.4. Reproducibility of overpotential vs. current dependence for $\text{La}_2\text{Ni}_{0.8}\text{Cu}_{0.2}\text{O}_{4+\delta}$ cathode, fabricated at 1473 K, in the course of the measurement cycles repeated several times.

The oxygen partial pressure dependence of electrode polarization resistance, under zero applied *dc* voltage, is presented in Fig.5.5. The slope parameter (*m*) of the simplest power model $R_\eta = R_\eta^0 \times p(\text{O}_2)^{1/m}$ is equal to (-3 ± 0.3) , being very different (higher) from the slope of $p(\text{O}_2)$ dependencies of the total conductivity and Seebeck coefficient (Table 3.8). This clearly indicates that, although the conductivity of $\text{La}_2\text{Ni}_{0.8}\text{Cu}_{0.2}\text{O}_{4+\delta}$ is 10-20 times lower than that of $\text{Ln}(\text{Sr})\text{CoO}_{3-\delta}$ (Chapter 1.5.1.3), the transport of electronic charge carriers cannot be considered as a rate-limiting step of the electrode reaction. Taking into account that the ionic conduction in $\text{La}_2\text{Ni}(\text{Cu})\text{O}_{4+\delta}$ is relatively high (Fig.3.25) and that oxygen permeation through $\text{La}_2\text{Ni}(\text{Cu})\text{O}_{4+\delta}$ ceramics at temperatures below 1150 K is primarily determined by the surface exchange kinetics (Fig.3.24),

one may expect a significant role of exchange rate at the electrode/gas interface [79]. In particular, the electrochemical reaction might be located not only at the triple phase boundary but also at the electrode surface, with subsequent oxygen ion diffusion through the bulk and, possibly, along the surface. Although in the case of porous electrode layers where the specific surface area is much larger (Fig.5.1), the overall exchange rate should be substantially higher compared to the dense ceramics, the surface exchange may still affect electrode performance, especially at moderate temperatures. For instance, oxygen permeation fluxes through La(Sr)MnO_{3-δ} ceramics are also surface-limited [147,196]; the oxygen reduction kinetics on La(Sr)MnO₃-based cathodes is determined by exchange-related factors, such as the concentration of oxygen vacancies on electrode surface, the role of which increases when temperature decreases [148,196,422].

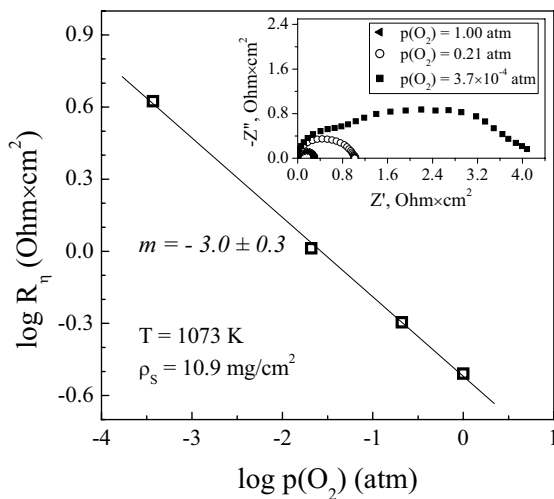


Fig.5.5. Oxygen partial pressure dependence of the polarization resistance of $\text{La}_2\text{Ni}_{0.8}\text{Cu}_{0.2}\text{O}_{4+\delta}$ electrode fabricated at 1473 K. Inset shows impedance spectra at various oxygen pressures, after correction for the electrode area and subtraction of the displacement from the origin of the Z' -axis resulting from ohmic losses.

Studying of $\text{La}_2\text{Ni}_{0.8}\text{Cu}_{0.2}\text{O}_{4+\delta}$ electrodes under high current densities (Figs.5.6 and 5.7) demonstrated a relatively high electrochemical activity. For example, at 1073 K and current density of 200 mA/cm^2 , the cathodic overpotential of electrode layer annealed at 1473 K was $46 \pm 2 \text{ mV}$. The overpotential vs. current dependencies follow Tafel equation without any indication of a limiting current density, thus implying an absence of gas diffusion limitations. At 1073 K, the anodic performance is worse than cathodic; at lower temperatures the anodic and cathodic overpotentials become similar. This may suggest that at 1073 K the exchange currents are affected by the surface concentration of active sites, such as oxygen vacancies, the coverage of which with oxygen species significantly depends on the current direction. High cathodic polarization is supposed to decrease oxygen content in the lattice of $\text{La}_2\text{Ni}_{0.8}\text{Cu}_{0.2}\text{O}_{4+\delta}$ electrode near surface, thus increasing the number of active sites participating in the reaction; this may decrease electrode polarization at a given current density. Under high anodic polarization, the situation is opposite. A

similar behavior is characteristic of $\text{La}(\text{Sr})\text{MnO}_{3-\delta}$ electrodes, where the electrochemical reaction mechanism involves oxygen vacancies on the surface [148,422]. Decreasing temperature seems to change the exchange mechanism, presumably to increase role of adsorption processes, in agreement with oxygen permeation data (Fig.3.24).

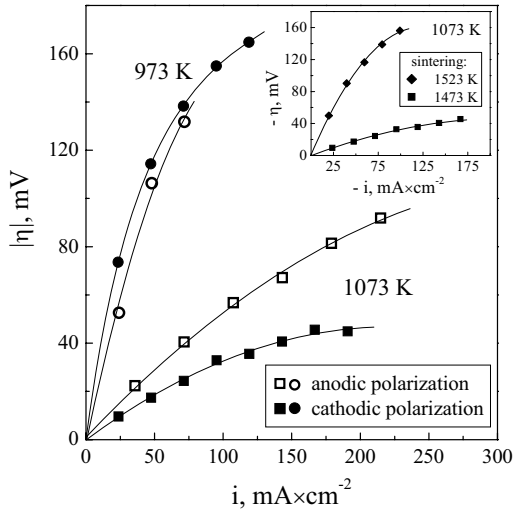


Fig.5.6. Comparison of anodic and cathodic polarization curves for $\text{La}_2\text{Ni}_{0.8}\text{Cu}_{0.2}\text{O}_{4+\delta}$ electrode layer, sintered at 1473 K, in contact with LSGM solid electrolyte in air. Inset compares overpotential vs. current dependencies for two $\text{La}_2\text{Ni}_{0.8}\text{Cu}_{0.2}\text{O}_{4+\delta}$ cathodes sintered at different temperatures, measured at 1073 K in air. Solid lines are for visual guidance.

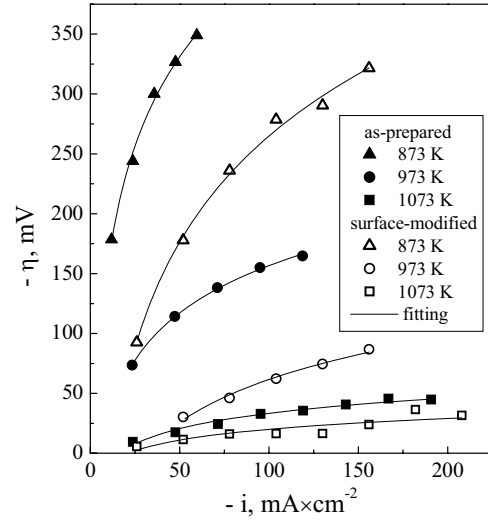
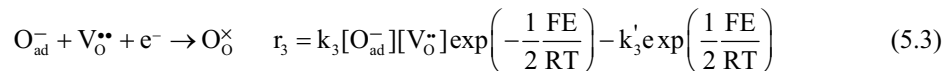
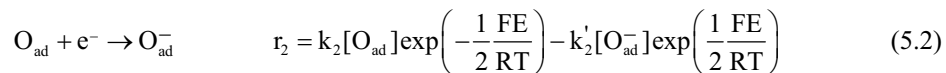


Fig.5.7. Current dependence of cathodic overpotential for one $\text{La}_2\text{Ni}_{0.8}\text{Cu}_{0.2}\text{O}_{4+\delta}$ electrode layer, as-prepared at 1473 K and surface-activated with PrO_x . Solid lines show fitting results according to Tafel equation.

If the overall rate is determined by surface-related processes, with no essential effect on the ionic charge carrier concentration in the electrode bulk under low polarization, a simplified model based on the assumptions [89] may include three consecutive steps:



where E is the electrode potential, r_i , k_i and k_i' are the total rate and the rate constants for the forward and backward reaction, respectively. The charge transfer coefficients (transport factors) in

the kinetic equations (5.2) and (5.3) are taken equal to 1/2 [89]. On assuming that cathodic process on oxygen-hyperstoichiometric $\text{La}_2\text{Ni}_{0.8}\text{Cu}_{0.2}\text{O}_{4+\delta}$ electrodes is associated with direct incorporation of interstitial oxygen ions, one should replace Eq.(5.3) by the reaction $\text{O}_{\text{ad}}^- + 2e^- \rightarrow \text{O}_i''$. However, the higher anodic overpotentials (Fig.5.6) are more consistent with Eq.(5.3).

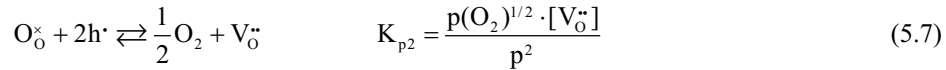
If the second elementary step Eq.(5.2) is considered as rate-limiting with two other steps being in virtual equilibrium, the concentrations of surface oxygen species can be expressed from Eqs.(5.1) and (5.3). Since the current (i) is equal to $(-2Fr)$, under high polarization the simplified expressions for anodic and cathodic currents can be derived from Eq.(5.2):

$$i_2^{\text{anodic}} = 2F \frac{k_2' k_3'}{k_3} [\text{V}_\text{O}^\bullet]^{-1} \exp\left(\frac{3}{2} \frac{FE}{RT}\right) \quad (5.4)$$

$$-i_2^{\text{cathodic}} = 2F \frac{k_2 k_1}{k_1'} p(\text{O}_2)^{\frac{1}{2}} \exp\left(-\frac{1}{2} \frac{FE}{RT}\right) \quad (5.5)$$

Comparison of Eqs.(5.4) and (5.5) may qualitatively explain the observed difference in anodic and cathodic performance (Fig.5.6).

Under equilibrium conditions, the oxygen vacancy concentration is determined by intrinsic Frenkel defect formation and oxygen exchange with gas phase



and the electroneutrality condition $p + 2[\text{V}_\text{O}^{\bullet\bullet}] = 2[\text{O}_i'']$, where p is the electron-hole concentration. If $[\text{V}_\text{O}^{\bullet\bullet}] \ll [\text{O}_i'']$, the total oxygen hyperstoichiometry should be proportional to $p(\text{O}_2)^{1/6}$. This is confirmed by experimental data on $\text{La}_2\text{NiO}_{4+\delta}$ [260] and $\text{La}_2\text{CuO}_{4+\delta}$ [319]. In these conditions $[\text{V}_\text{O}^{\bullet\bullet}] \approx K_v \cdot p(\text{O}_2)^{-1/6}$. The equilibrium electrode potential, $E_0 = \text{const} + (RT/mF) \ln p(\text{O}_2)$, can be calculated under conditions when $i^{\text{anodic}} = i^{\text{cathodic}} \equiv i_0$, with i_0 being the exchange current density. The overpotential is defined as $\eta = E - E_0$. When the polarization is low, the surface concentration of oxygen vacancies should be dependent of the oxygen pressure and essentially independent of current. Substituting E and $[\text{V}_\text{O}^{\bullet\bullet}]$ into Eqs.(5.4) and (5.5) and then inserting them into the steady-state current $i = i^{\text{anodic}} + i^{\text{cathodic}}$, one can obtain after simple transformations:

$$i_2 = 2F \left(\frac{k_2' k_3'}{k_3 K_v} \right)^{\frac{1}{4}} \left(\frac{k_2 k_1}{k_1'} \right)^{\frac{3}{4}} p(\text{O}_2)^{\frac{5}{12}} \left[\exp\left(\frac{3}{2} \frac{F\eta}{RT}\right) - \exp\left(-\frac{1}{2} \frac{F\eta}{RT}\right) \right] \quad (5.8)$$

Under low polarization ($|\eta| \ll RT/F$), one can calculate polarization resistance as $R_\eta = |\eta|/I$ by taking linear part of the exponential members. For the model expressed by Eq.(5.8), R_η is proportional to $p(\text{O}_2)^{-5/12}$. The slope of the experimental dependence (Fig.5.5), equal to -0.33, is

quite close to the model value of -0.41. Another approximation, based on the assumption that the concentration of surface active centers is $p(\text{O}_2)$ -independent, gives the slope of -0.375.

In general, by selecting a more complex exchange mechanism or by considering another rate-determining steps, one can easily obtain the values of $(1/n)$ in the range from $(-1/12)$ to $(-1/2)$; representative examples derived in a similar manner can be found in Refs.[32,89]. The data on R_{η} vs. $p(\text{O}_2)$ dependence cannot, therefore, be used to unambiguously identify a single process limiting exchange currents. Nevertheless, these results suggest that the rate-limiting steps are related to the gas/electrode interface; if the oxygen exchange kinetics would be limited by ion diffusion in the electrode bulk, a slope close to $(-1/6)$ could be supposed [263].

It should be separately noted that at high oxygen pressures, the impedance spectra of $\text{La}_2\text{Ni}_{0.8}\text{Cu}_{0.2}\text{O}_{4+\delta}$ cathodes consist of one single arc (Figs.5.3 and 5.5), which is attributed to the charge-transfer process, such as Eq.(5.2) or Eq.(5.3). On reduction, the electrode behavior becomes more complex, suggesting appearance of at least one additional reaction rate-determining step (Fig.5.5). The latter is supposed to have a diffusion-related nature [79,112].

5.1.3. $\text{YBaCo}_4\text{O}_{7+\delta}$ -based electrodes

As for the $\text{La}_2\text{Ni}_{0.8}\text{Cu}_{0.2}\text{O}_{4+\delta}$ cathodes at oxygen pressures close to atmospheric, the impedance spectra of $\text{YBa}(\text{Co,Fe})_4\text{O}_{7+\delta}$ porous layers comprise a well-resolved single arc; typical examples are shown in Fig.5.8. The reproducibility of electrochemical data was verified studying 2-3 similar electrodes prepared under identical conditions.

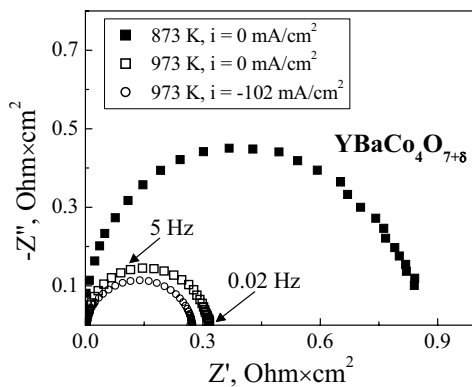


Fig.5.8. Examples of the impedance spectra of $\text{YBaCo}_4\text{O}_{7+\delta}$, corrected for ohmic contribution and normalized to electrode area, at open-circuit conditions and under polarization in air.

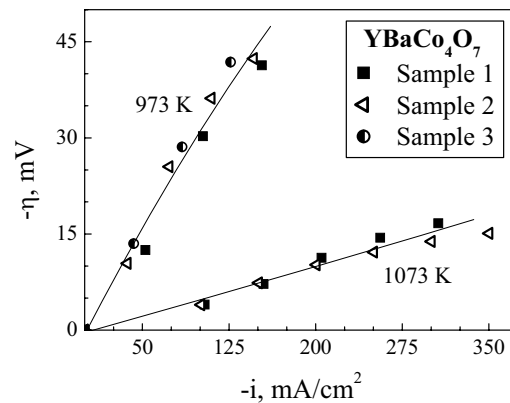


Fig.5.9. Reproducibility of overpotential vs. current dependence for $\text{YBaCo}_4\text{O}_{7+\delta}$ cathode, measured for three different cells.

YBa(Co,Fe)₄O_{7+δ} cathodes exhibit a very low polarization (Figs.5.9-5.11) and a good reproducibility of the performance in contact with LSGM solid electrolyte (Fig.5.9). At 873 K, the electrode overpotential was as low as -145 mV at current density of -200 mA/cm². The polarization resistance, which can be evaluated from the impedance spectra normalized to the electrode area, was lower than 1 Ohm×cm² at 873 K (Fig.5.8). The electrochemical activity of yttrium-barium cobaltite cathodes is higher than that of La₂Ni_{0.8}Cu_{0.2}O_{4+δ} (Table 5.1). For instance, at 873 K and *i* = 50 mA/cm², the overpotential of cobaltite electrodes is approximately 4.5 times lower than that of nickelate layers.

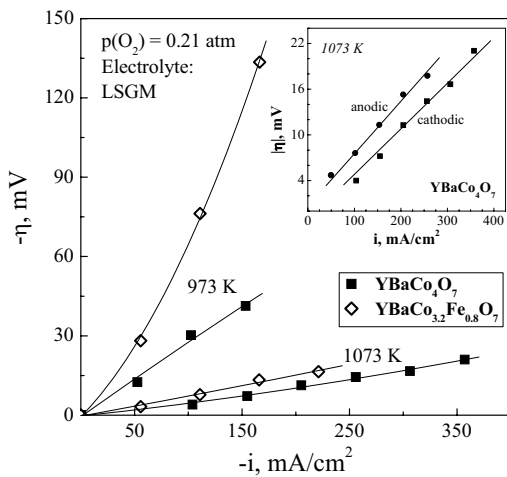


Fig.5.10. Current dependencies of cathodic overpotentials for YBa(Co,Fe)₄O₇ in contact with LSGM electrolyte, in air. Inset compares the anodic and cathodic polarization curves of YBaCo₄O_{7+δ} porous layer.

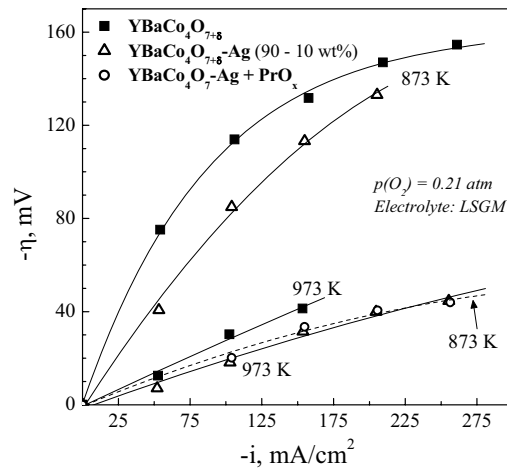


Fig.5.11. Current dependencies of the cathodic overpotentials of YBaCo₄O_{7+δ} layers with and without silver addition and after the surface-activation of the latter with PrO_x.

Table 5.1

Overpotentials (mV) of YBaCo₄O_{7+δ} and LaNi_{0.8}Cu_{0.2}O_{4+δ} porous cathode layers in contact with LSGM electrolyte

T, K	<i>i</i> , mA/cm ²	YBaCo ₄ O _{7+δ}	YBaCo ₄ O _{7+δ} -Ag (90-10 wt%)	LaNi _{0.8} Cu _{0.2} O _{4+δ}
1073	150 mA/cm ²	6.9	-	42.1
973	100 mA/cm ²	28.4	17.6	157
873	60 mA/cm ²	79.5	46.6	350

Most likely, this superior performance is due to their interaction with LSGM surface, particularly Ba and Co diffusion into the surface layer of lanthanum gallate ceramics, confirmed by the EDS studies (Fig.5.12). Incorporation of cobalt into LSGM should increase both ionic and electronic conductivities of solid electrolyte surface, thus promoting surface exchange; an increase in the oxygen exchange rates can also be expected due to Ba diffusion ([172,173] and references cited). Recently, a very good electrochemical activity in contact with Co-substituted LSGM was reported for BaCoO₃-based perovskite cathodes [173], the TECs of which, however, may be excessively high [146]. The excellent performance of YBaCo₄O_{7+δ} and Ba(La)CoO_{3-δ} electrodes should have a similar nature, probably due to enhanced oxygen exchange currents of the electrolyte. On the other hand, the activity of yttrium-barium cobaltite electrodes may be contributed by the lattice instability, especially due to oxygen activity variations under cathodic polarization. Doping of YBaCo₄O₇ with iron has a little influence on the electrode performance at 1073 K, but leads to significantly higher overpotentials at 973 K, probably due to an increasing tendency to the phase decomposition and volume changes associated with increasing oxygen content (Fig.5.10).

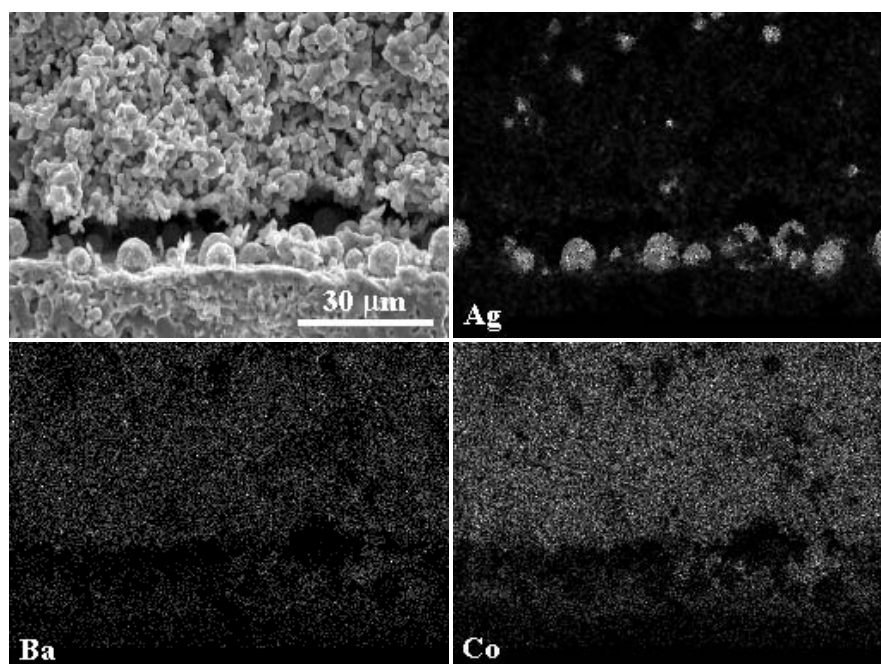


Fig.5.12. SEM micrograph of fractured YBaCo₄O_{7+δ}-Ag/LSGM cell and the corresponding distribution of Ag, Ba and Co, evaluated by EDS. The density of white dots corresponds to cation concentration.

Further decrease in the cathodic overpotentials at 873-973 K can be achieved by adding metallic silver (Fig.5.11 and Table 5.1), which spreads along the electrolyte surface and partly in the bulk of porous electrode layer, thus enhancing the TPB length and, probably, promoting the oxygen exchange rate of the electrode material. Nevertheless, taking into account the volume fractions of components, the porous layer of $\text{YBaCo}_4\text{O}_{7+\delta}$ should still play a dominant role in the electrochemical processes. One should separately mention that the $p(\text{O}_2)$ -independent conductivity values at decreased temperatures (Fig.3.35) suggest that high cathodic polarisation should have no effect on the electrical properties of electrode layers.

5.1.4. Critical role of ceramic microstructure and effects of surface modification

As expected, increasing the $\text{La}_2\text{Ni}_{0.8}\text{Cu}_{0.2}\text{O}_{4+\delta}$ electrode fabrication temperature from 1473 to 1523 K resulted in grain growth and agglomeration (Fig.5.1, B and C). This leads to considerably worse electrochemical activity (inset in Fig.5.6). Although such a behavior might be partly ascribed to decreasing triple-phase boundary length, the most likely reason relates to decreasing specific surface area and, thus, overall exchange currents. Therefore, the performance of $\text{La}_2\text{Ni}_{0.8}\text{Cu}_{0.2}\text{O}_{4+\delta}$ cathodes can be improved by reducing fabrication temperature, by further decrease of the grain size, and by the incorporation of electrocatalytically-active components onto electrode and electrolyte surfaces.

Fig.5.7 compares overpotential vs. current dependencies for one $\text{La}_2\text{Ni}_{0.8}\text{Cu}_{0.2}\text{O}_{4+\delta}$ layer after preparation at 1473 K and after surface modification with praseodymium oxide; the corresponding microstructures are shown in Figs. 5.1B and 5.1D. SEM/EDS, TEM/EDS and XRD analyses, performed before and after electrochemical tests, confirmed that praseodymia is distributed mainly in pores and on the surface of electrode and electrolyte; the interaction between $\text{La}_2\text{Ni}_{0.8}\text{Cu}_{0.2}\text{O}_{4+\delta}$ and PrO_x phases was below the detection limits. In particular, the lattice parameters of $\text{La}_2\text{Ni}_{0.8}\text{Cu}_{0.2}\text{O}_{4+\delta}$ remain essentially unchanged after surface activation and testing during 150-200 h. At the same time, surface interaction between these phases cannot be excluded. As for $\text{La}(\text{Sr})\text{MnO}_3$ -based cathodes [196], the activation drastically increases electrochemical activity, especially at reduced temperatures. For instance, at 873 K the cathodic overpotential is decreased by approximately 2 times, from 330 down to 175 mV at 50 mA/cm^2 .

Possible nature of such an enhancement in electrode performance was discussed in Ref.[196]. In fact, similar to other electrochemical data on mixed-conducting cathodes, this phenomenon cannot be unambiguously attributed to a single factor; the activation may lead to a faster surface exchange of both solid electrolyte and electrode, to an enlargement of TPB and electrode surface area, and even to an improvement of transport properties of the porous electrode layer due to significant mixed conductivity of praseodymium oxide (Refs.[33,196] and references

cited). The latter is indicated, in particular, by the substantial decrease in the ohmic resistance after the activation as illustrated by Fig.5.3. Most likely, a combination of all these factors is responsible for the enhanced electrochemical activity. Nonetheless, the data on surface-modified $\text{La}_2\text{Ni}_{0.8}\text{Cu}_{0.2}\text{O}_{4+\delta}$ based layers are in agreement with the assumption that their performance is influenced by surface-related processes.

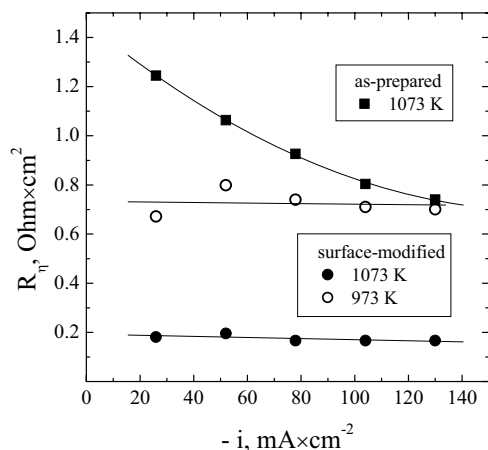


Fig.5.13. Dependence of the polarization resistance of $\text{La}_2\text{Ni}_{0.8}\text{Cu}_{0.2}\text{O}_{4+\delta}$ electrode, as-prepared at 1473 K and after surface modification with PrO_x , on the direct current passed through electrode. Solid lines are for visual guidance.

This hypothesis is also supported by the dependence of polarization resistance on the cathodic current density (Fig.5.13). For non-activated $\text{La}_2\text{Ni}_{0.8}\text{Cu}_{0.2}\text{O}_{4+\delta}$ layer, the values of R_η calculated from impedance spectra decrease with increasing current, which well corresponds to the relationship between cathodic and anodic overpotentials (Fig.5.6). Again, this behavior is very similar to literature data [196,148,422] on $\text{La}(\text{Sr})\text{MnO}_{3-\delta}$ and $\text{La}(\text{Sr})\text{CoO}_{3-\delta}$ electrodes, where cathodic polarization leads to formation of oxygen vacancies on the surface, contributing to the electrochemical activity enhancement. After the surface activation of $\text{La}_2\text{Ni}_{0.8}\text{Cu}_{0.2}\text{O}_{4+\delta}$ layer, the polarization resistance becomes current-independent (Fig.5.13). One may suggest that, due to an increase in the concentration of active centers on the electrode surface, the role of this factor decreased.

The major trends of $\text{YBa}(\text{Co},\text{Fe})_4\text{O}_{7+\delta}$ electrode behavior are quite similar to those of $\text{La}_2\text{Ni}_{0.8}\text{Cu}_{0.2}\text{O}_{4+\delta}$. In particular, praseodymia treatment enables to drastically decrease the polarization of $\text{YBaCo}_4\text{O}_{7+\delta}$ - Ag cathode layers (Fig.5.11). Since the ionic conductivity of $\text{YBaCo}_4\text{O}_{7+\delta}$ based phases is lower compared to that of $\text{La}_2\text{Ni}_{0.8}\text{Cu}_{0.2}\text{O}_{4+\delta}$, narrowing the electrochemically-active zone at the cathode surface and increasing role of the surface exchange kinetics [81,82]. The latter, and the surface diffusion processes, can be enhanced by the surface modification. Another possible reason for this behavior may be associated with increasing electrolyte surface-exchange currents. In fact, a significant role of the electrolyte surface is

indicated by the effect of Ag additions (see Fig.5.11). Also, this modification of porous layers might result in better electrical contacts between the electrode grains, which could worsen due to the phase transformations.

5.1.5. Concluding remarks: factors determining electrochemical activity

When the necessary level of electronic and oxygen ionic conductivity of a mixed-conducting electrode material is already achieved, the electrochemical activity seems determined by other factors. One relevant factor is the interaction between cathode material and solid electrolyte. The diffusion layers at the electrode/electrolyte interface may either promote oxygen exchange of the electrolyte ceramics surface, as for the barium cobaltites/LSGM or, oppositely, block the oxygen transport, e.g. in the case of LSM/YSZ electrodes. Another important parameter refers to activity of the electrode surface. Preserving the high surface area in the porous layer as well as enhancing the surface transport and catalytic properties is favorable for decreasing the electrode polarization. The effective method to reduce the overpotentials on the oxide cathodes is a deposition of highly-dispersed electrocatalytically active phase onto the electrode and electrolyte surfaces during or after the fabrication of porous layer. Indeed, as for the oxygen transport through dense $\text{La}_2\text{Ni}_{0.8}\text{Cu}_{0.2}\text{O}_{4+\delta}$ ceramics, the results on the electrode behavior suggest a considerable role of surface-related processes, such as oxygen sorption or discharge of oxygen ad-atoms on the electrode surface, with the active site concentration dependent on current. Due to this, the performance of $\text{La}_2\text{Ni}_{0.8}\text{Cu}_{0.2}\text{O}_{4+\delta}$ electrodes can be substantially enhanced by surface modification via impregnation with Pr-containing solutions, and also by decreasing fabrication temperature leading to greater surface area. Both silver and PrO_x additions improved the performance of $\text{YBaCo}_4\text{O}_{7+\delta}$ based cathodes.

The presence of phase transitions is considered quite important for the applicability of the electrode materials. First of all, phase transitions lead to unfavorable volume changes. On the other hand, the presence of morphotropic phase boundaries may weaken the bonds in the lattice [423], which would have a positive effect on the electrochemical activity. In most cases, however, the former factor plays more important role; therefore, the compositional modification is necessary to suppress the phase changes in $\text{YBaCo}_4\text{O}_{7+\delta}$ based materials.

5.2. Cellulose-precursor synthesis of SOFC anode components

Formation of single fluorite-type CGO phase in the course of calcinations was confirmed by XRD studies (Fig.5.14). After annealing, the oxide fibers were either converted into nanocrystalline powders by light mechanical action, or directly applied onto dense LSGM ceramics and sintered.

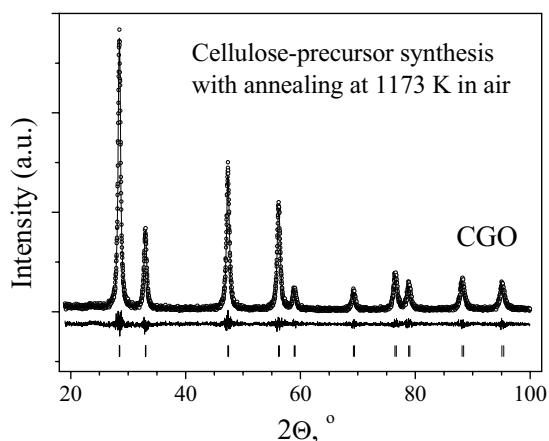


Fig.5.14. Observed, calculated and difference XRD pattern of $\text{Ce}_{0.8}\text{Gd}_{0.2}\text{O}_{2-\delta}$ prepared via the cellulose-precursor technique and annealed in air at 1173 K.

SEM studies of oxide fibers made of CGO (Fig.5.15A) showed that the precursor texture is retained after combustion; the fibers have a highly porous tubular-like microstructure (Fig.5.15B). Such a feature may be advantageous for the preparation of anodes with regular microstructures, which can further be optimized taking the electrode reaction mechanisms into account. In particular, by varying the type of cellulose precursor, the treatment conditions and the concentration of impregnating solution, this technique makes it possible to achieve necessary relationships between size and distribution of pores, specific surface area, distribution of electronically-conducting phase, triple-phase boundary length and other factors determining anode performance. Furthermore, sintering of the highly-porous oxide fibers onto solid-electrolyte substrate can be used to form ion-conducting ceramic matrix stabilizing metallic Ni with respect to sintering and redox cycling.

TEM inspection revealed that CGO particles constituting oxide fibers are nanocrystalline; their size varies in the range 8-35 nm (Fig.5.16). The crystallization of CGO phase was verified by electron diffraction studies; one example of the electron diffraction pattern is presented as the inset in Fig.5.16.

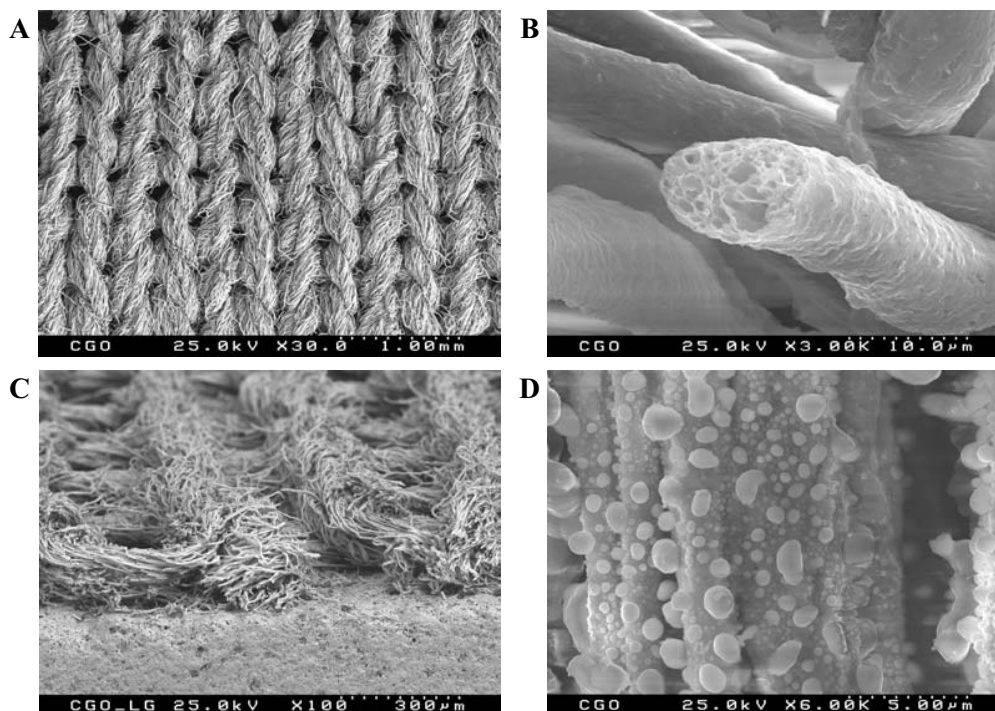


Fig.5.15. SEM micrographs of $\text{Ce}_{0.8}\text{Gd}_{0.2}\text{O}_{2-\delta}$ synthesized via the cellulose-precursor technique: (A, B), after synthesis and annealing in air at 1173 K; (C), applied onto LSGM substrate and annealed in air at 1573 K (cross-section view); (D), applied onto LSGM with subsequent deposition of metallic Ni (50 wt%) by impregnation with an aqueous $\text{Ni}(\text{NO}_3)_2 \cdot 6\text{H}_2\text{O}$ solution and reduction at 1273 K in flowing 10% H_2 -90% N_2 .

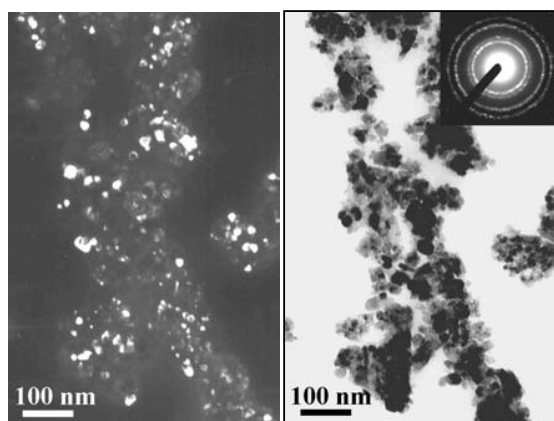


Fig.5.16. Dark- and bright-field TEM images and electron diffraction pattern of CGO powder prepared using the cellulose-precursor technique and annealed in air at 1173 K.

Owing to the potential advantages of anode microstructure control by cellulose precursor selection, direct application of oxide or cermet fibers onto solid-electrolyte ceramics might be of considerable interest. A series of electrode layers was thus prepared by applying CGO fibers onto LSGM, followed by annealing, impregnation with Ni-containing solutions and reduction. As an example, Fig.5.15C presents the cross-section SEM micrograph of one layer made of CGO fiber

after annealing at 1573 K for 2 h. The shrinkage of the oxide layer during the sintering process was about 16% in one direction and 6% in the other. The fiber forms a porous ceramic matrix with a relatively good adhesion to electrolyte and a regular microstructure suitable for metal incorporation. After impregnation with an aqueous solution of $\text{Ni}(\text{NO}_3)_2 \cdot 6\text{H}_2\text{O}$ and firing at 1273 K in a flow of 10% H_2 - 90% N_2 mixture for 0.25 h, metallic nickel is uniformly distributed in CGO fibres in the layer containing 50wt% Ni and 50wt% CGO (Fig.5.15D). At the same time, the stability of such Ni-CGO anodes in the course of redox cycling was found insufficient, most probably due to volume changes. Further developments necessary to prepare stable anode layers, by directly applying ceramic fibers onto electrolyte ceramics, are now in progress. In this work, therefore, the main emphasis is given to the CGO-containing cermets, where the nanocrystalline powders synthesized using cellulose-precursor technique were mixed with other components, as described in Table 5.2.

The same technique was used to synthesize the multicomponent cermets. In order to increase the electrochemical activity, catalytically-active CGO was incorporated in their composition. At the same time, relatively low (25 wt%) nickel concentration in the cermets was used in order to reduce the carbon deposition problems. Since the percolation threshold can be shifted varying the grain sizes of cermet components, the use of submicron NiO-CGO powders may enable decreasing the nickel content while preserving well-percolated grains and high conductivity in the porous layer. As an alternative approach to cope with the coking problem, attention was drawn to electrodes based on metallic copper, which possesses a considerably lower catalytic activity for C-C bond formation [160,307].

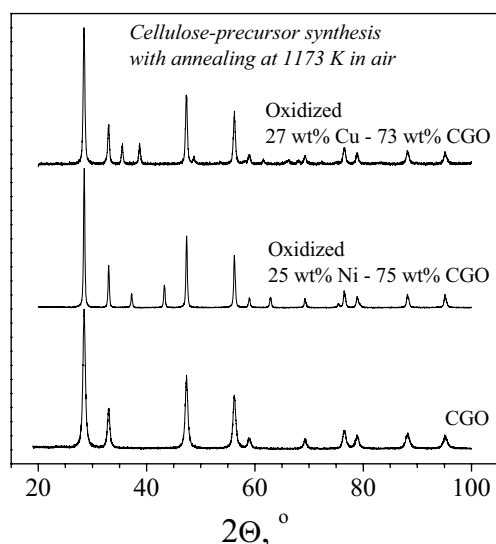


Fig.5.17. XRD patterns of CGO, NiO-CGO and CuO-CGO powders.

XRD results showed that the two-phase NiO-CGO and CuO-CGO composites were formed in the combustion front (Fig.5.17). The unit cell parameters of fluorite-type CGO phase, calculated from XRD data, were almost equal for all synthesized materials, 0.54250 ± 0.00005 nm. This suggests, in particular, that the interaction of CGO and NiO in the two-phase mixture is negligible.

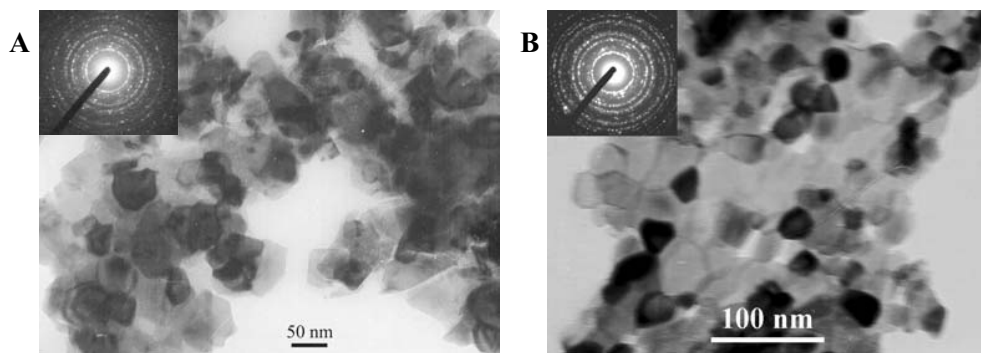


Fig.5.18. Bright-field TEM images and electron diffraction patterns of NiO-CGO (A) and CuO-CGO (B) powders prepared by cellulose-precursor technique.

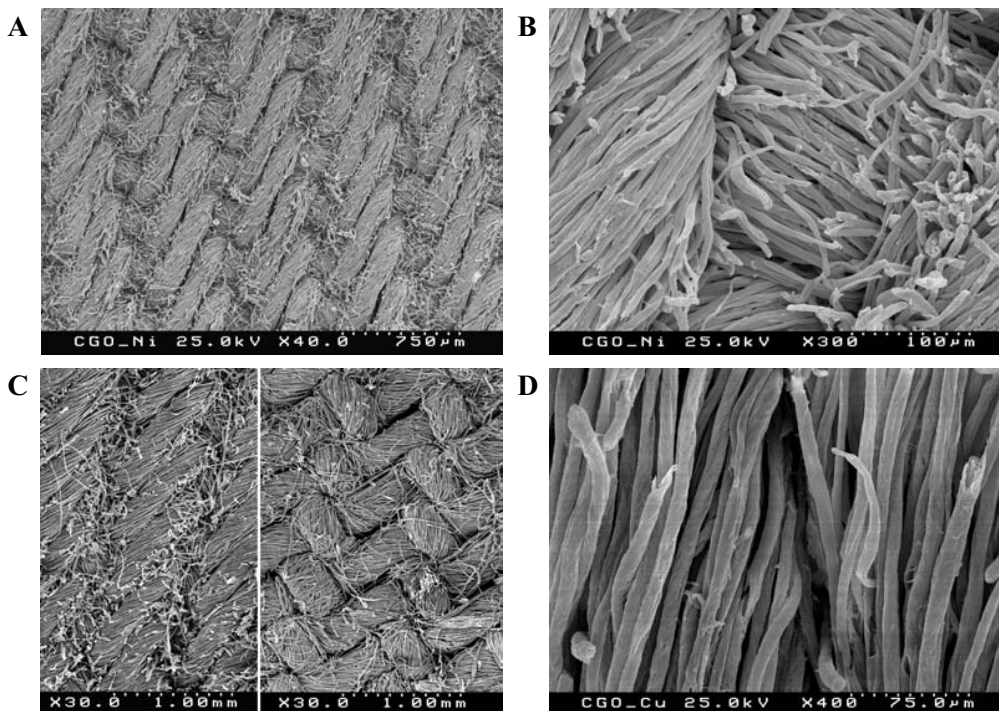


Fig.5.19. SEM micrographs NiO-CGO (A,B) and CuO-CGO (C,D) fibers prepared by cellulose-precursor technique and annealed in air at 1173 K.

The maximum concentration of the aqueous solution for impregnation of the cellulose fabric, permissible by this technique, seems close to 1M. After combustion of the cellulose material treated with higher-concentrated solutions, the fibers were destroyed.

The data shown above suggest that such method can be employed for fabrication of metallic grids, which may be of interest as components of multilayered anodes, improving their current collection. As discussed in Chapter 1.4.5, geometry of current collector should provide a homogeneous current distribution and should not limit the gas diffusion. In addition, highly-conductive Ni or Cu fibers could be incorporated in the anode layer improving the electronic transport and current distribution.

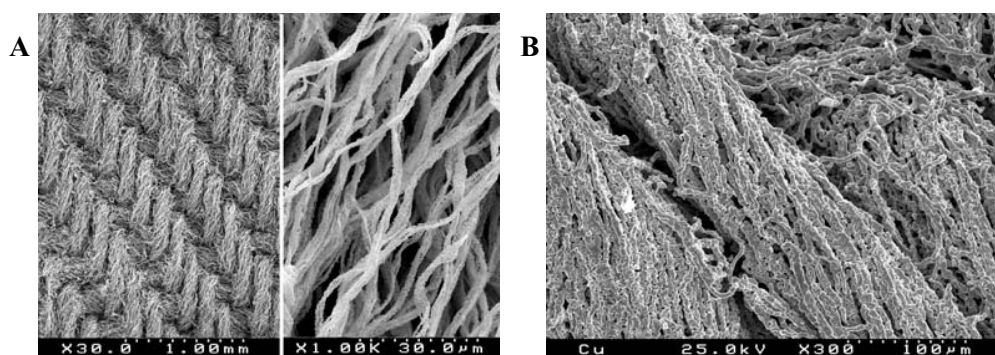


Fig.5.20. SEM micrographs of metallic Ni (A) and Cu (B) fibers prepared by cellulose-precursor technique and reduced at 1073 K under flowing H_2 - H_2O - N_2 gas mixture.

The NiO and CuO fibers were prepared analogously to CGO-containing materials, with subsequent reduction to corresponding metals in the H_2 - H_2O - N_2 gas flow at 1073 K. Thus obtained metallic meshes occurred very stable mechanically, as different from the oxide fibers. As expected, the materials considerably shrunk after reduction. The SEM images reflecting typical microstructures of these meshes are shown in Fig.5.20. Metallic fibers consist of well connected particles but remain quite porous. Thus, the possibility of obtaining the metal grids made of nickel and copper was evaluated.

5.3. Electrochemical performance of cermet anodes

5.3.1. Fabrication and characterization of porous anode layers

Table 5.2 summarizes the anode compositions and their preparation conditions. Nanocrystalline powders of single-phase $\text{Ce}_{0.8}\text{Gd}_{0.2}\text{O}_{2-\delta}$ (CGO) and two-phase NiO - CGO (Ni-CGO 25 – 75 wt% or 50 – 50 mol%) and CuO - $\text{Ce}_{0.8}\text{Gd}_{0.2}\text{O}_{2-\delta}$ (Cu - CGO 27 – 73 wt% or 50 – 50 mol%) mixtures, prepared via the cellulose-precursor technique (Table 2.1), were used for the fabrication of anode layers on the LSGM solid electrolyte. All YSZ materials were commercially available (Chapter 2.1). After annealing, the oxide fibers were either converted into nanocrystalline powders by light mechanical action, or directly applied onto dense LSGM ceramics and sintered. A series of Ni-containing cermets, including Ni - Y8SZ - CGO, Ni - $\text{Gd}_{1.86}\text{Ca}_{0.14}\text{Ti}_2\text{O}_{7-\delta}$ - CGO, Ni - Y8SZ - $\text{Ce}_{0.8}\text{Ca}_{0.2}\text{VO}_{4+\delta}$, Ni - $\text{TbZrO}_{4-\delta}$ - CGO and Ni - $\text{La}_{0.90}\text{Sr}_{0.10}\text{Al}_{0.65}\text{Fe}_{0.20}\text{Mg}_{0.15}\text{O}_{3-\delta}$ - CGO, where the weight ratio between the phases was 50-30-20%, and a metal-free Y8SZ - CGO (60 – 40 wt%) mixture were prepared using NiO obtained by thermal decomposition of $\text{Ni}(\text{NO}_3)_2 \cdot 6\text{H}_2\text{O}$, cellulose-precursor synthesized CGO and the powders of mixed conductors synthesized as specified in Table 2.1. The porous layers were prepared in a similar way as anodes comprising Y8SZ (Table 5.2). Ni - $\text{Zr}_{0.9}\text{Y}_{0.1}\text{O}_{2-\delta}$ - $\text{CeO}_{2-\delta}$ and Ni - $\text{Zr}_{0.9}\text{Y}_{0.1}\text{O}_{2-\delta}$ - CGO mixtures were prepared by grinding together the commercial powders and ceria obtained from thermally-decomposed $\text{Ce}(\text{NO}_3)_3 \cdot 6\text{H}_2\text{O}$, and deposited onto the $\text{Zr}_{0.9}\text{Y}_{0.1}\text{O}_{2-\delta}$ surface as described in Table 2.2.

The anode layers (5.1-7.2 mm in diameter) with loading density of 15-25 mg/cm^2 were screen-printed onto the surface of dense LSGM or $\text{Zr}_{0.9}\text{Y}_{0.1}\text{O}_{2-\delta}$ ceramics and annealed in air for 2 h; the sintering temperature was 1523 K for Ni - Y8SZ - CGO, 1273 K for Cu-based cermet, 1373 K for $\text{Zr}_{0.9}\text{Y}_{0.1}\text{O}_{2-\delta}$ -containing electrodes and 1573 K in all other cases. SEM inspections showed that the prepared electrode layers had a homogeneous porous microstructure; selected examples are shown below. After the electrochemical tests, selected anodes were surface-modified by impregnation with a saturated $\text{Ce}(\text{NO}_3)_3 \cdot 6\text{H}_2\text{O}$ solution in ethanol, followed by annealing at 1073-1273 K; then the overpotential-current dependencies were re-measured.

Table 5.2

Preparation conditions of selected ceria-containing SOFC anodes

Electrode composition	Electrolyte	Preparation conditions
Ni - Y8SZ - CGO 50 – 30 – 20 wt% [42 – 37 – 21 vol%]*	LSGM	<ul style="list-style-type: none"> ▪ decomposition of $\text{Ni}(\text{NO}_3)_2 \cdot 6\text{H}_2\text{O}$, cellulose-precursor synthesis of CGO ▪ mixing and grinding of NiO, CGO and commercial Y8SZ ▪ screen-printing ▪ annealing in air at 1523 K for 2 h ▪ reduction at 1073-1123 K in 10%H_2-90%N_2 atmosphere
Ni - $\text{Gd}_{1.86}\text{Ca}_{0.14}\text{Ti}_2\text{O}_{7-\delta}$ - CGO Ni - Y8SZ - $\text{Ce}_{0.8}\text{Ca}_{0.2}\text{VO}_{4+\delta}$ Ni - $\text{TbZrO}_{4-\delta}$ - CGO Ni - $\text{La}_{0.9}\text{Sr}_{0.1}\text{Al}_{0.65}\text{Fe}_{0.20}\text{Mg}_{0.15}\text{O}_{3-\delta}$ - CGO 50 – 30 – 20 wt%	LSGM	Analogously to Ni - Y8SZ - CGO cermet. The oxide components were synthesized as described in Chapter 2.1
Ni - CGO 25 – 75 wt% [21 – 79 vol%, 50 - 50 mol%]	LSGM	<ul style="list-style-type: none"> ▪ cellulose-precursor synthesis of NiO - CGO mixture ▪ screen-printing ▪ firing in air at 1573 K for 2 h ▪ reduction at 1073-1123 K in 10%H_2-90%N_2 atmosphere
Cu - CGO 27 – 73 wt% [23 – 77 vol%, 50 - 50 mol%]	LSGM	Analogously to Ni - CGO cermet but sintered at 1273 K
Y8SZ – CGO with Cu-mesh 60 – 40 wt%	LSGM	Analogously to Ni - Y8SZ - CGO cermet but cellulose-precursor-synthesized Cu-mesh was incorporated into the anode layer
Ni – $\text{Zr}_{0.9}\text{Y}_{0.1}\text{O}_{2-\delta}$ - $\text{CeO}_{2-\delta}$ 54 – (46-x) – x wt% [44 – (56-x) – x vol%] and Ni – $\text{Zr}_{0.9}\text{Y}_{0.1}\text{O}_{2-\delta}$ – CGO 54 – 17 – 29 wt% [47 – 22 – 31 vol%]	$\text{Zr}_{0.9}\text{Y}_{0.1}\text{O}_{2-\delta}$	<ul style="list-style-type: none"> ▪ decomposition of $\text{Ce}(\text{NO}_3)_2 \cdot 6\text{H}_2\text{O}$, mixing with commercial powders and ball-milling ▪ screen-printing ▪ firing at 1373 K in air ▪ reduction at 1173-1273 K in wet 10%H_2-90%N_2 atmosphere

* The volume percentage was estimated from the weight percentage and theoretical densities calculated from XRD data at room temperature in air, neglecting oxygen stoichiometry variations and accounting solid phases only.

5.3.2. Effects of metal/oxide ratio and phase components

Fig.5.21 shows the overpotential dependence on ceria content in anode layers at the fixed current density of 100 mA/cm²; the general composition of the anodes applied onto $\text{Zr}_{0.9}\text{Y}_{0.1}\text{O}_{2-\delta}$ electrolyte is 54 wt% Ni – (46-x) wt% $\text{Zr}_{0.9}\text{Y}_{0.1}\text{O}_{2-\delta}$ – x wt% $\text{CeO}_{2-\delta}$ (x = 0-40). When the temperature is high, the anode performance is moderately influenced by ceria additive. For

example, at 1223 K adding 10-20 wt% of ceria leads to decreasing overpotential from approximately 40 down to 25 mV; further additions result in a worse performance. This behavior seems in agreement with literature data [19,20,33,158,424] and may be explained by an enhancement of anode electrocatalytic activity due to the incorporation of $\text{CeO}_{2-\delta}$, which may be, however, quite passivated after thermal treatments at 1273-1373 K (Table 5.2). Although a significant oxygen nonstoichiometry of $\text{CeO}_{2-\delta}$ in reducing atmospheres [424] makes it possible to expect a substantial ionic transport, the conductivity of YSZ electrolyte at 1173-1223 K is also high [33]; only minor improvement due to ionic conduction of ceria could be expected in these conditions. For instance, a parallel anodic reaction path at 1273 K, with H_2 oxidation occurring at the Y8SZ surface, was suggested in Ref.[104]. The optimum anode performance is hence obtained when combining two ionically-conductive components, catalytically-active $\text{CeO}_{2-\delta}$ and cermet-stabilizing YSZ. When temperature decreases, a pronounced shift of the overpotential minimum towards higher Ce-concentrations is observed, indicating a greater role of electrocatalytic activity of anode layers (Fig.5.21). Nonetheless, the minimum overpotential is still achieved if combining yttria-stabilized zirconia and ceria in the cermets.

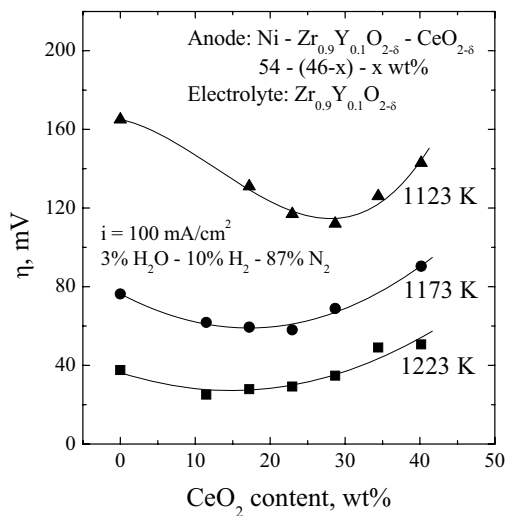


Fig.5.21. Anodic overpotentials of Ni - YSZ - $\text{CeO}_{2-\delta}$ cermet layers in contact with $\text{Zr}_{0.9}\text{Y}_{0.1}\text{O}_{2-\delta}$ solid electrolyte at 100 mA/cm^2 .

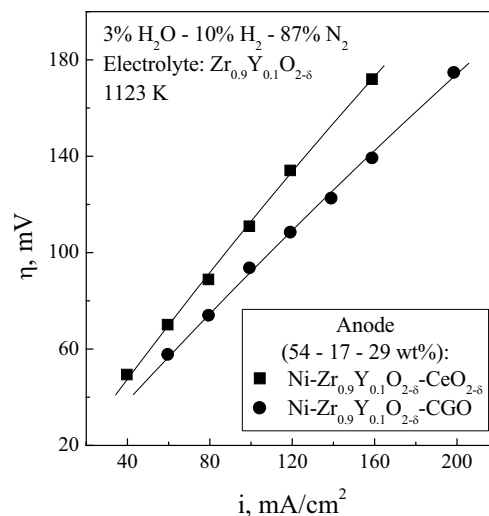


Fig.5.22. Anodic current density dependence of the overpotential for two cermet compositions, containing 29 wt% of $\text{CeO}_{2-\delta}$ or CGO, at 1123 K.

In order to assess role of the oxygen ionic conductivity of anode components, Fig.5.22 compares the overpotential vs. current dependencies for two cermet compositions containing Ni, $\text{Zr}_{0.9}\text{Y}_{0.1}\text{O}_{2-\delta}$, and $\text{CeO}_{2-\delta}$ or CGO; the microstructure of both cermets was similar. At 1123 K, the

polarization of CGO-containing anode is 15-25% lower with respect to the layer comprising undoped ceria. At higher temperatures this difference was found to become rather negligible; in fact, performance of the latter cermet composition at 1223 K was even slightly higher. This suggests that the effect of ionic transport in cermet components, resulting in an enlargement of the electrochemical reaction zone, becomes more important when temperature decreases, in agreement with literature [19,20].

Summarizing these results, one can conclude that the use of CGO in the intermediate temperature range is preferable as compared to undoped ceria. Although the ionic conductivity of YSZ at temperatures below 1123 K is insufficient for a high anode performance, incorporation of YSZ in the cermet compositions might still be important to provide necessary stability of the anode layers.

The steady-state anodic current density and overpotential varied in the ranges 0-300 mA/cm² and 0-460 mV, respectively; the time necessary to achieve steady-state conditions was 1-3 h. The reproducibility of results was separately checked after each measurement cycle; representative examples are given in Fig.5.23. For different anodes of identical composition, the standard deviation of the overpotential values at fixed current density was about 12-15% at 1073-1223 K; for one sample after approximately 200 h of testing, the maximum deviation from the initial overpotential values was lower than 5-7%.

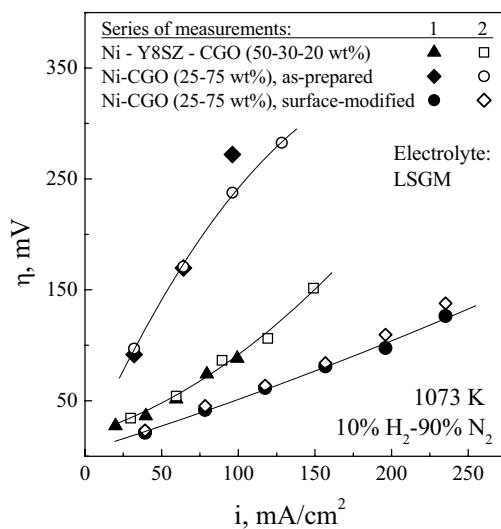


Fig.5.23. Selected results illustrating reproducibility tests of the overpotential vs. current density dependence for CGO-containing cermets.

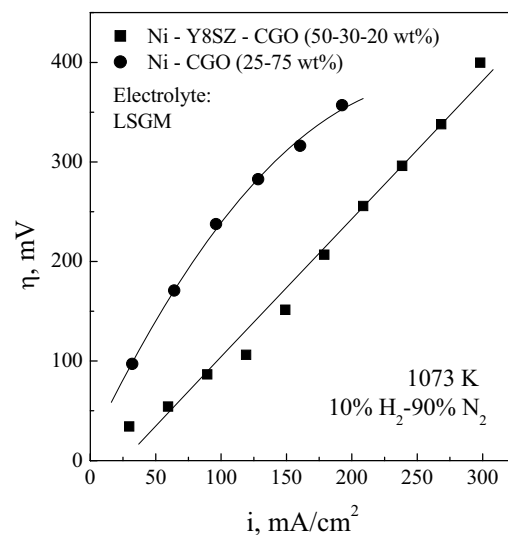


Fig.5.24. Overpotential vs. anodic current density dependencies of the CGO-containing anodes in contact with LSGM electrolyte at 1073 K.

Fig.5.24 compares overpotential vs. current dependencies of Ni - CGO and Ni - CGO - Y8SZ anodes, deposited onto LSGM, at 1073 K. The electrochemical performance of Ni - Y8SZ - CGO cermet in contact with LSGM electrolyte is higher than that of similar compositions applied onto YSZ (compare Figs.5.21 and 5.24). Most likely, this is associated with the higher activity of nano-sized CGO particles in the former case, and also with the influence of ionic conductivity of solid electrolyte on the anode exchange currents, which becomes significant at intermediate temperatures [20]. At 1073 K and a fixed current density of 200 mA/cm^2 , the overpotential of the Ni - Y8SZ - CGO anode is lower than 245 mV (Fig.5.24). SEM micrographs of this layer, as-prepared and after testing for approximately 200 h are presented in Figs.5.25A and 5.25B, respectively. Both microstructures are quite homogeneous; the grain agglomeration that occurs at elevated temperatures is insignificant.

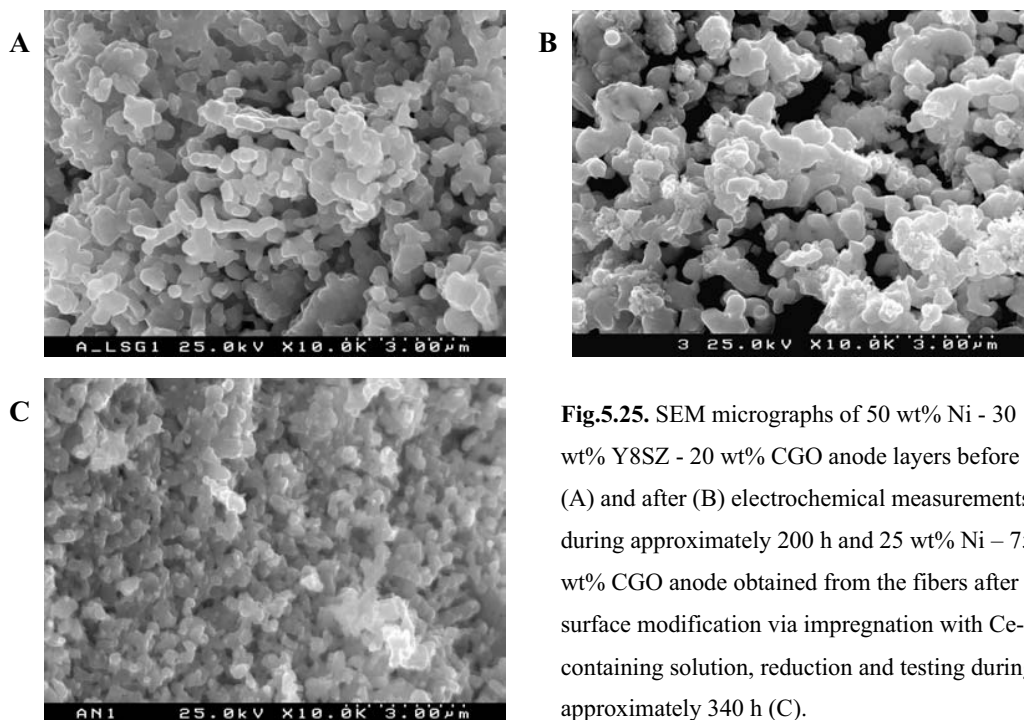


Fig.5.25. SEM micrographs of 50 wt% Ni - 30 wt% Y8SZ - 20 wt% CGO anode layers before (A) and after (B) electrochemical measurements during approximately 200 h and 25 wt% Ni - 75 wt% CGO anode obtained from the fibers after surface modification via impregnation with Ce-containing solution, reduction and testing during approximately 340 h (C).

The YSZ-containing anode exhibits a higher electrochemical activity compared to Ni - CGO (Fig.5.24), which could be attributed either to a stabilizing influence of zirconia or to higher Ni content in the Ni - CGO - Y8SZ cermet. However, the data on surface-activated Ni - CGO layer (Chapter 5.3.4) indicate that the performance can be improved by further ceria additions, decreasing Ni concentration down to 21 vol%. Therefore, the total Ni concentration above percolation limit cannot be considered as a performance-determining factor. Since the ionic conductivity of YSZ at 1073 K is considerably lower than that of CGO, one may suggest that the

major role of YSZ refers to mechanical stabilization of the cermet, in particular with respect to re-oxidation at high anodic currents. This well corresponds to the data on Ni - $Zr_{0.9}Y_{0.1}O_{2-\delta}$ - $CeO_{2-\delta}$ layers in contact with YSZ solid electrolyte (Fig.5.21).

5.3.3. Other factors influencing anode performance

Fig.5.26 presents selected overpotential-current dependencies of the mixed conductor-containing anodes. Compared to other layers without surface modification, the best performance was found for Ni - Y8SZ - CGO, Ni - Y8SZ - $Ce_{0.8}Ca_{0.2}VO_{4+\delta}$ and Ni - $Gd_{1.86}Ca_{0.14}Ti_2O_{7-\delta}$ - CGO compositions. The electrochemical activity of Ni - $TbZrO_{4-\delta}$ - CGO and Ni - $La_{0.90}Sr_{0.10}Al_{0.65}Fe_{0.20}Mg_{0.15}O_{3-\delta}$ - CGO layers is rather poor.

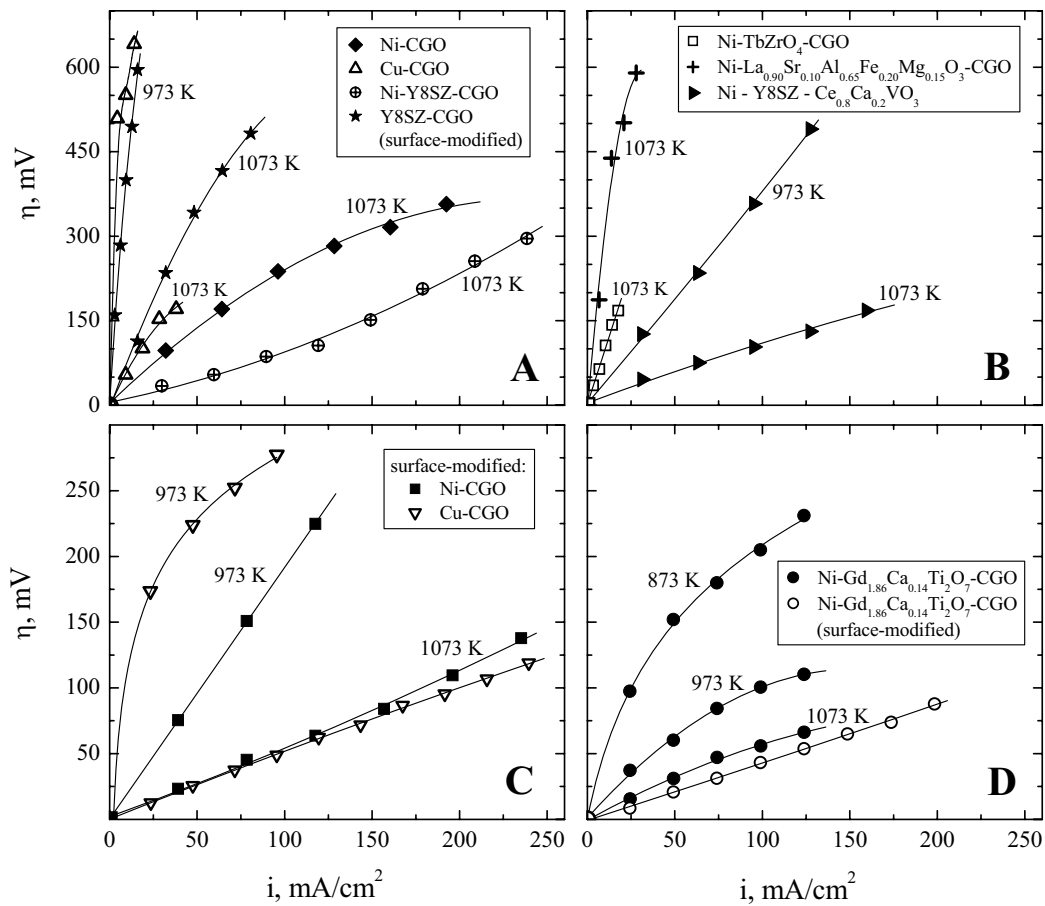


Fig.5.26. Current density dependence of the overpotential for various cermet anodes.

The Ni - CGO anode exhibits lower overpotentials with respect to the Cu-containing analogue; this behavior is generally associated with low catalytic activity and high sinterability of copper [160,307]. Despite the highest ionic conductivity of CGO (Fig.4.63A), the electrodes of Ni -

Y8SZ - CGO, Ni - Y8SZ - $\text{Ce}_{0.8}\text{Ca}_{0.2}\text{VO}_{4+\delta}$ and Ni - $\text{Gd}_{1.86}\text{Ca}_{0.14}\text{Ti}_2\text{O}_{7-\delta}$ - CGO show similar performance (Fig.5.26). Also, the role of electronic conductivity of the oxide components seems insignificant due to the presence of percolated metal phase.

In general, the results suggests that, when necessary level of ionic and electronic conduction in the cermets is achieved, minor variations of their transport properties are less important than the stability with respect to sintering of metal particles and volume changes induced by current changes. The stability can be improved using oxide phases where the oxygen stoichiometry and volume are essentially $p(\text{O}_2)$ -independent, including YSZ and $\text{Gd}_{1.86}\text{Ca}_{0.14}\text{Ti}_2\text{O}_{7-\delta}$. For instance, the worse performance of Ni - CGO anodes may indicate instability of Ni - CGO electrodes, particularly due to the volume changes caused by the variations of current and oxygen chemical potential.

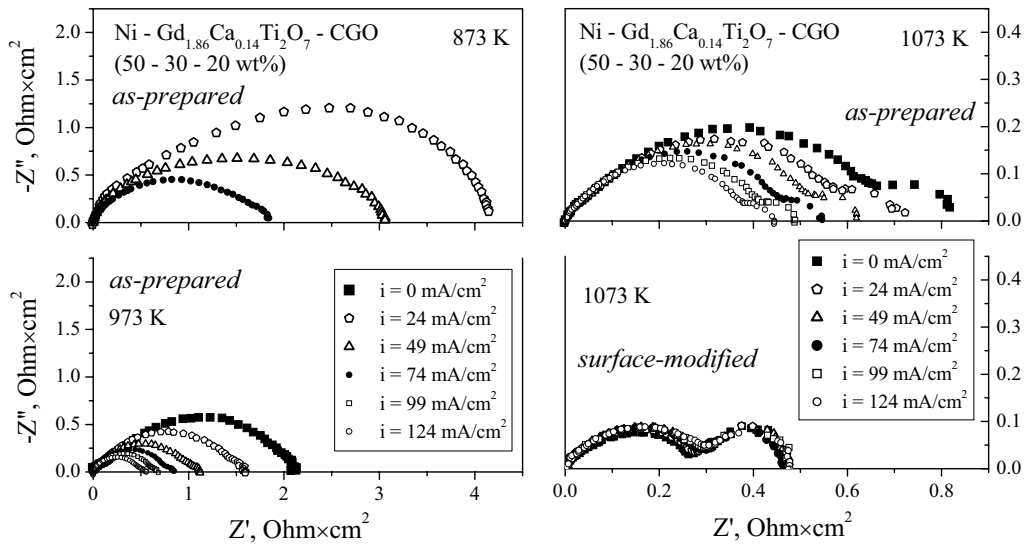


Fig.5.27. Selected impedance spectra of as-prepared and CeO_2 -activated anode made of Ni - $\text{Gd}_{1.86}\text{Ca}_{0.14}\text{Ti}_2\text{O}_{7-\delta}$ - CGO cermet. The ohmic contribution is subtracted. The spectra arc is corrected for the geometric surface area.

The evolution of electrode impedance spectra with temperature and anodic polarization is illustrated in Fig.5.27, by the example of Ni - $\text{Gd}_{1.86}\text{Ca}_{0.14}\text{Ti}_2\text{O}_{7-\delta}$ - CGO. At least two arcs can be recognized, indicating that the anode reaction is limited by two or more processes. Even at 873 K, the spectra cannot be approximated by one single semicircle. The resistance corresponding to the high-frequency electrode signal ($R_{\eta 1}$) decreases on heating and, at 973-1073 K, on increasing current density. The latter effect becomes much smaller at 873 K. The resistance corresponding to

the low-frequency arc (R_{η_2}) becomes dominating at 873 K and low polarization. In all cases, R_{η_2} decreases on increasing anodic current. Although the present study was not focused on a deep analysis of the anodic reaction mechanisms complex in the multicomponent electrode systems, one should mention that these impedance spectra are analogous to those reported for the common Ni-YSZ cermets [104,156]. As in Refs.[104,156], three semicircles might be actually necessary to fit the impedance data; one of them could be difficult to separate if the corresponding time constant is close to that of the other process [156]. Also, the high-frequency arc might be distorted due to the transport limitations [104,298]. Whatever the number of limiting steps, the high-frequency process may be attributed to the limiting protons transfer across the Ni/LSGM interface or oxygen ion transport through the oxide particles in electrode layer [156]. The process at lower frequencies may originate from changes in the gas phase composition and/or from the adsorption of charged species [156]. Similar to Ni - YSZ cermets [104,156], the total polarization resistance of studied cermets decreases with current, Fig.5.27. This trend can be ascribed to local increase in the water vapor content near the anode surface, towards an optimum value. The arc with lower time constant is reduced under anodic polarization probably due to promoted oxygen transfer to the reaction zone. The temperature-activated electrode reaction is observed in all cases, as expected.

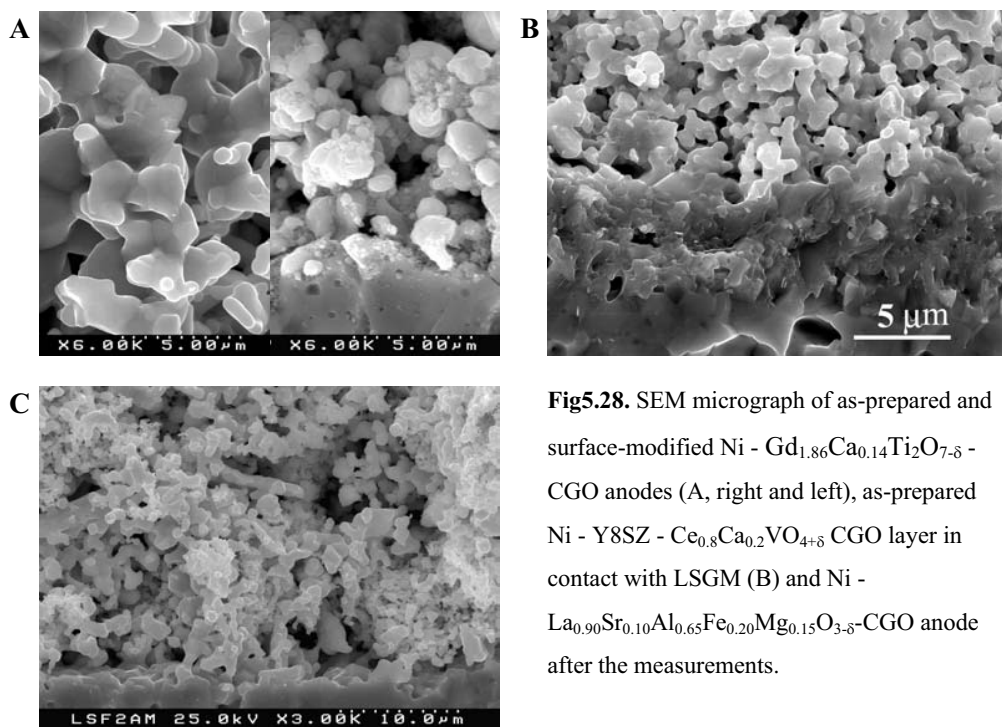


Fig5.28. SEM micrograph of as-prepared and surface-modified Ni - Gd_{1.86}Ca_{0.14}Ti₂O_{7-δ} - CGO anodes (A, right and left), as-prepared Ni - Y8SZ - Ce_{0.8}Ca_{0.2}VO_{4+δ} CGO layer in contact with LSGM (B) and Ni - La_{0.90}Sr_{0.10}Al_{0.65}Fe_{0.20}Mg_{0.15}O_{3-δ}-CGO anode after the measurements.

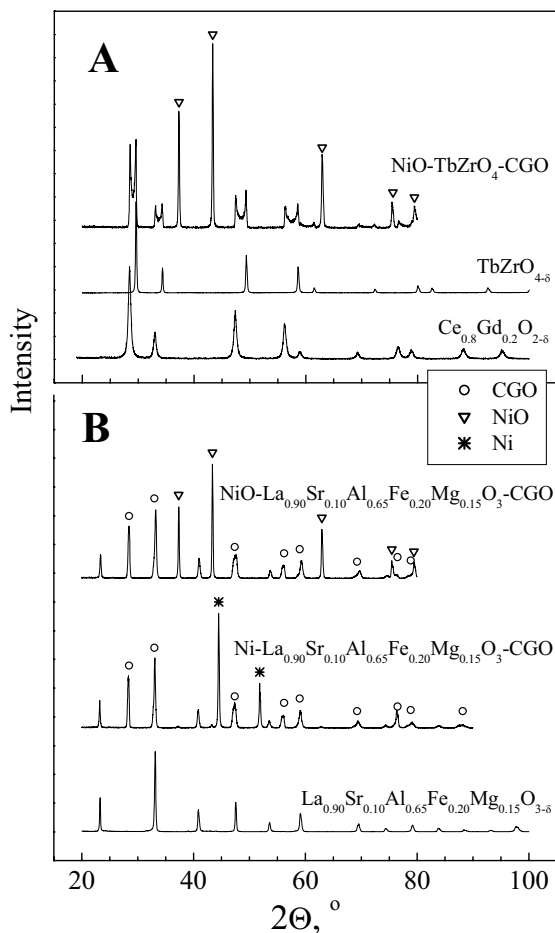


Fig.5.29. XRD patterns of $\text{Ce}_{0.8}\text{Gd}_{0.2}\text{O}_{2-\delta}$, $\text{TbZrO}_{4-\delta}$ and oxidized Ni - $\text{TbZrO}_{4-\delta}$ - CGO layer (A), and the oxidized and reduced layers containing $\text{La}_{0.90}\text{Sr}_{0.10}\text{Al}_{0.65}\text{Fe}_{0.20}\text{Mg}_{0.15}\text{O}_{3-\delta}$ perovskite (B).

The presence of Ce-containing phases with different composition and transport properties, such as CGO and $\text{Ce}_{0.8}\text{Ca}_{0.2}\text{VO}_{4+\delta}$, provides similar electrochemical activity. At the same time, one should take into account the formation of reactive layer between $\text{Ce}_{0.8}\text{Ca}_{0.2}\text{VO}_{4+\delta}$ with LSGM (Fig.5.28B), which may lead to time degradation of the electrode performance. The poor properties of anode with $\text{TbZrO}_{4-\delta}$ addition (Fig.5.26B) relates to chemical interaction between the two fluorite phases, $\text{TbZrO}_{4-\delta}$ and CGO. This reaction results in formation of a continuous series of solid solutions as demonstrated by XRD studies (Fig.5.29A). On the contrary, no essential reactivity of the cermet components were detected for Ni - $\text{La}_{0.90}\text{Sr}_{0.10}\text{Al}_{0.65}\text{Fe}_{0.20}\text{Mg}_{0.15}\text{O}_{3-\delta}$ - CGO (Fig.5.29B). Most likely, high overpotentials of the latter electrode are associated with large changes in the oxygen nonstoichiometry of the perovskite phase, having a destabilizing effect, and cation interdiffusion between $\text{La}_{0.90}\text{Sr}_{0.10}\text{Al}_{0.65}\text{Fe}_{0.20}\text{Mg}_{0.15}\text{O}_{3-\delta}$ and LSGM. Incorporation of Al^{3+} cations into LSGM surface should decrease ionic conduction through electrode/electrolyte

interface, whereas iron diffusion may cause formation of microcracks at the electrolyte surface when the current varies.

5.3.4. Surface modification of cermet layers

Although the ionic conductivity of CGO is higher than that of undoped ceria, incorporating $\text{CeO}_{2-\delta}$ via impregnation with Ce-containing solutions substantially increases electrochemical activity of CGO-containing anodes (Figs.5.26, A, C and D, and 5.30). Such a behavior is related, first of all, to increasing catalytic activity of the anode layer due to incorporation of fine ceria particles formed after thermal decomposition of cerium nitrate. At the same time, the anode performance enhancement may also be contributed by improved electrical contacts between particles, resulting from the significant electronic conductivity of ceria in reducing atmospheres [424]. Indeed, the microstructure of surface-modified anodes is less porous and, in the case of Ni(Cu) - CGO, more uniform if compared to non-activated layers (e.g. Figs.5.25 and 5.28).

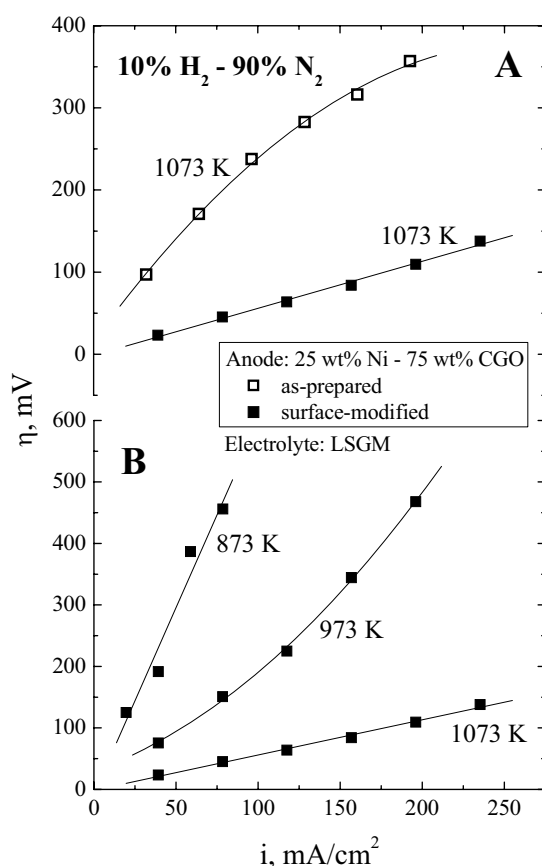


Fig.5.30. Overpotential vs. anodic current density dependencies of 25 wt% Ni - 75 wt% CGO electrode in contact with LSGM solid electrolyte: (A), comparison of as-prepared and surface-modified anode at 1073 K; (B), performance of surface-activated layer at 873 - 1073 K.

Finally, the electrochemical activity of surface-modified Ni - CGO and Cu - CGO layers at 1073 K becomes similar and relatively high; for example, the overpotentials of both Ni - CGO and

Cu - CGO anodes activated with ceria are about 80 mV at 1073 K and 150 mA/cm². Decreasing temperature below 973 K leads, however, to a rather poor performance (Figs.5.26B and 5.30). This makes it necessary to further optimize the anode composition and microstructure. Promising approaches include, in particular, incorporation of nanocrystalline YSZ into CGO fibers with subsequent applying on solid-electrolyte ceramics, use of higher Ni concentrations, modification of the electrolyte surface prior to anode deposition, and probably doping of CGO in order to increase n-type electronic transport.

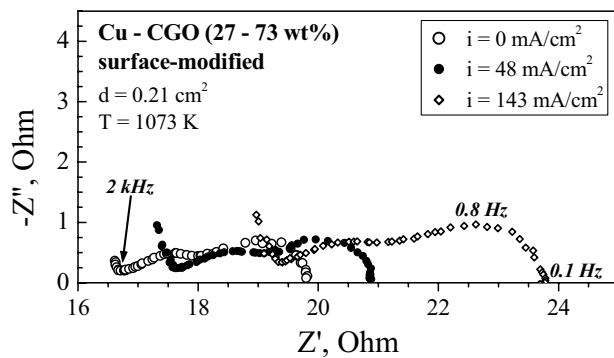


Fig.5.31 Examples of impedance spectra of Cu - CGO anode surface-activated with CeO_{2-δ}, obtained in the course of polarization measurements at 1073 K in H₂-H₂O-N₂ atmosphere.

The surface activation of the Ni - CGO anode layers 3-5 times decreases overpotentials at 1073 K (Fig.5.26, A and C). This suggests, again, that ceria might improve contacts at the electrode/electrolyte interface and also between the grains constituting porous electrode layer of the Ni - CGO and Cu - CGO cermets, dimensionally unstable on redox cycling. The contacts seem, however, still worsening on increasing anodic overpotential: even after ceria incorporation, both the ohmic and polarization resistances keep increasing on electrical current through the cell (e.g. Fig.5.31). Nonetheless, the results were quite reproducible (Fig.5.23).

Contrary to the Ni - CGO anodes, the modification with ceria has a much smaller effect on the performance of Ni - Gd_{1.86}Ca_{0.14}Ti₂O_{7-δ} - CGO cermets (Fig.5.26D). Moreover, R_η values of the surface-modified Ni - Gd_{1.86}Ca_{0.14}Ti₂O_{7-δ} - CGO electrodes are current-independent (Fig.5.27), while the ohmic losses decrease slightly on the anodic polarization. Another observation is that the surface activation affects mainly the high-frequency arc of the anode impedance spectra (Fig.5.27), indicating promotion of the charge-transfer processes. Indeed, the presence of ceria at the electrode surface could fasten both sorption processes and oxygen transport, and modify catalytic activity for the oxidation reactions. On the other hand, non-negligible contribution of the electrolyte surface is quite possible. The deposition of ceria is expected to promote the hydrogen oxidation at this surface.

5.3.5. Final remarks

The results on anodic polarization of Ni - YSZ - CGO ($\text{CeO}_{2-\delta}$) cermet layers in contact with YSZ solid electrolyte show that the anode performance at 1123-1223 K can be significantly increased by ceria-based additions. Due to an enlargement of the electrochemical reaction zone resulting from higher ionic conductivity of $\text{Ce}_{0.8}\text{Gd}_{0.2}\text{O}_{2-\delta}$ compared to undoped ceria, the use of CGO provides higher electrochemical activity. Although the role of catalytically-active ceria additions increases on cooling, the optimum performance is achieved if combining ceria with YSZ, which, most probably, stabilizes cermets with respect to re-oxidation. Since an additional improvement could be expected from the use of nano-structured CGO, submicron powders of $\text{Ce}_{0.8}\text{Gd}_{0.2}\text{O}_{2-\delta}$ (grain size of 8-35 nm) and MeO - CGO (Me = Ni, Cu) mixtures (10-80 nm) were prepared using the cellulose-precursor technique. This method makes it possible, in particular, to fabricate electrode layers with regular microstructures and to stabilize metal component of the cermets by dispersing in highly-porous oxide matrix. Testing of Ni - CGO - YSZ anodes, comprising nanocrystalline ceria-based powders and applied onto LSGM electrolyte, demonstrated a relatively high activity, which can be further improved by surface modification via the impregnation with Ce-containing solutions. The presence of YSZ in the anodes seems desirable even at intermediate temperatures, 873-1073 K. The overpotential of surface-modified anode, containing 25 wt% Ni and 75 wt% CGO, was approximately 110 mV at 1073 K and current density of 200 mA/cm² in flowing 10% H_2 -90% N_2 mixture.

In summary, the results of this work show that cermet anodes for IT SOFCs should combine at least one redox-stable material and, preferably, a Ce-containing component. In spite of their transport properties, activation with ceria improves anode performance due to increasing catalytic activity, improving intergranular contacts and, possibly, enhancing electronic conduction at the solid electrolyte surface. Any interaction between the electrolyte and/or anode components should be avoided.

Conclusions

1. In order to develop the novel electrochemically active electrode materials for intermediate-temperature solid oxide fuel cells (IT SOFCs), the physicochemical and electrochemical properties of hexagonal $\text{YBaCo}_{4-x}\text{Fe}_x\text{O}_{7+\delta}$ ($x = 0-0.8$), $\text{La}_2\text{Ni}_{1-x}\text{M}_x\text{O}_{4+\delta}$ ($M = \text{Co}, \text{Cu}; x = 0 - 0.20$) with K_2NiF_4 -type structure and perovskite-type ($\text{La}_{0.3}\text{Sr}_{0.7}$) $_{1-y}\text{CoO}_{3-\delta}$ ($y = 0-0.03$) and $\text{La}_{0.3}\text{Sr}_{0.7}\text{Co}_{0.8}\text{M}_{0.2}\text{O}_{3-\delta}$ ($M = \text{Al}, \text{Ga}$) were studied. Materials of the former two systems possessing moderate thermal expansion in air, $(7.3-9.0)\times 10^{-6} \text{ K}^{-1}$ and $(12.8-14.2)\times 10^{-6} \text{ K}^{-1}$ respectively, are compatible with common solid electrolyte materials, such as stabilized zirconia, doped ceria and $\text{La}(\text{Sr})\text{Ga}(\text{Mg})\text{O}_{3-\delta}$ (LSGM). The average thermal expansion coefficients of perovskite cobaltite ceramics in air, $(15.9-19.6)\times 10^{-6} \text{ K}^{-1}$ at 300-750 K and $(27.9-29.7)\times 10^{-6} \text{ K}^{-1}$ at 750-1240 K, are excessively high, making these materials inappropriate for the electrode applications due to the thermomechanical instability of the contact with electrolyte ceramics.
2. The oxygen permeation fluxes through dense ($\text{La}_{0.3}\text{Sr}_{0.7}$) $_{1-y}\text{CoO}_{3-\delta}$ ($y = 0-0.03$) and $\text{La}_{0.3}\text{Sr}_{0.7}\text{Co}_{0.8}\text{M}_{0.2}\text{O}_{3-\delta}$ ($M = \text{Al}, \text{Ga}$) membranes at 973-1223 K are limited by both bulk ionic conductivity and surface exchange kinetics. Substitution of cobalt with Al^{3+} or Ga^{3+} increases cubic perovskite unit cell volume, oxygen deficiency and Seebeck coefficient, whereas the thermal expansion, p-type electronic conductivity and oxygen permeability decrease. The analysis of oxygen partial pressure dependencies of the electrical properties, in combination with the oxygen nonstoichiometry data determined by thermogravimetry, suggests a broadband mechanism of hole conduction. Creation of A-site cation vacancies, compensated by Co^{4+} formation, leads to higher p-type electronic conductivity and thermal expansion at temperatures above 700 K, whilst the ionic transport in A-site deficient cobaltite is lower than that in the parent compound. Reducing oxygen pressure down to approximately 10^{-5} atm results in transition into brownmillerite-type phases having essentially $p(\text{O}_2)$ -independent electrical properties until decomposition, which occurs at $p(\text{O}_2)$ values 10^2-10^4 times higher compared to the CoO/Co boundary.
3. a) Mixed-conducting K_2NiF_4 -type $\text{La}_2\text{Ni}_{1-x}\text{M}_x\text{O}_{4+\delta}$ ($M = \text{Co}, \text{Cu}; x = 0 - 0.20$) possess significant p-type electronic conductivity and oxygen permeability. Oxygen permeation through $\text{La}_2\text{Ni}_{1-x}\text{M}_x\text{O}_{4+\delta}$ ceramics is limited by both bulk ionic conductivity and surface oxygen exchange. Despite moderate differences in the ceramic microstructures, the glycine-nitrate process (GNP)-synthesized membranes exhibit higher oxygen permeability than those prepared by the standard ceramic technique. Incorporation of copper into the

nickel sublattice was found to decrease sintering temperature necessary to achieve sufficient mechanical strength of highly porous electrode layers.

- b) $\text{La}_2\text{Ni}_{0.8}\text{Cu}_{0.2}\text{O}_{4+\delta}$ porous cathode layers show moderate polarization in contact with LSGM electrolyte, lower than 50 mV at 1073 K and current density of 200 mA/cm². As for the oxygen transport through dense membranes, the results on electrode behavior of $\text{La}_2\text{Ni}_{0.8}\text{Cu}_{0.2}\text{O}_{4+\delta}$ in contact with LSGM solid electrolyte, including the overpotential-microstructure relationships and the $p(\text{O}_2)$ dependence of polarization resistance, suggest that the cathodic reaction rate is affected by surface-related processes. Due to this, electrode performance can be considerably enhanced by surface activation, particularly via impregnation with Pr-containing solutions, and also by decreasing fabrication temperature. At 873 K, the surface modification with praseodymium oxide decreases cathodic overpotential from 330 down to approximately 175 mV at 50 mA/cm².
4. a) Moderate doping of $\text{YBaCo}_4\text{O}_{7+\delta}$ with iron decreases slightly the total conductivity, predominantly p-type electronic, and have no essential effect on the oxygen ion transport and cathodic polarization at 1073 K. The ion transference numbers, determined by the oxygen permeation and faradaic efficiency measurements at 1073-1223 K, vary in the range 3×10^{-5} to 4×10^{-4} and increase with temperature and iron content. The oxygen permeability through yttrium-barium cobaltite membranes is mainly limited by the bulk ionic conduction. The use of different synthesis methods, namely the standard ceramic technique and GNP, has no significant effect on the properties of $\text{YBaCo}_4\text{O}_{7+\delta}$ ceramics.
b) YBaCo_4O_7 , where the average cobalt oxidation state is +2.25, and its derivatives appear metastable below 1050-1100 K. Oxygen uptake at intermediate temperatures in air leads to the phase decomposition, accompanied by increasing conductivity and dramatic volume contraction.
c) Porous YBaCo_4O_7 -based cathodes show very high electrochemical activity in contact with LSGM solid electrolyte at 873-1073 K, superior to that of K_2NiF_4 -type nickelates, which is partly due to their interaction with the surface of lanthanum gallate ceramics. The cathode performance can further be improved by metallic silver additions and surface-activation with praseodymia. The overpotentials of YBaCo_4O_7 and $\text{YBaCo}_4\text{O}_7\text{-Ag}$ (90-10 wt%) electrode layers at current density of 60 mA/cm² and 873 K in air are less than 80 and 50 mV, respectively.
5. Oxygen ion transference numbers of $\text{Ce}_{1-x}\text{A}_x\text{VO}_{4+\delta}$, determined by faradaic efficiency measurements in air, vary in the range from 2×10^{-4} to 6×10^{-3} at 973-1223 K, increasing with temperature. The oxygen ionic conductivity has activation energy of 87-112 kJ/mol and is essentially independent of A-site dopant content. Contrary to the ionic transport, p-type

electronic conductivity and Seebeck coefficient of $Ce_{1-x}A_xVO_{4+\delta}$ are determined by the divalent cation concentration. The average thermal expansion coefficients of $Ce_{1-x}A_xVO_{4+\delta}$, calculated from high-temperature XRD and dilatometric data in air, are $(4.7 - 6.1) \times 10^{-6} K^{-1}$. Zircon-type $Ce_{1-x}A_xVO_{4+\delta}$ ($A = Ca, Sr; x = 0 - 0.2$) phases are stable in air up to approximately 1300 K, whilst further heating or reducing oxygen partial pressure leads to formation of A-site deficient zircon and $CeO_{2-\delta}$. Decreasing oxygen pressures below 10^{-15} atm leads to the formation of perovskite-type $CeVO_{3-\delta}$, possessing the high electronic conductivity in 10% H_2 - N_2 atmosphere, e.g. 15.3-15.9 S/cm at 873-1223 K for the composition with 20 mol% Ca.

6. a) Iron incorporation into lanthanum aluminate-based solid electrolyte leads to increasing oxygen ionic and p-type electronic conductivities. The oxygen ion transference numbers of perovskite-type $La_{0.90}Sr_{0.10}Al_{0.85-x}Fe_xMg_{0.15}O_{3-\delta}$ ($x = 0.2-0.4$), determined by faradaic efficiency measurements in air, vary from 6.9×10^{-4} to 1.6×10^{-2} at 1073-1223 K, increasing with temperature and decreasing when iron content increases.
- b) In order to study the behavior of transition metal cations dissolved in a lattice of cations with stable oxidation state, the total conductivity and Seebeck coefficient of $La_{0.90}Sr_{0.10}Al_{0.85-x}Fe_xMg_{0.15}O_{3-\delta}$ ($x = 0.2-0.5$) were measured at 973-1223 K in the oxygen partial pressure range from 10^{-20} to 0.5 atm. The results, in combination with Mössbauer spectroscopy data and ion transference numbers in air, show that increasing $p(O_2)$ leads to decreasing oxygen ionic conductivity, whilst no essential delocalization of the electronic charge carriers is observed. The variations of partial ionic and p- and n-type electronic conductivities can be adequately described by equilibrium processes of oxygen intercalation and iron disproportionation with the thermodynamic functions independent of defect concentrations. The p-type electronic conduction dominating under oxidizing conditions, occurs via a small-polaron mechanism within the whole $p(O_2)$ range studied. The activation energy for ionic transport, which becomes predominant at oxygen pressures lower than 10^{-10} atm, is 80-120 kJ/mol and decreases with reducing $p(O_2)$ due to decreasing contribution of the vacancy formation enthalpy. Reducing oxygen pressure below 10^{-18} - 10^{-16} atm results in noticeable n-type electronic conduction. No indications of the phase decomposition were observed.
7. Terbium hafnate and zirconate ceramics with submicron grain sizes were prepared via mechanically-activated synthesis. X-ray and electron diffraction and infrared absorption spectroscopy showed that $TbZrO_{4-\delta}$ has a disordered fluorite-type structure, while $TbHfO_{4-\delta}$ is partially ordered, containing pyrochlore microdomains. The oxygen ion transference numbers determined by the modified e.m.f. technique under oxygen/air gradient, vary in the range 0.08 - 0.26 at 873-1123 K, increasing with temperature. The activation energies for ionic and p-type

electronic transport are 82-83 and 29-40 kJ/mol, respectively. The ionic conduction becomes dominant in reducing atmospheres, but tends to decrease at low $p(\text{O}_2)$. Due to partial cation ordering, terbium hafnate exhibits lower ionic and hole transport as compared to $\text{TbZrO}_{4-\delta}$. The average thermal expansion coefficients of $\text{TbMO}_{4-\delta}$ (M= Zr, Hf) ceramics in air, calculated from dilatometric data, are $(11.5-12.4) \times 10^{-6} \text{ K}^{-1}$ at 600-1200 K and $(18.4-20.3) \times 10^{-6} \text{ K}^{-1}$ at 1200-1420 K.

8. a) Oxygen ion transference numbers of $\text{Gd}_{2-x}\text{Ca}_x\text{Ti}_2\text{O}_{7-\delta}$ ($x = 0.10-0.14$) pyrochlore ceramics vary in the range 0.95 - 0.98 in air, increasing when temperature or oxygen partial pressure decreases, as determined at 973-1223 K by the modified e.m.f. and faradaic efficiency techniques, taking into account electrode polarization, and from the oxygen permeation results. The activation energies for the ionic and p-type electronic transport in air are 74 – 77 and 87-91 kJ/mol, respectively. The p-type conductivity and oxygen permeability of $\text{Gd}_2\text{Ti}_2\text{O}_7$ -based pyrochlores can be adequately described by relationships common for other solid electrolytes. At temperatures below 1273 K under the gradient of 10% H_2 - N_2 / air, average ion transference numbers of doped gadolinium titanate are not less than 0.97. However, due to significant ohmic contribution to the cell resistance, the performance of fuel cells with pyrochlore solid electrolyte is poor. Thermal expansion coefficients of $\text{Gd}_{2-x}\text{Ca}_x\text{Ti}_2\text{O}_{7-\delta}$ ceramics, calculated from dilatometric data in air, are $(10.4 - 10.6) \times 10^{-6} \text{ K}^{-1}$ at 400 - 1300 K.
- b) In order to reveal the role of grain boundaries on the ionic and electronic conduction processes, small amounts of SiO_2 were added to $\text{Gd}_{2-x}\text{Ca}_x\text{Ti}_2\text{O}_{7-\delta}$ materials. For these ceramics having, as expected, high interfacial resistances, the ion transference numbers were considerably lower, 0.76-0.88, and increase with temperature. This behavior suggests a larger limiting effect of grain boundaries on ionic than on electronic transport. Increasing boundary resistivity may increase the relative role of electronic conductivity in solid oxide electrolytes, thus preventing their potential use in electrochemical cells at low temperatures. Also, the presence of even small electronic contributions to the total conductivity may lead to significant errors in the grain-boundary resistance values estimated from impedance spectroscopy data. Evaluation of the grain boundary exact contribution should be based on clear knowledge of the transference numbers.
- c) Despite the lower ionic conductivity in comparison with zirconia electrolytes, $(\text{Gd,Ca})_2\text{Ti}_2\text{O}_{7-\delta}$ materials are still of interest for employing as the SOFC anode components, taking into account the high stability, non-negligible electronic conduction and relatively low cost.

9. a) In order to assess the role of oxide components of Ni- and Cu-containing cermets, a series of electrodes containing 8% yttria-stabilized zirconia (Y8SZ), $\text{CeO}_{2-\delta}$, $\text{Ce}_{0.8}\text{Gd}_{0.2}\text{O}_{2-\delta}$ (CGO) and $\text{TbZrO}_{4-\delta}$ with fluorite-related structure, zircon-type $\text{Ce}_{0.8}\text{Ca}_{0.2}\text{VO}_{4+\delta}$, $\text{Gd}_{1.86}\text{Ca}_{0.14}\text{Ti}_2\text{O}_{7-\delta}$ pyrochlore and perovskite-like $\text{La}_{0.9}\text{Sr}_{0.1}\text{Al}_{0.65}\text{Mg}_{0.15}\text{Fe}_{0.20}\text{O}_{3-\delta}$, were studied in contact with YSZ and LSGM electrolytes.
- b) The polarization of cermet anodes, made of nickel, ceria and YSZ, can be significantly reduced by catalytically-active ceria additions, the relative role of which increases with decreasing temperature. Further improvement is observed when using $\text{Ce}_{0.8}\text{Gd}_{0.2}\text{O}_{2-\delta}$ having a high oxygen ionic conductivity instead of undoped ceria due to enlargement of the electrochemical reaction zone.
- c) Nanocrystalline CGO, Ni-CGO and Cu-CGO powders with grain size of 8-80 nm, synthesized via the cellulose-precursor technique, were then used to prepare the porous cermet layers. The best performance was found for anodes comprising a stable ion-conducting component, such as Y8SZ or $\text{Gd}_{1.86}\text{Ca}_{0.14}\text{Ti}_2\text{O}_{7-\delta}$, and one Ce-containing phase, such as CGO or cerium vanadate. The ionic conductivity of the oxide components seems less significant with respect to redox stabilization, whilst interaction between the materials decreases anode performance. Surface modification with ceria enables to substantially reduce electrode polarization for all cermets. In particular, after such activation the overpotentials of Ni-CGO and Cu-CGO anodes become quite similar, varying in the range 100-115 mV at 1073 K and 225 mA/cm² in 10%H₂-90%N₂ flow.

Future research: selected aspects

The results on oxide and cermet electrode materials, presented in this thesis, enable to mark out the groups of promising IT SOFC cathodes and anodes. An importance of the surface-related processes for the performance of both mixed ionic-electronic conducting dense ceramic membranes and porous electrode layers is also demonstrated. Close control of any kind of solid-state interaction between the electrolyte and/or electrode components was found necessary.

It was revealed in the course of this work that the cobaltite and nickelate materials with layered structures are of interest for the high-temperature electrochemical applications. The compositional optimization of the current phases derived from YBaCo_4O_7 should be undertaken to enhance their stability to lower temperatures. Among other nonperovskite yttrium-barium cobaltites possibly envisaging further development, one can mention the YBaCo_2O_5 -based phases, the stability limits and high-temperature properties of which have not yet been assessed. Concerning the $\text{La}_2\text{Ni}_{0.8}\text{Cu}_{0.2}\text{O}_4$ -based electrodes, partial substitution of lanthanum with praseodymium seems quite promising.

$\text{La}_{0.90}\text{Sr}_{0.10}(\text{Al},\text{Fe})_{0.85}\text{Mg}_{0.15}\text{O}_{3-\delta}$ perovskites possess substantial mixed conductivity, when extensively doped with iron, and high stability to reduction. These materials, therefore, show considerable promise for the use in gas-separation membranes, provided that their high thermal expansion is suppressed. Substitution of chromium for iron in $\text{La}_{0.90}\text{Sr}_{0.10}(\text{Al},\text{Fe},\text{Cr})_{0.85}\text{Mg}_{0.15}\text{O}_{3-\delta}$ may solve this problem.

The data on the SOFC anodes, studied in this thesis, suggest that one redox-stable material and a catalytically active Ce-containing oxide should be incorporated into the cermet layers. The metal to oxide ratio, as well as the composition of the oxide phases, determining their transport and catalytic properties, should be further optimized. In particular, higher concentration of gadolinium in $\text{Ce}(\text{Gd})\text{O}_{2-\delta}$ is expected to increase the electronic conduction at reduced oxygen partial pressures and to suppress, to some extent, unfavorable volume variations. The electrocatalytic activity of ceria doped or co-doped with other cations, such as Pr, Y, Ca, etc. should also be tested in contact with lanthanum gallate-based electrolytes.

The elaboration of less labor- and capital-consuming processing and fabrication techniques is of great importance for SOFC developments. For instance, the concept of functionally graded electrode layers presents certain interest for decreasing an interaction between electrode and electrolyte materials, but seems to increase the technological complexity. Simplification of the synthesis routes and methods of electrode deposition, resulting in porous layers with optimized microstructure, may be of further interest. The polymer-template synthesis seems to be quite attractive in this respect. Another possible approach refers to employing the sintering aids, such as copper- and bismuth-containing oxides, to decrease the electrode fabrication temperature. The

effects of these additions on the sintering process and electrochemical properties of porous layers should be thoroughly studied.

References

1. "Fuel Cell Handbook" (6th ed.), EG&G Technical Services, Inc. Science Applications International Corporation, Morgantown, West Virginia, 2002.
2. N.Q. Minh and T. Takahashi, "Science and Technology of Ceramic Fuel Cells", Elsevier, Amsterdam, 1995.
3. O. Yamamoto, Solid oxide fuel cells: fundamental aspects and prospects, *Electrochim. Acta* 45 (2000) 2423.
4. T.-P. Chen, J.D. Wright, K. Krist, System analysis of oxide fuel cell unit. In: U. Stimming, S.C. Singhal, H. Tagawa, W. Lehnert (eds.), SOFC V (1997) *Electrochem. Soc.*, Pennington, NJ, vol. 97-40, p. 69.
5. B.C.H. Steele Material science and engineering: The enabling technology for the commercialisation of fuel cell systems, *J. Mater. Sci.* 36 (2001) 1053.
6. S.C. Singhal, Science and technology of solid-oxide fuel cells, *Mater. Res. Soc. Bull.* 25 (2000) 16.
7. S.C. Singhal, Solid oxide fuel cells in stationary, mobile and military applications, *Solid State Ionics* 152-153 (2002) 405.
8. S. Park, J.M. Vohs, R.J. Gorte, Direct oxidation of hydrocarbons in a solid-oxide fuel cell, *Nature* 404 (2000) 265.
9. K. Eguchi, H. Kojo, T. Takeguchi, R. Kikuchi, K. Sasaki, Fuel flexibility in power generation by solid oxide fuel cells, *Solid State Ionics*, 152-153 (2002) 411.
10. H. Baur, H. Preis, Uber brennstoff-ketten mit festleitern, *Z. Elektrochem.* 6 (1937) 41.
11. J. Weissbart, R. Ruka, A solid electrolyte fuel cell, *J. Electrochem. Soc.* 109 (1962) 723.
12. C.S. Tedmon, H.S. Spacil, S.P. Mitoff, Cathode materials and performance in high-temperature zirconia electrolyte fuel cells, *J. Electrochem. Soc.* 116 (1969) 1170.
13. Siemens Westinghouse website. <http://www.powergeneration.siemens.com>
14. Tokyo Gas website. <http://www.tokyo-gas.co.jp/>
15. B.C.H. Steele, Appraisal of $\text{Ce}_{1-y}\text{Gd}_y\text{O}_{2-y/2}$ electrolytes for IT-SOFC operation at 500°C, *Solid State Ionics*, 129 (2000) 95.
16. A.J. McEvoy, S. Rambert, S. Widmer, Nanostructure, defect chemistry and operating protocols influence SOFC performance. In: B. Thorstensen (ed.), Proc. Second European Solid Oxide Fuel Cell Forum (1996) Oslo, vol. 1, p. 599.
17. S.P. Jiang, A comparison of O_2 reduction reactions on porous $(\text{La,Sr})\text{MnO}_3$ and $(\text{La,Sr})(\text{Co,Fe})\text{O}_3$ electrodes. *Solid State Ionics*, 146 (2002) 1.
18. J.P.P. Huijsmans, Ceramics in solid oxide fuel cells, *Curr. Opin. Solid State Mat. Sci.* 5 (2001) 317.
19. T. Ishihara, T. Shibayama, H. Nishiguchi, Y. Takita, Nickel-Gd-doped CeO_2 cermet anode for intermediate temperature operating solid oxide fuel cells using LaGaO_3 -based perovskite electrolyte *Solid State Ionics* 132 (2000) 209.
20. M. Watanabe, H. Uchida, M. Yoshida, Effect of ionic conductivity of zirconia electrolytes on the polarization behavior of ceria-based anodes in solid oxide fuel cells, *J. Electrochem. Soc.* 144 (1997) 1739.

21. J. Will, A. Mitterdorfer, C. Kleinlogel, D. Perednis, L.J. Gauckler, Fabrication of thin electrolytes for second-generation solid oxide fuel cells, *Solid State Ionics* 131 (2000) 79.
22. V.E.J. van Dieten, J. Schoonman, Thin film techniques for solid oxide fuel cells, *Solid State Ionics* 57 (1992) 141.
23. C. Lu, W.L. Worrell, C. Wang, S. Park, H. Kim, J.M. Vohs, R.J. Gorte, Development of solid oxide fuel cells for the direct oxidation of hydrocarbon fuels, *Solid State Ionics* 152-153 (2002) 393.
24. R. Ihringer, J. Van herle and A.J. McEvoy, Development of thin film electrolytes co-fired with NiO-YSZ substrates. In: U. Stimming, S.C. Singhal, H. Tagawa, W. Lehnert (eds.), *SOFC V (1997) Electrochem. Soc.*, Pennington, NJ, vol. 97-40, p. 340.
25. J.-W. Kim, A.V. Virkar, K.-Z. Fung, K. Mehta, S.C. Singhal, Polarization effects in intermediate temperature, anode-supported solid oxide fuel cells, *J. Electrochem. Soc.* 146 (1999) 69.
26. R. Doshi, Von L. Richard, J.D. Carter, X. Wang, M. Krumpelt, Development of solid-oxide fuel cells that operate at 500°C, *J. Electrochem. Soc.* 146 (1999) 1273.
27. J. Van herle, R. Ihringer, N.M. Sammes, G. Tompsett, K. Kendall, K. Yamada, C. Wen, T. Kawada, M. Ihara, J. Mizusaki, Concept and technology of SOFC for electric vehicles, *Solid State Ionics* 132 (2000) 333.
28. T. Tsai, S.A. Barnett, Increased solid-oxide fuel cell power density using interfacial ceria layers, *Solid State Ionics*, 98 (1997) 191.
29. T. Ishihara, M. Honda, H. Nishiguchi, Y. Takita, Solid oxide fuel cell operable at decreased temperature using LaGaO₃ perovskite oxide electrolyte. In: U. Stimming, S.C. Singhal, H. Tagawa, W. Lehnert (eds.), *SOFC V (1997) Electrochem. Soc.*, Pennington, NJ, vol. 97-40, p. 301.
30. I. Yasuda, Y. Matsuzaki, T. Yamakawa, T. Koyama, Electrical conductivity and mechanical properties of alumina-dispersed doped lanthanum gallates, *Solid State Ionics* 135 (2000) 381.
31. J.B. Goodenough, Ceramic solid electrolytes, *Solid State Ionics* 94 (1997) 17.
32. M.V. Perfilyev, A.K. Demin, B.L. Kuzin, A.S. Lipilin, "High-Temperature Electrolysis of Gases", Nauka, Moscow, 1988 (in Russian).
33. V.V. Kharton, E.N. Naumovich, A.A. Vecher, Research on the electrochemistry of oxygen ion conductors in the former Soviet Union. I. ZrO₂-based ceramic materials, *J. Solid State Electrochem.* 3 (1999) 61.
34. S.P.S. Badwal, F.T. Ciacchi, D. Milosevic, Scandia-zirconia electrolytes for intermediate temperature solid oxide fuel cell operation, *Solid State Ionics* 136-137 (2000) 91.
35. M. Mori, T. Abe, H. Itoh, O. Yamamoto, Y. Takeda, T. Kawahara, Cubic-stabilized zirconia and alumina composites as electrolytes in planar type solid oxide fuel cells, *Solid State Ionics* 74 (1994) 157.
36. O. Yamamoto, Y. Arati, Y. Takeda, N. Imanishi, Y. Mizutani, M. Kawai, Y. Nakamura, Electrical conductivity of stabilized zirconia with ytterbia and scandia, *Solid State Ionics* 79 (1995) 137.
37. J.-H. Lee, M. Yoshimura, Phase stability and electrical conductivity of the Zr_{0.5}Y_{0.5}O_{1.75}-Y_{0.75}Nb_{0.25}O_{1.75} system, *Solid State Ionics* 124 (1999) 185.
38. S.P.S. Badwal, Zirconia-based solid electrolytes: microstructure, stability and ionic conductivity, *Solid State Ionics*, 52 (1992) 23.

39. A.N. Vlasov, Some relationships in the aging of $ZrO_2+Y_2O_3$ and $ZrO_2+Ho_2O_3$ solid oxide electrolytes, Soviet Electrochem. 19 (1983) 1456.
40. V.K. Gil'derman, A.D. Neumin, S.F. Pal'guev, Oxygen permeability of solid electrolytes based on zirconium dioxide stabilized by scandium and calcium oxides, Doklady AN SSSR 218 (1974) 133.
41. V.V. Kharton, A.A. Yaremchenko, E.N. Naumovich, F.M.B. Marques, Research on the electrochemistry of oxygen ion conductors in the former Soviet Union III. HfO_2 -, CeO_2 - and ThO_2 -based oxides, J. Solid State Electrochem. 4 (2000) 243.
42. H. Yahiro, K. Eguchi, H. Arai, Electrical-properties and reducibilities of ceria rare earth oxide systems and their application to solid oxide fuel-cell, Solid State Ionics 36 (1989) 71.
43. V.V. Kharton, F.M. Figueiredo, L. Navarro, E.N. Naumovich, A.V. Kovalevsky, A.A. Yaremchenko, A.P. Viskup, A. Carneiro, F.M.B. Marques, J.R. Frade, Ceria-based materials for solid oxide fuel cells, J. Mater. Sci. 36 (2001) 1105.
44. T. Kudo, H. Obayashi, Mixed electrical-conduction in fluorite-type $Ce_{1-x}Gd_xO_{2-x/2}$, J. Electrochem. Soc. 123 (1976) 415.
45. S. Luebke, H.-D. Wiemhoefer, Electronic conductivity of Gd-doped ceria with additional Pr-doping, Solid State Ionics. 117 (1999) 229.
46. H. Hayashi, M. Kanoh, C. Quan, H. Inaba, S. Wang, M. Dokiya and H. Tagawa, Thermal expansion of Gd-doped ceria and reduced ceria, Solid State Ionics 132 (2000) 227.
47. V.V. Kharton, E.N. Naumovich, A.A. Yaremchenko, F.M.B. Marques, Research on the electrochemistry of oxygen ion conductors in the former Soviet Union IV. Bismuth oxide-based ceramics, J. Solid State Electrochem. 5 (2001) 160.
48. T. Ishihara, H. Matsuda, Y. Takita, Doped $LaGaO_3$ perovskite type oxide as a new oxide ionic conductor, J. Am. Chem. Soc. 116 (1994) 3801.
49. J.W. Stevenson, T.R. Armstrong, L.R. Pederson, J. Li, C.A. Levinsohn, S. Baskaran, Effect of A-site cation nonstoichiometry on the properties of doped lanthanum gallate, Solid State Ionics 113-115 (1998) 571.
50. J.W. Stevenson, K. Hasinska, N.L. Canfield, T.R. Armstrong, Influence of cobalt and iron additions on the electrical and thermal properties of $(La,Sr)(Ga,Mg)O_{3-d}$, J. Electrochem. Soc., 147 (2000) 3213.
51. T. Ishihara, T. Akbay, H. Furutani, Y. Takita, Improved oxide ion conductivity of Co doped $La_{0.8}Sr_{0.2}Ga_{0.8}Mg_{0.2}O_3$ perovskite type oxide, Solid State Ionics 113-115 (1998) 585.
52. J.-H. Kim, H.-I. Yoo, Partial electronic conductivity and electrolytic domain of $La_{0.9}Sr_{0.1}Ga_{0.8}Mg_{0.2}O_{3-\delta}$, Solid State Ionics 140 (2001) 105.
53. I.P. Marozau, D. Marrero-López, A.L. Shaula, V.V. Kharton, E.V. Tsipis, P. Núñez, J.R. Frade, Ionic and electronic transport in stabilized β - $La_2Mo_2O_9$ electrolytes, Electrochim. Acta, 49 (2004) 3517.
54. S. A. Kramer, H. L. Tuller, A novel titanate-based oxygen ion conductor: $Gd_2Ti_2O_7$, Solid State Ionics 82 (1995) 15.
55. M. Mori, G.M. Tompsett, N.M. Sammes, E. Suda, Y. Takeda, Compatibility of $Gd_xTi_2O_7$ pyrochlores ($1.72 \leq x \leq 2.0$) as electrolytes in high-temperature solid oxide fuel cells, Solid State Ionics 158 (2003) 79.
56. Hiroshi Arikawa, Hiroyasu Nishiguchi, Tatsumi Ishihara, Yusaku Takita, Oxide ion conductivity in Sr-

- doped $\text{La}_{10}\text{Ge}_6\text{O}_{27}$ apatite oxide, *Solid State Ionics*, 136-137 (2000) 31.
57. E.J. Abram, D.C. Sinclair and A.R. West, A novel enhancement of ionic conductivity in the cation-deficient apatite $\text{La}_{9.33}(\text{SiO}_4)_6\text{O}_2$, *J. Mater. Chem.* 11 (2001) 1978.
 58. J. Drennan, G. Auchterlonie, Microstructural aspects of oxygen ion conduction in solids, *Solid State Ionics* 134 (2000) 75.
 59. A. Yuzaki, A. Kishimoto, Effects of alumina dispersion on ionic conduction of toughened zirconia base composite, *Solid State Ionics* 116 (1999) 47.
 60. R.D. Shannon, Revised effective ionic-radii and systematic studies of interatomic distances in halides and chalcogenides, *Acta Cryst.*, A32 (1976) 751.
 61. K. Nomura, S. Tanase, Electrical conduction behaviour in $(\text{La}_{0.9}\text{Sr}_{0.1})\text{M}(\text{III})\text{O}_{3-d}$ (M(III)=Al, Ga, Sc, In and Lu) perovskites, *Solid State Ionics*, 98 (1997) 229-236.
 62. A. Tsoda, A. Gupta, A. Naoumoudis, D. Skarmoutsos, P. Nikolopoulos, Performance of double-layer CGO/YSZ electrolyte for solid oxide fuel cells, *Ionics* 4 (1998) 234.
 63. F. Tietz, Thermal expansion of SOFC materials, *Ionics* 5 (1999) 129.
 64. I.V. Murygin, "Electrode Processes in Solid Electrolytes", Nauka, Moscow, 1991.
 65. P. Fabry, M. Kleitz, Influence of the metal and the electrolyte composition on the characteristics of the oxygen electrode reaction on solid oxide electrolyte, *J. Electroanal. Chem.*, 57 (1974) 165.
 66. Da Yu Wang, A.S. Nowick, Diffusion-controlled polarization of Pt, Ag and Au electrodes with doped ceria electrolyte, *J. Electrochem. Soc.* 128 (1981) 55.
 67. A. Mitterdorfer, L.J. Gauckler, Identification of the reaction mechanism of the Pt, $\text{O}_2(\text{g})$ |yttria-stabilized zirconia system, Part I: General framework, modeling, and structural investigation, *Solid State Ionics* 117 (1999) 187.
 68. A. Mitterdorfer, L.J. Gauckler, Identification of the reaction mechanism of the Pt, $\text{O}_2(\text{g})$ |yttria-stabilized zirconia system, Part II: Model implementation, parameter estimation, and validation, *Solid State Ionics* 117 (1999) 203.
 69. B.C.H. Steele, Behavior of porous cathodes in high temperatures fuel cells, *Solid State Ionics* 94 (1997) 239.
 70. J. Mizusaki, H. Tagawa, K. Isobe, M. Tajika, I. Koshiro, H. Maruyama, K. Hirano, Kinetics of the electrode reaction at the H_2 - H_2O porous Pt/stabilized zirconia interface, *J. Electrochem. Soc.* 141 (1994) 1674.
 71. M.V. Perfilyev, "Temperature dependence of the electrode polarizability in the cells with solid oxide electrolyte", In: *Physical chemistry of salt melts and solid electrolytes*, AN SSSR, Urals scientific center, Ekaterinburg, 1978, p. 81. [in Russian]
 72. T. Horita, K. Yamaji, N. Sakai, Yu. Xiong, H. Yokokawa, T. Kawada, Application of novel SIMS technique for imaging the active sites of oxygen reduction at the SOFC cathode/electrolyte interfaces, *Ionics* 8 (2002) 108.
 73. M. Mogensen, S. Skaarup, Kinetic and geometric aspects of solid oxide fuel cell electrodes, *Solid State Ionics* 86-88 (1996) 1151.
 74. R. Jiménez, T. Klöidt, M. Kleitz, Reaction-zone expansions and mechanism of the O_2 , Ag|yttria-

- stabilized zirconia electrode reaction, *J. Electrochem. Soc.* 144 (1997) 582.
75. S.P. Yoon, S.W. Nam, S-G. Kim, S-A. Hong, S-H. Hyun, Characteristic of cathodic polarization at Pt/YSZ interface without the effect of electrode microstructure, *J. Power Sources* 115 (2003) 27.
 76. T. Kenjo, Y. Kanehira, Influence of the local variation of the polarization resistance on SOFC cathodes, *Solid State Ionics* 148 (2002) 1.
 77. M. Liu, Equivalent circuit approximation to porous mixed-conducting oxygen electrodes in solid-state cells, *J. Electrochem. Soc.* 145 (1998) 142.
 78. K. Sasaki, J.-P. Wurth, R. Gschwend, M. Gödickemeier, L.J. Gauckler, Microstructure-property relations of solid oxide fuel cell cathodes and current collectors, *J. Electrochem. Soc.* 143 (1996) 530.
 79. S.B. Adler, J.A. Lane, B.C.H. Steele, Electrode kinetics of porous mixed-conducting oxygen electrodes, *J. Electrochem. Soc.* 143 (1996) 3554.
 80. M. Kleitz, F. Petitbon, Optimized SOFC electrode microstructure, *Solid State Ionics* 92 (1996) 65.
 81. J. Fleig, On the width of the electrochemically active region in mixed conducting solid oxide fuel cell cathodes, *J. Power Sources* 105 (2002) 228.
 82. J. Fleig, J. Maier, The polarization of mixed conducting SOFC cathodes: Effects of surface reaction coefficient, ionic conductivity and geometry, *J. Eur. Ceram. Soc.* 24 (2004) 1343.
 83. J. Mizusaki, T. Saito, H. Tagawa, A chemical diffusion-controlled electrode reaction at the compact $\text{La}_{1-x}\text{Sr}_x\text{MnO}_3$ /stabilized zirconia interface in oxygen atmospheres, *J. Electrochem. Soc.* 143 (1996) 3065.
 84. A.M. Svensson, K. Nişancıoğlu, Current distribution at electrode-solid oxide electrolyte interface, *J. Electrochem. Soc.* 145 (1998) 3130.
 85. A.M. Svensson, S. Sunde, K. Nişancıoğlu, Mathematical modeling of oxygen exchange and transport in air-perovskite-YSZ interface regions I. Reduction of intermediately adsorbed oxygen, *J. Electrochem. Soc.* 144 (1997) 2719, and II. Direct exchange of oxygen vacancies, *J. Electrochem. Soc.* 145 (1998) 1390.
 86. S.P. Jiang, J.G. Love, Observation of structural change induced by cathodic polarization on $(\text{La,Sr})\text{MnO}_3$ electrodes of solid oxide fuel cells, *Solid State Ionics* 158 (2003) 45.
 87. E. Siebert, A. Hammouche, M. Kleitz, Impedance spectroscopy analysis $\text{La}_{1-x}\text{Sr}_x\text{MnO}_3$ -yttria-stabilized zirconia electrode kinetics, *Electrochim. Acta* 40 (1995) 1741.
 88. Y. Takeda, R. Kanno, M. Noda, Y. Tomida, O. Yamamoto, Cathodic polarization phenomena of perovskite oxide electrodes with stabilized zirconia, *J. Electrochem. Soc.* 134 (1987) 2656.
 89. F.H. van Heuveln, H.J.M. Bouwmeester, Electrode properties of Sr-doped LaMnO_3 on yttria-stabilized zirconia. II. Electrode kinetics, *J. Electrochem. Soc.* 144 (1997) 134.
 90. P. Kofstad, "Nonstoichiometry, Diffusion and Electrical Conductivity in Binary Metal Oxides", Wiley-Interscience, New York, 1972.
 91. S.H. Chan, K.A. Khor, Z.T. Xia, A complete polarization model of a solid oxide fuel cell and its sensitivity to the change of the cell components, *J. Power Sources* 93 (2001) 130.
 92. H.J.M. Bouwmeester, A.J. Burggraaf, Dense ceramic membranes for oxygen separation. In: A.J. Burggraaf, L. Cot (eds.), *Fundamentals of Inorganic Membrane Science and Technology*, Elsevier, Amsterdam, 1996, p. 435.

93. A.W. Marczewski, A. Derylo-Marczewska, M. Jaroniec, Unified theoretical description of physical adsorption from gaseous and liquid phases on heterogeneous solid surfaces and its application for predicting multicomponent adsorption equilibria, *Chem. Scripta* 28 (1988) 173.
94. A. Endo, H. Fukunaga, C. Wen, K. Yamada, Cathodic reaction mechanism of dense $\text{La}_{0.6}\text{Sr}_{0.4}\text{CoO}_3$ and $\text{La}_{0.81}\text{Sr}_{0.09}\text{MnO}_3$ electrodes for solid oxide fuel cells, *Solid State Ionics* 135 (2000) 353.
95. C.-L. Chang, T.-C. Lee, T.-J. Huang, Oxygen reduction mechanism and performance of $\text{Y}_1\text{Ba}_2\text{Cu}_3\text{O}_{7-8}$ as a cathode material in a high-temperature solid-oxide fuel cell, *J. Solid State Electrochem.* 2 (1998) 291.
96. M. Göddeckemeier, K. Sakai, L.J. Gauckler, I. Riess, Electrochemical characteristics of cathodes in solid oxide fuel cells based on ceria electrolytes, *J. Electrochem. Soc.* 144 (1997) 1635.
97. G.W. Coffey, L.R. Pederson, P.C. Rieke, Competition between bulk and surface pathways in mixed ionic electronic conducting oxygen electrodes, *J. Electrochem. Soc.* 150 (2003) A1139.
98. M. Kuznecov, P. Otschik, P. Obenaus, K. Eichler, W. Schaffrath, Diffusion controlled oxygen transport and stability at the perovskite/electrolyte interface, *Solid State Ionics* 157 (2003) 371.
99. S.B. Adler, Limitations of charge-transfer models for mixed-conducting oxygen electrodes, *Solid State Ionics* 135 (2000) 603.
100. J. Jamnic, J. Maier, Generalised equivalent circuits for mass and charge transport: chemical capacitance and its implications, *Phys. Chem. Chem. Phys.* 3 (2001) 1668.
101. Y. Bultel, L. Genies, O. Antoine, P. Ozil, R. Durand, Modeling impedance diagrams of active layers in gas diffusion electrodes: diffusion, ohmic drop effects and multistep reactions, *J. Electroanal. Chem.* 527 (2002) 143.
102. C. Gabrielli and M. Keddad, Contribution of electrochemical impedance spectroscopy to the investigation of the electrochemical kinetics, *Electrochim. Acta* 41 (1996) 957.
103. A. Bieberle, L.J. Gauckler, Reaction mechanism of Ni pattern anodes for solid oxide fuel cells, *Solid State Ionics* 135 (2000) 37.
104. M. Brown, S. Primdahl, M. Mogensen, Structure/performance relations for Ni/yttria-stabilized zirconia anodes for solid oxide fuel cells, *J. Electrochem. Soc.* 147 (2000) 475.
105. A. Bieberle, L.J. Gauckler, State-space modeling of the anodic SOFC system Ni, H_2 - H_2O |YSZ, *Solid State Ionics* 146 (2002) 23.
106. K. Tsuneyoshi, K. Mori, A. Sawata, J. Mizusaki, H. Tagawa, Kinetic studies on the reaction at the $\text{La}_{0.6}\text{Ca}_{0.4}\text{MnO}_3/\text{YSZ}$ interface, as an SOFC air electrode, *Solid State Ionics* 35 (1989) 263.
107. S.P. Jiang, J.G. Love, Y. Ramprakash, Electrode behavior at $(\text{La},\text{Sr})\text{MnO}_3/\text{Y}_2\text{O}_3\text{-ZrO}_2$ interface by electrochemical impedance spectroscopy, *J. Power Sources* 110 (2002) 201.
108. X.J. Chen, K.A. Khor, S.H. Chan, Identification of O_2 reduction process at yttria stabilized zirconia/doped lanthanum manganite interface, *J. Power Sources* 123 (2003) 17.
109. H. Kamata, A. Hosaka, J. Mizusaki, H. Tagawa, High temperature electrocatalytic properties of the SOFC air electrode $\text{La}_{0.8}\text{Sr}_{0.2}\text{MnO}_3/\text{YSZ}$, *Solid State Ionics* 106 (1998) 237.
110. E. Murray, T. Tsai, S. Barnett, Oxygen transfer process in $(\text{La},\text{Sr})\text{MnO}_3/\text{Y}_2\text{O}_3$ -stabilized ZrO_2 cathodes: an impedance spectroscopy study, *Solid State Ionics* 110 (2002) 235.
111. J. Mizusaki, H. Tagawa, M. Katou, K. Hirano, A. Sawata, K. Tsuneyoshi, Electrochemical properties of

- some perovskite-type oxides as oxygen gas electrodes on yttria stabilized zirconia. In: F. Grosz, P. Zegers, S.C. Singhal, O. Yamamoto (eds.), SOFC II (1991) Electrochem. Soc., Pennington, NJ, p. 487.
- 112.S.B. Adler, Mechanism and kinetics of oxygen reduction on porous $\text{La}_{1-x}\text{Sr}_x\text{CoO}_{3-\delta}$ electrodes, *Solid State Ionics* 111 (1998) 125.
113. H. Fukunaga, M. Koyama, N. Takahashi, C. Wen, K. Yamada, Reaction model of dense $\text{Sm}_{0.5}\text{Sr}_{0.5}\text{CoO}_3$ as SOFC cathode, *Solid State Ionics* 132 (2000) 279.
- 114.R. Baker, J. Guindet, M. Kleitz, Classification criteria for solid oxide fuel cell electrode materials, *J. Electrochem. Soc.* 144 (1997) 2427.
- 115.I. Drescher, W. Lehnert, J. Meusinger, Structural properties of SOFC anodes and reactivity, *Electrochim. Acta*, 43 (1998) 3059.
- 116.E.P. Murray, T. Tsai, S.A. Barnett, A direct-methane fuel cell with a ceria-based anode, *Nature* 400 (1999) 649.
- 117.I.V. Yentekakis, Y. Jiang, S. Neophytides, S. Bebelis. C.G. Vayenas, Catalysis, electrocatalysis and electrochemical promotion of the steam reforming of methane over Ni film and Ni-YSZ cermet anodes, *Ionics* 1 (1995) 491.
- 118.J. Liu, S.A. Barnett, Operation of anode-supported solid oxide fuel cells on methane and natural gas, *Solid State Ionics* 158 (2003) 11.
- 119.P. Vernoux, J. Guindet, E. Gehain, M. Kleitz, Catalysts for continuous methane reforming in medium temperature SOFC, In: U. Stimming, S.C. Singhal, H. Tagawa, W. Lehnert (eds.), SOFC V (1997) Electrochem. Soc., Pennington, NJ, vol. 97-40, p. 219.
- 120.K. Sato, J. Nakamura, T. Uchijima, T. Hayakawa, S. Hamakawa, T. Tsunoda, T. Shishido, K. Takehira, Role of rhodium anode in the YSZ-aided CH_4 oxidation into syngas, *Solid State Ionics* 136-137 (2000) 753.
- 121.A.M. Diskin, R.H. Cunningham, R.M. Ormerod, The oxidative chemistry of methane over supported nickel catalysts, *Catal. Today* 46 (1998) 147.
- 122.C.M. Finnerty, N.J. Coe, R.H. Cunningham, R.M. Ormerod, Carbon formation on and deactivation of nickel-based/zirconia anodes in solid oxide fuel cells running on methane, *Catal. Today* 46 (1998) 137.
- 123.B. de Boer, M. Gonzalez, H.J.M. Bouwmeester, H. Verweij, The effect of the presence of fine YSZ particles on the performance of porous nickel electrodes, *Solid State Ionics* 127 (2000) 269.
- 124.J. Mizusaki, H. Tagawa, T. Saito, K. Kamitani, T. Yamamura, K. Hirano, S. Ehara, T. Takagi, T. Hikita, M. Ippommatsu, S. Nakagawa, K. Hashimoto, Preparation of nickel pattern electrodes on YSZ and their electrochemical properties in H_2 - H_2O atmospheres, *J. Electrochem. Soc.* 141 (1994) 2129.
- 125.T. Iwata, Characterization of Ni-YSZ anode degradation for substrate-type solid oxide fuel cells, *J. Electrochem. Soc.* 143 (1996) 1521.
- 126.R.E. Williford, L.A. Chick, G.D. Maupin, S.P. Simner, J.W. Stevenson, Diffusion limitations in the porous anodes of SOFCs, *J. Electrochem. Soc.* 150 (2003) A1067
- 127.S.H. Chan, Z.T. Xia, Anode micro model of solid oxide fuel cell, *J. Electrochem. Soc.* 148 (2001) A388.
- 128.D. Arnošt, P. Schneider, Dynamic transport of multicomponent mixtures of gases in porous solids, *Chem. Eng. J.* 57 (1995) 91.

- 129.K. Eguchi, Y. Kunisa, K. Adachi, H. Arai, Effect of anodic concentration overvoltages on power generation characteristics of solid oxide fuel cells, *J. Electrochem. Soc.* 143 (1996) 3699.
130. C.Wen, R. Kato, H. Fukunaga, H. Ishitani, K. Yamada, The overpotential of nickel/yttria-stabilized zirconia cermet anodes used in solid oxide fuel cells, *J. Electrochem. Soc.* 147 (2000) 2076.
- 131.M. Ihara, T. Kusano, C. Yokoyama, Competitive adsorption reaction mechanism of Ni/yttria-stabilized zirconia cermet anodes in H₂-H₂O solid oxide fuel cells, *J. Electrochem. Soc.* 148 (2001) A209.
- 132.S.P. Jiang, Y. Ramprakash, H₂ oxidation on Ni/Y-TZP cermet electrodes – polarisation behaviour, *Solid State Ionics* 116 (1999) 145.
- 133.S.P. Jiang, S.P.S. Badwal, An electrode kinetics study of H₂ oxidation on Ni/Y₂O₃-ZrO₂ cermet electrode of the solid oxide fuel cell, *Solid State Ionics* 123 (1999) 209.
- 134.P. Holtappels, L.G.J. de Haart, U. Stimming, Reaction of Hydrogen/Water Mixtures on Nickel-Zirconia Cermet Electrodes I. DC Polarization Characteristics, *J. Electrochem. Soc.* 146 (1999) 1620.
- 135.V.N. Chebotin, M.V. Perfilyev, “Electrochemistry of Solid Electrolytes”, Khimia, Moscow, 1978 (in Russian).
- 136.M.V. Perfiliev, V.N. Chebotin, I.V. Murygin, Mutual influence of gas-mixture components in the electrode-kinetics of high-temperature cells with solid electrolytes, *Soviet Electrochemistry* 15 (1979) 1559.
- 137.A. Bieberle, L.P. Meier, L.J. Gauckler, The electrochemistry of Ni pattern anodes used as solid oxide fuel cell model electrodes, *J. Electrochem. Soc.* 148 (2001) A646.
138. F.Z. Mohamedi-Boulenouar, J. Guindet, A. Hammou, Influence of water vapor on electrochemical oxidation of hydrogen at the Ni/zirconia interface. In: U. Stimming, S.C. Singhal, H. Tagawa, W. Lehnert (eds.), SOFC V (1997) *Electrochem. Soc.*, Pennington, NJ, vol. 97-40, p. 441.
- 139., S.P. Jiang, Y. Ramprakash, H₂ oxidation on Ni/Y-TZP cermet electrodes – a comparison of electrode behaviour by GCI and EIS techniques *Solid State Ionics* 122 (1999) 211.
- 140.J. Mizusaki, H. Tagawa, Y. Miyaki, S. Yamauchi, K. Fueki, I. Koshiro, K. Hirano, Kinetics of the electrode reaction at the CO-CO₂, porous Pt/stabilized zirconia interface, *Solid State Ionics* 53-56 (1992) 126.
- 141.V.N. Chebotin, M.V. Glumov, S.F. Pal’guev, A.D. Neuimin, Polarization of gas electrode on solid oxide electrolyte, partially possessing the electronic conductivity, *Elektrokhimiya* 7 (1971) 491 (in Russian).
- 142.P. Vernoux, Lanthanum chromite as an anode material for solid oxide fuel cells, *Ionics* 3 (1997) 270.
- 143.O. Deutschmann, F. Behrendt, J. Warnatz, Formal treatment of catalytic combustion and catalytic conversion of methane, *Catal. Today* 46 (1998) 155.
- 144.A.G. Steghuis, J.G. van Ommen, J.A. Lercher, On the reaction mechanism for methane partial oxidation over yttria/zirconia, *Catal. Today* 46 (1998) 91.
- 145.M.A. Peña, J.P. Gómez, J.L.G. Fierro, New catalytic routes for syngas and hydrogen production, *Appl. Catal.* A144 (1996) 7.
- 146.V.V. Kharton, A.A. Yaremchenko, E.N. Naumovich, Research on the electrochemistry of oxygen ion conductors in the former Soviet Union. II. Perovskite-related oxides, *J. Solid State Electrochem.* 3 (1999) 303.

- 147.V.V. Kharton, A.V. Nikolaev, E.N. Naumovich, A.A. Vecher, Oxygen ion transport and electrode properties of La(Sr)MnO₃, *Solid State Ionics* 81 (1995) 201.
- 148.H.Y. Lee, W.S. Cho, S.M. Oh, H.-D. Wiemhöfer, W. Göpel, Active reaction sites for oxygen reduction in La_{0.9}Sr_{0.1}MnO₃/YSZ electrodes, *J. Electrochem. Soc.* 142 (1995) 2659.
- 149.H.J.M. Bouwmeester, H. Kruidhof, A.J. Burggraaf, Importance of the surface exchange kinetics as rate limiting step in oxygen permeation through mixed-conducting oxides, *Solid State Ionics* 72 (1994) 185.
- 150.B.C.H. Steele, Interfacial reactions associated with ceramic ion transport membranes, *Solid State Ionics* 75 (1995) 157.
- 151.A. Endo, S. Wada, Ch.-Ju Wen, H. Komiyama, K. Yamada, Low overvoltage mechanism of high ionic conducting cathode for solid oxide fuel cell, *J. Electrochem. Soc.* 145 (1998) L35.
- 152.J. Bockris, T. Otagawa, The electrocatalysis of oxygen evolution on perovskites, *J. Electrochem. Soc.* 131 (1984) 290.
- 153.T. Ioroi, T. Hara, Y. Uchimoto, Z. Ogumi, Z.-I. Takehara, Preparation of perovskite-type La_{1-x}Sr_xMnO₃ films by vapor-phase processes and their electrochemical properties, *J. Electrochem. Soc.* 145 (1998) 1999.
- 154.K. Yasumoto, N. Mori, J. Mizusaki, H. Tagawa, M. Dokiya, Effect of oxygen nonstoichiometry on electrode activity of La_{1-x}A_xMnO_{3±δ}, *J. Electrochem. Soc.* 148 (2001) A105.
- 155.D. Simwonis, F. Tietz, D. Stöver, Nickel coarsening in annealed Ni/8YSZ anode substrates for solid oxide fuel cells, *Solid State Ionics* 132 (2000) 241.
- 156.S. Primdahl, M. Mogensen, Oxidation of hydrogen on Ni/yttria-stabilized zirconia cermet anodes, *J. Electrochem. Soc.* 144 (1997) 3409.
- 157.S.P. Jiang, Y.Y. Duan, J.G. Love, Fabrication of high-performance Ni/Y₂O₃-ZrO₂ cermet anodes of solid oxide fuel cells by ion impregnation, *J. Electrochem. Soc.* 149 (2002) A1175.
- 158.V.V. Kharton, E.N. Naumovich, V.N. Tikhonovich, I.A. Bashmakov, L.S. Boginsky, A.V. Kovalevsky, Testing tubular solid oxide fuel cells in nonsteady-state conditions, *J. Power Sources* 79 (1999) 242.
- 159.O.A. Marina, C. Bagger, S. Primdahl, M. Mogensen, A solid oxide fuel cell with a gadolinia-doped ceria anode: preparation and performance, *Solid State Ionics* 123 (1999) 199.
- 160.Gorte, R.J., Park, S., Vohs, J.M. and Wang, C., Anodes for direct oxidation of dry hydrocarbons in a solid-oxide fuel cell, *Adv. Mater.* 12 (2000) 1465.
- 161.S. Wang, T. Kato, S. Nagata, T. Honda, T. Kaneko, N. Iwashita, M. Dokiya, Ni/ceria cermet as anode of reduced-temperature solid oxide fuel cells, *J. Electrochem. Soc.* 149 (2002) A927.
- 162.S. Primdahl, M. Mogensen, Mixed conductor anodes: Ni as electrocatalyst for hydrogen conversion, *Solid State Ionics* 152 (2002) 597.
- 163.H. Uchida, M. Yoshida, M. Watanabe, Effect of ionic conductivity of zirconia electrolytes on the polarization behavior of various cathodes in solid oxide fuel cells, *J. Electrochem. Soc.* 146 (1999) 1.
- 164.T. Ishihara, T. Shibayama, M. Honda, H. Nishiguchi, Y. Takita, Intermediate temperature solid oxide fuel cells using LaGaO₃ electrolyte II. Improvement of oxide ion conductivity and power density by doping Fe for Ga site of LaGaO₃, *J. Electrochem. Soc.* 147 (2000) 1332.
- 165.M. Liu, Z. Wu, Significance of interfaces in solid-state cells with porous electrodes of mixed ionic-

- electronic conductors, *Solid State Ionics* 107 (1998) 105.
- 166.Y. Mishima, H. Mitsuyasu, M. Ohtaki, K. Eguchi, Solid oxide fuel cell with composite electrolyte consisting of samaria-doped ceria and yttria-stabilized zirconia, *J. Electrochem. Soc.* 145 (1998) 1004.
- 167.T. Tsai, E. Perry, S. Barnett, Low-temperature solid oxide fuel cells utilizing thin bilayer electrolytes, *J. Electrochem. Soc.* 144 (1997) L130.
- 168.T. Horita, K. Yamaji, N. Sakai, H. Yokokawa, T. Kawada, T. Kato, Oxygen reduction sites and diffusion paths at $\text{La}_{0.9}\text{Sr}_{0.1}\text{MnO}_{3-x}$ /yttria-stabilized zirconia interface for different cathodic overvoltages by secondary-ion mass spectrometry, *Solid State Ionics* 127 (2000) 55.
- 169.E.J.L. Schouler, Relation between solid oxide electrolyte surface properties and electrode reaction kinetics, *Solid State Ionics* 9-10 (1983) 945.
- 170.P. Bohac, A. Orliukas, L. Gauckler, Lowering of the cathode overpotential of SOFC by electrolyte doping. In: R. Waser, S. Hoffmann, D. Bonnenberg, Ch. Hoffmann (eds.) *Electroc ceramics IV* (1994), IWE, University of Technology, Augustinus Buchhandlung, Aachen, v. II, p. 771.
- 171.B.A. van Hassel, B.A. Boukamp, A.J. Burggraaf, Electrode polarization at the Au, O_2 (g) / Fe implanted yttria-stabilized zirconia interface, *Solid State Ionics* 51 (1992) 161.
- 172.K. Yamaji, T. Horita, N. Sakai and H. Yokokawa, Comparison between $\text{La}_{0.9}\text{Ba}_{0.1}\text{Ga}_{0.8}\text{Mg}_{0.2}\text{O}_{2.85}$ and $\text{La}_{0.9}\text{Sr}_{0.1}\text{Ga}_{0.8}\text{Mg}_{0.2}\text{O}_{2.85}$ as SOFCs electrolytes *Solid State Ionics* 152-153 (2002) 517.
- 173.T. Ishihara, S. Fukui, H. Nishiguchi and Y. Takita, Mixed electronic-oxide ionic conductor of BaCoO_3 doped with La for cathode of intermediate-temperature-operating solid oxide fuel cell, *Solid State Ionics* 152-153 (2002) 609.
- 174.L. Qiu, T. Ichikawa, A. Hirano, N. Imanishi, Y. Takeda, $\text{Ln}_{1-x}\text{Sr}_x\text{Co}_{1-y}\text{Fe}_y\text{O}_{3-\delta}$ (Ln=Pr, Nd, Gd; $x=0.2, 0.3$) for the electrodes of solid oxide fuel cells, *Solid State Ionics* 158 (2003) 55.
- 175.M. de Ridder, A.G.J. Vervoort, R.G. van Welzenis, H.H. Brongersma, The limiting factor for oxygen exchange at the surface of fuel cell electrolytes, *Solid State Ionics* 156 (2003) 255.
- 176.S.P. Jiang, J.G. Love, L. Apateanu, Effect of contact between electrode and current collector on the performance of solid oxide fuel cells, *Solid State Ionics* 160 (2003) 15.
- 177.D.I. Bronin, B.L. Kuzin, H. Nāfe, F. Aldinger, Behavior of a dense In_2O_3 / YSZ electrode in oxygen containing atmospheres, *Ionics* 4 (1998) 249.
- 178.Y. Matsuzaki, I. Yasuda, Dependence of SOFC cathode degradation by chromium-containing alloy on compositions of electrodes and electrolytes, *J. Electrochem. Soc.* 148 (2001) A126.
- 179.S.P. Jiang, J.P. Zhang, K. Föger, Deposition of chromium species at Sr-doped LaMnO_3 electrodes in solid oxide fuel cells. II. Effect on O_2 reduction reaction, *J. Electrochem. Soc.* 147 (2000) 3195.
- 180.S.F. Pal'guyev, V.K. Gil'derman, V.I. Zemtsov, "High-temperature oxide electronic conductors for electrochemical devices", Nauka, Moscow, 1990 (in Russian).
- 181.Y. Sakaki, Y. Takeda, A. Kato, N. Imanishi, O. Yamamoto, M. Hattori, M Iio, Y. Esaki, $\text{Ln}_{1-x}\text{Sr}_x\text{MnO}_3$ (Ln = Pr, Nd, Sm and Gd) as cathode material for solid oxide fuel cells, *Solid State Ionics* 118 (1999) 187.
- 182.Yu.S. Gaiduk, V.V. Kharton, E.N. Naumovich, A.V. Nikolaev, V.V. Samokhval, Physicochemical and electrochemical properties of $\text{La}_{1-x}\text{Pb}_x\text{MnO}_3$ ($x = 0.1-0.6$) solid solutions, *Inorg. Mater.* 30 (1994) 1360.

- 183.L.A. Tikhonova, G.I. Samal, P.P. Zhuk, A.A. Tonoyan, A.A. Vecher, Physicochemical properties of lanthanum manganite doped with strontium, *Inorg. Mater.* 26 (1990) 149.
- 184.Y. Takeda, H.Y. Tu, H. Sakaki, S. Watanabe, N. Imanishi, O. Yamamoto, M.B. Phillipps, N.M. Sammes, $Gd_{1-x}A_xMnO_3$ (A = Ca and Sr) for the electrode of solid oxide fuel cells, *J. Electrochem. Soc.* 144 (1997) 2810.
- 185.Y. Takeda, Y. Sakaki, T. Ichikawa, N. Imanishi, O. Yamamoto, M. Mori, N. Mori, T. Abe, Stability of $La_{1-x}A_xMnO_3$ (A = Ca and Sr) as cathode materials for solid oxide fuel cells, *Solid State Ionics* 72 (1994) 257.
- 186.T. Ishihara, T. Kudo, H. Matsuda, Y. Takita, Doped $PrMnO_3$ oxide as a new cathode of solid oxide fuel cells for low temperature operation, *J. Electrochem. Soc.* 142 (1995) 1519.
- 187.S.W. Hashimoto, H. Iwahara, Structural, thermal and electrical properties of Ce-doped $SrMnO_3$, *J. Electroceram.* 4 (2000) 225.
- 188.X. Huang, J. Liu, Zhe Lu, Wei Liu, Li Pei, T. He, Zh. Liu, W. Su, Properties of nonstoichiometric $Pr_{0.6-x}Sr_{0.4}MnO_3$ as the cathodes of SOFCs, *Solid State Ionics* 130 (2000) 195.
- 189.R. Schachtner, E. Ivers-Tiffée, W. Weppner, R. Männer, W. Wersing, Investigations on stoichiometric and substoichiometric $La_{1-x-y}Sr_xMnO_{3-\delta}$ used as cathode material in the solid oxide fuel cell, *Ionics* 1 (1995) 63.
- 190.M. Al Daroukh, V.V. Vashook, H. Ullmann, F. Tietz and I. Arual Raj, Oxides of the AMO_3 and A_2MO_4 -type: structural stability, electrical conductivity and thermal expansion *Solid State Ionics* 158 (2003) 141.
- 191.S.P. Jiang, Issues on development of (La,Sr) MnO_3 cathode for solid oxide fuel cells, *J. Power Sources* 124 (2003) 390.
- 192.S.T. Aruna, M. Muthuraman, K.C. Patil, Studies on strontium substituted rare earth manganites, *Solid State Ionics* 120 (1999) 275.
- 193.W. Huebner, D.M. Reed, H.U. Anderson, Structure-property relationships in solid oxide fuel cells. In: U. Stimming, S.C. Singhal, H. Tagawa, W. Lehnert (eds.), *SOFC V* (1997) *Electrochem. Soc.*, Pennington, NJ, vol. 97-40, p. 411.
- 194.J.A.M. van Roosmalen, E.H.P. Cordfunke, Chemical reactivity and interdiffusion of (La,Sr) MnO_3 and (Zr,Y) O_2 solid oxide fuel cell cathode and electrolyte materials, *Solid State Ionics* 52 (1992) 303.
- 195.A. Weber, R. Männer, R. Waser, E. Ivers-Tiffée, Interaction between microstructure and electrical properties of screen printed cathodes in SOFC single cells, *Denki Kagaku* 64 (1996) 582.
- 196.V.N. Tikhonovich, V.V. Kharton, E.N. Naumovich, A.A. Savitsky, Surface modification of $La(Sr)MnO_3$ electrodes, *Solid State Ionics* 106 (1998) 197.
- 197.A. Mitterdorfer, L.J. Gauckler, $La_2Zr_2O_7$ formation and oxygen reduction kinetics of the $La_{0.85}Sr_{0.15}Mn_yO_3$, $O_2(g)|YSZ$ system, *Solid State Ionics* 111 (1998) 185.
- 198.H. Yokokawa, N. Sakai, T. Kawada, M. Dokiya, Chemical Thermodynamic Stability of the Interface, In: S.P.S. Badwal, M.J. Bannister, R.H.J. Hannink (eds.) *Science and Technology of Zirconia V*, The Australian Ceram. Soc., Technomic, 1993, p. 752.
- 199.H.-R. Rim, S.-Ki. Jeung, E. Jung, Ju-S. Lee, Characteristics of $Pr_{1-x}M_xMnO_3$ (M=Ca, Sr) as cathode

- material in solid oxide fuel cells, *Mater. Chem. Phys.* 52 (1998) 54.
200. Yu.S. Gaiduk, V.V. Kharton, E.N. Naumovich, V.V. Samokhval, Properties of solid solutions $\text{La}_{0.6}\text{Sr}_{0.4}\text{Mn}_{1-x}\text{Ni}_x\text{O}_3$ ($x = 0 - 0.5$), *Inorg. Mater.* 30 (1994) 759.
201. Tikhonovich VN, Kharton VV, Naumovich EN, Oxygen transport in $\text{La}_{0.6}\text{Sr}_{0.4}\text{Mn}_{1-x}\text{Fe}_x\text{O}_3$ perovskite-like oxides, *Inorg. Mater.* 33 (1997) 602.
202. J. Holc, D. Kuščer, M. Hrovat, S. Bernik, D. Kolar, Electrical and microstructural characterisation of $(\text{La}_{0.8}\text{Sr}_{0.2})(\text{Fe}_{1-x}\text{Al}_x)\text{O}_3$ and $(\text{La}_{0.8}\text{Sr}_{0.2})(\text{Mn}_{1-x}\text{Al}_x)\text{O}_3$ as possible SOFC cathode materials, *Solid State Ionics* 95 (1997) 259.
203. M.B. Phillipps, N.M. Sammes, O. Yamamoto, $\text{Gd}_{1-x}\text{A}_x\text{Co}_{1-y}\text{Mn}_y\text{O}_3$ (A=Sr, Ca) as a cathode for SOFC, *Solid State Ionics*, 123 (1999) 131.
204. S. Srilomsak, D. Schilling, H.U. Anderson, Thermal expansion studies on cathode and interconnect oxides. In: S.C. Singhal (ed.), *SOFC I* (1989), Electrochem. Soc., Pennington, NJ, p. 129.
205. I. Yasuda, K. Ogasawara, M. Hishinuma, T. Kawada, M. Dokiya, Oxygen tracer diffusion coefficient of $(\text{La, Sr})\text{MnO}_{3\pm\delta}$, *Solid State Ionics* 86-88 (1996) 1197.
206. Phase Equilibria Diagrams. CD-Rom Database, Ed. P. Schenck, The American Ceramic Society, Westerville, OH, 1998.
207. T. Sasamoto, J. Mizusaki, M. Yoshimura, W.R. Cannon, H.K. Bowen, Phase relationships and electrical conductivity of the perovskite-type solid solutions in the system strontium zirconium trioxide-lanthanum iron trioxide- $\text{SrFeO}_{3-\delta}$ in air, *Yogyo Kyokaiishi* 90 (1982) 24.
208. M. Schmidt, S.J. Campbell, Crystal and magnetic structures of $\text{Sr}_2\text{Fe}_2\text{O}_5$ at elevated temperature, *J. Solid State Chem.* 156 (2000) 292.
209. J.P. Hodges, S. Short, J.D. Jorgensen, X. Xiong, S.M. Dabrowski, S.M. Mini, C.W. Kimball, Evolution of Oxygen-Vacancy Ordered Crystal Structures in the Perovskite Series $\text{Sr}_n\text{Fe}_n\text{O}_{3n-1}$ ($n=2, 4, 8$, and ∞), and the Relationship to Electronic and Magnetic Properties *J. Solid State Chem.* 151 (2000) 190.
210. V.V. Kharton, A.A. Yaremchenko, A.L. Shaula, A.P. Viskup, F.M.B. Marques, J.R. Frade, E.N. Naumovich, J.R. Casanova, I.P. Marozau, Oxygen permeability and thermal expansion of ferrite-based mixed conducting ceramics, *Defect Diffusion Forum* 226-228 (2004) 141.
211. A.J. Jennings, S.J. Skinner, Ö. Helgason, Structural properties of $\text{La}_x\text{Sr}_{2-x}\text{FeO}_{4\pm\delta}$ at high temperature and under reducing conditions, *Journal of Solid State Chemistry* 175 (2003) 207.
212. M.V. Patrakeev, J.A. Bahteeva, E.B. Mitberg, I.A. Leonidov, V.L. Kozhevnikov, K.R. Poeppelmeier, Electron/hole and ion transport in $\text{La}_{1-x}\text{Sr}_x\text{FeO}_{3-\delta}$, *J. Solid State Chem.* 172 (2003) 219.
213. V.V. Kharton, A.A. Yaremchenko, M.V. Patrakeev, E.N. Naumovich, F.M.B. Marques, Thermal and chemical induced expansion of $\text{La}_{0.3}\text{Sr}_{0.7}(\text{Fe,Ga})\text{O}_{3-\delta}$ ceramics, *J. Europ. Ceram. Soc.* 23 (2003) 1417.
214. M. Schwartz, J.H. White, A.F. Sammells, Solid state oxygen anion and electron mediating membrane and catalytic membrane reactors containing them. US Patent 6214757 (2001).
215. M.V. Patrakeev, E.B. Mitberg, A.A. Lakhtin, I.A. Leonidov, V.L. Kozhevnikov, V.V. Kharton, M. Avdeev, F.M.B. Marques, Oxygen nonstoichiometry, conductivity, and Seebeck coefficient of $\text{La}_{0.3}\text{Sr}_{0.7}\text{Fe}_{1-x}\text{Ga}_x\text{O}_{2.65\pm\delta}$ perovskites, *J. Solid State Chem.* 167 (2002) 203.

- 216.V.V. Kharton, A.A. Yaremchenko, A.P. Viskup, M.V. Patrakee, I.A. Leonidov, V.L. Kozhevnikov, F.M. Figueiredo, A.L. Shaulo, E.N. Naumovich, F.M.B. Marques, Oxygen permeability and ionic conductivity of perovskite-related $\text{La}_{0.3}\text{Sr}_{0.7}\text{Fe}(\text{Ga})\text{O}_{3-\delta}$, *J. Electrochem. Soc.* 149 (2002) E125.
- 217.T.J. Mazanec, T.L. Cable, J.G. Frye, W.R. Kliever, Solid-component membranes electrochemical reactor components electrochemical reactors use of membranes reactor components and reactor for oxidation reactions, US patent 5591315, 1997.
- 218.V.V. Kharton, A.V. Kovalevsky, A.P. Viskup, J.R. Jurado, F.M. Figueiredo, E.N. Naumovich and J.R. Frade, Transport properties and thermal expansion of $\text{Sr}_{0.97}\text{Ti}_{1-x}\text{Fe}_x\text{O}_{3-\delta}$ ($x = 0.2-0.8$), *J. Solid State Chem.* 156 (2001) 437.
- 219.D.P. Fagg, V.V. Kharton, A.V. Kovalevsky, A.P. Viskup, E.N. Naumovich, J.R. Frade, The stability and mixed conductivity in La and Fe doped SrTiO_3 in the search for potential SOFC anode materials, *Journal of the European Ceramic Society* 21 (2001) 1831.
- 220.Q. Ming, J. Huang, Y.L. Yang, M. Nersesyan, A.J. Jacobson, J.T. Richardson, D. Luss, Combustion synthesis of $\text{La}_{0.2}\text{Sr}_{0.8}\text{Cr}_{0.2}\text{Fe}_{0.8}\text{O}_{3-x}$, *Combust. Sci. Technol.* 138 (1998) 279.
- 221.L. Kindermann, D. Das, H. Nickel, K. Hilpert, Chemical compatibility of the LaFeO_3 base perovskites $(\text{La}_{0.6}\text{Sr}_{0.4})_z\text{Fe}_{0.8}\text{M}_{0.2}\text{O}_{3-\delta}$ ($z = 1, 0.9$; $\text{M} = \text{Cr, Mn, Co, Ni}$) with yttria stabilized zirconia, *Solid State Ionics* 89 (1996) 215.
- 222.L. Kindermann, D. Das, H. Nickel, K. Hilpert, C.C. Appel, F.W. Poulsen, Chemical compatibility of $(\text{La}_{0.6}\text{Ca}_{0.4})_z\text{Fe}_{0.8}\text{M}_{0.2}\text{O}_{3-\delta}$ with yttria-stabilized zirconia, *J. Electrochem. Soc.* 144 (1997) 717.
- 223.G.Ch. Kostoglou, G. Tsiniarakis, Ch. Ftikos, Chemical reactivity of perovskite oxide SOFC cathodes and yttria stabilized zirconia, *Solid State Ionics* 135 (2000) 529.
- 224.S. P. Simner, J. P. Shelton, M. D. Anderson and J. W. Stevenson, Interaction between $\text{La}(\text{Sr})\text{FeO}_3$ SOFC cathode and YSZ electrolyte, *Solid State Ionics* 161 (2003) 11.
- 225.L.-W. Tai, M.M. Nasrallah, H.U. Anderson, D.M. Sparlin, S.R. Sehlin, Structure and electrical properties of $\text{La}_{1-x}\text{Sr}_x\text{Co}_{1-y}\text{Fe}_y\text{O}_3$. Part 1. The system $\text{La}_{0.8}\text{Sr}_{0.2}\text{Co}_{1-y}\text{Fe}_y\text{O}_3$, *Solid State Ionics* 76 (1995) 259.
- 226.L.-W. Tai, M.M. Nasrallah, H.U. Anderson, D.M. Sparlin, S.R. Sehlin, Structure and electrical properties of $\text{La}_{1-x}\text{Sr}_x\text{Co}_{1-y}\text{Fe}_y\text{O}_3$. Part 2. The system $\text{La}_{1-x}\text{Sr}_x\text{Co}_{0.2}\text{Fe}_{0.8}\text{O}_3$, *Solid State Ionics* 76 (1995) 273.
- 227.A. Petric, P. Huang, F. Tietz, Evaluation of La–Sr–Co–Fe–O perovskites for solid oxide fuel cells and gas separation membranes, *Solid State Ionics* 135 (2000) 719.
- 228.G.Ch. Kostoglou, Ch. Ftikos, Properties of A-site-deficient $\text{La}_{0.6}\text{Sr}_{0.4}\text{Fe}_{0.8}\text{Co}_{0.2}\text{O}_{3-\delta}$ -based perovskite oxides, *Solid State Ionics* 126 (1999) 143.
- 229.F. Riza, Ch. Ftikos, F. Tietz, W. Fischer, Preparation and characterization of $\text{Ln}_{0.8}\text{Sr}_{0.2}\text{Fe}_{0.8}\text{Co}_{0.2}\text{O}_{3-x}$ ($\text{Ln}=\text{La, Pr, Nd, Sm, Eu, Gd}$), *J. European Ceram. Soc.* 21 (2001) 1769.
- 230.E. Maguire, B. Gharbage, F.M.B. Marques, J.A. Labrincha, Cathode materials for intermediate temperature SOFCs, *Solid State Ionics* 127 (2000) 329.
- 231.J.-M. Bae, B.C.H. Steele, Properties of $\text{La}_{0.6}\text{Sr}_{0.4}\text{Co}_{0.2}\text{Fe}_{0.8}\text{O}_{3-\delta}$ (LSCF) double layer cathodes on

- gadolinium-doped cerium oxide (CGO) electrolytes I. Role of SiO₂, Solid State Ionics 106 (1998) 247.
- 232.H. Ohbayashi, T. Kudo, T. Gejo, Crystallographic, Electric and thermochemical properties of the perovskite-type Ln_{1-x}Sr_xCoO₃ (Ln: lanthanoid element), Jpn. J. Appl. Phys. 13 (1974) 1.
- 233.W.T.A. Harrison, S.L. Hegwood, A.J. Jacobson, A powder neutron-diffraction determination of the structure of Sr₆Co₅O_{15x}, formerly described as the low-temperature hexagonal form of SrCoO_{3-x}, J. Chem. Soc.-Chem. Commun. 19 (1995) 1953.
- 234.A.N. Petrov, V.A. Cherepanov, A.Yu. Zuev, Oxygen nonstoichiometry of lanthanum, praseodymium and neodymium cobaltates with the perovskite structure, Z. Fiz. Khim. 61 (1987) 630.
- 235.T. Vogt, P.M. Woodward, P. Karen, B.A. Hunter, P. Henning, A.R. Moodenbaugh, Low to high spin state transition induced by charge ordering in antiferromagnetic YBaCo₂O₅, Phys. Rev. Lett. 84 (2000) 2969.
- 236.F. Fauth, E. Suard, V. Caignaert, B. Domengès, I. Mirebeau, L. Keller, Interplay of structural, magnetic and transport properties in the layered Co-based perovskite LnBaCo₂O₅ (Ln = Tb, Dy, Ho), Eur. Phys. J. B21 (2001) 163.
- 237.D.V. Sheptyakov, A. Podlesnyak, S.N. Barilo, S.V. Shiryaev, D.D. Khalyavin, D.Yu. Chernyshov, N.I. Leonyuk, Crystal structure of the new cobaltite HoBaCo₄O₇. In: J. Schefer, D. Castellazzi, M. Braun-Shea (eds.), PSI Sci. Rep. (2001) vol. 3, p. 64.
- 238.M. Valldor, Syntheses and structures of compounds with YBaCo₄O₇-type structure, Solid State Sci., 6 (2004) 251.
- 239.V.V. Kharton, E.N. Naumovich, A.A. Vecher, A.V. Nikolaev, Oxide ion conduction in solid solutions Ln_{1-x}Sr_xCoO_{3-δ} (Ln = La, Pr, Nd), J. Solid State Chem. 120 (1995) 128.
- 240.A.V. Kovalevsky, V.V. Kharton, V.N. Tikhonovich, E.N. Naumovich, A.A. Tonoyan, O.P. Reut, L.S. Boginsky Oxygen permeation through Sr(Ln)CoO_{3-δ} (Ln=La, Nd, Sm, Gd) ceramic membranes, Mater. Sci. Eng. B52 (1998) 105.
- 241.R.H.E. van Doorn, A.J. Burggraaf, Structural aspects of the ionic conductivity of La_{1-x}Sr_xCoO_{3-δ}, Solid State Ionics 128 (2000) 65.
- 242.S. Pei, M.S. Kleefisch, T.P. Kobylinski, J. Faber, C.A. Udovich, V. Zhang-McCoy, B. Dabrowski, U. Balachandran, R.L. Mieville, R.B. Poeppel, Failure mechanisms of ceramic membrane reactors in partial oxidation of methane to synthesis gas, Catal. Lett. 30 (1995) 201.
- 243.K. Huang, H.Y. Lee, J.B. Goodenough, Sr- and Ni-doped LaCoO₃ and LaFeO₃ perovskites. New cathode materials for solid-oxide fuel cells, J. Electrochem. Soc. 145 (1998) 3220.
- 244.S. Uhlenbruck, F. Tietz, High-temperature thermal expansion and conductivity of cobaltites: potentials for the adaptation of the thermal expansion to the demands for solid oxide fuel cells, Mater. Sci. Eng. B107 (2004) 277.
- 245.W. Chen, T. Wen, H. Nie, R. Zheng, Study of Ln_{0.6}Sr_{0.4}Co_{0.8}Mn_{0.2}O_{3-δ} (Ln = La, Gd, Sm or Nd) as the cathode materials for intermediate temperature SOFC, Mater. Res. Bull. 38 (2003) 1319.
- 246.H.Y. Tu, Y. Takeda N. Imanishi, O. Yamamoto, Ln_{1-x}Sr_xCoO₃ (Ln = Sm, Dy) for the electrode of solid oxide fuel cells, Solid State Ionics 100 (1997) 283.
- 247.T. Ishihara, M. Honda, T. Shibayama, H. Furutani, Y. Takita, An intermediate temperature solid oxide

- fuel cell utilizing superior oxide ion conducting electrolyte, doubly doped LaGaO₃ perovskite, *Ionics* 4 (1998) 395.
- 248.Y. Takeda, H. Ueno, N. Imanishi, O. Yamamoto, N. Sammes, M.B. Phillipps, Gd_{1-x}Sr_xCoO₃ for the electrode of solid oxide fuel cells, *Solid State Ionics* 86-88 (1996) 1187.
- 249.F. Chen, Ch. Xia, M. Liu, Preparation of ordered macroporous Sm_{0.5}Sr_{0.5}CoO₃ as cathode for solid oxide fuel cells, *Chem. Lett.* 30 (2001) 1032.
- 250.H. Uchida, Sh. Arisaka, M. Watanabe, High performance electrode for medium-temperature solid oxide fuel cells. Control of microstructure of La(Sr)CoO₃ cathodes with highly dispersed Pt electrocatalysts, *J. Electrochem. Soc.* 149 (2002) A13.
- 251.H.Y. Tu, Y. Takeda, N. Imanishi, O. Yamamoto, Ln_{0.4}Sr_{0.6}Co_{0.8}Fe_{0.2}O₃ (Ln = La, Pr, Nd, Sm, Gd) for the electrode in solid oxide fuel cells, *Solid State Ionics* 117 (1999) 277.
- 252.H.Y. Lee, S.M. Oh, Il-Y. Seo, F. Rocholl, H.-D. Wiemhöfer, The cathodic activity and interfacial stability of Y_{0.8}Ca_{0.2}Co_{1-x}Fe_xO₃/YSZ electrodes, In: *Stimming U, Singhal SC, H. Tagawa, W. Lehnert (eds.) SOFC V, PV 97-40. The Electrochemical Society, 1997, Pennington, NJ, pp 520-529.*
- 253.G.Ch. Kostoglou, Ch. Ftikos, A. Ahmad-Khanlou, A. Naoumidis, D. Stöver, Chemical compatibility of alternative perovskite oxide SOFC cathodes with doped lanthanum gallate solid electrolyte, *Solid State Ionics* 134 (2000) 127.
- 254.T. Nakamura, G. Petzow, L.J. Gauckler, Stability of the perovskite phase LaBO₃ (B = V, Cr, Mn, Fe, Co, Ni) in reducing atmosphere I. Experimental results, *Mat. Res. Bul.* 14 (1979) 649.
- 255.M.T. Colomer, A. Martinez Juarez, P. Recio, C. Pascual, J.R. Jurado, LaNiO₃ cathode material for low temperature SOFCs. In: P. Stevens (ed.), *Proc. 3rd Eur. SOFC Forum, Nantes, France, 1994, p. 55.*
- 256.R. Chiba, F. Yoshimura, Y. Sakurai, An investigation of LaNi_{1-x}Fe_xO₃ as a cathode material for solid oxide fuel cells *Solid State Ionics* 124 (1999) 281.
- 257.R. Chiba, F. Yoshimura, Y. Sakurai, Properties of La_{1-y}Sr_yNi_{1-x}Fe_xO₃ as a cathode material for a low-temperature operating SOFC, *Solid State Ionics* 152-153 (2002) 575.
- 258.E.Boehm, J.-M.Bassat, M.C.Steil, P.Dordor, F.Mauvy, J.-C.Grenier, Oxygen transport properties of La₂Ni_{1-x}Cu_xO_{4+δ} mixed conducting oxides, *Solid State Sciences* 5 (2003) 973.
- 259.S.J. Skinner, J.A. Kilner, Oxygen diffusion and surface exchange in La_{2-x}Sr_xNiO_{4+δ}, *Solid State Ionics* 135 (2000) 709.
- 260.V.V. Vashook, I.I. Yushkevich, L.V. Kokhanovsky, L.V. Makhnach, S.P. Tolochko, I.F. Kononyuk, H. Ullmann, H. Altenburg, Composition and conductivity of some nickelates, *Solid State Ionics* 119 (1999) 23.
- 261.J.A. Kilner, C.K.M. Shaw, Mass transport in La₂Ni_{1-x}Co_xO_{4+δ} oxides with the K₂NiF₄ structure, *Solid State Ionics* 154-155 (2002) 523.
- 262.G. Amow, P.S. Whitfield, I.J. Davidson, R.P. Hammond, C.N. Munnings, S.J. Skinner, Structural and sintering characteristics of the La₂Ni_{1-x}Co_xO_{4+δ} series, *Ceramics International* 30 (2004) 1635.
- 263.V.V. Kharton, A.P. Viskup, A.V. Kovalevsky, E.N. Naumovich, F.M.B. Marques, Ionic transport in oxygen-hyperstoichiometric phases with K₂NiF₄-type structure, *Solid State Ionics* 143 (2001) 337.
- 264.F. Mauvy, C. Lalanne, J.M. Bassat, J.C. Grenier, H. Zhao, Ph. Dordor, P. Stevens, Oxygen reduction on

- porous $\text{Ln}_2\text{NiO}_{4+\delta}$ electrodes, *J. Electrochem. Soc.* 25 (2005) 2669.
- 265.D.M. Bochkov, V.V. Kharton, A.V. Kovalevsky, A.P. Viskup, E.N. Naumovich, Oxygen permeability of $\text{La}_2\text{Cu}(\text{Co})\text{O}_{4+\delta}$ solid solutions, *Solid State Ionics* 120 (1999) 281.
- 266.E.J. Opila, H.L. Tuller, B.J. Wuensch, J. Maier, Oxygen Tracer Diffusion in $\text{La}_{2-x}\text{Sr}_x\text{CuO}_{4-y}$ Single Crystals, *J. Am. Ceram. Soc.* 76 (1993) 2363.
- 267.J.L. Routbort, S.J. Rothman, B.K. Flandermeier, L.J. Nowicki, J.E. Baker, Oxygen diffusion in $\text{La}_{2-x}\text{Sr}_x\text{CuO}_{4-y}$, *J. Mater. Res.* 3 (1988) 116.
- 268.M.V. Patrakeev, I.A. Leonidov, V.L. Kozhevnikov, V.I. Tsidilkovskii, A.K. Demin, A.V. Nikolaev, The oxygen permeation through $\text{YBa}_2\text{Cu}_3\text{O}_{6+x}$, *Solid State Ionics* 66 (1993) 61.
- 269.M.J. Jørgensen, S. Primdahl, C. Bagger, M. Mogensen, Effect of sintering temperature on microstructure and performance of LSM-YSZ composite cathodes, *Solid State Ionics* 139 (2001) 1.
- 270.J.-D. Kim, G.-D. Kim, Ji-W. Moon, H.-W. Lee, Ki-T. Lee, C.-E. Kim, The effect of percolation on electrochemical performance, *Solid State Ionics* 133 (2000) 67.
- 271.R.P. Kusy, Influence of particle size ratio on the continuity of aggregates, *J. Appl. Phys.* 48 (1977) 5301.
- 272.M. Juhl, S. Primdahl, C. Manon, M. Mogensen, Performance/structure correlation for the composite cathodes, *J. Power Sources* 61 (1996) 173.
- 273.T. Kenjo, M. Nishiya, LaMnO_3 air cathodes containing ZrO_2 electrolyte for high temperature solid oxide fuel cells, *Solid State Ionics* 57 (1992) 295.
- 274.Sh. Wang, Yi Jiang, Y. Zhang, J. Yan, W. Li, The role of 8 mol % yttria stabilized zirconia in the improvement of electrochemical performance of lanthanum manganite composite electrodes, *J. Electrochem. Soc.* 145 (1998) 1932.
- 275.S. Sunde, Calculation of conductivity and polarization resistance of composite SOFC electrodes from random resistor networks, *J. Electrochem. Soc.* 142 (1995) L50.
- 276.X.J. Chen, S.H. Chan, K.A. Khor, Simulation of a composite cathode in solid oxide fuel cells, *Electrochim. Acta* 49 (2004) 1851.
- 277.J.R. Gavarry, L. Tortet, J. Musso, Transport properties and percolation in two-phase composites, *Solid State Ionics* 117 (1999) 75.
- 278.E.P. Murray, S.A. Barnett, $(\text{La},\text{Sr})\text{MnO}_3-(\text{Ce},\text{Gd})\text{O}_{2-x}$ composite cathodes for solid oxide fuel cells, *Solid State Ionics* 143 (2001) 265.
- 279.H. Zhao, L. Huo, Sh. Gao, Electrochemical properties of LSM-CBO composite cathode, *J. Power Sources* 125 (2004) 149.
- 280.Ch. Xia, W. Rauch, F. Chen, M. Liu, $\text{Sm}_{0.5}\text{Sr}_{0.5}\text{CoO}_3$ cathodes for low-temperature SOFCs, *Solid State Ionics* 149 (2002) 11.
- 281.E.P. Murray, M.J. Sever, S.A. Barnett, Electrochemical performance of $(\text{La},\text{Sr})(\text{Co},\text{Fe})\text{O}_3-(\text{Ce},\text{Gd})\text{O}_{2-x}$ composite cathodes, *Solid State Ionics* 148 (2002) 27.
- 282.Sh. Wang, T. Kato, S. Nagata, T. Honda, T. Kaneko, N. Iwashita, M. Dokiya, Performance of a $\text{La}_{0.6}\text{Sr}_{0.4}\text{Co}_{0.8}\text{Fe}_{0.2}\text{O}_3-\text{Ce}_{0.8}\text{Gd}_{0.2}\text{O}_{1.9-\text{Ag}}$ cathode for ceria electrolyte SOFCs, *Solid State Ionics* 146 (2002) 203.
- 283.Yi Jiang, A.V. Virkar, $\text{La}_{1-x}\text{Sr}_x\text{CoO}_{3-\delta}$ (LSC)- $\text{Ce}_{0.8}\text{Sm}_{0.2}\text{O}_{2-\delta}$ (SDC) composite cathodes for anode

- supported, YSZ-SDC bi-layer electrolyte, thin film, solid oxide fuel cell, In: T.A. Ramanarayanan, W.L. Worrell, M. Mogensen, (eds.), Proc. Ionic and Mixed Conducting Ceramics (2001), Pennington, NJ.
284. Y. Liu, W. Rauch, Sh. Zha, M. Liu, Fabrication of $\text{Sm}_{0.5}\text{Sr}_{0.5}\text{CoO}_{3-\delta}$ - $\text{Sm}_{0.1}\text{Ce}_{0.9}\text{O}_{2-\delta}$ cathodes for solid oxide fuel cells using combustion CVD, *Solid State Ionics* 166 (2004) 261.
285. N.T. Hart, N.P. Brandon, M.J. Day, J.E. Shemilt, Functionally graded cathodes for solid oxide fuel cells, *J. Mater. Sci.* 36 (2001) 1077.
286. N.T. Hart, N.P. Brandon, M.J. Day, N. Lapeña-Rey, Functionally graded cathodes for solid oxide fuel cells, *J. Power Sources* 106 (2002) 42.
287. Zh. Wu, M. Liu, Ag-Bi_{1.5}Y_{0.5}O₃ composite cathode materials for BaCe_{0.8}Gd_{0.2}O₃-based solid oxide fuel cells, *J. Am. Ceram. Soc.* 81 (1998) 1215.
288. H. Ullmann, N. Trofimenko, F. Tietz, D. Stöver, A. Ahmad-Khanlou, Correlation between thermal expansion and oxide ion transport in mixed conducting perovskite-type oxides for SOFC cathodes, *Solid State Ionics* 138 (2000) 79.
289. Y. Teraoka, Influence of constituent metal cations in substituted LaCoO₃ on mixed conductivity and oxygen permeability, *Solid State Ionics* 48 (1991) 207.
290. O. Yamamoto, Y. Takeda, R. Kanno, T. Kojima, Stability of perovskite oxide electrode with stabilized zirconia In: S.C. Singhal (ed.), SOFC I, Electrochem. Soc., Pennington, NJ, 1989, p. 242.
291. D. Skarmoutsos, A. Tsoga, A. Naoumidis, P. Nikolopoulos, 5 mol% TiO₂-doped Ni-YSZ anode cermets for solid oxide fuel cells, *Solid State Ionics* 135 (2000) 439.
292. S.T. Aruna, M. Muthuraman, K.C. Patil, Synthesis and properties of Ni-YSZ cermet: anode material for solid oxide fuel cells, *Solid State Ionics* 111 (1998) 45.
293. F.P.F. van Berkel, F.H. van Heuveln, J.P.P. Huijsmans, Characterization of solid oxide fuel cell electrodes by impedance spectroscopy and I-V characteristics, *Solid State Ionics* 72 (1994) 240.
294. D.-S. Lee, J.-H. Lee, J. Kim, H.-W. Lee, H.S. Song, Tuning of the microstructure and electrical properties of SOFC anode via compaction pressure control during forming, *Solid State Ionics* 166 (2004) 13.
295. T. Fukui, K. Murata, S. Ohara, H. Abe, M. Naito, K. Nogi, Morphology control of Ni-YSZ cermet anode for lower temperature operation of SOFCs, *J. Power Sources* 125 (2004) 17.
296. S.P. Jiang, S.H. Chan, A review of anode materials development in solid oxide fuel cells, *J. Mater. Sci.* 39 (2004) 4405.
297. S. Sunde, Simulations of composite electrodes in fuel cells, *J. Electroceram.* 5:2 (2000) 153.
298. S. Sunde, Calculations of impedance of composite anodes for solid oxide fuel cells, *Electrochim. Acta*, 42 (1997) 2637.
299. S. Sunde, Monte Carlo simulations of conductivity of composite electrodes for solid oxide fuel cells, *J. Electrochem. Soc.* 143 (1996) 1123.
300. U. Anselmi-Tamburini, G. Chiodelli, M. Arimondi, F. Maglia, G. Spinolo, Z.A. Munir, Electrical properties of Ni/YSZ cermets obtained through combustion synthesis, *Solid State Ionics* 110 (1998) 35.
301. S.F. Corbin, Xin Qiao, Metal-coated pore-forming agents, *J. Amer. Ceram. Soc.* 86 (2003) 401.
302. H. Koide, Y. Someya, T. Yoshida, T. Maruyama, Properties of Ni/YSZ cermet as anode for SOFC, *Solid*

- State Ionics, 132 (2000) 253.
- 303.J.-H. Lee, H. Moon, H.-W. Lee, J. Kim, J.-D. Kim, K.-H. Yoon, Tuning of the microstructure and electrical properties of SOFC anode via compaction pressure control during forming, *Solid State Ionics* 166 (2004) 13.
- 304.D.W. Dees, T.D. Claar, T.E. Easler, D.C. Fee, F.C. Mrazek, Conductivity of porous Ni/ZrO₂-Y₂O₃ cermets, *J. Electrochem. Soc.* 134 (1987) 2141.
- 305.D. Fouquet, A.C. Müller, A. Weber, E. Ivers-Tiffée, Kinetics of oxidation and reduction of Ni/YSZ cermets, *Ionics* 8 (2003) 103.
- 306.M. Mori, Y. Hiei, H. Itoh, G. A. Tompsett, N.M. Sammes, Evaluation of Ni and Ti-doped Y₂O₃ stabilized ZrO₂ cermet as an anode in high-temperature solid oxide fuel cells, *Solid State Ionics* 160 (2003) 1.
- 307.H. Kim, C. Liu, W.L. Worrell, J.M. Vohs, R.J. Gorte, Cu-Ni cermet anodes for direct oxidation of methane in solid-oxide fuel cells, *J. Electrochem. Soc.* 149 (2002) A247.
- 308.H.H. Möbius, B. Rohland, Method of producing fuel cell with solid electrolytes and ceramic oxide electrode layers, US Patent 3377203, 1968, (filed in 1964).
- 309.B.C.H. Steele, Running on natural gas, *Nature* 400 (1999) 619.
- 310.H. Uchida, H. Suzuki, M. Watanabe, High performance electrode for medium-temperature solid oxide fuel cells. Effects of composition and microstructure on performance of ceria-based anodes, *J. Electrochem. Soc.* 145 (1998) 615.
- 311.M. Watanabe, H. Uchida, M. Shibata, N. Mochizuki, K. Amikura, High performance catalyzed-reaction layer for medium temperature operating solid oxide fuel cells, *J. Electrochem. Soc.* 141 (1994) 342.
- 312.X. Zhang, S. Ohara, R. Maric, K. Mukai, T. Fukui, H. Yoshida, M. Nishimura, T. Inagaki, K. Miura, Ni-SDC cermet anode for medium-temperature solid oxide fuel cell with lanthanum gallate electrolyte, *J. Power Sources* 83 (1999) 170.
- 313.Ch. Xia, M. Liu, Microstructures, conductivities, and electrochemical properties of Ce_{0.9}Gd_{0.1}O₂ and GDC-Ni anodes for low-temperature SOFCs, *Solid State Ionics* 152–153 (2002) 423.
- 314.R. Maric, S. Ohara, T. Fukui, T. Inagaki, Jun-ichi Fujita, High-Performance Ni-SDC cermet anode for solid oxide fuel cells at medium operating temperature, *Electrochem. Solid-State Lett.* 1 (1998) 201.
- 315.X. Huang, Zhe Lu, Li Pei, Zh. Liu, Yu. Liu, R. Zhu, J. Miao, Zh. Zhang, W. Su, An anode for solid oxide fuel cells: NiO+(Ce_{0.9}Ca_{0.1}O_{1.9})_{0.25}(YSZ)_{0.75} solid solution, *J. Alloy. Compd.* 360 (2003) 294.
- 316.J.C. Ruiz-Morales, P. Núñez, R. Buchanan, J.T.S. Irvine, Electrochemical studies of nickel and copper/yttria titania zirconia ceria cermets, *J. Electrochem. Soc.* 150 (2003) A1030.
- 317.T. Katsura, K. Kitayama, T. Sugihara, N. Kimizuka, Thermochemical properties of lanthanoid-iron-perovskite at high-temperatures, *Bull. Chem. Soc. Japan* 48 (1975) 1809.
- 318.D.E. Rice, D.J. Buttrey, An X-ray diffraction study of the oxygen content phase diagram of La₂NiO_{4+δ}, *J. Solid State Chem.* 105 (1993) 197.
- 319.H. Kanai, J. Mizusaki, H. Tagawa, S. Hoshiyama, K. Hirano, K. Fujita, M. Tezuka, T. Hashimoto, Defect chemistry of La_{2-x}Sr_xCuO_{4-δ}: Oxygen nonstoichiometry and thermodynamic stability, *J. Solid State Chem.* 131 (1997) 150.
- 320.T. Atsumi, T. Ohgushi, N. Kamegashira, Studies on oxygen dissociation pressure of LnMnO₃ (Ln = rare

- earth) with the e.m.f. technique, *J. Alloy. Compd.* 238 (1996) 35.
321. J. Sfeir, LaCrO₃-based anodes: stability considerations, *J. Power Sources* 118 (2003) 276.
322. J. Sfeir, P.A. Buffat, P. Mückli, N. Xanthopoulos, R. Vasquez, H.J. Mathieu, J. Van herle, K.R. Thampi, Lanthanum chromite based catalysts for oxidation of methane directly on sofc anodes, *J. Catal.* 202 (2001) 229.
323. R.T. Baker, I.S. Metcalfe, P.H. Middleton, B.C.H. Steele, Evaluation of perovskite anodes for the complete oxidation of dry methane in solid oxide fuel cells, *Solid State Ionics* 72 (1994) 328.
324. A.-L. Sauvet, J. Guindet, J. Fouletier, La_{0.8}Sr_{0.2}Cr_{0.95}Ru_{0.05} (LSCRu) as a new anode material for SOFC using natural gas, *Ionics* 5 (1999) 150.
325. S. Primdahl, J.R. Hansen, L. Grahl-Madsen, P.H. Larsen, Sr-doped LaCrO₃ anode for solid oxide fuel cells, *J. Electrochem. Soc.* 148 (2001) A74.
326. P. Vernoux, M. Guillo, J. Fouletier, A. Hammou, Alternative anode material for gradual methane reforming in solid oxide fuel cells, *Solid State Ionics* 135 (2000) 425.
327. G. Pudmich, B.A. Boukamp, M. Gonzalez-Cuenca, W. Jungen, W. Zipprich, F. Tietz, Chromite/titanate based perovskites for application as anodes in solid oxide fuel cells, *Solid State Ionics* 135 (2000) 433.
328. S. Tao, J.T.S. Irvine, Conductivity and electrochemical performance of a new perovskite-type SOFC anode material. In: S.C. Singhal and M. Dokiya (eds.) SOFC-VIII (2003) *Electrochem. Soc.*, Pennington, NJ, 2003, vol. 2003-07, p. 793.
329. S. Tao, J.T.S. Irvine, A redox-stable efficient solid-oxide fuel cells, *Nature Mater.* 2 (2003) 320.
330. S. Hui, A. Petric, Evaluation of yttrium-doped SrTiO₃ as an anode for solid oxide fuel cells, *J. European Ceram. Soc.* 22 (2002) 1673.
331. D.P. Fagg, S.M. Fray, J.T.S. Irvine, Reduced magnesium titanate electrodes for solid oxide fuel cells, *Solid State Ionics* 72 (1994) 235.
332. P.R. Slater, D.P. Fagg, J.T.S. Irvine, Synthesis and electrical characterization of doped perovskite titanates as potential anode materials for solid oxide fuel cells, *J. Mater. Chem.* 7 (1997) 2495.
333. J. Canales-Vásques, S.W. Tao, J.T.S. Irvine, Electrical properties in La₂Sr₄Ti₆O_{19.8}: a potential anode for high temperature fuel cells, *Solid State Ionics* 159 (2003) 159.
334. A. Kaiser, J.L. Bradley, P.R. Slater, J.T.S. Irvine, Tetragonal tungsten bronze type phases (Sr_{1-x}Ba_x)_{0.6}Ti_{0.2}Nb_{0.8}O_{3-δ}: Material characterisation and performance as SOFC anodes, *Solid State Ionics* 135 (2000) 519.
335. P.R. Slater, J.T.S. Irvine, Synthesis and electrical characterisation of the tetragonal tungsten bronze type phases, (Ba/Sr/Ca/La)_{0.6}M_xNb_{1-x}O_{3-δ} (M = Mg, Ni, Mn, Cr, Fe, In, Sn): evaluation as potential anode materials for solid oxide fuel cells, *Solid State Ionics* 124 (1999) 61.
336. Sh. Tao, J.T.S. Irvine, Optimization of mixed conducting properties of Y₂O₃-ZrO₂-TiO₂ and Sc₂O₃-Y₂O₃-ZrO₂-TiO₂ solid solutions as potential SOFC anode materials, *J. Solid State Chem.* 165 (2002) 12.
337. M.K. Dongare, A.M. Dongare, V.B. Tare, E. Kemnitz, Synthesis and characterization of copper-stabilized zirconia as an anode material for SOFC, *Solid State Ionics* 152-153 (2002) 455.
338. E.Kh. Kurumchin, M.V. Perfil'yev, An isotope exchange study of the behaviour of electrochemical systems, *Solid State Ionics* 42 (1990) 129.

- 339.A.J. McEvoy, Activation processes, electrocatalysis and operating protocols enhance SOFC performance, *Solid State Ionics* 135 (2000) 331.
- 340.L.J. Olmer, J.C. Vicuie, E.J.L. Schouler, An increase in the water vapor reduction rate by using an yttria-stabilized zirconia electrolyte with ceria-doped surface, *Solid State Ionics* 7 (1982) 23.
- 341.D. Scholten and A. J. Burggraaf, Surface modification of $ZrO_2 - Y_2O_3$ ss by ion implantation, *Solid State Ionics* 16 (1985) 147.
- 342.B. A. van Hassel, B. A. Boukamp and A. J. Burggraaf, Oxygen transfer properties of ion-implanted yttria-stabilized zirconia, *Solid State Ionics* 53-56 (1992) 890.
- 343.M. de Ridder, R.G. van Welzenis, H.H. Brongersma, U. Kreissig, Oxygen exchange and diffusion in the near surface of pure and modified yttria-stabilized zirconia, *Solid State Ionics* 158 (2003) 67.
- 344.K.R. Thampi, A.J. McEvoy, J. Van herle, Electrocatalysis in solid oxide fuel cell electrode domains, *J. Electrochem. Soc.* 142 (1995) 506.
- 345.E.Kh. Kurumchin. Isotope exchange studies of electrochemical systems with solid oxide electrolytes, *Ionics* 4 (1998) 390.
- 346.K. Asano, H. Iwahara, Performance of a one-chamber solid oxide fuel cell with a surface-modified zirconia electrolyte, *J. Electrochem. Soc.* 144 (1997) 3125.
- 347.D. Rutenbeck, V.A.C. Haanappel, S. Uhlenbruck, F. Tietz, I.C. Vinke, D. Stöver, Noble metals in SOFC cathodes: processing and electrochemical performance, In: S.C. Singhal and M. Dokiya (eds.) SOFC-VIII (2003) *Electrochem. Soc.*, Pennington, NJ, 2003, vol. 2003-07, p. 615.
- 348.E.N. Naumovich, V.V. Kharton, V.V. Samokhval, A.V. Kovalevsky, Oxygen separation using Bi_2O_3 -based solid electrolytes, *Solid State Ionics* 93 (1997) 95.
- 349.S. Uhlenbruck, F. Tietz, V.A.C. Haanappel, D. Sebold, H.-P. Buchkremer, D. Stöver, Silver incorporation into cathodes for solid oxide fuel cells operating at intermediate temperature, *J. Solid State Electrochem.* 8 (2004) 923.
- 350.K. Sasaki, M. Gödickemeier, P. Bohac, A. Orliukas, L.J. Gauckler, Microstructure Design of mixed-conducting solid oxide fuel cell cathodes. In: Proc. 5th IEA Workshop (1993), Juelich, Germany, p. 187.
- 351.B.L. Kuzin, M.A. Komarov, Oxygen nonstoichiometry, resistance, and electrochemical-behavior of thin $La_{0.7}Sr_{0.3}CoO_{3-\delta}$ layers applied to a solid oxide electrolyte, *Soviet Electrochem.* 26 (1990) 1287.
- 352.H.L. Tuller, Ionic conduction in nanocrystalline materials, *Solid State Ionics* 131 (2000) 143.
- 353.G.M. Christie, F.P.F. van Berkel, Microstructure — ionic conductivity relationships in ceria-gadolinia electrolytes *Solid State Ionics* 83 (1996) 17.
- 354.L.A. Chick, L.R. Pederson, G.D. Maupin, J.L. Bates, L. Thomas, G.L. Exarhos, Glycine-nitrate combustion synthesis of oxide ceramic powders *Mater. Lett.* 10 (1990) 6.
- 355.P. Yu. Butyagin, I. K. Pavlichev, Determination of energy yield of mechanochemical reactions, *React. Solids*, 1 (1986) 361.
- 356.J. Rodríguez-Carvajal, Recent advances in magnetic structure determination by neutron powder diffraction, *Physica B* 192 (1993) 55.
- 357.B.A. Boukamp, A nonlinear least squares fit procedure for analysis of immitance data of electrochemical systems, *Solid State Ionics* 20 (1986) 31.

- 358.V.P. Gorelov, *Elektrokhimiya*, 24 (1988) 1380 [in Russian].
- 359.M. Liu, H. Hu, Effect of interfacial resistance on determination of transport properties of mixed-conducting electrolytes, *J. Electrochem. Soc.* 143 (1996) L109.
- 360.F.M. Figueiredo, J. Frade, F.M.B. Marques, Role of the reference position on overpotential measurements, *Bol. Soc. Esp. Ceram. Vidrio* 38 (1999) 639.
- 361.N. Ramadass, ABO₃-type oxides—Their structure and properties—A bird's eye view, *Mater. Sci. Eng.* 36 (1978) 231.
- 362.K.K. Singh, P. Ganguly, J.B. Goodenough, Unusual effects of anisotropic bonding in Cu(II) and Ni(II) oxides with K₂NiF₄ structure *J. Solid State Chem.* 52 (1984) 254.
- 363.R.H.E. van Doorn, I.C. Fullarton, R.A. de Souza, J.A. Kilner, H.J.M. Bouwmeester, A.J. Burggraaf, Surface oxygen exchange of La_{0.3}Sr_{0.7}CoO_{3-δ} *Solid State Ionics*, 96 (1997) 1.
- 364.V.V. Kharton, A.V. Kovalevsky, A.A. Yaremchenko, F.M. Figueiredo, E.N. Naumovich, A.L. Shaulo, F.M.B. Marques, Surface modification of La_{0.3}Sr_{0.7}CoO_{3-δ} ceramic membranes, *J. Membrane Sci.*, 195 (2002) 277.
- 365.V.V. Kharton, A.V. Kovalevsky, A.P. Viskup, A.L. Shaula, F.M. Figueiredo, E.N. Naumovich, F.M.B. Marques, Oxygen transport in Ce_{0.8}Gd_{0.2}O_{2-δ}-based composite membranes, *Solid State Ionics*, 160 (2003) 247.
- 366.V.V. Kharton, E.N. Naumovich and A.V. Nikolaev, Oxide ion and electron conjugate diffusion in perovskite-like SrCo_{1-x}M_xO_{3-δ} (M=Cr..Cu; x=0..0.5), *Solid State Phenom.*, 39-40 (1994) 147.
- 367.V.V. Kharton, A.V. Nikolaev, E.N. Naumovich, V.V. Samokhval, Electronic and oxygen conductivity of SrCo(Fe, Cu)O_{3-δ} solid-solutions, *Inorg. Mater.*, 30 (1994) 492.
- 368.M.Yu. Avdeev, M.V.Patrakeev, V.V. Kharton, J.R. Frade, Oxygen vacancy formation and ionic transport in Sr₄Fe₆O_{13±δ}, *J. Solid State Electrochem.*, 6 (2002) 217.
- 369.V.V. Kharton, I.P. Marozau, N.P. Vyshatko, A.L. Shaula, A.P. Viskup, E.N. Naumovich, F.M.B. Marques, Oxygen ionic conduction in brownmillerite CaAl_{0.5}Fe_{0.5}O_{2.5+δ}, *Mater. Res. Bul.*, 38 (2003) 773.
- 370.A.L. Shaula, A.P. Viskup, V.V. Kharton, D.I. Logvinovich, E.N. Naumovich, J.R. Frade, F.M.B. Marques, Oxygen permeability of LaGa_{0.65}Ni_{0.20}Mg_{0.15}O_{3-δ} ceramics: effect of synthesis method, *Mater. Res. Bul.* 38 (2003) 353.
- 371.V.V. Kharton, A.P. Viskup, E.N. Naumovich, V.N. Tikhonovich, Oxygen permeability of LaFe_{1-x}Ni_xO_{3-δ} solid solutions, *Mater. Res. Bul.* 34 (1999) 1311.
- 372.A.A. Yaremchenko, V.V. Kharton, A.P. Viskup, E.N. Naumovich, N.M. Lapchuk, V.N. Tikhonovich, , Oxygen ionic and electronic transport in LaGa(Ni)O_{3-δ} perovskites *J. Solid State Chem.* 142 (1999) 325.
- 373.S. Nishiyama, D. Sakaguchi, T. Hattori, Electrical conduction and thermoelectricity of La₂NiO_{4+δ} and La₂(Ni,Co)O_{4+δ}, *Solid State Commun.* 94 (1995) 279.
- 374.V.V. Kharton, F.M.B. Marques, Mixed ionic-electronic conductors: effects of ceramic microstructure on transport properties, *Curr. Opin. Solid State Mater. Sci.* 6 (2002) 261.
- 375.J.B. Goodenough, J.-S. Zhou, in *Localized to Itinerant Electronic Transition in Perovskite Oxides*, Ed. J.B. Goodenough, Springer-Verlag, Berlin-Heidelberg, 2001, p.17.

376. A. Mineshige, M. Kobune, S. Fujii, Z. Ogumi, M. Inaba, T. Yao, K. Kikuchi, Metal-insulator transition and crystal structure of $\text{La}_{1-x}\text{Sr}_x\text{CoO}_3$ as functions of sr-content, temperature, and oxygen partial pressure, *J. Solid State Chem.* 142 (1999) 374.
377. E.B. Mitberg, M.V. Patrakeev, I.A. Leonidov, V.L. Kozhevnikov, K.R. Poeppelmeier, High-temperature electrical conductivity and thermopower in nonstoichiometric $\text{La}_{1-x}\text{Sr}_x\text{CoO}_{3-\delta}$ ($x=0.6$), *Solid State Ionics* 130 (2000) 325.
378. J. Mizusaki, Y. Mima, S. Yamaguchi, K. Fueki, H. Tagawa, Nonstoichiometry of the perovskite-type oxides $\text{La}_{1-x}\text{Sr}_x\text{CoO}_{3-\delta}$, *J. Solid State Chem.* 80 (1989) 102.
379. E. Jacobsson, E. Rosén, Thermodynamic studies of high-temperature equilibria 25. Solid-state emf studies of the systems Fe-FeO, Ni-NiO and Co-CoO in the temperature-range 1000-1600 K, *Scand. J. Metall.*, 10 (1981) 39.
380. V.A. Cherepanov, L.Ya. Gavrilova, L.Yu. Barkhatova, V.I. Voronin, M.V. Trifonova, O.A. Bukhner, Phase equilibria in the La-Me-Co-O (Me=Ca, Sr, Ba) systems, *Ionics* 4 (1998) 309.
381. Yu.D. Tretiakov "Chemistry of Nonstoichiometric Oxides", Moscow State University, Moscow, 1974.
382. V.N. Tikhonovich, E.N. Naumovich, D.I. Logvinovich, V.V. Kharton, A.A. Vecher, Oxygen deficiency and phase transitions in $\text{SrCo}_{1-x-y}\text{Fe}_x\text{Cr}_y\text{O}_{3-\delta}$ ($x = 0.10-0.40$, $y = 0-0.05$), *J. Solid State Electrochem.* 7 (2003) 77.
383. L.-M. Liu, T.H. Lee, L. Qiu, Y.L. Yang, A.J. Jacobson, *Mater. Res. Bul.* 31 (1996) 29.
384. E.N. Naumovich, M.V. Patrakeev, V.V. Kharton, A.A. Yaremchenko, D.I. Logvinovich, F.M.B. Marques, Oxygen nonstoichiometry in $\text{La}_2\text{Ni}(\text{M})\text{O}_{4+\delta}$ ($\text{M} = \text{Cu}, \text{Co}$) under oxidizing conditions, *Solid State Sciences*, accepted for publication (2005).
385. A. Watanabe, Highly conductive oxides, CeVO_4 , $\text{Ce}_{1-x}\text{M}_x\text{VO}_{4-0.5x}$ ($\text{M}=\text{Ca}, \text{Sr}, \text{Pb}$) and $\text{Ce}_{1-y}\text{Bi}_y\text{VO}_4$, with zircon-type structure prepared by solid-state reaction in air, *J. Solid State Chem.* 153 (2000) 174.
386. T. Hirata, A. Watanabe, Raman and infrared spectroscopic study of $\text{Ce}_{1-x}\text{M}_x\text{VO}_{4-0.5x}$ ($\text{M}=\text{Pb}, \text{Sr}, \text{and Ca}$) and $\text{Ce}_{1-x}\text{Bi}_x\text{VO}_4$ solid solutions, *J. Solid State Chem.* 158 (2001) 254.
387. K. Gaur, H.B. Lal, Electrical transport in light rare-earth vanadates, *J. Mater. Sci.*, 20 (1985) 3167.
388. R.F. Reidy, K.E. Swider, Determination of the cerium oxidation state in cerium vanadate, *J. Am. Ceram. Soc.* 78 (1995) 1121.
389. A. F. Sammells, R. L. Cook, J. H. White, J. J. Osborne, R. C. MacDuff, Rational selection of advanced solid electrolytes for intermediate temperature fuel cells, *Solid State Ionics* 52 (1992) 111.
390. H. Hayashi, H. Inaba, M. Matsuyama, N.G. Lan, M. Dokiya, H. Tagawa, Structural consideration on the ionic conductivity of perovskite-type oxides, *Solid State Ionics* 122 (1999) 1.
391. L.-P. Li, G.-S. Li, Y.-F. Xue, H. Inomata, Structure, luminescence, and transport properties of EuVO_4 , *J. Electrochem. Soc.* 148 (2001) J45.
392. S. Yamaguchi, K. Kobayashi, K. Abe, S. Yamazaki and Y. Iguchi, Electrical conductivity and thermoelectric power measurements of $\text{Y}_2\text{Ti}_2\text{O}_7$, *Solid State Ionics* 113 (1998) 393.
393. I.A. Leonidov, A.A. Fotiev, M.Ya. Khodos, Defect structure and nature of the conductivity of acceptor-doped $\text{Ca}_3(\text{VO}_4)_2$, *Inorg. Mater.* 23 (1987) 107.
394. I. S. Kulikov, "Thermodynamics of Oxides", Metallurgia, Moscow, 1986. (in Russian)

- 395.H. C. Nguyen, J. B. Goodenough, Magnetic and transport properties of CeVO₃, *J. Solid State Chem.* 119 (1995) 24.
- 396.J. Matta, D. Courcot, E. Abi-Aad, A. Aboukais, Identification and evaluation of the redox properties of the V species in the V-Ce-O catalysts used in the elimination of diesel soot particles, In: *Environment and Solar, Proc. 2000 Mediterranean Conf., IEEE, Piscataway, NJ, 2001*, p. 236.
- 397.A.L. Shaula, A.A. Yaremchenko, V.V. Kharton, D.I. Logvinovich, E.N. Naumovich, A.V. Kovalevsky, J.R. Frade, F.M.B. Marques, Oxygen permeability of LaGaO₃-based ceramic membranes, *J. Memb. Sci.* 221 (2003) 69.
- 398.D. Lybye, F.W. Poulsen, M. Mogensen, Conductivity of A- and B-site doped LaAlO₃, LaGaO₃, LaScO₃ and LaInO₃ perovskites, *Solid State Ionics* 128 (2000) 91.
- 399.T.L. Nguyen, M. Dokiya, S. Wang, H. Tagawa, T. Hashimoto, The effect of oxygen vacancy on the oxide ion mobility in LaAlO₃-based oxides, *Solid State Ionics* 130 (2000) 229.
- 400.V.V. Kharton, A.A. Yaremchenko, A.P. Viskup, G.C. Mather, E.N. Naumovich, F.M.B. Marques, Synthesis, physicochemical characterization and partial ionic conductivity of LaGa_{0.4}Mg_{0.2}M_{0.4}O_{3-δ} (M = Cr, Mn, Fe, Co), *J. Electroceram.* 7 (2001) 57.
- 401.A.A. Yaremchenko, A.L. Shaula, D.I. Logvinovich, V.V. Kharton, A.V. Kovalevsky, E.N. Naumovich, J.R. Frade and F.M.B. Marques, Oxygen ionic conductivity of perovskite-type La_{1-x}Sr_xGa_{1-y}Mg_yM_{0.20}O_{3-δ} (M = Fe, Co, Ni), *Mater. Chem. Phys.* 82 (2003) 684.
- 402.T. Ishigaki, S. Yamauchi, K. Kishio, J. Mizusaki, K. Fueki, Diffusion of oxide ion vacancies in perovskite-type oxides, *J. Solid State Chem.* 73 (1988) 179.
- 403.J.E. ten Elshof, H.J.M. Bouwmeester, H. Verweij, Oxygen transport through La_{1-x}Sr_xFeO_{3-δ} membranes. I. Permeation in air/He gradients, *Solid State Ionics* 81 (1995) 97.
- 404.J.Y. Park, G.M. Choi, Electrical conductivity of Sr and Mg doped LaAlO₃, *Solid State Ionics* 154-155 (2002) 535.
- 405.F.A. Kröger, "The Chemistry of Imperfect Crystals", North-Holland, Amsterdam, 1964.
- 406.J.B. Goodenough, Crystalline solid electrolytes II: Material design, In: P. Bruce (ed.), *Solid State Electrochemistry*, Cambridge University Press, Cambridge, 1995, p 43.
- 407.V.N. Tikhonovich, O.M. Zharkovskaya, E.N. Naumovich, I.A. Bashmakov, V.V. Kharton, A.A. Vecher, Oxygen nonstoichiometry of Sr(Co,Fe)O_{3-δ}-based perovskites. I. Coulometric titration of SrCo_{0.85}Fe_{0.10}Cr_{0.05}O_{3-δ} by the two-electrode technique, *Solid State Ionics* 160 (2003) 259.
- 408.A.A. Yaremchenko, M.V. Patrakev, V.V. Kharton, F.M.B. Marques, I.A. Leonidov, V.L. Kozhevnikov, Oxygen ionic and electronic conductivity of La_{0.3}Sr_{0.7}Fe(Al)O_{3-δ} perovskites, *Solid State Sciences* 6 (2004) 357.
- 409.J. Mizusaki, T. Sasamoto, W.R. Cannon, H.K. Bowen, Electronic conductivity, Seebeck coefficient, and defect structure of La_{1-x}Sr_xFeO₃ (x = 0.1, 0.25), *J. Am. Ceram. Soc.* 66 (1983) 247.
- 410.M.P. van Dijk, K.J. de Vries, A.J. Burggraaf, Oxygen ion and mixed conductivity in compounds with the fluorite and pyrochlore structure, *Solid State Ionics* 9-10 (1983) 913.
- 411.R.L. Withers, J.G. Thompson, P.J. Barlow, An electron, and X-ray powder, diffraction study of cubic,

- fluorite-related phases in various ZrO_2 - Ln_2O_3 systems, *J. Solid State Chem.* 94 (1991) 89.
- 412.M.P. van Dijk, F.C. Mijlhoff, A.J. Burggraaf, Pyrochlore microdomain formation in fluorite oxides, *J. Solid State Chem.* 62 (1986) 377.
- 413.E.L. Karyakina, E.I. Zoz, A.M. Gavrish, N.V. Gulko, Crystal-chemistry and heat physics of lanthanum zirconate and hafnate, *Zh. Neorg. Khim.* 23 (1978) 3202.
- 414.B.J. Wuensch, K.W. Eberman, C.Heremans, E.M. Ku, P.Onnerud, E.M.E. Yeo, S.M. Haile, J.K. Stalik, J.D. Jorgensen, Connection between oxygen-ion conductivity of pyrochlore fuel-cell materials and structural change with composition and temperature, *Solid State Ionics* 129 (2000) 111.
- 415.M.P. van Dijk, K.J. de Vries, A.J. Burggraaf, Electrical conductivity and defect chemistry of the system $(Tb_xGd_{1-x})_2Zr_2O_{7+y}$ ($0 \leq x \leq 1$; $0 \leq y < 0.25$), *Solid State Ionics* 16 (1985) 211.
- 416.J. Nell, B.J. Wood, S.E. Dorris, T.O. Mason, Jonker-type analysis of small polaron conductors, *J. Solid State Chem.* 82 (1989) 247.
- 417.H. Rickert, "Electrochemistry of Solids. An Introduction.", Springer-Verlag, Berlin-Heidelberg-NY, 1982.
- 418.S. Kramer, M. Spears, H.L. Tuller, Conduction in titanate pyrochlores: role of dopants, *Solid State Ionics* 72 (1994) 59.
- 419.U. Heider, L. Jörissen, R.A. Huggins, W. Witschel, Oxygen ion conductivity in doped $Gd_2Ti_2O_7$ with the pyrochlore structure. *Ionics*, 2 (1996) 7.
- 420.P. Huang, A. Petric, Superior oxygen ion conductivity of lanthanum gallate doped with strontium and magnesium, *J. Electrochem. Soc.* 143 (1996) 1644.
- 421.X. Guo, J. Fleig, J. Maier, Separation of electronic and ionic contributions to the grain boundary conductivity in acceptor-doped $SrTiO_3$. *J. Electrochem. Soc.* 148 (2001) J50-53.
- 422.G. Reinhardt, V. Baitinger, W. Göpel, Oxygen electrodes of zirconia electrolytes: Fundamentals and application to analysis of oxygen containing gases, *Ionics* 1 (1995) 504.
- 423.V.V. Kharton, J.C. Waerenborgh, D.P. Rojas, A.A. Yaremchenko, A.A. Valente, A.L. Shaula, M.V. Patrakeev, F.M.B. Marques, J. Rocha, Mössbauer spectra and catalytic behavior of perovskite-like $SrFe_{0.7}Al_{0.3}O_{3-\delta}$, *Catal. Lett.* 99 (2005) 249.
- 424.M. Mogensen, N.M. Sammes, G.A. Tompsett, Physical, chemical and electrochemical properties of pure and doped ceria, *Solid State Ionics* 129 (2000) 63.
- 425.J.C. Waerenborgh, F.M. Figueiredo, J.R. Frade, M.T. Colomer, J.R.Jurado, Fe^{4+} content and ordering of anion vacancies in partially reduced $AFe_xTi_{1-x}O_{3-y}$ ($A = Ca, Sr$; $x \leq 0.6$) perovskites. An ^{57}Fe Mössbauer spectroscopy study, *J. Phys.: Cond. Mater.* 13 (2001) 8171.
- 426.A. Lebon, P. Adler, C. Bernhard, A.V. Boris, A.V. Pimenov, A. Maljuk, C.T. Lin, C. Ulrich, B. Keimer, Magnetism, charge order, and giant magnetoresistance in $SrFeO_{3-\delta}$ single crystals, *Phys. Rev. Lett.* 92 (2004) 037202.
- 427.S.E. Dann, D.B. Currie, M.T. Weller, M.F. Thomas, A.D. Al-Rawwas, The effect of oxygen stoichiometry on phase relations and structure in the system $La_{1-x}Sr_xFeO_{3-\delta}$ ($0 \leq x \leq 1$, $0 \leq \delta \leq 0.5$), *J. Solid State Chem.* 109 (1994) 134.
- 428.P.D. Battle, T.C. Gibb, S. Nixon, A study of charge disproportionation in the nonstoichiometric

perovskite $\text{Sr}_2\text{LaFe}_3\text{O}_{8+y}$ by Mössbauer spectroscopy, *J. Solid State Chem.*, 77 (1988) 124.

Appendix 1. Properties of selected glass-ceramics

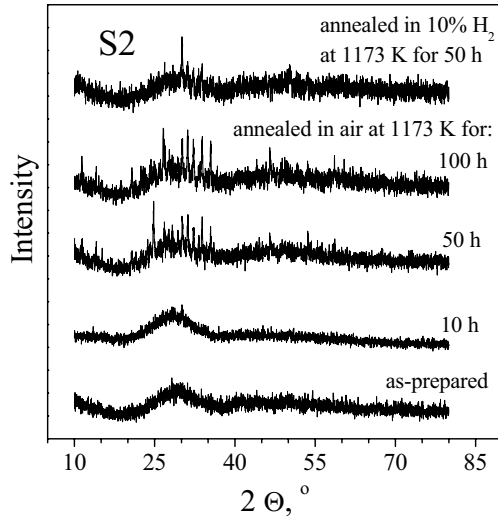


Fig.A1.1. XRD patterns showing the phase evolution of S2 sample treated after sintering.

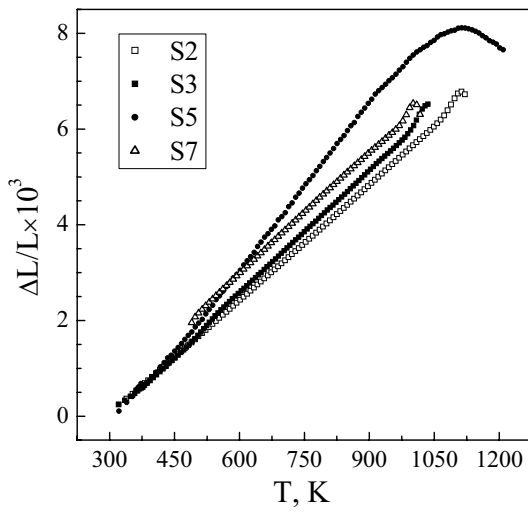


Fig.A1.2. Dilatometric curves of glass-ceramic materials in air (right).

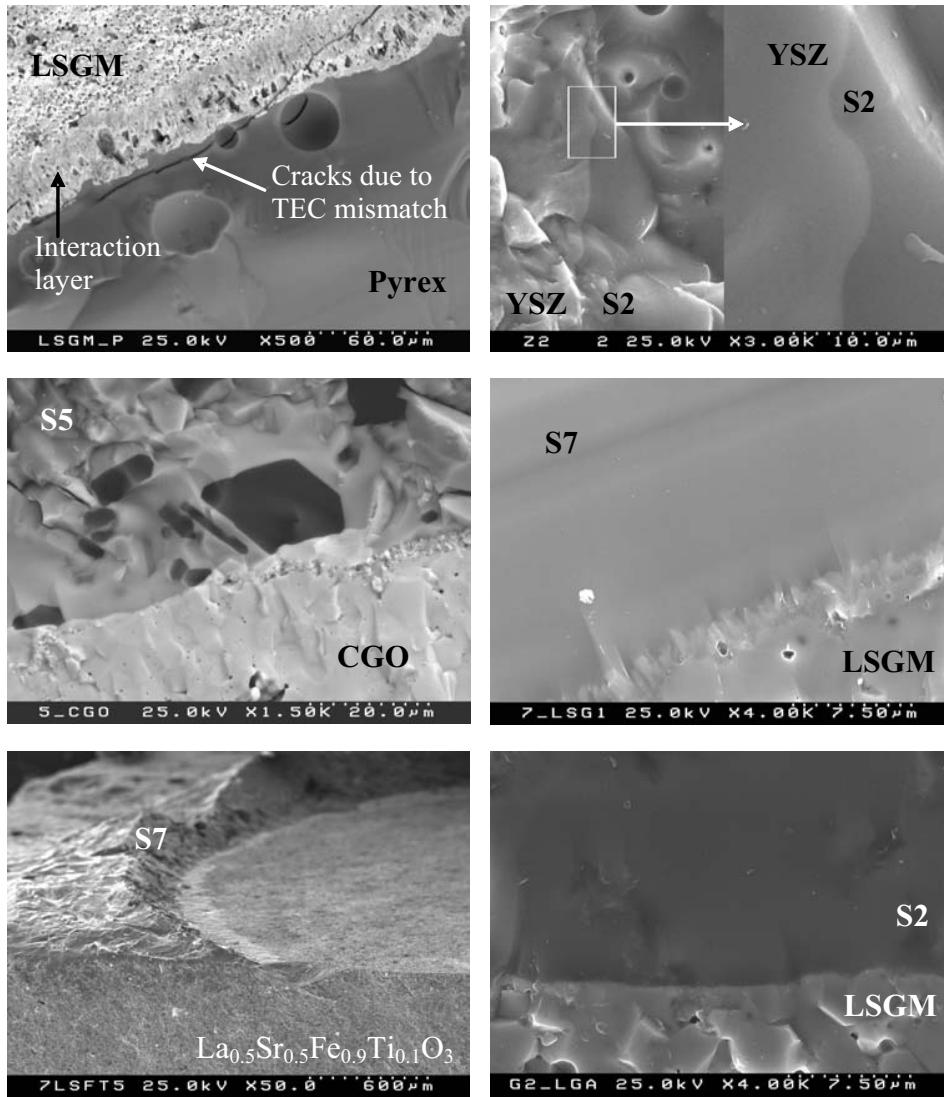


Fig.A1.3. SEM micrographs of glass-ceramic sealants in contact with various ceramics. Two bottom images are taken from the real cells fractured after measurements of oxygen permeability (left) and electrode properties (right).

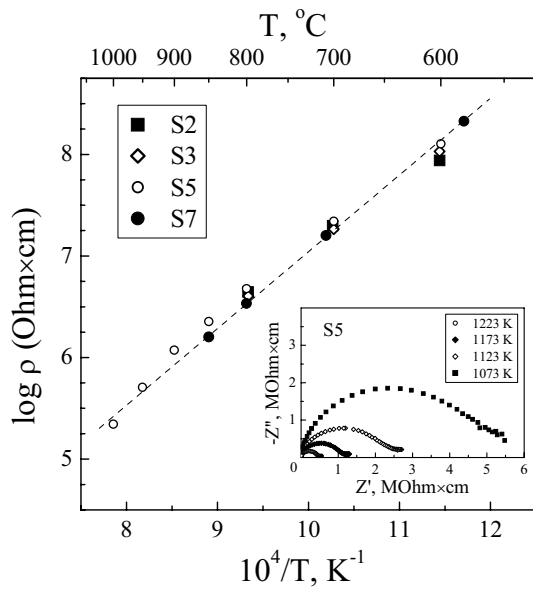


Fig.A1.4. Temperature dependencies of the total resistivity measured by the impedance spectroscopy. Inset shows the typical examples of impedance spectra.

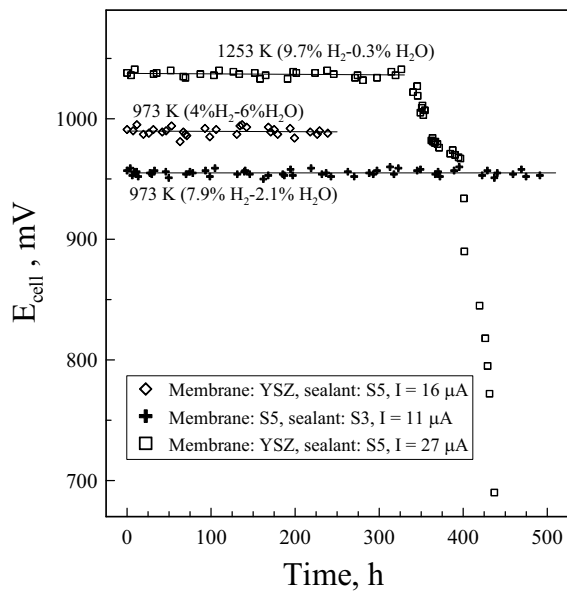


Fig.A1.5. Selected examples of time-dependencies of emf of the YSZ cells, similar to that shown in Fig.2.2 (left) but with controllable external atmosphere, at fixed gas composition in the chamber and current through the oxygen pump.

Appendix 2. Mössbauer spectroscopy results

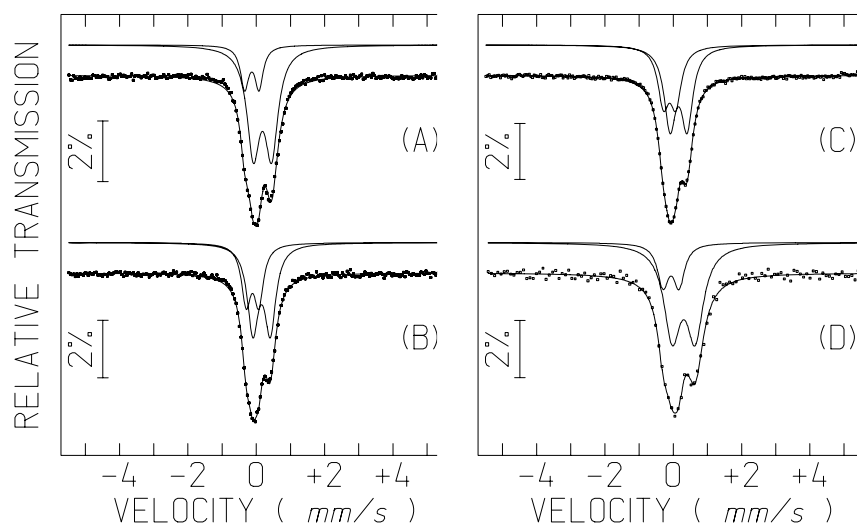


Fig.A2.1. Mössbauer spectra of $\text{La}_{0.90}\text{Sr}_{0.10}\text{Al}_{0.45}\text{Fe}_{0.40}\text{Mg}_{0.15}\text{O}_{3-\delta}$ perovskite after different treatments in air: quenched from 1223 K (A and D), quenched from 973 K (B), and slowly cooled down to room temperature (C). The spectra were collected at 295 K (A-C) and at 20 K (D). The lines plotted on the experimental points are the sum of two quadrupole doublets attributed to Fe^{3+} and Fe^{4+} , shown slightly shifted, for clarity.

The room-temperature Mössbauer spectra of $\text{La}_{0.90}\text{Sr}_{0.10}\text{Al}_{0.85-x}\text{Fe}_x\text{Mg}_{0.15}\text{O}_{3-\delta}$ ($x = 0.20-0.40$) (Figs.A2.1 and A2.2, A-C), similar to those of Fe^{3+} -containing $\text{SrFeO}_{3-\delta}$ or $\text{Sr}(\text{Fe}_{1-x}\text{Ti}_x)\text{O}_{3-\delta}$ [209,425,426], may be fitted with two doublets corresponding to the tri- and tetravalent iron cations. The final parameters are summarized in Table A2.1. The highest estimated IS values are low for hexacoordinated Fe^{3+} , particularly in the case of LaFeO_3 [427]. Most likely, the Fe^{3+} quadrupole doublet in $\text{La}_{0.90}\text{Sr}_{0.10}\text{Al}_{0.85-x}\text{Fe}_x\text{Mg}_{0.15}\text{O}_{3-\delta}$ is due to the sum of unresolved contributions of 6- and 5-coordinated Fe^{3+} , as found earlier for $\text{Sr}(\text{Fe}_{1-x}\text{Ti}_x)\text{O}_{3-\delta}$ [425]. The latter coordination gives rise to lower IS values, thus shifting the average IS estimated for the observed unresolved contributions down to values lower than those typical of hexacoordinated Fe^{3+} .

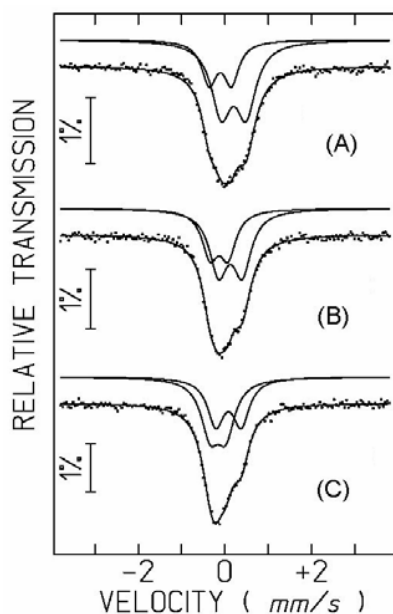


Fig.A2.1. Room temperature Mössbauer spectra of the $\text{La}_{0.90}\text{Sr}_{0.10}\text{Al}_{0.65}\text{Fe}_{0.20}\text{Mg}_{0.15}\text{O}_{3-\delta}$ samples after different heat treatments in air: quenched from 1223 K (A), quenched from 973 K (B), and slowly cooled down to room temperature (C). The lines plotted on the experimental points are the sum of two quadrupole doublets attributed to Fe^{3+} and Fe^{4+} , shown slightly shifted, for clarity.

One should note that the room-temperature spectra of $\text{La}_{0.33}\text{Sr}_{0.66}\text{FeO}_{3-\delta}$ [428] showed a single broad peak ascribed to an "averaged" oxidation state. This was attributed to fast electron transfer between Fe^{3+} and Fe^{4+} with respect to the ^{57}Fe Mössbauer spectroscopy observation time [428]. For oxidized $\text{La}_{0.9}\text{Sr}_{0.1}\text{FeO}_3$ with an orthorhombic structure, charge delocalization was detected as well [427]. In this case, however, the electron transfer is not as fast as in $\text{La}_{0.33}\text{Sr}_{0.66}\text{FeO}_{3-\delta}$, since the different oxidation states ("3+" and "5+" according to the notation of Ref.[427]) are observed as resolved magnetic sextets. The presence of magnetic sextets also indicates that $\text{La}_{0.9}\text{Sr}_{0.1}\text{FeO}_3$ is magnetically ordered at room temperature, in contrast to paramagnetic $\text{La}_{0.33}\text{Sr}_{0.66}\text{FeO}_{3-\delta}$. In the case of $\text{La}_{0.90}\text{Sr}_{0.10}\text{Al}_{0.85-x}\text{Fe}_x\text{Mg}_{0.15}\text{O}_{3-\delta}$ ($x \leq 0.40$), the delocalization seems hampered due to relatively high concentrations of Al^{3+} and Mg^{2+} in the B sites; as a result, the 3+ and 4+ states of iron cations can be clearly distinguished in the Mössbauer spectra.

Another necessary comment is that both $\text{La}_{0.9}\text{Sr}_{0.1}\text{FeO}_3$ and $\text{La}_{0.33}\text{Sr}_{0.66}\text{FeO}_{3-\delta}$ order magnetically above 80 K [427,428], while $\text{La}_{0.90}\text{Sr}_{0.10}\text{Al}_{0.45}\text{Fe}_{0.40}\text{Mg}_{0.15}\text{O}_{3-\delta}$ is paramagnetic down to 20 K. In the title material, the concentrations of Al^{3+} and Mg^{2+} cations, with no unpaired spin electrons, are high enough to prevent long-range magnetic ordering of iron ions. The Mössbauer spectra taken at 20 K consist therefore of paramagnetic peak doublets similar to those observed at 295 K; one example is presented in Fig.A2.1D. Decreasing the temperature leads to higher IS as expected from the second order Doppler shifts, whereas the relative areas are temperature-independent within the limits of experimental error (Table A2.1).

Table A2.1.

Parameters estimated from the Mössbauer spectra at 295 K of $\text{La}_{0.90}\text{Sr}_{0.10}\text{Al}_{0.85-x}\text{Fe}_x\text{Mg}_{0.15}\text{O}_{3-\delta}$
after quenching or slow cooling in air

x	T, K	Thermal pre-treatment	Fe^{3+}				Fe^{4+}				$\sigma(I)$, %
			IS, mm/s	QS, mm/s	W, mm/s	I, %	IS, mm/s	QS, mm/s	W, mm/s	I, %	
0.2	295	Quenching from 1223 K	0.30	0.57	0.55	69	0.00	0.51	0.42	31	7
		Quenching from 973 K	0.24	0.54	0.51	61	-0.02	0.41	0.45	39	4
		Slow cooling	0.20	0.58	0.46	45	0.00	0.36	0.51	55	4
0.4	295	Quenching from 1223 K	0.30	0.53	0.45	79	-0.02	0.42	0.30	21	1
		Quenching from 973 K	0.27	0.51	0.39	63	0.00	0.37	0.33	37	2
		Slow cooling	0.27	0.50	0.41	60	0.00	0.36	0.39	40	1
0.4	20	Quenching from 1223 K	0.42	0.67	0.59	77	0.04	0.47	0.39	23	1

Notes:

- IS, QS and W are the isomer shift relative to metallic α -Fe at 295 K, the quadrupole splitting and the full width at half maximum, respectively;
- I and $\sigma(I)$ are the relative area and its standard deviation, correspondingly;
- Estimated standard deviations for the other parameters are lower than 0.02 mm/s.

Appendix 3. List of publications containing major results of the thesis

Publications in SCI journals:

1. E.V. Tsipis, M.V. Patrakeev, V.V. Kharton, N.P. Vyshatko and J.R. Frade, Ionic and p-type electronic transport in zircon-type $Ce_{1-x}A_xVO_{4\pm\delta}$ ($A = Ca, Sr$), *Journal of Materials Chemistry*, 2002, vol. 12, pp. 3738-3745.
2. E.V. Tsipis, V.V. Kharton, N.P. Vyshatko, A.L. Shaula, M.V. Patrakeev and J.R. Frade, Mixed conductivity of zircon-type $Ce_{1-x}A_xVO_{4\pm\delta}$ ($A = Ca, Sr$), *Ionics*, 2003, vol. 9, pp.231-237.
3. V.V. Kharton, F.M.B. Marques, E.V. Tsipis, A.P. Viskup, M.V. Patrakeev, A.V. Harkavy, R. Samigullina and J.R. Frade, Mixed conductivity of gadolinium titanate-based pyrochlore ceramics: the grain boundary effects, *Ionics*, 2003, vol. 9, pp.122-126.
4. E.V. Tsipis, V.V. Kharton, N.P. Vyshatko, A.L. Shaula and J.R. Frade, Stability and oxygen ionic conductivity of zircon-type $Ce_{1-x}A_xVO_{4\pm\delta}$ ($A = Ca, Sr$), *Journal of Solid State Chemistry*, 2003, vol. 176, pp. 47-56.
5. V.V. Kharton, E.V. Tsipis, A.A. Yaremchenko, N.P. Vyshatko, A.L. Shaula, E.N. Naumovich and J.R. Frade, Oxygen ionic and electronic transport in $Gd_{2-x}Ca_xTi_2O_{7-\delta}$ pyrochlores, *Journal of Solid State Electrochemistry*, 2003, vol. 7, pp. 468-476.
6. E.V. Tsipis, A.V. Shlyakhtina, L.G. Shcherbakova, I.V. Kolbanev, V.V. Kharton, N.P. Vyshatko and J.R. Frade, Mechanically-activated synthesis and mixed conductivity of $TbMO_{4-\delta}$ ($M = Zr, Hf$) ceramics, *Journal of Electroceramics*, 2003, vol. 10, pp. 153-164.
7. V.V. Kharton, E.V. Tsipis, A.A. Yaremchenko and J.R. Frade, Surface-limited oxygen transport and electrode properties of $La_2Ni_{0.8}Cu_{0.2}O_{4+\delta}$, *Solid State Ionics*, 2004, vol. 166, pp. 327-337.
8. V.V. Kharton, A.A. Yaremchenko, E.V. Tsipis, A.A. Valente, M.V. Patrakeev, A.L. Shaula, J.R. Frade and J. Rocha, Characterization of mixed-conducting $La_2Ni_{0.9}Co_{0.1}O_{4+\delta}$ membranes for dry methane oxidation, *Applied Catalysis A: General*, 2004, vol. 261, pp. 25-35.
9. V.V. Kharton, F.M.B. Marques, E.V. Tsipis, A.P. Viskup, N.P. Vyshatko, M.V. Patrakeev, E.N. Naumovich and J.R. Frade, Interfacial effects in electrochemical cells for oxygen ionic conduction measurements. III. Transference numbers vs. grain-boundary resistivity, *Solid State Ionics*, 2004, vol. 168, pp. 137-151.
10. E.V. Tsipis, V.V. Kharton, I.A. Bashmakov, E.N. Naumovich and J.R. Frade, Cellulose-precursor synthesis of nanocrystalline $Ce_{0.8}Gd_{0.2}O_{2-\delta}$ for SOFC anodes, *Journal of Solid State Electrochemistry*, 2004, vol. 8, pp.674-680.
11. V.V. Kharton, E.V. Tsipis, I.P. Marozau, A.A. Yaremchenko, A.A. Valente, A.P. Viskup, J.R. Frade, E.N. Naumovich and J. Rocha, Transport and electrocatalytic properties of $La_{0.3}Sr_{0.7}Co_{0.8}Ga_{0.2}O_{3-\delta}$ membranes, *Journal of Solid State Electrochemistry*, 2005, vol. 9, pp.10-20.
12. E.V. Tsipis, V.V. Kharton and J.R. Frade, Mixed conducting components of solid oxide fuel cell anodes, *Journal of the European Ceramic Society*, 2005, vol. 25, pp.2623–2626.

13. E.V. Tsipis, V.V. Kharton, N.V. Vyshatko, J.R. Frade and F.M.B. Marques, Ion transport properties and Seebeck coefficient of Fe-doped La(Sr)Al(Mg)O_{3-δ}, *Solid State Sciences*, 2005, vol. 7, pp. 257-267.
14. E.V. Tsipis, V.V. Kharton, J.R. Frade and P. Núñez, High-temperature transport and electrochemical properties of YBaCo₄O_{7+δ}, *Journal of Solid State Electrochemistry*, 2005, vol. 9, pp. 547-557.
15. E.V. Tsipis, D.D. Khalyavin, S.V. Shiryaev, K.S. Redkina and P. Núñez, Electrical and magnetic properties of YBaCo₄O_{7+δ}, *Materials Chemistry & Physics*, 2005, vol. 92/1, pp.33-38.
16. J.R. Frade, V.V. Kharton, A.A. Yaremchenko and E.V. Tsipis, Applicability of emf measurements under external load resistance conditions for ion transport number determination, *Journal of Solid State Electrochemistry*, 2006, vol. 10, pp. 96-103.

Publications in proceedings of international conferences:

17. V.V. Kharton, A.A. Yaremchenko, E.V. Tsipis and J.R. Frade, Oxygen transport and electrochemical activity of La₂NiO₄-based cathode materials, *Proc. Int. Symp. "SOFC-VIII"*, Eds. S.C. Singhal and M. Dokiya (27 April - 2 May 2003, Paris, France), PV2003-07, The Electrochemical Society, Pennington, NJ, 2003, pp.561-570.
18. E.V. Tsipis, I.A. Bashmakov, V.V. Kharton, E.N. Naumovich and J.R. Frade, Cellulose-precursor synthesis of electrocatalytically active components of SOFCs and mixed-conducting membrane reactors, *Proc. NATO ARW "Fuel Cell Technologies: State and Perspectives"*, Eds. N. Sammes and O. Vasylyev (6-10 June 2004, Kyiv, Ukraine), Springer, 2005, pp. 223-229.
19. V.V. Kharton, E.V. Tsipis, A.P. Carvalho, A.V. Kovalevsky, E.N. Naumovich, F.M.B. Marques, J.R. Frade and A.L. Shaula, Glass-ceramic sealants for SOFC-based systems, *Proc. NATO ARW "Fuel Cell Technologies: State and Perspectives"*, Eds. N. Sammes and O. Vasylyev (6-10 June 2004, Kyiv, Ukraine), Springer, 2005, pp. 231-238.

List of symbols

A	electrochemically-active area near the TPB	cm^2
A_0	pre-exponential factor	$\text{S}\times\text{cm}^{-1}\times\text{K}$
a	unit cell parameter	nm or Å
a_i	activity	$\text{mol}\times\text{cm}^{-3}$
b	unit cell parameter	nm or Å
C	capacitance	F or $\text{F}\times\text{cm}^{-1}$ (specific)
c	unit cell parameter	nm
c_i	concentration	$\text{mol}\times\text{cm}^{-3}$ or mol/l (solution)
D	diffusion coefficient	$\text{cm}^2\times\text{s}^{-1}$
$D_{\text{O}_2-\text{B}}$	gas-phase binary (O_2 -B) diffusion coefficient	$\text{cm}^2\times\text{s}^{-1}$
$D_{\text{O}_2}^{\text{eff}}$	effective oxygen diffusion coefficient	$\text{cm}^2\times\text{s}^{-1}$
$D_{\text{O}_2}^{\text{K}}$	Knudsen diffusion coefficient of oxygen	$\text{cm}^2\times\text{s}^{-1}$
d	thickness	m
$d_{\text{exp,theor}}$	density	$\text{g}\times\text{cm}^{-3}$
E	cell voltage	V
E^0	open-circuit cell voltage	V
E_a	activation energy	$\text{J}\times\text{mol}^{-1}$
e	electron charge	1.6022×10^{-19} C
e^-	electron	
F	Faraday constant	96484.56 C $\times\text{mol}^{-1}$
f	gas flow rate	$\text{cm}^3\times\text{min}^{-1}$
ΔH	enthalpy	$\text{J}\times\text{mol}^{-1}$
ΔH_{298}^0	standard enthalpy	$\text{J}\times\text{mol}^{-1}$
h^+	electron-hole	
I	electrical current	A
IR	ohmic losses	V
IS	isomer shift	mm/s
i	current density	$\text{A}\times\text{cm}^{-2}$ or $\text{A}\times\text{cm}^{-1}$ (per unit TPB length)
I_0	exchange current	A
i_0	exchange current density	$\text{A}\times\text{cm}^{-2}$ or $\text{A}\times\text{cm}^{-1}$ (per unit TPB length)
I_{lim}	limiting current	A

j	flux density	$\text{mol}\times\text{s}^{-1}\times\text{cm}^{-2}$
j^0	exchange flux density	$\text{mol}\times\text{s}^{-1}\times\text{cm}^{-2}$
$J(\text{O}_2)$	specific oxygen permeability	$\text{mol}\times\text{s}^{-1}\times\text{cm}^{-1}$
K	equilibrium constant	-
K_A	Knudsen number	dimensionless
k	Boltzman constant	$1.3806\times 10^{-23} \text{ J}\times\text{K}^{-1}$
$k_{1,2,3}$	forward reaction constant	-
k'	backward reaction constant	-
L, l	length, thickness	m
M	molecular weight	$\text{g}\times\text{mol}^{-1}$
m	weight	g
N	total concentration of sites participating in the conduction process	$\text{mol}\times\text{cm}^{-3}$ or cm^{-3}
N^*	density of states	$\text{mol}\times\text{cm}^{-3}$ or cm^{-3}
N_A	Avogadro number	$6.022\times 10^{23} \text{ mol}^{-1}$
N_{fu}	number of formula units per unit cell	
n	electron concentration	$\text{mol}\times\text{cm}^{-3}$ or cm^{-3}
O_{ad}	oxygen ad-atom	
O_i''	oxygen interstitial	
P	porosity, power density	dimensionless, $\text{W}\times\text{cm}^{-2}$
p	electron-hole concentration, partial pressure	$\text{mol}\times\text{cm}^{-3}$ or cm^{-3}
$p(\text{O}_2)$	oxygen partial pressure	atm
Q^0	the transported heat of oxygen ions	J
QS	quadrupole splitting	mm/s
R	universal gas constant	$8.3144 \text{ J}\times\text{K}^{-1}\times\text{mol}^{-1}$
R_η	polarization resistance	$\text{Ohm}\times\text{cm}^2$
r	ion radius	nm
r_i	reaction rate	
S	surface area	cm^2
ΔS	entropy change	$\text{J}\times\text{mol}^{-1}\times\text{K}^{-1}$
s	active site	
T	absolute temperature	K
t	time	h
t_i	transference number	dimensionless
U	voltage	V

u	mobility	$\text{cm}^2 \times \text{V}^{-1} \times \text{s}^{-1}$
V	volume	cm^3, l
V_{uc}	unit cell volume	nm^3
V_{O}^{\bullet}	oxygen vacancy	
W	full width at half maximum	mm/s
x, y	mole fraction	dimensionless
Z	impedance	Ohm
z	number of electrons	
$[k]$	defect concentration	$\text{mol} \times \text{cm}^{-3}$ or cm^{-3}

Greek

α	Seebeck coefficient	$\text{V} \times \text{K}^{-1}$
$\bar{\alpha}$	average linear TEC	K^{-1}
β	charge transfer coefficient	dimensionless
δ	oxygen nonstoichiometry	-
ϕ	electrochemical potential	V
γ	number of electrons	
η	overpotential	V
φ	electrical potential of electrode	V
φ^0	equilibrium electrode potential	V
λ	wave length	nm
μ	chemical potential	$\text{J} \times \text{mol}^{-1}$
ν	frequency	cm^{-1}
Θ	angle	$^\circ$
θ	relative surface coverage	dimensionless
ρ	specific resistance	$\text{Ohm} \times \text{cm}$
ρ_s	sheet density	$\text{g} \times \text{cm}^{-2}$
σ	electrical conductivity	$\text{S} \times \text{cm}^{-1}$
σ^0	conductivity at unit $p(\text{O}_2)$	$\text{S} \times \text{cm}^{-1}$
τ	gas-phase tortuosity	dimensionless

Additional subscripts

ad	adsorbed
e	electronic
exp	experimental
i, k	denotation of the sort of species
n	n-type electronic
O, O ²⁻	oxygen ionic
O ₂	molecular oxygen
obs	observed
p	p-type electronic
sens	sensor
th, theor	theoretical
V	oxygen vacancy

List of abbreviations

<i>ac</i>	alternating current
CE	counter electrode
CGO	20 mol% gadolinia-doped ceria
CYO	yttria-doped ceria
<i>dc</i>	direct current
DTA	differential thermal analysis
EDS	energy-dispersive spectroscopy
EIS	electrochemical impedance spectroscopy
e.m.f.	electromotive force
emf	measurement technique based on the e.m.f. of the oxygen concentration cells
FE	faradaic efficiency
GE	gas/electrolyte interface
GM	gas/mixed conductor interface
GNP	glycine-nitrate process
ICP	inductively coupled plasma
IR	infrared
IT SOFC	intermediate-temperature solid oxide fuel cell
LSGM	(La,Sr)(Ga,Mg)O _{3-δ}
LSM	(La,Sr)MnO _{3-δ}
LSFC	(La,Sr)(Fe,Co)O _{3-δ}
MC	mixed conductor
ME	mixed conductor/electrolyte interface
Method 1	standard ceramic synthesis technique
Method 2	glycine-nitrate process
mol	mole
OP	oxygen permeability
RE	reference electrode
redox	reduction-oxidation
S	sealant
SAED	selected area electron diffraction
SEM	scanning electron microscopy
S.G.	space group
SOFC	solid oxide fuel cell

TEC	thermal expansion coefficient
TEM	transmission electron microscopy
TGA	thermogravimetric analysis
TPB	triple-phase boundary
vol	volume
WE	working electrode
wt	weight
XRD	X-ray diffraction
YSZ	yttria-stabilized zirconia

Index of Materials

Composition	Property	Page
$Ce_{1-x}Gd_xO_{2-\delta}$	ionic transport	8, 183, 191
	thermal expansion	12
	performance as anode component	68, 74, 212
$Ce_{1-x}A_xVO_{4+\delta}$ (A = Ca, Sr)		135, 191, 216
$Gd_{2-x}Ca_xTi_2O_{7-\delta}$	ionic transport	8, 181, 189
	thermal expansion	12, 179
	performance as anode component	69, 216
$La_2Ni_{1-x}M_xO_{4+\delta}$ (M = Co, Cu)	electrical conductivity	41, 57, 105
	ionic transport	58, 112
	thermal expansion	57, 103, 133
	electrode performance	58, 196, 203
$La_{0.9}Sr_{0.1}Al_{0.85-x}Mg_{0.15}Fe_xO_{3-\delta}$		154, 191, 216
$(La_{0.3}Sr_{0.7})_{1-y}Co_{1-x}M_xO_{3-\delta}$ (M = Al, Ga)	electrical conductivity	96
	ionic transport	106
	thermal expansion	94, 132
$La_{1-x}A_xCr_{1-y}M_yO_{3-\delta}$ (A = Ca, Sr; M = Mn, Fe, Co, Ni)		70, 74
$(La_{1-x}Sr_x)_{1-z}Ga_{1-y}Mg_yO_{3-\delta}$	ionic transport	8, 182
	thermal expansion	12
	electrolyte performance	195, 211
$(La_{1-x}Sr_x)_{1-y}MnO_{3-\delta}$		38, 41, 63, 74
$La_{1-x}Sr_xFe_{1-y}Co_yO_{3-\delta}$		41, 48, 63
$TbMO_{4-\delta}$ (M = Zr, Hf)		166, 191, 216
$YBaCo_{4-x}Fe_xO_{7+\delta}$	electrical conductivity	101
	ionic transport	109
	thermal expansion	98, 132
	electrode performance	199, 204
$Zr_{1-x}Y_xO_{2-\delta}$	ionic transport	7, 183, 191
	thermal expansion	12
	performance as anode component	36, 64, 74, 212